WIND LOADING STRUCTURES

SECOND EDITION

JOHN HOLMES

Wind Loading of Structures

Also available from Taylor & Francis

Structures
Jennings
Hb: ISBN 0–415–26842–7
Pb: ISBN 0–415–26843–5

Buckling of Thin Metal Shells
J.G.Teng et al.
Hb: ISBN 0–419–24190–6

Ductility of Seismic-Resistant Steel Structures
F.Mazzolani et al.
Hb: ISBN 0–419–22550–1

Moment-Resistant Connections of Steel Frames in Seismic Areas
F.Mazzolani
Hb: ISBN 0–415–23577–4

Dynamic Loading and Design of Structures
A.Kappos
Hb: ISBN 0–419–22930–2

Programming the Dynamic Analysis of Structures
P.Bhatt
Hb: ISBN 0–419–15610–0

Monitoring and Assessment of Structures
G.Armer
Hb: ISBN 0–419–23770–4

Wind Loading of Structures

Second Edition

John D.Holmes

Taylor & Francis
Taylor & Francis Group

LONDON AND NEW YORK

First published 2001
by Taylor & Francis

Second edition published 2007 by Taylor & Francis
2 Park Square, Milton Park, Abingdon, Oxon OX14 4RN

Simultaneously published in the USA and Canada
by Taylor & Francis
270 Madison Ave, New York, NY 10016, USA

Taylor & Francis is an imprint of the Taylor & Francis Group, an informa business

This edition published in the Taylor & Francis e-Library, 2007.

"To purchase your own copy of this or any of
Taylor & Francis or Routledge's collection of thousands of eBooks
please go to www.eBookstore.tandf.co.uk."

British Library Cataloguing in Publication Data
A catalogue record for this book is available from the British Library

Library of Congress Cataloging in Publication Data
Holmes, John D., 1942–
Wind loading of structures/John D.Holmes.—2nd ed.
p. cm.
Includes bibliographical references and index.
ISBN 0-415-40946-2 (hardback: alk. paper) 1. Wind-pressure.
2. Structural dynamics. 3. Buildings—Aerodynamics. I. Title.
TA654.5.H65 2007
624.1′75—dc22
2006014139

ISBN 0-203-96428-4 Master e-book ISBN

ISBN10: 0-415-40946-2 (hbk)
ISBN10: 0-203-96428-4 (ebk)
ISBN13: 978-0-415-40946-9 (hbk)
ISBN13: 978-0-203-96428-6 (ebk)

Table of contents

Preface to the second edition

More than 5 years have elapsed since the first edition of *Wind Loading of Structures* was published. In that time, the need for good design of structures against the effects of wind has become even more obvious, with the great increase in destructive wind storms that have affected many parts of the world. In particular, this was emphasized by the unprecedented two successive hurricane seasons of 2004 and 2005 on the southern coastline of the United States.

Although the original chapter topics of the first edition of the book have remained unchanged, there have been changes to nearly every chapter and appendix. The importance of strong winds generated by thunderstorms has become more recognized by wind engineering researchers in the last 5 years, and Chapters 1 and 3 have been expanded with new material on the structure of tornadoes and downbursts. Chapter 5 also includes a new section on the transient dynamic response to winds of this type. In Chapter 7, the laboratory simulation of tornadoes is discussed; although pioneer work in this area was carried out in the 1960s and 1970s, this was not included in the first edition. Chapter 7 has also been expanded with a new section on the simulation of internal pressures in a wind tunnel.

There are changes and additions to Chapters 8, 9, 11, 12 and 14, but none in Chapters 10 and 13. However, Chapter 15 on 'Wind loading codes and standards' has been completely re-written. This has been necessary because four out of the six major codes and standards reviewed in the first edition have been revised extensively during the last 5 years (twice in the case of ASCE-7!). However, clearly this chapter will become out of date again quite quickly.

Appendix D has also been greatly extended, with basic extreme wind information given for an additional 16 countries or regions. I would like to thank the many people who have provided me with additional information for that part of the book.

I would also like to thank the many people who have provided useful comments on the first edition of the book, the several University staff who have adopted the book for teaching post-graduate courses, Dr M.Matsui (Tokyo Polytechnic University) for providing Figure 11.6 and my daughters Lucy and Julia Holmes for the drafting of most of the new figures in the second edition, and assisting with the indexing. I am grateful for the efficient editing and typesetting carried out by Integra Software Services Pvt. Ltd. Finally, thanks are due to Taylor & Francis for supporting this book into a second edition, and acceding to most of my requests.

Preface to the first edition

The wind loading of structures has had significant research effort in many countries during the last 30–35 years. Several thousand research papers have been published in journals and conference proceedings in all aspects of the subject. In many countries, wind loading governs the design of many structures; yet, even there, a good knowledge and understanding of wind loading amongst practising engineers is not widespread, despite the wealth of material available. Why is this the case? There are probably several reasons. The multi-disciplinary nature of the subject—involving probability and statistics, meteorology, the fluid mechanics of bluff bodies and structural dynamics—undoubtedly is a deterrent to structural engineers whose expertise is in the analysis and design of structures under nominally static loads. The subject is usually not taught in University and College courses, except as final year undergraduate electives, or at post-graduate level, although exposure to wind loading codes of practice or standards often occurs in design courses. Like many subjects, the jargon used by specialists and researchers in wind loading can be a deterrent to many non-specialists.

This book has been written with the practising structural engineer in mind, based on many years of experience working with clients in this profession. I hope it may also find use in advanced University courses. Although there are several other books on the subject, in this one I have attempted to fill gaps in a number of areas:

- An overview of wind loading on structures of all types is given (not just buildings).
- The method of effective static wind load distributions is covered in some detail (mainly in Chapter 5). I have found this approach to fluctuating and dynamic wind loading to have good acceptance amongst structural engineers, raised on a diet of static load analysis.
- Internal pressures are discussed in some detail (Chapter 6).
- An attempt has been made (Appendix D) to give an overview of extreme and design wind speeds for the whole world. This is probably a first anywhere, but it is an important step, and one that needs to be expanded in the future, as design projects are now routinely carried out by structural engineers in countries other than their own. The need for such information will become more important in the future as the expansion in world trade (including engineering services) continues.

I have tried to minimize the amount of mathematics, and concentrate on the physical principles involved. In some chapters (e.g. Chapter 5), I have found it necessary to include a significant amount of mathematics, but, hopefully, not at the expense of the physical principles. These sections could be omitted in a first reading.

I have been influenced by the work of many outstanding researchers and colleagues in this field over a period of 30 years. They are too many to list but most of their names will be found in the reference lists attached to each chapter. However, a number of people have assisted with the production of this book: Professor K.C.S.Kwok for contributing

most of Section 15.9; Dr John Ginger, Michael Syme, Dr Ignatius Calderone and Dr Jannette Frandsen for reading parts of the manuscript; Heather Fordham, Paul Bowditch, Maryjeanne Watt and Harry Fricke for the drafting of figures; Shob Narayan for typing permission letters; and Elizabeth Gray for assisting with indexing. I am most grateful for their assistance. I would also like to thank the staff of E.F. and N.Spon for their patience in waiting for delivery of the manuscript.

I would be most happy to receive constructive comments and suggestions from readers.

John D.Holmes
Mentone, Australia

1
The nature of wind storms and wind-induced damage

1.1 Introduction

Wind loading competes with seismic loading as the dominant environmental loading for structures. They have produced roughly equal amounts of damage over a long time period, although large damaging earthquakes occur less often than severe wind storms. On almost every day of the year a severe wind storm is happening somewhere on the earth—although many storms are small and localized. In the tropical oceans, the most severe of all wind events—tropical cyclones (including hurricanes and typhoons)—are generated. When these storms make landfall on populated coastlines, their effects can be devastating.

In this introductory chapter, the meteorology of severe wind storms—*gales* produced by large extra-tropical depressions, *tropical cyclones* and *downbursts*, squall lines and *tornadoes* associated with thunderstorms—is explained, including the expected horizontal variation in wind speed during these events. The history of damaging wind events, particularly those of the last 30 years, is discussed, focussing on the lessons learnt from them by the structural engineering profession. The behaviour of flying debris, a major source of damage in severe wind storms, is outlined. Insurance aspects are discussed, including the recent development of loss models, based on historical data on the occurrences of large severe storms, the spatial characteristics for the wind speeds within them, and assumed relationships between building damage and wind speed.

1.2 Meteorological aspects

Wind is air movement relative to the earth, driven by several different forces, especially pressure differences in the atmosphere, which are themselves produced by differential solar heating of different parts of the earth's surface, and forces generated by the rotation of the earth. The differences in solar radiation between the poles and the equator produce temperature and pressure differences. These, together with the effects of the earth's rotation, set up large-scale circulation systems in the atmosphere, with both horizontal and vertical orientations. The result of these circulations is that the prevailing wind directions in the tropics and near the poles tend to be easterly. Westerly winds dominate in the temperate latitudes.

Local severe winds may also originate from local convective effects *(thunderstorms)* or from the uplift of air masses produced by mountain ranges *(downslope winds)*. Severe tropical cyclones, known in some parts of the world as *hurricanes* and *typhoons*, generate

extremely strong winds over some parts of the tropical oceans and coastal regions, in latitudes from 10° to about 30°, both north and south of the equator.

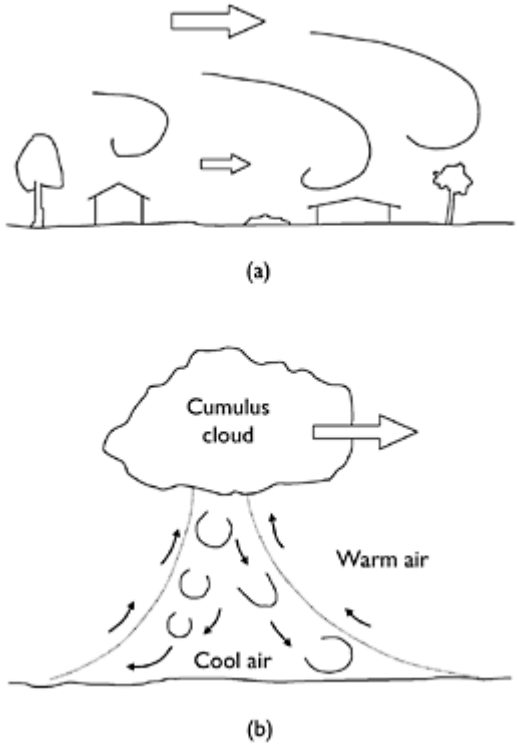

Figure 1.1 The generation of turbulence in boundary-layer winds and thunderstorm downdrafts.

For all types of severe storms, the wind is highly turbulent or gusty. The turbulence or gustiness is produced by eddies or vortices within the air flow, which are generated by frictional interaction at ground level or shearing action between air moving in opposite directions at altitude. These processes are illustrated in Figure 1.1 for downdrafts generated by thunderstorms and for larger storms such as gales or tropical cyclones, which are of the 'boundary-layer' type.

1.2.1 Pressure gradient

The two most important forces acting on the upper level air in the 'free atmosphere', i.e. above the frictional effects of the earth's boundary layer, are the pressure gradient force and the Coriolis force.

It is shown in elementary texts on fluid mechanics that, at a point in a fluid in which there is a pressure gradient, $\partial p/\partial x$, in a given direction, x, in a Cartesian coordinate system, there is a resulting force per unit mass given by Equation (1.1):

$$\text{Pressure gradient force per unit mass} = -\left(\frac{1}{\rho_a}\right)\frac{\partial p}{\partial x} \tag{1.1}$$

where ρ_a is the density of air.

This force acts from a high-pressure region to a low-pressure region.

1.2.2 Coriolis force

The *Coriolis* force is an apparent force due to the rotation of the earth. It acts to the right of the direction of motion in the northern hemisphere and to the left of the velocity vector in the case of the southern hemisphere; at the equator, the Coriolis force is zero. Figure 1.2 gives a simple explanation of the Coriolis force by observing the motion of a particle of air northwards from the South Pole.

Consider a parcel of air moving horizontally away from the South Pole, *P*, with a velocity *U*, in the direction of point *A* (Figure 1.2, left). As the earth is rotating clockwise with angular velocity, Ω, the point originally at *A* will have moved to *B*, and a point originally at *A′* will have moved to *A*, as the air parcel arrives. *Relative to the earth's surface*, the particle will have appeared to follow the path *PA′*, i.e. to have undergone a continuous deflection to the left. At the North Pole, the deflection is to the right. These deflections can be associated with an apparent acceleration acting at right angles to the velocity of the parcel—the Coriolis acceleration.

Consider a small time interval, δt (Figure 1.2, right); AA' is then small compared with PA. In this case,

$$AA' = \Omega U(\delta t)^2 \tag{1.2}$$

Let the Coriolis acceleration be denoted by a. As AA' is the distance travelled under this acceleration, it can also be expressed by:

$$AA' = (1/2)a(\delta t)^2 \tag{1.3}$$

Equating the two expressions for AA', Equations (1.2) and (1.3),

$$a = 2U\Omega \tag{1.4}$$

This gives the Coriolis acceleration, or force per unit mass, at the poles.

At other points on the earth's surface, the angular velocity is reduced to $\Omega \sin \lambda$, where λ is the latitude. Then the Coriolis acceleration is equal to $2U\Omega \sin \lambda$. The term $2\Omega \sin \lambda$ is a constant for a given latitude and is called the 'Coriolis parameter', often denoted by the symbol, *f*. The Coriolis acceleration is then equal to *fU*.

Thus, the Coriolis force is an apparent, or effective, force acting to the right of the direction of air motion in the northern hemisphere and to the left of the air motion in the southern hemisphere. At the equator, the Coriolis force is zero, and in the equatorial region, within about 5° of the equator, is negligible in magnitude. The latter explains why tropical cyclones (Section 1.3.2), or other cyclonic systems, will not form in the equatorial regions.

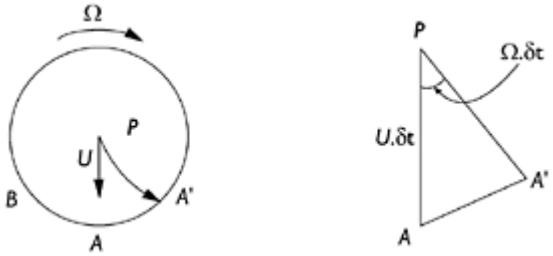

Figure 1.2 The apparent (Coriolis) force due to the earth's rotation (southern hemisphere).

1.2.3 Geostrophic wind

Steady flow under equal and opposite values of the *pressure gradient* and the *Coriolis* force is called 'balanced geostrophic flow'. Equating the pressure gradient force per unit mass from Equation (1.1) and the Coriolis force per unit mass given by *fU*, we obtain:

$$U = -\left(\frac{1}{\rho_a f}\right)\frac{\partial p}{\partial x} \tag{1.5}$$

This is the equation for the *geostrophic wind speed*, which is proportional to the magnitude of the pressure gradient *(∂p/∂x)*.

The directions of the pressure gradient and Coriolis forces and of the flow velocity are shown in Figure 1.3, for both northern and southern hemispheres. It may be seen that the flow direction is parallel to the isobars (lines of constant pressure) in both hemispheres. In the northern hemisphere, the high pressure is to the right of an observer facing the flow direction; in the southern hemisphere, the high pressure is on the left. This results in anti-clockwise rotation of winds around a low-pressure centre in the northern hemisphere and

a clockwise rotation in the southern hemisphere. In both hemispheres, rotation about a low-pressure centre (which usually produces strong winds) is known as a 'cyclone' to meteorologists. Conversely, rotation about a high-pressure centre is known as an 'anti-cyclone'.

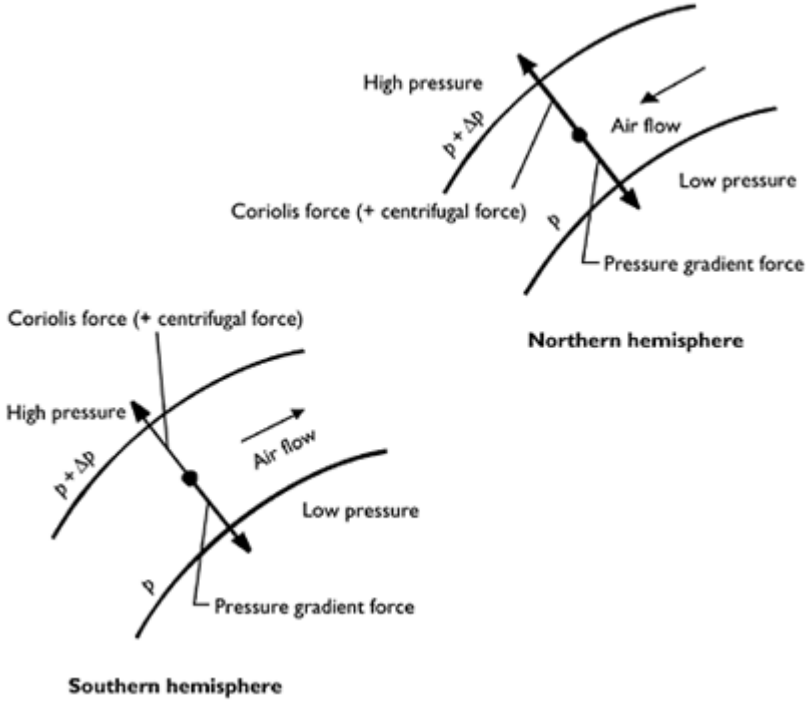

Figure 1.3 Balanced geostrophic flow in northern and southern hemispheres.

1.2.4 Gradient wind

If the isobars have significant curvature (as for example near the centre of a tropical cyclone), then the *centrifugal* force acting on the air particles cannot be neglected. The value of the centrifugal force per unit mass is (U^2/r), where U is the resultant wind velocity and r the radius of curvature of the isobars.

The direction of the force is away from the centre of curvature of the isobars. If the path of the air is around a high-pressure centre (anti-cyclone), the centrifugal force acts in the same direction as the pressure gradient force and in the opposite direction to the Coriolis force. For flow around a low-pressure centre (cyclone), the centrifugal force acts in the same direction as the Coriolis force and opposite to the pressure gradient force.

The equation of motion for a unit mass of air moving at a constant velocity, *U*, is then Equation (1.6) for an anti-cyclone and Equation (1.7) for a cyclone:

$$\frac{U^2}{r} - |f|\,U + \frac{1}{\rho_a}\left|\frac{\partial p}{\partial r}\right| = 0 \tag{1.6}$$

$$\frac{U^2}{r} + |f|\,U - \frac{1}{\rho_a}\left|\frac{\partial p}{\partial r}\right| = 0 \tag{1.7}$$

Equations (1.6) and (1.7) apply to both hemispheres. Note that the pressure gradient *(∂p/∂r)* is negative in an anti-cyclone and *f* is negative in the southern hemisphere. These equations are quadratic equations for the *gradient wind speed*, *U*. In each case, there are two theoretical solutions, but if the pressure gradient is zero, then *U* must be zero, so that the solutions become:

$$U = \frac{|f|\,r}{2} - \sqrt{\frac{f^2 r^2}{4} - \frac{r}{\rho_a}\left|\frac{\partial p}{\partial r}\right|} \tag{1.8}$$

for an anti-cyclone and

$$U = -\frac{|f|\,r}{2} + \sqrt{\frac{f^2 r^2}{4} + \frac{r}{\rho_a}\left|\frac{\partial p}{\partial r}\right|} \tag{1.9}$$

for a cyclone.

Examining Equation (1.8), it can be seen that a maximum value of *U* occurs when the term under the square root sign is zero. This value is ($|f|r/2$), which occurs when $|\partial p/\partial r|$ is equal to $\rho_a f^2 r/4$. Thus, in a anti-cyclone, there is an upper limit to the gradient wind; *anti-cyclones are normally associated with low wind speeds*.

Now considering Equation (1.9), it is clear that the term under the square root sign is always positive. The wind speed in a cyclone is therefore only limited by the pressure gradient; *cyclones are therefore associated with strong winds*.

1.2.5 Frictional effects

As the earth's surface is approached, *frictional* forces, transmitted through shear between layers of air in the atmospheric boundary layer, gradually play a larger role. This force acts in a direction opposite to that of the flow direction, which in order to achieve a vector balance is now not parallel to the isobars, but directed towards the low-pressure region. Figure 1.4 shows the new balance of forces in the boundary layer.

Thus, as the ground surface is approached from above, the wind vector gradually turns towards the low-pressure centre, as the height reduces. This effect is known as the *Ekman Spiral*. The total angular change between gradient height and the surface is about 30°. However, the angular change over the height of most tall structures is quite small.

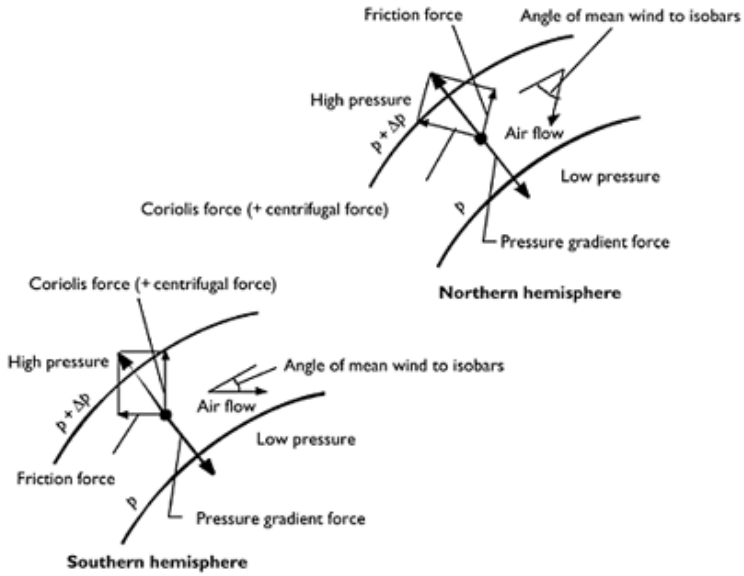

Figure 1.4 Force balance in the atmospheric boundary layer.

1.3 Types of wind storms

1.3.1 Gales from large depressions

In the mid-latitudes from about 40° to 60°, the strongest winds are gales generated by large and deep depressions or (extra-tropical) cyclones, of synoptic scale. They can also be significant contributors to winds in lower latitudes. Navigators, particularly in sailing ships, are familiar with the strong westerly winds of the ‘roaring forties’, of which those of the North Atlantic and at Cape Horn are perhaps the most notorious. As shown in Section 1.4.1, severe building damage has been caused by winter gales in north-west Europe.

These systems are usually large in horizontal dimension—they can extend for more than 1000 km, so can influence large areas of land during their passage—several countries in the case of Europe. They may take several days to pass, although winds may not blow continuously at their maximum intensity during this period. The winds tend to be quite turbulent near the ground, as the flow has adjusted to the frictional effects of the earth’s surface over hundreds of kilometres. The direction of the winds remains quite constant over many hours. These features are illustrated in a typical anemograph (wind speed and direction versus time) from this type of event reproduced in Figure 1.5.

1.3.2 Tropical cyclones

Tropical cyclones are intense cyclonic storms which occur over the tropical oceans, mainly in late summer and autumn. They are driven by the latent heat of the oceans and require a minimum sea temperature of about 26° C to sustain them; they rapidly degenerate when they move over land or into cooler waters. They will not form within about 5° of the equator and do not reach full strength until they reach at least 10° latitude. They are usually at full strength when they are located between 20° and 30° latitude, but can travel to higher latitudes if there are warm ocean currents to sustain them.

The strongest tropical cyclones have occurred in the Caribbean where they are known as *hurricanes*, in the South China Sea where they are called *typhoons*, and off the north-west coast of Australia. Areas of medium tropical cyclone activity are the eastern Pacific Ocean off the coast of Mexico, the southern Indian Ocean, the Bay of Bengal, the South Pacific, southern Japan, the Coral Sea (off eastern Australia) and the south-east Atlantic Ocean. Regions of lesser activity or weaker storms are the Arabian sea, the Gulf of Thailand and the north coast of Australia (including the Gulf of Carpentaria).

A developed tropical cyclone has a three-dimensional vortex structure, which is shown schematically in Figure 1.6. The horizontal dimensions of these storms are less than the extra-tropical cyclones or depressions, discussed earlier, but their effects can extend for several hundred kilometres. The circulation flows with a radial component towards the 'eye', outside of which is a region of intense thermal convection with air currents spiralling upwards. Inside the eye is a region of relative calm with slowly sinking air; the diameter of the eye can range between 8 and 80 km. Often clear skies have been observed in this region. The strongest winds occur just outside the eye wall.

Figure 1.7 gives an example of an anemograph measured at a height of 10 m above the ground for a tropical cyclone. This example shows a fortuitous situation when the eye of the storm passed nearly directly over the recording station, resulting in a period of about an hour of very low winds. The direction changed nearly 180° during the passage of the vortex over the measuring station.

Outside of the eye of a tropical cyclone, the wind speed at upper levels decays with the radial distance from the storm centre. The gradient wind equation, Equation (1.9), can be used to determine this wind speed:

$$U = -\frac{|f|\,r}{2} + \sqrt{\frac{f^2 r^2}{4} + \frac{r}{\rho_a}\left|\frac{\partial p}{\partial r}\right|} \tag{1.9}$$

where f is the Coriolis parameter (= $2\Omega \sin \lambda$), r the radius from the storm centre, ρ_a the density of air and p the atmospheric pressure.

To apply Equation (1.9), it is necessary to establish a suitable function for the pressure gradient. A commonly assumed expression is (Holland, 1980)

$$\frac{p - p_0}{p_a - p_0} = \exp\left(\frac{-A}{r^B}\right) \tag{1.10}$$

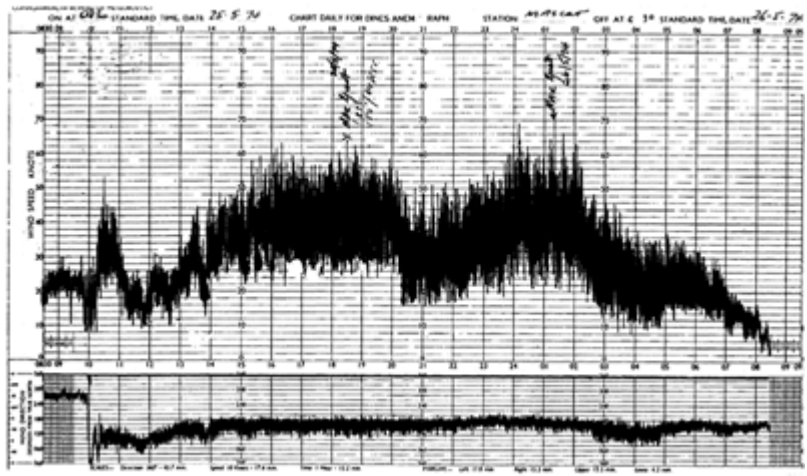

Figure 1.5 Anemograph for large extra-tropical depression.

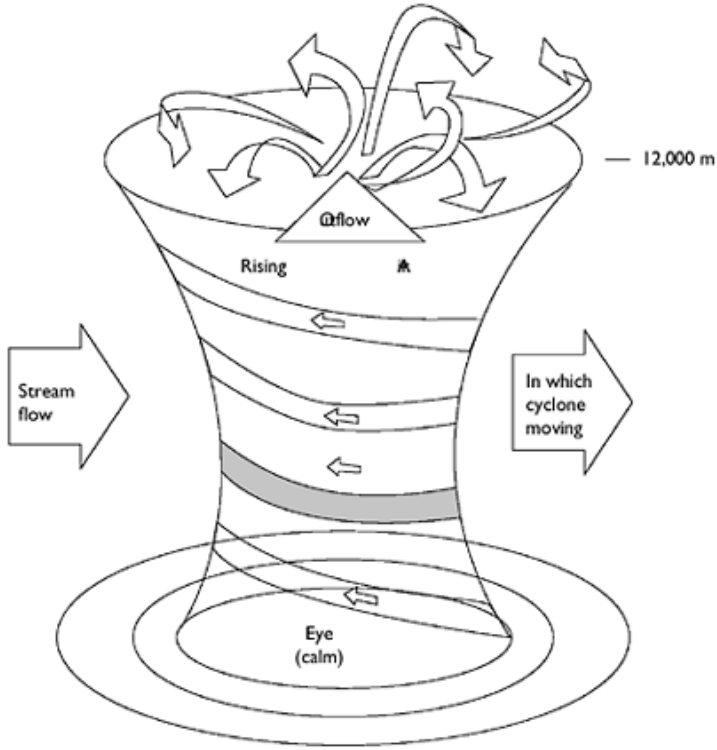

Figure 1.6 Three-dimensional structure for a developed tropical cyclone.

where p_0 is the central pressure of the tropical cyclone, p_n is the atmospheric pressure at the edge of the storm and A and B are scaling parameters.

The pressure difference $(p_n - p_0)$ can be written as Δp and is an indication of the strength of the storm.

Differentiating Equation (1.10) and substituting in Equation (1.9), we have:

$$U = -\frac{|f|\,r}{2} + \sqrt{\frac{f^2 r^2}{4} + \frac{\Delta p}{\rho_a}\frac{AB}{r^B}\exp\left(-\frac{A}{r^B}\right)} \qquad (1.11)$$

This is an equation for the mean wind field at upper levels in a tropical cyclone as a function of radius from the storm centre, r; the characteristic parameters, A and B; the pressure drop across the cyclone, Δp; and the Coriolis parameter, f.

Near the centre of a tropical cyclone, the Coriolis forces, i.e. the first two terms in Equations (1.9) and (1.11), are small, and it can be shown by differentiating the remaining term that the maximum value of U occurs when r equals $A^{1/B}$. Thus $A^{1/B}$ is, to a good approximation, the radius of maximum winds in the cyclone. The exponent B is found to be in the range 1.0–2.5 and to reduce with increasing central pressure, p_0 (Holland, 1980).

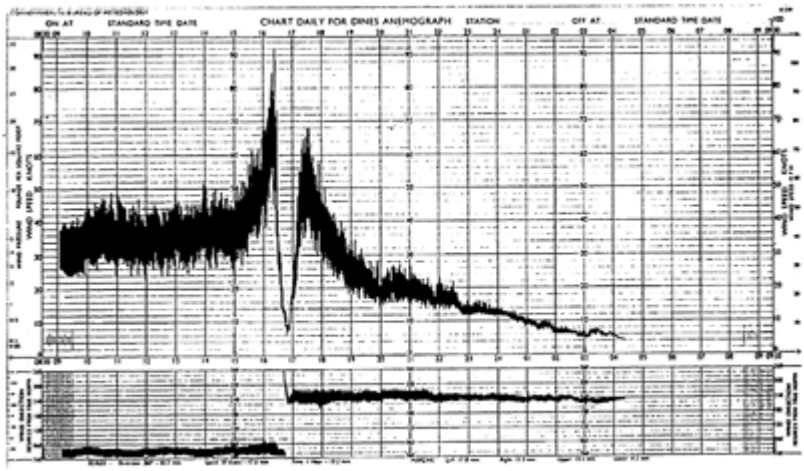

Figure 1.7 Anemograph at 10 m height for a tropical cyclone.

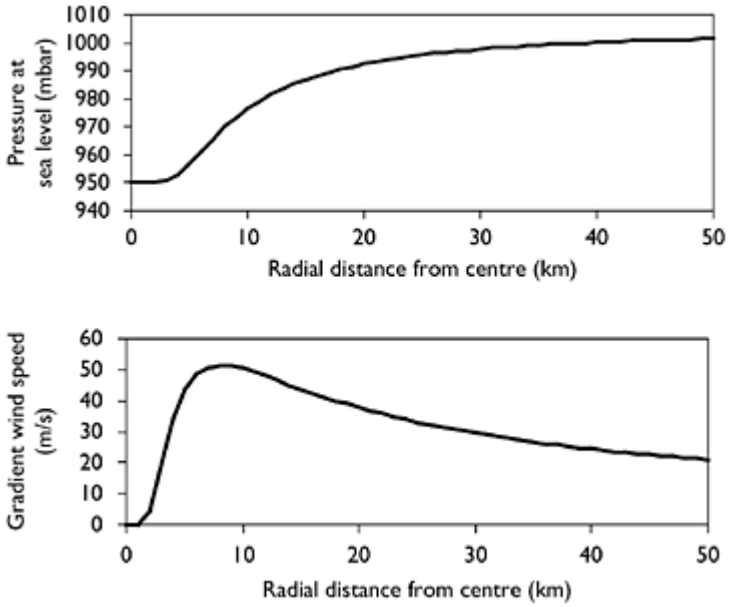

Figure 1.8 Pressure and gradient wind speeds for Cyclone 'Tracy', 1974. (a) Sea level pressure, (b) gradient wind speed.

Figure 1.8 shows the profiles of pressure and gradient wind speed with radial distance from the centre of the storm calculated from Equations (1.10) and (1.11) for Cyclone 'Tracy' which severely damaged Darwin, Australia, in 1974. The parameters A and B were taken as 23 and 1.5 (where r is measured in kilometres), respectively, following Holland (1980). The gradient wind speed in Figure 1.8(b) is approximately equal to the gust wind speed near ground level. The radius of maximum winds, in this case about 8 km, approximately coincides with the maximum pressure gradient.

The forward motion of the moving storm adds an additional vector component to the wind speed given by Equation (1.11), which gives the wind speed *relative* to the moving storm.

An intensity scale for North Atlantic and Caribbean hurricanes has been proposed by Saffir and Simpson. This is reproduced in Table 1.1.

Table 1.1 Saffir-Simpson intensity scale for hurricanes

Category	*Central pressure (mbar)*	*Wind speed range (3s gust, m/s)*
I	>980	42–54
II	965–979	55–62
III	945–964	63–74

IV	920–944	75–88
V	<920	>88

This scale is widely used for forecasting and emergency management purposes. However, the wind speed ranges given in Table 1.1 should be used with caution, as the estimated wind speeds in hurricanes are usually obtained from upper level aircraft readings. A similar, but not identical, scale is used in the Australian region.

1.3.3 Thunderstorms

Thunderstorms, both isolated storms and those associated with advancing cold fronts, are small disturbances in horizontal extent, compared with extra-tropical depressions and tropical cyclones, but they are capable of generating severe winds, through tornadoes and downbursts. They contribute significantly to the strongest gusts recorded in many countries, including the United States, Australia and South Africa. They are also the main source of high winds in the equatorial regions (within about 10° of the equator), although their strength is not high in these regions.

Thunderstorms also derive their energy from heat. Warm moist air is convected upwards to mix with the drier upper air. With evaporation, rapid cooling occurs and the air mass loses its buoyancy and starts to sink. Condensation then produces heavy rain or hail which falls, dragging cold air with it. A strong downdraft reaches the ground and produces a strong wind for a short period of time—perhaps 5–10 min. The strongest winds produced by this mechanism are known as *downbursts*, which are further subdivided into *microbursts* and *macrobursts*, depending on their size. The strongest winds produced by these events have a large component of wind speed due to the forward motion of the convection cell.

The conditions for generation of severe thunderstorms are

- water vapour in the atmosphere at low levels, i.e. high humidity;
- instability in the atmosphere, i.e. a negative temperature gradient with height greater than the adiabatic rate of the neutral atmosphere;
- a lifting mechanism that promotes the initial rapid convection—this may be provided by a mountain range or a cold front, for example.

1.3.4 Tornadoes

The strongest convection cells that often generate tornadoes are known as *supercells*. They are larger and last longer than ‘ordinary’ convection cells. The tornado, a vertical funnel-shaped vortex created in thunderclouds, is the most destructive of wind storms. Fortunately they are quite small in their horizontal extent—of the order of 100 m—but they can travel for quite long distances of up to 50 km before dissipating, producing a long narrow path of destruction. They occur mainly in large continental plains in countries such as the United States, Argentina, Russia and South Africa.

Periodically, atmospheric conditions in the central United States are such that severe outbreaks with many damaging tornadoes can occur in a short period. For example, they have occurred in April 1974 and May 2003. In the former case, 335 fatalities and

destruction of about 7500 dwellings resulted from the 'super-outbreak' of 148 tornadoes within a 2-day period (3–4 April 1974) with 13 states affected. In the latter case, a total of 393 tornadoes were reported in 19 states of the United States in a period of about a week. Of these, 15 resulted in 41 fatalities.

A detailed survey of tornadoes in South Africa has been given by Goliger *et al.* (1997). They occur in that country at the rate of about four per year, with a concentration in Gauteng Province in the north of the country, with an occurrence rate of 1×10^{-4} per square kilometre per year. This compares with a rate of about 2×10^{-4} per square kilometre per year in the mid-west of the United States.

Tornadoes are sometimes confused with downbursts (described in the following section); however, tornadoes can be identified by the appearance of the characteristic funnel vortex, a long narrow damage 'footprint' and evidence of varying wind directions.

The wind speed in a tornado can be related to the radial pressure gradient by neglecting the Coriolis term in the equation of motion. Hence, from either Equation (1.7) or Equation (1.9):

$$U=\sqrt{\frac{r}{\rho_a}\left|\frac{\partial p}{\partial r}\right|} \tag{1.12}$$

This is known as the *cyclostrophic* wind speed. Assuming that the pressure is constant along the edge of a tornado funnel (actually a line of condensed water vapour), Equation (1.12) has been used to estimate wind speeds in tornadoes.

Measurement of wind speeds in tornadoes is very difficult. Because of their small size, they seldom pass over a weather recording station. If one does, the anemometer is quite likely to be destroyed. For many years, photogrammetric analyses of movie film shot by eyewitnesses were used to obtain reasonable estimates (Fujita *et al.*, 1976; Golden, 1976). The method involves the tracking of clouds, dust and solid debris from the film frames and was first applied to the Dallas, Texas, tornado of 2 April 1957 by Hoecker (1960). This method is subject to a number of errors—e.g. distortion produced by the camera or projector lenses or tracked large objects not moving with the local wind speed. Also, the method is not able to detect velocities normal to the image plane.

However, the photogrammetric method has enabled several significant features of tornadoes such as 'suction vortices'—smaller vortex systems rotating around the main vortex core—and high vertical velocities. In the latter case, analysis of a tornado at Kankakee, Illinois, in 1963 (Golden, 1976) indicated vertical velocities of 55–60 m/s, at a height above the ground of less than 200 m.

Analyses of failures of engineered buildings in tornadoes have generally indicated lower maximum wind speeds in tornadoes than those obtained by photogrammetric or other methods (e.g. Mehta, 1976). After considering all the available evidence at that time, Golden (1976) estimated the maximum wind speeds in tornadoes to be no more than 110 m/s.

In recent years, portable Doppler radars have been successfully used in the United States for more accurate determination of wind speeds in tornadoes.

An intensity scale for tornadoes was originally proposed in 1971 (Fujita, 1971). Several F-scale classifications are associated with wind speed ranges, although, in practice, classifications are applied based on observed damage to buildings and other

structures. The original scaling has recently been criticized by engineers for several reasons, e.g. for failing to account for variations in the quality of construction and that it has not been based on a proper correlation of damage descriptions and wind speeds. The original and proposed (McDonald and Mehta, 2004) wind speed ranges for F0 to F5 categories are given in Table 1.2.

An engineering model of wind speed distributions in a tornado is discussed in Section 3.2.7.

Table 1.2 Fujita intensity scale for tornadoes

Category	*Original wind speed range (m/s)*	*Proposed wind speed range (m/s)*
F0	18–32	29–38
F1	33–50	39–49
F2	51–70	50–61
F3	71–92	62–74
F4	93–116	75–89
F5	117–142	90–105

1.3.5 Downbursts

Figure 1.9 shows an anemograph from a severe thunderstorm downburst, recorded at the Andrews Air Force Base near Washington, DC, in 1983, with a time scale in minutes. The short duration of the storm is quite apparent, and there is also a rapid change of wind direction during its passage across the measurement station. Such events typically produce a damage footprint 2–3 km wide and 10–15 km long.

The horizontal wind speed in a thunderstorm downburst with respect to the moving storm is similar to that in a jet of fluid impinging on a plain surface. It varies approximately linearly from the centre of impact to a radius where the wind speed is maximum, and then decays with increasing radius. The forward velocity of the moving storm can be a significant component of the total wind speed produced at ground level and must be added as a vector component to that produced by the jet.

1.3.6 Downslope winds

In certain regions such as those near the Rocky Mountains of the United States, Switzerland and the southern Alps of New Zealand, extreme winds can be caused by thermal amplification of synoptic winds on the leeward slopes of mountains. The regions affected are usually quite small, but are often identified as special regions, in wind loading codes and standards (see Appendix D).

1.4 Wind damage

Damage to buildings and other structures by wind storms has been a fact of life for human beings from the time they moved out of cave dwellings to the present day. Trial and error has played an important part in the development of construction techniques and roof shapes for small residential buildings, which have usually suffered the most damage during severe winds. In the past centuries, heavy masonry construction, as used for important community buildings such as churches and temples, was seen, by intuition, as the solution to resist wind forces (although somewhat less effective against seismic action). For other types of construction, wind storm damage was generally seen as an 'Act of God', as it is still viewed today by many insurance companies.

The nineteenth century was important as it saw the introduction of steel and reinforced concrete as construction materials and the beginnings of stress analysis methods for the design of structures. The latter was developed further in the twentieth century, especially

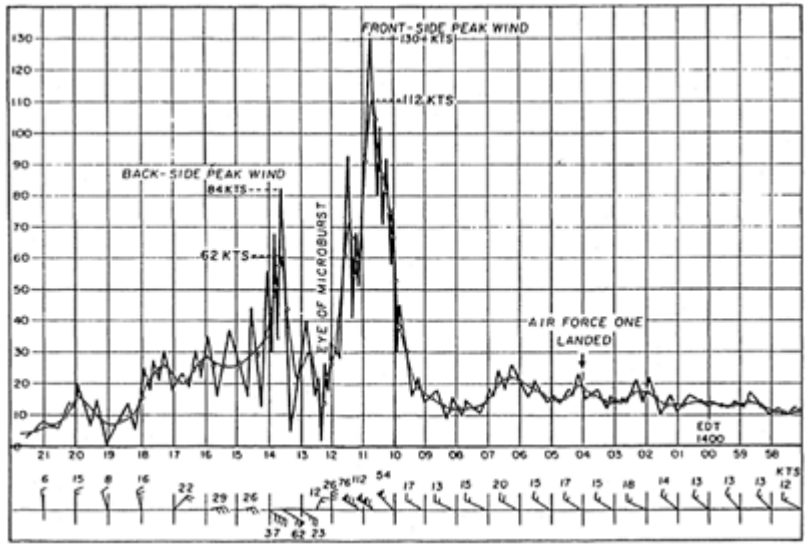

Figure 1.9 Anemograph for a severe downburst at Andrews Air Force Base, Maryland, 1983 (source: Fujita, 1985).

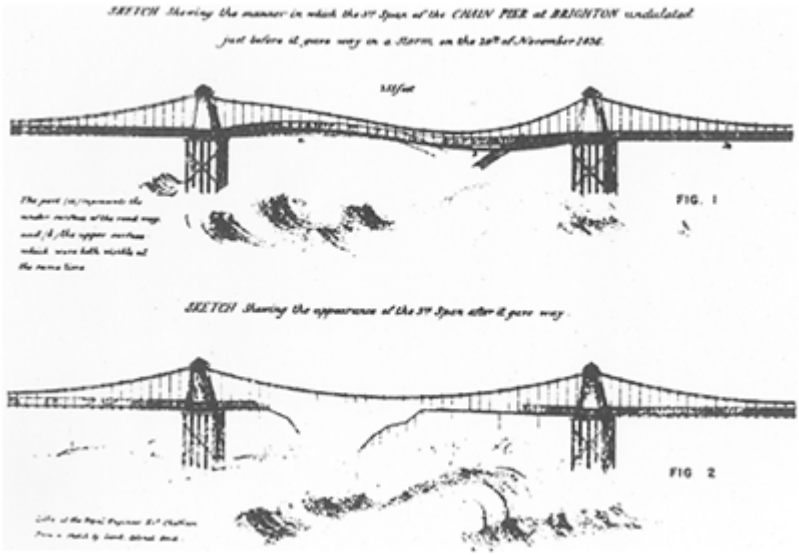

Figure 1.10 Failure of the Brighton Chain Pier, 1836.

in the second half, with the development of computer methods. During the last two centuries, major structural failures due to wind action have occurred periodically and provoked much interest in wind forces by engineers. Long-span bridges often produced the most spectacular of these failures, with the Brighton Chain Pier, England (1836) (Figure 1.10), the Tay Bridge, Scotland (1879), and Tacoma Narrows Bridge, Washington State (1940) being the most notable, with the dynamic action of wind playing a major role.

Other large structures have experienced failures as well—e.g. the collapse of the Ferrybridge Cooling Tower in the United Kingdom in 1965 (Figure 1.11) and the permanent deformation of the columns of the Great Plains Life Building in Lubbock, Texas, during a tornado (1970). These events were notable, not only as events in themselves, but also for the part they played as a stimulus to the development of research into wind loading in the respective countries. Another type of structure which has proved to be dynamically sensitive to wind is the guyed mast; it has also suffered a high failure rate—in one 10-year period (from the mid-1980s to the mid-1990s) there were 83 failures of this type of structure worldwide. In many cases of mast failures, a combination of wind and ice action was involved.

Some major wind storms, which have caused large-scale damage to residential buildings as well as some engineered structures, are also important for the part they have played in promoting research and understanding of wind loads on structures. The Yorkshire (United Kingdom) storms of 1962, Cyclone ‘Tracy’ in Darwin, Australia, in 1974 and Hurricane ‘Andrew’ in Florida, United States, in 1992 can be mentioned as seminal events of this type. However, these extreme events occur intermittently, and it is

unfortunate that the collective human memory after them is only about 10 years, and often old lessons have to be relearned by a new generation. However, an encouraging sign is the recent interest of some major insurance and re-insurance groups in natural hazards, in the estimation of the potential financial losses and the beginnings of a realization that any structure can be made wind-resistant, with appropriate knowledge of the forces involved and suitable design approaches.

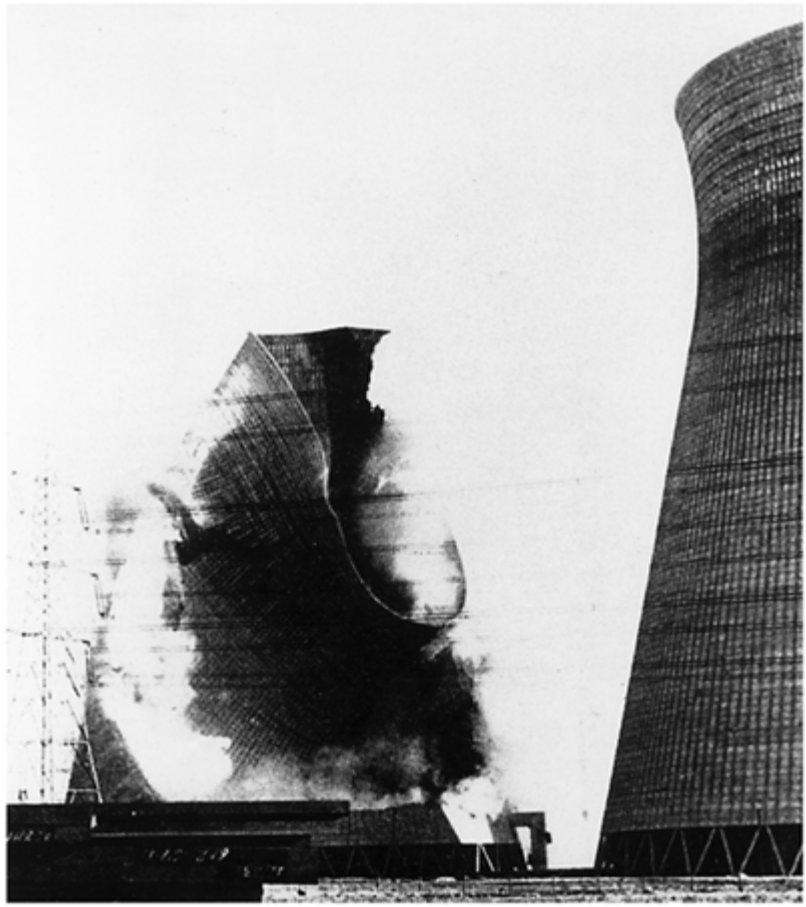

Figure 1.11 Ferrybridge Cooling Tower failures, 1965.

1.4.1 Recent history of wind damage

Figure 1.12 shows the annual insured losses in billions of US$ from all major natural disasters, from 1970 to 2005. Wind storms account for about 70% of the total insured losses. Bearing in mind that property insurance is much less common in the less-developed economies, Figure 1.12 does not show the total property damage from natural

events and, in fact, is biased towards losses in Europe and North America. However, the graph does show that the level of insured losses from natural disasters increased dramatically after about 1987. The major contributor to the increase was wind storms, especially tropical cyclones such as hurricanes 'Hugo' (1989), 'Andrew' (1992), 'Charley' (2004), 'Ivan' (2004) and 'Katrina' (2005) in the United States and winter gales in Europe in 1987, 1990 and 1999.

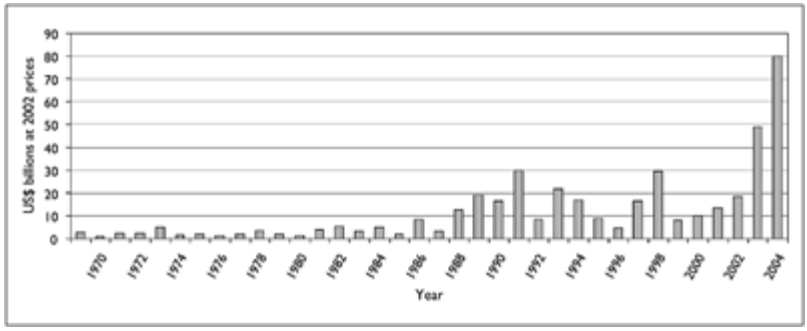

Figure 1.12 World insurance losses from natural disaters 1970–2004 (source: Swiss Reinsurance Company).

Table 1.3 Some disastrous wind storms of the last 30 years

Year	*Name*	*Country or region*	*Approximate economic losses (US$ million)*	*Lives lost*
1974	Cyclone 'Tracy'	Australia	500	52
1987	Gales	W. Europe	3700	17
1989	Hurricane 'Hugo'	Caribbean, United States	9000	61
1990	Gales	W. Europe	15,000	230
1992	Hurricane 'Andrew'	United States	30,000	44
1999	Gales	France	10,000	140
2003	Typhoon 'Maemi'	Japan, Korea	6000	131
2004	Hurricane 'Ivan'	Caribbean, United States	11,000	124

Source of data apart from Cyclone 'Tracy': Munich Reinsurance and Swiss Reinsurance.

In 2005, there was an estimated US$80 billion of insured losses from natural disasters, of which the majority originated from hurricanes and typhoons.

Some notable wind storms and the losses resulting from them are listed in Table 1.3. Cyclone 'Tracy' and Hurricane 'Andrew' have already been mentioned, but in fact all the events listed in Table 1.3 have had a major influence on the insurance industry and structural engineering profession.

Table 1.3 does not include tornadoes. However, the aggregate damage from multiple events can be substantial. For example, in the 'super-outbreak' of 3–4 April 1974, the total damage in the state of Ohio alone was estimated to be US$100 million.

1.5 Wind-generated debris

As well as damage to buildings produced by direct wind forces—either overloads caused by overstressing under peak loads or fatigue damage under fluctuating loads of a lower level—a major cause of damage in severe wind storms is flying debris. Penetration of the building envelope by flying missiles has a number of undesirable results: high internal pressures threatening the building structure, wind and rain penetration of the inside of the building, the generation of additional flying debris, and the possibility of flying missiles inside the building endangering the occupants.

The area of a building most vulnerable to impact by missiles is the windward wall region, although impacts could also occur on the roof and side walls. As the air approaches the windward wall its horizontal velocity reduces rapidly. Heavier objects in the flow with higher inertia will probably continue with their velocity little changed until they impact on the wall. Lighter and smaller objects may lose velocity in this region or even be swept around the building with the flow if they are not directed at the stagnation point (see Chapter 4).

1.5.1 Threshold of flight

Wills *et al.* (1998) carried out an analysis of debris flight conditions and the resulting building damage in severe winds. They considered 'compact' objects, sheet objects and rods and poles (Figure 1.13) and established relationships between the body dimensions and the wind speed, U_f, at which flight occurs and the objects become missiles. For each of the three categories, these relationships are

$$\ell = \frac{\frac{1}{2}\rho_a U_f^2 C_F}{I\rho_m g} \tag{1.13}$$

$$t = \frac{\frac{1}{2}\rho_a U_f^2 C_F}{I\rho_m g} \tag{1.14}$$

$$d = \frac{\frac{2}{\pi}\rho_a U_f^2 C_F}{I\rho_m g} \tag{1.15}$$

where ℓ is a characteristic dimension for 'compact' objects, t the thickness of sheet objects, d the effective diameter of rod-type objects, ρ_a the density of air, ρ_m the density of the object material, C_F an aerodynamic force coefficient (see Section 4.2.2), U_f the wind speed at which flight occurs, I a fixing strength integrity parameter, i.e. the value of force required to dislodge the objects expressed as a multiple of their weight (for objects resting on the ground $I \cong 1$), and g the gravitational constant.

Equations (1.13), (1.14) and (1.15) illustrate the important point that the larger the value of the characteristic dimension, ℓ, t or d, the higher the wind speed at which flight occurs. These equations also show that the higher the value of the density, ρ_m, the higher the wind speed for lift off. Thus as the wind speed in a cyclone builds up, the smaller,

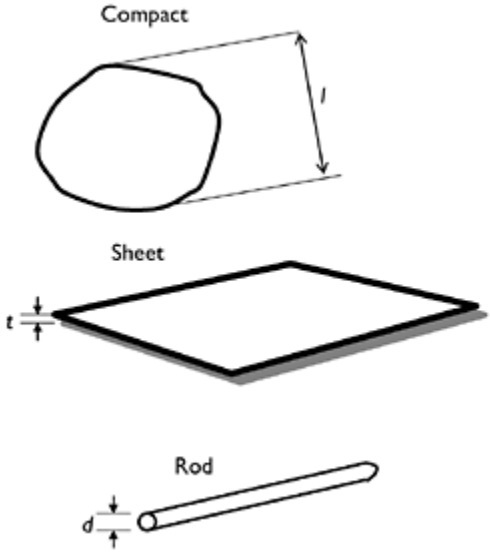

Figure 1.13 Three types of flying debris (after Wills *et al.,* 1998).

lighter objects—e.g. gravel, small loose objects in gardens and backyards—'fly' first. At higher wind speeds appurtenances on buildings are dislodged as the wind forces exceed their fixing resistance, and they also commence flight. At even higher wind speeds, substantial pieces of building structure such as roof sheeting and purlins may be removed and become airborne.

As examples of the application of Equation (1.13), Wills *et al.* (1998) considered wooden compact objects (ρ_m=500 kg/m^3) and stone objects (ρ_m=2700 kg/m^3). Assuming C_F=1 and I=1, Equation (1.12) gives ℓ equal to 110 mm for the wooden missile, but only 20 mm for the stone missile, for a lift-off speed of 30 m/s.

For sheet objects, Equation (1.14) shows that the wind speed for flight depends on the thickness of the sheet, but not on the length and width. Wills *et al.* expressed Equation (1.14) in a slightly different form:

$$\rho_m t = \frac{\frac{1}{2}\rho_a U_f^2 C_F}{lg} \tag{1.16}$$

The left-hand side of Equation (1.16) is the mass per unit area of the sheet. This indicates the wind speed for flight for a loose object depends essentially on its mass per unit area. Thus, a galvanized iron sheet of 1 mm thickness with mass per unit area of 7.5 kg/m^2 will fly at about 20 m/s (C_F=0.3).

2 For 'rod'-like objects, which include timber members of rectangular cross-section, a similar formula to Equation (1.16) can be derived from Equation (1.15), with the *'t'* replaced by *'d'*, the equivalent rod diameter. Using this Wills *et al.* calculated that a timber rod of 10 mm diameter will fly at about 11 m/s, and a 100 mm by 50 mm timber member, with an equivalent diameter of 80 mm, will fly at about 32 m/s, assuming C_F is equal to 1.0.

1.5.2 Trajectories of compact objects

A missile, once airborne, will continue to accelerate until its flight speed approaches the wind speed or until its flight is terminated by impact with the ground or with an object such as a building. The trajectories of compact objects are produced by drag forces (Section 4.2.2), acting in the direction of the relative wind with respect to the body.

Consider first the aerodynamic force on a compact object (such as a sphere) in a horizontal wind of speed, *U*. Neglecting the vertical air resistance initially, the aerodynamic force can be expressed as:

$$\text{Accelerating force} = \frac{1}{2}\rho_a (U - v_m)^2 C_D A$$

where v_m is the horizontal velocity of the missile with respect to the ground and *A* the reference area for the drag coefficient, C_D (Section 4.2.2).

Applying Newton's law, the instantaneous acceleration of the object (characteristic dimension, ℓ) is given by:

$$\text{Acceleration} = \frac{dv_m}{dt} = \frac{\frac{1}{2}\rho_a (U - v_m)^2 C_D A}{\rho_m \ell^3} = \frac{\frac{1}{2}\rho_a (U - v_m)^2 C_D}{\rho_m \ell} \tag{1.17}$$

taking A equal to ℓ^2.

Table 1.4 Flight times and distances for a steel ball (neglecting vertical air resistance)

Object/speed	*Time taken (s)*	*Horizontal distance travelled (m)*
Steel ball/20 m/s	5.4	71
Steel ball/30 m/s	49	1270

Equation (1.17) shows that heavier and larger objects have lower accelerations, and hence their flight speeds are likely to be lower than smaller or lighter objects. The equation also shows that the initial acceleration from rest (v_m=0) is high, but the acceleration rapidly reduces as the difference between the missile speed and the wind speed reduces, so that the wind speed is approached very slowly. Of course the missile speed cannot exceed the wind speed in steady winds.

Equation (1.17) can be integrated to obtain the time taken to accelerate to a given speed, v_m, and the distance travelled in this time. These equations are as follows:

$$\text{Time taken to accelerate from 0 to } v_m = T = \frac{v_m}{kU(U - v_m)} \tag{1.18}$$

$$\text{Distance travelled} = U\left[T - \left(\frac{1}{kU}\right)\ln(1 + kUT)\right] \tag{1.19}$$

where $k=(\rho_a C_D)/(2\rho_m \ell)$ with units of (1/m).

Using Equation (1.19), the flight times and distance travelled by a steel ball of 8mm diameter and 2 g mass have been calculated for a wind speed, *U*, of 32 m/s and are given in Table 1.4.

The calculations show that it takes nearly a minute and 1.27 km for the steel ball to reach 30 m/s—i.e. within 2 m/s of the wind speed. In reality, such a long flight time and distance would not occur as the object would strike a building, or the ground, and lose its kinetic energy.

A more accurate analysis of the trajectories of compact objects requires the vertical air resistance to be included, and neglect of it results in underestimation of the missile speed and distance travelled in a given time (Holmes, 2004).

1.5.3 Trajectories of sheet and rod objects

Tachikawa (1983) carried out a fundamental study of the trajectories of missiles of the sheet type. Aerodynamic forces on auto-rotating plates were measured in a wind tunnel. These results were then used to calculate the trajectories of the plates released into a wind stream. Free-flight tests of model plates with various aspect ratios were made in a small wind tunnel and compared with the calculated trajectories. A distinct change in the mode of motion and the trajectory, with initial angle of attack of the plate, was observed. The calculated trajectories predicted the upper and lower limits of the observed trajectories, with reasonable accuracy. A later study by Tachikawa (1990) extended the experiments

to small prismatic models as well as flat plates and gave a method of estimating the position of a missile impact on a downstream building. The critical non-dimensional parameter for determination of trajectories was $K=\rho_a U^2 A/2mg$, where ρ_a is the density of air, U the wind speed, A the plan area of a plate, m the mass of the missile and g the gravitational constant.

This parameter represents the ratio of aerodynamic forces to gravity forces and can also be expressed as the product of three other non-dimensional parameters:

$$K = \frac{1}{2}\frac{\rho_a}{\rho_m}\frac{U^2}{g\ell}\frac{\ell}{t} \tag{1.20}$$

where ρ_m is the missile density, t the plate thickness and ℓ is equal to $\sqrt{A}$, i.e. a characteristic plan dimension.

In Equation (1.20), ρ_a/ρ_m is a density ratio and $(U^2/g\ell)$ is a Froude number, both important non-dimensional quantities in aerodynamics (see also Section 7.4).

The equations of motion for horizontal, vertical and rotational motion of a flat plate moving in a vertical plane must be solved numerically. Good agreement has been obtained when such numerical solutions are compared with measurements of trajectories of many small plates in a wind tunnel (Holmes *et al.*, 2006; Lin *et al.*, 2006).

1.5.4 Damage potential of flying debris

Wills *et al.* (1998) carried out an analysis of the damage potential of flying missiles, based on the assumption that the damage of a given missile is proportional to its kinetic energy in flight. A number of interesting conclusions arose from this work:

- For compact objects, lower density objects have more damage potential.
- Sheet and rod objects have generally more damage potential than compact objects.
- Very little energy is required to break glass (e.g. a 5 g steel ball travelling at 10 m/s is sufficient to break a 6 mm annealed glass).
- Based on an assumed distribution of available missile dimensions, Wills *et al.* found that the total damage is proportional to U^n, where n is a power equal to about 5.

1.5.5 Standardized missile testing criteria

In regions subjected to hurricanes and tropical cyclones (Section 1.3.2), where the occurrence of damage to buildings by wind-generated missiles has been shown to be a major problem, standardized missile tests have been devised. These demonstrate the ability of wall claddings of various types to resist penetration by flying debris or assist in the development of window protection screens.

When specifying appropriate test criteria for missile impact resistance, the following principles should be followed:

- The missiles should be representative of actual objects available.
- The criteria should be physically realistic, i.e. if the flight threshold speed is greater than the expected wind speed in the storm, then the object should not be regarded as a potential missile.

• Realistic missile speeds should be specified for the expected separation distances between buildings.

Missile testing criteria were included in the *Darwin Area Building Manual*, following Cyclone 'Tracy' in 1974, in Australia. This specified that windows and doors should withstand impact at any angle of a piece of 100 mm by 50 mm timber weighing 4 kg, travelling at 20 m/s. A more severe test was specified for cyclone refuge shelters: 'end-on' impact of a piece of 100 mm by 50 mm timber weighing 8 kg, travelling at 30 m/s. Later the test requirement for windows and doors of buildings was modified to a piece of 100 mm by 50 mm timber weighing 4 kg, travelling at 15 m/s.

Wind-borne debris impact test standards in the United States were discussed by Minor (1994). Following investigations of glass breakage (mainly in high-rise buildings), during several US hurricanes, Pantelides *et al.* (1992) proposed a test protocol involving impacts from small spherical missiles of 2 g. This was taken up in South Florida following Hurricane Andrew in 1992. The Dade County and Broward County editions of the South Florida Building Code required windows, doors and wall coverings to withstand impacts from large and small debris. The large missile test, which is similar to the Australian one, is only applicable to buildings below 9 m in height. The small missile test is only applicable to windows, doors and wall coverings above 9 m and differs between the two counties. The Dade County protocol uses ten 2 g pieces of roof gravel impacting simultaneously at 26 m/s, while the Broward County version uses ten 2 g steel balls impacting successively at 43 m/s.

1.6 Wind storm loss prediction

The trend towards increased losses from wind storms has provoked concern in the insurance and re-insurance industries, and many of these groups now require detailed assessments of the potential financial losses from the exposure of their portfolios of buildings to large-scale severe wind storms. Government bodies also now require predictions of economic losses to aid in planning for disaster and emergency management.

The prediction of average annual loss or accumulated losses over an extended period, say 50 years, requires two major inputs: hazard models and vulnerability curves. The hazard model focuses on the wind storm hazard itself and makes use of historical meteorological data and statistics to predict potential wind speeds at a site in the future. Vulnerability curves attempt to predict building (and sometimes contents) damage, given the occurrence of a particular wind speed.

1.6.1 Hazard models

The purpose of wind hazard models is to define the risk of occurrence of extreme wind speeds at the site of a single structure, on a system such as a transmission line or on a complete city or region. The basis for these models is usually the historical record of wind speeds from anemometer stations, but often larger scale storm parameters such as central pressures for tropical cyclones and atmospheric stability indices for thunderstorm

occurrences are studied. The methods of statistics and probability are extensively used in the development of hazard models in wind engineering.

The application of statistical methods to the prediction of extreme wind speeds is discussed in Chapter 2 of this book.

An understanding of the structure of the wind within a storm enables predictions of 'footprints' such as that shown in Figure 1.14 (Holmes and Oliver, 2000), which shows simulated contours of maximum wind speeds, occurring at some time during the passage of a downburst (Section 1.3.5). This information, in combination with knowledge of the strength or 'vulnerability' of structures, enables predictions of potential damage to be made.

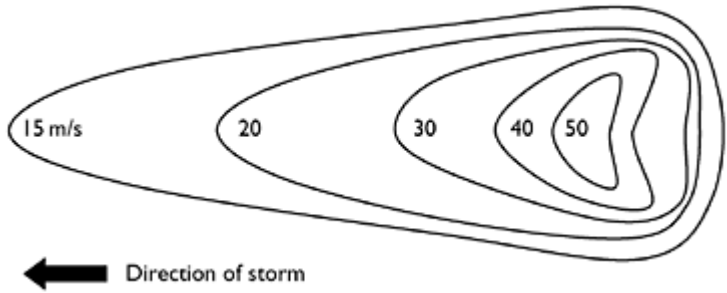

Figure 1.14 Wind speed threshold footprint during the passage of a downburst (Holmes and Oliver, 1999).

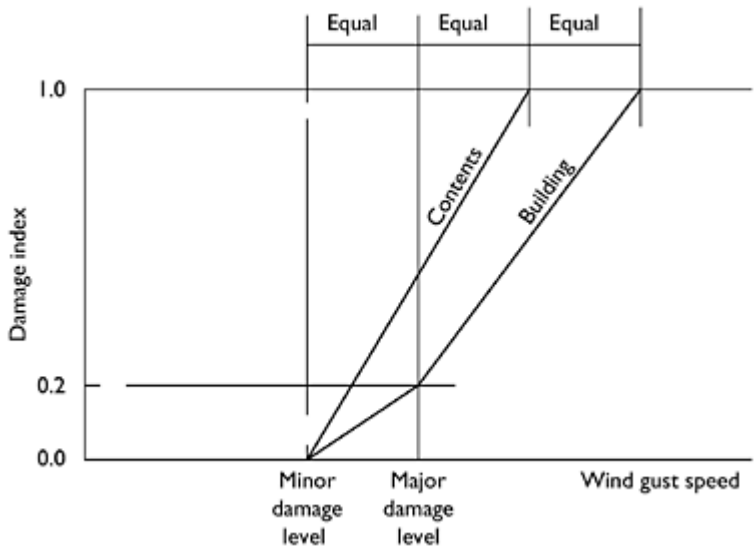

Figure 1.15 Form of vulnerability curve proposed by Leicester (1981).

1.6.2 Vulnerability curves

Insurance loss predictions are quite sensitive to the assumed variations of relative building and contents damage as a function of the local wind speed. Such graphs are known as 'vulnerability curves'. Vulnerability curves can be derived in a number of ways. Leicester (1981) proposed the simplified form, with straight-line segments, for Australian houses, shown in Figure 1.15. The ordinate is a 'damage index' defined as follows for the building:

Damage index *(D)*=(repair cost)/(initial cost of building)

For insurance purposes it may be more appropriate to replace the denominator with the insured value of the building. A similar definition can be applied to the building contents, with 'replacement cost' in the numerator.

Separate lines are given for building and contents. Two parameters only need be specified—a threshold gust speed for the onset of minor damage and a speed for the onset of major building damage (damage index>0.2).

Walker (1995) proposed the following relationships for housing in Queensland, Australia.

For pre-1980 buildings:

$$D = 0.2\left(\frac{U-30}{30}\right)^2 + 0.5\left(\frac{U-30}{30}\right)^6 \tag{1.21}$$

For post-1980 buildings:

$$D = 0.2\left(\frac{U-37.5}{37.5}\right)^2 + 0.5\left(\frac{U-37.5}{37.5}\right)^6 \tag{1.22}$$

Clearly in both cases D is limited to the range 0–1.0.

The relationship of Equation (1.21) was also found to agree well with the recorded damage and wind speed estimates of Hurricane 'Andrew' (see Table 1.1).

A simple form of a vulnerability curve for a fully engineered structure consisting of a large number of members or components with strengths of known probability distribution can be derived. The failure of each component is assumed to be independent of all the others, and they are all designed to resist the same wind load, or speed. Thus, the expected fractional damage to the complete structure, for a given wind speed, is the proportion of failed components expected at that wind speed. If all the components have the same probability distribution of strength, which would be true if they were all designed to the same codes, then the vulnerability curve can simply be derived from the cumulative distribution of strength of any element.

A curve derived in this way (Holmes, 1996) is shown in Figure 1.16, for a structure comprising components with a lognormal distribution of strength, with a mean/nominal strength of 1.20 and a coefficient of variation of 0.13, values which are appropriate for steel components. The nominal design gust wind speed is taken as 65 m/s. This curve can

be compared with that proposed by Walker, for post-1980 Queensland houses, in the tropical cyclone-affected coastal region (Equation 1.22). The theoretical curve, representing fully engineered structures, is steeper than the Walker curve, which has been derived empirically, and incorporates the greater variability in the components of housing structures.

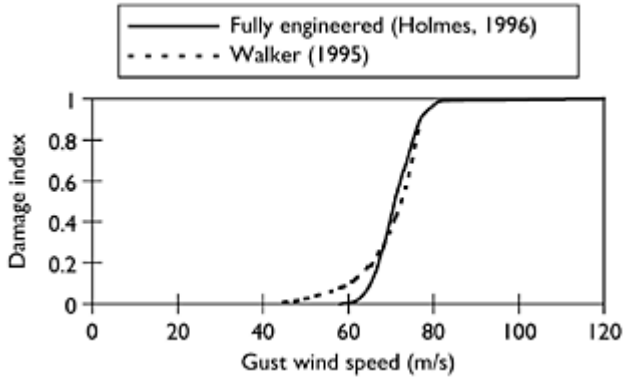

Figure 1.16 Theoretical and empirical vulnerability curves.

1.7 Summary

In this chapter, the physical mechanisms and meteorology of strong wind storms of all types have been described. The balance of forces in a large-scale synoptic system was established and the gradient wind equation derived. Smaller scale storms—tornadoes and downbursts—were also introduced.

The history of significant damaging wind storms was discussed. The mechanics of wind-generated flying debris was considered, and vulnerability curves relating fractional damage potential to wind speed, for insurance loss prediction, were derived.

1.8 The following chapters and appendices

Following this introductory chapter, Chapters 2–7 are directed towards fundamental aspects of wind loading, common to all or most structures—e.g. atmospheric wind structure and turbulence (Chapter 3), bluff-body aerodynamics (Chapter 4), resonant dynamic response of structures (Chapter 5) and wind-tunnel techniques (Chapter 7). Chapters 8–14 deal with aspects of wind loading for particular types of structures: buildings, bridges, towers, etc. Finally, Chapter 15 discusses contemporary wind loading codes and standards—the most common point of contact of practising structural engineers with wind loads.

Appendices A and B cover the terminology of wind engineering and the symbols used in this book, respectively. Appendix C describes probability distributions relevant to wind loading. Appendix D attempts to summarize the extreme wind climate of over 70 countries, and Appendix E gives some approximate formulae for natural frequencies of structures. Appendix F gives a simple example of the calculation of effective static wind load distributions.

References

Fujita, T.T. (1971) Proposed characterization of tornadoes and hurricanes by area and intensity. Report SMRP No. 91, University of Chicago, Chicago, IL.

Fujita, T.T. (1985) The downburst. Report on projects NIMROD and JAWS. Published by the author at the University of Chicago, Chicago, IL.

Fujita, T.T., Pearson, A.D., Forbes, G.S., Umenhofer, T.A., Pearl, E.W. and Tecson, J.J. (1976) Photogrammetric analyses of tornados. *Symposium on Tornadoes: Assessment of Knowledge and Implications for Man*, Texas Tech University, Lubbock, TX, 22–24 June, pp. 43–88.

Golden, J.H. (1976) An assessment of windspeeds in tornados. *Symposium on Tornadoes: Assessment of Knowledge and Implications for Man*, Texas Tech University, Lubbock, TX, 22–24 June, pp. 5–42.

Goliger, A.M., Milford, R.V., Adam, B.F. and Edwards, M. (1997) Inkanyamba: tornadoes in South Africa. CSIR Building Technology and S.A. Weather Bureau.

Hoecker, W.H. (1960) Wind speed and airflow patterns in the Dallas tornado of April 2, 1957. *Monthly Weather Review*, 88:167–80.

Holland, G.J. (1980) An analytic model of the wind and pressure profiles in a hurricane. *Monthly Weather Review*, 108:1212–18.

Holmes, J.D. (1996) Vulnerability curves for buildings in tropical-cyclone regions for insurance loss assessment. *ASCE EMD/STD Seventh Specialty Conference on Probabilistic Mechanics and Structural Reliability*, Worcester, MA, 7–9 August.

Holmes, J.D. (2004) Trajectories of spheres in strong winds with applications to wind-borne debris. *Journal of Wind Engineering & Industrial Aerodynamics*, 92:9–22.

Holmes, J.D. and Oliver, S.E. (2000) An empirical model of a downburst. *Engineering Structures*, 22:1167–72.

Holmes, J.D., Letchford, C.W. and Lin, N. (2006) Investigations of plate-type windborne debris. II. Computed trajectories. *Journal of Wind Engineering & Industrial Aerodynamics*, 94:21–39.

Leicester, R.H. (1981) A risk model for cyclone damage to dwellings. *Proceedings, 3rd International Conference on Structural Safety and Reliability*, Trondheim, Norway.

Lin, N., Letchford, C.W. and Holmes, J.D (2006) Investigations of plate-type windborne debris. I. Experiments in full scale and wind tunnel. *Journal of Wind Engineering & Industrial Aerodynamics*, 94:51–76.

McDonald, J.R. and Mehta, K.C. (2004) A recommendation for an enhanced Fujita Scale. Wind Science and Engineering Research Center, Texas Tech University.

Mehta, K.C. (1976) Windspeed estimates: engineering analyses. *Symposium on Tornadoes: Assessment of Knowledge and Implications for Man*, Texas Tech University, Lubbock, TX, 22–24 June, pp. 89–103.

Minor, J.E. (1994) Windborne debris and the building envelope. *Journal of Wind Engineering & Industrial Aerodynamics*, 53:207–27.

Pantelides, C.P., Horst, A.D. and Minor, J.E. (1992) Post-breakage behaviour of architectural glazing in wind storms. *Journal of Wind Engineering & Industrial Aerodynamics*,
41–44: 2425–35.

Tachikawa, M. (1983) Trajectories of flat plates in uniform flow with application to wind-generated missiles. *Journal of Wind Engineering & Industrial Aerodynamics*, 14:443–53.

Tachikawa, M. (1990) A method for estimating the distribution range of trajectories of wind-borne missiles. *Journal of Wind Engineering & Industrial Aerodynamics*, 29:175–84.

Walker, G.R. (1995) Wind vulnerability curves for Queensland houses. Alexander Howden Insurance Brokers (Australia) Ltd.

Wills, J., Wyatt, T. and Lee, B.E. (1998) Warnings of high winds in densely populated areas. United Kingdom National Coordination Committee for the International Decade for Natural Disaster Reduction.

2
Prediction of design wind speeds and structural safety

2.1 Introduction and historical background

The establishment of appropriate design wind speeds is a critical first step towards the calculation of design wind loads for structures. It is also usually the most uncertain part of the design process for wind loads, and requires the statistical analysis of historical data on recorded wind speeds.

In the 1930s, the use of the symmetrical bell-shaped *Gaussian* distribution (Section C3.1) to represent extreme wind speeds for the prediction of long-term design wind speeds was proposed. However, this failed to take note of the earlier theoretical work of Fisher and Tippett (1928), establishing the limiting forms of the distribution of the largest (or smallest) value in a fixed sample, depending on the form of the tail of the parent distribution. The identification of the three types of *extreme value distribution* was of prime significance to the development of probabilistic approaches in engineering in general.

The use of extreme value analysis for design wind speeds lagged behind the application to flood analysis. Gumbel (1954) strongly promoted the use of the simpler Type I extreme value distribution for such analyses. However, Jenkinson (1955) showed that the three asymptotic distributions of Fisher and Tippett could be represented as a single *Generalized Extreme Value Distribution*—this is discussed in detail in a following section. In the 1950s and the early 1960s, several countries had applied extreme value analyses to predict design wind speeds. In the main, Type I (by now also known as the 'Gumbel distribution') was used for these analyses. The concept of *return period* also arose at this time.

The use of probability and statistics as the basis for the modern approach to wind loads was, to a large extent, a result of the work of Davenport in the 1960s, recorded in several papers (e.g. Davenport, 1961).

In the 1970s and 1980s, the enthusiasm for the then standard 'Gumbel analysis' was tempered by events such as Cyclone 'Tracy' in Darwin, Australia (1974), and severe gales in Europe (1987), when the previous design wind speeds determined by a Gumbel fitting procedure were exceeded considerably. This highlighted the importance of:

- sampling errors inherent in the recorded database, usually less than 50 years, and
- the separation of data originating from different storm types.

The need to separate the recorded data by storm type was recognized in the 1970s by Gomes and Vickery (1977a).

The development of probabilistic methods in structural design generally, developed in parallel with their use in wind engineering, followed pioneering work by Freudenthal (1947, 1956) and Pugsley (1966). This area of research and development is known as 'structural reliability' theory. Limit states design, which is based on probabilistic concepts, was steadily introduced into design practice from 1970 onwards.

This chapter discusses modern approaches to the use of extreme value analysis for the prediction of extreme wind speeds for the design of structures. Related aspects of structural design and safety are discussed in Section 2.6.

2.2 Principles of extreme value analysis

The theory of extreme value analysis of wind speeds or other geophysical variables such as flood heights or earthquake accelerations is based on the application of one or more of the three asymptotic extreme value distributions identified by Fisher and Tippett (1928), and is discussed in the following section. They are asymptotic in the sense that they are the correct distributions for the largest of an *infinite* population of independent random variables of known probability distribution. In practice, of course, there will be a finite number in a population, but in order to make predictions, the asymptotic extreme value distributions are still used as empirical fits to the extreme data. Which one of the three is theoretically 'correct' depends on the form of the tail of the underlying parent distribution. However, unfortunately, this form is not usually known with certainty due to lack of data. Physical reasoning has sometimes been used to justify the use of one or other of the asymptotic extreme value distributions.

Gumbel (1954, 1958) has covered the theory of extremes in detail. A useful review of the various methodologies available for the prediction of extreme wind speeds, including those discussed in this chapter, has been given by Palutikof *et al.* (1999).

2.2.1 The generalized extreme value distribution

The generalized extreme value distribution (GEV) introduced by Jenkinson (1955) combines the three extreme value distributions into a single mathematical form:

$$F_U(U)=\exp\{-[1-k(U-u)/a]^{1/k}\} \tag{2.1}$$

where $F_U(U)$ is the cumulative probability distribution function (see Appendix C) of the maximum wind speed in a defined period (e.g. 1 year).

In Equation (2.1), k is a shape factor, a a scale factor and u a location parameter. When $k<0$, the GEV is known as the *Type II Extreme Value* (or *Frechet*) *Distribution;* when $k>0$, it becomes a *Type III Extreme Value Distribution* (a form of the *Weibull*

distribution). As k tends to 0, Equation (2.1) becomes Equation (2.2) in the limit. Equation (2.2) is the *Type I Extreme Value Distribution* or *Gumbel Distribution:*

$$F_U(U)=\exp\{-\exp[-(U-u)/a]\} \tag{2.2}$$

The GEV with k equal to −0.2, 0 and 0.2 is plotted in Figure 2.1 in a form that Type I appears as a straight line. As can be seen Type III (k=+0.2) curves in a way to approach a limiting value—it is therefore appropriate for variables that are 'bounded' on the high side. It should be noted that Type I and Type II predict unlimited values—they are therefore suitable distributions for variables that are 'unbounded'. As we would expect that there is an upper limit to the wind speed that the atmosphere can produce, the Type III distribution may be more appropriate for wind speed.

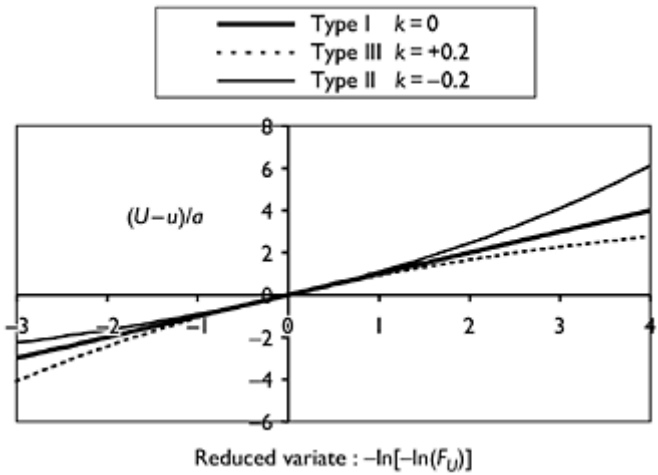

Figure 2.1 The generalized extreme value distribution (k=−0.2, 0, +0.2).

A method of fitting the generalized extreme value distribution to wind data is discussed in Section 2.4. An alternative method is the method of probability-weighted moments described by Hosking *et al.* (1985).

2.2.2 Return period

At this point it is appropriate to introduce the term *return period, R.* It is simply the inverse of the complementary cumulative distribution of the extremes,

$$\text{i.e. Return period, } R = \frac{1}{\text{Probability of exceedence}} = \frac{1}{1-F_U(U)}$$

Thus, if the annual maximum is being considered, then the return period is measured in years. Thus, a 50-year return period wind speed has a probability of exceedence of 0.02 (1/50) in any 1 year. It should not be interpreted as recurring regularly every 50 years. The probability of a wind speed, of given return period, being exceeded in a lifetime of a structure is discussed in Section 2.5.3.

2.2.3 Separation by storm type

In Chapter 1, the various types of wind storm that are capable of generating winds strong enough to be important for structural design were discussed. These different event types will have different probability distributions and therefore should be statistically analysed separately; however, this is usually quite a difficult task as weather bureaus or meteorological offices do not normally record the necessary information. If anemograph records such as those shown in Figures 1.5 and 1.7 are available, these can be used for identification purposes—although this is a time-consuming and painstaking task!

The relationship between the combined return period, R_c for a given extreme wind speed due to winds of either type and for those calculated separately for storm types 1 and 2 (R_1 and R_2) is:

$$\left(1-\frac{1}{R_c}\right)=\left(1-\frac{1}{R_1}\right)\left(1-\frac{1}{R_2}\right) \tag{2.3}$$

Equation (2.3) relies on the assumption that exceedence of wind speeds from the two different storm types is an independent event.

2.2.4 Simulation methods for tropical cyclone wind speeds

The winds produced by severe tropical cyclones also known as ‘hurricanes’ and ‘typhoons’ are the most severe on earth (apart from those produced by tornadoes which affect very small areas). However, their infrequent occurrence at particular locations often makes the historical record of recorded wind speeds an unreliable predictor for design wind speeds. An alternative approach, which gained popularity in the 1970s and early 1980s, was the simulation or ‘Monte Carlo’ approach, introduced originally for offshore engineering by Russell (1971). In this procedure, satellite and other information on storm size, intensity and tracks are made use of to enable a computer-based simulation of wind speed (and in some cases direction) at particular sites. Usually, established probability distributions are used for parameters such as central pressure and radius to maximum winds. A recent use of these models is for damage prediction for insurance companies. The disadvantage of this approach is the subjective aspect resulting from the complexity of the problem. Significantly varying predictions could be obtained by adopting different assumptions. Clearly whatever recorded data that are available should be used to calibrate these models.

2.2.5 Compositing data from several stations

No matter what type of probability distribution is used to fit historical extreme wind series or what fitting method is used, extrapolations to high return periods for ultimate limit states design (either explicitly or implicitly through the application of a wind load factor) are usually subject to significant sampling errors. This results from the limited record lengths usually available to the analyst. In attempts to reduce the sampling errors, a recent practice has been to combine records from several stations with perceived similar wind climates to increase the available records for extreme value analysis. Thus, 'superstations' with long records can be generated in this way.

For example, in Australia, stations in a huge region in the southern part of the country have been judged to have similar statistical behaviour, at least as far as the all-direction extreme wind speeds are concerned. A single set of design wind speeds has been specified for this region (Standards Australia, 1989, 2002; Holmes, 2002). A similar approach has been adopted in the United States (ASCE, 1998, 2006; Peterka and Shahid, 1998).

2.2.6 Incorporation of wind direction effects

Increased knowledge of the aerodynamics of buildings and other structures, through wind-tunnel and full-scale studies, has revealed the variation of structural response as a function of wind direction as well as speed. The approaches to probabilistic assessment of wind loads including direction can be divided into those based on the parent distribution of wind speed and those based on extreme wind speeds. In many countries, the extreme winds are produced by rare severe storms such as thunderstorms and tropical cyclones, and there is no direct relationship between the parent population of regular everyday winds and the extreme winds. For such locations (which would include most tropical and subtropical countries), the latter approach is more appropriate. Where a separate analysis of extreme wind speeds by direction sector has been carried out, the relationship between the return period, Ra, for exceedence of a specified wind speed from *all* direction sectors and the return periods for the same wind speed from direction sectors θ_1, θ_2, etc. is given in the following equation:

$$\left(1-\frac{1}{R_a}\right)=\prod_{i=1}^{N}\left(1-\frac{1}{R_{\theta_i}}\right) \tag{2.4}$$

Equation (2.4) follows from the assumption that wind speeds from each direction sector are statistically independent of each other and is a statement of the following:

Probability that a wind speed U is *not* exceeded for all wind directions =
(probability that U is not exceeded from direction 1)
× (probability that U is not exceeded from direction 2)
× (probability that U is not exceeded from direction 3)
……etc.

Equation (2.4) is a similar relationship to Equation (2.3) for combining extreme wind speeds from different types of storms.

2.3 Extreme wind estimation by the Type I distribution

2.3.1 Gumbel's method

Gumbel (1954) gave an easily usable methodology for fitting recorded annual maxima to the Type I extreme value distribution. This distribution is a special case of the GEV discussed in Section 2.2.1. The Type I distribution takes the form of Equation (2.2) for the cumulative distribution $F_U(U)$:

$$F_U(U)=\exp\{-\exp[-(U-u)/a]\}$$

where u is the mode of the distribution and a a scale factor.

The return period, R, is directly related to the cumulative probability distribution, $F_U(U)$, of the annual maximum wind speed at a site as follows:

$$R = \frac{1}{1 - F_U(U)} \tag{2.5}$$

Substituting for $F_U(U)$ from Equation (2.5) in Equation (2.2), we obtain:

$$U_R = u + a\left\{-\log_e\left[-\log_e\left(1-\frac{1}{R}\right)\right]\right\} \tag{2.6}$$

For large values of return period, R, Equation (2.6) can be written as:

$$U_R \cong u + a\log_e R \tag{2.7}$$

In Gumbel's original extreme value analysis method (applied to flood prediction as well as extreme wind speeds), the following procedure is adopted:

- The largest wind speed in each calendar year of the record is extracted.
- The series is ranked in order of smallest to largest: 1, 2,…m… to N.
- Each value is assigned a probability of non-exceedence, p, according to:

$$p \approx m/(N+1) \tag{2.8}$$

• A reduced variate, *y*, is formed from:

$$y=-\log_e(-\log_e p) \tag{2.9}$$

where *y* is an estimate of the term in {} brackets in Equation (2.6).

• The wind speed, *U*, is plotted against *y*, and a line of 'best fit' is drawn, usually by means of linear regression.

As may be seen from Equation (2.7) and Figure 2.1, the Type I or Gumbel distribution will predict unlimited values of U_R as the return period, *R*, increases; i.e. as *R* becomes larger, U_R as predicted by Equation (2.6) or (2.7) will also increase without limit. As discussed in Section 2.2.1, this can be criticized on physical grounds, as there must be upper limits to the wind speeds that can be generated in the atmosphere in different types of storms. This behaviour, although unrealistic, may be acceptable for codes and standards.

2.3.2 Gringorten's method

The Gumbel procedure, as described in Section 2.3.1, has been used many times to analyse extreme wind speeds for many parts of the world.

Assuming that the Type I extreme value distribution is in fact the correct one, the fitting method, due to Gumbel, is biased, i.e. Equation (2.8) gives distorted values for the probability of non-exceedence, especially for high values of *p* near 1. Several alternative fitting methods have been devised which attempt to remove this bias. However, most of these are more difficult to apply, especially if *N* is large, and some involve the use of computer programs to implement. A simple modification to the Gumbel procedure, which gives nearly unbiased estimates for this probability distribution, is due to Gringorten (1963). Equation (2.8) is replaced by the following modified formula:

$$p \approx (m-0.44)/(N+1-0.88)=(m-0.44)/(N+0.12) \tag{2.10}$$

Fitting of a straight line to *U* versus the plotting parameter, *p*, then proceeds as for the Gumbel method.

2.3.3 Method of moments

The simplest method of fitting the Type I extreme value distribution to a set of data is known as the *Method of Moments*. It is based on the following relationships between the mean and the standard deviation of the distribution, and the mode and the scale factor (or slope):

$$\text{mean} = u + 0.5772a \tag{2.11}$$

$$\text{standard deviation} = \left(\frac{\pi}{\sqrt{6}}\right)a \tag{2.12}$$

The method to estimate the parameters, u and a of the distribution simply entails the calculation of the sample mean, μ, and standard deviation, σ, from the data, then estimating u and a by using the inverse of Equations (2.11) and (2.12), i.e.

$$a \cong \left(\frac{\sqrt{6}}{\pi}\right)\sigma \tag{2.13}$$

$$u \cong \mu - 0.5772a \tag{2.14}$$

Once the parameters u and a have been determined, predictions of the extreme wind speed for a specified return period, R, are made using Equation (2.6) or (2.7).

Another procedure is the 'best linear unbiased estimators' proposed by Lieblein (1974), in which the annual maxima are ordered and the parameters of the distribution are obtained by weighted sums of the extreme values.

2.3.4 Example of fitting the Type I distribution to annual maxima

Wind gust data have been obtained from a military airfield at East Sale, Victoria, Australia, continuously since late 1951. The anemometer position has been constant throughout that period, and the height of the anemometer head has always been the standard meteorological value of 10 m. Thus, in this case no corrections for height and terrain are required. Also the largest gusts have almost entirely been produced by gales from large synoptic depressions (Section 1.3.1). However, the few gusts that were produced by thunderstorm downbursts were eliminated from the list to produce a statistically consistent population (see Section 2.2.3).

The annual maxima for the 47 calendar years 1952–98 are listed in Table 2.1. The values in Table 2.1 are sorted in order of increasing magnitude (Table 2.2) and assigned a probability, p, according to (i) the Gumbel formula (Equation (2.8)), and (ii) the Gringorten formula (Equation (2.10)). The reduced variate, $-\log_e(-\log_e p)$, according to Equation (2.9) is formed for both cases. These are tabulated in Table 2.2. The wind speed is plotted against the reduced variates and straight lines are fitted by linear regression ('least squares' method). The results of this are shown in Figures 2.2 and 2.3, for the Gumbel and Gringorten methods, respectively. The intercept and slope of these lines give the mode, u, and slope, a, of the fitted Type I extreme value distribution according to Equation (2.1).

u and a can also be estimated from the calculated mean and standard deviation (shown in Table 2.1) by the method of moments using Equations (2.13) and (2.14).

Predictions of extreme wind speeds for various return periods can then be readily obtained by the application of either Equation (2.6) or (2.7). Table 2.3 lists these predictions based on the Gumbel and Gringorten fitting methods and by the method of moments. For return periods up to 500 years, the predicted values by the three methods are within 1 m/s of each other. However, these small differences are swamped by sampling errors, i.e. the errors inherent in trying to make predictions for return periods of 100 years or more from less than 50 years of data. This problem is illustrated in the following Exercise. The problem of high sampling errors can often be circumvented by compositing data, as discussed in Section 2.2.5.

Table 2.1 Annual maximum gust speeds from East Sale, Australia 1952–1998

Year	*Maximum gust speed (m/s)*
1952	31.4
1953	33.4
1954	29.8
1955	30.3
1956	27.8
1957	30.3
1958	29.3
1959	36.5
1960	29.3
1961	27.3
1962	31.9
1963	28.8
1964	25.2
1965	27.3
1966	23.7
1967	27.8
1968	32.4
1969	27.8
1970	26.2
1971	30.9
1972	31.9
1973	27.3

1974	25.7
1975	32.9
1976	28.3
1977	27.3
1978	28.3
1979	28.3
1980	29.3
1981	27.8
1982	27.8
1983	30.9
1984	26.7
1985	30.3
1986	28.3
1987	30.3
1988	34.0
1989	28.8
1990	30.3
1991	27.3
1992	27.8
1993	28.8
1994	30.9
1995	26.2
1996	25.7
1997	24.7
1998	42.2
Mean	29.27
SD	3.196

Table 2.2 Processing of East Sale data

Rank	*Gust speed (m/s)*	*Reduced variate (Gumbel)*	*Reduced variate (Gringorten)*
1	23.7	−1.354	−1.489
2	24.7	−1.156	−1.226
3	25.2	−1.020	−1.069
4	25.7	−0.910	−0.949
5	25.7	−0.816	−0.848
6	26.2	−0.732	−0.759
7	26.2	−0.655	−0.679
8	26.7	−0.583	−0.604
9	27.3	−0.515	−0.534
10	27.3	−0.450	−0.467
11	27.3	−0.388	−0.403
12	27.3	−0.327	−0.340
13	27.3	−0.267	−0.279
14	27.8	−0.209	−0.220
15	27.8	−0.151	−0.161
16	27.8	−0.094	−0.103
17	27.8	−0.037	−0.045
18	27.8	0.019	0.013
19	27.8	0.076	0.071
20	28.3	0.133	0.129
21	28.3	0.190	0.187
22	28.3	0.248	0.246
23	28.3	0.307	0.306
24	28.8	0.367	0.367
25	28.8	0.427	0.428
26	28.8	0.489	0.492
27	29.3	0.553	0.556
28	29.3	0.618	0.623
29	29.3	0.685	0.692

30	29.8	0.755	0.763
31	30.3	0.827	0.837
32	30.3	0.903	0.914
33	30.3	0.982	0.995
34	30.3	1.065	1.081
35	30.3	1.152	1.171
36	30.9	1.246	1.268
37	30.9	1.346	1.371
38	30.9	1.454	1.484
39	31.4	1.572	1.607
40	31.9	1.702	1.744
41	31.9	1.848	1.898
42	32.4	2.013	2.075
43	32.9	2.207	2.285
44	33.4	2.442	2.544
45	34.0	2.740	2.885
46	36.5	3.157	3.391
47	42.2	3.861	4.427

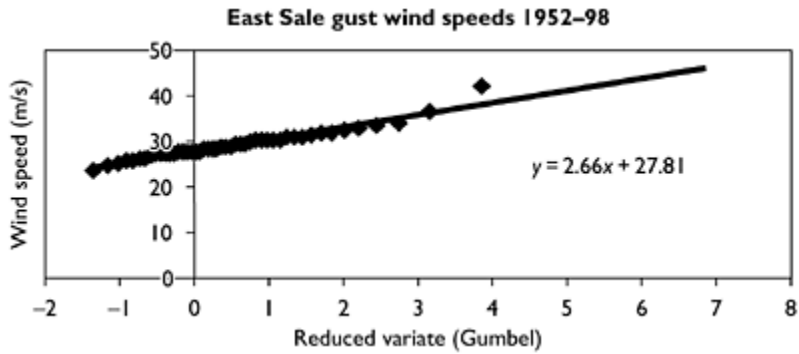

Figure 2.2 Analysis of annual maximum wind gusts from East Sale using the Gumbel method.

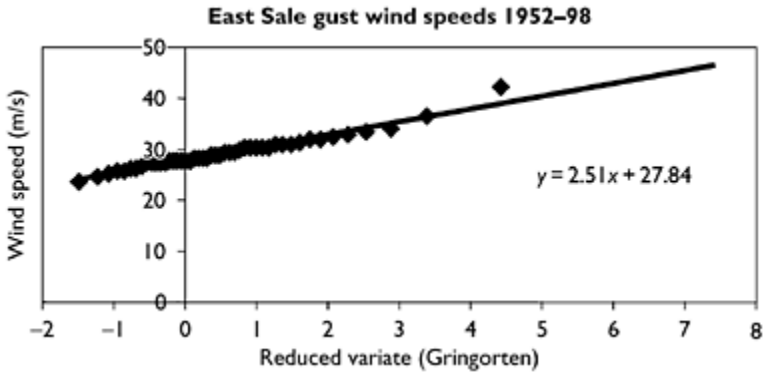

Figure 2.3 Analysis of East Sale data using the Gringorten fitting method.

Table 2.3 Prediction of extreme wind speeds for East Sale (synoptic winds)

Return period (years)	*Predicted gust speed (m/s) (Gumbel)*	*Predicted gust speed (m/s) (Gringorten)*	*Predicted gust speed (m/s) (method of moments)*
10	33.8	33.5	33.4
20	35.7	35.3	35.2
50	38.2	37.6	37.6
100	40.0	39.4	39.3
200	41.9	41.1	41.0
500	44.3	43.5	43.3
1000	46.2	45.2	45.0

2.3.4.1 Exercise

Re-analyse the annual maximum gust wind speeds for East Sale for the years 1952–97, i.e. ignore the high value recorded in 1998. Compare the resulting predictions of design wind speeds for (a) 50-year return period and (b) 1000-year return period, and comment.

2.3.5 General penultimate distribution

For extreme wind speeds that are derived from a Weibull parent distribution (see Section 2.5), Cook and Harris (2004) have proposed a ‘general penultimate’ Type I or Gumbel distribution. This takes the form of Equation (2.15):

$$F_U(U)=\exp\{-\exp[-(U^w-u^w)/a^w]\} \tag{2.15}$$

where w is the Weibull exponent of the underlying parent distribution (see Equation (2.21)).

Comparing Equation (2.15) with Equation (2.2), it can be seen that Equation (2.15) represents a Gumbel distribution for a transformed variable, Z, equal to U^w.

If the parent wind speed data are available for a site, w can be obtained directly from fitting a Weibull distribution to that. Alternatively, the penultimate distribution of Equation (2.15) can be treated as a three-parameter (u, a and w) distribution and fitted directly to the extreme wind data without knowing the parent distribution directly.

The Weibull exponent, w, is typically in the range of 1.3–2.0; in that case, when Equation (2.15) is plotted in the Gumbel form (Figure 2.2), the resulting line curves downwards, and is similar in shape to the Type III extreme value distribution. The main difference is that the latter has a finite upper limit, whereas for the penultimate distribution, U^w, and hence U, is unlimited. However, for practical design situations, the two distributions give very similar predictions (Holmes and Moriarty, 2001).

2.4 The peaks over threshold approach

The approach of extracting a single maximum value of wind speed from each year of historical data obviously has limitations in that there may be many storms during any year and only one value from all these storms is being used. A shorter reference period than a year could, of course, be used to increase the amount of data. However, it is important for extreme value analysis that the data values be statistically independent—this will not be the case if a period as short as 1 day is used. An alternative approach which makes use of only the data of relevance to extreme wind prediction is the *peaks*, or *excesses, over threshold* approach (e.g. Davison and Smith, 1990; Lechner *et al.*, 1992; Holmes and Moriarty, 1999). The method is also known as the 'conditional mean exceedence' (CME) method.

A brief description of the method is given here. This is a method which makes use of all wind speeds from independent storms above a particular minimum threshold wind speed, u_0 (say 20 m/s). There may be several of these events or none, during a particular year. The basic procedure is as follows:

- Several threshold levels of wind speed are set: u_0, u_1, u_2, *etc.* (e.g. 20, 21, 22,… m/s).
- The exceedences of the lowest level u_0 by the maximum storm wind are identified and the number of crossings of this level per year, λ, is calculated.
- The differences $(U-u_0)$ between each storm wind and the threshold level u_0 are calculated and averaged (only positive excesses are counted).
- The previous step is repeated for each level, u_1, u_2, etc. in turn.
- The mean excess is plotted against the threshold level.
- A scale factor, σ, and a shape factor, k, are determined from the following equations (Davison and Smith, 1990):

$$\text{slope} = \frac{-k}{(1+k)} \quad \text{intercept} = \frac{\sigma}{(1+k)} \tag{2.16}$$

Prediction of the *R*-year return period wind speed, U_R, can then be calculated from:

$$U_R = u0 + \sigma[1-(\lambda R)^{-k}]/k \tag{2.17}$$

In Equation (2.17), the shape factor, *k*, is normally found to be positive (usually around 0.1). As *R* increases to very large values, the upper limit to U_R of $u_0+(\sigma/k)$ is gradually approached.

When *k* is zero, it can be shown mathematically that Equation (2.17) reduces to Equation (2.18):

$$U_R = u_0 + \sigma \log_e(\lambda R) \tag{2.18}$$

The similarity between Equations (2.7) and (2.18) should be noted.

The highest threshold level, u_n, should be set so that it is exceeded by at least 10 wind speeds. An example of this method is given in the following section.

2.4.1 Example of the use of the 'peaks over threshold' method

Daily wind gusts at several stations in Melbourne, Australia, have been recorded since 1940. Those at the four airport locations of Essendon, Moorabbin, Melbourne Airport (Tullamarine) and Laverton are the most useful as the anemometers are located at positions most closely matching the ideal open country conditions and away from the direct influence of buildings. Table 2.4 summarizes the data available from these four stations.

The two most common types of events producing extreme wind in the Melbourne area are gales produced by the passage of large low-pressure or frontal systems ('synoptic' winds—see Section 1.3.1) and severe thunderstorm 'downbursts' (Section 1.3.3). Downbursts are usually accompanied by thunder, but the occurrence of thunder does not necessarily mean that an extreme gust has been generated by a downburst. The occurrences of downbursts in the data from the four stations were identified by inspection of the charts stored by the Australian Bureau of Meteorology or the National Archives. Table 2.4 shows that the rate of occurrence of downbursts greater than 21 m/s is quite low (around one per year at each station); however, as will be seen they are significant contributors to the largest gusts.

Table 2.4 Summary of data for Melbourne stations

Station	*Station number*	*Years*	*Maximum recorded gust (m/s)*	*Rate/year (synoptic gusts 21 m/s)*	*Rate/year (downburst gusts 21 m/s)*
Essendon	86038	1940–71	40.6	34.6	1.1
Moorabbin	86077	1972–92	41.2	19.3	0.7
Tullamarine	86282	1970–97	38.6	30.1	1.3
Laverton	87031	1946–95	42.7	28.4	0.8

Note: 1953, 1954 and 1956 are missing from Laverton data.

The largest recorded gusts in the Melbourne area are listed in Table 2.5. Approximately half of these were generated by downbursts.

Extreme value analysis of the data was carried out in the following stages:

- Daily gusts over 21 m/s were retained for analysis.
- Gusts generated by downbursts were identified by inspection of anemometer charts and separated from the synoptic gusts.
- The data from the four stations were composited into single data sets, for both downburst gusts and synoptic gusts.
- The synoptic data were corrected to a uniform height (10m) and approach terrain (open country), using correction factors according to direction derived from wind-tunnel tests for each station.
- For both data sets, the 'excesses over threshold' analysis was used to derive relationships between wind speed and return period.

The last stage enabled a scale factor, σ, and a shape factor, k, to be determined in the relationship in Equation (2.17):

$$U_R = u_0 + \sigma[1 - (\lambda R)^{-k}]/k$$

where u_0 is the lowest threshold, in this case 21 m/s, and λ is average annual rate of exceedence of u_0 for the combined data sets. For the current analysis, λ was 23.4 for the synoptic data and 0.97 for the downburst data.

The results of the two analyses were expressed in the following forms for the Melbourne data:

Table 2.5 Largest recorded gusts in the Melbourne area 1940–97

Date	*Station*	*Gust speed (knots)*	*Gust speed (m/s)*	*Type*
14/1/1985	Laverton	83	42.7	Synoptic
25/12/1978	Moorabbin	80	41.2	Downburst
6/9/1948	Essendon	79	40.6	Synoptic
15/11/1982	Tullamarine	75	38.6	Downburst
3/1/1981	Tullamarine	74	38.1	Downburst
26/10/1978	Laverton	71	36.5	Downburst
4/8/1947	Essendon	70	36.0	Synoptic
27/2/1973	Laverton	70	36.0	Downburst
8/11/1988	Tullamarine	70	36.0	Synoptic
1/7/1942	Essendon	67	34.5	Downburst
5/8/1959	Laverton	67	34.5	Synoptic
24/1/1982	Laverton	67	34.5	Downburst
10/8/1992	Tullamarine	67	34.5	Synoptic

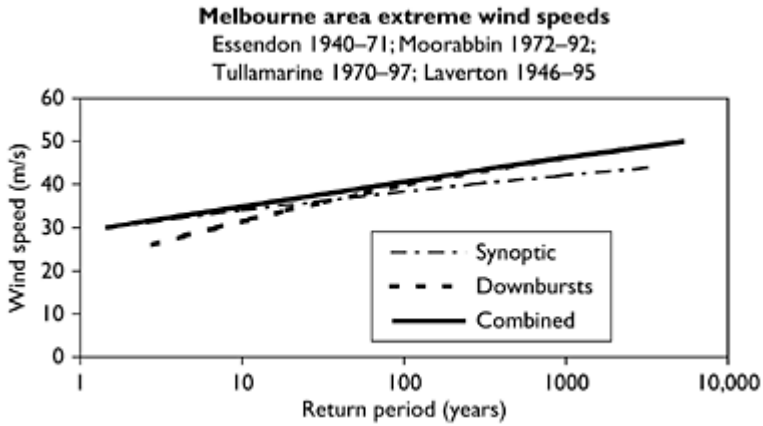

Figure 2.4 Wind speed versus return period for the Melbourne area.

For synoptic winds:

$$U_R = 68.3 - 39.3R_1^{-0.059} \tag{2.19}$$

For downburst winds:

$$U_R = 69.0 - 48.1R_2^{-0.108} \tag{2.20}$$

The combined probability of exceedence of a given gust speed from either type of wind is obtained by substituting in Equation (2.3):

$$\frac{1}{R_c} = 1 - \left[1 - \left(\frac{68.3 - U_R}{39.3}\right)^{1/0.059}\right]\left[1 - \left(\frac{69.0 - U_R}{48.1}\right)^{1/0.108}\right] \tag{2.21}$$

Equations (2.19), (2.20) and (2.21) are plotted in Figure 2.4. The lines corresponding to Equations (2.19) and (2.20) cross at a return period of 30 years. It can also be seen that the combined wind speed return period relationship is asymptotic to the synoptic line at low return periods and to the downburst line at high return periods.

2.5 Parent wind distributions

For some design applications it is necessary to have information on the distribution of the complete population of wind speeds at a site. An example is the estimation of fatigue damage for which account must be taken of damage accumulation over a range of wind storms (see Section 5.6). The population of wind speeds produced by synoptic wind storms at a site is usually fitted with a distribution of the Weibull type:

$$f_U(\tilde{U}) = \frac{w\tilde{U}^{w-1}}{c^w} \exp\left[-\left(\frac{\tilde{U}}{c}\right)^w\right] \tag{2.22}$$

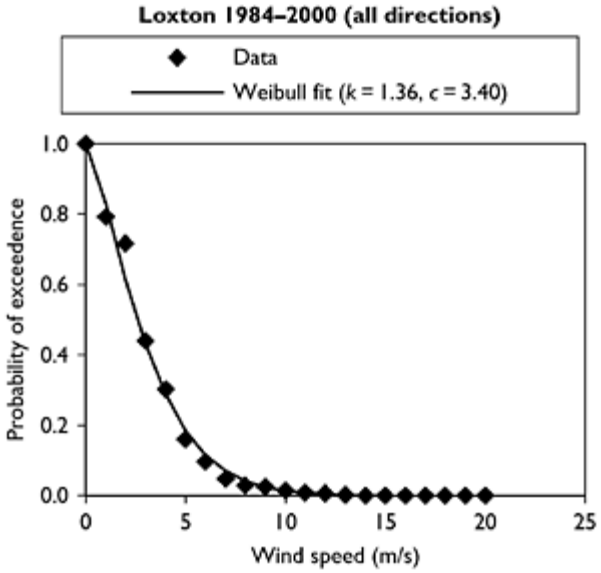

Figure 2.5 Example of a Weibull distribution fit to parent population of synoptic winds.

Equation (2.22) represents the probability density function for mean wind speeds produced by synoptic events. There are two parameters: a *scale factor, c*, which has units of wind speed, and a *shape factor, w*, which is dimensionless (see also Section C3.4). The probability of exceedence of any given wind speed is given by Equation (2.23):

$$1 - F(\tilde{U}) = \exp\left[-\left(\frac{\tilde{U}}{c}\right)^{w}\right] \tag{2.23}$$

Typical values of *c* are 3–10 m/s and *w* usually falls in the range 1.3–2.0. An example of a Weibull fit to recorded meteorological data is shown in Figure 2.5.

Several attempts have been made to predict extreme winds from knowledge of the parent distribution of wind speeds and thus make predictions from quite short records of wind speed at a site (e.g. Gomes and Vickery, 1977b). The ‘asymptotic’ extreme value distribution for a Weibull parent distribution is the Type I or Gumbel distribution. However, for extremes drawn from a finite sample (e.g. annual maxima), the ‘penultimate’ Type I, as discussed in Section 2.3.2, is the more appropriate extreme value distribution.

However, it should be noted that both the Weibull distribution and the Type I extreme value distribution will give unlimited wind speeds with reducing probability of exceedence.

2.6 Wind loads and structural safety

The development of structural reliability concepts, i.e. the application of probabilistic methods to the structural design process, has accelerated the adoption of probabilistic methods into wind engineering since the 1970s. The assessment of wind loads is only one part of the total structural design process, which also includes the determination of other loads and the resistance of structural materials. The structural engineer must proportion the structure so that collapse or overturning has a very low risk of occurring and defined serviceability limits on deflection, acceleration, etc. are not exceeded very often.

2.6.1 Limit states design

Limit states design is a rational approach to the design of structures, which has gradually become accepted around the world. As well as explicitly defining the ultimate and serviceability limit states for design, the method takes a more rational approach to structural safety by defining 'partial' load factors ('gamma' factors) for each type of loading and a separate resistance factor ('phi' factor) for the resistance. The application of the limit states design method is not, in itself, a probabilistic process, but probability is usually used to derive the load and resistance factors.

A typical ultimate limit states design relationship involving wind loads is as follows:

$$\varphi R \geq \gamma_D D + \gamma_w W \tag{2.24}$$

where ϕ is a resistance factor, R the nominal structural resistance, γ_D the dead load factor, D the nominal dead load, γ_w the wind load factor and W the nominal wind load.

In this relationship, the partial factors ϕ, γ_D and γ_w are adjusted separately to take account of the variability and uncertainty in the resistance, dead load and wind load. The values used also depend on what particular nominal values have been selected. Often a final calibration of a proposed design formula is carried out by evaluating the safety, or reliability, index as discussed in the following section, for a range of design situations, e.g. various combinations of nominal dead and wind loads.

2.6.2 Probability of failure and the safety index

A quantitative measure of the safety of structures known as the *safety index*, or *reliability index*, is used in many countries as a method of calibration of existing and future design methods for structures. As will be explained in this section, there is a one-to-one relationship between this index and a probability of failure, based on the exceedence of a design resistance by an applied load (but not including failures by human errors and other accidental causes).

The design process is shown in its simplest form in Figure 2.6. The design process consists of comparing a structural load effect, S, with the corresponding resistance, R. In the case of limit states associated with structural strength or collapse, the load effect could be an axial force in a member or a bending moment, or the corresponding stresses.

In the case of serviceability limit states, *S* and *R* may be deflections, accelerations or crack widths.

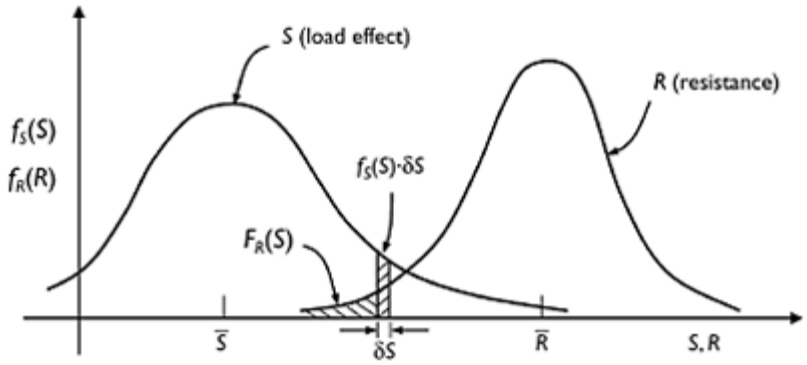

Figure 2.6 Probability densities for load effects and resistance.

The probability density functions $f_s(S)$ and $f_R(R)$ for a load effect, *S*, and the corresponding structural resistance, *R*, are shown in Figure 2.6. (Probability density is defined in Section C2.1.) Clearly, *S* and *R* must have the same units. The dispersion or 'width' of the two distributions represents the uncertainty in *S* and *R*.

Failure (or unserviceability) occurs when the resistance of the structure is less than the load effect. The probability of failure will now be determined assuming *S* and *R* are statistically independent:

The probability of failure occurring at a load effect between *S* and $S+dS$ =[probability of load effect lying between *S* and $S+\delta S$] ×[probability of resistance, *R*, being less than *S*]=$[f_s(S)\delta S]\times F_R(S)$ (2.25)

where $F_R(R)$ is the cumulative probability distribution of *R* and

$$F_R(S) = \int_{-\infty}^{S} f_R(R)\,\mathrm{d}R \tag{2.26}$$

The terms in the product in Equation (2.25) are the areas shown in Figure 2.6.

The total probability of failure is obtained by summing or integrating Equation (2.25) over all possible values of *S* (between $-\infty$ and $+\infty$):

$$p_f = \int_{-\infty}^{\infty} f_S(S)\cdot F_R(S)\,\mathrm{d}S \tag{2.27}$$

Substituting for $F_R(S)$ from Equation (2.26) into Equation (2.27),

$$p_f = \int_{-\infty}^{\infty}\int_{-\infty}^{S} f_S(S)\cdot f_R(R)\cdot dR\cdot dS = \int_{-\infty}^{\infty}\int_{-\infty}^{S} f(S,R)\cdot dR\cdot dS \tag{2.28}$$

where $f(S, R)$ is the *joint* probability density of S, R.

The values of the probability of failure computed from Equation (2.28) are normally very small numbers, typically 1×10^{-2} to 1×10^{-5}.

The safety or reliability index is defined according to Equation (2.29) and normally takes values in the range 2–5:

$$\beta = -\Phi^{-1}(Pf) \tag{2.29}$$

where $\Phi^{-1}()$ is the inverse cumulative probability distribution of a unit normal (Gaussian) variate, i.e. a normal variate with a mean of zero and a standard deviation of one.

The relationship between the safety index, β, and the probability of failure, p_f, according to Equation (2.29) is shown plotted in Figure 2.7.

Equations (2.28) and (2.29) can be evaluated exactly when S and R are assumed to have Gaussian (normal) or lognormal (Section C3.2) probability distributions.

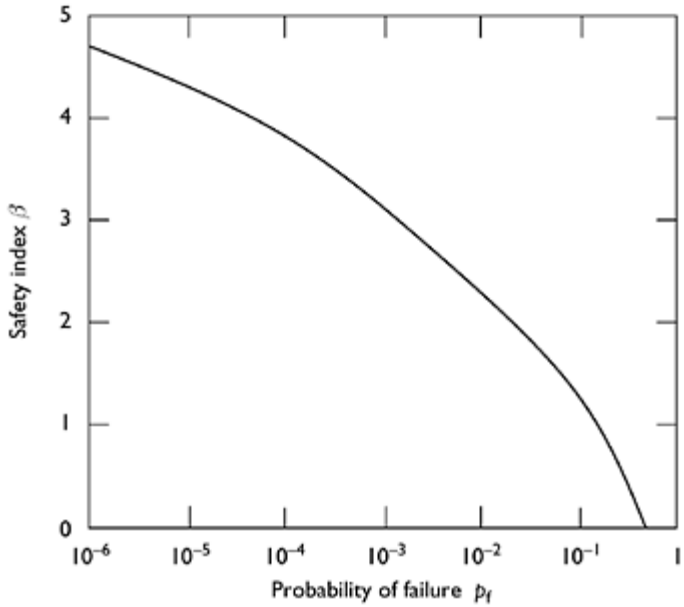

Figure 2.7 Relationship between safety index and probability of failure.

However, in other cases (which includes those involving wind loading), numerical methods must be used. Numerical methods must also be used when, as is usually the case, the load effect, *S*, and resistance, *R*, are treated as combinations (sums and products) of separate random variables with separate probabilistic characteristics.

Details of structural reliability theory and practice can be found in a number of texts on the subject (e.g. Blockley, 1980; Melchers, 1987; Ang and Tang, 1990).

2.6.3 Nominal return period for design wind speeds

The return periods (or annual risk of exceedence) for the nominal design wind speeds in various wind loading codes and standards are discussed in Chapter 15. The most common choice is 50 years. There should be no confusion between return period, *R*, and expected lifetime of a structure, *L*. The return period is just an alternative statement of annual risk of exceedence, e.g. a wind speed with a 50-year return period is one with an expected risk of exceedence of 0.02 (1/50) in any 1 year. However, the risk, r, of exceedence of a wind speed *over the lifetime* can be determined by assuming that all years are statistically independent of each other.

Then,

$$r = 1 - \left[1 - \left(\frac{1}{R}\right)\right]^L \tag{2.30}$$

Equation (2.30) is very similar to Equation (2.4) in which the combined probability of exceedence of a wind speed occurring over a range of wind directions was determined.

Setting both *R* and *L* as 50 years in Equation (2.30), we arrive at a value of *r* of 0.636. There is thus a nearly 64% chance that the 50-year return period wind speed will be exceeded at least once during a 50-year lifetime—i.e. a better than even chance that it *will occur*. Wind loads derived from wind speeds with this level of risk must be factored up when used for ultimate limit states design. Typical values of wind load factor, γ_w, are in the range of 1.4–1.6. Different values may be required for regions with different wind speed/return period relationships.

The use of a return period for the nominal design wind speed substantially higher than the traditional 50 years, avoids the need to have different wind load factors in different regions. This was an important consideration in the revision of the Australian Standard for Wind Loads in 1989 (Standards Australia, 1989), which, in previous editions, required the use of a special ‘Cyclone Factor’ in the regions of northern coastline affected by tropical cyclones. The reason for this factor was the greater rate of change of wind speed with return period in the cyclone regions. A similar ‘hurricane importance factor’ appeared in some editions of the American National Standard (ASCE, 1993), but was later incorporated into the specified basic wind speed (ASCE, 1998).

In AS 1170.2–1989, the wind speeds for ultimate limit states design had a nominal probability of exceedence of 5% in a lifetime of 50 years (a return period of 1000 years approximately).

However, a load factor of 1.0 was applied to the wind loads derived in this way—and this factor was the same in both cyclonic and non-cyclonic regions.

2.6.4 Uncertainties in wind load specifications

A reliability study of structural design involving wind loads requires an estimation of all the uncertainties involved in the specification of wind loads—wind speeds; multipliers for terrain, height, topography, etc.; pressure coefficients; local and area averaging effects, etc. Some examples of this type of study for buildings and communication towers are given by Pham *et al.* (1983, 1992).

2.7 Summary

In Chapter 2, the application of extreme value analysis to the prediction of design wind speeds has been discussed. In particular, the Gumbel and 'peaks over threshold' approaches were described in detail. The need to separate wind speeds caused by wind storms of different types was emphasized and wind direction effects were considered.

The main principles of the application of probability to structural design and safety were also introduced.

References

American Society of Civil Engineers (1993) Minimum design loads for buildings and other structures. ASCE Standard, ANSI/ASCE 7–93, American Society of Civil Engineers, New York.

American Society of Civil Engineers (1998) Minimum design loads for buildings and other structures. ASCE Standard, ANSI/ASCE 7–98, American Society of Civil Engineers, New York.

American Society of Civil Engineers (2006) Minimum design loads for buildings and other structures. ASCE/SEI 7–05, American Society of Civil Engineers, New York.

Ang, A.H. and Tang, W. (1990) *Probability Concepts in Engineering Planning and Design. Volume II. Decision, Risk and Reliability.* Published by the authors.

Blockley, D. (1980) *The Nature of Structural Design and Safety.* Ellis Horwood, Chichester.

Cook, N.J. and Harris, R.I. (2004) Exact and general FT1 penultimate distributions of extreme winds drawn from tail-equivalent Weibull parents. *Structural Safety,* 26:391–420.

Davenport, A.G. (1961) The application of statistical concepts to the wind loading of structures. *Proceedings of the Institution of Civil Engineers,* 19:449–71.

Davison, A.C. and Smith, R.L. (1990) Models for exceedances over high thresholds. *Journal of the Royal Statistical Society, Series B,* 52:339–442.

Fisher, R.A. and Tippett, L.H.C. (1928) Limiting forms of the frequency distribution of the largest or smallest member of a sample. *Proceedings of the Cambridge Philosophical Society Part 2,* 24:180–90.

Freudenthal, A.M. (1947) The safety of structures. *Transactions of ASCE,* 112:125–59.

Freudenthal, A.M. (1956) Safety and the probability of structural failure. *Transactions of ASCE,* 121:1337–97.

Gomes, L. and Vickery, B.J. (1977a) Extreme wind speeds in mixed wind climates. *Journal of Industrial Aerodynamics,* 2:331–44.

Gomes, L. and Vickery, B.J. (1977b) On the prediction of extreme wind speeds from the parent distribution. *Journal of Industrial Aerodynamics,* 2:21–36.

Gringorten, I.I. (1963) A plotting rule for extreme probability paper. *Journal of Geophysical Research,* 68:813–14.

Gumbel, E.J. (1954) Statistical theory of extreme values and some practical applications. *Applied Math Series 33*, National Bureau of Standards, Washington, DC.

Gumbel, E.J. (1958) *Statistics of Extremes.* Columbia University Press, New York.

Holmes, J.D. (2002) A re-analysis of recorded extreme wind speeds in region A. *Australian Journal of Structural Engineering*, 4:29–40.

Holmes, J.D. and Moriarty, W.W. (1999) Application of the generalized Pareto distribution to extreme value analysis in wind engineering. *Journal of Wind Engineering & Industrial Aerodynamics*, 83:1–10.

Holmes, J.D. and Moriarty, W.W. (2001) Response to discussion by N.J.Cook and R.I.Harris of: 'Application of the generalized Pareto distribution to extreme value analysis in wind engineering'. *Journal of Wind Engineering & Industrial Aerodynamics*, 89:225–7.

Hosking, J.R.M., Wallis, J.R. and Wood, E.F. (1985) Estimates of the Generalized extreme value distribution by the method of probability-weighted moments. *Technometrics*, 27: 251–61.

Jenkinson, A.F. (1955) The frequency distribution of the annual maximum (or minimum) values of meteorological elements. *Quarterly Journal of the Royal Meteorological Society*, 81:158–71.

Lechner, J.A., Leigh, S.D. and Simiu, E. (1992) Recent approaches to extreme value estimation with application to wind speeds. Part 1: the Pickands method. *Journal of Wind Engineering & Industrial Aerodynamics*, 41:509–19.

Lieblein, J. (1974) Efficient methods of extreme-value methodology. Report NBSIR 74–602, National Bureau of Standards, Washington, DC.

Melchers, R. (1987) *Structural Reliability—Analysis and Prediction.* Ellis Horwood, Chichester.

Palutikof, J.P., Brabson, B.B., Lister, D.H. and Adcock, S.T. (1999) A review of methods to calculate extreme wind speeds. *Meteorological Applications*, 6:119–32.

Peterka, J.A. and Shahid, S. (1998) Design gust wind speeds in the United States. *ASCE Journal of Structural Engineering*, 124:207–14.

Pham, L., Holmes, J.D. and Leicester, R.H. (1983) Safety indices for wind loading in Australia. *Journal of Wind Engineering & Industrial Aerodynamics*, 14:3–14.

Pham, L., Holmes, J.D. and Yang, J. (1992) Reliability analysis of Australian communication lattice towers. *Journal of Constructional Steel Research*, 23:255–72.

Pugsley, A.G. (1966) *The Safety of Structures.* Edward Arnold, London.

Russell, L.R. (1971) Probabilistic distributions for hurricane effects. *ASCE Journal of Waterways, Harbours and Coastal Engineering*, 97:139–54.

Standards Australia (1989) SAA loading code. Part 2: wind loads. Australian Standard, AS1170.2–1989, Standards Australia, North Sydney, New South Wales, Australia.

Standards Australia (2002) Structural design actions. Part 2: wind actions. Australian/New Zealand Standard, AS/NZS1170.2:2002, Standards Australia, Sydney, New South Wales, Australia.

3
Strong wind characteristics and turbulence

3.1 Introduction

As the earth's surface is approached, frictional forces play an important role in the balance of forces on the moving air. For larger storms such as extra-tropical depressions, this zone extends up to 500–1000 m height. For thunderstorms, the boundary layer is much smaller—probably around 100 m(see Section 3.2.6). The region of frictional influence is called the 'atmospheric boundary layer' and is similar in many respects to the turbulent boundary layer on a flat plate or airfoil at high wind speeds.

Figure 3.1 shows wind speeds recorded at three heights on a tall mast at Sale in southern Australia (as measured by sensitive cup anemometers, during a period of strong wind produced by gales from a synoptic depression (Deacon, 1955)). The records show the main characteristics of fully developed 'boundary-layer' flow in the atmosphere:

- the increase of the average wind speed as the height increases;
- the gusty or turbulent nature of the wind speed at all heights;
- the broad range of frequencies in the gusts in the air flow;
- there is some similarity in the patterns of gusts at all heights, especially for the more slowly changing gusts, or lower frequencies.

The term 'boundary layer' means the region of wind flow affected by friction at the earth's surface, which can extend up to 1 km. The Coriolis forces (Section 1.2.2) become gradually less in magnitude as the wind speed falls near the earth's surface. This causes the geostrophic balance, as discussed in Chapter 1, to be disturbed, and the mean wind vector turns from being parallel to the isobars to having a component towards the low pressure, as the height above the ground reduces. Thus, the mean wind speed may change in direction slightly with height, as well as magnitude. This effect is known as the *Ekman Spiral*. However, the direction change is small over the height range of normal structures and is normally neglected in wind engineering.

The following sections will mainly be concerned with the characteristics of the mean wind and turbulence, near the ground, produced by severe gales in the higher latitudes. These winds have been studied in detail for more than 40 years and are generally well understood, at least over flat homogeneous terrain. The wind and turbulence characteristics in tropical cyclones (Section 1.3.2) and thunderstorm downbursts (Section 1.3.5), which produce the extreme winds in the lower latitudes, are equally important, but are much less well understood. However, existing knowledge of their characteristics is presented in Sections 3.2.5 and 3.2.6. Tornadoes are rare events, but can produce significant damage in some parts of the world. A simple horizontal profile of wind components in a tornado vortex is discussed in Section 3.2.7.

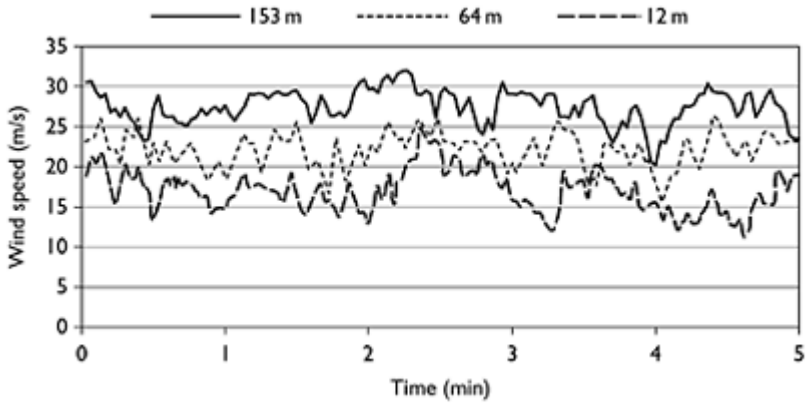

Figure 3.1 Wind speeds at three heights during gales (Deacon, 1955).

3.2 Mean wind speed profiles

3.2.1 The 'logarithmic law'

In this section we will consider the variation of the mean or time-averaged wind speed with height above the ground near the surface (in first 100–200 m—the height range of most structures). In strong wind conditions, the most accurate mathematical expression is the 'logarithmic law'. The logarithmic law was originally derived for the turbulent boundary layer on a flat plate by Prandtl; however, it has been found to be valid in an unmodified form in strong wind conditions in the atmospheric boundary layer near the surface. It can be derived in a number of ways. The following derivation is the simplest and is a form of dimensional analysis.

We postulate that the wind shear, i.e. the rate of change of mean wind speed, $\bar{U}$, with height, is a function of the following variables:

- the height above the ground, *z;*
- the retarding force per unit area exerted by the ground surface on the flow—known as the surface shear stress, τ_0;
- the density of air, ρ_a.

Note that near the ground, the effect of the earth's rotation (Coriolis forces) is neglected. Also because of the turbulent flow, the effect of molecular viscosity can be neglected.

Combining the wind shear with the above quantities, we can form a non-dimensional wind shear:

$$\frac{d\bar{U}}{dz} z \sqrt{\frac{\rho_a}{\tau_0}}$$

$\sqrt{(\tau_0/\rho a)}$ has the dimensions of velocity and is known as the *friction velocity, u_** (note that this is not a physical velocity). Then, as there are no other non-dimensional quantities involved,

$$\frac{d\overline{U}}{dz}\frac{z}{u_*} = \text{a constant, say}\frac{1}{k} \tag{3.1}$$

Integrating,

$$\overline{U}(z) = \frac{u_*}{k}(\log_e z - \log_e z_0) = \frac{u_*}{k}\log_e(z/z_0) \tag{3.2}$$

where z_0 is a constant of integration, with the dimensions of length, known as the *roughness length.*

Equation (3.2) is the usual form of the logarithmic law. *k* is known as *von Karman's constant* and has been found experimentally to have a value of about 0.4. z_0, the roughness length, is a measure of the roughness of the ground surface.

Another measure of the terrain roughness is the *surface drag coefficient, κ,* which is a non-dimensional surface shear stress, defined as:

$$\kappa = \frac{\tau_0}{\rho\overline{U}_{10}^2} = \frac{u_*^2}{\overline{U}_{10}^2} \tag{3.3}$$

where $\bar{U}_{10}$ is the mean wind speed at 10 mheight.

For urban areas and forests, where the terrain is very rough, the height, *z,* in Equation (3.2) is often replaced by an effective height, $(z-z_h)$, where z_h is a 'zero-plane displacement'. Thus, in this case,

$$\overline{U}(z) = \frac{u_*}{k}\log_e\left[\frac{z-z_h}{z_0}\right] \tag{3.4}$$

The zero-plane displacement can be taken as about three-quarters of the general rooftop height.

Usually the most useful way of applying Equation (3.4) is to use it to relate the mean wind speeds at two different heights as follows:

$$\frac{\overline{U}(z_1)}{\overline{U}(z_2)} = \frac{\log_e[(z_1-z_h)/z_0]}{\log_e[(z_2-z_h)/z_0]} \tag{3.5}$$

In the application of Equation (3.3), the 10 m reference height should be taken as 10m above the zero-plane displacement or $(10+z_h)$ metres above the actual ground level.

By applying Equations (3.3) and (3.4) for *z* equal to 10m, a relationship between the surface drag coefficient and the roughness length can be determined:

$$\kappa = \left[\frac{k}{\log_e\left(\frac{10}{z_0}\right)}\right]^2 \tag{3.6}$$

Table 3.1 gives the appropriate value of roughness length and surface drag coefficient for various types of terrain (adapted from the Australian Standard for Wind Loads, AS/NZS 1170.2:2002).

Although the logarithmic law has a sound theoretical basis, at least for fully developed wind flow over homogeneous terrain, these ideal conditions are rarely met in practice. Also the logarithmic law has some mathematical characteristics which may cause problems: first, as logarithms of negative numbers do not exist, it cannot be evaluated for heights, z, below the zero-plane displacement, z_h, and if $z-z_h$ is less than z_0, a negative wind speed is given. Second, it is less easy to integrate. To avoid some of these problems, wind engineers have often preferred to use the power law.

Table 3.1 Terrain types, roughness length and surface drag coefficient

Terrain type	*Roughness length (m)*	*Surface drag coefficient*
Very flat terrain (snow, desert)	0.001–0.005	0.002–0.003
Open terrain (grassland, few trees)	0.01–0.05	0.003–0.006
Suburban terrain (buildings 3–5 m)	0.1–0.5	0.0075–0.02
Dense urban (buildings 10–30m)	1–5	0.03–0.3

3.2.2 The 'power law'

The power law has no theoretical basis but is easily integrated over height—a convenient property when wishing to determine bending moments at the base of a tall structure, for example.

To relate the mean wind speed at any height, z, with that at 10 m(adjusted if necessary for rougher terrains, as described in the previous section), the power law can be written as:

$$\overline{U}(z) = \overline{U}_{10}\left(\frac{z}{10}\right)^{\alpha} \tag{3.7}$$

The exponent, α, in Equation (3.7) will change with the terrain roughness and also with the height range, when matched to the logarithmic law. A relationship that can be used to relate the exponent to the roughness length, z_0, is as follows:

$$\alpha = \left(\frac{1}{\log_e(z_{ref}/z_0)}\right) \tag{3.8}$$

where z_{ref} is a reference height at which the two 'laws' are matched. z_{ref} may be taken as the average height in the range over which matching is required or half the maximum height over which the matching is required.

Figure 3.2 shows a matching of the two laws for a height range of 100m, using Equation (3.8), with z_{ref} taken as 50m. It is clear the two relationships are extremely close, and that the power law is quite adequate for engineering purposes.

3.2.3 Mean wind profiles over the ocean

Over land the surface drag coefficient, κ, is found to be nearly independent of mean wind speed. This is not the case over the ocean, where higher winds create higher waves, and hence higher surface drag coefficients. The relationship between κ and $\bar{U}_{10}$ has been the subject of much study, and a large number of empirical relationships have been derived.

Charnock (1955), using dimensional arguments, proposed a mean wind profile over the ocean, which implies that the roughness length, z_0, should be given by:

$$z_0 = \frac{a u_*^2}{g} = \frac{a \kappa \bar{U}_{10}^2}{g} \tag{3.9}$$

where g is the gravitational constant and a an empirical constant.

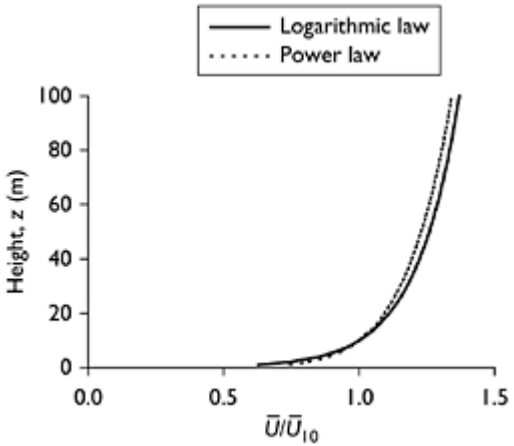

Figure 3.2 Comparison of the logarithmic (z_0=0.02m) and power laws (α=0.128) for mean velocity profile.

Equation (3.9), with the constant a lying between 0.01 and 0.02, is valid over a wide range of wind speeds. It is not valid at very low wind speeds, under aerodynamically smooth conditions and also may not be valid at very high wind speeds, during which the air-sea surface experiences intensive wave breaking and spray.

Substituting for the surface drag coefficient, κ, from Equation (3.6) into Equation (3.9), Equation (3.10) is obtained:

$$z_0 = \frac{a}{g}\left[\frac{k\bar{U}_{10}}{\log_e(10/z_0)}\right]^2 \tag{3.10}$$

(z_h is usually taken as zero over the ocean.)

The implicit nature of the relationship between z_0 (or κ) and $\bar{U}_{10}$ in Equations (3.9) and (3.10) makes them difficult to apply, and several simpler forms have been suggested.

Garratt (1977) examined a large amount of experimental data and suggested a value for *a* of 0.0144. Using this value for *a*, taking *g* equal to 9.81 m/s^2 and *k* equal to 0.41, the relationship between z_0 and $\bar{U}_{10}$ given in Table 3.2 is obtained.

The values given in Table 3.2 can be used in non-tropical cyclone conditions. Mean wind profiles over the ocean in tropical cyclones (typhoons and hurricanes) are discussed in a following section.

Table 3.2 Roughness length over the ocean as a function of mean wind speed

$\bar{U}$10(m/s)	*Roughness length (mm)*
10	0.21
15	0.59
20	1.22
25	2.17
30	3.51

3.2.4 Relationship between upper level and surface winds

For large-scale atmospheric boundary layers in synoptic winds, dimensional analysis gives a functional relationship between a *geostrophic drag coefficient, C_g=u_*/Ug,* and the *Rossby number, Ro=U_g/fz_0. u_** is the friction velocity and U_g is the geostrophic (Section 1.2.3) or gradient wind; *f* is the Coriolis parameter (Section 1.2.2) and z_0 is the roughness length (Section 3.2.1). Lettau (1959) proposed the following relationship based on a number of full-scale measurements:

$$C_g = 0.16Ro^{-0.09} \tag{3.11}$$

Applying the above relationship for a latitude of 40°(*f*=0.935×10^{-4} s^{-1}), a value of U_g equal to 40 m/s and a roughness length of 20 mm gives a friction velocity of 1.40 m/s and, from Equation (3.2), a value of $\bar{U}_{10}$ of 21.8 m/s. Thus, in this case, the wind speed near the surface is equal to 0.54 times the geostrophic wind—the upper level wind away from the frictional effects of the earth's surface.

3.2.5 Mean wind profiles in tropical cyclones

A number of low-level flights into Atlantic Ocean and Gulf of Mexico hurricanes have been made by the National Oceanic and Atmospheric Administration (NOAA) of the United States. However, the flight levels were not low enough to provide useful data on wind speed profiles below about 200m. Measurements from fixed towers are also extremely limited. However, some measurements were made from a 390 mcommunications mast close to the coast near Exmouth, Western Australia, in the late 1970s (Wilson, 1979). SODAR (sonic radar) profiles have been obtained from typhoons on Okinawa, Japan (Amano *et al.*, 1999). These show similar characteristics near the regions of maximum winds: a steep logarithmic-type profile up to a certain height (60–200 m), followed by a layer of strong convection, with nearly constant mean wind speed. More recently probes, known as 'dropwindsondes', have been dropped from aircraft flying through hurricanes and their positions continually tracked by GPS satellites, enabling estimation of horizontal wind speeds to be made (Hock and Franklin, 1999).

Based on averages of the dropwindsonde data, the following mean wind speed profile has been proposed for the eye wall region (Franklin *et al.*, 2003):

$$\overline{U}_z = \overline{U}_{10}\frac{\log_e(z/0.0001)}{\log_e(10/0.0001)} \quad \text{for } z < 300\,\text{m}; \quad \overline{U}(z) = \overline{U}_{100} \quad \text{for } z \geq 300\,\text{m} \tag{3.12}$$

Equation (3.12) is applicable over the ocean or the adjacent coastline. As the tropical cyclone crosses the coast it weakens (see Chapter 1), and the mean wind profiles would be expected to adjust to the underlying ground roughness. However, measurements are virtually non-existent at the present time.

3.2.6 Wind profiles in thunderstorm winds

The most common type of severe wind generated by a thunderstorm is a downburst, discussed in Section 1.3.5. Downbursts may produce severe winds for short periods and are transient in nature, and it is therefore meaningless to try to define a 'mean' wind speed for this type of event (see Figure 1.9). However, we can separate the slowly varying part, representing the downward air flow which becomes a horizontal 'outflow' near the ground, from any superimposed turbulence of higher frequency.

Thanks to Doppler radar measurements in the United States and some tower anemometer measurements in Australia and the United States, there are some indications of the wind structure in the downburst type of thunderstorm wind, including the 'macroburst' and 'microburst' types identified by Fujita (1985). At the horizontal location where the maximum gust occurs, the wind speed increases from ground level up to a maximum value at a height of 50–100m. Above this height, the wind speed reduces relatively slowly.

A useful model of the velocity profiles in the vertical and horizontal directions in a downburst was provided by Oseguera and Bowles (1988). This model satisfies the requirements of fluid mass continuity, but does not include any effect of storm movement. The horizontal velocity component is expressed as:

$$U = \left(\frac{\lambda R^2}{2r}\right)\left[1 - e^{-(r/R)^2}\right]\left(e^{-z/z^*} - e^{-z/\varepsilon}\right) \tag{3.13}$$

where r is the radial coordinate from the centre of the downburst; R the characteristic radius of the downburst 'shaft'; z the height above the ground; z^* a characteristic height out of the boundary layer; ε a characteristic height in the boundary layer; and λ a scaling factor, with dimensions of $[\text{time}]^{-1}$.

The velocity profile at the radius of maximum winds (r=1.121R) is shown in Figure 3.3. The profile clearly shows a maximum at the height of the boundary layer on the ground surface. Radar observations have shown that this height is 50–100 m in actual downbursts.

3.2.7 Wind profiles in tornadoes

There have been many studies of the wind structure in tornadoes based on full-scale studies using photogrammetry and portable Doppler radars (see also Section 1.3.4), laboratory studies of tornado-like vortices and theoretical analyses.

The simplest model of horizontal wind profile in a tornado is based on the Rankine, or combined, vortex (Figure 3.4). This consists of an inner 'core' with solid body rotation, in which the product of the tangential wind velocity component, U_θ, and the radius from the centreline of the tornado is a constant. In the outer region *(r>R)*, the tangential velocity component is inversely proportional to the radius, r. This satisfies the equation of angular momentum (Lewellen, 1976), except the discontinuity at r equal to R.

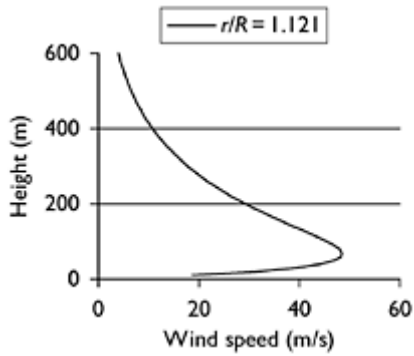

Figure 3.3 Profile of horizontal velocity near the ground during a stationary downburst.

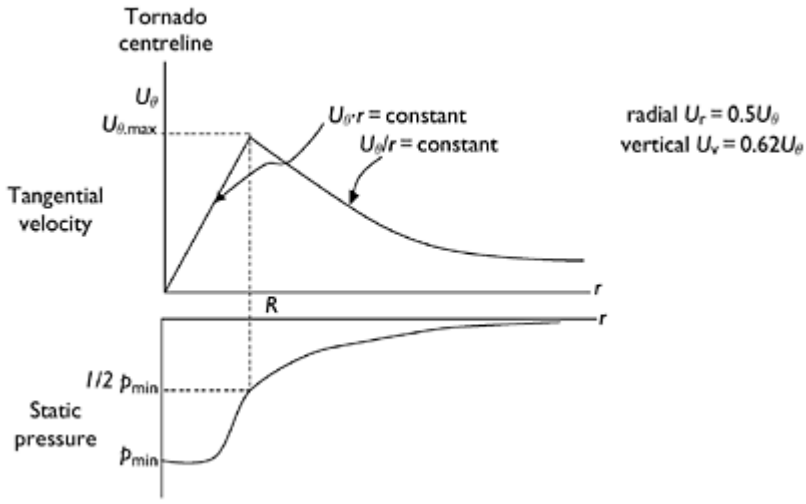

Figure 3.4 Velocity components in a tornado.

This model does not define the radial, U_r, or vertical, U_v, velocity components, but empirical values of these are shown in Figure 3.4.

Several alternative theoretical models are discussed by Lewellen (1976).

3.3 Turbulence

The general level of turbulence or 'gustiness' in the wind speed such as that shown in Figure 3.1 can be measured by its standard deviation or root-mean-square. First we subtract out the steady or mean component (or the slowly varying component in the case of a transient storm, like a thunderstorm), then quantify the resulting deviations. As both positive and negative deviations can occur, we first square the deviations before averaging them, and finally the square root is taken to give a quantity with the units of wind speed. Mathematically, the formula for standard deviation can be written as:

$$\sigma_u = \left\{ \frac{1}{T} \int_0^T \left[U(t) - \overline{U} \right]^2 \mathrm{d}t \right\}^{1/2} \tag{3.14}$$

where $U(t)$ is the total velocity component in the direction of the mean wind, equal to $\bar{U}+u(t)$, where $u(t)$ is the 'longitudinal' turbulence component, i.e. the component of the fluctuating velocity in the mean wind direction.

Other components of turbulence in the lateral horizontal direction denoted by $v(f)$ and in the vertical direction denoted by $w(t)$ are quantified by their standard deviations σ_v and σ_w, respectively.

3.3.1 Turbulence intensities

The ratio of the standard deviation of each fluctuating component to the mean value is known as the *turbulence intensity* of that component.

Thus,

$I_u=\sigma_u/\bar{U}$ (longitudinal) (3.15)

$I_v=\sigma_v/\bar{U}$ (lateral) (3.16)

$I_w=\sigma_w/\bar{U}$ (vertical) (3.17)

Near the ground, in gales produced by large-scale depression systems, measurements have found that the standard deviation of longitudinal wind speed, σ_u, is equal to $2.5u_*$ to a good approximation, where u_* is the friction velocity (Section 3.2.1). Then the turbulence intensity, I_u, is given by:

$$I_u = \frac{2.5u_*}{(u_*/0.4)\log_e(z/z_0)} = \frac{1}{\log_e(z/z_0)} \tag{3.18}$$

Thus, the turbulence intensity is simply related to the surface roughness, as measured by the roughness length, z_0. For a rural terrain, with a roughness length of 0.04 m, the longitudinal turbulence intensities for various heights above the ground are given in Table 3.3.

Thus, the turbulence intensity decreases with height above the ground.

The lateral and vertical turbulence components are generally lower in magnitude than the corresponding longitudinal value. However, for well-developed boundary-layer winds, simple relationships between standard deviation and the friction velocity u_* have been suggested. Thus, approximately the standard deviation of lateral (horizontal) velocity, σ_v, is equal to 2.20_{u*}, and for the vertical component, σ_w is given approximately by $1.3-1.4_{u*}$. Then equivalent expressions to Equation (3.18) for the variation of I_v and I_w with height can be derived:

$$I_v \cong 0.88/\log_e(z/z_0) \tag{3.19}$$

$$I_w \cong 0.55/\log_e(z/z_0) \tag{3.20}$$

The turbulence intensities in tropical cyclones (typhoons and hurricanes) are generally believed to be higher than those in gales in temperate latitudes. Choi (1978) found that the longitudinal turbulence intensity was about 50% higher in tropical cyclone winds compared to synoptic winds. From measurements on a tall mast in north-western Australia during the passage of severe tropical cyclones, convective ‘squall-like’

turbulence was observed (Wilson, 1979). This was considerably more intense than the 'mechanical turbulence' seen closer to the ground and was associated with the passage of bands of rain clouds.

Table 3.3 Longitudinal turbulence intensities for rural terrain (z_0=0.04m)

Height, z (m)	I_u
2	0.26
5	0.21
10	0.18
20	0.16
50	0.14
100	0.13

Turbulence intensities in thunderstorm downburst winds are even less well defined than for tropical cyclones. However, the Andrews Air Force Base event of 1983 (Figure 1.9) indicates a turbulence 'intensity' of the order of 0.1 (10%) superimposed on the underlying transient flow (see also Section 3.3.7).

3.3.2 Probability density

As shown in Figure 3.1, the variations of wind speed in the atmospheric boundary layer are generally random in nature and do not repeat in time. The variations are caused by eddies or vortices within the air flow, moving along at the mean wind speed. These eddies are never identical, and we must use statistical methods to describe the gustiness.

The probability density, $f_u(u_0)$, is defined so that the proportion of time that the wind velocity, $U(t)$, spends in the range u_0+d_u is $f_u(u_0) \cdot du$. Measurements have shown that the wind velocity components in the atmospheric boundary layer follow closely the Normal or Gaussian probability density function, given by:

$$f_u(u) = \frac{1}{\sigma_u\sqrt{2\pi}} \exp\left[-\frac{1}{2}\left(\frac{u-\bar{U}}{\sigma_u}\right)^2\right] \qquad (3.21)$$

This function has the characteristic bell shape. It is defined only by the mean value, $\bar{U}$, and standard deviation, σu(see also Section C3.1 in Appendix C).

Thus, with the mean value and standard deviation, the probability of any wind velocity occurring can be estimated.

3.3.3 Gust wind speeds and gust factors

In many design codes and standards for wind loading (see Chapter 15), a peak gust wind speed is used for design purposes. The nature of wind as a random process means that the peak gust within an averaging period of, say, 10min is itself also a random variable. However, we can define an *expected*, or average, value within the 10min period. Assuming that the longitudinal wind velocity has a Gaussian probability distribution, it can be shown that the expected peak gust, $\hat{U}$, is given approximately by:

$$\hat{U}=\bar{U}+g\sigma_u \tag{3.22}$$

where g is a peak factor equal to about 3.5.

Thus, for various terrains, a profile of peak gust with height can be obtained. Note, however, that gusts do not occur simultaneously at all heights, and such a profile would represent an envelope of the gust wind speed with height.

Meteorological instruments used for long-term wind measurements do not have a perfect response, and the peak gust wind speed they measure is dependent on their response characteristics. The response is usually indicated as an equivalent averaging time. For instruments of the pressure tube type (such as the Dines anemometer used for many years in the United Kingdom and Australia) and small cup anemometers, an averaging time of 2–3 s is usually quoted.

The *gust factor*, G, is the ratio of the maximum gust speed within a specified period to the mean wind speed. Thus, in general,

$$G=\frac{\hat{U}}{\overline{U}} \tag{3.23}$$

For gales (synoptic winds in temperate climates), the magnitude of gusts for various averaging times, τ, was studied by Durst (1960) and Deacon (1965). Deacon gave gust factors at a height of 10m, based on a 10min mean wind speed, of about 1.45 for ‘open country with few trees’ and 1.96 for suburban terrain.

Several authors have provided estimates of gust factors over land, for tropical cyclones or hurricanes. Based on measurements in typhoons in Japan, Ishizaki (1983) proposed the following expression for gust factor, G:

$$G=\frac{\hat{U}_{1\text{sec}}}{\overline{U}_{T\text{sec}}}=1+0.5\,I_u\ln(T/t) \tag{3.24}$$

where I_u is the longitudinal turbulence intensity (Section 3.3.1), T the averaging period for the mean speed and t the gust duration.

A typical value of I_u at 10 m height in open country is 0.2. Then, taking T equal to 600 s and s equal to 2 s, Equation (3.24) gives a value of gust factor of 1.57. A study by Krayer and Marshall (1992) of four US hurricanes gave a similar value of 1.55. These values are based on tropical cyclone winds with a wide range of wind speeds, to values as low as 10 m/s.

An analysis by Black (1992), which appeared to be based on higher wind speeds in hurricanes, gave a higher value of 1.66 for the gust factor, $\hat{U}_{2s,10m}/\bar{U}_{10min,10m}$.

3.3.4 Wind spectra

The probability density function (Section 3.3.2) tells us something about the magnitude of the wind velocity, but nothing about how slowly or quickly it varies with time. In order to describe the distribution of turbulence with frequency, a function called the *spectral density*, usually abbreviated to 'spectrum', is used. It is defined so that the contribution to the variance (σ_u^2, or square of the standard deviation), in the range of frequencies from n to $n+\mathrm{d}n$, is given by $S_u(n) \cdot \mathrm{d}n$, where $S_u(n)$ is the spectral density function for $u(t)$. Then, integrating over all frequencies,

$$\sigma_u^{\,2} = \int_0^\infty S_u(n)\mathrm{d}n \tag{3.25}$$

There are many mathematical forms that have been used for $S_u(n)$ in meteorology and wind engineering. The most common and mathematically correct of these for the longitudinal velocity component (parallel to the mean wind direction) is the von Karman–Harris form (developed for laboratory turbulence by von Karman (1948) and adapted for wind engineering by Harris (1968)). This may be written in several forms; Equation (3.26) is a commonly used non-dimensional form:

$$\frac{n \cdot S_u(n)}{\sigma_u^{\,2}} = \frac{4\left(\frac{n\ell_u}{\bar{U}}\right)}{\left[1+70.8\left(\frac{n\ell_u}{\bar{U}}\right)^2\right]^{5/6}} \tag{3.26}$$

where ℓ, is a turbulence length scale.

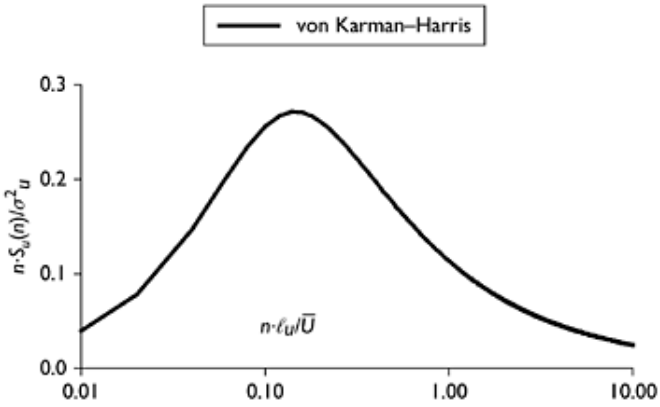

Figure 3.5 Normalised spectrum of longitudinal velocity component (von Karman–Harris).

In this form, the curve of $n \cdot S_u(n)/\sigma_u^2$ versus $n/\bar{U}$ has a peak; the value of ℓ_u determines the value of $(n/\bar{U})$ at which the peak occurs—the higher the value of ℓ_u, the higher the value of $(\bar{U}/n)$ at the peak or λ, known as the 'peak wavelength'. For the von Karman–Harris spectrum, λ is equal to $6.85\ell_u$. The length scale, ℓ_u, varies with both terrain roughness and height above the ground. The form of the von Karman–Harris spectrum is shown in Figure 3.5.

The other orthogonal components of atmospheric turbulence have spectral densities with somewhat different characteristics. The spectrum of vertical turbulence is the most important of these, especially for horizontal structures such as bridges. A common mathematical form for the spectrum of vertical turbulence (w') is the Busch and Panofsky (1968) form which can be written as:

$$\frac{n \cdot S_w(n)}{\sigma_w^2} = \frac{2.15\left(\frac{nz}{\bar{U}}\right)}{\left[1 + 11.16\left(\frac{nz}{\bar{U}}\right)^{5/3}\right]} \tag{3.27}$$

In this case, the length scale is directly proportional to the height above the ground, z. The Busch and Panofsky spectrum for vertical turbulence (w') is shown in Figure 3.6.

3.3.5 Correlation

Covariance and *correlation* are two important properties of wind turbulence in relation to wind loading. The latter is the same quantity that is calculated in linear regression analysis. In the present context, it relates the fluctuating wind velocities at two points in space or wind pressures at two points on a building (such as a roof).

For example, consider the wind speed at two different heights on a tower (for example, Figure 3.1). The covariance between the fluctuating (longitudinal) velocities at two different heights, z_1 and z_2, is defined according to:

$$\overline{u'(z_1)u'(z_2)} = \frac{1}{T}\int_0^T \left[U(z_1,t) - \overline{U}(z_1)\right]\left[U(z_2,t) - \overline{U}(z_2)\right]\mathrm{d}t \tag{3.28}$$

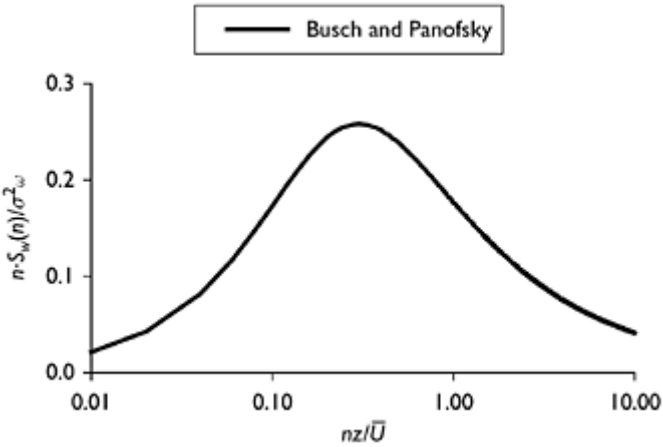

Figure 3.6 Normalized spectrum of vertical velocity component (Busch and Panofsky).

Thus, the covariance is the product of the fluctuating velocities at the two heights, averaged over time. Note that the mean values, $\bar{U}(z_1)$ and $\bar{U}(z_2)$, are subtracted from each velocity in the right-hand side of Equation (3.28). Note that in the special case when z_1 is equal to z_2, the right-hand side is then equal to the variance (σ_w^2) of the fluctuating velocity at the single height.

The correlation coefficient, ρ, is defined by:

$$\rho = \frac{\overline{u'(z_1)u'(z_2)}}{\sigma_w(z_1)\cdot\sigma_u(z_2)} \tag{3.29}$$

When z_1 is equal to z_2, the value of ρ is +1 (i.e. we have full correlation). It can be shown that ρ must lie between −1 and +1. A value of 0 indicates no correlation (i.e. no statistical relationship between the wind velocities)—this usually occurs when the heights z_1 and z_2 are widely separated.

The covariance and correlation are very useful in calculating the fluctuating wind loads on tall towers, large roofs, etc. and for estimating span reduction factors for transmission lines. In the latter case, the points would be separated horizontally, rather than vertically.

A mathematical function which is useful for describing the correlation, ρ, is the exponential decay function:

$$\rho \approx \exp[-C|z_1 - z_2| \tag{3.30}$$

This function is equal to +1 when z_1 is equal to z_2 and tends to zero when $|z_1 - z_2|$ becomes very large (very large separations).

Figure 3.7 shows Equation (3.30) with C equal to (1/40) m^{-1}. It is compared with some measurements of longitudinal velocity fluctuations in the atmospheric boundary, at a height of 13.5 m, with horizontal separations, over urban terrain (Holmes, 1973).

3.3.6 Co-spectrum and coherence

When considering the resonant response of structures to wind (Chapter 5), the correlation of wind velocity fluctuations from separated points *at different frequencies* is important. For example, the correlations of vertical velocity fluctuations with span-wise separation at the natural frequencies of vibration of a large-span bridge are important in determining its response to buffeting.

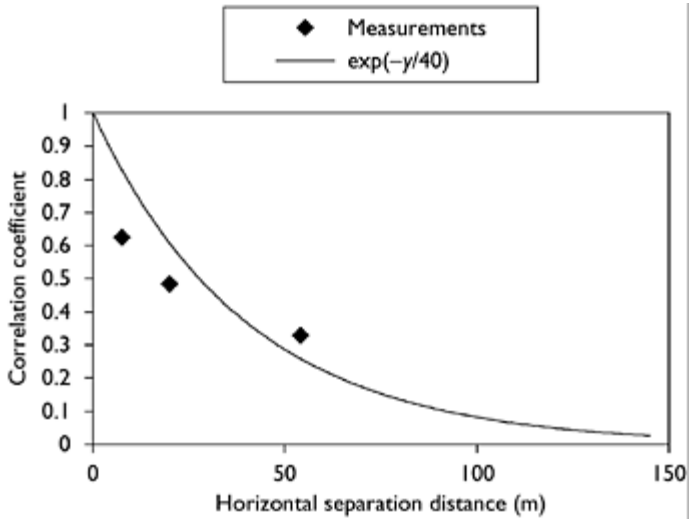

Figure 3.7 Cross-correlation of longitudinal velocity fluctuations in the atmospheric boundary layer at a height of 13.5 m (Holmes, 1973).

The frequency-dependent correlation can be described by functions known as the *cross-spectral density*, *co-spectral density* and *coherence*. Mathematical definitions of these functions are given by Bendat and Piersol (1999) and others. The cross-spectral density, as well as being a function of frequency, is a complex variable, with real and imaginary components. The co-spectral density is the real part and may be regarded as a frequency-dependent covariance (Section 3.3.5). The coherence is a normalized magnitude of the cross-spectrum, approximately equivalent to a frequency-dependent correlation coefficient. The normalized co-spectrum is very similar to coherence, but does not include the imaginary components; this is in fact the relevant quantity when considering the wind forces from turbulence on structures.

The normalized co-spectrum and coherence are often represented by an exponential function of separation distance and frequency:

$$\rho(\Delta z, n) = \exp\left[-\left(\frac{k \cdot n \cdot \Delta z}{\overline{U}}\right)\right] \tag{3.31}$$

where k is an empirical constant, used to fit measured data; a typical range of values for atmospheric turbulence is 10–20. Δz is the vertical separation distance. A similar function is used to represent the co-spectrum when lateral (horizontal) separations, Δy, are considered.

As for Equation (3.30), Equation (3.31) does not allow negative values—a theoretical problem, but of little practical significance. A more important disadvantage is that it implies full correlation at very low frequencies, no matter how large the separation distance, Δz. As the equation only needs to be evaluated at high frequencies corresponding to resonant frequencies, this is also not a great disadvantage.

More mathematically acceptable (but more complex) expressions for the normalized co-spectrum and coherence are available (e.g. Deaves and Harris, 1978).

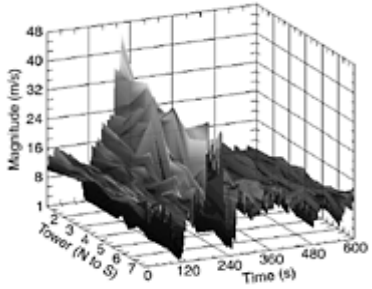

Figure 3.8 Space-time history of a rear-flank downdraft at 10 m height at Lubbock, Texas—June 4, 2002 (image provided by Kirsten Orwig and John Schroeder, Texas Tech University). *Note:* Data shown for Towers 1 and 7 were extrapolated from 3m height; values shown for Tower 2 were interpolated from Towers 1 and 3.

3.3.7 Turbulence in a downdraft

The ‘rear-flank’ thunderstorm downdraft recorded by several towers near Lubbock, Texas, on 4 June 2002, gave a unique opportunity to study the fluctuating wind characteristics, near the ground, in a severe event of this type.

Figure 3.8 shows space-time histories from several anemometer towers at 10 mheight, for this event. This plot shows a series of ‘ridges’ which indicates remarkable similarity between time histories over a lateral distance of more than 1 km.

An individual time history from one tower is shown in Figure 3.9(a). By applying a simple moving-average filter, a smoothed time history that shows the main features of the event can be extracted. This is shown in Figure 3.9(b), in which a 40s moving average has been applied; this record can be called a ‘running mean’. Subtracting the ‘filtered’ history from the original ‘unfiltered’ history results in a residual time history that is more or less random in nature and can be described as ‘turbulence’ (Figure 3.9(c)). This is a non-stationary time history, and the conventional ‘turbulence intensity’ (Section 3.3.1), as defined for stationary synoptic winds, cannot be used here in the same way. However, Figure 3.9(a) shows that the level of random fluctuation varies with the running mean (Figure 3.9(b)), with an approximate ‘intensity’ of 10%. This is somewhat lower than the level obtained in stationary boundary-layer winds at this height in open country (for example, Table 3.3 gives a value of 18%), but is similar to that obtained in the Andrews AFB downburst (Figure 1.9).

Data such as that shown in Figure 3.9 will need further analysis in the future to understand the characteristics of this type of strong wind event, for applications such as the dynamic response of structures (Chapter 5).

3.4 Modification of wind flow by topography

Mean and gust wind speeds can be increased considerably by natural and man-made topography in the form of escarpments, embankments, ridges, cliffs and hills. These effects were the subject of considerable research in the 1970s and 1980s, with the incentive of the desire to exploit wind power and to optimize the siting of wind turbines. This work greatly improved the prediction of mean wind speeds over shallow topography. Less well defined are the speed-up effects on turbulence and gust wind speeds and the effects of steep topography—often of interest with respect to structural design.

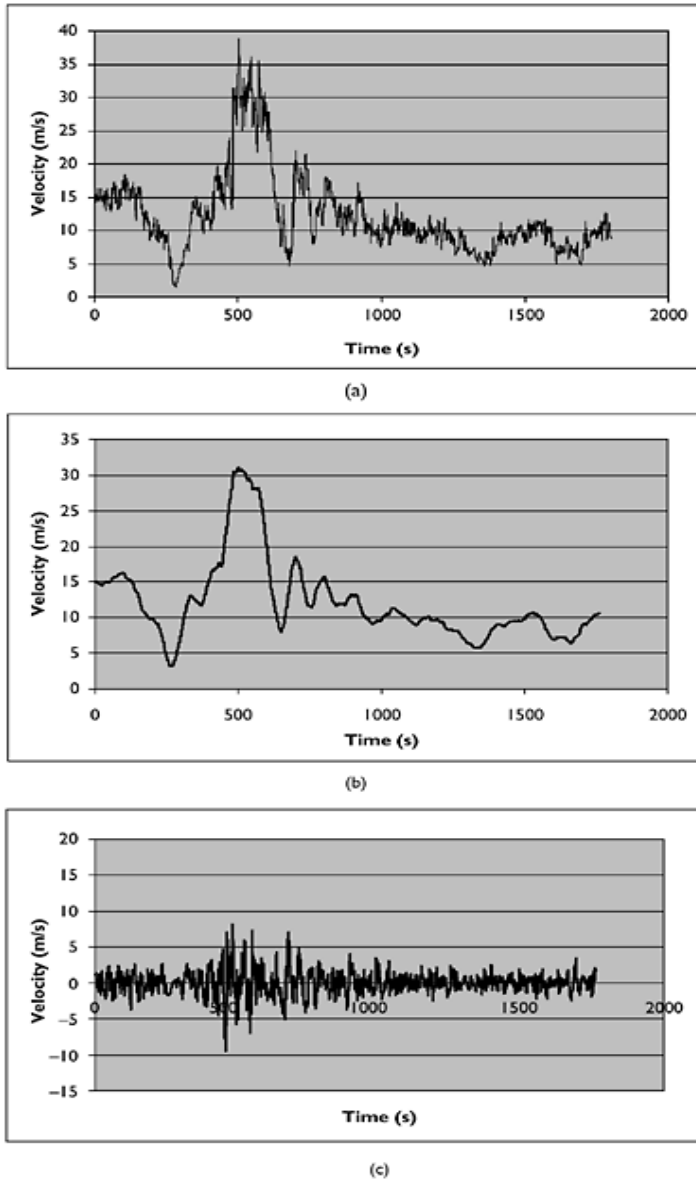

Figure 3.9 Time histories from rear-flank downdraft, June 4, 2002, Lubbock, Texas, (a) Velocities as recorded (unfiltered record); (b) time history filtered with 40 s moving-average filter; (c) residual 'turbulence' obtained by subtraction.

3.4.1 General effects of topography

Figure 3.10 shows the *general* features of boundary-layer wind flow over a shallow escarpment, a shallow ridge, a steep escarpment and a steep ridge.

As the wind approaches a shallow feature, its speed first reduces slightly as it encounters the start of the slope upwards. It then gradually increases in speed as it flows up the slope towards the crest. The maximum speed-up occurs at the crest, or slightly upwind of it. Beyond the crest, the flow speed gradually reduces to a value close to that well upwind of the topographic feature; the adjustment is somewhat faster for a feature with a downwind slope such as a ridge than for an escarpment with a plateau downwind of the crest.

On steeper features, flow 'separation' (see also Section 4.1) may occur, as the flow is not able to overcome the increasing pressure gradients in the along-wind direction. Separations may occur at the start of the upwind slope, immediately downwind of the crest, and on the downwind slope for a ridge.

For steeper slopes (greater than about 0.3), the upwind separation 'bubble' presents an 'effective slope' of approximately constant value, independent of the actual slope underneath. This is often used in codes and standards to specify an upper limit to the speed-up effects of an escarpment or ridge.

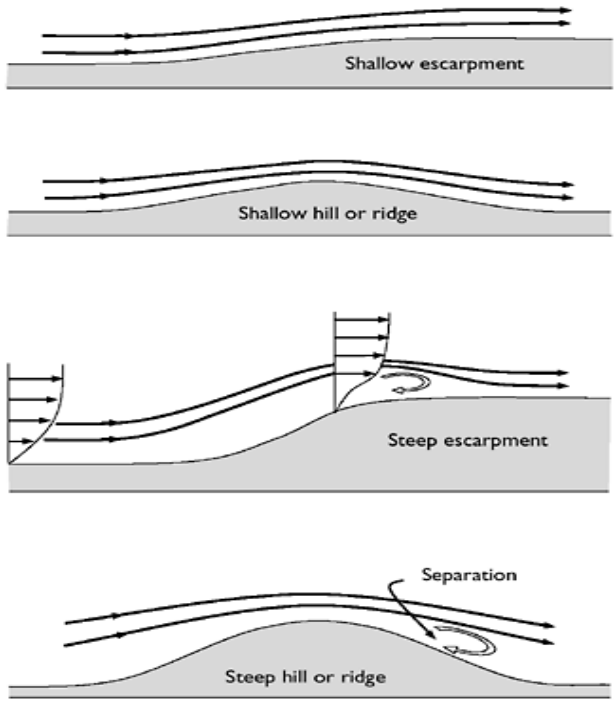

Figure 3.10 Flow over shallow and steep topography.

The speed-up effects are greatest near the surface and reduce with height above the ground. This can have the effect of producing mean velocity profiles, near the crest of a topographic feature, that are nearly constant or have a peak (see Figure 3.10).

The above discussion relates to topographic features, which are two-dimensional in nature, i.e. they extend for an infinite distance normal to the wind direction. This may be a sufficient approximation for many long ridges and escarpments. Three-dimensional effects occur when air flow can occur around the ends of a hill or through gaps or passes. These alternative air paths reduce the air speeds over the top of the feature and generally reduce the speed-up effects. For structural design purposes, it is often convenient, and usually conservative, to ignore the three-dimensional effects and to calculate wind loads only for the speed-up effects of the upwind and downwind slopes parallel to the wind direction of interest.

3.4.2 Topographic multipliers

The definition of topographic multiplier used in this book is as follows:

$$\text{Topographic multiplier} = \frac{\text{Wind speed at height, } z, \text{ above the feature}}{\text{Wind speed at height, } z, \text{ above the flat ground upwind}} \tag{3.32}$$

This definition applies to mean, peak gust and standard deviation wind speeds, and these will be denoted by $\overline{M}_t$, $\hat{M}_t$ and M'_t, and M'_t, respectively.

Topographic multipliers measured in full scale or in wind tunnels or calculated by computer programs can be greater or less than one. However, in the cases of most interest for structural design, we are concerned with speed-up effects for which the topographic multiplier for mean or gust wind speeds will exceed unity.

3.4.3 Shallow hills

The analysis by Jackson and Hunt (1975) of the mean boundary-layer wind flow over a shallow hill produced the following form for the mean topographic multiplier:

$$\overline{M}_t = 1 + ks\phi \tag{3.33}$$

where ϕ is the upwind slope of the topographic feature; k a constant for a given shape of topography; and s a position factor.

Equation (3.33) has been used in various forms for specifying topographic effects in several codes and standards. It indicates that the 'fractional speed-up', equal to $(\overline{M}_t - 1)$, is directly proportional to the upwind slope, ϕ. The latter is defined as $H/2L_u$, where H is the height of the crest above level ground upwind and L_u the horizontal distance from the crest to where the ground elevation drops to $H/2$.

Taylor and Lee (1984) proposed the following values of the constant, *k*, for various types of topography:

- 4.0 for two-dimensional ridges,
- 1.6 for two-dimensional escarpments, and
- 3.2 for three-dimensional (axisymmetric) hills.

The position factor, *s*, is 1.0 close to the crest of the feature and falls upwind and downwind and with height, *z*, above local ground level. The reduction of *s* with height is more rapid near the ground, becoming more gradual as *z* increases.

To a first approximation, the longitudinal turbulence component, σ_u, does not change over the hill or escarpment. This results in the following equation for the gust topographic multiplier, $\hat{M}_t$:

$$\hat{M}_t = 1 + k' s \phi \tag{3.34}$$

where k' is a constant for the gust multiplier, related to *k* by:

$$k' = \frac{k}{1 + g\left(\frac{\sigma_u}{\bar{U}}\right)} \tag{3.35}$$

$(\sigma_u/\bar{U})$ is the longitudinal turbulence intensity (over flat level ground) defined in Section 3.3.1, and *g* is the peak factor (Section 3.3.3).

Equations (3.33)–(3.35) show that the gust topographic multiplier is lower than the mean topographic multiplier for the same type of topography and height above the ground.

There is a slight dependence of the topographic multipliers on the Jensen number (Section 4.4.5) based on the hill height (H/Z_0).

3.4.4 Steep hills, cliffs and escarpments

Once the upwind slope of a hill or escarpment reaches a value of about 0.3 (about 17°), separations occur on the upwind face (Figure 3.10) and the simple formulae given in Section 3.4.3 cannot be applied directly.

For slopes between about 0.3 and 1 (17°–45°), the separation bubble on the upwind slope presents an effective slope to the wind which is relatively constant, as discussed in Section 3.4.1. The topographic multipliers, at or near the crest, are therefore also fairly constant with upwind slope in this range. Thus, for this range of slopes, Equations (3.33) and (3.34) can be applied with ϕ replaced by an effective slope ϕ', equal to about 0.3 (Figure 3.11).

For slopes greater than about 1, e.g. steep cliffs, the flow stream lines near ground level at the crest originate from the upwind flow at levels near cliff height above the upwind ground level, rather than near ground level upwind (Figure 3.12). The concept of the topographic multiplier as defined by Equation (3.32) is less appropriate in such cases. Some of the apparent speed-up is caused by the upstream boundary-layer profile rather than a perturbation produced by the hill or cliff.

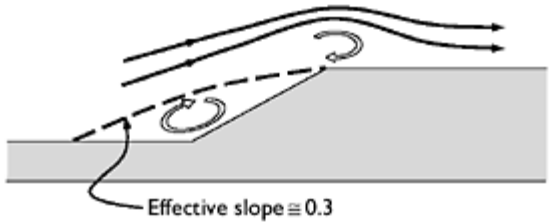

Figure 3.11 Effective upwind slope for steep escarpments.

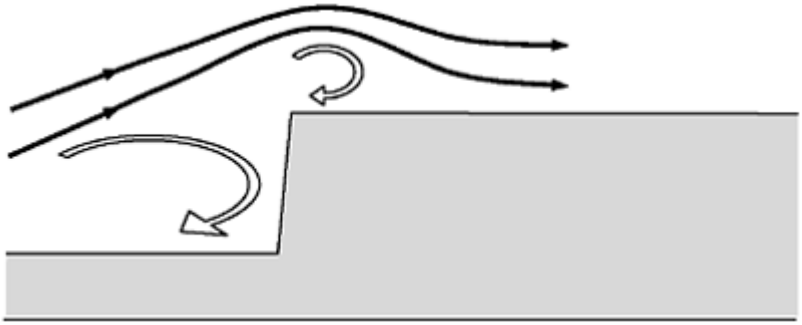

Figure 3.12 Wind flow over a steep cliff.

An additional complication for steep features is that separations can occur at or downwind of the crest (see Figure 3.10). Separated flow was found within the first 50 mheight above the crest of a 480 m high feature, with an upwind slope of only 0.48 (average angle of 26°), in both full-scale and 1/1000 scale wind-tunnel measurements (Glanville and Kwok, 1997). This has the effect of decreasing the mean velocity and increasing the turbulence intensity, as shown in Figure 3.13.

3.4.5 Effect of topography on tropical cyclones and thunderstorm winds

The effect of topographic features on wind near the ground in tropical cyclones and thunderstorm downbursts is much less clearly understood than those in the well-developed boundary layers of large-scale synoptic systems.

Tropical cyclones are large storms with similar boundary layers to extra-tropical depressions on their outer edges. Near the region of strongest winds, they appear to have much lower boundary-layer heights—of the order of 100m. Topographic features greater than this height would therefore be expected to interact with the structure of the storm itself.

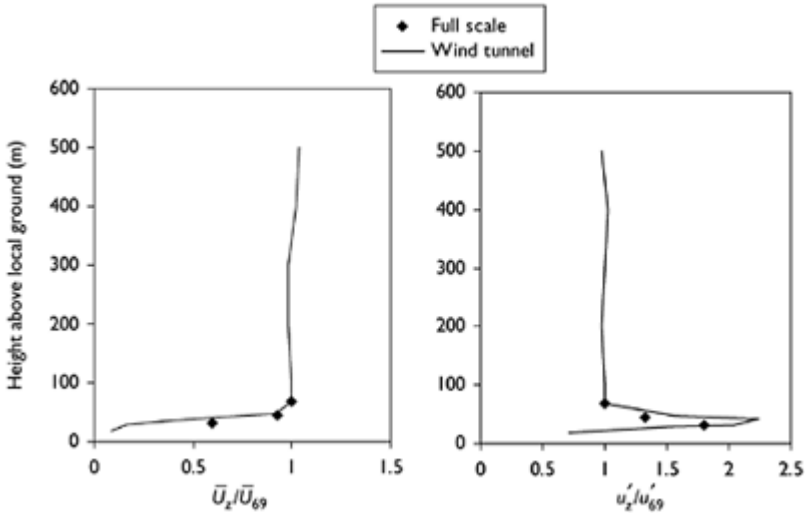

Figure 3.13 Mean velocity profile and r.m.s. longitudinal turbulence velocity near the crest of a steep escarpment (H=480m, upwind slope=0.48).

Thunderstorm downdrafts also have 'boundary layers' with peaks in the velocity profiles at 50–100m. They also do not have fully developed boundary-layer velocity profiles. There have been some basic studies using wind-tunnel jets impinging on a flat board (Letchford and Illidge, 1999; Wood *et al.*, 1999) to indicate considerably lower topographic multipliers compared with developed thick boundary-layer flows. However, the effect of forward motion of the storm is uncertain.

3.5 Change of terrain

When strong winds in a fully developed boundary layer encounter a change of surface roughness, e.g. winds from open country flowing over the suburbs of a town or city, a process of adjustment in the turbulent boundary-layer flow properties develops. The adjustment starts at the ground level and gradually moves upwards. The result is the development of an internal boundary layer over the new terrain as shown in Figure 3.14.

Deaves (1981), from numerical studies, developed the following relationships for the horizontal position of the inner boundary layer as a function of its height, *z:*

For flow from smooth terrain (roughness length z_{01}) to rougher terrain (z_{02}) with $z_{01}>z_{02}$*:*

$$x_i(z) = z_{02}\left(\frac{z}{0.36z_{02}}\right)^{4/3} \tag{3.36}$$

For flow from rough terrain (roughness length z_{01}) to smoother terrain (z_{02}) with $z_{01} > z_{02}$:

$$x_i(z) = 14z\left(\frac{z_{01}}{z_{02}}\right)^{1/2} \tag{3.37}$$

Setting z_{02} equal to 0.2m, approximately the value for suburban terrain with low-rise buildings 3–5 m high (see Table 3.1), and z equal to 10m, Equation (3.36) gives a value for $x_i(10)$ of 144m. Beyond this distance, the shape of the mean velocity profile below 10 m has the characteristics of the new terrain. However, the *magnitude* of the mean velocity continues to reduce for many kilometres, until the complete atmospheric boundary layer has fully adjusted to the rougher terrain.

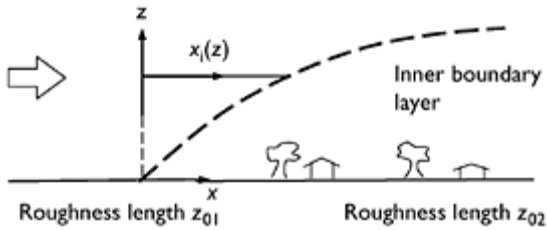

Figure 3.14 Internal boundary-layer development at a change of terrain roughness.

Melbourne (1992) found the *gust* wind speed at a height of 10 m adjusts to a new terrain approximately exponentially with a distance constant of about 2000 m. Thus, the peak gust at a distance x (in metres) into the new terrain (2) can be represented by:

$$\hat{U}_{2,x} = \hat{U}_1 + (\hat{U}_2 - \hat{U}_1)\left[1 - \exp\left(\frac{-x}{2000}\right)\right] \tag{3.38}$$

where $\hat{U}_1$ and $\hat{U}_2$ are the asymptotic gust velocities over fully developed terrain of types 1 (upstream) and 2 (downstream).

Equation (3.38) was found to fit data from a wind tunnel for flow from rough to smooth, as well as smooth to rough, and when there were several changes of roughness.

3.6 Other sources

A well-documented and detailed description of the atmospheric boundary in temperate synoptic systems, for wind-loading purposes, is given in a series of data items published by the Engineering Sciences Data Unit (ESDU, 1974–99). These include the effects of topographic and terrain changes. The mathematical model of atmospheric turbulence in

temperate gale conditions of Deaves and Harris (1978), which used data only from measurements that satisfied rigorous conditions such as very uniform upstream terrain, is also well known and contains mathematically acceptable expressions for turbulence quantities in the atmospheric boundary layer. Cook (1985) has described, for the designer, a structure of the atmospheric boundary layer, which is consistent with the above models.

These references are strongly recommended for descriptions of strong wind structure in temperate zones. However, as discussed in this chapter, the strong wind structure in tropical and semi-tropical locations such as those produced by thunderstorms and tropical cyclones is different, and such models should be used with caution in these regions.

3.7 Summary

In this chapter, the structure of strong winds near the earth's surface, relevant to wind loads on structures, has been described. The main focus has been the atmospheric boundary layer in large synoptic winds over land. The mean wind speed profile and some aspects of the turbulence structure have been described. However, some aspects of wind over the oceans and, in tropical cyclones, thunderstorm downbursts and tornadoes have also been discussed.

The modifying effects of topographic features and of changes in terrain have also been briefly covered.

References

Amano, T., Fukushima, H., Ohkuma, T., Kawaguchi, A. and Goto, S. (1999) The observation of typhoon winds in Okinawa by Doppler sodar. *Journal of Wind Engineering & Industrial Aerodynamics*, 83:11–20.

Bendat, J.S. and Piersol, A.G. (1999) *Random Data: Analysis and Measurement Procedures*, 3rd Edition. Wiley, New York.

Black, P.G. (1992) Evolution of maximum wind estimates in typhoons. *ICSU/WMO Symposium on Tropical Cyclone Disasters*, Beijing, China, 12–18 October.

Busch, N. and Panofsky, H. (1968) Recent spectra of atmospheric turbulence. *Quarterly Journal of the Royal Meteorological Society*, 94:132–48.

Charnock, H. (1955) Wind stress on a water surface. *Quarterly Journal of the Royal Meteorological Society*, 81:639–40.

Choi, E.C.C. (1978) Characteristics of typhoons over the South China Sea. *Journal of Industrial Aerodynamics*, 3:353–65.

Cook, N.J. (1985) *The Designer's Guide to Wind Loading of Building Structures. Part 1 Background, Damage Survey, Wind Data and Structural Classification*. Building Research Establishment and Butterworths, London.

Deacon, E.L. (1955) Gust variation with height up to 150 metres. *Quarterly Journal of the Royal Meteorological Society*, 81:562–73.

Deacon, E.L. (1965) Wind gust speed: averaging time relationship. *Australian Meteorological Magazine*, 51:11–14.

Deaves, D.M. (1981) Computations of wind flow over changes in surface roughness. *Journal of Wind Engineering & Industrial Aerodynamics*, 7:65–94.

Deaves, D.M. and Harris, R.I. (1978) A mathematical model of the structure of strong winds. Report 76, Construction Industry Research and Information Association (UK).

Durst, C.S. (1960) Wind speeds over short periods of time. *Meteorological Magazine*, 89: 181–6.

ESDU (1974–99) Wind speeds and turbulence. Engineering Sciences Data Unit (ESDU International, London), Wind Engineering series volumes la and 1b. ESDU data items 74030, 82026, 83045, 84011, 84031, 85020, 86010, 86035, 91043, 92032.

Franklin, J.L., Black, M.L. and Valde, K. (2003) GPS dropwindsonde wind profiles in hurricanes and their operational implications. *Weather and Forecasting*, 18:32–44.

Fujita, T.T. (1985) The downburst. Report on projects NIMROD and JAWS. Published by the author at the University of Chicago, Chicago, IL.

Garratt, J.R. (1977) Review of drag coefficients over oceans and continents. *Monthly Weather Review*, 105:915–29.

Glanville, M.J. and Kwok, K.C.S. (1997) Measurements of topographic multipliers and flow separation from a steep escarpment. Part II. Model-scale measurements. *Journal of Wind Engineering & Industrial Aerodynamics*, 69–71:893–902.

Harris, R.I. (1968) On the spectrum and auto-correlation function of gustiness in high winds. Report 5273, Electrical Research Association.

Hock, T.F. and Franklin, J.L. (1999) The NCAR GPS dropwindsonde. *Bulletin, American Meteorological Society*, 80:407–20.

Holmes, J.D. (1973) Wind pressure fluctuations on a large building. Ph.D. thesis, Monash University, Australia.

Ishizaki, H. (1983) Wind profiles, turbulence intensities and gust factors for design in typhoonprone regions. *Journal of Wind Engineering & Industrial Aerodynamics*, 13:55–66.

Jackson, P.S. and Hunt, J.C.R. (1975) Turbulent flow over a low hill. *Quarterly Journal of the Royal Meteorological Society*, 101:929–55.

Krayer, W.R. and Marshall, R.D. (1992) Gust factors applied to hurricane winds. *Bulletin, American Meteorological Society*, 73:613–17.

Letchford, C.W. and Illidge, G. (1999) Turbulence and topographic effects in simulated thunderstorm downdrafts by wind tunnel jet. *Proceedings, 10th International Conference on Wind Engineering*, Copenhagen, Denmark, 21–24 June, Balkema, Rotterdam.

Lettau, H.H. (1959) Wind profile, surface stress and geostrophic drag coefficients in the atmospheric boundary layer. *Proceedings, Symposium on Atmospheric Diffusion and Air Pollution*, Oxford, UK, Academic Press, New York.

Lewellen, W.S. (1976) Theoretical models of the tornado vortex. *Symposium on Tornadoes: Assessment of Knowledge and Implications for Man*, Texas Tech University, Lubbock, TX, 22–24 June, pp. 107–43.

Melbourne, W.H. (1992) Unpublished course notes, Monash University.

Oseguera, R.M. and Bowles, R.L. (1988) A simple analytic 3-dimensional downburst model based on boundary layer stagnation flow. N.A.S.A. Technical Memorandum 100632, National Aeronautics and Space Administration, Washington, DC.

Taylor, P.A. and Lee, R.J. (1984) Simple guidelines for estimating windspeed variation due to small scale topographic features. *Climatological Bulletin (Canada)*, 18:3–32.

von Karman, T. (1948) Progress in the statistical theory of turbulence. *Proceedings of the National Academy of Sciences of the United States of America*, 34:530–9.

Wilson, K.J. (1979) Characteristics of the subcloud layer wind structure in tropical cyclones. *International Conference on Tropical Cyclones*, Perth, Western Australia, November.

Wood, G.S., Kwok, K.C.S., Motteram, N. and Fletcher, D.F. (1999) Physical and numerical modelling of thunderstorm downbursts. *Proceedings, 10th International Conference on Wind Engineering*, Copenhagen, Denmark, 21–24 June, Balkema, Rotterdam.

4
Basic bluff-body aerodynamics

4.1 Flow around bluff bodies

Structures of interest in this book can generally be classified as *bluff* bodies with respect to the air flow around them, in contrast to *streamlined* bodies such as aircraft wings and yacht sails (when the boat is sailing across the wind). Figure 4.1 shows the flow patterns around an airfoil (at low angle of attack) and around a two-dimensional body of rectangular cross-section. The flow patterns are shown for steady free-stream flow; turbulence in the approaching flow, which occurs in the atmospheric boundary layer, as discussed in Chapter 3, can modify the flow around a bluff body, as will be discussed later.

It can be seen in Figure 4.1 that the flow streamlines around the airfoil closely follow the contours of the body. The free-stream flow is separated from the surface of the airfoil by only a thin boundary layer, in which the tangential flow is brought to rest at the surface. The flow around the rectangular section (a typical bluff body) in Figure 4.1 is characterized by a 'separation' of the flow at the leading edge corners. The separated flow region is divided from the outer flow by a thin region of high shear and vorticity, a region known as a free shear layer, which is similar to the boundary layer on the airfoil

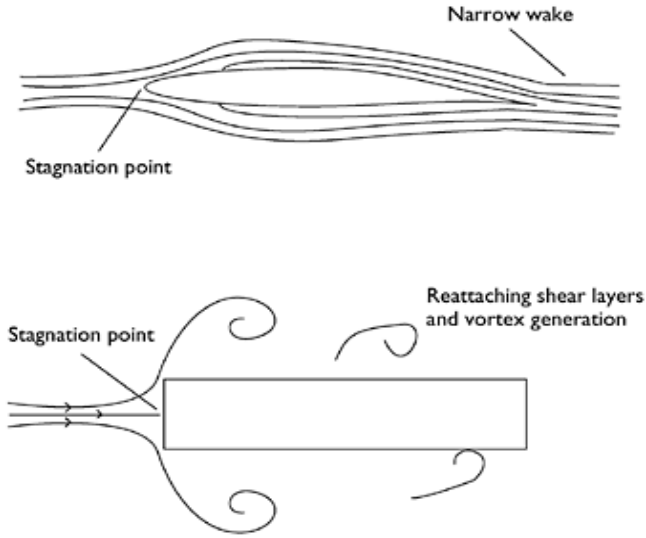

Figure 4.1 Flow around streamlined and bluff bodies.

but not attached to a surface. These layers are unstable in a sheet form and will roll up towards the wake to form concentrated vortices, which are subsequently shed downwind.

In the case of bluff body with a long 'after-body' in Figure 4.1, the separated shear layer 're-attaches' on to the surface. However, the shear layer is not fully stabilized and vortices may be formed on the surface and subsequently roll along the surface.

4.2 Pressure and force coefficients

4.2.1 Bernoulli's equation

The region outside the boundary layers in the case of the airfoil and the outer region of the bluff-body flow are regions of *inviscid* (zero viscosity) and *irrotational* (zero vorticity) flow, and the pressure, p, and velocity, U, in the fluid are related by *Bernoulli's equation:*

$$p + \frac{1}{2}\rho_a U^2 = \text{a constant} \tag{4.1}$$

Denoting the pressure and velocity in the region outside the influence of the body by p_0 and U_0, we have:

$$p + \frac{1}{2}\rho_a U^2 = p_0 + \frac{1}{2}\rho_a U_0^2$$

Hence,

$$p - p_0 = \frac{1}{2}\rho_a \left(U_0^2 - U^2\right)$$

The surface pressure on the body is usually expressed in the form of a non-dimensional *pressure coefficient:*

$$C_p = \frac{p - p_0}{\frac{1}{2}\rho_a U_0^2} \tag{4.2}$$

In the region in which Bernoulli's equation holds,

$$C_p = \frac{\frac{1}{2}\rho_a \left(U_0^2 - U^2\right)}{\frac{1}{2}\rho_a U_0^2} = 1 - \left(\frac{U}{U_0}\right)^2 \tag{4.3}$$

At the stagnation point where U is zero, Equation (4.3) gives a pressure coefficient of one. This is the value measured by a *total* pressure or *pilot* tube pointing into a flow. The pressure $(1/2)\rho_a U_0^2$ is known as the *dynamic* pressure. Values of pressure coefficient near 1.0 also occur on the stagnation point on a circular cylinder, but the largest (mean) pressure coefficients on the windward faces of buildings are usually less than this theoretical value.

In the regions where the flow velocity is greater than U_0, the pressure coefficients are negative. Strictly, Bernoulli's equation is not valid in the separated flow and wake regions, but reasonably good predictions of surface pressure coefficients can be obtained from Equation (4.3) by taking the velocity, U, as that just outside the shear layers and wake region.

4.2.2 Force coefficients

Force coefficients are defined in a similar non-dimensional way to pressure coefficients:

$$C_F = \frac{F}{\frac{1}{2}\rho_a U_0^2 A} \tag{4.4}$$

where F is the total aerodynamic force and A a reference area (not necessarily the area over which the force acts). Often A is a projected frontal area.

In the case of long or two-dimensional bodies, a force coefficient per unit length is usually used:

$$C_f = \frac{f}{\frac{1}{2}\rho_a U_0^2 b} \tag{4.5}$$

where f is the aerodynamic force per unit length and b a reference length, usually the breadth of the structure normal to the wind.

Aerodynamic forces are conventionally resolved into two orthogonal directions. These may be parallel and perpendicular to the wind direction (or mean wind direction in the case of turbulent flow), in which case the axes are referred to as *wind axes*, or parallel and perpendicular to a direction related to the geometry of the body *(body axes)*. These axes are shown in Figure 4.2.

Following the terminology of aeronautics, the terms 'lift' and 'drag' are commonly used in wind engineering for cross-wind and along-wind force components, respectively. Substituting 'L' and 'D' for 'F' in Equation (4.4) gives the definition of *lift and drag coefficients*.

The relationship between the forces and force coefficients resolved with respect to the two axes can be derived using trigonometry, in terms of the angle, a, between the sets of axes, as shown in Figure 4.3. α is called the *angle of attack* (or sometimes the angle of incidence).

4.2.3 Dependence of pressure and force coefficients

Pressure and force coefficients are non-dimensional quantities, which are dependent on a number of variables related to the geometry of the body and to the upwind flow characteristics. These variables can be grouped together into non-dimensional groups, using processes of dimensional analysis or by inspection.

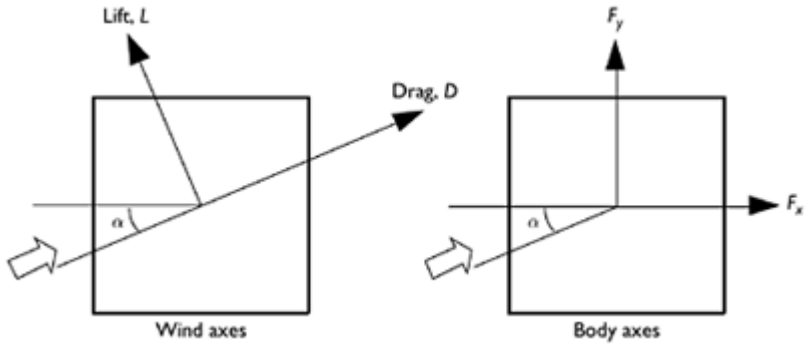

Figure 4.2 Wind axes and body axes.

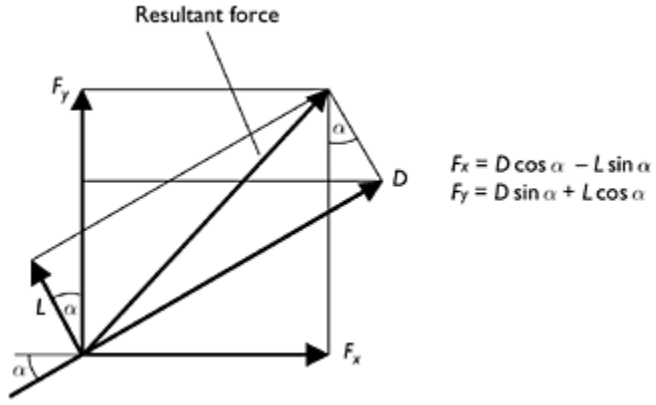

Figure 4.3 Relationship between resolved forces.

Assume that we have a number of bluff bodies of geometrically similar shape, which can be characterized by a single length dimension (e.g. buildings with the same ratio of height, width and length and with the same roof pitch, characterized by their height, *h*). Then the pressure coefficients for pressures at corresponding points on the surface of the body may be a function of a number of other non-dimensional groups: $\pi 1$, $\pi 2$, $\pi 3$, etc. Thus,

$$C_p = f(\pi_1, \pi_2, \pi_3, \ldots) \tag{4.6}$$

Examples of relevant non-dimensional groups are:

- h/z_0 (Jensen number; where z_0 is the roughness length as discussed in Section 3.2.1);
- I_u, I_v, I_w the turbulence intensities in the approaching flow;
- (ℓ_u/h), (ℓ_v/h), (ℓ_w/h) representing ratios of turbulence length scales in the approaching flow to the characteristic body dimension; and
- (Uh/υ), Reynolds number, where υ is the kinematic viscosity of air.

Equation (4.6) is relevant to the practice of wind-tunnel model testing, in which geometrically scaled models are used to obtain pressure (or force) coefficients for application to full-scale prototype structures (see Section 7.4). The aim should be to ensure that all relevant non-dimensional numbers (π_1, π_2, π_3, etc.) should be equal in both model and full scale. This is difficult to achieve for all the relevant numbers, and methods have been devised for minimizing the errors resulting from this. Wind-tunnel testing techniques are discussed in Chapter 7.

4.2.4 Reynolds number

Reynolds number is the ratio of fluid inertia forces in the flow to viscous forces and is an important parameter in all branches of fluid mechanics. In bluff-body flows, viscous forces are only important in the surface boundary layers and free shear layers (Section 4.1). The dependence of pressure coefficients on Reynolds number is often overlooked for sharpedged bluff bodies such as most buildings and industrial structures. For these bodies, separation of flow occurs at sharp edges and corners such as wall-roof junctions, over a very wide range of Reynolds number. However, for bodies with curved surfaces such as circular cylinders or arched roofs, the separation points *are* dependent on Reynolds number, and this parameter should be considered. However, the addition of turbulence to the flow reduces the Reynolds number dependence for bodies with curved surfaces.

4.3 Flat plates and walls

4.3.1 Flat plates and walls normal to the flow

The flat plate, with its plane normal to the air stream, represents a common situation for wind loads on structures. Examples are elevated hoardings and signboards, which are mounted so that their plane is vertical. Solar panels are another example but, in this case, the plane is normally inclined to the vertical to maximize the collection of solar radiation. Free-standing walls are another example, but the fact that they are attached to the ground has a considerable effect on the flow and the resulting wind loading. In this section, some fundamental aspects of flow and drag forces on flat plates and walls are discussed.

For a flat plate or wall with its plane normal to the flow, the only aerodynamic force will be one parallel to the flow, i.e. a drag force. Then, if p_w and p_L are the average pressures on the front (windward) and rear (leeward) faces, respectively, the drag force, D, will be given by:

$$D=(p_{\mathrm{w}}-p_{\mathrm{L}})A$$

where A is the frontal area of the plate or wall.

Then dividing both sides by $(1/2)\rho_{\mathrm{a}}U^2A$, we have:

$$\begin{aligned} C_D&=C_{p,\mathrm{w}}-C_{p,\mathrm{L}}\\ &=C_{p,\mathrm{w}}+(-C_{p,\mathrm{L}}) \end{aligned} \tag{4.7}$$

In practice, the windward wall pressure, p_{w}, and pressure coefficient, $C_{p,\mathrm{w}}$, vary considerably with the position on the front face. The leeward (or 'base') pressure, however, is nearly uniform over the whole rear face, as this region is totally exposed to the wake region, with relatively slow-moving air.

The mean drag coefficients for various plate and wall configurations are shown in Figure 4.4. The drag coefficient for a square plate in a smooth, uniform approach flow is about 1.1, slightly greater than the total pressure in the approach flow, averaged over the face of the plate. Approximately 60% of the drag is contributed by positive pressures (above static pressure) on the front face and 40% by negative pressures (below static pressure) on the rear face (ESDU, 1970).

The effect of free-stream turbulence is to increase the drag on the normal plate slightly. The increase in drag is caused by a decrease in leeward or base pressure, rather than an increase in front face pressure. The hypothesis is that the free-stream turbulence causes an increase in the rate of entrainment of air into the separated shear layers. This leads to a reduced radius of curvature of the shear layers and a reduced base pressure (Bearman, 1971).

Figure 4.4 also shows the drag coefficient on a long flat plate with a theoretically infinite width into the paper—the 'two-dimensional' flat plate. The drag coefficient of 1.9 is higher than that for the square plate. The reason for the increase on the wide plates can be explained as follows. For a square plate, the flow is deflected around the plate equally around the four sides. The extended width provides a high-resistance flow path into (or out of) the paper, thus forcing the flow to travel faster over the top edge and under the bottom edge. This faster flow results in more entrainment from the wake into the shear layers, thus generating lower base, or leeward face, pressure and higher drag.

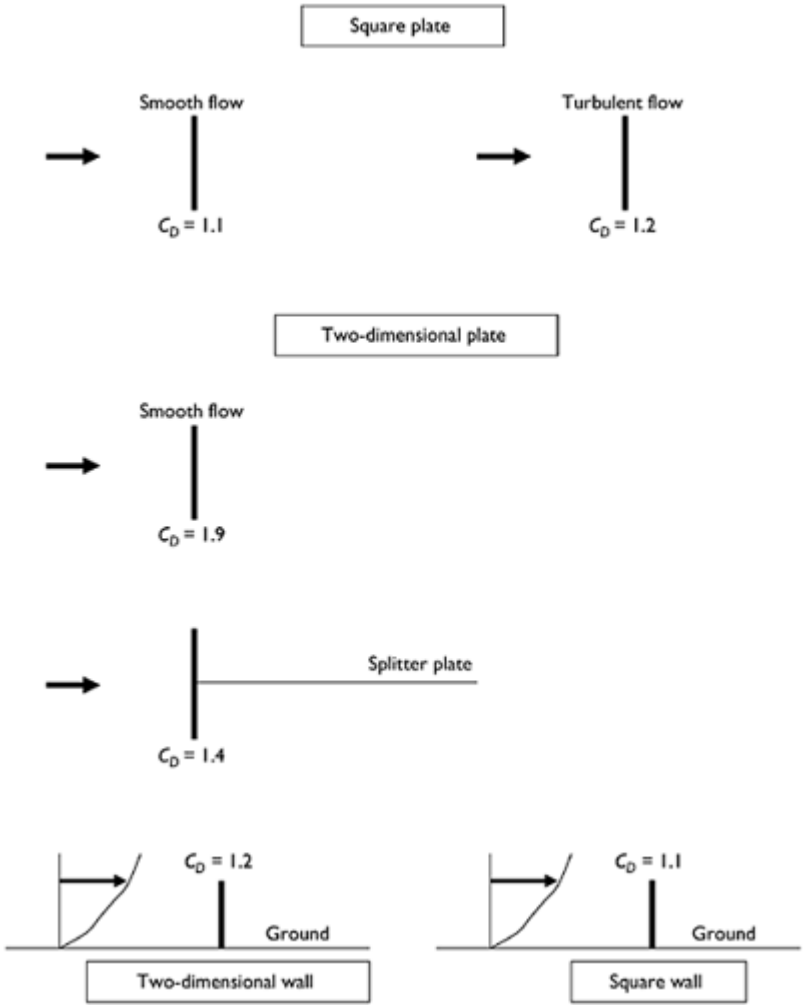

Figure 4.4 Drag coefficients for normal plates and walls.

Rectangular plates with intermediate values of width to height have intermediate values of drag coefficient. A formula given by ESDU (1970) for the drag coefficient on plates of height/breadth ratio in the range $1/30<h/b<30$, in smooth uniform flow normal to the plate, is reproduced in Equation (4.8):

$$C_D=1.10+0.02[(h/b)+(b/h)] \tag{4.8}$$

In the case of the two-dimensional plate, strong vortices are shed into the wake alternately from top and bottom, in a similar way to the bluff-body flow shown in Figure 4.1. These contribute greatly to the increased entrainment into the wake of the two-dimensional plate. Suppression of these vortices by a splitter plate has the effect of reducing the drag coefficient to a lower value, as shown in Figure 4.4.

This suppression of vortex shedding is nearly complete when a flat plate is attached to a ground plane and becomes a wall, as shown in the lower sketch in Figure 4.4. In this case, the approach flow will be of a boundary-layer form with a wind speed increasing with height as shown. The value of drag coefficient, with U taken as the mean wind speed at the top of the wall, $\bar{U}_h$, is very similar for the two-dimensional wall and finite wall of square planform, i.e. a drag coefficient of about 1.2 for an infinitely long wall. The effect of the finite length of wall is shown in Figure 4.5. Little change in the mean drag coefficient occurs, although a slightly lower value occurs for an aspect ratio (length/height) of about 5 (Letchford and Holmes, 1994).

The case of two thin normal plates in series, normal to the flow, as shown in Figure 4.6, is an interesting one. At zero spacing, the two plates act like a single plate with a combined drag coefficient (based on the frontal area of one plate) of about 1.1, for a square plate. For spacings in the range of 0 to about 2 h, the combined drag coefficient is actually *lower* than that for a single plate, reaching a value of about 0.8 at a spacing of about 1.5h for two square plates. As the spacing is allowed to increase, the combined drag coefficient then increases so that, for very high spacings, the plates act like individual plates with no interference from each other and a combined drag coefficient of about 2.2. The mechanism that produces the reduced drag at the critical spacing of 1.5h has not been studied in detail, but clearly there is a large interference in the wake and vortex shedding, generated by the downstream plate.

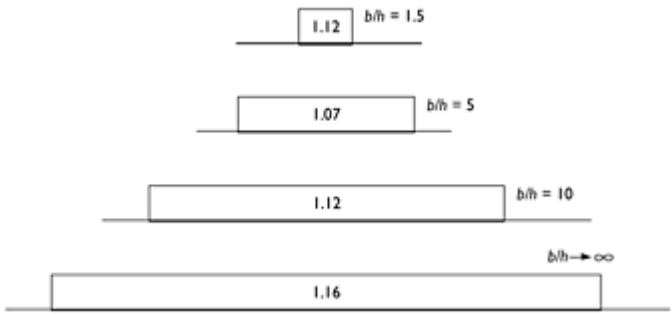

Figure 4.5 Mean drag coefficients on walls in boundary-layer flow.

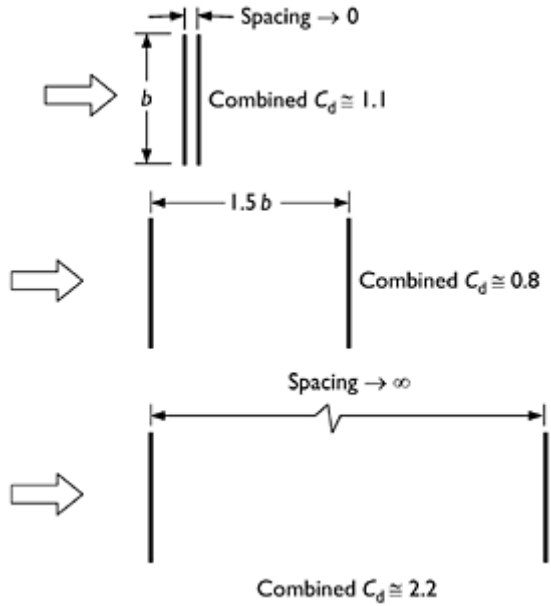

Figure 4.6 Drag coefficients for two square plates in series.

The drag force on two flat plates separated by small distances normal to the flow is also a relevant situation in wind engineering, with applications for clusters of lights or antennas together on a frame, for example. Experiments by Marchman and Werme (1982) found increases in drag of up to 15% when square, rectangular or circular plates were within half a width (or diameter) from each other.

If uniform porosity is introduced, the drag on a normal flat plate or wall reduces, as some air is allowed to flow through the plate and reduce the pressure difference between front and rear faces. The reduction in drag coefficient can be represented by the introduction of a porosity factor, K_p, which is dependent on the solidity of the plate, δ, being the ratio of the 'solid' area of the plate to the total elevation area as indicated in Equation (4.9):

$$C_{D,\delta}=C_D \cdot K_p \tag{4.9}$$

K_p is not linearly related to the solidity. An approximate expression for K_p, which fits the data quite well for plates and walls with ratios of height to breadth between about 0.2 and 5, is given by:

$$K_p \cong 1-(1-\delta)^2 \tag{4.10}$$

Equation (4.10) has the required properties of equalling one for a value of δ equal to 1, i.e. an impermeable plate or wall, and tending to zero as the solidity tends to zero. For very small values of δ (e.g. an open truss plate made up of individual members), K_p tends to a value of 2δ, as, from Equation (4.10),

$$K_p = 1 - (1 - 2\delta + \delta^2) \cong 2\delta$$

because δ^2 is very small in comparison with 2δ for small δ.

Considering the application of this to the drag coefficient for an open truss plate of square planform, we have from Equations (4.9) and (4.10),

$$C_{D,A_t} \cong 1.1(2\delta) = 2.2\delta$$

where C_{D,A_t} denotes that the drag coefficient, defined as in Equation (4.4), is with respect to the total (enclosed) elevation area of A_t. With respect to the elevation area of the actual members in the truss A_m, the drag coefficient is larger, being given by:

$$C_{D,A_m} = C_{D,A_t}(A_t/A_m) = C_{D,A_t} \cdot (1/\delta) \cong 2.2$$

In this case of a very open plate, the members will act like isolated bluff bodies with individual values of drag coefficient of 2.2.

Cook (1990) discusses in detail the effect of porosity on aerodynamic forces on bluff bodies.

4.3.2 Flat plates and walls inclined to the flow

Figure 4.7 shows the case with the wind at an oblique angle of attack, α, to a two-dimensional flat plate. In this case, the resultant force remains primarily at right angles to the plate surface, i.e. it is no longer a drag force in the direction of the wind. There is also a tangential component, or 'skin friction' force. However, this is not significant in comparison with the normal force, for angles of attack greater than about 10°.

For small angles of attack, α (less than 10°), the normal force coefficient, C_N, with respect to the total plan area of the plate viewed normal to its surface, is approximately given by:

$$C_N \cong 2\pi\alpha \qquad (4.11)$$

(where α is measured in radians, not in degrees).

Equation (4.11) comes from the theory used in aeronautics. The 'centre of pressure', denoting the position of the line of action of the resultant normal force, is at, or near, one-quarter of the height h from the leading edge, again a result from aeronautical theory.

As the angle of attack, α, increases, the normal force coefficient, C_N, progressively increases towards the normal plate case (α=90°), discussed in Section 4.3.1, with the centre of pressure at a height of 0.5 *h*. For example, the normal force coefficient for an angle of attack of 45° is about 1.5, with the centre of pressure at a distance of about 0.4 *h* from the leading edge, as shown in Figure 4.7. The corresponding values for *a* equal to 30° are about 1.2 and 0.38 *h* (ESDU, 1970).

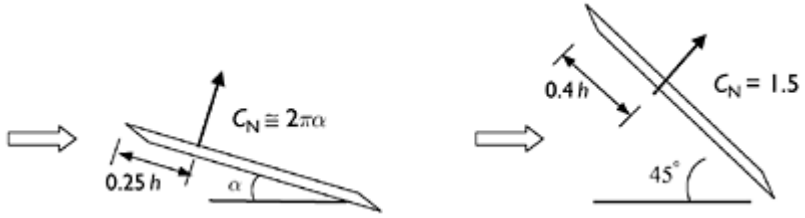

Figure 4.7 Normal force coefficients for an inclined two-dimensional plate.

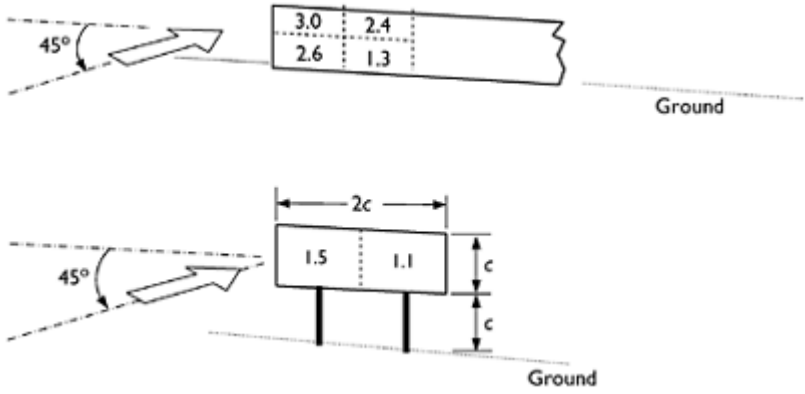

Figure 4.8 Area-averaged mean pressure coefficients on walls and hoardings for oblique wind directions.

Now, we will consider finite length walls and hoardings, at or near ground level, and hence in a highly sheared and turbulent boundary-layer flow. The mean net pressure coefficients at the windward end of the wall, for an oblique wind blowing at 45° to the normal, are quite high due to the presence of a strong vortex system behind the wall. Some values of area-averaged mean pressure coefficients are shown in Figure 4.8; these high values are usually the critical cases for the design of free-standing walls and hoardings for wind loads.

4.4 Rectangular prismatic shapes

4.4.1 Drag on two-dimensional rectangular prismatic shapes

Understanding of the wind forces on rectangular prismatic shapes is clearly of importance for many structures, especially buildings of all heights and bridge decks. We will first consider the drag coefficients for two-dimensional rectangular prisms.

Figure 4.9 shows how the drag coefficient varies for two-dimensional rectangular prisms with sharp corners as a function of the ratio, *d/b*, where *d* is the along-wind or after-body length and *b* the cross-wind dimension. The flow is normal to a face of width *b* and is 'smooth', i.e. the turbulence level is low. As previously shown in Figure 4.4, the value of the drag coefficient is 1.9 for *(d/b)* close to zero, i.e. for a flat plate normal to a flow stream. As *(d/b)* increases to 0.65–0.70, the drag coefficient increases to about 2.9 (e.g. Bearman and Trueman, 1972). The drag coefficient then decreases with increasing *(d/b)*, reaching 2.0 for a square cross-section. The drag coefficient continues to decrease with further increases in *(d/b)*, reaching about 1.0 for values of *(d/b)* of 5 or greater.

These variations can be explained by the behaviour of the free shear layers separating from the upstream corners. These shear layers are unstable, as was shown in Figure 4.1, and eventually form discrete vortices. During the formation of these vortices, air is entrained from the wake region behind the prism; it is this continual entrainment process which sustains a base pressure lower than the static pressure. As *(d/b)* increases to the range 0.65–0.70, the size of the wake decreases simply because of the increased volume of the prism occupying part of the wake volume. Thus, the same entrainment process acts

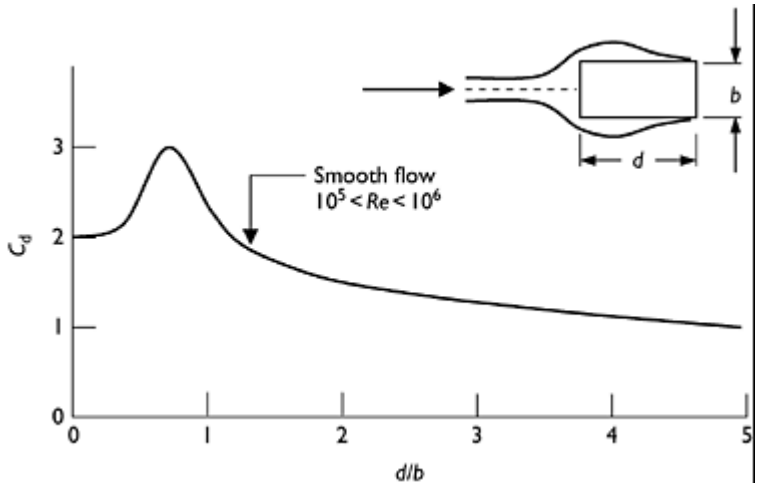

Figure 4.9 Drag coefficients for two-dimensional rectangular prisms in smooth flow.

on a smaller volume of wake air, causing the base pressure to decrease further and the drag to increase. However, as *(d/b)* increases beyond 0.7, the rear or downstream corners interfere with the shear layers, and if the length *d* is long enough, the shear layers will stabilize, or 're-attach', on to the sides of the prisms. Although the attached shear layers will eventually separate again from the *rear* corners of the prism, the wake is smaller for prisms with long after-bodies (high *d/b*), and the entrainment is weaker. The result is a lower drag coefficient, as shown in Figure 4.9.

4.4.2 Effect of aspect ratio

The effect of a finite aspect ratio (height/breadth) is to introduce an additional flow path around the end of the body and a means of increasing the pressure in the wake cavity. The reduced air flow normal to the axis results in a lower drag coefficient for finite length bodies in comparison to two-dimensional bodies of infinite aspect ratio. Figure 4.10 shows the drag coefficient for a square cross-section with one free end exposed to the flow, which was smooth (Scruton and Rogers, 1972). The aspect ratio in this case is calculated as *2h/b*, where *h* is the height, as it is assumed that the flow is equivalent to that around a body with a 'mirror image' added to give an overall height of 2 *h*, with two free ends.

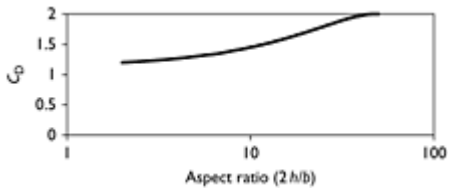

Figure 4.10 Effect of aspect ratio on drag coefficient for a square cross-section.

4.4.3 Effect of turbulence

Free-stream turbulence containing scales of the prism dimensions, or smaller, can have significant effects on the mean drag coefficients of rectangular prisms, as well as producing fluctuating forces. As shown in Figure 4.4, the effect of free-stream turbulence on a flat plate normal to an air stream is to increase the drag coefficient slightly (Bearman, 1971). This results from increased mixing and entrainment into the free shear layers induced by the turbulence. Observations have also shown a reduction in the radius of curvature of the mean shear layer position (Figure 4.11). As the after-body length increases, the drag first increases and then decreases, as occurs in smooth flow. However, because of the decrease in the mean radius of curvature of the shear layers caused by the free-stream turbulence, the *(d/b)* ratio for maximum drag will decrease with increasing turbulence intensity, as shown in Figure 4.12 (Gartshore, 1973; Laneville *et al.*, 1975).

The drag coefficients for two-dimensional rectangular prisms on the ground in turbulent boundary-layer flow are shown in Figure 4.13. In comparison with rectangular prisms in smooth uniform flow (Figure 4.9), the drag coefficients, based on the mean wind speed at the height of the top of the prism, are much lower; because of the high turbulence in the boundary-layer flow, they do not show any maximum value.

Melbourne (1995) has discussed the important effects of turbulence on flow around bluff bodies in more detail.

4.4.4 Drag and pressures on a cube and a prism

The mean pressure distributions on a cube in a turbulent boundary-layer flow are shown in Figure 4.14 (Baines, 1963). These pressure coefficients are based on the mean wind speed at the height of the top of the cube. The drag coefficient of 0.8 is lower than that of the two-dimensional square section prism (*d/h* equal to 1.0 in Figure 4.13). This is due to the three-dimensional flows that occur around the side walls of the block which increase the base pressure (decrease the negative pressure).

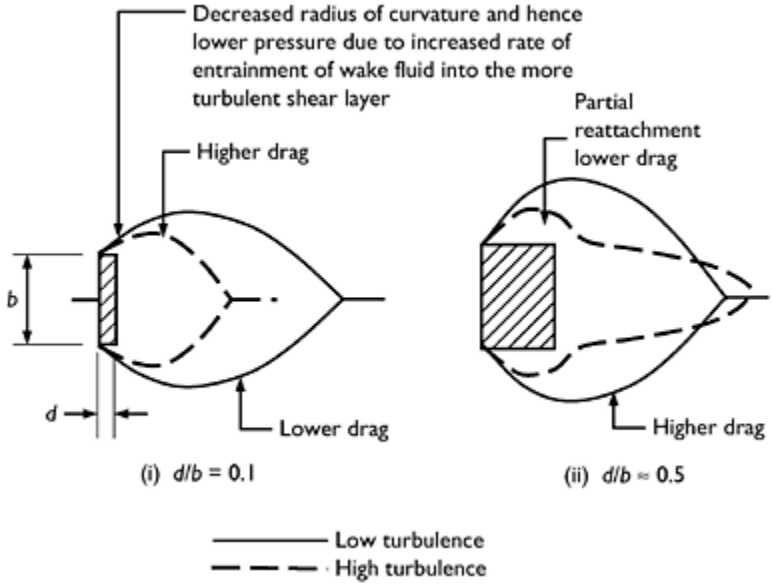

Figure 4.11 Effect of turbulence on shear layers from rectangular prisms (Gartshore, 1973).

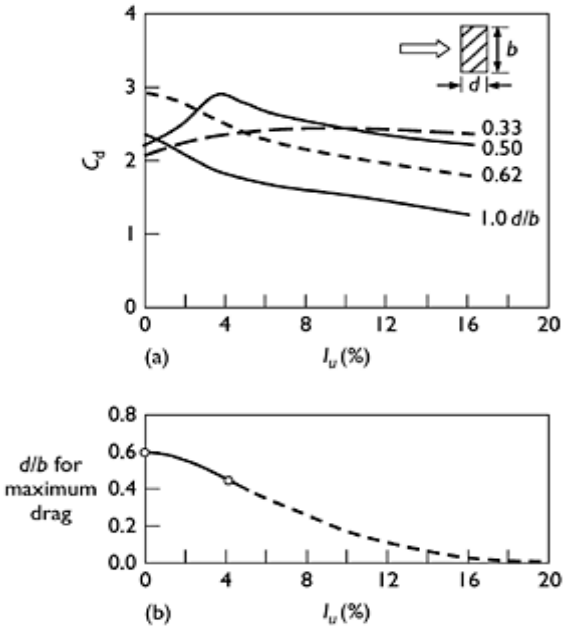

Figure 4.12 Effect of turbulence on drag coefficients for rectangular prisms (Laneville *et al.*, 1975).

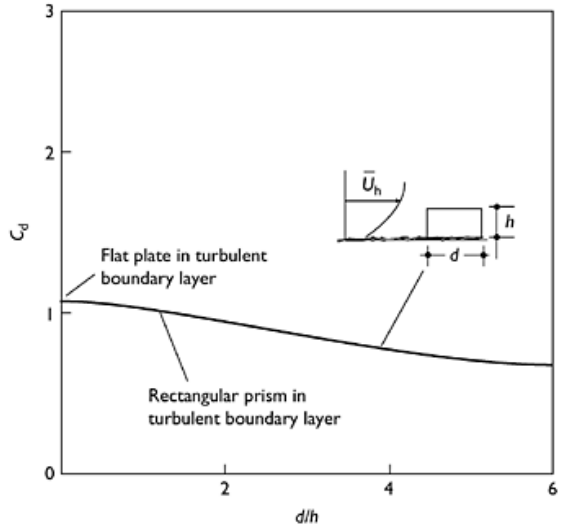

Figure 4.13 Mean drag coefficients for rectangular prisms in turbulent boundary-layer flow.

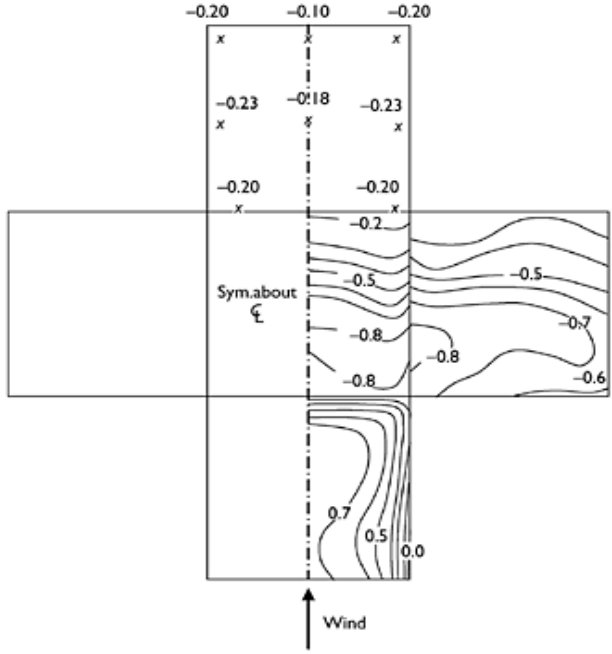

Figure 4.14 Mean pressure coefficients on a cube in turbulent boundary-layer flow (Baines, 1963).

The mean pressure distribution on a tall prism of square cross-section in a turbulent boundary-layer flow is shown in Figure 4.15 (Baines, 1963). This is representative of the pressure distribution on a tall building in the atmospheric boundary layer. The mean pressure coefficients are again based on the dynamic pressure calculated from the mean wind speed at the top of the prism. The effect of the vertical velocity profile on the windward wall pressure is clearly seen. The maximum pressure occurs at about 85% of the height. On the windward face of unshielded tall buildings, the strong pressure gradient can cause a strong downwards flow, often causing high wind speeds which may cause problems for pedestrians at ground level.

4.4.5 Jensen number

For bluff bodies such as buildings immersed in a turbulent boundary-layer flow, the ratio of characteristic body dimension, usually the height, h, in the case of a building, to the characteristic boundary-layer length, represented by the roughness length, z_0, is known as the Jensen number. In a classic series of experiments, Jensen (1958) established the need for equality of (h/z_0) in order for wind-tunnel mean pressure measurements on a model of a small building to match those in full scale. The effect is greatest on the roof and side walls, where the increased turbulence in the flow over the rougher ground surfaces promotes shorter flow re-attachment lengths.

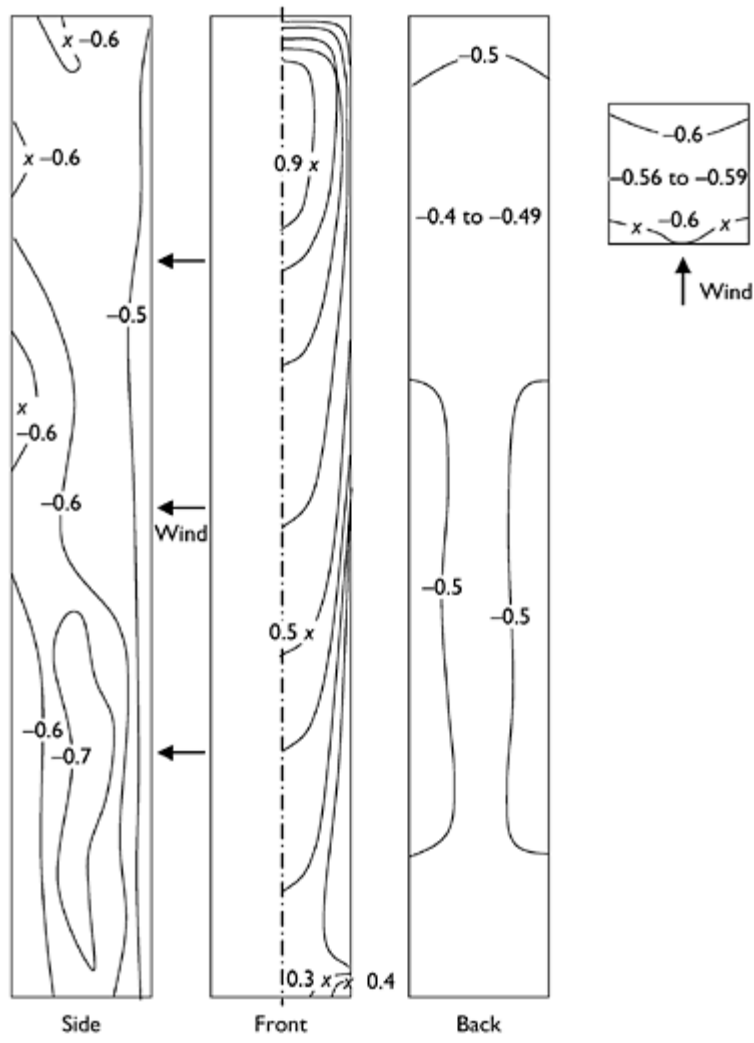

Figure 4.15 Mean pressure coefficients on a tall prism in turbulent boundary-layer flow (Baines, 1963).

For a given height, *h*, greater values of roughness length, z_0, and lower values of Jensen number imply rougher ground surface and hence greater turbulence intensities at the height of the body. Thus, fluctuating pressure coefficients also depend on Jensen number—decreasing Jensen number generally giving increasing root-mean-square (r.m.s.) pressure coefficients.

4.5 Circular cylinders

4.5.1 Effects of Reynolds number and surface roughness

For bluff bodies with curved surfaces such as the circular cylinder, the positions of the separation of the local surface boundary layers are much more dependent on viscous forces than is the case with sharp-edged bodies. This results in a variation of drag forces

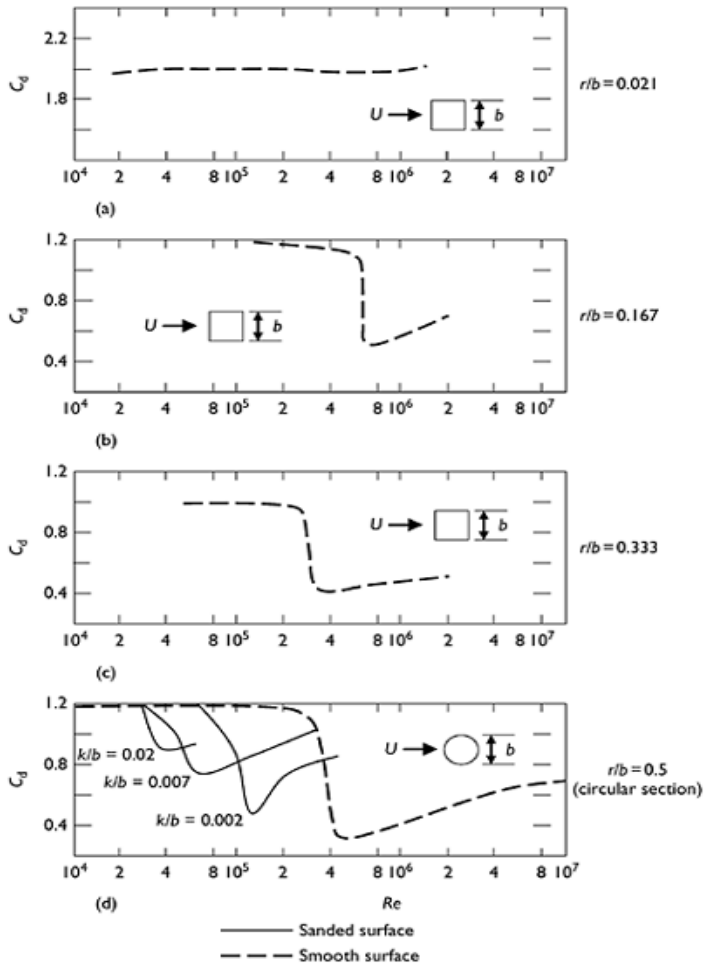

Figure 4.16 Effect of Reynolds number, corner radius and surface roughness on drag coefficients of square sections (Scruton, 1981).

with Reynolds number, which is the ratio of inertial forces to viscous forces in the flow (see Section 4.2.4). Figure 4.16 shows the variation of drag coefficient with Reynolds number for square section bodies with various corner radii (Scruton, 1981). The appearance of a 'critical' Reynolds number, at which there is a sharp fall in drag coefficient, occurs at a relatively low corner radius.

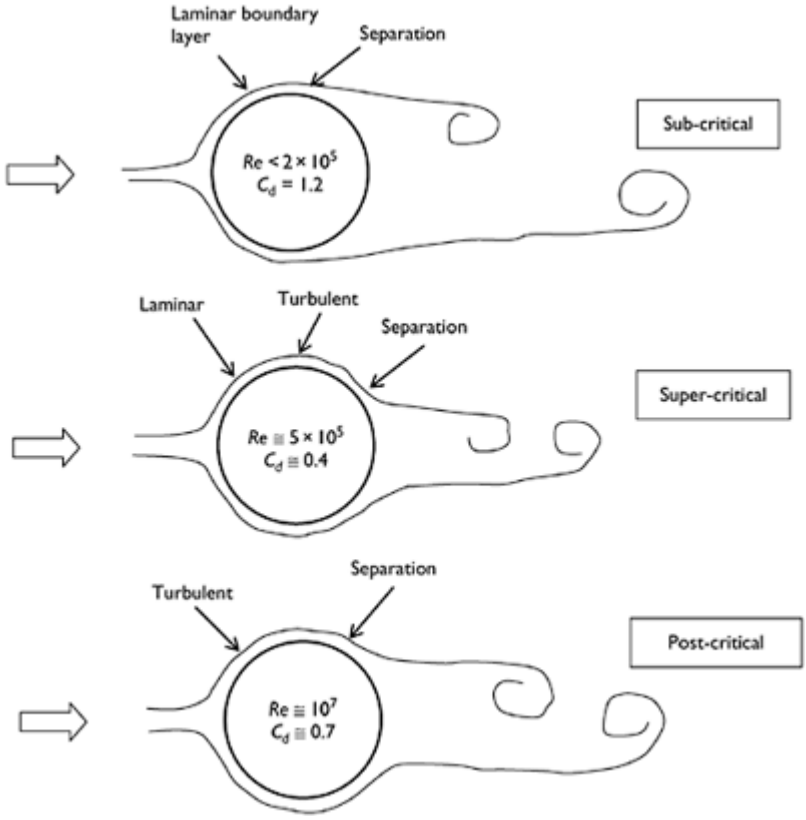

Figure 4.17 Flow regimes for a circular cylinder in smooth flow.

The various flow regimes for a circular cylinder with a smooth surface finish in smooth (low turbulence) flow are shown in Figure 4.17. The sharp fall in drag coefficient at a Reynolds number of about 2×10^5 is caused by a transition to turbulence in the surface boundary layers ahead of the separation points. This causes separation to be delayed to an angular position of about 140° from the front stagnation point, instead of 90°, which is the case for sub-critical Reynolds numbers. This delay in the separation results in a narrowing in the wake and an increased (less negative) base pressure and a lower drag coefficient. The pressure distributions at sub-critical and super-critical Reynolds numbers are shown in Figure 4.18.

As shown in Figure 4.16, the presence of a rough surface on a circular cylinder causes the critical Reynolds number range to be lower than that for a smooth cylinder. The minimum drag coefficient is higher for the rougher surfaces (ESDU, 1980).

4.5.2 Effect of aspect ratio

The reduction in drag coefficient for a circular cylinder of finite aspect ratio (single free end) in smooth flow (sub-critical) is shown in Figure 4.19 (Scruton and Rogers, 1972). This figure is analogous to Figure 4.10 for a square cross-section. As for the square section, the reduction in drag for a circular cylinder results from the additional flow path provided by the free end on the body.

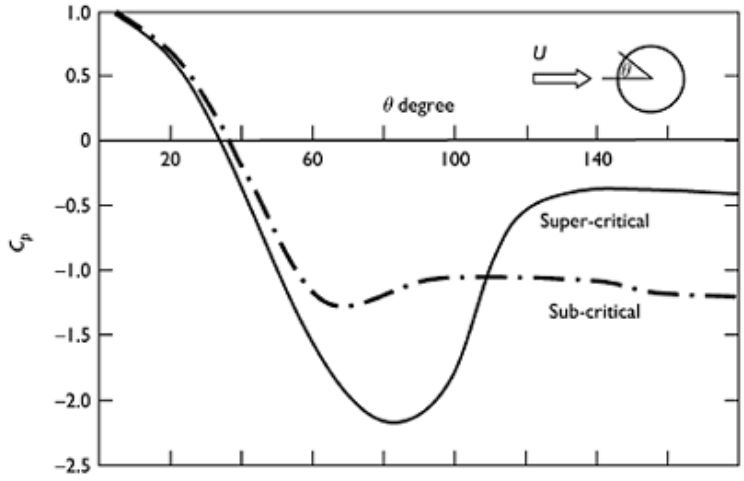

Figure 4.18 Pressure distributions around a two-dimensional circular cylinder at sub-critical and trans-critical Reynolds numbers.

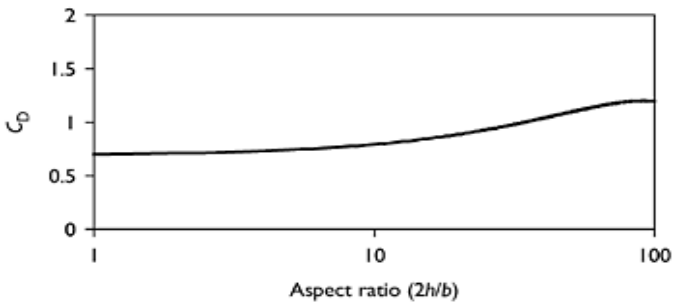

Figure 4.19 Effect of aspect ratio on drag coefficient of a circular cylinder (sub-critical Reynolds number).

The mean pressure distribution around a circular cylinder with a height to diameter (aspect) ratio of 1, with its axis vertical in a turbulent boundary-layer flow, is shown in Figure 4.20 (Macdonald *et al.,* 1988). The minimum mean pressure coefficient on the side occurs at an angular position of about 80° and is about −1.2, lower in magnitude than the value of about −2.0 for a two-dimensional cylinder in super-critical flow (see Figure 4.18). The minimum $\overline{C}_p$ increases in magnitude with increasing aspect ratio, reaching the two-dimensional value at an aspect ratio of about 2.0.

4.6 Fluctuating forces and pressures

4.6.1 Introduction

The turbulent and fluctuating nature of wind flow in the atmospheric boundary layer has been described in Chapter 3. This and the unstable nature of flow around bluff bodies which results in flow separations, and sometimes re-attachments, produce pressures and forces on bodies in the natural wind, which are also highly fluctuating.

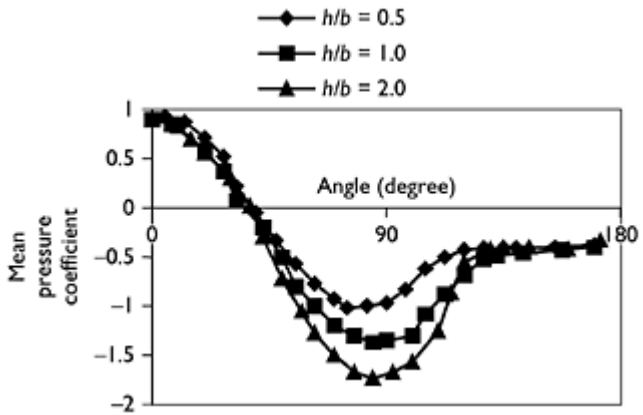

Figure 4.20 Effect of aspect ratio (height/diameter) on pressure distributions around circular cylinders.

The main sources of the fluctuating pressures and forces are as follows:

- Natural turbulence or gustiness in the free-stream flow. This is often called ‘buffeting’. If the body dimensions are small relative to the length scales of the turbulence, the pressure and force variations will tend to follow the variations in velocity (see Section 4.6.2 on the quasi-steady assumption).
- Unsteady flow generated by the body itself, by phenomena such as separations, re-attachments and vortex shedding.
- Fluctuating forces due to movement of the body itself (e.g. aerodynamic damping).

The third source arises only for very flexible vibration-prone 'aeroelastic structures'. In the following sections, only the first two sources will be considered.

4.6.2 The quasi-steady assumption

The 'quasi-steady' assumption is the basis of many wind-loading codes and standards. The fluctuating pressure on a structure is assumed to follow the variations in longitudinal wind velocity upstream. Thus,

$$p(t)=C_{p0}(1/2)\rho_a[U(t)]^2 \tag{4.12}$$

where C_{p0} is a quasi-steady pressure coefficient.

Expanding $U(t)$ into its mean and fluctuating components,

$$\begin{aligned} p(t) &= C_{p_0}(1/2)\rho_a[\overline{U}+u'(t)]^2 \\ &= C_{p_0}(1/2)\rho_a[\overline{U}^2+2\overline{U}u'(t)+u'(t)^2] \end{aligned} \tag{4.13}$$

Taking mean values,

$$\overline{p} = C_{p_0}(1/2)\rho_a\left[\overline{U}^2+\sigma_u^2\right]$$

For small turbulence intensities, σ_u^2 is small in comparison with $\overline{U}^2$. Then the quasi-steady pressure coefficient, C_{p0}, is approximately equal to the mean pressure coefficient, $\overline{C}_p$.

Then,

$$\overline{p} \cong C_{p_0}(1/2)\rho_a\,\overline{U}^2 = \overline{C}_p(1/2)\rho_a\overline{U}^2 \tag{4.14}$$

Subtracting the mean values from both sides of Equation (4.13), we have,

$$p'(t) = C_{p_0}(1/2)\rho_a[2\overline{U}u'(t)+u'(t)^2]$$

Neglecting the second term in the square brackets (valid for low turbulence intensities), squaring and taking mean values,

$$\overline{p'^2} \cong \overline{C}_p{}^2(1/4)\rho_a{}^2[4\overline{U}^2\overline{u'^2}] = \overline{C}_p{}^2\rho_a{}^2\overline{U}^2\overline{u'^2} \tag{4.15}$$

Equation (4.15) is a quasi-steady relationship between mean-square pressure fluctuations and mean-square longitudinal velocity fluctuations.

To predict peak pressures by the quasi-steady assumption,

$$\hat{p}, \breve{p} = C_{p_0}(1/2)\rho_a[\hat{U}^2] \cong \overline{C_p}(1/2)\rho_a[\hat{U}^2] \tag{4.16}$$

Thus, according to the quasi-steady assumption, we can predict peak pressures (maxima and minima) by using mean pressure coefficients with a peak gust wind speed. This is the basis of many codes and standards that use a peak gust as a basic wind speed (see Chapter 15). Its main disadvantage is that building-induced pressure fluctuations (the second source described in Section 4.6.1) are ignored. Also when applied to wind pressures over large areas, it is conservative because full correlation of the pressure peaks is implied. These effects and the way they are treated in codes and standards are discussed in Chapter 15.

4.6.3 Body-induced pressure fluctuations and vortex-shedding forces

The phenomena of separating shear layers and vortex shedding have already been introduced in Sections 4.1, 4.3.1, 4.4.1 and 4.5 in descriptions of the flow around some basic bluff-body shapes. These phenomena occur whether the flow upstream is turbulent or not, and the resulting surface pressure fluctuations on a bluff body can be distinguished from those generated by the flow fluctuations in the approaching flow.

The regular vortex shedding into the wake of a long bluff body results from the rolling-up of the separating shear layers alternately on one side, then the other, and occurs on bluff bodies of all cross-sections. A regular pattern of decaying vortices, known as the von Karman vortex ‘street’, appears in the wake. Turbulence in the approaching flow tends to make the shedding less regular, but the strengths of the vortices are maintained, or even enhanced. Vibration of the body may also enhance the vortex strength, and the vortex-shedding frequency may change to the frequency of vibration, in a phenomenon known as *lock-in*.

As each vortex is shed from a bluff body, a strong cross-wind force is induced towards the side of the shed vortex. In this way, the alternate shedding of vortices induces a nearly harmonic (sinusoidal) cross-wind force variation on the structure.

For a given cross-sectional shape, the frequency of vortex shedding, n_s, is proportional to the approaching flow speed and inversely proportional to the width of the body. It may be expressed in a non-dimensional form, known as the *Strouhal number, St:*

$$St = \frac{n_s b}{\overline{U}} \tag{4.17}$$

where b is the cross-wind body width and U the mean flow speed.

The Strouhal number varies with the shape of the cross-section, and for circular and other cross-sections with curved surfaces varies with the Reynolds number. Some

representative values of Strouhal number for a variety of cross-sections are shown in Figure 4.21.

An inclined two-dimensional flat plate with an angle of attack, α (Figure 4.7), has a Strouhal number of about 0.15 based on the breadth, b, normal to the flow or (0.15/sin α) based on the chord, c, where $b=c$ sin α (Chen and Fang, 1996).

The variation with Reynolds number for a circular cylinder is shown in Figure 4.22 (Scruton, 1963; Schewe, 1983). In the sub-critical range, up to a Reynolds number of 2×10^5, the Strouhal number is quite constant at a value of 0.20. In the critical Reynolds number range, coinciding with the sharp fall in drag coefficient (see Figure 4.16), the Strouhal number jumps to 0.3 and then 0.48, although in this range the vortex shedding is random and not clearly defined. A slightly decreasing Strouhal number to about 0.4, in the super-critical range, is followed by a fall to about 0.2 again, at a Reynolds number of 2×10^6. Helical strakes (Figure 4.23) are often used to inhibit vortex shedding and the resulting cross-wind forces on structures with circular sections such as chimney stacks (Scruton and Walshe, 1957).

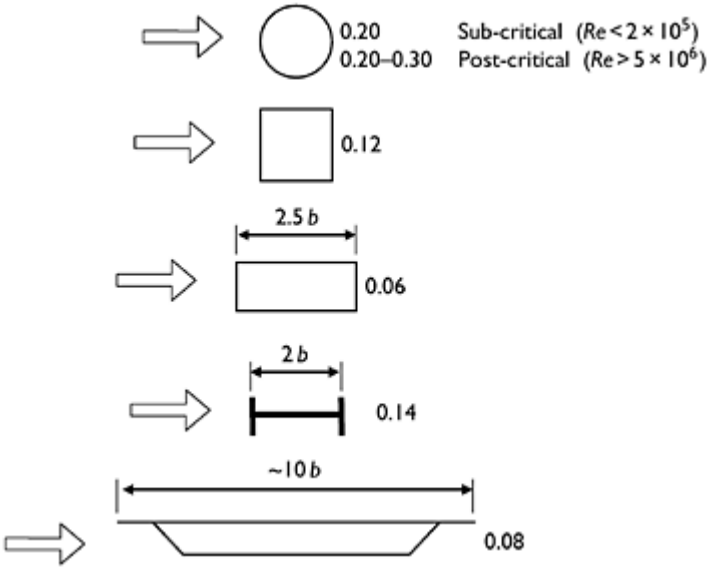

Figure 4.21 Strouhal numbers for vortex shedding for various cross-sections.

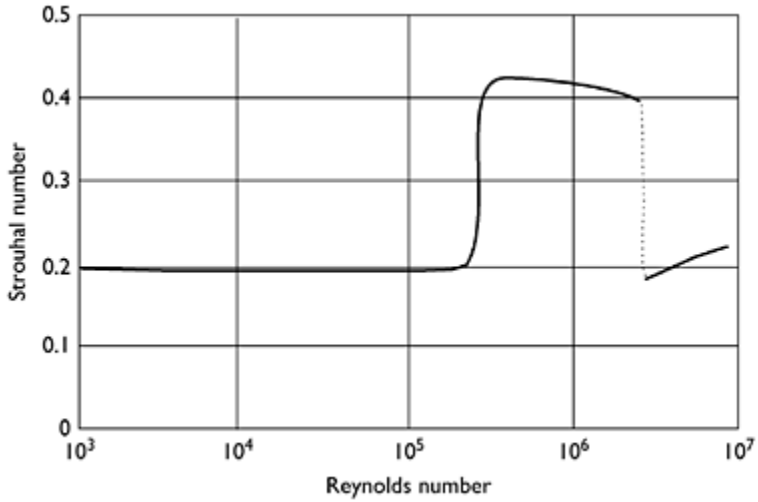

Figure 4.22 Strouhal number versus Reynolds number for circular cylinders.

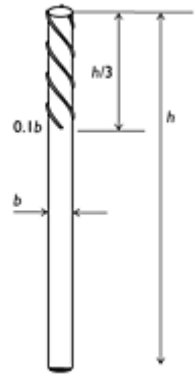

Figure 4.23 Helical strakes for inhibiting vortex shedding.

4.6.4 Fluctuating pressure and force coefficients

The r.m.s. fluctuating (standard deviation) pressure coefficient at a point on a bluff body is defined by:

$$C_p' = \frac{\sqrt{\overline{p'^2}}}{\frac{1}{2}\rho_a \overline{U}^2} \tag{4.18}$$

$\sqrt{\overline{p'^2}}$ is the r.m.s. fluctuating, or standard deviation, pressure (also denoted by σ_p).

The r.m.s. fluctuating sectional force coefficient per unit length of a two-dimensional cylindrical or prismatic body is defined by:

$$C'_f = \frac{\sqrt{\overline{f'^2}}}{\frac{1}{2}\rho_a \overline{U}^2 b} \tag{4.19}$$

$\sqrt{\overline{f'^2}}$ is the r.m.s. fluctuating force per unit length, b is a reference dimension—usually the cross-wind breadth.

For a whole body,

$$C'_F = \frac{\sqrt{\overline{F'^2}}}{\frac{1}{2}\rho_a \overline{U}^2 A} \tag{4.20}$$

$\sqrt{\overline{F'^2}}$ is the r.m.s. fluctuating force acting on the complete body. A is a reference area—usually the frontal area.

The total fluctuating force acting on a cylindrical body of finite length can be calculated from the fluctuating sectional force, knowing the correlation function or correlation length.

With the quasi-steady assumption (Section 4.6.2), the r.m.s. fluctuating pressure coefficient can be estimated from Equations (4.15) and (4.18):

$$C'_p = \frac{\sqrt{\overline{p'^2}}}{\frac{1}{2}\rho \overline{U}^2} \approx \frac{\overline{C}_p \rho_a \overline{U} \sqrt{\overline{u'^2}}}{\frac{1}{2}\rho_a \overline{U}^2} = 2\overline{C}_p I_u \tag{4.21}$$

where I_u is the longitudinal turbulence intensity $(= \sqrt{\overline{u'^2}}/\overline{U}$ or $\sigma_u/\overline{U})$—as defined in Section 3.3.1.

Similarly the r.m.s. fluctuating drag coefficient can be estimated using the quasi-steady assumption:

$$C'_D \approx 2\overline{C}_D I_u \tag{4.22}$$

Fluctuating forces in the cross-wind direction, however, are usually determined by experiment. Measurements have shown that square cross-sections experience stronger cross-wind fluctuating forces due to vortex shedding, than do circular cross-sections. Figure 4.24 shows the variation of r.m.s. fluctuating cross-wind force per unit length, for a circular cylinder, as a function of Reynolds number (Wootton and Scruton, 1970). The value is around 0.5 at sub-critical Reynolds numbers, falling to much lower values in the critical and super-critical ranges, coinciding with a reduction in drag coefficient (Section 4.5.1).

The fluctuating cross-wind force coefficient for a square cross-section with sharp corners is higher than that for a circular section, due to the greater strength of the shed vortices. In smooth flow, the r.m.s. fluctuating cross-wind force coefficient is about 1.3; this drops to about 0.7 in turbulent flow of 10% intensity (Vickery, 1966).

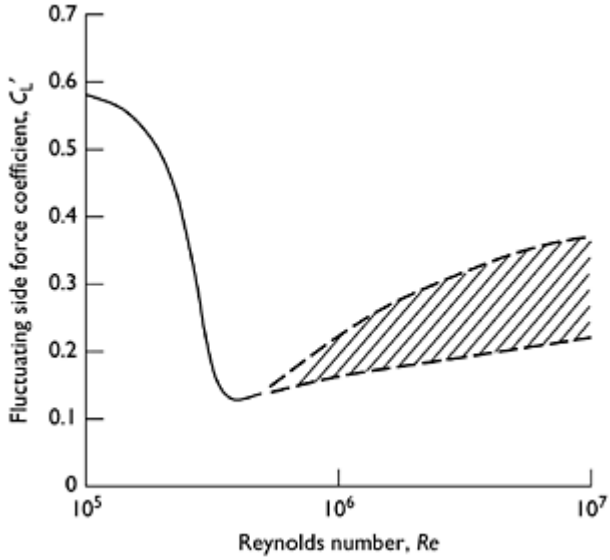

Figure 4.24 Variation of fluctuating cross-wind force coefficient per unit length with Reynolds number for a circular cylinder (smooth flow).

4.6.5 Correlation length

The spatial correlation coefficient for fluctuating forces at two points along a cross-section is defined by:

$$\rho = \frac{\overline{f_1'(t) f_2'(t)}}{\overline{f'^2}} = \frac{\overline{f_1'(t) f_2'(t)}}{\sigma_f{}^2} \tag{4.23}$$

where $f_1'(t)$, $f_2'(t)$ are the fluctuating forces per unit length at two sections along a cylindrical or prismatic body. (This was previously discussed in relation to atmospheric turbulence in Section 3.3.5.)

We have assumed that the mean-square fluctuating force per unit length is constant along the body, so that:

$$\overline{f_1'^2} = \overline{f_2'^2} = \overline{f'^2}$$

As the separation distance, *y*, between the two sections 1 and 2 approaches zero, the correlation function, $\rho(y)$, approaches 1. As the separation distance becomes very large, $\rho(y)$ tends to zero; this means there is no statistical relationship between the fluctuating forces.

The *correlation length*, ℓ, is then defined as:

$$\ell = \int_0^\infty \rho(y)\, dy \tag{4.24}$$

The correlation length is thus the area under the graph of $\rho(y)$ plotted against *y*.

Measurements of correlation length for a smooth circular cylinder in smooth flow are shown in Figure 4.25 (Wootton and Scruton, 1970). The correlation length falls from about five diameters to one diameter over the critical Reynolds number range.

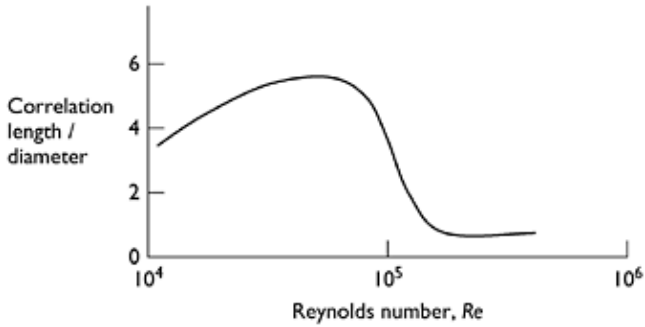

Figure 4.25 Variation of correlation length with Reynolds number for a stationary circular cylinder (smooth flow).

4.6.6 Total fluctuating forces on a slender body

Consider a long cylindrical, or prismatic, body of length, *L*, subjected to fluctuating wind forces along its length. Divide the body into a large number, *N*, of sections of width, δy_1, δy_2,…, δy_N, as shown in Figure 4.26. Assume that the mean-square fluctuating force is the same at all sections.

At any section, *i*, the total force per unit length can be separated into a mean, or time-averaged, component and a fluctuating component with a zero mean:

$$f_i(t) = \overline{f}_i + f_i'(t) \tag{4.25}$$

The *total* mean force acting on the whole body is given by:

$$\overline{F} = \Sigma \overline{f}_i\, \delta y_i$$

where the summation is taken from i equal to 1 to N.

As we let the number of sections tend to infinity, δy_i tends to zero, and the right-hand side becomes an integral:

$$\overline{F} = \int_0^L \overline{f_i}\, \mathrm{d}y_i \tag{4.26}$$

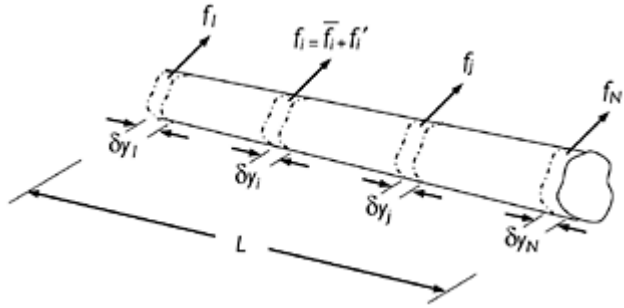

Figure 4.26 Sectional force fluctuations on a long cylinder.

The instantaneous fluctuating force on the body as a whole is:

$$\begin{aligned} F'(t) &= \Sigma f_i'(t)\,\delta y_i \\ &= f_1'(t)\,\delta y_1 + f_2'(t)\,\delta y_2 + \cdots + f_N'(t)\,\delta y_N \end{aligned}$$

Squaring both sides,

$$\begin{aligned} [F'(t)]^2 &= [f_1'(t)\,\delta y_1 + f_2'(t)\,\delta y_2 + \cdots + f_N'(t)\,\delta y_N]^2 \\ &= [f_1'(t)\,\delta y_1]^2 + [f_2'(t)\,\delta y_2]^2 \cdots + [f_N'(t)\,\delta y_N]^2 + f_1'(t) f_2'(t)\,\delta y_1\ \delta y_2 \\ &\quad + f_1'(t) f_3'(t)\,\delta y_1\ \delta y_3 + \cdots \\ &= \sum_i^N \sum_j^N f_i'(t) f_j'(t)\,\delta y_i\,\delta y_j \end{aligned}$$

Now taking means (time averages) of both sides,

$$\overline{F'^2} = \sum_i^N \sum_j^N \overline{f_i'(t) f_j'(t)}\,\delta y_i\ \delta y_j \tag{4.27}$$

As δy_i, δy_j tend to zero,

$$\overline{F'^2} = \int_0^L \int_0^L \overline{f_i'(t) f_j'(t)}\, dy_i\, dy_j \tag{4.28}$$

Equations (4.27) and (4.28) are important equations, which illustrate how to obtain a total fluctuating force from the fluctuating force on small elements. The integrand in Equation (4.28) is the *covariance* of the sectional force fluctuations.

Now assume that the integrand can be written in the form:

$$\overline{f_i'(t) f_j'(t)} = \overline{f'^2} \rho(y_i - y_j)$$

where $\rho(y_i - y_j)$ is the correlation coefficient for the fluctuating sectional forces, which is assumed to be a function of the separation distance, $(y_i - y_j)$, but not of the individual positions, y_i and y_j—i.e. we assume that the wind forces are horizontally or vertically *homogeneous*.

Then,

$$\overline{F'^2} = \overline{f'^2(t)} \int_0^L \int_0^L \rho(y_i - y_j)\, dy_i\, dy_j \tag{4.29}$$

This is the fundamental equation for the total mean-square fluctuating force on the body, in terms of the mean-square fluctuating force per unit length.

By introducing a new variable equal to $(y_i - y_j)$, Equation (4.29) can be written as:

$$\overline{F'^2} = \overline{f'^2} \int_0^L dy_j \int_{-y_j}^{L-y_j} \rho(y_i - y_j)\, d(y_i - y_j) \tag{4.30}$$

Equations (4.29) or (4.30) can be evaluated in two special cases:

(i) *Full correlation*

This assumption implies that $\rho(y_i - yj)$ equals 1 for all separations, $(y_i - yj)$. Then Equation (4.29) becomes:

$$\overline{F'^2} = \overline{f'^2(t)}\, L^2$$

In this case, the fluctuating forces are treated like static forces,

(ii) *Rapidly decreasing correlation length*

In this case, ℓ is much less than L, and the second part of Equation (4.29) can be approximated by:

$$\int_{-y_j}^{L-y_j} \rho(y_i - y_j)\, d(y_i - y_j) = \int_{-\infty}^{\infty} \rho(y_i - y_j)\, d(y_i - y_j) = 2\ell$$

from Equation (4.24).

Then from Equation (4.30),

$$\overline{F'^2} = \overline{f'^2(t)}\, L \cdot 2\ell \tag{4.31}$$

Thus, the mean-square total fluctuating force is directly proportional to the correlation length, ℓ This is an important result that is applicable to structures such as slender towers.

4.7 Summary

This chapter has attempted to summarize the relevant aspects of bluff-body aerodynamics, itself a large subject with applications in many fields, to wind loads on structures. The basic fluid mechanics of stagnation, separation and wakes has been described, and pressure and force coefficients are defined. The characteristics of pressures and forces on the basic shapes of flat plates and walls, cubes and rectangular prisms and circular cylinders have been described. The effect of turbulence and the ground surface are covered.

Fluctuating pressures and forces, particularly those generated by upwind turbulence, and the regular shedding of vortices by a bluff body are discussed. The concept of correlation length and the averaging process by which fluctuating total forces on a body can be calculated are described.

References

Baines, W.D. (1963) Effects of velocity distributions on wind loads and flow patterns on buildings. *Proceedings, International Conference on Wind Effects on Buildings and Structures,* Teddington UK, 26–28 June, pp. 198–225.

Bearman, P.W. (1971) An investigation of the forces on flat plates normal to a turbulent flow. *Journal of Fluid Mechanics,* 46:177–98.

Bearman, P.W. and Trueman, D.H. (1972) An investigation of the flow around rectangular cylinders. *Aeronautical Quarterly,* 23:229–37.

Chen, J.M. and Fang, Y.-C. (1996) Strouhal numbers of inclined flat plates. *Journal of Wind Engineering & Industrial Aerodynamics,* 61:99–102.

Cook, N.J. (1990) *The Designer's Guide to Wind Loading of Building Structures. Part 2 Static Structures.* Building Research Establishment and Butterworths, London.

ESDU (1970) Fluid forces and moments on flat plates. Engineering Sciences Data Unit (ESDU International, London). ESDU data item 70015.

ESDU (1980) Mean forces, pressures and flow field velocities for circular cylindrical structures: single cylinder with two-dimensional flow. Engineering Sciences Data Unit (ESDU International, London). ESDU data item 80025.

Gartshore, I.S. (1973) The effects of freestream turbulence on the drag of rectangular two-dimensional prisms. Boundary Layer Wind Tunnel Report, BLWT-4–73, University of Western Ontario.

Jensen, M. (1958) The model law for phenomena in the natural wind. *Ingenioren,* 2:121–8.

Laneville, A., Gartshore, I.S. and Parkinson, G.V. (1975) An explanation of some effects of turbulence on bluff bodies. *Fourth International Conference on Wind Effects on Buildings and structures,* London, UK, September.

Letchford, C.W. and Holmes, J.D. (1994) Wind loads on free-standing walls in turbulent boundary layers. *Journal of Wind Engineering & Industrial Aerodynamics,* 51:1–27.

Macdonald, P.A., Kwok, K.C.S. and Holmes, J.D. (1988) Wind loads on circular storage bins, silos and tanks: I point pressure measurements on isolated structures. *Journal of Wind Engineering & Industrial Aerodynamics,* 31:165–88.

Marchman, J.F. and Werme, T.D. (1982) Mutual interference drag on signs and luminaires. *ASCE Journal of the Structural Division,* 108:2235–44.

Melbourne, W.H. (1995) Bluff body aerodynamics for wind engineering. In: *A State of the Art in Wind Engineering,* ed. P.Krishna, Wiley Eastern, New Delhi.

Schewe, G. (1983) On the force fluctuations acting on a circular cylinder in crossflow from subcritical up to transcritical Reynolds numbers. *Journal of Fluid Mechanics,* 133:265–85.

Scruton, C. (1963) On the wind-excited oscillations of stacks, towers and masts. *Proceedings, International Conference on Wind Effects on Buildings and Structures,* Teddington, UK, 26–28 June, pp. 798–832.

Scruton, C. (1981) An *Introduction to Wind Effects on Structures.* Oxford University Press, Oxford.

Scruton, C. and Rogers, E.W.E. (1972) Steady and unsteady wind loading of buildings and structures. *Philosophical Transactions of the Royal Society of London, Series A,* 269:353–83.

Scruton, C. and Walshe, D.E.J. (1957) A means for avoiding wind-excited oscillations of structures of circular or near-circular cross section. National Physical Laboratory, UK, N.P.L. Aero Report 335 (unpublished).

Vickery, B.J. (1966) Fluctuating lift and drag on a long cylinder of square cross-section in a smooth and turbulent flow. *Journal of Fluid Mechanics,* 25:481–94.

Wootton, L.R. and Scruton, C.P. (1970) Aerodynamic stability. *Proceedings, CIRIA Seminar on the Modern Design of Wind-Sensitive Structures,* CIRIA, London, 18 June, pp. 65–81.

5
Resonant dynamic response and effective static load distributions

5.1 Introduction

Due to the turbulent nature of the wind velocities in storms of all types, the wind loads acting on structures are also highly fluctuating. There is a potential to excite resonant dynamic response for structures or parts of structures with natural frequencies less than about 1 Hz. The resonant response of a structure introduces the complication of a time-history effect, in which the response at any time depends not just on the instantaneous wind gust velocities acting along the structure but also on the previous time history of wind gusts.

This chapter will introduce the principles and analysis of dynamic response to wind. Some discussion of aeroelastic and fatigue effects is included. Also in this chapter, the method of equivalent or effective static wind loading distributions is introduced.

Treatment of dynamic response is continued in Chapters 9–12 on tall buildings, large roofs and sports stadiums, slender towers and masts and bridges, with emphasis on the particular characteristics of these structures. In Chapter 15 code approaches to dynamic response are considered.

5.2 Principles of dynamic response

The fluctuating nature of wind velocities, pressures and forces, as discussed in Chapters 3 and 4, may cause the excitation of significant resonant vibratory response in structures or parts of structures, provided their natural frequencies and damping are low enough. This resonant dynamic response should be distinguished from the background fluctuating response to which all structures are subjected. Figure 5.1 shows the response spectral density of a dynamic structure under wind loading; the area under the entire curve represents the total mean-square fluctuating response (note that the mean response is not included in this plot). The resonant responses in the first two modes of vibration are shown hatched in this diagram. The background response, made up largely of low-frequency contributions below the lowest natural frequency of vibration, is the largest contributor in Figure 5.1 and, in fact, is usually the dominant contribution in the case of along-wind loading. Resonant contributions become more and more significant, and will eventually dominate, as structures becomes taller or longer in relation to their width and their natural frequencies become lower and lower.

Figure 5.2(a) shows the characteristics of the time histories of an along-wind (drag) force; the structural response for a structure with a *high* fundamental natural frequency is shown in Figure 5.2(b), and the response with a *low* natural frequency in Figure 5.2(c). In the former case, the resonant, or vibratory component, clearly plays a minor role in the response, which generally follows closely the time variation of the exciting forces.

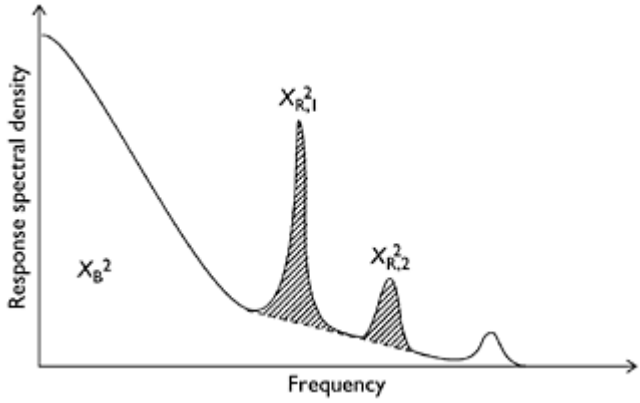

Figure 5.1 Response spectral density for a structure with significant resonant contributions.

However, in the latter case, the resonant response in the fundamental mode of vibration is important, although response in higher modes than the first can usually be neglected.

In fact, the majority of structures fall into the category of Figure 5.2(b), and will *not* experience significant resonant dynamic response. A well-known rule of thumb is that the lowest natural frequency should be below 1 Hz for the resonant response to be significant. However, the amount of resonant response also depends on the damping, aerodynamic or structural, present. For example, high-voltage transmission lines usually have fundamental sway frequencies which are well below 1 Hz; however, the *aerodynamic* damping is very high—typically around 25% of critical—so that the resonant response is largely damped out. Lattice towers, because of their low mass, also have high aerodynamic damping ratios. Slip-jointed steel lighting poles have high *structural* damping due to friction at the joints—this energy-absorbing mechanism will limit the resonant response to wind.

Resonant response, when it does occur, may occasionally produce complex interactions, in which the movement of the structure itself results in additional aeroelastic forces being produced (Section 5.5). In some extreme cases, for example the Tacoma Narrows Bridge failure of 1940 (see Chapter 1), catastrophic failure has resulted. These are exceptional cases, which of course must be avoided, but in the majority of structures with significant resonant dynamic response, the dynamic component is superimposed on a significant or dominant mean and background fluctuating response.

The two major sources of fluctuating wind loads are discussed in Section 4.6. The first and obvious source, exciting resonant dynamic response, is the natural unsteady or turbulent flow in the wind produced by shearing actions as the air flows over the rough surface of the earth, as discussed in Chapter 3. The other main source of fluctuating loads is the alternate vortex shedding which occurs behind bluff cross-sectional shapes such as circular cylinders or square cross-sections. A further source is buffeting forces from the wakes of other structures upwind of the structure of interest.

When a structure experiences resonant dynamic response, counteracting structural forces come into play to balance the wind forces:

- inertial forces proportional to the mass of the structure;
- damping or energy-absorbing forces—in their simplest form, these are proportional to the velocity, but this is not always the case;
- elastic or stiffness forces proportional to the deflections or displacements.

When a structure does respond dynamically, i.e. the resonant response is significant, an important principle to remember is that the condition of the structure, i.e. stresses, deflections, at any given time depends not only on the wind forces acting at the time, but also on the *past history* of wind forces. In the case of quasi-static loading, the structure responds directly to the forces acting instantaneously at any given time.

The effective load distribution due to the resonant part of the loading (Section 5.4.4) is given to a good approximation by the distribution of inertial forces along the structure. This is based on the assumption that the fluctuating wind forces at the resonant frequency approximately balance the damping forces once a stable amplitude of vibration is established.

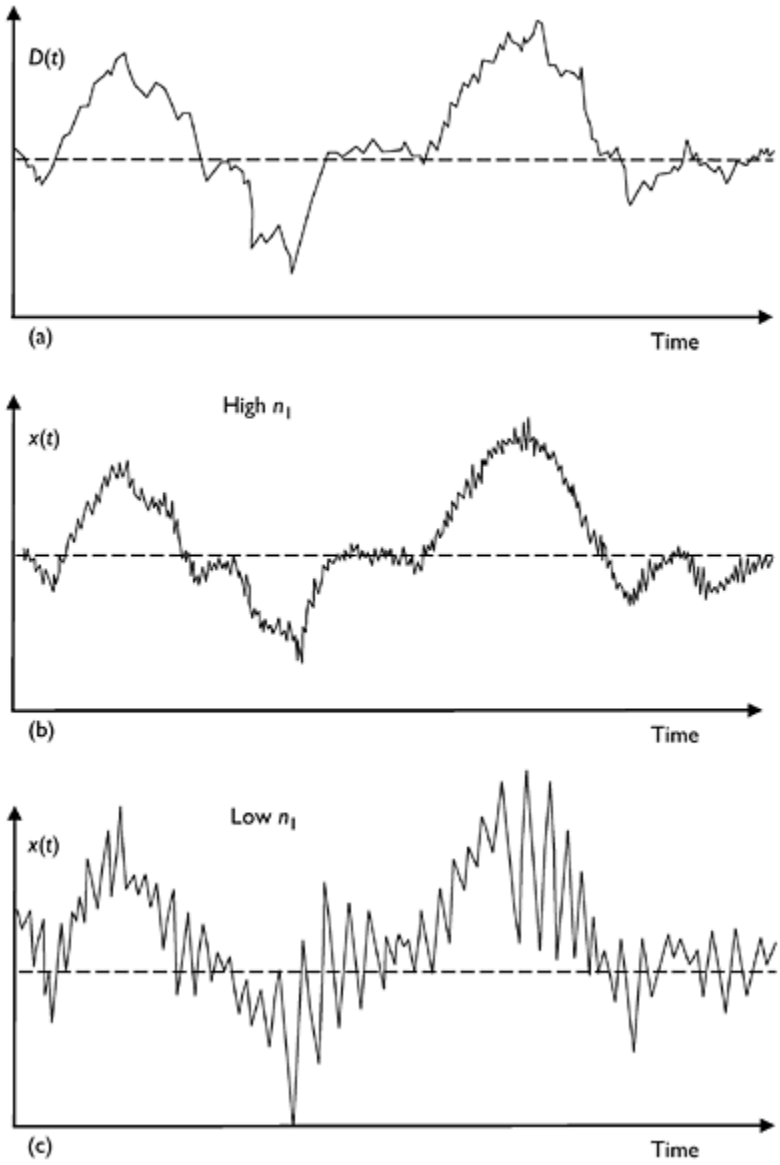

Figure 5.2 Time histories of: (a) wind force; (b) response of a structure with a high natural frequency; (c) response of a structure with a low natural frequency.

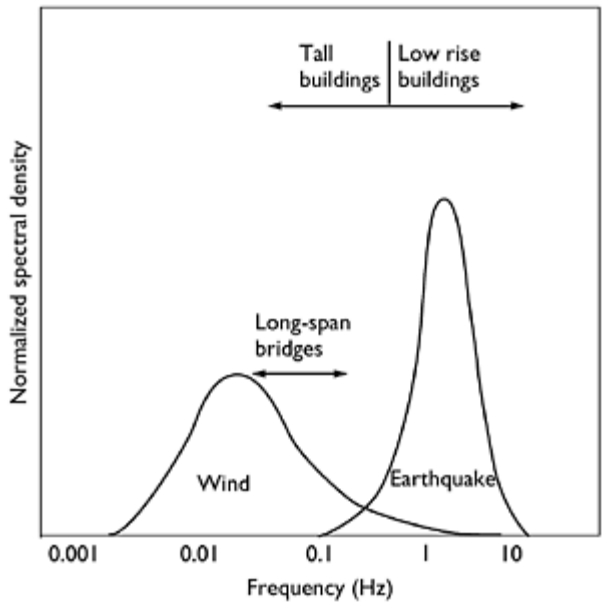

Figure 5.3 Dynamic excitation frequencies of structures by wind and earthquake.

At this point, it is worth noting the essential differences between dynamic response of structures to wind and earthquake. The main differences between the excitation forces due to these two natural phenomena are:

- Earthquakes are of much shorter duration than wind storms (with the possible exception of the passage of a tornado) and are thus treated as transient loadings.
- The predominant frequencies of the earthquake ground motions are typically 10–50 times those of the frequencies in fully developed wind storms. This means that structures will be affected in different ways, e.g. buildings in a certain height range may not experience significant dynamic response to wind loadings, but may be prone to earthquake excitation.
- The earthquake ground motions will appear as *fully* correlated equivalent forces acting over the height of a tall structure. However, the eddy structure in wind storms results in *partially* correlated wind forces acting over the height of the structure. Vortex-shedding forces on a slender structure are also not fully correlated over the height.

Figure 5.3 shows the various frequency ranges for excitation of structures by wind and earthquake actions.

5.3 The random vibration or spectral approach

In some important papers in the 1960s, Davenport outlined an approach to the wind-induced vibration of structures based on random vibration theory (Davenport, 1961, 1963, 1964). Other significant early contributions to the development of this approach were made by Harris (1963) and Vickery (1965, 1966).

The approach uses the concept of the stationary random process to describe wind velocities, pressures and forces. This assumes that the complexities of nature are such that we can never describe, or predict, perfectly (or 'deterministically') the forces generated by wind storms. However, we are able to use averaged quantities like standard deviations, correlations and spectral densities (or 'spectra') to describe the main features of both the exciting forces and the structural response. The *spectral density*, which has already been introduced in Section 3.3.4 and Figure 5.1, is the most important quantity to be considered in this approach, which primarily uses the *frequency domain* to perform calculations and is alternatively known as the *spectral approach*.

Wind speeds, pressures and resulting structural response have generally been treated as stationary random processes in which the time-averaged or mean component is separated from the fluctuating component. Thus:

$$X(t) = \overline{X} + x'(t) \tag{5.1}$$

where $X(t)$ denotes either a wind velocity component, a pressure (measured with respect to a defined reference static pressure) or a structural response such as bending moment, stress resultant, deflection, etc.; $\overline{X}$ the mean or time-averaged component; and $x'(t)$ the fluctuating component such that $\overline{x'(t)} = 0$. If x is a response variable, $x'(t)$ should include any resonant dynamic response resulting from excitation of any natural modes of vibration of the structure.

Figure 5.4 (after Davenport, 1963) illustrates graphically the elements of the spectral approach. The main calculations are done in the bottom row, in which the total meansquare fluctuating response is computed from the spectral density or 'spectrum' of the response. The latter is calculated from the spectrum of the aerodynamic forces, which are, in turn, calculated from the wind turbulence or gust spectrum. The frequency-dependent *aerodynamic* and *mechanical admittance* functions form links between these spectra. The amplification at the resonant frequency, for structures with a low fundamental frequency, will result in a higher mean-square fluctuating and peak response, than is the case for structures with a higher natural frequency, as previously illustrated in Figure 5.2.

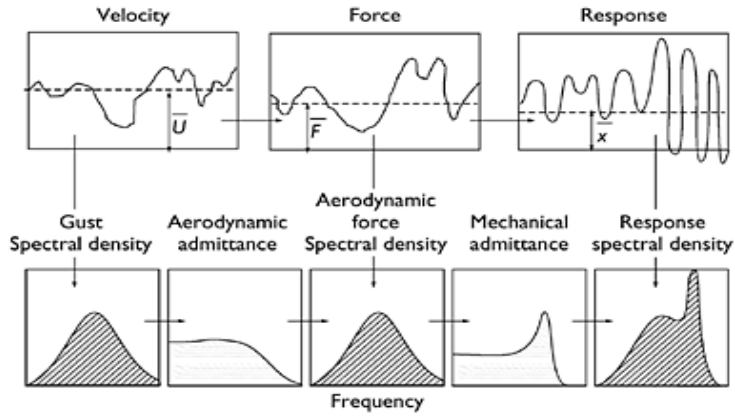

Figure 5.4 The random vibration (frequency domain) approach to resonant dynamic response (Davenport, 1963).

The use of stationary random processes and Equation (5.1) is appropriate for large-scale wind storms such as gales in temperate latitudes and tropical cyclones. It may not be appropriate for some short-duration, transient storms such as downbursts or tornadoes associated with thunderstorms. Methods for these types of storms are still under development.

5.3.1 Along-wind response of a single-degree-of-freedom structure

We will consider first the along-wind dynamic response of a small body whose dynamic characteristics are represented by a simple mass-spring-damper (Figure 5.5) and which does not disturb the approaching turbulent flow significantly. This is a single-degree-of freedom system and is reasonably representative of a structure consisting of a large mass supported by a column of low mass such as a lighting tower or mast with a large array of lamps on top.

The equation of motion of this system under an aerodynamic drag force, *D(t)*, is given by Equation (5.2):

$$m\ddot{x} + c\dot{x} + kx = D(t) \tag{5.2}$$

The quasi-steady assumption (Section 4.6.2) for small structures allows the following relationship between mean-square fluctuating drag force and fluctuating longitudinal wind velocity to be written:

$$\overline{D^2} = C_{D_0}^2 \rho_a \overline{U}^2 \overline{u^2} A^2 \cong \overline{C_D}^2 \rho_a \overline{U}^2 \overline{u^2} A^2 = \frac{4\overline{D}^2}{\overline{U}^2} \overline{u^2} \tag{5.3}$$

Equation (5.3) is analogous to Equation (4.15) for pressures.

Writing Equation (5.3) in terms of spectral density,

Hence,

$$\int_0^\infty S_D(n)\cdot dn = \frac{4\overline{D}^2}{\overline{U}^2}\int_0^\infty S_u(n)\cdot dn$$

$$S_D(n) = \frac{4\overline{D}^2}{\overline{U}^2} S_u(n) \tag{5.4}$$

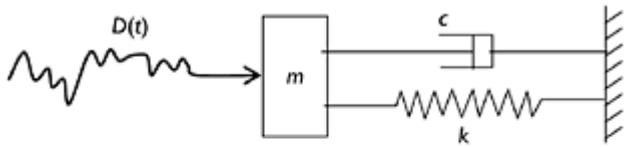

$$n_1 = \frac{1}{2\pi}\sqrt{\frac{k}{m}} \qquad \eta = \frac{c}{2\sqrt{mk}}$$

Figure 5.5 Simplified dynamic model of a structure.

To derive the relationship between fluctuating force and the response of the structure, represented by the simple dynamic system of Figure 5.5, the deflection is first separated into mean and fluctuating components, as in Equation (5.1):

$$X(t) = \overline{X} + x'(t) \tag{5.1}$$

The relationship between mean drag force, $\overline{D}$, and mean deflection, $\overline{X}$, is as follows:

$$\overline{D} = k\,\overline{X} \tag{5.5}$$

where k is the spring stiffness in Figure 5.5.

The spectral density of the deflection is related to the spectral density of the applied force as follows:

$$S_x(n) = \frac{1}{k^2}\,|H(n)|^2\, S_D(n) \tag{5.6}$$

where $|H(n)|^2$ is known as the *mechanical admittance* for the single-degree-of-freedom dynamic system under consideration, given by:

$$|H(n)|^2 = \frac{1}{\left[1-\left(\frac{n}{n_1}\right)^2\right]^2 + 4\eta^2\left(\frac{n}{n_1}\right)^2} \tag{5.7}$$

$|H(n)|$, i.e. the square root of the mechanical admittance, may be recognized as the *dynamic amplification factor* or *dynamic magnification factor* which arises when the response of a single-degree-of-freedom system to a harmonic or sinusoidal, excitation force is considered. n_1 is the undamped natural frequency and η is the ratio of the damping coefficient, c, to critical damping, as shown in Figure (5.5).

By combining Equations (5.4) and (5.6), the spectral density of the deflection response can be related to the spectral density of the wind velocity fluctuations:

$$S_x(n) = \frac{1}{k^2}|H(n)|^2 \frac{4\overline{D}^2}{\overline{U}^2} S_u(n) \tag{5.8}$$

Equation (5.8) applies to structures which have small frontal areas in relation to the length scales of atmospheric turbulence.

For larger structures, the velocity fluctuations do not occur simultaneously over the windward face and their correlation over the whole area, A, must be considered. To allow for this effect, an *aerodynamic admittance*, $\chi^2(n)$, is introduced:

$$S_x(n) = \frac{1}{k^2}|H(n)|^2 \frac{4\overline{D}^2}{\overline{U}^2} \cdot \chi^2(n) \cdot S_u(n)$$

Substituting for $\overline{D}$ from Equation (5.5),

$$S_x(n) = \frac{4\overline{X}^2}{\overline{U}^2}|H(n)|^2 \cdot \chi^2(n) \cdot S_u(n) \tag{5.9}$$

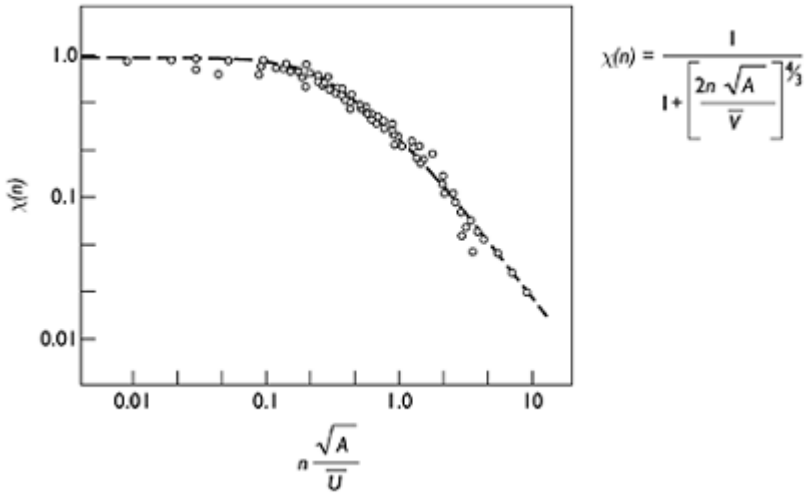

Figure 5.6 Aerodynamic admittance—experimental data and fitted function (Vickery, 1965, 1968).

For open structures such as lattice frame towers which do not disturb the flow greatly, $\chi^2(n)$ can be determined from the correlation properties of the upwind velocity fluctuations (see Section 3.3.6). This assumption is also made for solid structures, but $\chi^2(n)$ has also been obtained experimentally.

Figure 5.6 shows some experimental data with an empirical function fitted. Note that $\chi(n)$ tends towards 1.0 at low frequencies and for small bodies. The low-frequency gusts are nearly fully correlated and fully envelope the face of a structure. For high frequencies or very large bodies, the gusts are ineffective in producing total forces on the structure, due to their lack of correlation, and the aerodynamic admittance tends towards zero.

To obtain the mean-square fluctuating deflection, the spectral density of deflection given by Equation (5.8) is integrated over all frequencies:

$$\sigma_x^2 = \int_0^\infty S_x(n)\cdot \mathrm{d}n = \int_0^\infty \frac{4\overline{X}^2}{\overline{U}^2}|H(n)|^2\cdot\chi^2(n)\cdot S_u(n)\cdot \mathrm{d}n \tag{5.10}$$

The area underneath the integrand in Equation (5.10) can be approximated by two components, *B* and *R*, representing the 'background' and resonant parts, respectively (Figure 5.7).

Thus,

$$\sigma_x^2 = \frac{4\overline{X}^2\sigma_u^2}{\overline{U}^2}\int_0^\infty |H(n)|^2\cdot\chi^2(n)\cdot\frac{S_u(n)^2}{\sigma_u}\cdot \mathrm{d}n \cong \frac{4\overline{X}^2\sigma_u^2}{\overline{U}^2}[B+R] \tag{5.11}$$

where,

$$B = \int_0^\infty \chi^2(n) \cdot \frac{S_u(n)}{\sigma_u^2} \cdot \mathrm{d}n \tag{5.12}$$

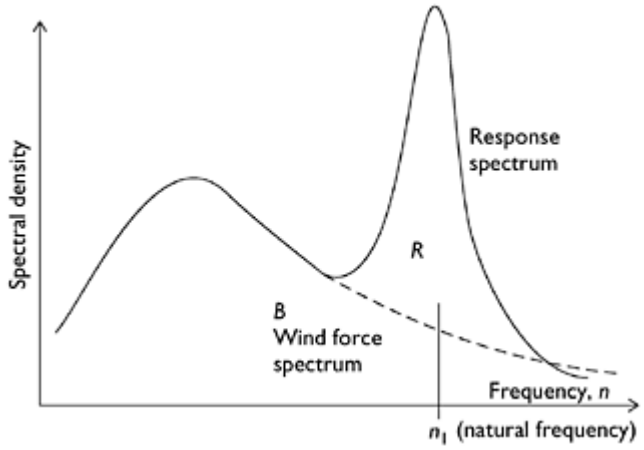

Figure 5.7 Background and resonant components of response.

$$R = \chi^2(n_1) \cdot \frac{S_u(n_1)}{\sigma_u^2} \int_0^\infty |H(n)|^2 \cdot \mathrm{d}n \tag{5.13}$$

The approximation of Equation (5.11) is based on the assumption that over the width of the resonant peak in Figure 5.7, the functions $\chi^2(n)$, $S_u(n)$ are constant at the values $\chi^2(n_1)$, $S_u(n_1)$. This is a good approximation for the flat spectral densities, characteristic of wind loading, and when the resonant peak is narrow, as occurs when the damping is low (Ashraf Ali and Gould, 1985). The integral $\int |H(n)|^2 \cdot \mathrm{d}n$ integrated for n from 0 to ∞ can be evaluated by the method of poles (Crandall and Mark, 1963) and shown to be equal to $(\pi n_1/4\eta)$.

The approximation of Equation (5.11) is used widely in code methods of evaluating along-wind response and will be discussed further in Chapter 15.

The background factor, B, represents the quasi-static response caused by gusts below the natural frequency of the structure. Importantly, it is independent of frequency as shown by Equation (5.12) in which the frequency appears only in the integrand and thus is 'integrated out'. For many structures under wind loading, B is considerably greater than R, i.e. the background response is dominant in comparison with the resonant response. An example of the response of such a structure is shown in Figure 5.2(b).

5.3.2 Gust response factor

A commonly used term in wind engineering is *gust response factor*. The term *gust loading factor* was used by Davenport (1967) and *gust factor* by Vickery (1966). These essentially have the same meaning, although sometimes the factor is applied to the effective applied loading and sometimes to the response of the structure. The term 'gust factor' is better applied to the wind speed itself (Section 3.3.3).

The *gust response factor, G,* may be defined as the ratio of the expected maximum response (e.g. deflection or stress) of the structure in a defined time period (e.g. 10 minutes or 1 h) to the mean or time-averaged response in the same time period. It really has meaning only in stationary or near-stationary winds such as those generated by large-scale synoptic wind events such as gales from depressions in temperate latitudes or tropical cyclones (see Chapter 2).

The expected maximum response of the simple system described in Section 5.3.1 can be written:

$$\hat{X} = \overline{X} + g\sigma_x$$

where g is a *peak factor* which depends on the time interval for which the maximum value is calculated and the frequency range of the response.

From Equation (5.11),

$$G = \frac{\hat{X}}{\overline{X}} = 1 + g\frac{\sigma_x}{\overline{X}} = 1 + 2g\frac{\sigma_u}{\overline{U}}\sqrt{B+R} \tag{5.14}$$

Equation (5.14) or variations of it are used in many codes and standards for wind loading, for simple estimations of the along-wind dynamic loading of structures. The usual approach is to calculate G for the modal coordinate in the first mode of vibration, a_1, and then to apply it to a mean load distribution on the structure from which all responses such as bending moments are calculated. This is an approximate approach which works reasonably well for some structures and load effects such as the base bending moment of tall buildings. However, in other cases it gives significant errors and should be used with caution (e.g. Holmes, 1994; Vickery, 1995—see also Chapter 11).

5.3.3 Peak factor

The along-wind response of structures to wind has a probability distribution which is closely Gaussian. For this case, Davenport (1964) derived the following expression for the peak factor, *g:*

$$g = \sqrt{2\ \log_e(\upsilon T)} + \frac{0.577}{\sqrt{2\ \log_e(\upsilon T)}} \tag{5.15}$$

where υ is the 'cycling rate' or effective frequency for the response; this is often conservatively taken as the natural frequency, n_1. T is the time interval over which the maximum value is required.

5.3.4 Dynamic response factor

In transient or non-stationary winds such as downbursts from thunderstorms, for example, the use of a gust factor or gust response factor is meaningless. The gust response factor is also meaningless in cases when the mean response is very small or zero (such as cross-wind response). In these cases, use of a 'dynamic response factor' is more appropriate. This approach has been adopted recently in some codes and standards for wind loading. The dynamic response factor may be defined in the following way:

Dynamic response factor= (maximum response including resonant and correlation effects)/(maximum response calculated ignoring both resonant and correlation effects)

The denominator is in fact the response calculated using 'static' methods in codes and standards. The dynamic response factor defined as above will usually have a value close to 1. A value greater than 1 can only be caused by a significant resonant response.

The use of the gust response factor and dynamic response factor in wind loading codes and standards will be discussed further in Chapter 15.

5.3.5 Influence coefficient

When considering the action of a time-dependent and spatially varying load such as wind loading on a continuous structure, the *influence coefficient* or *influence line* is an important parameter. To appreciate the need for this, we must understand the concept, familiar to structural designers, of 'load effect'. A load effect is not the load itself but a parameter resulting from the loading which is required for comparison with design criteria. Examples are internal forces or moments such as bending moments or shear forces, stresses or deflections. The influence line represents the value of a single load effect as a unit (static) load is moved around the structure.

Two examples of influence lines are given in Figure 5.8. Figure 5.8(a) shows the influence lines for the bending moment and shear force at a level, *s*, halfway up a lattice tower. These are relatively simple functions; in the case of the shear force, loads (or wind pressures) above the level *s* have uniform effect on the shear force at that level. The influence line for the bending moment varies linearly from unity at the top to zero at the level *s;* thus, wind pressures at the top of the structure have a much larger effect than those lower down on the bending moment, which, in turn, is closely related to the axial forces in the leg members of the tower. It should be noted that loads or wind pressures below the level *s* have *no* effect on the shear force or bending moment at that level.

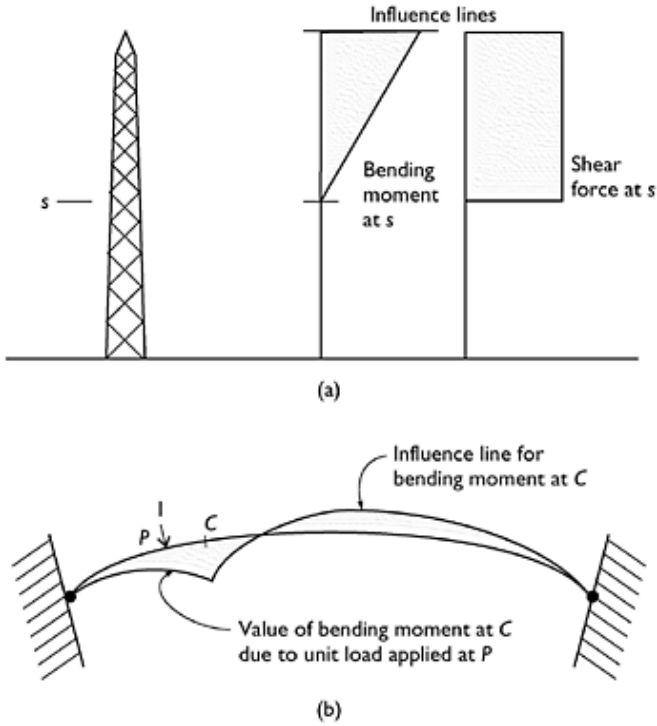

Figure 5.8 Examples of influence lines for an arch roof and a tower.

Figure 5.8(b) shows the influence line for the bending moment at a point in an arch roof. In this case, the sign of the influence line changes along the arch. Thus, wind pressures applied in the same direction at different parts of the roof may have opposite effects on the bending moment at *C*, M_c.

It is important to take into account these non-uniform influences when considering the structural effects of wind loads, even for apparently simple structures, especially for the fluctuating part of the loading.

5.3.6 Along-wind response of a structure with distributed mass—modal analysis

The usual approach to the calculation of the dynamic response of multi-degree-of-freedom structures to dynamic forces, including resonance effects, is to expand the complete displacement response as a summation of components associated with each of the natural modes of vibration:

$$x(z,t) = \Sigma a_j(t)\phi_j(z) \tag{5.16}$$

where j denotes the natural modes; z a spatial coordinate on the structure; $a_j(t)$ a time-varying modal (or generalized) coordinate; and $\phi_j(z)$ a mode shape for the jth mode.

Modal analysis is discussed in most texts on structural dynamics (e.g. Clough and Penzien, 1975; Warburton, 1976).

The approach will be described here in the context of a two-dimensional or 'line-like' structure, with a single spatial coordinate, z, but it can easily be extended to more complex geometries.

Equation (5.16) can be used to determine the complete response of a structure to random forcing, i.e. including the mean component, $\bar{x}$, and the sub-resonant (background) fluctuating component, as well as the resonant responses.

The result of this approach is that separate equations of motion can be written for the modal coordinate $a_j(t)$ for each mode of the structure:

$$G_j\ddot{a}_j + C_j\dot{a}_j + K_j a_j = Q_j(t) \tag{5.17}$$

where G_j is the generalized mass equal to $\int_0^L m(z)\phi_j^2(z)\,dz$, $m(z)$ the mass per unit length along the structure, L the length of the structure, C_j the modal damping $(=2\eta_j G_j\omega_j)$, K_j the modal stiffness, η_j the damping as a fraction of critical for the jth mode, to ω_j the natural undamped circular frequency for the jth mode $(=2\pi n_j = \sqrt{K_j/G_j})$, $Q_j(t)$ the generalized force equal to $\int_0^L f(z,t)\phi_j(z)dz$ and $f(z, t)$ the force per unit length along the structure.

$f(z, t)$ can be taken as along-wind or cross-wind forces. For along-wind forces, by applying a 'strip' assumption which relates the forces on a section of the structure with the flow conditions upstream of the section, it can be written as:

$$f(z,t) = C_d(z).b(z)\frac{1}{2}\rho_a U^2(z,t) \tag{5.18}$$

where $C_d(z)$ is a local drag coefficient, $b(z)$ the local breadth and $U(z, t)$ the longitudinal velocity upstream of the section. If the structure is moving, this should be a relative velocity, which then generates an aerodynamic damping force (Section 5.5.1 and Holmes, 1996a). However, at this point we will assume the structure is stationary, in which case $U(z, t)$ can be written as:

$$U(z, t)=\bar{U}(z)+u'(z, t)$$

where $u'(z, t)$ is the fluctuating component of longitudinal velocity (zero mean).

Then from Equation (5.18),

$$f(z,t) = C_d(z)\cdot b(z)\rho_a\left[\frac{1}{2}\overline{U}^2(z) + \overline{U}(z)u'(z,t) + \frac{1}{2}u'^2(z,t)\right]$$

Neglecting the third term within the square brackets, the fluctuating sectional along-wind force is given by:

$$f'(z,t) = C_d(z) \cdot b(z) \rho_a \overline{U}(z) u'(z,t)$$

and the instantaneous fluctuating generalized force is therefore:

$$Q'_j(t) = \int_0^L f'(z,t)\phi_j(z)\,\mathrm{d}z = \int_0^L C_d(z) \cdot b(z)\rho_a \overline{U}(z) u'(z,t)\phi_j(z)\,\mathrm{d}z$$

Applying the same procedure used in Section 4.6.6, the mean-square generalized force is:

$$\overline{Q_j^2} = \int_0^L \int_0^L \overline{f'(z_1)f'(z_2)}\,\phi_j(z_1)\phi_j(z_2)\,\mathrm{d}z_1\,\mathrm{d}z_2$$
$$= \rho_a{}^2 \int_0^L \int_0^L \overline{u'(z_1)u'(z_2)}\; C_d(z_1) \cdot C_d(z_2) b(z_1) b(z_2) \overline{U}(z_1)\overline{U}(z_2)\phi_j(z_1)\phi_j(z_2)\,\mathrm{d}z_1\,\mathrm{d}z_2$$

This can be simplified for a uniform cross-section with $C_d(z)$ and $b(z)$ constant with z:

$$\overline{Q_j^2} = (\rho_a C_d b)^2 \int_0^L \int_0^L \overline{u'(z_1)u'(z_2)}\;\overline{U}(z_1)\overline{U}(z_2)\phi_j(z_1)\phi_j(z_2)\,\mathrm{d}z_1\,\mathrm{d}z_2 \qquad (5.19)$$

where $\overline{u'(z_1)u'(z_2)}$ is the covariance for the fluctuating velocities at heights z_1 and z_2. If the standard deviation of velocity fluctuations is constant with z, then the covariance can be written as:

$$\overline{u'(z_1)u'(z_2)} = \sigma_u^2 \rho_{uu}(z_1, z_2)$$

where $\rho_{uu}(z_1, z_2)$ is the correlation coefficient for fluctuating velocities at heights z_1 and z_2, defined in Section 3.3.5.

The spectral density of $Q'_j(t)$ can be obtained in analogous way to the mean-square value:

$$S_{Q_j}(n) = (\rho C_d b)^2 \int_0^L \int_0^L \mathrm{Co}(z_1, z_2, n)\;\overline{U}(z_1)\overline{U}(z_2)\phi_j(z_1)\phi_j(z_2)\,\mathrm{d}z_1\,\mathrm{d}z_2 \qquad (5.20)$$

where $Co(z_1, z_2, n)$ is the co-spectral density of the longitudinal velocity fluctuations (Section 3.3.6) (defined in random process theory—e.g. Bendat and Piersol, 1999).

Analogously with Equation (5.6), the spectral density of the modal coordinate $a_j(t)$ is given by:

$$S_{a_j}(n) = \frac{1}{K_j^2} |H_j(n)|^2 S_{Q_j}(n) \tag{5.21}$$

where the mechanical admittance for the jth mode is:

$$|H_j(n)|^2 = \frac{1}{\left[1 - \left(\frac{n}{n_j}\right)^2\right]^2 + 4\eta_j^2 \left(\frac{n}{n_j}\right)^2} \tag{5.22}$$

The mean-square value of $a_j(t)$ can then be obtained by integration of equation (5.21) with respect to frequency:

$$\overline{a_j^2} = \int_0^\infty S_{a_j}(n) \cdot \mathrm{d}n$$

Applying Equation (5.16), the mean-square displacement is obtained from:

$$\overline{x^2} = \sum_{j=1}^{N} \sum_{k=1}^{N} \overline{a_j a_k} \phi_j(z) \phi_k(z)$$

If cross-coupling between modes can be neglected (however, see Section 5.3.7), the above equation becomes:

$$\overline{x^2} = \sum_{j=1}^{N} \overline{a_j^2} \phi_j^2(z) \tag{5.23}$$

The mean-square value of any other response, r (e.g. bending moment, stress) can similarly be obtained if the response, R_j for a unit value of the modal coordinate, a_j, is known. That is:

$$\overline{r^2} = \sum_{j=1}^{N} \overline{a_j^2} R_j^2 \tag{5.24}$$

5.3.7 Along-wind response of a structure with distributed mass—separation of background and resonant components

In the case of wind loading, the method described in the previous section is not an efficient one. For the vast majority of structures, the natural frequencies are at the high end of the range of forcing frequencies from wind loading. Thus, the resonant components become very small as j increases in Equation (5.16). However, the contributions to the mean and background fluctuating components for j greater than 1 in Equation (5.16) *may not be small*. Thus, it is necessary to include higher modes (j>1) in Equation (5.16) not for their resonant contributions, but to accurately determine the mean and background contributions. For example, Vickery (1995) found that over 20 m odes were required to determine the mean value of a response and over 10 values were need to compute the variance. Also for the background response, cross-coupling of modes cannot be neglected, i.e. Equation (5.23) is not valid.

A much more efficient approach is to separately compute the mean and background components as for a quasi-static structure. Thus, the total peak response, $\hat{r}_*$ can be taken to be:

$$\hat{r} = \bar{r} + \sqrt{\hat{r}_B^2 + \sum_j (\hat{r}_{R,j}^2)} \tag{5.25}$$

where $\hat{r}_B$ is the peak background response equal to $g_B\sigma_B$; and $\hat{r}_{R,j}$ is the peak resonant response computed for the jth mode equal to $g_j\sigma_{R,j}$. This approach is illustrated in Figure 5.1.

g_B and gj are peak factors which can be determined from Equation (5.15); in the case of the resonant response, the cycling rate, υ, in Equation (5.15), can be taken as the natural frequency, n_j.

The mean-square value of the quasi-static fluctuating (background) value of any reponse, r, is:

$$\begin{aligned}\overline{r_B^2} = \sigma_B^2 &= \int_0^L \int_0^L \overline{f'(z_1)f'(z_2)}\, I_r(z_1) I_r(z_2)\, \mathrm{d}z_1\, \mathrm{d}z_2 \\ &= \rho_a^2 \int_0^L \int_0^L \overline{u'(z_1)u'(z_2)}\, C_d(z_1) \cdot C_d(z_2) b(z_1) b(z_2) \overline{U}(z_1) \overline{U}(z_2) I_r(z_1) I_r(z_2)\, \mathrm{d}z_1\, \mathrm{d}z_2\end{aligned} \tag{5.26}$$

where $I_r(z)$ is the influence line for r, i.e. the value of r when a unit load is applied at z.

The resonant component of the response in mode j can be written to a good approximation as:

$$\overline{r_{R,j}^2} = \frac{S_{Q_j}(n_j) R_j^2}{K_j^2} \int_0^\infty |H_j(n)|^2 \cdot \mathrm{d}n = \frac{\pi n_1 \cdot S_{Q_j}(n_j) R_j^2}{4\eta_j K_j^2} \tag{5.27}$$

because the integral $\int_0^\infty |H_j(n)|^2 \cdot \mathrm{d}n$, evaluated by the method of poles (Crandall and Mark, 1963) is equal to ($\pi n_j/4\eta_j$).

5.3.8 Along-wind response to non-stationary (transient) winds

It is clear that downburst winds as generated by severe thunderstorms produce time histories which are non-stationary, as shown in Figure 3.9. Calculation of dynamic response to such winds requires a different approach to those described earlier in this chapter for turbulent winds generated within the boundary layers of synoptic winds—which can be considered statistically stationary. One such approach has been 'borrowed' from earthquake engineering.

The use of Duhamel's Integral is a standard technique for the calculation of the dynamic response of structures to transient loadings such as blast loadings or earthquakes. As it represents the response to an arbitrary loading as the superposition of the response to many discrete impulses, this technique is limited to linear structures. However, structures with non-linear characteristics (e.g. stiffness and damping) can usually be linearized with sufficient accuracy to make use of this very convenient technique.

The displacement response of any linear system to an arbitrary force input *D(t)* can be written as:

$$x(t) = \int_0^t h(t-\tau) \cdot D(\tau)\mathrm{d}\tau \tag{5.28}$$

where *h(t)* is the unit impulse response function. Equation (5.28) is a 'convolution integral'.

The unit impulse response function for a simple mass-spring-damper system (Figure 5.5), with an equation of motion given by Equation (5.2), depends on the value of the damping ratio, η, and the natural circular frequency, ω_1, where $\eta = c/2\sqrt{(mk)}$ and $\omega_1 = \sqrt{(k/m)}$.

For $\eta < 1$,

$$h(t) = \left(\frac{1}{m \cdot \omega_1 \sqrt{1-\eta^2}}\right) \exp\left[-\eta\omega_1 t\right] \cdot \sin\left[\omega_1 \sqrt{1-\eta^2} \cdot (t)\right] \tag{5.29}$$

Hence, from Equation (5.28),

$$x(t) = \left(\frac{1}{m \cdot \omega_1 \sqrt{1-\eta^2}}\right) \int_0^t \exp\left[-\eta\omega_1 (t-\tau)\right] \cdot \sin\left[\omega_1 \sqrt{1-\eta^2} \cdot (t-\tau)\right] \cdot D(\tau)\mathrm{d}\tau \tag{5.30}$$

The right-hand side of Equation (5.30) is known as 'Duhamel's Integral', e.g. Clough and Penzien (1975).

The effective quasi-static along-wind force, $D_{eff}(t)$, is then given by the product of the displacement response, $x(t)$, and the stiffness, k:

$$D_{eff}(t) = k \cdot x(t) = \left(\frac{\omega_1}{\sqrt{1-\eta^2}}\right) \int_0^t \exp[-\eta\omega_1(t-\tau)] \cdot \sin\left[\omega_1\sqrt{1-\eta^2}\cdot(t-\tau)\right] \cdot D(\tau)\mathrm{d}\tau \tag{5.31}$$

The dynamic response factor (Section 5.3.4) can then be obtained as the ratio of the maximum value of the effective static force, $D_{eff}(t)$, in the time history to the maximum value of the applied force $D(t)$ in the same time history. Note that these maxima will generally not occur at the same time, t.

Figure 5.9 shows calculated dynamic response factors to the downburst measured in 2002 at Lubbock, Texas (Figure 3.9), for structures with periods of 6–100 s (circular frequencies of 0.06–1 rad/s) and damping ratios from 0.1 to 3 (Holmes *et al.*, 2005). For structures with shorter periods, more closely spaced time intervals are required in the recorded wind time histories. The information in Figure 5.9 resembles closely that provided in 'response spectra' for earthquake design.

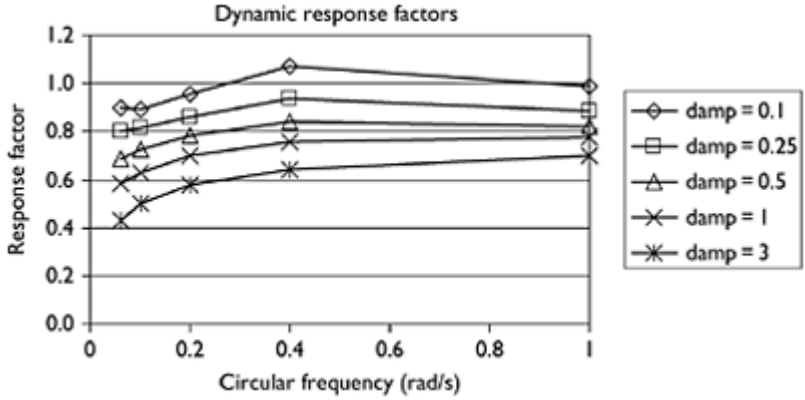

Figure 5.9 Dynamic response factors for the response of structures of various frequencies and damping to the Lubbock downburst of 2002.

5.4 Effective static loading distributions

5.4.1 Introduction

Effective static wind load distributions are those loadings that produce the correct expected values of peak load effects such as bending moments, axial forces in members or deflections, generated by the fluctuating wind loading. The effective peak loading distributions associated with the mean wind loading, the fluctuating quasi-static or

background response and the resonant response are identified and combined to give a total effective peak wind loading distribution.

Following the procedure described in the previous sections, effective static peak loading distributions can be separately derived for the following three components:

(a) mean component;
(b) background or sub-resonant component; and
(c) resonant components.

The background component is derived making use of a formula derived by Kasperski and Niemann (1992), and depends on the load effect in question. The resonant component comprises an inertial loading, similar to that used in earthquake engineering.

The approach will be illustrated by examples of buildings with long-span roofs and free-standing lattice towers and chimneys. Simplifications will be suggested to make the method more palatable to structural engineers used to analysing and designing with static loadings.

The main advantage of the effective static load distribution approach is that the distributions can be applied to static structural analysis computer programs for use in final structural design. The approach can be applied to any type of structure (Holmes and Kasperski, 1996).

5.4.2 Mean load distributions

The mean wind loading on a structure which does not distort the air flow significantly can be obtained simply by relating the mean local pressure or force per unit length to the mean wind speed. Thus, for the mean along-wind force per unit height acting on a tower:

$$\overline{f}(z) = [0.5\rho_a \overline{U}(z)^2] C_d b(z) \tag{5.32}$$

where ρ_a is the density of air; $\bar{U}(z)$ the mean wind speed at height z; C_d is a drag coefficient; and $b(z)$ is the reference breadth at the height z.

The mean value of any load effect (e.g. shear force, bending moment, deflection) can be obtained by integrating the local load with the influence line over the appropriate height. However, if the purpose is to derive an equivalent static loading, then Equation (5.32) is already in this form.

In the case of 'solid' structures (such as cooling towers and most buildings) with at least two dimensions comparable to the size of turbulent eddies in the atmosphere, Equation (5.32) cannot be used, but wind-tunnel tests can be employed to determine mean pressure coefficients, $\overline{C}_p$, which can then be used with a reference wind speed, $\bar{U}_h$, to determine local mean pressures on the structure:

$$\overline{p}(z) = [0.5\ \rho_a\ \overline{U}_h^2] \overline{C}_p \tag{5.33}$$

5.4.3 Background loading distributions

As discussed previously, the background wind loading is the quasi-static loading produced by fluctuations due to turbulence, but with frequencies too low to excite any resonant response. Over the duration of a wind storm, because of the incomplete correlations of pressures at various points on a structure, loadings varying both in space and time will be experienced. It is necessary to identify those instantaneous loadings which produce the critical load effects in a structure. The formula which enables this to be done is the 'Load-Response Correlation' formula derived by Kasperski and Niemann (1992).

This formula gives the expected 'instantaneous' pressure distribution associated with the maximum or minimum load effect. Thus, for the maximum value, $\hat{r}$, of a load effect, *r:*

$$(p_i)_{\hat{r}} = \overline{p}_i + g_B \cdot \rho_{r,p_i} \cdot \sigma_{p_i} \tag{5.34}$$

where $\overline{p}_i$ and σ_{pi} are the mean and root-mean-square (r.m.s.) pressures at point or panel, *i;* $\rho_{r,\,pi}$ the correlation coefficient between the fluctuating load effect and the fluctuating pressure at point *i* (this can be determined from the correlation coefficients for the fluctuating pressures at all points on the tributary area and from the influence coefficients); and g_B the peak factor for the background response which normally lies in the range 2.5–5.

A simple example of the application of this formula is given in Appendix F.

The second term on the right-hand side of Equation (5.34) represents the background fluctuating load distribution. This term can also be written in the form of a continuous distribution:

$$f_B(z) = g_B \rho(z)\, \sigma_p(z) \tag{5.35}$$

where $\rho(z)$ denotes the correlation coefficient between the fluctuating load at position *z* on the structure and the load effect of interest; and $\sigma_p(z)$ is the r.m.s. fluctuating load at position *z*.

In Equation (5.34), the correlation coefficient, $\rho_{r,\,pi}$, can be shown to be given by:

$$\rho_{r,p_i} = \sum_k \left[\overline{p_i(t) p_k(t)}\; I_k\right] / (\sigma_{p_i}\, \sigma_r) \tag{5.36}$$

where I_k is the influence coefficient for a pressure applied at position, *k*.

The standard deviation of the structural load effect, σ_r, is given by (Holmes and Best, 1981):

$$\sigma_r^2 = \sum_i \sum_k \overline{p_i(t) p_k(t)}\; I_i I_k \tag{5.37}$$

When the continuous form is used, Equations (5.36) and (5.37) are replaced by an integral form (Holmes, 1996b):

$$\rho(z) = \frac{\int_s^h \overline{f'(z)f'(z_1)} I_r(z_1) b(z_1) \mathrm{d}z_1}{\left\{ \int_s^h \int_s^h \overline{f'(z_1)f'(z_2)} I_r(z_1) I_r(z_2) b(z_1) b(z_2) \mathrm{d}z_1 \, \mathrm{d}z_2 \right\}^{1/2} \sqrt{\overline{f'^2(z)}}} \tag{5.38}$$

where $I_r(z)$ now denotes the influence function for the load effect, r, as a function of position z and $b(z)$ the breadth of the structure at position z. For a vertical structure, the integrations in Equation (5.38) are carried out for the height range from s, the height at which the load effect (e.g. bending moment, shearing force, member force) is being evaluated, and the top of the structure, h.

Clearly, because the correlation coefficient, $\rho_{r,\,pi}$, calculated by Equation (5.36) or $\rho(z)$ calculated by Equation (5.38) are dependent on the particular load effect, then the background load distribution will also depend on the nature of the load effect.

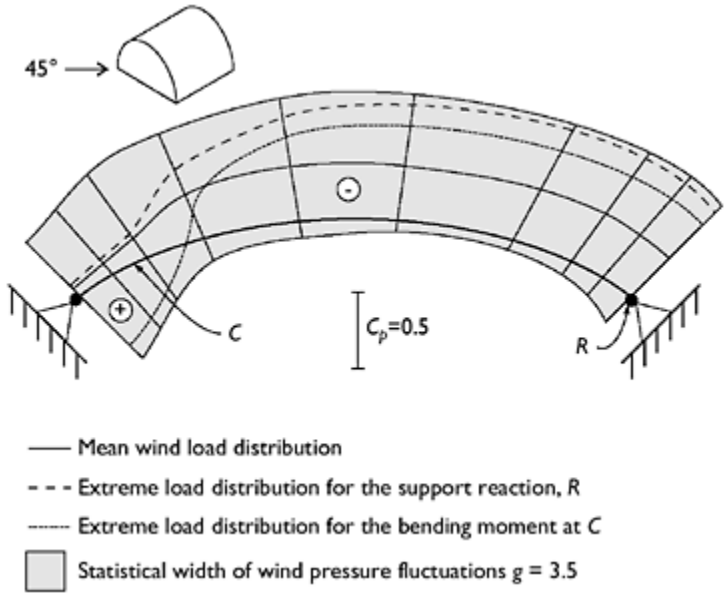

Figure 5.10 Mean and effective background loading distributions for an arch roof (Kasperski and Niemann, 1992).

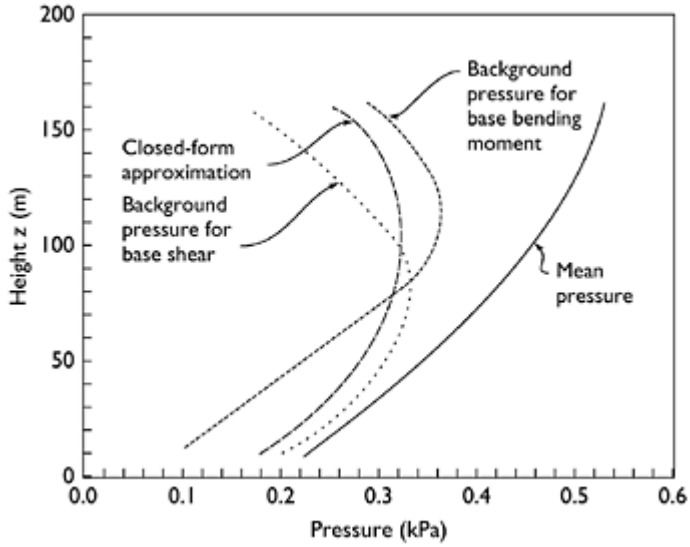

Figure 5.11 Mean and effective background load distributions for a 160 m tower (Holmes, 1996b).

Figures 5.10 and 5.11 give examples of background loading distributions calculated using these methods. Figure 5.10 shows examples of peak load (mean+background) distributions for a support reaction (dashed) and a bending moment (dotted) in an arch roof. These distributions fall within an envelope formed by the maximum and minimum pressure distributions along the arch. It should also be noted that the distribution for the bending moment at *C* includes a region of positive pressure.

Figure 5.11 shows the background pressure distribution for the base shear force and base bending moment on a lattice tower 160 m high, determined by calculation using Equation (5.35) (Holmes, 1996b). The maxima for these distributions occur at around 70 m height for the base shear and about 120 m for the base bending moment. An approximation (Holmes, 1996b) to these distributions, which is independent of the load effect but dependent on the height at which the load effect is evaluated, is also shown in Figure 5.11.

5.4.4 Load distributions for resonant response (single resonant mode)

The equivalent load distribution for the resonant response in the first mode can be represented as a distribution of inertial forces over the length of the structure. Thus, an equivalent load distribution for the resonant response, $f_R(z)$, is given by:

$$f_R(z) = g_R m(z)(2\pi n_1)^2 \sqrt{\overline{a^2}}\, \phi_1(z) \tag{5.39}$$

where g_R is the peak factor for resonant response; *m(z)* a mass per unit length; n_1 the first mode natural frequency; $\sqrt{\overline{a^2}}$ the r.m.s. modal coordinate (resonant contribution only) and $\phi_1(z)$ the mode shape for the first mode of vibration.

Determination of the r.m.s. modal coordinate requires knowledge of the spectral density of the exciting forces, the correlation of those forces at the natural frequency (or aerodynamic admittance) and the modal damping and stiffness, as discussed in Sections 5.3.1 and 5.3.6.

5.4.5 Combined load distribution

The combined effective static load distribution for mean, background and resonant components (one mode) is obtained as follows:

$$f_c(z) = \overline{f}(z) + W_{back}\, f_B(z) + W_{res}(z)\, f_R(z) \tag{5.40}$$

where the absolute values of the weighting factors W_{back} and W_{res} are given by:

$$|W_{back}| = \frac{g_B \sigma_{r,B}}{\left(g_B^2 \sigma_{r,B}^2 + g_R^2 \sigma_{r,R}^2\right)^{1/2}} \qquad |W_{res}| = \frac{g_R \sigma_{r,R}}{\left(g_B^2 \sigma_{r,B}^2 + g_R^2 \sigma_{r,R}^2\right)^{1/2}} \tag{5.41}$$

The above equation assumes that the fluctuating background and resonant components are uncorrelated with each other, so that Equation (5.25) applies. W_{back} and W_{res} will be positive if the influence line of the load effect, *r*, and the mode shape are both all positive, but either could be negative in many cases.

Multiplying by the influence coefficient and summing over the whole structure, Equation (5.40) will give Equation (5.25) for the total peak load effect.

An alternative to Equation (5.40) is to combine the background and resonant distributions in the same way that the load effects themselves were combined (Equation (5.25)), i.e.:

$$f_c(z) = \overline{f}(z) + \sqrt{[f_B(z)]^2 + [f_R(z)]^2} \tag{5.42}$$

The second term on the right-hand side is an approximation to the correct combination formula (Equation 5.40) and is independent of the load effect or its influence line. Equation (5.42) with positive and negative signs taken in front of the square root is, in fact, an ‘envelope’ of the combined distributions for all load effects. However, it is a good approximation for cases where the influence line $I_r(z)$ and the mode shape have the same sign for all *z* (Holmes, 1996b).

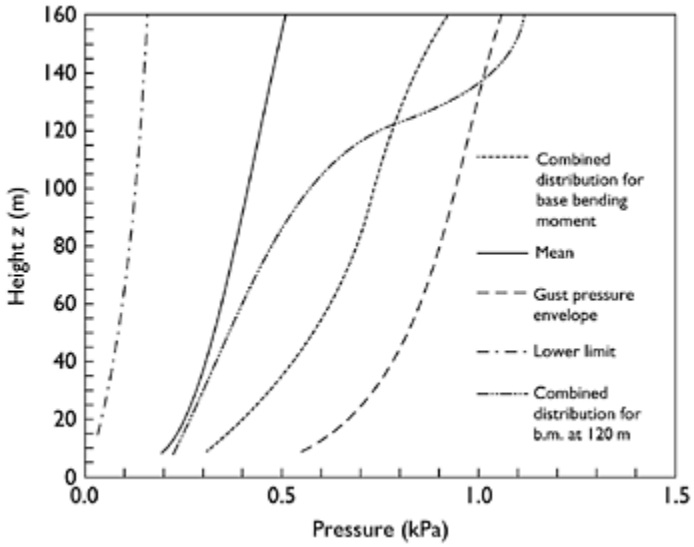

Figure 5.12 Combined mean, background and resonant load distributions for a 160 m tower (Holmes, 1996b).

Examples of the combined distribution calculated using Equation (5.42) are given in Figure 5.12 for a 160 m lattice tower (Holmes, 1996b). When the resonant component is included, the combined loading can exceed the 'peak gust pressure envelope', i.e. the expected limit of non-simultaneous peak pressures, as is the case in Figure 5.12 for the bending moment at 120 m.

Equations (5.40) and (5.41) can be extended to cover more than one resonant mode by introducing an additional term for each participating mode of vibration. An example of combined equivalent static load distributions when more than one resonant mode contributes significantly is discussed in Section 12.3.4.

5.5 Aeroelastic forces

For very flexible, dynamically wind-sensitive structures, the motion of the structure may itself generate aerodynamic forces. In extreme cases, the forces may be of such a magnitude and act in a direction to sustain or increase the motion; in these cases, an unstable situation may arise such that a small disturbance may initiate a growing amplitude of vibration. This is known as 'aerodynamic instability'—examples of which are the 'galloping' of iced-up transmission lines and the flutter of long suspension bridges (such as the Tacoma Narrows Bridge failure of 1940).

On the other hand 'aerodynamic damping' forces may act to reduce the amplitude of vibration induced by wind. This is the case with the along-wind vibration of tall structures such as lattice towers of relatively low mass.

The subject of aeroelasticity and aerodynamic stability is a complex one, and one which most engineers will not need to be involved with. However, some discussion of the principles will be given in this section. A number of general reviews of this aspect of wind loads are available (e.g. Scanlan, 1982).

5.5.1 Aerodynamic damping

Consider the along-wind motion of a structure with a square cross-section, as shown in Figure 5.13. Ignoring the effects of turbulence initially, we will consider only the mean wind speed, $\bar{U}$. If the body itself is moving in the along-wind direction with a velocity, $\dot{x}$, the relative velocity of the air with respect to the moving body is $(\overline{U} - \dot{x})$. We then have a drag force per unit length of the structure equal to:

$$D = C_D \frac{1}{2}\rho_a b(\overline{U} - \dot{x})^2 \cong C_D \frac{1}{2}\rho_a b\overline{U}^2 \left(1 - \frac{2\dot{x}}{\overline{U}}\right)$$
$$= C_D \frac{1}{2}\rho_a b\overline{U}^2 - C_D \rho_a b\overline{U}\dot{x}$$

for small values of $\dot{x}/\overline{U}$. The second term on the right-hand side is a quantity proportional to the structure velocity, $\dot{x}$, and this represents a form of damping. When transferred to the left-hand side of the equation of motion (Equation 5.2), it combines with the structural damping term, $c\dot{x}$, to reduce the aerodynamic response.

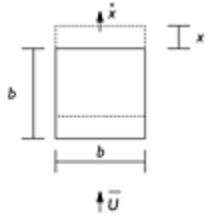

Figure 5.13 Along-wind relative motion and aerodynamic damping.

For a continuous structure, the along-wind aerodynamic damping coefficient in mode *j* can be shown to be (Holmes, 1996a):

$$C_{\text{aero},j} = \rho_a \int_0^L C_d(z) b(z) \overline{U}(z) \phi_j^2(z)\, dz$$

giving a critical aerodynamic damping ratio, $\eta_{\text{aero},j}$, equal

$$\eta_{\text{aero},j} = \frac{\rho_a \int_0^L C_d(z) b(z) \overline{U}(z) \phi_j^2(z)\, dz}{4\pi n_j G_j} \qquad (5.43)$$

5.5.2 Galloping

Galloping is a form of single-degree-of-freedom aerodynamic instability, which can occur for long bodies with certain cross-sections. It is a pure translational, cross-wind vibration. Consider a section of a body with a square cross-section as shown in Figure 5.14.

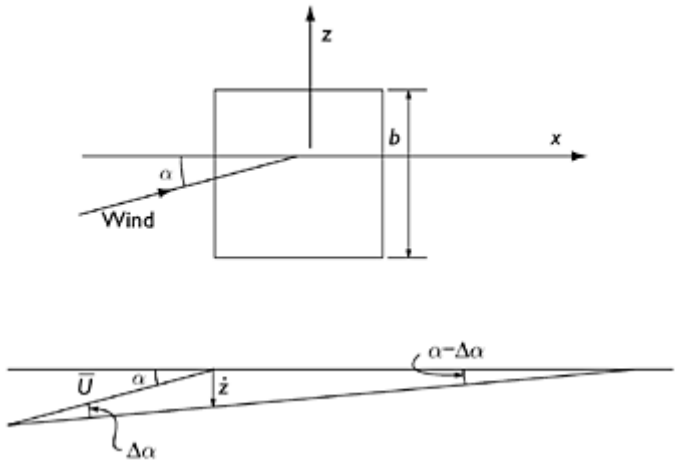

Figure 5.14 Cross-wind relative motion and galloping.

The aerodynamic force per unit length, in the z-direction, is obtained from the lift and drag by a change of axes (Figure 4.3):

$$F_z = D\sin\alpha + L\cos\alpha = \frac{1}{2}\rho_a \overline{U}^2 b(C_D \sin\alpha + C_L \cos\alpha)$$

Hence,

$$\frac{dF_z}{d\alpha} = \frac{1}{2}\rho_a \overline{U}^2 b\left(C_D \cos\alpha + \frac{dC_D}{d\alpha}\sin\alpha - C_L \sin\alpha + \frac{dC_L}{d\alpha}\cos\alpha\right)$$

Setting α equal to zero (for flow in the *x*-direction),

$$\frac{dF_z}{d\alpha} = \frac{1}{2}\rho_a \overline{U}^2 b\left(C_D + \frac{dC_L}{d\alpha}\right) \tag{5.44}$$

If the body is moving in the *z*-direction with velocity, ż there will be a reduction in the apparent angle of attack of the flow by ż/Ū or an increase in angle of attack by −ż/Ū.

From Equation (5.44),

$$\Delta F_z \cong \frac{1}{2}\rho_a \overline{U}^2 b\left(C_D + \frac{dC_L}{d\alpha}\right)\Delta\alpha$$

Substituting, $\Delta\alpha = -\dot{z}/\bar{U}$,

$$\Delta F_z \cong \frac{1}{2}\rho_a \overline{U}^2 b\left(C_D + \frac{dC_L}{d\alpha}\right)\left(-\frac{\dot{z}}{\overline{U}}\right)$$
$$= -\frac{1}{2}\rho_a \overline{U} b\left(C_D + \frac{dC_L}{d\alpha}\right)\dot{z} \qquad (5.45)$$

If $(C_D + dC_L/d\alpha) < 0$, there will be an aerodynamic force in the z-direction proportional to the velocity of the motion, $\dot{z}$, or a *negative* aerodynamic damping term when it is transposed to the left-hand side of the equation of motion. This is known as 'den Hartog's criterion'.

This situation can arise for a square section, which has a negative slope $dC_L/d\alpha$, with a magnitude greater than C_D, for α equal to zero (Figure 5.14).

5.5.3 Flutter

Consider now a two-dimensional bluff body able to move, with elastic restraint, in both vertical translation and rotation (i.e. bending and torsion deflections).

The body shown in Figure 5.15 is being twisted and the section shown is rotating with an angular velocity, $\dot{\theta}$, radians per second. This gives the relative wind, with respect to the rotating body, a vertical component of velocity at the leading edge of $\dot{\theta}d/2$, and hence a relative angle of attack between the apparent wind direction and the rotating body of $-\dot{\theta}d/2\overline{U}$. This effective angle of attack can generate both a vertical force and a moment if the centre of pressure is not collinear with the centre of rotation of the body. These aeroelastic forces can generate instabilities, if they are not completely opposed by the structural damping in the rotational mode. Aerodynamic instabilities involving rotation are known as 'flutter', using aeronautical parlance, and are a potential problem with the suspended decks of long-span bridges.

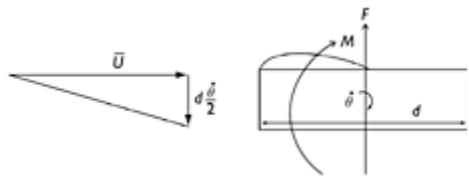

Figure 5.15 Aeroelastic forces generated by rotation of a cross-section.

The equations of motion (per unit mass or moment of inertia) for the two degrees of freedom of a bluff body can be written (Scanlan and Tomko, 1971; Scanlan and Gade, 1977; Matsumoto, 1996) as:

$$\ddot{z} + 2\eta_z\omega_z\dot{z} + \omega_z^2 z = \frac{F_z(t)}{m} + H_1\dot{z} + H_2\dot{\theta} + H_3\theta \tag{5.46}$$

$$\ddot{\theta} + 2\eta_\theta\omega_\theta\dot{\theta} + \omega_\theta^2\theta = \frac{M(t)}{I} + A_1\dot{z} + A_2\dot{\theta} + A_3\theta \tag{5.47}$$

The terms A_i and H_i are linear aeroelastic coefficients or *flutter derivatives* which are usually determined experimentally for particular cross-sections. They are functions of non-dimensional or *reduced* frequency. $F_z(t)$ and $M(t)$ are forces and moments due to other mechanisms which act on a static body (e.g. turbulent buffeting or vortex shedding). $\omega_z(=2\pi n_z)$ and $\omega_\theta(=2\pi n_\theta)$ are the undamped circular frequencies in still air for vertical motion and rotation, respectively.

Note that Equations (5.46) and (5.47) have been 'linearized', i.e. they only contain terms in $\dot{z}$, θ, $\dot{\theta}$, etc. There could be smaller terms in $\dot{z}^2$, θ^2, $\dot{\theta}^3$, etc. The two equations are 'coupled' second-order linear differential equations. The coupling arises from the ocurrence of terms in z and θ, or their derivatives in both equations. This can result in coupled aeroelastic instabilities, which are a combination of vertical (bending) and rotational (torsion) motions, depending on the signs and magnitudes of the A_i and H_i derivatives. All bridge decks will reach this state at a high enough wind speed.

Several particular types of instability for bluff bodies have been defined. Three of these are summarized in Table 5.1.

Coupled aeroelastic instabilities in relation to long-span bridge decks and flutter derivatives are further discussed in Chapter 12—Bridges.

5.5.4 Lock-in

Motion-induced forces can occur during vibration produced by vortex shedding (Section 4.6.3). Through a feedback mechanism, the frequency of the shedding of vortices can 'lock-in' to the frequency of motion of the body. The strength of the vortices shed and the resulting fluctuating forces are also enhanced. *Lock-in* has been observed many times during the vibration of lightly damped cylindrical structures such as steel chimneys and occasionally during the vortex-induced vibration of long-span bridges.

Table 5.1 Types of aerodynamic instabilities

Name	*Conditions*	*Type of motion*	*Type of section*
Galloping	$H_1>0$	Translational	Square section
'Stall' flutter	$A_2>0$	Rotational	Rectangle, H-section
'Classical' flutter	$H_2>0$, $A_1>0$	Coupled	Flat plate, airfoil

5.6 Fatigue under wind loading

5.6.1 Metallic fatigue

The ‘fatigue’ of metallic materials under cyclic loading has been well researched, although the treatment of fatigue damage under the random dynamic loading characteristic of wind loading is less well developed.

In the usual failure model for the fatigue of metals it is assumed that each cycle of a sinusoidal stress response inflicts an increment of damage which depends on the amplitude of the stress. Each successive cycle then generates additional damage which accumulates in proportion to the number of cycles until failure occurs. The results of constant amplitude fatigue tests are usually expressed in the form of an *s–N* curve, where *s* is the stress amplitude and *N* is the number of cycles until failure. For many materials, the *s–N* curve is well approximated by a straight line when log *s* is plotted against log *N* (Figure 5.16). This implies an equation of the form:

$$Ns^m=K \tag{5.48}$$

where *K* is a constant which depends on the material, and the exponent *m* varies between about 5 and 20.

A criterion for failure under repeated loading with a range of different amplitudes is Miner’s Rule:

$$\sum\left(\frac{n_i}{N_i}\right)=1 \tag{5.49}$$

where n_i is the number of stress cycles at an amplitude for which N_i cycles are required to cause failure. Thus, failure is expected when the sum of the fractional damage for all stress levels is unity.

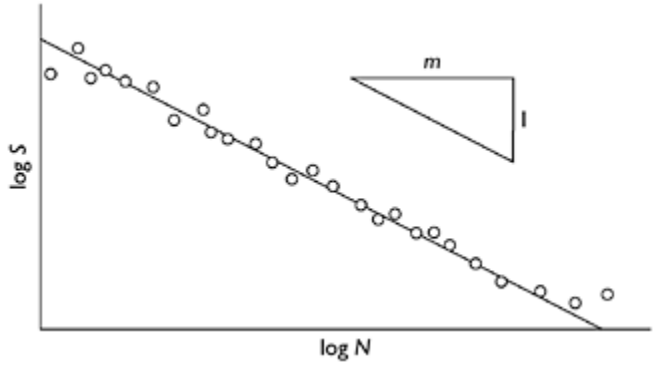

Figure 5.16 Form of a typical *s–N* curve.

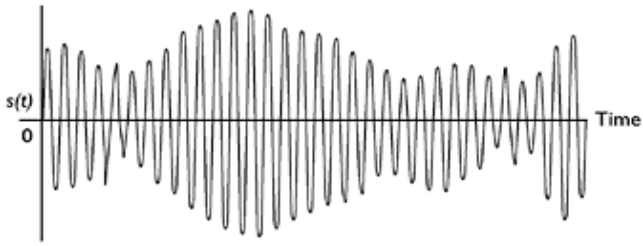

Figure 5.17 Stress-time history under narrow-band random vibrations.

Note that there is no restriction on the *order* in which the various stress amplitudes are applied in Miner's Rule. Thus, we may apply it to a random loading process which can be considered as a series of cycles with randomly varying amplitudes.

5.6.2 Narrow-band fatigue loading

Some wind loading situations produce resonant 'narrow-band' vibrations. For example, the along-wind response of structures with low natural frequencies (Section 5.3.1) and cross-wind vortex-induced response of circular cylindrical structures with low damping. In these cases, the resulting stress variations can be regarded as quasi-sinusoidal with randomly varying amplitudes, as shown in Figure 5.17.

For a narrow-band random stress $s(t)$, the proportion of cycles with amplitudes in the range from s to $s+\delta s$ is $f_p(s)\cdot\delta s$, where $f_p(s)$ is the probability density of the peaks. The total number of cycles in a time period, T, is $\upsilon_0^+ T$, where υ_0^+ is the rate of crossing of the mean stress. For narrow-band resonant vibration, υ_0^+ may be taken to be equal to the natural frequency of vibration.

Then the total number of cycles with amplitudes in the range s to δs is given by:

$$n(s) = \upsilon_0^+ T\, f_p(s)\cdot\delta s \tag{5.50}$$

If $N(s)$ is the number of cycles at amplitude s to cause failure, then the fractional damage at this stress level:

$$\frac{n(s)}{N(s)} = \frac{\upsilon_o^+ T f_p(s)\, s^m\, \delta s}{K}$$

where Equation (5.50) has been used for $n(s)$ and Equation (5.48) for $N(s)$.

The total expected fractional damage over all stress amplitudes is then, by Miner's Rule:

$$D = \sum_0^\infty \frac{n(s)}{N(s)} = \frac{\upsilon_o^+ T \int_0^\infty f_p(s)\, s^m\, \mathrm{d}s}{K} \tag{5.51}$$

Wind-induced narrow-band vibrations can be taken to have a normal or Gaussian probability distribution (Section C3.1). If this is the case then the peaks or amplitudes, *s*, have a Rayleigh distribution (e.g. Crandall and Mark, 1963):

$$f_p(s) = \frac{s}{\sigma^2} \exp\left(-\frac{s^2}{2\sigma^2}\right) \tag{5.52}$$

where σ is the standard deviation of the entire stress history. Derivation of Equation (5.52) is based on the level-crossing formula of Rice (1944–5).

Substituting into Equation (5.51),

$$D = \frac{v_0^+ T}{K\sigma^2} \int_0^\infty s^{m+1} \exp\left(-\frac{s^2}{2\sigma^2}\right) \mathrm{d}s = \frac{v_0^+ T}{K} (\sqrt{2}\sigma)^m \Gamma\left(\frac{m}{2}+1\right) \tag{5.53}$$

Here the following mathematical result has been used (Crandall and Mark, 1963):

$$\int_0^\infty x^n \exp\left(-\frac{x^2}{2\sigma^2}\right) \mathrm{d}x = \frac{(\sqrt{2}\sigma)^{n+1}}{2} \Gamma\left(\frac{n+1}{2}\right) \tag{5.54}$$

where $\Gamma(x)$ is the Gamma Function.

Equation (5.53) is a very useful 'closed-form' result, but it is restricted by two important assumptions:

- 'high-cycle' fatigue behaviour in which steel is in the elastic range, and for which an *s*–*N* curve of the form of Equation (5.48) is valid, has been assumed;
- narrow-band vibration in a single resonant mode of the form shown in Figure 5.17 has been assumed. In wind loading this is a good model of the behaviour for vortex-shedding-induced vibrations in low turbulence conditions. For along-wind loading, the background (sub-resonant) components are almost always important and result in a random wide-band response of the structure.

5.6.3 Wide-band fatigue loading

Wide-band random vibration consists of contributions over a broad range of frequencies with a large resonant peak—this type of response is typical for wind loading (Figure 5.7). A number of cycle counting methods for wide-band stress variations have been proposed (Bowling, 1972). One of the most realistic of these is the 'rainflow' method proposed by Matsuishi and Endo (1968). In this method, which uses the analogy of rain flowing over the undulations of a roof, cycles associated with complete hysteresis cycles of the metal are identified. Use of this method rather than a simple level-crossing approach which is the basis of the narrow-band approach described in Section 5.6.2, invariably results in fewer cycle counts.

A useful empirical approach has been proposed by Wirsching and Light (1980). They proposed that the fractional fatigue damage under a wide-band random stress variation can be written as:

$$D=\lambda D_{nb} \tag{5.55}$$

where D_{nb} is the damage calculated for narrow-band vibration with the same standard deviation, σ (Equation 5.53). A is a parameter determined empirically. The approach used to determine λ was to use simulations of wide-band processes with spectral densities of various shapes and bandwidths and rainflow counting for fatigue cycles.

The formula proposed by Wirsching and Light to estimate λ was:

$$\lambda=a+(1-a)(1-\varepsilon)^b \tag{5.56}$$

where a and b are functions of the exponent m (Equation 5.48) obtained by least-squares fitting as follows:

$$a \cong 0.926 - 0.033\,m \tag{5.57}$$

$$b \cong 1.587\,m - 2.323 \tag{5.58}$$

ε is a spectral bandwidth parameter equal to:

$$\varepsilon = 1 - \frac{\mu_2^2}{\mu_0 \mu_4} \tag{5.59}$$

where μ_k is the kth moment of the spectral density defined by:

$$\mu_k = \int_0^\infty n^k S(n)\,dn \tag{5.60}$$

For narrow-band vibration ε tends to zero and, from Equation (5.56), λ approaches 1. As ε tends to its maximum possible value of 1, λ approaches a given by Equation (5.57). These values enable upper and lower limits on the damage to be determined.

5.6.4 Effect of varying wind speed

Equation (5.53) applies to a particular standard deviation of stress, σ, which in turn is a function of mean wind speed, $\bar{U}$. This relationship can be written in the form:

$$\sigma=AU^n \tag{5.61}$$

The mean wind speed, $\bar{U}$, itself, is a random variable. Its probability distribution can be represented by a Weibull distribution (see Sections 2.5 and C.3.4):

$$f_U(\overline{U}) = \frac{k\overline{U}^{k-1}}{c^k} \exp\left[-\left(\frac{\overline{U}}{c}\right)^k\right] \tag{5.62}$$

The total damage from narrow-band vibration for all possible mean wind speeds is obtained from Equations (5.53), (5.61) and (5.62) and integrating over all wind speeds.

The fraction of the time T during which the mean wind speed falls between U and $U+\delta U$ is $f_U(U)\cdot\delta U$.

Hence the amount of damage generated while this range of wind speed occurs is from Equations (5.53) and (5.61):

$$D_U = \frac{v_0^+ T f_U(U)\delta U}{K}(\sqrt{2}AU^n)^m \Gamma\left(\frac{m}{2}+1\right)$$

The total damage in time T during all mean wind speeds between 0 and ∞ is given by,

$$\begin{aligned} D &= \frac{v_o^+ T(\sqrt{2}A)^m}{K}\Gamma\left(\frac{m}{2}+1\right)\int_0^\infty U^{mn} f_U(U)\,\mathrm{d}U \\ &= \frac{v_o^+ T(\sqrt{2}A)^m}{K}\Gamma\left(\frac{m}{2}+1\right)\int_0^\infty U^{mn+k-1}\frac{k}{c^k}\exp\left[-\left(\frac{U}{c}\right)^k\right]\mathrm{d}U \end{aligned} \tag{5.63}$$

This can be integrated numerically for general values of k. Usually k is around 2, in which case,

$$D = \frac{2v_0^+ T(\sqrt{2}A)^m}{Kc^2}\Gamma\left(\frac{m}{2}+1\right)\int_0^\infty U^{mn+1}\exp\left[-\left(\frac{U}{c}\right)^2\right]\mathrm{d}U$$

This is now of the form of Equation (5.54), so that:

$$\left.\begin{aligned} D &= \frac{2v_0^+ T(\sqrt{2}A)^m}{Kc^2}\Gamma\left(\frac{m}{2}+1\right)\frac{c^{mn+2}}{2}\Gamma\left(\frac{mn+2}{2}\right) \\ &= \frac{v_0^+ T(\sqrt{2}A)^m c^{mn}}{K}\Gamma\left(\frac{m}{2}+1\right)\Gamma\left(\frac{mn+2}{2}\right) \end{aligned}\right| \tag{5.64}$$

This is a useful closed-form expression for the fatigue damage over a lifetime of wind speeds, assuming narrow-band vibration.

For wide-band vibration, Equation (5.64) can be modified, following Equation (5.55), to:

$$D = \frac{\lambda v_0^+ T(\sqrt{2}A)^m c^{mn}}{K} \Gamma\left(\frac{m}{2}+1\right)\Gamma\left(\frac{mn+2}{2}\right) \tag{5.65}$$

By setting D equal to 1 in Equations (5.64) and (5.65), we can obtain lower and upper limits to the fatigue life as follows:

$$T_{lower} = \frac{K}{v_o^+(\sqrt{2}A)^m c^{mn}\Gamma\left(\frac{m}{2}+1\right)\Gamma\left(\frac{mn+2}{2}\right)} \tag{5.66}$$

$$T_{upper} = \frac{K}{\lambda v_o^+(\sqrt{2}A)^m c^{mn}\Gamma\left(\frac{m}{2}+1\right)\Gamma\left(\frac{mn+2}{2}\right)} \tag{5.67}$$

5.6.4.1 Example

To enable the calculation of fatigue life of a welded connection at the base of a steel pole using Equations (5.66) and (5.67), the following values are assumed:

$m = 5$; $n = 2$; $v_0^+ = 0.5$ Hz (say one half of the natural frequency of the pole)

$K = 2 \times 10^{15}$ [MPa]^5; $c = 8$ m/s; $A = 0.1 \dfrac{\text{MPa}}{(\text{m/s})^2}$

$\Gamma\left(\dfrac{m}{2}+1\right) = \Gamma(3.5) = e^{1.201} = 3.323$

$\Gamma\left(\dfrac{mn+2}{2}\right) = \Gamma(6) = 5! = 120$

Then from Equation (5.66),

$$T_{lower} = \frac{2 \times 10^{15}}{1.0 \times (\sqrt{2} \times 0.1)^5 \times 8^{10} \times 3.323 \times 120.0} = 1.651 \times 10^8\, s$$

$$= \frac{1.651 \times 10^8}{365 \times 24 \times 3600}\text{years} = \underline{5.24 \text{ years}}$$

From Equation (5.57), a=0.926–0.033 m=0.761

From Equation (5.56), this is a lower limit for λ

$$T_{upper} = \frac{T_{lower}}{\lambda} = \frac{5.24}{0.761}\text{years} = \underline{6.88 \text{ years}}$$

This example illustrates the sensitivity of the estimates of fatigue life to the values of both A and c. For example, increasing A to 0.15 MPa/(m/s)^2 would decrease the fatigue

life by 7.6 times (1.5^5). Decreasing c from 8 to 7 m/s will increase the fatigue life by 3.8 times $(8/7)^{10}$.

5.7 Summary

This chapter has covered a wide range of topics relating to the dynamic response of structures to wind forces. For wind loading, the sub-resonant or background response should be distinguished from the contributions at the resonant frequencies and calculated separately.

The along-wind response of structures that can be represented as single- and multi-degree-of-freedom systems has been considered. The effective static load approach in which the distributions of the mean, background and resonant contributions to the loading are considered separately, and assembled as a combined effective static wind load, has been presented.

Aeroelastic effects such as aerodynamic damping, and the instabilities of galloping and flutter have been introduced. Finally wind-induced fatigue has been treated resulting in usable formulae for the calculation of fatigue life of a structure under along-wind loading.

Cross-wind dynamic response from vortex shedding has not been treated in this chapter, but is discussed in Chapters 9 and 11.

References

Ashraf Ali, M. and Gould, P.L. (1985) On the resonant component of the response of single degree-of-freedom systems under wind loading. *Engineering Structures,* 7:280–2.

Bendat, J.S. and Piersol, A.G. (1999) *Random Data: Analysis and Measurement Procedures,* 3rd Edition. Wiley, New York.

Clough, R.W. and Penzien, J. (1975) *Dynamics of Structures.* McGraw-Hill, New York.

Crandall, S.H. and Mark, W.D. (1963) *Random Vibration in Mechanical Systems.* Academic Press, New York.

Davenport, A.G. (1961) The application of statistical concepts to the wind loading of structures. *Proceedings of the Institution of Civil Engineers,* 19:449–71.

Davenport, A.G. (1963) The buffeting of structures by gusts. *Proceedings, International Conference on Wind Effects on Buildings and Structures,* Teddington, UK, 26–28 June, pp. 358–91.

Davenport, A.G. (1964) Note on the distribution of the largest value of a random function with application to gust loading. *Proceedings of the Institution of Civil Engineers,* 28:187–96.

Davenport, A.G. (1967) Gust loading factors. *ASCE Journal of the Structural Division,* 93: 11–34.

Dowling, N.E. (1972) Fatigue failure predictions for complicated stress-strain histories. *Journal of Materials,* 7:71–87.

Harris, R.I. (1963) The response of structures to gusts. *Proceedings, International Conference on Wind Effects on Buildings and Structures,* Teddington, UK, 26–28 June, pp. 394–421.

Holmes, J.D. (1994) Along-wind response of lattice towers: part I—derivation of expressions for gust response factors. *Engineering Structures,* 16:287–92.

Holmes, J.D. (1996a) Along-wind response of lattice towers: part II—aerodynamic damping and deflections. *Engineering Structures,* 18:483–8.

Holmes, J.D. (1996b) Along-wind response of lattice towers: part III—effective load distributions. *Engineering Structures,* 18:489–94.

Holmes, J.D. and Best, R.J. (1981) An approach to the determination of wind load effects for low-rise buildings. *Journal of Wind Engineering & Industrial Aerodynamics,* 7:273–87.

Holmes, J.D. and Kasperski, M. (1996) Effective distributions of fluctuating and dynamic wind loads. *Civil Engineering Transactions, Institution of Engineers, Australia,* CE38:83–8.

Holmes, J.D., Forristall, G. and McConochie, J. (2005) Dynamic response of structures to thunderstorm winds. *10th Americas Conference on Wind Engineering,* Baton Rouge, LA, 1–4 June.

Kasperski, M. and Niemann, H.-J. (1992) The L.R.C. (load-response-correlation) method: a general method of estimating unfavourable wind load distributions for linear and non-linear structural behaviour. *Journal of Wind Engineering & Industrial Aerodynamics,* 43:1753–63.

Matsuishi, M. and Endo, T. (1968) Fatigue of metals subjected to varying stress. *Japan Society of Mechanical Engineers Meeting,* Fukuoka, March.

Matsumoto, M. (1996) Aerodynamic damping of prisms. *Journal of Wind Engineering & Industrial Aerodynamics,* 59:159–75.

Rice, S.O. (1944–5) Mathematical analysis of random noise. *Bell System Technical Journal,* 23:282–332 (1944) and 24:46–156. Reprinted in N.Wax (1954) *Selected Papers on Noise and Stochastic Processes.* Dover, New York.

Scanlan, R.H. (1982) Developments in low-speed aeroelasticity in the civil engineering field. *AIAA Journal,* 20:839–44.

Scanlan, R.H. and Gade, R.H. (1977) Motion of suspended bridge spans under gusty winds. *ASCE Journal of the Structural Division,* 103:1867–83.

Scanlan, R.H. and Tomko, J.J. (1971) Airfoil and bridge deck flutter derivatives. *ASCE Journal of the Engineering Mechanics Division,* 97:1717–37.

Vickery, B.J. (1965) On the flow behind a coarse grid and its use as a model of atmospheric turbulence in studies related to wind loads on buildings. Aero Report 1143, National Physical Laboratory (UK).

Vickery, B.J. (1966) On the assessment of wind effects on elastic structures. *Australian Civil Engineering Transactions,* CE8:183–92.

Vickery, B.J. (1968) Load fluctuations in turbulent flow. *ASCE Journal of the Engineering Mechanics Division,* 94:31–46.

Vickery, B.J. (1995) The response of chimneys and tower-like structures to wind loading. In: *A State of the Art in Wind Engineering,* ed. P.Krishna, Wiley Eastern, New Delhi.

Warburton, G.B. (1976) *The Dynamical Behaviour of Structures,* 2nd Edition. Pergamon Press, Oxford.

Wirsching, P.H. and Light, M.C. (1980) Fatigue under wide band random stresses. *ASCE Journal of the Structural Division,* 106:1593–1607.

6
Internal pressures

6.1 Introduction

Internal pressures induced by wind can form a high proportion of the total design wind load in some circumstances—e.g. for low-rise buildings when there are dominant openings in the walls. On high-rise buildings, a critical design case for a window at a corner may be an opening in the wall at the adjacent wall at the same corner—perhaps caused by glass failure due to flying debris.

In this chapter, the fundamentals of the prediction of wind-induced internal pressures within enclosed buildings are discussed. A number of cases are considered: a single dominant opening in one wall, multiple wall openings and the effect of background wall porosity. The possibility of Helmholtz resonance occurring is also discussed.

6.2 Single windward opening

We will first consider the case of a dominant windward wall opening—a situation which often arises in severe wind storms—often after the failure of a window glass due to flying debris. In a steady flow situation, the internal pressure will quickly build up to equal external pressure on the windward wall in the vicinity of the opening—there may be some oscillations in internal pressure (Section 6.2.4), but these will die out after a short time. However, when a building is immersed in a turbulent boundary-layer wind, the external pressure will be highly fluctuating and the internal pressure will respond in some way to these fluctuations. As there is only a single opening, flow into the building resulting from an increase in external pressure will cause an increase in the density of the air within the internal volume; this, in turn, will produce an increase in internal pressure. The pressure changes produced by wind are only about 1% of atmospheric pressure (1000 Pa compared to atmospheric pressure of about 100,000 Pa) and the relative density changes are of the same order. These small density changes can be maintained by small mass flows in and out of the building envelope, and consequently the internal pressure can be expected to respond quite quickly to external pressure changes, except for very small opening areas.

6.2.1 Dimensional analysis

It is useful to first carry out a dimensional analysis for the fluctuating internal pressures, resulting from a single windward opening to establish the non-dimensional groups involved.

The fluctuating internal pressure coefficient, $C_{pi}(t)$, can be written as:

$$C_{pi} = \frac{p_i - p_0}{\frac{1}{2}\rho_a \bar{U}^2} = F(\pi_1, \pi_2, \pi_3, \pi_4, \pi_5) \tag{6.1}$$

$\pi_1 = A^{3/2}/V_0$—where A is the area of the opening and V_0 is the internal volume;

$\pi_2 = p_0/(\frac{1}{2}\rho_a \bar{U}^2)$—where p_0 is the atmospheric pressure;

$\pi_3 = \rho_a \bar{U} A^{1/2}/\mu$—where μ is the dynamic viscosity of air (Reynolds number);

$\pi_4 = \sigma_u/\bar{U}$—where σ_u is the standard deviation of the longitudinal turbulence velocity upstream;

$\pi_5 = \ell_u/\sqrt{A}$—where ℓ_u is the length scale of turbulence (Section 3.3.4).

π_1 is a non-dimensional parameter related to the geometry of the opening and the internal volume, π_3 is a Reynolds number (Section 4.2.4) based on a characteristic length of the opening, π_5 is a ratio between characteristic length scales in the approaching flow and of the opening. π_2, the ratio of atmospheric pressure to the reference dynamic pressure, is a parameter closely related to Mach number.

Amongst these parameters, π_1 and π_4 are the most important. This is fortunate when wind-tunnel studies of internal pressures are carried out, as it is difficult or impossible to maintain equality of the other three parameters between full scale and model scale.

6.2.2 Response time

If the inertial (i.e. mass times acceleration) effects are initially neglected, an expression for the time taken for the internal pressure to become equal to a sudden increase in pressure outside the opening such as that caused by a sudden window failure can be derived (Euteneur, 1970).

For conservation of mass, the rate of mass flow-in through the opening must equal the rate of mass increase inside the volume:

$$\rho_i Q = \left(\frac{\mathrm{d}\rho_i}{\mathrm{d}t}\right) V_0 \tag{6.2}$$

where ρ_i denotes the air density within the internal volume.

For turbulent flow through an orifice, the following relationship between flow rate, Q, and the pressure difference across the orifice, $p_e - p_i$, applies:

$$Q = kA\sqrt{\frac{2(p_e - p_i)}{\rho_a}} \tag{6.3}$$

where k is an orifice constant, typically around 0.6.

Assuming an adiabatic law relating the internal pressure and density,

$$\frac{p_i}{\rho_i^{\gamma}} = \text{constant} \tag{6.4}$$

where γ is the ratio of specific heats of air.

Substituting Equations (6.2) and (6.4) in Equation (6.3) and integrating the differential equation, the following expression for the response, or equilibrium, time, τ, when the internal pressure becomes equal to the external pressure, can be obtained:

$$\tau = \frac{\rho_a V_0 \overline{U}}{\gamma k A p_0} \sqrt{C_{pe} - C_{pi0}} \tag{6.5}$$

where the pressures have been written in terms of pressure coefficients:

$$C_{pe} = \frac{p_e - p_0}{\frac{1}{2}\rho_a \overline{U}^2} \quad \text{and} \quad C_{pi} = \frac{p_i - p_0}{\frac{1}{2}\rho_a \overline{U}^2}$$

and C_{pi0} is the initial value of C_{pi} (i.e. at t=0).

Example

It is instructive to apply Equation (6.5) to a practical example. The following numerical values will be substituted:

$$\rho_a = 1.20\,\text{kg/m}^3;\ V_0 = 1000\,\text{m}^3;\ \overline{U} = 40\,\text{m/s}$$
$$\gamma = 1.4;\ k = 0.6;\ A = 1.0\,\text{m}^2;\ p_0 = 10^5\,\text{Pa}$$
$$C_{pe} = +0.7;\ C_{pi_0} = -0.2$$

Then the response time,

$$\tau = \frac{1.2 \times 1000 \times 40}{1.4 \times 0.6 \times 1.0 \times 10^5} \sqrt{0.7 - (-0.2)} = 0.54\,\text{s}$$

Thus, even for a relatively large internal volume of 1000 m^3, Equation (6.5) predicts a response time of just over half a second for the internal pressure to adjust to the external pressure, following the creation of an opening on the windward face of 1 m^2.

6.2.3 Helmholtz resonator model

In the previous example, inertial effects on the development of internal pressure following a sudden opening were neglected. These will now be included in a general model of internal pressure, which can be used for the prediction of the response to turbulent external pressures (Holmes, 1979).

The Helmholtz resonator is a well-established concept in acoustics (Rayleigh, 1896; Malecki, 1969), which describes the response of small volumes to the fluctuating external pressures. Although originally applied to the situation where the external pressures are caused by acoustic sources, it can be applied to the case of external wind pressures 'driving' the internal pressures within a building. It also describes the low-frequency fluctuations felt by occupants of a travelling motor vehicle, with an open window.

Acoustic resonators made from brass or earthenware, based on this principle, were used to improve the acoustic quality in the amphitheatres of ancient Greece and Rome (Malecki, 1969).

Figure 6.1 illustrates the concept as applied to internal pressures in a building. It is assumed that a defined 'slug' of air moves in and out of the opening in response to the external pressure changes. Thus, mixing of the moving air either with the internal air or the external air is disregarded in this model of the situation.

A differential equation for the motion of the slug of air can be written as follows:

$$\rho_a A \ell_e \ddot{x} + \frac{\rho_a A}{2k^2} \dot{x} |\dot{x}| + \frac{\gamma p_0 A^2}{V_0} x = A \, \Delta p_e(t) \tag{6.6}$$

The dependent variable, x, in this differential equation is the displacement of the air 'slug' from its initial or equilibrium position. The first term on the left-hand side of Equation (6.6) is an inertial term proportional to the acceleration, $\ddot{x}$, of the air slug, whose mass is $\rho_a A \ell_e$, in which ℓ_e is an effective length for the slug. The second term is a loss term associated with energy losses for flow through the orifice, and the third term is a 'stiffness' associated with the resistance of the air pressure already in the internal volume to the movement of the 'slug'.

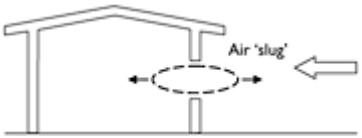

Figure 6.1 The Helmholtz resonator model of fluctuating internal pressures with a single dominant opening.

A movement x in the air slug can be related to the change in density $\Delta\rho_i$, and hence pressure Δp_i within the internal volume:

$$\rho_a A x = V_0 \Delta \rho_i = \frac{\rho_i V_0}{\gamma p_0} \Delta p_i \tag{6.7}$$

Making use of Equation (6.4) and converting the internal and external pressures to pressure coefficients, Equation (6.6) can be rewritten in the form of a differential equation for the fluctuating internal pressure coefficient, $C_{pi}(t)$:

$$\frac{\rho_a \ell_e V_0}{\gamma p_0 A} \ddot{C}_{p_i} + \left(\frac{\rho_a V_0 \overline{U}}{2k\gamma \, A p_0} \right)^2 \dot{C}_{p_i} |\dot{C}_{p_i}| + C_{p_i} = C_{p_e} \tag{6.8}$$

Equation (6.8) can also be derived (Vickery, 1986) by writing the discharge equation for unsteady flow through the orifice in the form:

$$p_e - p_i = \left(\frac{1}{k^2}\right)\frac{1}{2}\rho_a u_0^2 + \rho_a \ell_e \frac{du_0}{dt} \tag{6.9}$$

where ρ_a is taken as the air density within the volume (ρ_i) and u_0 as the (unsteady) spatially averaged velocity through the opening.

Equations (6.6) and (6.8) give the following equation for the (undamped) natural frequency for the resonance of the movement of the air slug and of the internal pressure fluctuations. This frequency is known as the Helmholtz frequency, n_H given by,

$$n_H = \frac{1}{2\pi}\sqrt{\frac{\gamma A p_0}{\rho_a \ell_e V_0}} \tag{6.10}$$

Internal pressure resonances at, or near, the Helmholtz frequency have been measured both in wind-tunnel (Holmes, 1979; Liu and Rhee, 1986) and in full-scale studies.

The effective length, ℓ_e, varies with the shape and depth of the opening, and is theoretically equal to $\sqrt{(\pi A/4)}$ for a thin circular orifice. For practical purposes (openings in thin walls), it is sufficiently accurate to take ℓ_e as equal to $1.0\sqrt{A}$ (Vickery, 1986).

Equation (6.10) assumes that the building or enclosure has rigid walls and roof. Real buildings have considerable flexibility. In this case, it can be shown (Vickery, 1986) that the equation for the Helmholtz frequency becomes:

$$n_H = \frac{1}{2\pi}\sqrt{\frac{\gamma A p_0}{\rho_a \ell_e V_0[1 + (K_A/K_B)]}} \tag{6.11}$$

where K_A is the bulk modulus of air, $(\rho_a \Delta p)/\Delta\rho$, equal to γp_0, and K_B is the bulk modulus for the building—i.e. the internal pressure for a unit change in relative internal volume.

The ratio K_A/K_B for low-rise buildings is in the range of 0.2–5.

6.2.4 Sudden windward opening with inertial effects

Equation (6.8) can be solved numerically for the case of a step change in external pressure coefficient, C_{pe} (representative of the situation after a sudden window failure). Figure 6.2(a) and (b) shows the response of a 600 m^3 volume (rigid walls and roof) with opening areas of 1 and 9 m^2, respectively (Holmes, 1979). For these simulations, the effective length, ℓ_e, was equivalent to $0.96\sqrt{A}$ and the discharge coefficient, k, was taken as 0.6.

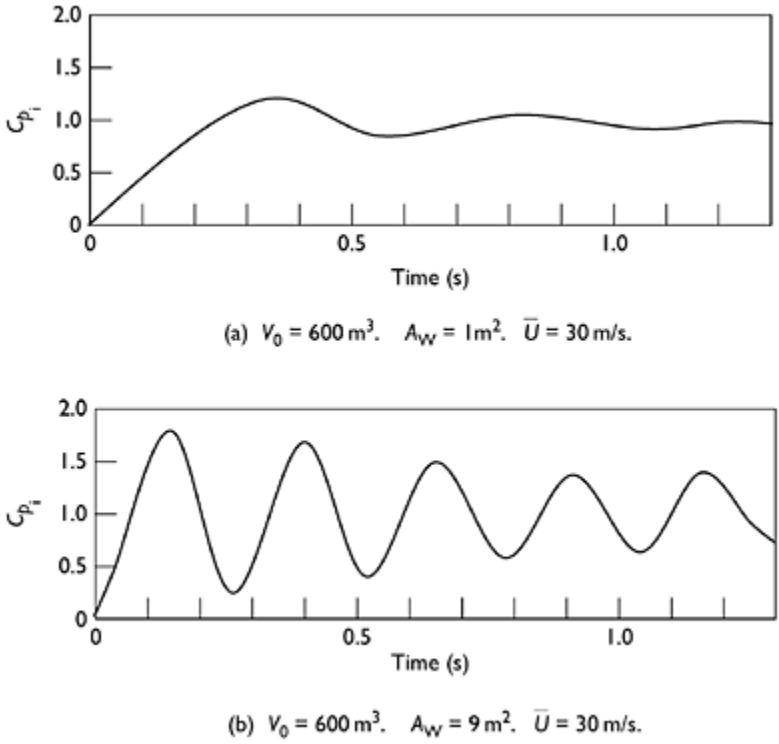

Figure 6.2 Response to a step change in external pressure, V_0=600 m^3, $\bar{U}$=30 m/s. (a) A= 1 m^2; (b) A=9 m^2.

It is apparent from Figure 6.2(b) that the inertial effects are significant for the larger opening when the damping term in Equation (6.8) is much smaller (note that the area, A, is in the denominator in this term). Many oscillatory cycles in internal pressure occur before equilibrium conditions are reached in this case. However, the flexibility of the walls and roof of real buildings, discussed in the previous section, also increases the damping term (Vickery, 1986), and hence causes more rapid attenuation of the oscillations.

6.2.5 Helmholtz resonance frequencies

Section 6.2.3 discussed the phenomenon of Helmholtz resonance in the interior of buildings, when there is a single opening, and Equations (6.10) and (6.11) gave formulae to calculate the Helmholtz frequency, given the opening area, internal volume and flexibility of the roof and walls.

Applying Equation (6.10) for the Helmholtz resonance frequency and setting $p_0=10^5$ Pa (atmospheric pressure), ρ=1.2 kg/m^3 (air density), γ=1.4 (ratio of specific heats) and $\ell_e=1.0\sqrt{A}$, we have the following approximate formula for n_H:

$$n_H \approx 55\frac{A^{1/4}}{V_0^{1/2}[1+(K_A/K_B)]^{1/2}} \tag{6.12}$$

where K_A is the bulk modulus for air ($=\gamma p_0$) and K_B the volume stiffness of the building structure (theoretically it is the internal pressure required to double the internal volume).

Equation (6.12) can be used to calculate n_H for typical low-rise buildings in Table 6.1 (Vickery, 1986).

Table 6.1 indicates that for the two smallest buildings, the Helmholtz frequencies are greater than 1 Hz, and hence significant resonant excitation of internal pressure fluctuations by natural wind turbulence is unlikely. However, for the large arena this would certainly be possible. However, in this case the structural frequency of the roof is likely to be considerably greater than the Helmholtz resonance frequency of the internal pressures and the latter will therefore not excite any structural vibration of the roof (Liu and Saathoff, 1982). It is clear, however, that there could be an intermediate combination of area and volume (such as the 'concert hall' in Table 6.1), for which the Helmholtz frequency is similar to the natural structural frequency of the roof and in a range which could be excited by the natural turbulence in the wind. However, such a situation has not yet been recorded.

Table 6.1 Helmholtz resonance frequencies for some typical buildings

Type	*Internal volume (m^3)*	*Opening area (m^2)*	*Stiffness ratio, K_A/K_B*	*Helmholtz frequency (Hz)*
House	600	4	0.2	2.9
Warehouse	5000	10	0.2	1.3
Concert hall	15,000	15	0.2	0.8
Arena (flexible roof)	50,000	20	4	0.23

6.3 Multiple windward and leeward openings

6.3.1 Mean internal pressures

The mean internal pressure coefficient inside a building with total areas (or effective areas if permeability is included) of openings on the windward and leeward walls of A_w and A_L, respectively, can be derived by using Equation (6.3) and applying mass conservation. The latter relation can be written for a total of N openings in the envelope:

$$\sum_{1}^{N} \rho_a Q_j = 0 \tag{6.13}$$

If quasi-steady and incompressible flow is assumed initially, we can assume the density, ρ_a, to be constant. Then, applying Equation (6.3) for the flow through each of the N openings, Equation (6.13) becomes:

$$\sum_{1}^{N} A_j \sqrt{|p_{e,j} - p_i|} = 0 \tag{6.14}$$

where the modulus, $|p_{e,j} - p_i|$, allows for the fact that for some openings the flow is from the interior to the exterior.

Figure 6.3 shows a building (or a floor of a high-rise building) with five openings in the envelope. Applying Equation (6.14) to this case:

$$A_1\sqrt{|p_{e,1} - p_i|} + A_2\sqrt{|p_{e,2} - p_i|} + A_3\sqrt{|p_{e,3} - p_i|} = A_4\sqrt{|p_{e,4} - p_i|} + A_5\sqrt{|p_{e,5} - p_i|} \tag{6.15}$$

In Equation (6.15), the inflows through the windward openings on the left-hand side balance the outflows through openings on the leeward and side walls on the right-hand side. Equation (6.15), or similar equations for a large number of openings, can be solved by iterative numerical methods.

For the simpler case of a single windward opening with a single leeward opening, Equation (6.14) can be applied, with a conversion to pressure coefficients, to give:

$$A_W\sqrt{C_{pw} - C_{pi}} = A_L\sqrt{C_{pi} - C_{pL}}$$

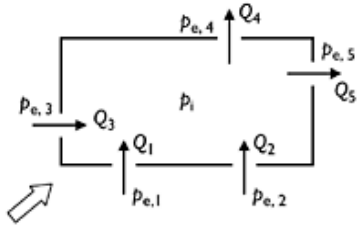

Figure 6.3 Inflows and outflows for multiple openings.

This can be re-arranged to give Equation (6.16) for the coefficient of internal pressure:

$$C_{pi} = \frac{C_{pw}}{1 + \left(\frac{A_L}{A_W}\right)^2} + \frac{C_{pL}}{1 + \left(\frac{A_W}{A_L}\right)^2} \tag{6.16}$$

Equation (6.16) can be applied with A_w taken as the combined open area for several openings on a windward wall and C_{pw} taken as an average mean pressure coefficient with similar treatment for the leeward/side walls. It has been applied to give specified values of internal pressures in design codes and standards (see Chapter 15), in which case the coefficients are used with mean pressure coefficients to predict peak internal pressures, making use of the quasi-steady assumption (see Section 4.6.2).

Measurements of mean internal pressure coefficients for a building model with various ratios of windward/leeward opening area are shown in Figure 6.4. The solid line in this figure is Equation (6.16) with C_{pw} taken as +0.7 and C_{pL} taken as −0.2. These values were the values of mean external pressure coefficients on the walls at or near the windward and leeward openings, respectively. It may be seen that the agreement between the measurements and Equation (6.16) is good.

6.3.2 Fluctuating internal pressures

The analysis of fluctuating internal pressures when there are openings on more than one wall of a building is more difficult than for a single opening. In general, numerical solutions are required (Saathoff and Liu, 1983). However, some useful results can be obtained if the inertial terms are neglected and the damping term is linearized (Vickery, 1986, 1991; Harris, 1990). The neglect of the inertial term in comparison to the damping term is justified when there is background porosity in the walls of a building, but may not be so when there are one or more large openings.

It can be shown (Harris, 1990) that when there is a combined open area on a windward wall of A_w and external pressure coefficient C_{pw}, and on a leeward wall with total open area A_L and external pressure coefficient C_{PL}, then there is a characteristic response time given by:

$$\tau = \frac{\rho_a V_0 \overline{U} A_w A_L}{\gamma k p_0 (A_w^2 + A_L^2)^{3/2}} \sqrt{C_{p_w} - C_{p_L}} \tag{6.17}$$

There is some similarity between Equations (6.16) and (6.5) for a single opening, but they are not exactly equivalent. External pressure fluctuations which have periods much greater than τ are transmitted as internal pressures in a quasi-steady manner—i.e. they will follow Equation (6.15). Fluctuations with periods of the same order as τ will be significantly attenuated; those with periods less than τ will have negligible effect on the fluctuating internal pressures.

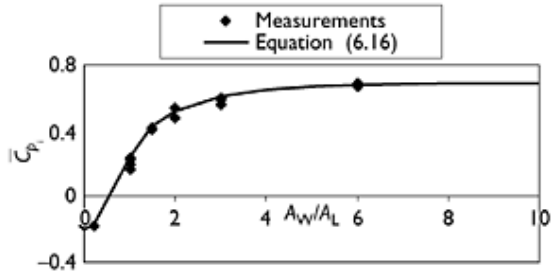

Figure 6.4 Mean internal pressure coefficient as a function of windward/leeward open area.

The effect of building wall and roof flexibility is such as to increase the response time according to Equation (6.18) (Vickery, 1986):

$$\tau = \frac{\rho_a V_0 \overline{U} A_W A_L [1 + (K_A/K_B)]}{\gamma k p_0 (A_W^2 + A_L^2)^{3/2}} \sqrt{C_{Pw} - C_{PL}} \tag{6.18}$$

For 'normal' low-rise building construction, K_A/K_B is about 0.2 (Vickery, 1986 and Section 6.2.5) and the response time therefore increases by about 20%.

6.4 Nominally sealed buildings

The situation of buildings that are nominally sealed, but have some leakage distributed over all surfaces, can be treated by neglecting the inertial terms and lumping together windward and leeward leakage areas (Vickery, 1986, 1994; Harris, 1990).

A characteristic frequency, n_c, is obtained. Pressure fluctuations below this frequency are effectively communicated to the interior of the building. n_c is given by Equation (6.19) (Vickery, 1994):

$$\frac{n_c V_0}{\overline{U} A_{W,total}} = \frac{\varphi}{2\pi} \frac{k}{1 + (K_A/K_B)} \left(\frac{a_s}{\overline{U}}\right)^2 \frac{r^{1/2}\left(r + \frac{1}{r}\right)^{3/2}}{\sqrt{C_{Pw} - C_{PL}}} \tag{6.19}$$

where r is the ratio of total leeward wall surface area to windward wall surface area, a_s the speed of sound and the other parameters were defined previously. $A_{w,\,total}$ is the total surface area of the windward wall and φ is the wall porosity. Equation (6.19) is essentially the same as Equation (6.18), with τ equal to $(1/2\pi n_c)$.

The peak internal pressure coefficient can be estimated by:

$$\hat{C}_{p_i} \cong \overline{C}_{p_i}\left[1 + 2g\frac{\sigma_u'}{\overline{U}}\right] \tag{6.20}$$

where σ_u' is an effective, filtered standard deviation of velocity fluctuations that are capable of generating internal pressure fluctuation given by:

$$\sigma_u'^2 = \int_0^\infty S_u(n)/[1+(n/n_c)]^2 \, dn \tag{6.21}$$

Equation (6.21) has been evaluated using Equation (3.26) for the longitudinal turbulence spectrum, and σ_u'/σ_u is shown plotted against $(n_c\ell_u/\bar{U})$ in Figure 6.5 (Vickery, 1994). g is a peak factor which lies between 3.0 and 3.5. The mean internal pressure coefficient in Equation (6.20) can be evaluated using Equation (6.16).

Evaluation of Equation (6.21) for a large warehouse building with a wall porosity of 0.0005 gave a value of σ_u'/σ_u equal to 0.7, i.e. there is a 30% reduction in the effective velocity fluctuations resulting from the filtering effect of the porosity of the building (Vickery, 1994).

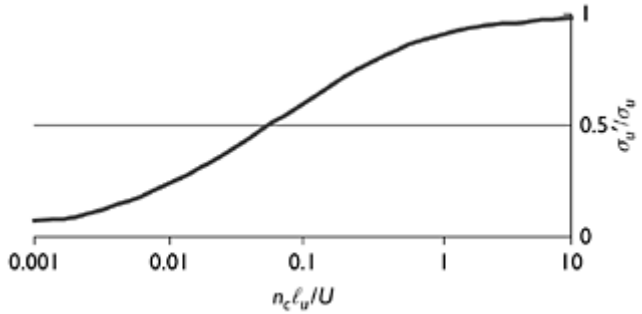

Figure 6.5 Reduction factor for fluctuating internal pressures for a building with distributed porosity (Vickery, 1994).

6.5 Modelling of internal pressures

To correctly model internal pressures in wind-tunnel tests, it is necessary to ensure that the frequencies associated with the internal pressure fluctuations are scaled correctly with respect to the frequencies in the external flow. The relevant internal pressure frequencies are the Helmholtz resonance frequency (Sections 6.2.3 and 6.2.5) and the 'characteristic frequency' (Section 6.4).

For correct scaling of internal pressure fluctuations at full-scale design wind speeds, it is usually necessary to increase the internal volume above that obtained from normal geometric scaling. The details of the scaling rules for internal pressures are discussed in Chapter 7 (Section 7.4.2).

6.6 Summary

The topic of internal pressures produced by wind has been covered in this chapter. The relevant non-dimensional parameters are introduced, and the response time of the interior of a building or a single room to a sudden increase in external pressure at an opening has been evaluated.

The dynamic response of an internal volume to excitation by a sudden generation of a windward wall opening, or by turbulence, using the Helmholtz resonator model, which includes inertial effects, has been considered. The effect of multiple windward and leeward openings on mean and fluctuating internal pressures is introduced. The case of a nominally sealed building with distributed porosity is also considered.

The requirements for modelling of internal pressures in wind-tunnel studies have also been mentioned; however, the full details of this are given in Chapter 7.

Most of the results in this chapter have been validated by wind-tunnel studies and, more importantly, by full-scale measurements (e.g. Ginger *et al.*, 1997).

References

Euteneur, G.A. (1970) Druckansteig im Inneren von Gebauden bei Windeinfall. *Der Bauingenieur*, 45:214–16.

Ginger, J.D., Mehta, K.C. and Yeatts, B.B. (1997) Internal pressures in a low-rise full-scale building. *Journal of Wind Engineering & Industrial Aerodynamics*, 72:163–74.

Harris, R.L (1990) The propagation of internal pressures in buildings. *Journal of Wind Engineering & Industrial Aerodynamics*, 34:169–84.

Holmes, J.D. (1979) Mean and fluctuating internal pressures induced by wind. *Proceedings, 5th Internal Conference on Wind Engineering*, Fort Collins, CO, pp. 435–50, Pergamon Press, Oxford.

Liu, H. and Rhee, K.H. (1986) Helmholtz oscillation in building models. *Journal of Wind Engineering & Industrial Aerodynamics*, 24:95–115.

Liu, H. and Saathoff, P.J. (1982) Internal pressure and building safety. *ASCE Journal of the Structural Division*, 108:2223–34.

Malecki, I. (1969) *Physical Foundations of Technical Acoustics.* Pergamon Press, Oxford.

Rayleigh, Lord (1896) *Theory of Sound—Volume 2*. Macmillan, London. (Reprinted by Dover Publications, 1945.)

Saathoff, P.J. and Liu, H. (1983) Internal pressure of multi-room buildings. *Journal of the Engineering Mechanics Division, American Society of Civil Engineers*, 109:908–19.

Vickery, B.J. (1986) Gust factors for internal pressures in low-rise buildings. *Journal of Wind Engineering & Industrial Aerodynamics*, 23:259–71.

Vickery, B.J. (1991) Discussion of 'The propagation of internal pressures in buildings', by R.I.Harris. *Journal of Wind Engineering & Industrial Aerodynamics*, 37:209–12.

Vickery, B.J. (1994) Internal pressures and interaction with the building envelope. *Journal of Wind Engineering & Industrial Aerodynamics*, 53:125–44.

7
Laboratory simulation of strong winds and wind loads

7.1 Introduction

Practising structural engineers will not generally themselves operate wind tunnels or other laboratory equipment, for simulation of strong wind effects on structures, but they may be clients of specialist groups who will provide wind loading information for new or existing structures, usually by means of model tests. For this reason, this chapter will not attempt to describe in detail wind-tunnel or other simulation techniques. There are detailed references, guide books and manuals of practice available which perform this function (e.g. Cermak, 1977; Reinhold, 1982; American Society of Civil Engineers, 1999; Australasian Wind Engineering Society, 2001). However, sufficient detail is given here to enable the educated client to be able to 'ask the right questions' of their wind-tunnel contractors.

In the following sections, a brief description of wind-tunnel layouts is given, and methods of simulation of natural wind flow and experimental measurement techniques are discussed.

7.2 Wind-tunnel layouts

7.2.1 Historical

The first use of a wind tunnel to measure wind forces on buildings is believed to have been made by Kernot in Melbourne, Australia (1893). A sketch of the apparatus, which he called a 'blowing machine', is given in Figure 7.1 (Aynsley *et al.*, 1977). This would now be described as an 'open-circuit, open-test section' arrangement. With this equipment, Kernot studied wind forces on a variety of bluff bodies—cubes, pyramids, cylinders, etc. and on roofs of various pitches.

At about the same time, Irminger (1894) in Copenhagen, Denmark, used the flow in a flue of a chimney to study wind pressures on some basic shapes (Larose and Franck, 1997).

Wind tunnels for aeronautical applications developed rapidly during the first half of the twentieth century, especially during and between the two World Wars. The two basic wind-tunnel layouts—the *open circuit* or 'NPL (National Physical Laboratory) type' and the *closed circuit* or 'Göttingen type'—were developed during this period, named after the research establishments in the United Kingdom and Germany where they originated. These two types are outlined in the following sections.

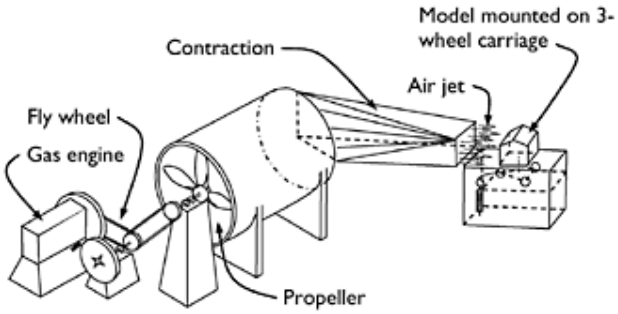

Figure 7.1 Sketch of W.C.Kernot's 'blowing machine' of 1893.

7.2.2 Open-circuit type

The simplest type of wind-tunnel layout is the open-circuit or NPL type. The main components are shown in Figure 7.2. The contraction, usually with a flow straightener and fine mesh screens, has the function of smoothing out mean flow variations and reducing turbulence in the test section. For modelling atmospheric boundary-layer flows, which are themselves very turbulent, as described in Chapter 3, it is not essential to include a contraction, although it is better to start with a reasonably uniform and smooth flow before commencing to simulate atmospheric profiles and turbulence.

The function of the diffuser, shown in Figure 7.2, is to conserve power by reducing the amount of kinetic energy that is lost with the discharging air. Again this is not an essential item, but omission will be at the cost of higher electricity charges.

Figure 7.2 shows an arrangement with an axial-flow fan downstream of the test section. This arrangement is conducive to better flow, but, as the function of the fan is to produce a pressure rise to overcome the losses in the wind tunnel, there will be a pressure drop across the walls and floor of the test section that can be a problem if leaks exist. An alternative is a 'blowing' arrangement in which the test section is downstream of the fan (see Figure 7.5). Usually a centrifugal blower is used, and a contraction with screens is essential to eliminate the swirl downstream of the fan. However, in this arrangement the test section is at or near atmospheric pressure.

Both the arrangements described above have been used successfully in wind engineering applications.

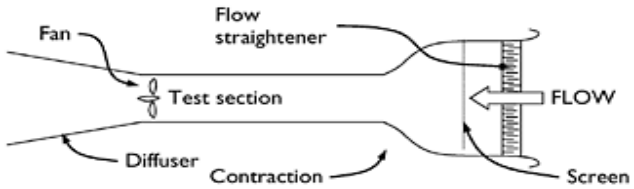

Figure 7.2 Layout of an open-circuit wind tunnel.

7.2.3 Closed-circuit type

In the closed-circuit, or Göttingen-type, wind tunnel, the air is continually recirculated, instead of being expelled. The advantages of this arrangement are as follows:

- It is generally less noisy than the open-circuit type.
- It is usually more efficient. Although the longer circuit gives higher frictional losses, there is no discharge of kinetic energy at exit.
- More than one test section with different characteristics can be incorporated.

However, this type of wind tunnel has a higher capital cost and the air heats up over a long period of operation before reaching a steady-state temperature. This can be a problem when operating temperature-sensitive instruments, such as hot-wire or other types of thermal anemometers, which use a cooling effect of the moving air for their operation.

7.3 Simulation of the natural wind flow

In this section, methods of simulation of strong wind characteristics in a wind tunnel are reviewed. Primarily, the simulation of the atmospheric boundary layer in gale, or large-scale synoptic conditions, is discussed. This type of large-scale storm is dominant in the temperate climates for latitudes greater than about 40°, as discussed in Chapter 1.

Even in large-scale synoptic wind storms, flows over sufficiently long homogeneous fetch lengths, so that the boundary layer is fully developed, are relatively uncommon. They will occur over open sea with consistent wave heights, and following large fetches of flat open country or desert terrain. However, buildings or other structures, which are exposed to these conditions, are few in number. Urban sites, with flat homogeneous upwind roughness of sufficient length to produce full development of the boundary layer, are also relatively uncommon. However, there have been sufficient measurements in conditions that are close to ideal to produce generally accepted semi-theoretical models of the strong wind atmospheric boundary layer for engineering purposes. These models have been validly used as the basis for wind-tunnel modelling of phenomena in the atmosphere, and the salient points have been discussed in Chapter 3.

In the case of the wind loading and response of structures, such as buildings, towers, bridges, etc., gales produced by large, mature, extra-tropical depressions are adequately described by these models, and they form a benchmark by which wind-tunnel flows are usually assessed. However, there are significant differences of opinion regarding some turbulence properties, such as length scales and spectra, which are important in determining wind forces and dynamic response. These uncertainties should be considered when assessing the reliability of wind-tunnel tests as a predictor of wind effects on real structures.

As outlined in Chapter 3, these models are also not good ones for storm winds produced by localized thermal mechanisms, namely tropical cyclones (hurricanes, typhoons), thunderstorms (including tornadoes) and monsoons. Winds produced by these storms are the dominant ones for design of structures in latitudes within about 40° from the equator.

The following sections consider natural growth methods requiring long test sections, methods used for wind tunnels with short test sections and methods developed for simulating only the inner or surface layer of the atmospheric boundary layer. Finally, some possibilities for simulations of strong winds in tropical cyclone and thunderstorm conditions are discussed. Laboratory modelling of these phenomena is still in an early stage of development, but some ideas on the subject are presented in Section 7.3.4.

7.3.1 Similarity criteria and natural growth methods

The 'ideal' neutral atmospheric boundary layer has two characteristic length scales—one for the outer part of the flow which depends on the rate of rotation of the earth and the latitude and on a velocity scale, and one for the flow near the surface itself which depends on the size and density of the roughness on the surface. The region near the surface, which is regarded as being independent of the effects of the earth's rotation, has a depth of about 100 m and is known as the *inner* or *surface layer*.

The first deliberate use of boundary-layer flow to study wind pressure on buildings was apparently by Flachsbart (1932). However, the work of Martin Jensen in Denmark provided the foundation for modern boundary-layer wind-tunnel testing techniques. Jensen (1958) suggested the use of the inner layer length scale or roughness length, z_0 (see Section 3.2.1), as the important length scale in the atmospheric boundary-layer flow, so that for modelling phenomena in the natural wind, ratios such as building height to roughness length (h/z_0)—later known as the Jensen number—are important. Jensen (1965) later described model experiments carried out in a small wind tunnel in Copenhagen, in which natural boundary layers were allowed to grow over a fetch of uniform roughness on the floor of the wind tunnel. In the 1960s, larger 'boundary-layer' wind tunnels were constructed and were used for wind engineering studies of tall buildings, bridges and other large structures (Davenport and Isyumov, 1967; Cermak, 1971). These tunnels are either of closed-circuit design (Section 7.2.3) or of open circuit of the 'sucking' type, with the axial-flow fan mounted downstream of the test section (Section 7.2.2). In more recent years, several open-circuit wind tunnels of the 'blowing' type have been constructed with a centrifugal fan upstream of the test section, supplying it through a rapid diffuser, a settling chamber containing screens and a contraction. As discussed in Section 7.2.2, the latter system has the advantage of producing nearly zero static pressure difference across the wind-tunnel walls at the end of the boundary-layer test section.

A naturally grown rough-wall boundary layer will continue to grow until it meets the boundary layer on the opposite wall or roof. In practical cases, this equilibrium situation is not usually reached, and tests of tall structures are carried out in boundary layers that are still developing, but are sufficient to envelop the model completely. In most cases of structural tests, more rapid boundary-layer growth must be promoted by a 'tripping' fence or grid at the start of the test section. Dimensional analysis indicates that the full height of the atmospheric boundary layer depends on the wind speed and the latitude. However, the typical height is about 1000m. Assuming a geometric scaling ratio of 1/500, this means that a *minimum* wind-tunnel height of 2 m is required to model the full atmospheric boundary layer. Usually a lower boundary-layer height is accepted, but the turbulent boundary-layer flow should completely envelop any structure under test.

In the early days of boundary-layer wind tunnels, it was common to install a roof of adjustable height for the purpose of maintaining a constant pressure gradient in the along-wind direction. This allows for the increasing velocity deficit in the flow direction and maintains the 'free-stream' velocity outside of the boundary layer approximately constant. This should also reduce the errors due to blockage for large models. For smaller models with lower blockage ratios, the errors in the measurements when the roof is maintained at a constant height or with a fixed slope are quite small, and it has been found to be unnecessary to continuously adjust the roof, in most situations. Blockage errors and corrections are discussed in Section 7.7.

As noted previously, the real atmospheric boundary layer is affected by the earth's rotation, and apparent forces of the Coriolis type must be included when considering the equations of motion of air flow in the atmosphere. One effect of this is to produce a mean velocity vector which is not constant in direction with height; it is parallel to the pressure gradient at the top of the boundary layer (or 'gradient' height) and rotates towards the lower static pressure side as the ground level is approached. This effect is known as the 'Ekman Spiral' (although the original solution by Ekman was obtained by assuming a shear stress in the flow proportional to the vertical velocity gradient—an assumption later shown to be unrealistic) and it has been shown to occur in full scale, with mean flow direction changes up to 30° having been measured. This effect cannot be achieved in conventional wind tunnels and the direction change is usually regarded as unimportant over the heights of most structures.

7.3.2 Methods for short test sections

In the 1960s and 1970s, to avoid the costs of constructing new boundary-layer wind tunnels, several methods of simulating the atmospheric boundary layer in existing (aeronautical) wind tunnels with test sections of low aspect ratio, i.e. short with respect to their height and width, were investigated. These usually make use of tapered fins or spires, which produce an immediate velocity gradient downstream, and which develops into a mean velocity profile representative of that in the atmosphere within a short downstream distance. Other bluff devices, such as grids or barriers, are required upstream, together with roughness on the floor of the wind tunnel, to increase the turbulence intensities to full-scale values.

Flows produced by these methods are likely to be still in a process of rapid development at the end of the short test section, and the interaction of the vortex structures produced in the wakes of the various devices may well result in unwanted characteristics in the turbulence at the measurement position. Unless detailed fluctuating velocity measurements, including spatial correlations, are made, such characteristics may never be detected. Fortunately, wind pressures and forces on structures appear to be dependent mainly on single-point statistics, such as turbulence intensities, and integral length scales in the along-wind direction, and not on the detailed eddy structures within the turbulence, in the approach flow.

Of the several methods developed in the late 1960s and early 1970s, that of Counihan (1969) is perhaps the best documented. The upstream devices consisted of a castellated fence, or barrier, several elliptical 'sharks-fins' and a short fetch of surface roughness

(Figure 7.3). Detailed measurements of mean velocity and turbulence intensity profiles at various spanwise stations and of cross-correlations and spectra were made.

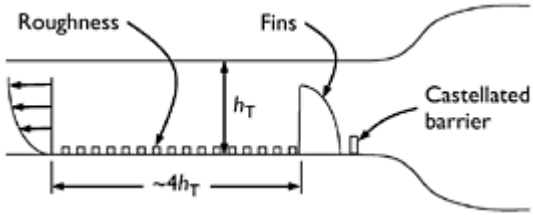

Figure 7.3 The Counihan method for short test sections.

7.3.3 Simulation of the surface layer

For simulation of wind forces and other wind effects on low-rise buildings, say less than 10 m in height, geometric scaling ratios of 1/400 result in extremely small models and do not allow any details on the building to be reproduced. The large differences in Reynolds numbers between model and full scale may mean that the wind-tunnel test data is quite unreliable. For this type of structure, no attempt should be made to model the complete atmospheric boundary layer. Simulation of the inner or surface layer, which is approximately 100 m thick in full scale, is sufficient for such tests. If this is done, larger and more practical scaling ratios in the range of 1/50–1/200 can be used for the models.

Cook (1973) developed a method for simulation of the lower third of the atmospheric boundary layer. This system consists of a castellated barrier, a mixing grid and surface roughness. A simpler system consisting of a plain barrier, or wall, at the start of the test section followed by several metres of uniform surface roughness has also been used (Figure 7.4) (Holmes and Osonphasop, 1983). This system has the advantage that simultaneous control of the longitudinal turbulence intensity and the longitudinal length scale of turbulence, to match the model scaling ratio, is obtained by adjustment of the height of the barrier. Larger scales of turbulence can be produced by this method than by other approaches—large horizontal vortices with their axes normal to the flow are generated in the wake of the barrier. Studies of the development of the flow in the wake of the barrier (Holmes and Osonphasop, 1983) showed that a fetch length of at least 30 times the barrier height is required to obtain a stable and monotonically increasing mean velocity profile. However, there is still a residual peak in the shear stress profile at the height of the barrier at this downstream position; this shows that the flow is still developing at the measurement position, but the effect of this on pressures on and flow around single buildings should not be significant.

7.3.4 Simulation of tropical cyclone and thunderstorm winds

As discussed in Chapter 1, strong winds produced by tropical cyclones and thunderstorms dominate the populations of extreme winds in most locations with latitudes less than 40°, including many sites in the United States, Australia, India and South Africa.

Unfortunately, full-scale measurements of such events are few in number, and there are no reliable analytical models for the surface wind structures in these storms. However, the few full-scale measurements, and some meso-scale numerical models, have enabled qualitative characteristics of the winds to be determined.

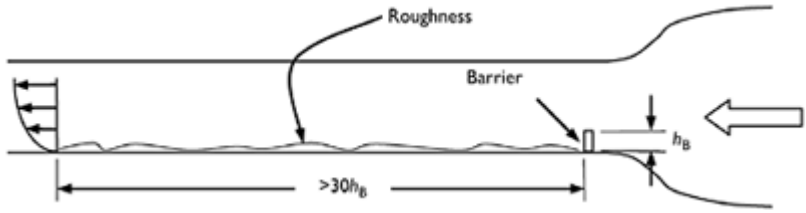

Figure 7.4 The barrier-roughness technique.

Tropical cyclones, known also as ‘hurricanes’ and ‘typhoons’ in some parts of the world, are circulating systems with a complex three-dimensional wind structure near their centre (Section 1.3.2). At the outer radii, where the wind speeds are lower, a boundary-layer structure should exist and conventional boundary-layer wind tunnels should be quite adequate for flow modelling. However, the region of maximum horizontal winds occurs just outside the eye wall. Here the winds near the surface turn towards the low-pressure centre and in a spiralling upward direction at greater heights. Measurements have indicated a steeper mean velocity profile than would be expected for gales, for the surface roughness conditions around the site, up to the height of about 100 m. Above that height, the mean wind velocity is approximately constant up to the top of the tower (Section 3.2.5). Measurements of turbulence intensities in typhoons have shown higher values than occurring at the same site in non-cyclonic conditions (Section 3.3.1). As most structures do not exceed 100 m in height, a reasonable approximation to the tropical cyclone flow can be obtained by using a boundary-layer flow generated for urban terrain conditions, even for directions with lower roughness lengths, such as off-water winds for coastal sites.

The laboratory modelling of thunderstorm winds is a more difficult problem for a number of reasons. First, there are a number of different types of local wind storms associated with thunderstorms, although some of these have similar characteristics. Second, these storms are individually transient, although a number of them may occur sequentially in the same day. The length of an individual storm rarely exceeds 30min. Third, thunderstorm winds are driven by thermodynamic processes which probably cannot be reproduced in a laboratory simulation.

The velocity profile in a thunderstorm downdraft is quite similar to a wall jet. The latter has been proposed as a laboratory model of the flow in a downdraft, and some studies have been conducted using the outlet jet from a wind tunnel impinging on a vertical board, as shown in Figure 7.5. Measurements can be carried out at various radial positions from the centre of the board. This system gives velocity profiles which are quite similar to those measured by radar in microbursts, but the transient characteristics of the real downdraft flow are not reproduced and the turbulence characteristics in the two flows could be quite different.

7.3.5 Laboratory simulation of tornadoes

Some characteristics of tornadoes and their effects on structures were discussed in Chapter 1 (Section 1.3.4) and Chapter 3 (Section 3.2.7). Davies-Jones (1976) gave a detailed review of the simulation of tornadoes or 'tornado-like vortices' in laboratories. These have produced reasonable kinematic and dynamic similarity with full-scale tornadoes.

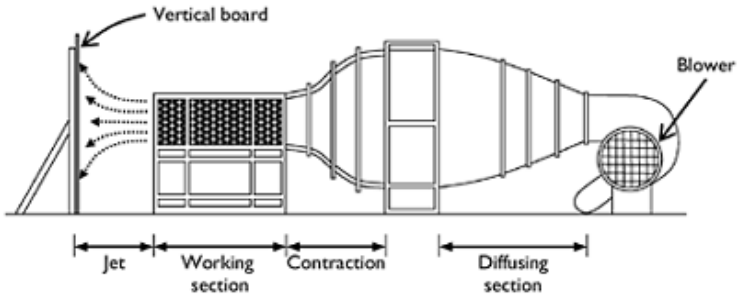

Figure 7.5 Simulation of thunderstorm downburst by impinging jet.

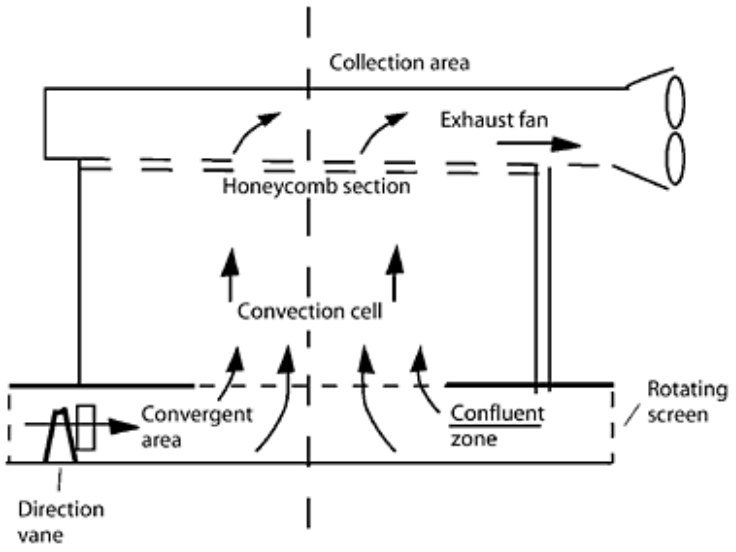

Figure 7.6 Laboratory simulation of tornado-like vortex (Ward, 1972).

Chang (1971) and Ward (1972) used a ducted fan above a flat board, with rotary motion imparted to the air flowing into a convective chamber above the board by means of a rotating screen. In the Ward type, the rising air exits the apparatus to an upper plenum, through a fine-mesh honeycomb, which prevents fan-induced vorticity from

entering the apparatus (Figure 7.6). In these systems, the rotational velocity is controlled by the rotational speed of the screen, and the core radius is controlled by the size of the opening to the upper plenum.

However, although methods of simulating tornadoes in laboratories are quite well developed, relatively few studies of wind pressures or forces on structures in laboratory simulations of tornadoes have been carried out, and virtually none since the 1970s.

7.4 Modelling of structures for wind effects

7.4.1 General approach for structural response

The modelling of structures for wind effects, in boundary-layer winds, requires knowledge of dimensional analysis and the theory of modelling (e.g. Whitbread, 1963).

The general approach is as follows. It may be postulated that the response of a structure to wind loading, including resonant dynamic response, is dependent on a number of basic variables such as the following (not necessarily exclusive).

$\bar{U}$—the mean wind speed at some reference position;
Z_0—roughness length defining the approaching terrain and velocity profile (Section 3.2.1);
σ_u—standard deviation of longitudinal turbulence;
σ_v—standard deviation of lateral turbulence;
σ_w—standard deviation of vertical turbulence;
ℓ_u—length scale of longitudinal turbulence (Section 3.3.4);
ℓ_v—length scale of lateral turbulence;
ℓ_w—length scale of vertical turbulence;
ρ_a—density of air;
υ—viscosity of air;
g—acceleration due to gravity;
ρ_s—density of the structure;
E—Young's modulus for the structural material;
G—shear modulus for the structural material;
η—structural damping ratio;
L—characteristic length of the structure.

The above list has been simplified considerably. For example, for a bridge there will usually be different structural properties for the deck, the towers, the cables, etc. However, the above list will suffice to illustrate the principles of structural modelling.

The above 16 dimensioned variables can be reduced to 13 (16–3) independent dimensionless groups, according to the Buckingham-Pi Theorem. A possible list of these is as follows:

L/z_0—Jensen number;
$\sigma_u/\bar{U}$—longitudinal turbulence intensity;
$\sigma_v/\bar{U}$—lateral turbulence intensity;

$\sigma_w/\bar{U}$—vertical turbulence intensity;
ℓ_u/L—length ratio;
ℓ_v/L—length ratio;
ℓ_w/L—length ratio;
$\bar{U}/L\upsilon$—Reynolds number (Section 4.2.4);
ρ_s/ρ_a—density ratio;
$\bar{U}/\sqrt{Lg}$—Froude number (inertial forces (air)/gravity forces (structure));
$E/\rho_a\bar{U}^2$—Cauchy number (normal internal forces in structure/inertial forces (air));
$G/\rho_a\bar{U}^2$—Cauchy number (internal shear forces in structure/inertial forces (air));
η—critical damping ratio.

For correct scaling, or similarity in behaviour between the model and the full-scale structure, these non-dimensional groups should be numerically equal for the model (wind tunnel) and prototype situation.

The 13 groups are not a unique set. Other non-dimensional groups can be formed from the 16 basic variables, but there are only 13 *independent* groups, and it will be found that the additional groups can be formed by taking products of the specified groups or their powers.

For example, it is often convenient to replace a Cauchy number by a reduced frequency $(n_sL/\bar{U})$, where n_s is a structural frequency. For structures or structural members in bending, n_s is proportional to $\sqrt{(E/\rho_sL^2)}$.

Then the reduced frequency,

$$\frac{n_sL}{\bar{U}} = K\sqrt{\frac{E}{\rho_sL^2}}\cdot\frac{L}{\bar{U}} = K\sqrt{\frac{E}{\rho_a\bar{U}^2}}\cdot\sqrt{\frac{\rho_a}{\rho_s}} \tag{7.1}$$

where K is a constant.

Thus, the reduced frequency is proportional to the square root of the Cauchy number divided by the density ratio.

7.4.2 Modelling of internal pressures

The phenomenon of Helmholtz resonance of internal pressures when the interior of a building is vented at a single opening was described in Chapter 6 (Sections 6.2.3 and 6.2.5). The ‘characteristic’ frequency of a building with distributed openings on windward and leeward walls was also discussed (Section 6.4). It is clearly important when simulating internal pressures in a wind-tunnel model of a building that these frequencies be scaled correctly with respect to the frequencies in the external flow. The scaling requirements to ensure this are derived as follows.

For a single dominant opening (area A), the Helmholtz resonance frequency is given by Equation (6.10):

$$n_H = \frac{1}{2\pi}\sqrt{\frac{\gamma A p_0}{\rho_a \ell_e V_0}}$$

$$\text{i.e. } n_H \propto \sqrt{\frac{\sqrt{A}p_0}{\rho_a V_0}}$$

$$n_H^2 \propto \frac{\sqrt{A}\cdot p_0}{\rho_a V_0}$$

Denoting the ratio of model to full-scale quantities by $[]_r$, the ratio of model to full-scale frequency is given by:

$$[n_H]_r^2 = \frac{[L]_r [p_0]_r}{[\rho_a]_r [V_0]_r} = \frac{[L]_r}{[V_0]_r}$$

as $[p_0]_r = [\rho_a]_r = 1.0$, for testing in air at normal atmospheric pressures.

However, for scaling with frequencies in the external flow:

$$[n_H]_r = \frac{[U]_r}{[L]_r}$$

Hence, for correct scaling,

$$[n_H]_r^2 = \frac{[L]_r}{[V_0]_r} = \frac{[U]_r^2}{[L]_r^2}$$

$$\text{i.e. } [V_0]_r = \frac{[L]_r^3}{[U]_r^2} \qquad (7.2)$$

Thus, if the velocity ratio, $[U]_r$, is equal to 1.0, i.e. when the wind-tunnel speed is the same as full-scale design speeds, then the internal volume should be scaled according to the geometrical scaling ratio,

$$[V_0]_r = [L]_r^3 \times 1.0$$

However, usually in wind-tunnel testing, the wind speed is considerably less than full-scale design wind speeds. Thus, $[U]_r$ is usually less than 1.0, and the internal volume should then be increased by a factor of $1/[U]_r^2$. For example, if the velocity ratio is 0.5, then the internal volume, V_0, should be increased by a factor of 4.

The characteristic response time for internal pressures in a building with distributed openings on the windward side, A_w, and on the leeward side, A_L, is given by Equation (6.17) (neglecting inertial effects):

$$\tau = \frac{\rho_a V_0 \overline{U} A_W A_L}{\gamma k p_0 (A_W^2 + A_L^2)^{3/2}} \sqrt{C_{p_W} - C_{p_L}}$$

For A_w=A_L=A and fixed C_{pw} and C_{PL},

$$\tau \propto \frac{\rho_a V_0 \overline{U}}{p_0 A}$$

and the characteristic frequency,

$$n_C \propto \frac{p_0 A}{\rho_a V_0 \overline{U}}$$

Then, the ratio of model to full-scale frequency is given by:

$$[n_C]_r = \frac{[p_0]_r [L]_r^2}{[\rho_a]_r [V_0]_r [U]_r} = \frac{[L]_r^2}{[V_0]_r [U]_r}$$

For correct scaling with frequencies in the external flow,

$$[n_C]_r = \frac{[U]_r}{[L]_r} = \frac{[L]_r^2}{[V_0]_r [U]_r}$$

Hence,

$$[V_0]_r = \frac{[L]_r^3}{[U]_r^2} \qquad (7.2)$$

Thus, the same scaling criterion applies, as for Helmholtz resonance frequency—i.e. the internal volume needs to be distorted if velocity ratio is not equal to 1.0.

The additional internal volume required when the velocity ratio is less than 1.0 can usually be provided beneath a wind-tunnel floor and connected to the interior of the model.

Failing to provide a sufficiently large volume will generally result in over-prediction of the fluctuating internal pressures, but it is difficult to quantify the errors involved. Thus, it is advisable to correctly scale the internal volume, unless it is particularly difficult or inconvenient to do this.

7.4.3 Simulation requirements for structures in tornadoes

The similarity requirements in laboratory models of tornadoes, for simulating wind pressures on model structures, were discussed by Chang (1971) and Jischke and Light (1979).

The latter proposed that the following non-dimensional parameters should be made the same in full and model scales for correct similarity:

$$\frac{h_i}{r_c}, \frac{\Gamma r_u}{Q}, \frac{z_0}{h_i}, \frac{L}{r_c}$$

where the dependent variables are as follows:

h_i—depth of the layer of horizontal inflow into the tornado;
r_c—radius of the core;
Γ—imposed circulation far from the axis of the tornado;
r_u—radius of the updraft region;
Q—volume flow rate;
z_0—surface roughness length on the ground surface;
L—characteristic length of the structure.

7.5 Measurement of local pressures

Modern cheap sensitive solid-state pressure sensors, either as individual transducers or as part of a multi-channel electronic scanning system, enable near-simultaneous measurements of fluctuating wind pressures on wind-tunnel models of buildings and structures for up to several hundred measurement positions (Holmes, 1995).

For reasons of cost or geometric constraint, it is usually necessary to mount the pressure sensor or scanning unit remotely from the point where the pressure measurement is required. Then the fluctuating pressure must be transmitted by tubing between the measurement and sensing points. The dynamic frequency response of the complete pressure measurement system, including the sensor itself, the volume exposed to the diaphragm and the tubing, is an important consideration.

Inadequate response can lead to significant errors especially when measuring peak pressures or suctions on building models (e.g. Durgin, 1982; Holmes, 1984; Irwin, 1988). As a rule of thumb, the equivalent full-scale upper frequency response limit should not be less than about 2 Hz. To convert this to model frequency, the frequency ratio is obtained by dividing the velocity ratio by the geometric length scaling ratio, e.g. for a typical velocity ratio of 1/3 and a geometric ratio of 1/300, the frequency ratio is 100 and the desirable upper limit is 200 Hz.

The transmission of pressure fluctuations is affected by the mass inertia, compressibility and energy dissipation in the transmitting fluid (e.g. Bergh and Tijdeman, 1965). Standing waves can produce unwanted resonant peaks in the amplitude frequency response characteristics of the system and a non-linear variation of phase lag with frequency.

An ideal system would have an amplitude response which is constant over the frequencies of interest and a linear phase variation with frequency. The latter characteristic guarantees that there is no distortion of transient pressure 'signatures' by the system.

As well as pressure measurement at a single point, systems in which pressures from a number of points are connected to a common manifold or *pneumatic averager* have become widely used. In wind engineering, this arrangement has been used to obtain fluctuating and peak pressures appropriate to a finite area, or panel, on a building model in a turbulent wind-tunnel flow (e.g. Surry and Stathopoulos, 1977; Holmes and Rains, 1981; Gumley, 1984; Holmes, 1987; Kareem *et al.*, 1989).

7.5.1 Single-point measurements

Three common systems are in use:

1. 'Short' tube systems

   This system uses a relatively short length of tubing to connect the measurement point to the sensor. Typically, for wind-tunnel testing, this may consist of 20–100 mm long tubes with 1–2 mm internal diameter. The short tube lengths will result in resonant frequencies that are high, hopefully well above the range of interest for the measurements. However, the short tube also results in low dissipation of energy and the amplitude response rises to a high value at the peak.

2. 'Restricted' tube systems

   Restricted-tube systems may be defined as those involving one or more changes in internal diameter along the tube length. Such systems often allow location of pressure sensors at distances of 150–500 mm from the measurement point, with good amplitude and phase characteristics up to 200 Hz, or more. The simplest system of this type is the two-stage type, in which a section of narrower tube is inserted between the main tube section and the transducer. Restricted tube systems are very effective in removing resonant peaks and giving linear phase response characteristics (e.g. Surry and Isyumov, 1975; Irwin *et al.*, 1979; Holmes and Lewis, 1987a). An effective frequency range can be obtained which is better than that for a constant diameter tubing with a fraction of the length.

3. 'Leaked' tube systems

   The leaked tube system was proposed by Gerstoft and Hansen (1987). A theoretical model was developed by Holmes and Lewis (1989). A relatively flat amplitude frequency response to frequencies of 500 Hz with 1 m of connecting tubing is possible with a system of this type. This is achieved by inserting a controlled side leak part-way along the main connecting tube, usually close to the transducer. It has the effect of attenuating the amplitude response to low-frequency fluctuations, and to steady pressures, to the level of a conventional closed system at higher frequencies. Thus, the leak effectively introduces a high-pass filter into the system. The amplitude ratio at frequencies approaching zero is simply a function of the resistance to steady laminar flow of the main tube and

leak tube. For multiple pressure tap measurements with this system, it is normally necessary to connect all the leaks to a common reference pressure, usually that inside a closed chamber, or plenum, to which the reference static pressure is also connected.

The general arrangement of the three types of single-point measurements are shown in Figure 7.7.

7.5.2 Measurement of area-averaged pressures

Systems which average the pressure fluctuations from a number of measurement points, so that area-averaged wind loads on finite areas of a structure can be obtained, are now in common use. Averaging manifolds were first used in wind tunnels by Surry and Stathopoulos (1977). Gumley (1981, 1983) developed a theoretical model for their response.

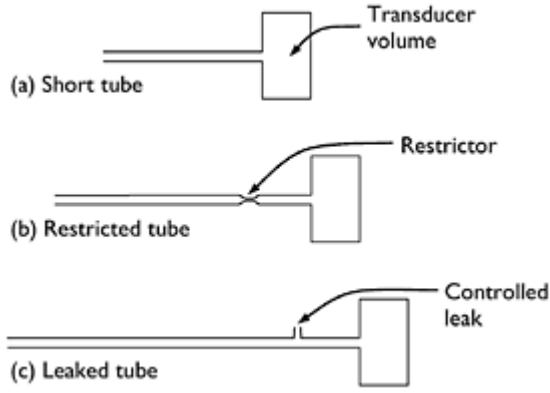

Figure 7.7 Tubing arrangements for measurement of point pressures.

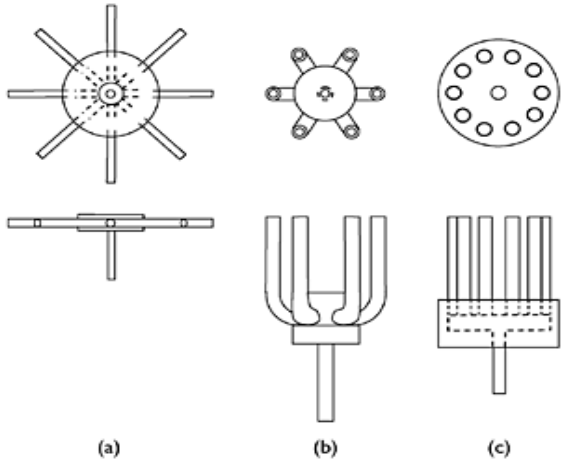

Figure 7.8 Manifolds for pressure averaging.

Figure 7.8 shows the types of parallel tube and manifold arrangement that have been commonly used in wind engineering work. Provided that the inlet tubes are identical in length and diameter, such a system should provide a true average in the manifold, of the fluctuating pressures at the entry to the input tubes, assuming that laminar flow exists in them. Usually, flatter amplitude response curves to higher frequencies can be obtained with the multi-tube-manifold systems, compared with single-point measurements using the same tube lengths, due to the reinforcement of the higher frequencies in the input tubes. However, once the number of input tubes exceeds about five, there is little change to the response characteristics. The response is also not greatly sensitive to the volume of the averaging manifold.

The assumption that the average of discrete fluctuating point pressures, sampled within a finite area of a surface, adequately approximates the continuous average aerodynamic load on the surface requires consideration (Surry and Stathopoulos, 1977; Holmes and Lewis, 1987b).

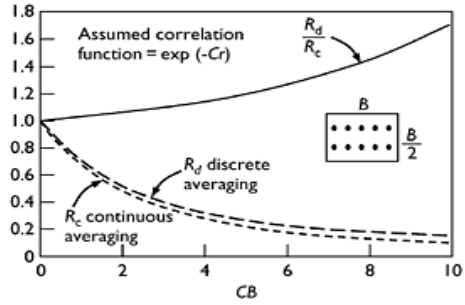

Figure 7.9 Discrete and continuous averaging of fluctuating pressures.

Figure 7.9 shows the ratio of the variance of the averaged panel force to the variance of the point pressure, using first the correct continuous averaging over the panel denoted by R_c, and second the discrete averaging approximation performed using the pneumatic averaging system with the 10 pressure tappings within a panel, denoted by R_d. Calculations of these ratios were made, assuming a correlation coefficient for the fluctuating pressures of the form, $\exp(-Cr)$, where r is a separation distance and C a constant. The variance of the local pressure fluctuations across the panel of dimensions B by $B/2$ was assumed to be constant.

It can be seen that R_d exceeds R_c for all values of CB. This is due to the implied assumption, in the discrete averaging, that the pressure fluctuations are fully correlated in the tributary area around each pressure tap. Clearly, the error increases with increasing C due to the lower correlation of the pressure fluctuations and with increasing panel size, B. The errors can be decreased by increasing the number of pressure tappings within a panel of a certain size. However, it should be noted that the errors are larger at higher frequencies than at lower frequencies; a more detailed analysis of the errors requires knowledge of the coherence of the pressure fluctuations.

7.5.3 Equivalent time averaging

An alternative procedure for determining wind loads acting over finite surface areas from point pressures is known as ‘equivalent time averaging’. In this approach, the time histories of fluctuating point pressures are filtered by means of a moving average filter. As originally proposed by Lawson (1976), the averaging time, τ, was estimated to be given by the following formula:

$$\tau \cong 4.5\frac{L}{\bar{U}} \tag{7.3}$$

where L is usually taken as the length of the diagonal for the panel of interest.

However, a later analysis (Holmes, 1997) showed Equation (7.3) to be unconservative, and that a more correct relationship is:

$$\tau \cong 1.0\frac{L}{\bar{U}} \tag{7.4}$$

However, the ‘constants’ in the above equations are likely to vary considerably depending on the location of the pressure measurement position on a building model—i.e. windward wall, roof, etc. This method is less accurate than the area-averaging technique by manifolding described in Section 7.5.2.

7.6 Modelling of overall loads and response of structures

7.6.1 Base-pivoted model testing of tall buildings

This section describes the procedure for the conducting of aeroelastic wind-tunnel testing of high-rise buildings, using rigid models.

The use of rigid-body aeroelastic modelling of tall buildings is based on three basic assumptions:

1. The resonant response of the building to wind loads in torsional (twisting) modes can be neglected.
2. The response in sway modes higher than the first in each orthogonal direction can be neglected.
3. The mode shapes of the fundamental sway modes can be assumed to be linear.

With these assumptions, the motion of a rigid model of the building, pivoted at, or near, ground level and located in a wind tunnel in which an acceptable model of the atmospheric boundary layer in strong winds has been set up, can be taken to represent the sway motion of the prototype building. The fact that a scaled reproduction of the building motion has been obtained means that fluctuating aerodynamic forces that depend upon that motion have been reproduced in the wind tunnel. This is not the case when fixed models are used to measure the fluctuating wind pressures or the 'base-balance' technique is used. In both these cases, the resonant response of the building is not reproduced.

Even buildings that have a non-linear mode shape can often be modelled by means of rigid-body rotation, but in these cases it may be appropriate to position the pivot point at a different level to ground level. For example, a building supported on stiff columns near ground level might be modelled by a rigid model pivoted at a height above ground level (e.g. Isyumov *et al.*, 1975). The disadvantage of this approach is that the bending moment at ground level cannot be measured.

There is a direct analogy between the generalized mass of the prototype building, G_1, and the moment of inertia of the model building, including the contributions from the support shaft and any other moving parts.

Assuming that the mode shape of the building is given by:

$$\phi_1(z) = (z/h) \tag{7.5}$$

the generalized mass is given by:

$$G_1 = \int_0^h m(z)\phi_1^2(z)\,\mathrm{d}z \tag{7.6}$$

The equivalent prototype moment of inertia for rigid-body rotation about ground level is given by

$$I_p = \int_0^h m(z)z^2 dz = (1/h^2)\, G_1 \tag{7.7}$$

The equivalent model moment of inertia is then given by:

$$I_m = M_r L_r^2 I_p = L_r^5 (1/h^2)\, G_1 \tag{7.8}$$

where M_r and L_r and are the mass ratio and length ratio, respectively. To maintain a density ratio of unity in both model and full scale, assuming that air is the working fluid in both cases,

$$M_r = L_r^3 \tag{7.9}$$

Equation (7.8) can be used to establish the required model moment of inertia.

To obtain the correct moment of inertia, and at the same time to achieve a relatively rigid model, it is normally necessary to manufacture the model from a light material such as expanded foam or balsa wood. A typical mounting is shown in Figure 7.10. The model is supported by gimbals of low friction, and rotation about any horizontal axis is permitted. Elastic support can be provided by springs whose position can be adjusted vertically. In the case of the system shown in Figure 7.10, damping is provided by an eddy current device, but vanes moving in a container of viscous liquid can also be used.

The moment of inertia of the model and the supporting rod and damper plates can be determined in one or more of the following three ways:

1. By swinging the model, supporting rod and attachments, as a compound pendulum and measuring the period of oscillation;
2. By measuring the frequency of vibration in the mounted position, and knowing the spring constants;
3. By measuring the angular deflection of the supporting rod for known overturning moments applied to the model in position and using the measured frequencies.

The support system shown in Figure 7.10 is the most common arrangement, but a method of support based on a cantilever support has also been used. The vertical position of the model on the cantilever is adjusted to minimize the rotation at ground level. The advantage of this method is that base shear, as well as base bending moment, can be measured.

Testing of the model to determine either the base bending moment or the tip deflection over a range of reduced velocities should be carried out. The assumptions made to justify the rigid model aeroelastic testing result in a relationship between the base bending moment, M_b, and the tip deflection, x, as follows:

$$M_b = (\omega_1^2 I_p/h)x = (\omega_1^2 G_1/h^3)x \cong (\omega_1^2 m h^2/3)x \tag{7.10}$$

where ω_1 is the natural circular frequency and m is the average mass/unit height.

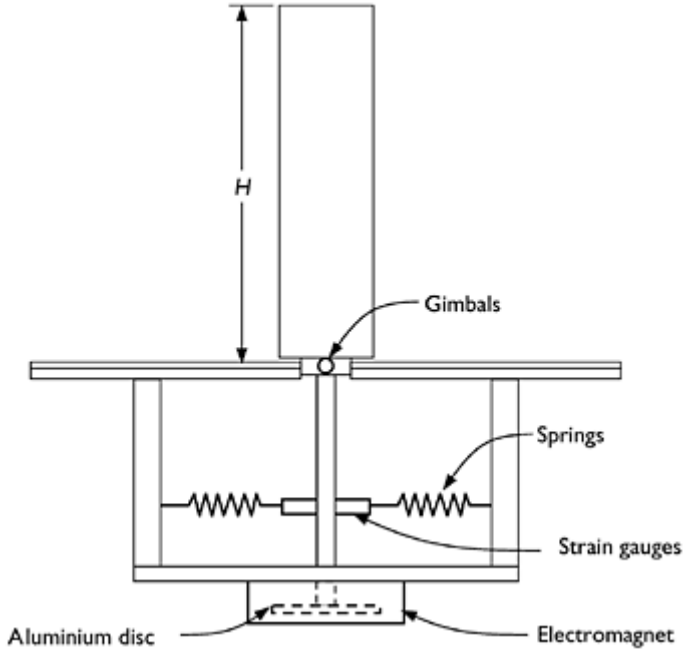

Figure 7.10 A base-pivoted tall building model.

The relationship in Equation (7.10) implies that the mean and background wind loads are distributed over the height of the building in the same way as the resonant response, i.e. according to the distribution of inertial forces for first mode response. This is a consequence of the neglect of the higher modes of vibration.

The upper limit of reduced velocity should correspond to a mean wind speed which is larger than any design value for any wind direction. As it will be required to fit a relationship between response (either peak or rms) and mean wind speed, testing should be carried out for at least three reduced velocities.

It is wise to conduct aeroelastic tests for at least two different damping ratios—a value representative of that expected at perceptible accelerations for the height and construction type, and a higher value that may be achieved at ultimate conditions, or at serviceability

design conditions when an auxiliary system is added. If the resonant response is dominant, values outside these conditions can be estimated by assuming that the rms response varies as the inverse of the square root of the damping ratio.

The final stage of an aeroelastic investigation should be to provide the structural engineer with vertical distributions of loads which are compatible with the base bending moments obtained from the experiments and subsequent processing. As discussed in Chapter 5, there are different distributions for the mean component, background or subresonant fluctuating component and the resonant component of the peak response, for any wind direction. If wind-tunnel pressure measurements are available, these can be used to determine the mean load distribution. Pressure measurements could, in principle, also be used to determine the background fluctuating loads, although this requires extensive correlation measurements; also the loading distribution should be 'tailored' to the particular load effect, such as a column load.

For tall buildings, a linear loading distribution with a maximum at the top, reducing to zero at the pivot point, is often assumed. Then the load per unit height at the top of the building, w_0, is given by:

$$w_0 = \frac{3M_b}{h^2} \tag{7.11}$$

For a linear mode of vibration, this is a realistic distribution for the inertial loading of the resonant part of the response (Section 5.4.4). However, this is not a realistic distribution for the mean (Section 5.4.2) or the background response (Section 5.4.3), when the loading is primarily along-wind.

7.6.2 The high-frequency base-balance technique

For most tall buildings, the 'high-frequency base-balance' (HFBB) technique (Tschanz and Davenport, 1983) has now replaced aeroelastic model testing. In this method, there is no attempt to model the dynamic properties of the building—in fact the support system is made deliberately stiff to put the building model above the range of the exciting forces of the wind. A rigid model, which reproduces the building shape, is used. The model is supported at the base by a measurement system, which is capable of measuring the mean and fluctuating wind forces and moments to a high frequency, without significant amplification or attenuation. The spectral densities of the base forces and moments are measured, and the resonant response of the building, with appropriate dynamic properties incorporated, is computed using a spectral or random vibration approach, similar to that described in Section 5.3. A range of damping ratios and mean wind speeds can be simulated using this approach.

Note that the HFBB measures the mean and background fluctuating (quasi-static) base moments directly. Calculation is required only for the *resonant* components.

Figure 7.11 shows how the spectrum of wind force varies with different speeds in a wind tunnel. For a given design of balance, there will be an upper limit to the wind force (proportional to wind speed squared) that is capable of being measured by the balance; this will be proportional to the stiffness of the balance for a particular force component.

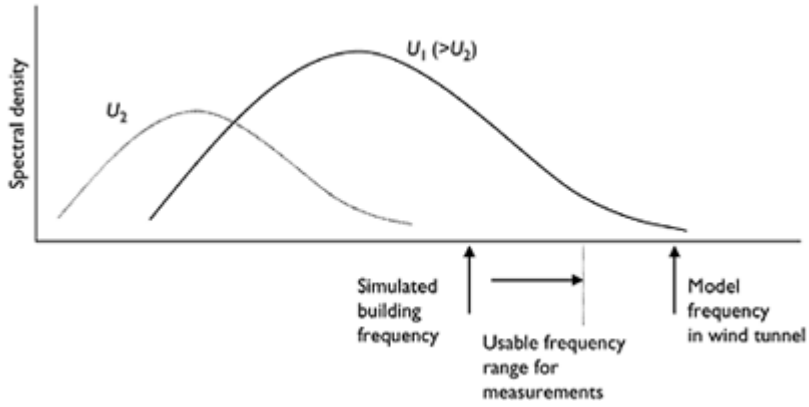

Figure 7.11 Frequency relationships for a high-frequency base balance.

Thus, the maximum wind-tunnel speed for which a balance can be used is proportional to the square root of the stiffness. As the natural frequency of a model of given mass is also proportional to the square root of the stiffness, the ratio of maximum wind speed to maximum usable frequency will be a constant for a given design of balance.

When the prototype building does not have a linear sway mode shape, corrections are required to the computed resonant response, as they are for the base-pivoted aeroelastic model technique. Base torque can also be measured and used to determine the response in torsional mode of vibration, although quite large mode shape corrections are required as discussed in the following.

A variety of mode shape correction factors have been developed for the HFBB (e.g. Holmes, 1987; Boggs and Peterka, 1989). These depend on the assumptions made for the variation of the fluctuating wind forces (or torques) with height and the correlation between the fluctuating sectional forces at different heights (Holmes *et al.*, 2003). There appear to be considerable differences between various commercial laboratories with regard to the corrections made, especially for the torsional, or twist, modes. Some laboratories make use of the measured base shears, as well as the base bending moments, available from a high-frequency base balance and assume a linear variation of the instantaneous wind force with height (Xie and Irwin, 1998). However, such methods do not eliminate the need for mode shape corrections (Chen and Kareem, 2005a).

The base moments $M_x(t)$, $M_y(t)$ and $M_z(t)$ measured by the HFBB must be converted into generalized forces for the two fundamental sway modes and twist mode. For example, using mode shape corrections proposed by Holmes (1987) and Holmes *et al.* (2003):

$$Q_x(t) = \left(\frac{1}{h}\right)\sqrt{\frac{4}{1+3\beta_x}}.M_y(t) \tag{7.12}$$

$$Q_y(t) = \left(\frac{1}{h}\right)\sqrt{\frac{4}{1+3\beta_y}}.M_x(t) \tag{7.13}$$

$$Q_z(t) = \sqrt{\frac{1}{1+2\beta_z}}.M_z(t) \tag{7.14}$$

where $Q_x(t)$, $Q_y(t)$, $Q_z(t)$ are the generalized forces in the *x*- and *y*-sway modes and twist modes, respectively; h is the building height.

It has been assumed that the mode shapes can be represented by power functions, i.e.

$$\phi_x = \left(\frac{z}{h}\right)^{\beta_x} \tag{7.15}$$

$$\phi_y = \left(\frac{z}{h}\right)^{\beta_y} \tag{7.16}$$

$$\phi_z = \left(\frac{z}{h}\right)^{\beta_z} \tag{7.17}$$

If the mode shape exponent for the twist mode β_z is 1.0 (i.e. the dynamic twist varies linearly with height from the ground to the top of the building), then from Equation (7.14) the mode shape correction term is $\sqrt{(1/3)}$ or 0.58. This is significantly different from 1.0 because the HFBB measures the base torsional moment *uniformly* weighted with height, whereas the generalized force for the twist mode requires a *linear* weighting with height. On the other hand, the generalized forces for the sway modes usually have mode shape correction factors close to 1.0 (equal to 1.0 for linear mode shapes).

Many modern tall buildings have dynamic modes that involve *coupled* sway and twist motions. This often results from differences between the average positions of the centre of mass and centre of stiffness (shear centre) of the cross-sections of the building. It is extremely difficult (and expensive) to manufacture accurate aeroelastic wind-tunnel models of buildings with coupled modes. However, methods are available to make reasonable predictions of the resonant contributions from the coupled modes of tall buildings using the HFBB technique (Holmes *et al.*, 2003; Chen and Kareem, 2005b).

The high-frequency base-balance technique requires relatively simple models and clearly reduces the amount of wind-tunnel testing time by a large factor, at the expense of computing resources, which have rapidly become cheaper. There are methodologies to account for complex coupled sway and twist dynamic modes. Most tall buildings can adequately be studied using the HFBB technique—a very cost-effective method.

7.6.3 Sectional and taut strip models of bridges

A common, and long-standing, technique to confirm the aerodynamic stability of the decks of long-span suspension or cable-stayed bridges is the section model test. This is another form of rigid-body aeroelastic modelling. The technique dates back to the investigations following the failure of the first Tacoma Narrows bridge (Farquarson *et al.*, 1949–54). A short section of the bridge deck is supported on springs and allowed to move in translation and rotation. By suitable adjustment of the springs, the model frequencies in rotation and vertical translation can be arranged to have the same ratio as those for the primary bending and torsional modes of the prototype bridge. Then in order to achieve

similarity between model, m, and prototype, p, the reduced frequencies (Section 7.4) should be kept equal:

$$\left(\frac{n_s L}{U}\right)_m = \left(\frac{n_s L}{U}\right)_p \tag{7.18}$$

where n_s should be taken both as the lowest frequencies in vertical translation (bending) and in rotation (torsion).

The models are made as rigid as possible, but they are also required to satisfy the density scaling requirement that the ratio ρ_s/ρ_a should be the same in model and full scale, where ρ_s is the average density of the structure and ρ_a the air density. The details of the deck at the leading edge—such as edge beams and guard railings—are usually modelled in some detail, as these have been found to affect the aeroelastic behaviour.

Section models are primarily used to determine the critical flutter speeds of the section in both smooth and turbulent flows. The static aerodynamic coefficients can also be determined for use in calculations of turbulent buffeting of the section. A more advanced use is for determination of the aeroelastic coefficients, or flutter derivatives (Sections 5.5.3 and 12.3.2), for subsequent use in more complete computational modelling of bridge behaviour; both free (Scanlan and Tomko, 1971) and forced vibration (e.g. Matsumoto *et al.*, 1992) methods have been developed.

Sectional models are primarily a two-dimensional simulation, and cannot readily be used in turbulent flow, which of course is more representative of atmospheric flow and three-dimensional in nature. A more advanced test method for bridges, known as ‘taut strip’, involves the central span of the model bridge deck supported on two parallel wires, pulled into an appropriate tension and separated by an appropriate distance, so that the bending and torsional modes are approximately matched. The deck is made in elements or short sections, so that no stiffness is provided. Such a model can be tested in full simulated boundary-layer flows, but is more economical than a full aeroelastic model test.

Scanlan (1983) and Tanaka (1990) have given useful reviews of the section model and taut-strip techniques for bridge decks, together with a discussion of full aeroelastic model testing of bridges.

7.6.4 Multi-mode aeroelastic modelling

For the modelling of structures with non-linear mode shapes or for structures which respond dynamically to wind in several of their natural resonant modes of vibration, such as tall towers and long-span bridges, the rigid-body modelling technique is not sufficient. In the case of long-span bridges, the aerodynamic influences of the cables and the supporting towers, which are not included in section model or taut-strip testing (Section 7.6.3), may often be significant. More complete aeroelastic and structural modelling techniques are then required.

There are three different types of these multi-mode models:

1. ‘Replica’ models—in which the construction of the model replicates that of the prototype structure.

2. ‘Spine’ models which reproduce the stiffness properties of the prototype structure by means of smaller central members or ‘spines’. Added sections reproduce the mass and aerodynamic shape of the prototype.
3. ‘Lumped mass’ models, in which the mass of the model is divided into discrete ‘lumps’, connected together by flexible elements. The number of vibration modes that can be reproduced by this type of model is limited by the number of lumped masses.

The design of these models generally follows the scaling laws based on dimensional analysis, as outlined in Section 7.4. Full model testing of suspension bridges and cable suspended roofs, where stiffness is, at least partially, provided by gravitational forces, requires equality of Froude number, $U/\sqrt{(Lg)}$ (introduced in Section 7.4), between model and full scale. Thus:

$$\left(\frac{U}{\sqrt{Lg}}\right)_m = \left(\frac{U}{\sqrt{Lg}}\right)_p$$

since the gravitational constant, g, is the same in model and full scale, this results in a velocity scaling given by:

$$\frac{U_m}{U_p} = \sqrt{\frac{L_m}{L_p}} \qquad (7.19)$$

Thus, the velocity ratio is fixed at the square root of the length ratio (or model scale). Thus for a 1/100 scale suspension bridge model, the velocity in the wind tunnel is one-tenth of the equivalent velocity in full scale.

For the majority of structures, in which the stiffness is provided by internal stresses (e.g. axial, bending, shear), Froude number scaling is not required for aeroelastic models, and a free choice can be made of the velocity scaling when designing a model. Usually a fine adjustment of the velocity scaling is made after the model is built, to ensure equality of reduced frequency (see Equation 7.18).

Examples of aeroelastic models are shown in Figure 11.6 (observation tower) and Figure 12.7 (bridge under construction). These are both ‘spine’ models.

A further simplification of dynamic models, which is occasionally employed, is to distort, by equal factors, the stiffness and mass properties of the model from those required by the correct scaling laws. This retains the correct value of reduced frequency (Section 7.4) and preserves the correct relationship between the frequencies associated with the flow (e.g. turbulence and vortex shedding), and those related to the structure. Although internal forces and moments in the structure are correctly modelled, deflections, velocities and accelerations of the model, and hence motion-induced forces, such as aerodynamic damping (Section 5.5.1), are not scaled correctly. This type of simplification is used to reduce the cost of model making, when aeroelastic effects are not regarded as important (Section 7.6.6).

7.6.5 Aeroelastic modelling of chimneys

Chimneys and other slender structures of circular cross-sections are vulnerable to cross-wind excitation by fluctuating pressures due to vortex shedding (Sections 4.6.3 and 11.5). In the 1950s and 1960s, it was quite common to investigate this behaviour with small-scale wind-tunnel models. However, the forces from vortex shedding are quite dependent on Reynolds number (Section 4.2.4), and wind-tunnel tests will severely over-estimate the cross-wind response of prototype large chimneys (Vickery and Daly, 1984). The prediction of full-scale response of such structures is better undertaken by the use of mathematical models of the response (Section 11.5) with input parameters derived from full-scale measurements at high Reynolds numbers.

7.6.6 Distorted 'dynamic' models

In many cases the resonant response of a structure may be significant, but the prototype structure may be stiff enough such that aeroelastic forces (i.e. the motion dependent forces) are not significant. Furthermore, the scaling requirements (Section 7.4.1) and properties of the available modelling materials may make it difficult, or even impossible, to simultaneously scale the mass, stiffness and aerodynamic shape of a structure.

In such cases, the mass and stiffness properties of the structure can both be distorted by the same factor (usually greater than 1.0). Then the correct frequency relationship for the applied fluctuating wind forces and the structural frequencies is obtained. Internal forces and moments are correctly modelled (including resonant effects, but neglecting aeroelastic effects), but the deflections, accelerations and aerodynamic forces are not scaled correctly.

Such 'distorted' dynamic models have been used on certain open-frame structures, where aeroelastic 'spine' models were not possible.

7.6.7 Structural loads through pressure measurements

For structures such as large roofs of sports stadiums, or large low-rise buildings, with structural systems that are well-defined and for which resonant dynamic action is not dominant, or can be neglected, wind-tunnel pressure measurements on rigid models can be used effectively to determine load effects such as member forces and bending moments, or deflections. This method is normally used in conjunction with the area-averaging pressure technique described in Section 7.5.2. Also required are *influence coefficients*, representing the values of a load effect under the action of a single uniformly distributed static 'patch load' acting on the area corresponding to a panel on the wind-tunnel model. Two methods are possible.

1. Direct on-line weighting of the fluctuating panel pressures recorded in the wind-tunnel test with the structural influence coefficients, to determine directly fluctuating and peak values of the load effects (Surry and Stathopoulos, 1977; Holmes, 1988).
2. Measurement of correlation coefficients between the fluctuating pressures on pairs of panels and calculation of rms and peak load effects by integration (Holmes and Best, 1981; Holmes *et al.*, 1997).

The latter method has advantages that the influence coefficients are not required at the time of the wind-tunnel testing, and also that the information can be used to determine equivalent static load distributions, as discussed in Chapter 5. When resonant response is of significance, as may be the case for the largest stadium roofs, time histories of the fluctuating pressures can be used to generate a time history of generalized force for each mode of significance. From the spectral density of the generalized force, the mean square generalized displacement (modal coordinate) and effective inertial forces acting can be determined (Section 5.4.4). The application of pressure model studies to large roofs is discussed in Chapter 10.

Pressure-based methods can also be used for structural loads and response of tall buildings (ASCE, 1999). Although these methods require a large number of simultaneous pressure measurements and extensive post-processing of the wind-tunnel data, accurate account of non-linear resonant mode shapes can be made, and in many cases this method has replaced the high-frequency base-balance technique. A significant advantage is that the same building model used to determine local cladding pressures can be used to determine overall wind loads and response. However, a practical difficulty with this technique is the installation of a sufficient number of tubes for pressure measurement within the available cross-section of a model.

7.7 Blockage effects and corrections

In a wind tunnel with a closed test section, the walls and roof of the wind tunnel provide a constraint on the flow around a model building or group of buildings, which depends on the blockage ratio. The blockage ratio is the maximum cross-sectional area of the model at any cross-section divided by the area of the wind-tunnel cross-section. If this ratio is high enough, there may be significant increases in the flow velocities around, and pressures on, the model. In the case of an open-test section, the errors are in the opposite direction, i.e. the velocities around the model are reduced. To deal with the blockage problem, several approaches are possible:

- Ensure that the blockage ratio is small enough that the errors introduced are small, and no corrections are required. The usual rule for this approach is that the blockage ratio should not exceed 5%.
- Accept a higher blockage ratio and attempt to make corrections. The difficulty with this approach is that the appropriate correction factors may themselves be uncertain. Although there are well-documented correction methods for drag and base pressure on stalled airfoils, and other bluff bodies in the centre of a wind tunnel with uniform or homogeneous turbulent flow, there is very little information for buildings or other structures mounted on the floor of a wind tunnel in turbulent boundary-layer flow. McKeon and Melbourne (1971) provided corrections for *mean* windward and leeward pressures, and total drag force, on simple plates and blocks. However, no corrections are available for pressures, mean or fluctuating, in separated flow regions, such as those which occur on roofs or side walls of building models.
- Design the walls and/or roof of the working section in such a way as to minimize the blockage errors. The most promising method for doing this appears to be the *slotted wall* concept (Parkinson, 1984; Parkinson and Cook, 1992). In this system, the walls

and roof of the test sections are composed of symmetrical aerofoil slats, backed with a plenum chamber. The optimum open area ratio is about 0.55, and it is claimed that blockage area ratios of up to 30% can be used without correction.

7.8 Computational wind engineering

Computational fluid dynamics (CFD) techniques as applied to wind engineering have been under development for a number of years. There have been several conferences on the subject. It is clear that wind flow around buildings is a very complex fluid mechanics problem, involving a large range of turbulence scales—varying from the very large eddy structures of atmospheric turbulence (see Chapter 3) to the small scales generated by the flow around the bluff-body shapes of buildings and other structures (Chapter 4). The result of this is that, at the time of writing, the most common CFD techniques are capable of predicting the *mean* pressures on buildings with reasonable accuracy, but are not sufficiently accurate for the fluctuating and peak pressures. As an example, mean pressures on arched-roof buildings generated by CFD are discussed in Section 10.3.

The poor representation of the pressure fluctuations is primarily because it is necessary to incorporate over-simplified representations of the turbulence in the fluid flow equations. At the current rate of progress, this situation is unlikely to change until well into the twenty-first century.

CFD techniques are, however, capable currently of providing useful insights into wind flow around buildings for environmental considerations. Useful reviews of such techniques are given by Baskaran and Kashev (1996) and Stathopoulos and Baskaran (1996).

7.9 Summary

In this chapter, a review of methods of laboratory simulation of natural strong wind characteristics for the investigation of wind pressures, forces and structural response has been given. Early methods used natural growth of boundary layers on the floor of wind tunnels to simulate the mean flow and turbulence structure in the fully developed boundary layer in gale wind conditions. To make use of shorter test sections in aeronautical wind tunnels, rapid growth methods were developed and described. For investigations on smaller structures, such as low-rise buildings, methods of simulating only the lower part, or surface layer, of the atmospheric boundary layer were devised.

Laboratory methods of simulating tornadoes, which were quite advanced as early as the 1970s, are discussed. Methods of simulating strong winds in tropical cyclones and thunderstorms, which are the dominant types for structural design at locations in the tropics and subtropics at latitudes from 0° to 40°, are still at an early stage of development. A major problem is the lack of good full-scale data of the wind structure on which the simulations can be based.

Experimental methods of measuring local pressures and overall structural loads in wind-tunnel tests are described in Sections 7.5 and 7.6, and the problem of wind-tunnel blockage and its correction is discussed in Section 7.7.

References

American Society of Civil Engineers (1999) Wind tunnel studies of buildings and structures. ASCE Manual and Reports on Engineering Practice No. 67, ASCE, New York.

Australasian Wind Engineering Society (2001) Wind-engineering studies of buildings. Quality Assurance Manual, AWES-QAM-1–2001.

Aynsley, R.D., Melbourne, W.H. and Vickery, B.J. (1977) *Architectural Aerodynamics.* Applied Science Publishers, London.

Baskaran, A. and Kashev, A. (1996) Investigation of air flow around buildings using computational fluid dynamics techniques. *Engineering Structures*, 18:861–75.

Bergh, H. and Tijdeman, H. (1965) Theoretical and experimental results for the dynamic response of pressure measurement systems. Report NLR-TR-F. 238, National Aero- and Astronautical Research Institute (Netherlands), January.

Boggs, D.W. and Peterka, J.A. (1989) Aerodynamic model tests of tall buildings. *Journal of Engineering Mechanics*, 115:618–35.

Cermak, J.E. (1971) Laboratory simulation of the atmospheric boundary layer. *AIAA Journal*, 9:1746–54.

Cermak, J.E. (1977) Wind-tunnel testing of structures. *ASCE Journal of the Engineering Mechanics Division*, 103:1125–40.

Chang, C.C. (1971) Tornado effects on buildings and structures by laboratory simulation. *Proceedings, 3rd International Conference on Wind effects on Buildings and Structures*, Tokyo, Japan, 6–9 September, pp. 231–40.

Chen, X. and Kareem, A. (2005 a) Validity of wind load distribution based on high frequency force balance measurements. *Journal of Structural Engineering*, 131:984–7.

Chen, X. and Kareem, A. (2005b) Dynamic wind effects on buildings with 3D coupled modes: application of high frequency force balance measurements. *Journal of Engineering Mechanics*, 131:1115–25.

Cook, N.J. (1973) On simulating the lower third of the urban adiabatic boundary layer in a wind tunnel. *Atmospheric Environment*, 7:691–705.

Counihan, J. (1969) An improved method of simulation of an atmospheric boundary layer in a wind tunnel. *Atmospheric Environment*, 3:197–214.

Davenport, A.G. and Isyumov, N. (1967) The application of the boundary layer wind tunnel to the prediction of wind loading. *Proceedings, International Research Seminar on Wind effects on Buildings and Structures*, Ottawa, Canada, 11–15 September, pp. 201–230.

Davies-Jones, R.F. (1976) Laboratory simulation of tornadoes. *Symposium on Tornadoes: Assessment of Knowledge and Implications for Man*, Texas Tech University, Lubbock, TX, 22–24 June, pp. 151–74.

Durgin, F. (1982) Instrumentation requirements for measuring aerodynamic pressures and forces on buildings and structures. In: *Wind Tunnel Modeling for Civil Engineering Applications*, ed. T.Reinhold, Cambridge University Press, Cambridge.

Farquarson, F.B., Smith, F.C. and Vincent, G.S. (1949–54) Aerodynamic stability of suspension bridges with special reference to the Tacoma Narrows Bridge. *University of Washington Engineering Experiment Station. Bulletin No. 116*, Parts I–V.

Flachsbart, O. (1932) Winddruck auf geschlossene und offene Gebäude. In: *Ergebnisse der aerodynamischen Versuchanstalt zu Göttingen, IV. Lieferung*, eds L.Prandl and A.Betz, Verlag von R.Oldenbourg, Munich and Berlin.

Gerstoft, P. and Hansen, S.O. (1987) A new tubing system for the measurement of fluctuating pressures. *Journal of Wind Engineering & Industrial Aerodynamics*, 25:335–54.

Gumley, S.J. (1981) Tubing systems for the measurement of fluctuating pressures in wind engineering. D.Phil. thesis, University of Oxford, Oxford.

Gumley, S.J. (1983) Tubing systems for pneumatic averaging of fluctuating pressures. *Journal of Wind Engineering & Industrial Aerodynamics*, 12:189–228.

Gumley, S.J. (1984) A parametric study of extreme pressures for the static design of canopy structures. *Journal of Wind Engineering & Industrial Aerodynamics*, 16:43–56.

Holmes, J.D. (1984) Effect of frequency response on peak pressure measurements. *Journal of Wind Engineering & Industrial Aerodynamics*, 17:1–9.

Holmes, J.D. (1987) Mode shape corrections for dynamic response to wind. *Engineering Structures*, 9:210–12.

Holmes, J.D. (1988) Distribution of peak wind loads on a low-rise building. *Journal of Wind Engineering & Industrial Aerodynamics*, 29:59–67.

Holmes, J.D. (1995) Methods of fluctuating pressure measurement in wind engineering. In: *A State of the Art in Wind Engineering*, ed. P.Krishna, Wiley Eastern, New Delhi.

Holmes, J.D. (1997) Equivalent time averaging in wind engineering. *Journal of Wind Engineering & Industrial Aerodynamics*, 72:411–19.

Holmes, J.D. and Best, R.J. (1981) An approach to the determination of wind load effects for low-rise buildings. *Journal of Wind Engineering & Industrial Aerodynamics*, 7:273–87.

Holmes, J.D. and Lewis, R.E. (1987a) Optimization of dynamic-pressure-measurement systems. I. Single point measurements. *Journal of Wind Engineering & Industrial Aerodynamics*, 25:249–73.

Holmes, J.D. and Lewis, R.E. (1987b) Optimization of dynamic-pressure-measurement systems. II. Parallel tube-manifold systems. *Journal of Wind Engineering & Industrial Aerodynamics*, 25:275–90.

Holmes, J.D. and Lewis, R.E. (1989) A re-examination of the leaked-tube dynamic pressure measurement system. *10th Australasian Fluid Mechanics Conference*, University of Melbourne, December, pp. 5.39–5.42.

Holmes, J.D. and Osonphasop, C. (1983) Flow behind two-dimensional barriers on a roughened ground plane, and applications for atmospheric boundary-layer modelling. *Proceedings, 8th Australasian Fluid Mechanics Conference*, Newcastle, NSW.

Holmes, J.D. and Rains, G.J. (1981) Wind Loads on flat and curved roof low rise buildings. *Colloque 'Construire avec le Vent'*, Nantes, France, July.

Holmes, J.D., Rofail, A. and Aurelius, L. (2003) High frequency base balance methodologies for tall buildings with torsional and coupled resonant modes. *Proceedings, 11th International Conference on Wind Engineering*, Lubbock, TX, USA, 1–5 June.

Holmes, J.D., Denoon, R.O., Kwok, K.C.S. and Glanville, M.J. (1997) Wind loading and response of large stadium roofs. *International Symposium on Shell and Spatial Structures*, Singapore, 10–14 November.

Irminger, J.O.V. (1894) Nogle forsog over trykforholdene paa planer og legemer paavirkede af luftstrominger. *Ingenioren*, 17.

Irwin, P.A. (1988) Pressure model techniques for cladding wind loads. *Journal of Wind engineering & Industrial Aerodynamics*, 29:69–78.

Irwin, H.P.A.H., Cooper, K.R. and Girard, R. (1979) Correction of distortion effects caused by tubing systems in measurements of fluctuating pressures. *Journal of Industrial Aerodynamics*, 5:93–107.

Isyumov, N., Holmes, J.D., Surry, D. and Davenport, A.G. (1975) A study of wind effects for the First National City Corporation Project, New York. Boundary Layer Wind Tunnel Special Study Report, BLWT-SS1–75, University of Western Ontario.

Jensen, M. (1958) The model law for phenomena in the natural wind, *Ingenioren* (International edition), 2:121–8.

Jensen, M. (1965) Model scale tests in the natural wind. (Parts I and II). Danish Technical Press, Copenhagen.

Jischke, M.C. and Light, B.D. (1979) Laboratory simulation of tornadic wind loads on a cylindrical structure. *Proceedings, 5th International Conference on Wind Engineering*, Fort Collins, CO, July 1979, pp. 1049–59, Pergamon Press, New York.

Kareem, A. Cheng, C.-M. and Lu, P.C. (1989) Pressure and force fluctuations on isolated circular cylinders of finite height in boundary layer flows. *Journal of Fluids and Structures*, 3:481–508.

Kernot, W.C. (1893) Wind pressure. *Proceedings, Australasian Society for the Advancement of Science*, V: 573–81.

Larose, G.L. and Franck, N. (1997) Early wind engineering experiments in Denmark. *Journal of Wind Engineering & Industrial Aerodynamics*, 72:493–9.

Lawson, T.V. (1976) The design of cladding. *Building and Environment*, 11:37–8.

Matsumoto, M., Shirato, H. and Hirai, S. (1992) Torsional flutter mechanism of 2-d H-shaped cylinders and effect of flow turbulence. *Journal of Wind Engineering & Industrial Aerodynamics*, 41:687–98.

McKeon, R. and Melbourne, W.H. (1971) Wind-tunnel blockage effects and drag on bluff bodies in rough wall turbulent boundary layers. *Third International Conference on Wind Effects on Buildings and Structures*, Saikon Shuppan Publishers, Tokyo.

Parkinson, G.V. (1984) A tolerant wind tunnel for industrial aerodynamics. *Journal of Wind Engineering & Industrial Aerodynamics*, 16:293–300.

Parkinson, G.V. and Cook, N.J. (1992) Blockage tolerance of a boundary-layer wind tunnel. *Journal of Wind Engineering & Industrial Aerodynamics*, 42:873–84.

Reinhold, T. (ed.) (1982) Wind tunnel modeling for civil engineering applications. *International Workshop on Wind Tunnel Modeling Criteria and Techniques in Civil Engineering Applications*, Gaithersburg, MD, Cambridge University Press, Cambridge.

Scanlan, R.H. (1983) Aeroelastic simulation of bridges. *ASCE Journal of Structural Engineering*, 109:2829–37.

Scanlan, R.H. and Tomko, J.J. (1971) Airfoil and bridge deck flutter derivatives. *ASCE Journal of the Engineering Mechanics Division*, 97:1717–37.

Stathopoulos, T. and Baskaran, B.A. (1996) Computer simulation of wind environmental conditions around buildings. *Engineering Structures*, 18:876–85.

Surry, D. and Isyumov, N. (1975) Model studies of wind effects—a perspective on the problems of experimental technique and instrumentation. *6th International Congress on Aerospace Instrumentation*, Ottawa.

Surry, D. and Stathopoulos, T. (1977) An experimental approach to the economical measurement of spatially-averaged wind loads. *Journal of Industrial Aerodynamics*, 2:385–97.

Tanaka, H. (1990) Similitude and modelling in wind tunnel testing of bridges. *Journal of Wind Engineering & Industrial Aerodynamics*, 33:283–300.

Tschanz, T. and Davenport, A.G. (1983) The base balance technique for the determination of dynamic wind loads. *Journal of Wind Engineering & Industrial Aerodynamics*, 13:429–39.

Vickery, B.J. and Daly, A. (1984) Wind tunnel modelling as a means of predicting the response to vortex shedding. *Engineering Structures*, 6:363–8.

Ward, N.B. (1972) The exploration of certain features of tornado dynamics using a laboratory model. *Journal of Atmospheric Sciences*, 29:1194–204.

Whitbread, R.E. (1963) Model simulation of wind effects on structures. *Proceedings, International Conference on Wind Effects on Buildings and Structures*, Teddington, UK, 26–28 June, pp. 284–302.

Xie, J. and Irwin, P.A. (1998) Application of the force balance technique to a building complex. *Journal of Wind Engineering & Industrial Aerodynamics*, 77/78:579–90.

8
Low-rise buildings

8.1 Introduction

For the purposes of this chapter, *low-rise buildings* are defined as roofed low-rise structures less than 15 m in height. Large roofs on major structures such as sports stadia, including arched roofs, are discussed in Chapter 10; free-standing roofs and canopies are covered in Chapter 14.

The following factors make the assessment of wind loads for low-rise buildings as difficult as for taller buildings and other larger structures:

- They are usually immersed within the layer of aerodynamic roughness on the earth's surface, where the turbulence intensities are high, and interference and shelter effects are important, but difficult to quantify.
- Roof loadings, with all the variations due to changes in geometry, are of critical importance for low-rise buildings. The highest wind loadings on the surface of a low-rise structure are generally the suctions on the roof, and many structural failures are initiated there.
- Low-rise buildings often have a single internal space, and internal pressures can be very significant, especially when a dominant opening occurs in a windward wall. The magnitude of internal pressure peaks, and their correlation with peaks in external pressure, must be assessed.

However, resonant dynamic effects can normally be neglected for smaller buildings. The majority of structural damage in wind storms is incurred by low-rise buildings, especially family dwellings, which are often non-engineered and lacking in maintenance.

The following sections will discuss the history of research on wind loads on low-rise buildings, the general characteristics of wind pressures and model scaling criteria and a summary of the results of the many studies that were carried out in the 1970s, 1980s and 1990s.

Several comprehensive reviews of wind loads on low-rise buildings have been made by Holmes (1983), Stathopoulos (1984, 1995), Krishna (1995) and Surry (1999).

8.2 Historical

8.2.1 Early wind-tunnel studies

Some of the earliest applications of wind tunnels were in the study of wind pressures on low-rise buildings. The two earliest investigations were by Irminger (1894) in Copenhagen, Denmark, and Kernot (1893) in Melbourne, Australia. Irminger used a

small tunnel driven by the suction of a factory chimney and measured pressures on a variety of models, including one of a house. He demonstrated the importance of roof suction, a poorly understood concept at the time. Kernot used what would now be called an open-jet wind tunnel (see Section 7.2.1), as well as a whirling arm apparatus, and measured forces on a variety of building shapes. The effects of roof pitch, parapets and adjacent buildings were all examined.

Over the following 30 years, isolated studies were carried out in aeronautical wind tunnels at the National Physical Laboratory (NPL) in the United Kingdom, the DLR laboratories at Göttingen, Germany, the National Bureau of Standards in the United States and the Central Aero-Hydrodynamical Institute of the USSR. These early measurements showed some disagreement with each other, although they were all measurements of steady wind pressures in nominally steady flow conditions. This was probably due to small but different levels of turbulence in the various wind tunnels (Chapter 4 discusses the effect of turbulence on the mean flow and pressures on bluff bodies) and other effects such as blockage.

In Denmark, Irminger, with Nokkentved (1930), carried out further wind-tunnel studies on low-rise buildings. These tests were again carried out in steady, uniform flow conditions, but included some innovative work on models with porous walls and the measurement of internal as well as external pressures. Similar but less extensive measurements were carried out by Richardson and Miller (1932) in Australia.

In 1936, the American Society of Civil Engineers (1936) surveyed the data available at that time on wind loads on steel buildings. This survey included consideration of ‘rounded and sloping roofs’. These data consisted of a variety of early wind-tunnel measurements presumably carried out in smooth flow.

Flachsbart, at the Göttingen Laboratories in Germany, is well known for his extensive wind-tunnel measurements on lattice frames and bridge trusses, in the 1930s. Less well known, however, is the work he did in comparing wind pressures on a low-rise building in smooth and boundary-layer flow. Unfortunately this work—probably the first boundary-layer wind-tunnel study—was not published at the time; however, it has been rediscovered, and reported, by Simiu and Scanlan (1996).

Recognition of the importance of boundary-layer flow was also made by Bailey and Vincent (1943) at the NPL. In doing so, they were able to make some progress in explaining differences between wind-tunnel and full-scale measurements of pressures, on a low-rise shed.

However, it was not until the 1950s that Jensen (1958), at the Technical University of Denmark, satisfactorily explained the differences between full-scale and wind-tunnel model measurements of wind pressures. Figure 8.1 reproduces some of his measurements, which fully established the importance of using a turbulent boundary-layer flow to obtain pressure coefficients in agreement with full-scale values. The non-dimensional ratio of building height to roughness length, h/z_0, was later named the *Jensen number* (see Section 4.4.5), in recognition of this work. Jensen and Franck (1965) later carried out extensive wind-tunnel measurements on a range of building shapes in a small boundary-layer wind tunnel.

The work of Jensen and Franck was the precursor to a series of generic, wind-tunnel studies of wind loads on low-rise buildings in the 1970s and 1980s, including those on

industrial buildings by Davenport *et al.* (1977) and on houses by Holmes (1983, 1994). Results from these studies are discussed in later sections.

Important contributions to the understanding of the effect of large groupings of bluff bodies in turbulent boundary layers, representative of large groups of low-rise buildings,

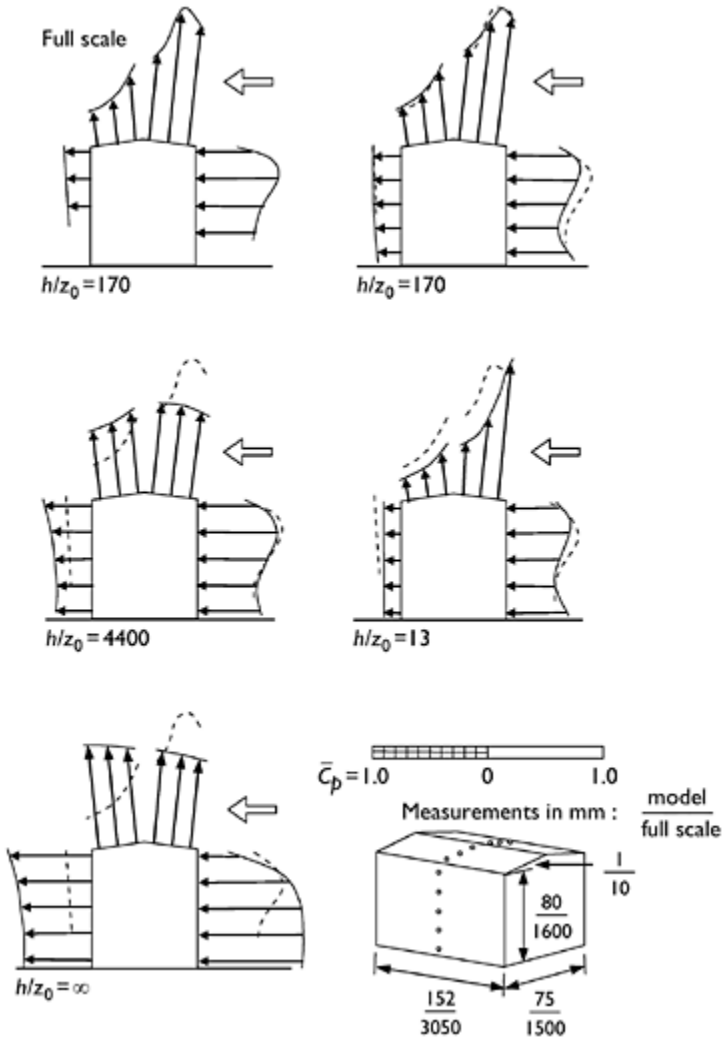

Figure 8.1 Pioneer boundary-layer measurements of Jensen (1958).

were made by Lee and Soliman (1977) and Hussain and Lee (1980). Three types of flow were established, depending on the building spacing: *skimming* flow (close spacing), *wake-interference* flow (medium spacing) and *isolated-roughness* flow (far spacing).

8.2.2 Full-scale studies

The last three decades of the twentieth century were notable for a number of full-scale studies of wind loads on low-rise buildings. In these studies, advantage was taken of the considerable developments that had taken place in electronic instrumentation and computer-based statistical analysis techniques and provided a vast body of data which challenged wind-tunnel modelling techniques.

In the early 1970s, the Building Research Establishment in the United Kingdom commenced a programme of full-scale measurements on a specially constructed

Figure 8.2 Aylesbury Experimental Building (United Kingdom, 1970–75).

experimental building, representative of a two-storey low-rise building at Aylesbury, England. The building had the unique feature of a roof pitch which was adjustable between 5° and 45° (Figure 8.2).

The results obtained in the Aylesbury experiment emphasized the highly fluctuating nature of the wind pressures and the high-pressure peaks in separated flow regions near the roof eaves and ridge, and near the wall corners (Eaton and Mayne, 1975; Eaton *et al.*, 1975). Unfortunately, the experiment was discontinued, and the experimental building dismantled only after 2 years at the Aylesbury site. However, interest of wind-tunnel researchers in the Aylesbury data continued through the 1980s, when an International Aylesbury Comparative Experiment was established. Seventeen wind-tunnel laboratories around the world tested identical 1/100 scale models of the Aylesbury building, using various techniques for modelling the upwind terrain and approaching flow conditions. This unique experiment showed significant differences in the measured pressure coefficients—attributed mainly to different techniques used to obtain the reference static

and dynamic pressures and in modelling the hedges in the upwind terrain at the full-scale site (Sill *et al.*, 1989, 1992).

In the late 1980s, two new full-scale experiments on low-rise buildings were set up in Lubbock, Texas, United States, and Silsoe, United Kingdom. The Lubbock experiment, known as the Texas Tech Field Experiment, comprised a small steel shed of height 4.0 m and plan dimensions 9.1 and 13.7 m; the building had a near-flat roof (Figure 8.3). The building had the unique capability of being mounted on a turntable, thus enabling control of the building orientation relative to the mean wind direction. Pressures were measured with high-response pressure transducers mounted close to the pressure tappings on the roof and walls; the transducers were moved around to different positions at different times during the course of the experiments. A 50 m-high mast upwind of the building, in the prevailing wind direction, had several levels of

Figure 8.3 Texas Tech Field Experiment (United States 1987–).

anemometers, enabling the approaching wind properties to be well defined. The upwind terrain was quite flat and open. The reference static pressure was obtained from an underground box, 23 m away from the centre of the test building (Levitan and Mehta, 1992a, b).

The Texas Tech Experiment produced a large amount of wind pressure data for a variety of wind directions. External and internal pressures, with and without dominant openings in the walls, were recorded. Very high extreme pressures at the windward corner of the roof for ‘quartering’ winds blowing directly on to the corner, at about 45° to the walls, were measured; these were considerably greater than those measured at equivalent positions on small 1/100 scale wind-tunnel models. The internal pressures, however, showed similar characteristics to those measured on wind-tunnel models and predicted by theoretical models.

The Silsoe Structures Building was a larger steel portal-framed structure, 24 m long, 12.9 m span and 4 m to the eaves, with a 10° roof pitch, located in open country. As well as 70 pressure tapping points on the building roof and walls, the building was equipped with 12 strain gauge positions on the central portal frame to enable measurements of structural response to be made (Robertson, 1992).

The building could be fitted with both curved and sharp eaves. The curved eaves were found to give lower mean negative pressures immediately downwind of the windward wall, than those produced by the sharp eaves. Measurements of strain in the portal frame were found to be predicted quite well by a structural analysis computer program when the correct column fixity was applied. Spectral densities of the strains were also measured—these showed the effects of Helmholtz resonance (Section 6.2.3) on the internal pressures, when there was an opening in the end wall of the building. Generally these measurements justified a *quasi-steady* approach to wind loads on low-rise buildings (Section 4.6.2).

8.3 General characteristics of wind loads on low-rise buildings

Full-scale measurements of wind pressures on low-rise buildings, such as those described in Section 8.2.2, show the highly fluctuating nature of wind pressures, area-averaged wind loads and load effects, or responses, on these structures. The fluctuations with time can be attributed to two sources (see also Section 4.6.1):

1. Pressure fluctuations induced by upwind turbulent velocity fluctuations (see Chapter 3). In an urban situation, the turbulence may arise from the wakes of upwind buildings.
2. Unsteady pressures produced by local vortex shedding and other unsteady flow phenomena, in the separated flow regions near sharp corners, roof eaves and ridges (see Chapter 4).

These two phenomena may interact with each other to further complicate the situation.

It should be noted that, as well as a variation with time, as shown for a single point on a building in Figure 8.4, there is a variation with space, i.e. the same pressure or response variation with time may not occur simultaneously at different points separated from each other on a building.

8.3.1 Pressure coefficients

The basic definition of a pressure coefficient for a bluff body was given in Section 4.2.1, and the rms fluctuating (standard deviation) pressure coefficient was defined in Section 4.6.4. A general time-varying pressure coefficient, $C_p(t)$, for buildings in stationary, or synoptic, wind storms is as follows:

$$C_p(t) = \frac{p(t) - p_0}{\frac{1}{2}\rho_a \overline{U}^2} \tag{8.1}$$

where p_0 is a static reference pressure (normally atmospheric pressure measured at a convenient location near the building, but not affected by the flow around the building),

ρ_a is the density of air and $\bar{U}$ is the mean (time-averaged) velocity measured at an appropriate defined reference height. As in the atmospheric boundary layer, there is a

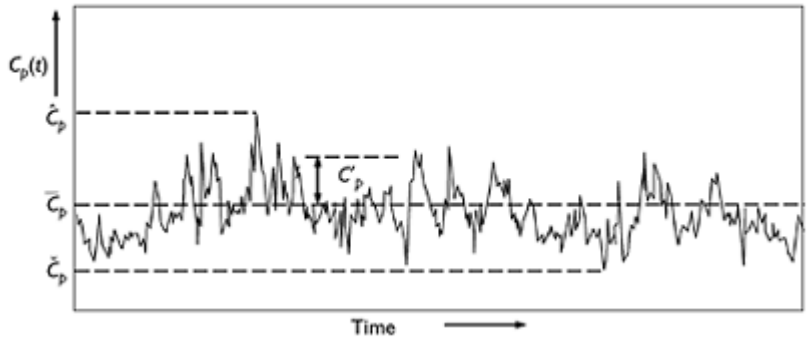

Figure 8.4 Typical variation of wind pressure and definition of pressure coefficients.

variation of mean wind speed with height (Section 3.2). In the case of a low-rise building, this is usually taken to be at roof height, either at eaves level, mid-height of the roof, or at the highest level of the roof; as for the static pressure, this must be away from the direct influence of the building.

Figure 8.4 shows a typical variation of $C_p(t)$ on a low-rise building and four significant values of the pressure coefficient:

1. $\bar{C}_p$—the mean or time-averaged pressure coefficient;
2. $C'_p \left(= \sigma_{C_p}\right)$—the rms fluctuating value, or standard deviation, representing the average departure from the mean;
3. $\hat{C}_p$ (or $C_{\hat{p}}$)—the maximum value of the pressure coefficient in a given time period;
4. C_p (or $C_{\check{p}}$)—the minimum value of the pressure coefficient in a given time period.

8.3.2 Dependence of pressure coefficients

The dependence of pressure coefficients on other non-dimensional quantities such as Reynolds number and Jensen number, in the general context of bluff-body aerodynamics, was discussed in Section 4.2.3. This dependence is applicable to wind loads on low-rise buildings.

For bodies which are sharp-edged and on which points of flow separation are generally fixed, the flow patterns and pressure coefficients are *relatively* insensitive to viscous effects and hence Reynolds number. This means that, provided an adequate reproduction of the turbulent flow characteristics in atmospheric boundary-layer flow is achieved and the model is geometrically correct, wind-tunnel tests can be used to predict pressure and force coefficients on full-scale buildings. However, the full-scale studies from the Texas Tech Field Experiment have indicated that for certain wind directions, pressure peaks in some separated flow regions are not reproduced in wind-tunnel tests with small-scale models, and some Reynolds number dependency is indicated.

As discussed in Section 8.2.1, Martin Jensen identified the Jensen number, h/z_0, the ratio of building height to the aerodynamic roughness length in the logarithmic law (Sections 3.2.1 and 4.4.5), as the most critical parameter in determining mean pressure coefficients on low-rise buildings. The Jensen number clearly directly influences the mean pressure distributions on a building through the effect of the mean velocity profile with height. However, in a fully developed boundary layer over a rough ground surface, the turbulence quantities such as intensities (Section 3.3.1) and spectra (Section 3.3.4) should also scale with the ratio z/z_0 near the ground. There is an indirect influence of the turbulence properties on the mean pressure coefficients (Section 4.4.3), which would have been responsible for some of the differences observed by Jensen (1958), and seen in Figure 8.1. In wind-tunnel tests, the turbulence intensity similarity will be achieved only with h/z_0 equality, if the turbulent inner surface layer in the atmospheric boundary layer has been correctly simulated in the boundary layer in the wind tunnel. Many researchers prefer to treat parameters such as turbulence intensities and ratios of turbulence length scale to building dimension as independent non-dimensional quantities (see Section 4.2.3), but unfortunately it is difficult to independently vary these parameters in wind-tunnel tests.

Fluctuating and peak external pressures on low-rise buildings, which are most relevant to structural design, are highly dependent on the turbulence properties in the approach flow, especially turbulence intensities. Consequently peak load effects, such as bending moments in framing members, are also dependent on the upwind turbulence. For 'correctly' simulated boundary layers, in which turbulence quantities near the ground scale as z/z_0, as discussed previously, peak load effects can be reduced to a variation with Jensen number (e.g. Holmes and Carpenter, 1990).

Finally, the question of the dependency of pressures and load effects on low-rise buildings in wind storms of the downdraft type (Section 1.3.5) arises. As discussed in Section 3.2.6, these winds have boundary layers which are not strongly dependent on the surface roughness of the ground—hence the Jensen number may not be such an important parameter. Further research is required to identify non-dimensional parameters in the downdraft flow which are relevant to wind pressures on buildings in these types of storms.

8.3.3 Flow patterns and mean pressure distributions

Figure 8.5 shows the main features of flow over a building with a low-pitched roof, which has many of the features of flow around a two-dimensional bluff body described in Section 4.1. The flow separates at the top of the windward wall and *re-attaches* at a region further downwind on the roof, forming a separation zone or 'bubble'. However, this bubble exists only as a time average. The separation zone is bounded by a free shear layer, a region of high velocity gradients, and high turbulence. This layer rolls up intermittently to form vortices; as these are shed downwind, they may produce high negative pressure peaks on the roof surface. The effect of turbulence in the approaching flow is to cause the vortices to roll up closer to the leading edge, and a shorter distance to the re-attachment zone results.

The longitudinal intensities of turbulence at typical roof heights of low-rise buildings are 20% or greater, and separation zone lengths are shorter, compared to those in smooth,

or low turbulence, flow. Small separation zones with high shear layer curvatures are associated with low pressures, i.e. high initial negative pressures, but rapid pressure recovery downwind.

Roof pitches up to about 10°, for wind normal to a ridge or gable end, are *aerodynamically flat*. When the mean wind direction is parallel to a ridge line, the roof is also seen as aerodynamically flat, for any roof pitch. For winds normal to the ridge line and roof

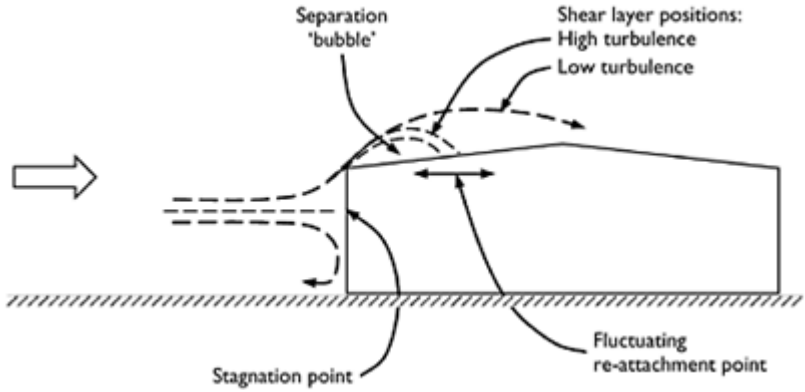

Figure 8.5 Wind flow around a low-rise building.

pitches between 10° and 20°, a second flow separation occurs at the ridge, producing regions of high negative pressures on both sides of the ridge. Downwind of the ridge, a second re-attachment of the flow occurs with an accompanying recovery in pressure. At roof pitches greater than about 20°, positive mean pressures occur on the upwind roof face, and fully separated flows without re-attachment occur downwind of the ridge giving relatively uniform negative mean pressures on the downwind roof slope.

It should be noted that the above comments are applicable only to low-rise buildings with height/downwind depth *(h/d)* ratios less than about 0.5. As this ratio increases, roof pressures generally become more negative. This influence can be seen in Figure 8.6, which shows the mean pressure distribution along the centreline of low-rise buildings for various roof pitches and *h/d* ratios; the horizontal dimension across the wind (into the paper in Figure 8.6) is about twice the along-wind dimension. For higher buildings with *h/d* ratios of 3 or greater, the roof pressure will be negative on both faces, even for roof slopes greater than 20°.

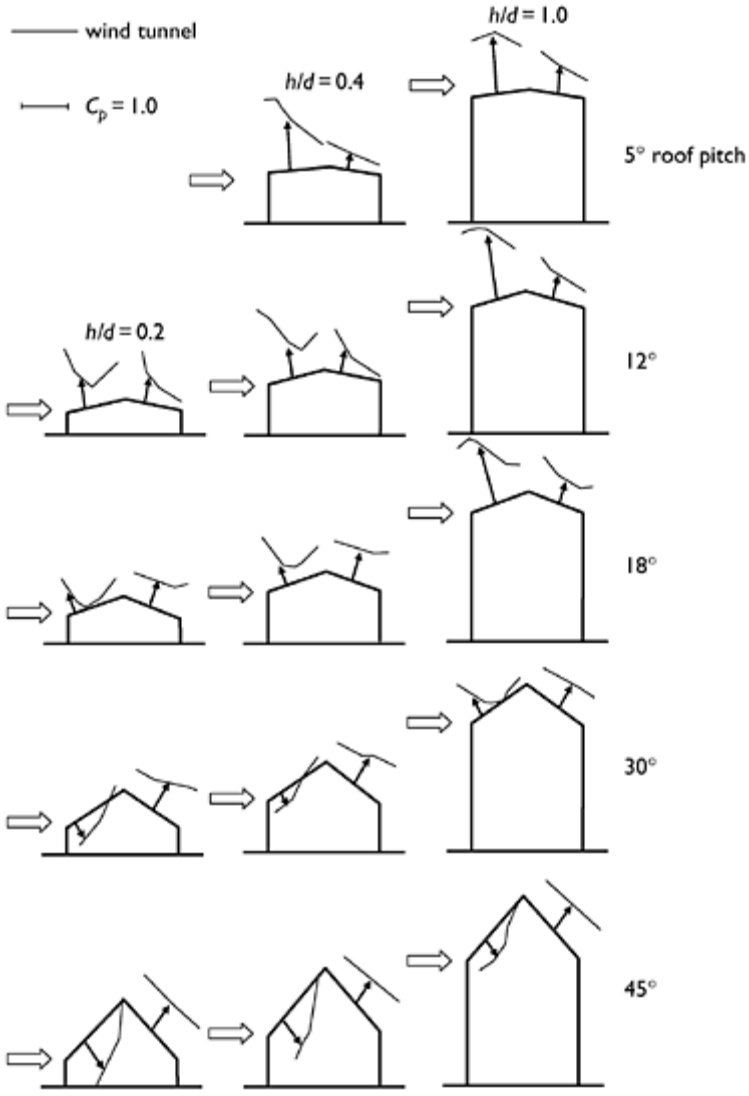

Figure 8.6 Mean pressure distributions on pitched roofs.

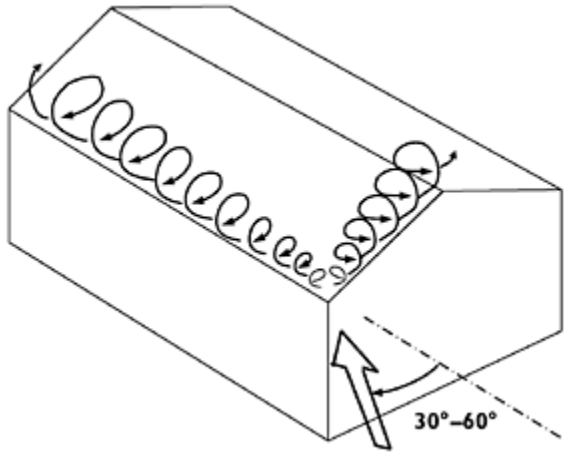

Figure 8.7 Conical vortices for oblique wind directions.

Similar flow separation and re-attachment, as described for roofs, occur on the side walls of low-rise buildings, although the magnitude of the mean pressure coefficients is generally lower. The mean pressures on windward walls are positive with respect to the free-stream static pressure. Leeward walls are influenced by the recirculating wake and generally experience negative pressures of lower magnitude; however, the values depend on the building dimensions, including the roof pitch angle.

When the wind blows obliquely on to the corner of a roof, a more complex flow pattern emerges as shown in Figure 8.7. *Conical* vortices similar to those found on delta-wings of aircraft occur. Figure 8.8 shows these vortices visualized by smoke—their axes are inclined slightly to the adjacent walls forming the corner. The pressures underneath these are the largest to occur on the low-pitched roofs, square or rectangular in planform, although the areas over which they act are usually quite small, and are more significant for pressures on small areas of cladding than for the loads in major structural members.

In the following sections, the effects of building geometries on design loads will be discussed in more detail.

8.3.4 Fluctuating pressures

The root-mean-squared fluctuating, or standard deviation, pressure coefficient, defined in Sections 4.6.4 and 8.3.1, is a measure of the general level of pressure fluctuations at a point on a building. As discussed in Section 8.3.2, the values obtained on a particular building are generally dependent on the turbulence intensities in the approaching flow, which in turn are dependent on the Jensen number. In boundary-layer winds over open country terrain, for which longitudinal turbulence intensities are typically around 20%, at heights typical of eaves heights on low-rise buildings, the values of rms pressure coefficients (based on a dynamic pressure calculated from the mean wind speed at eaves height) on windward walls are typically in the range of 0.3–0.4. In separated-reattaching

flow regions on side walls, values of C_p of 0.6 or greater can occur. Even higher values can occur at critical points on roofs, with values greater than 1.0 being not uncommon.

Figure 8.8 Corner vortices generated by quartering winds (from the Texas Tech Field Experiment).

High instantaneous peak pressures tend to occur at the same locations as high rms fluctuating pressures. The highest negative peak pressures are associated with the conical vortices generated at the roof corners of low-pitch buildings, for quartering winds blowing on to the corner in question (Figures 8.7 and 8.8). Figure 8.9 shows a short sample of pressure-time history, from a pressure measurement position near the formation point of one of these vortices, on the Texas Tech building (Mehta *et al.*, 1992). This shows that high pressure peaks occur as 'spikes' over very short time periods. Values of negative peak pressure coefficients as high as −10 often occur, and magnitudes of −20 have occasionally been measured.

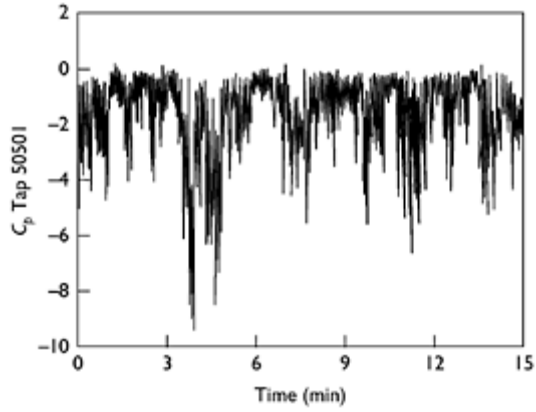

Figure 8.9 Pressure coefficient versus time from a corner pressure tap (Texas Tech Field Experiment).

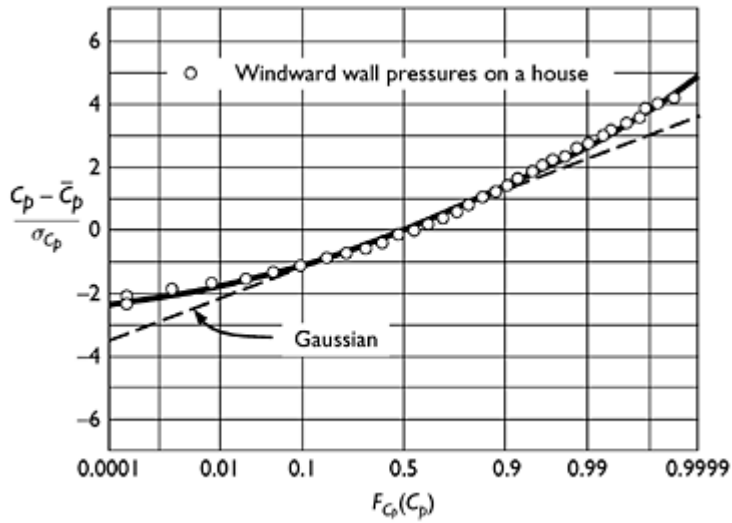

Figure 8.10 Cumulative probability distribution for pressure fluctuations on the windward wall of a house.

The probability density function (pdf) and cumulative distribution function (cdf) are measures of the amplitude variations in pressure fluctuations at a point. Even though the upwind velocity fluctuations in boundary-layer winds are nearly Gaussian (Sections 3.3.2 and C3.1), this is not the case for pressure fluctuations on buildings. Figure 8.10 shows a wind-tunnel measurement of the cdf for pressure fluctuations on the windward wall of a low-rise building model (Holmes, 1981, 1983). On this graph, a straight line indicates a

Gaussian distribution. Clearly the measurements showed upward curvature, or positive skewness (Figure C3). This can, in part, be explained by the square-law relationship between pressure and velocity (see Equation (4.12); Holmes, 1981 and Section C3.3). Negative skewness occurs for pressure fluctuations in separated flow regions of a building.

The spatial structure of fluctuating pressures on low-rise buildings has been investigated in detail by a number of researchers, using a technique known as *Proper Orthogonal Decomposition* (e.g. Best and Holmes, 1983; Holmes, 1990a; Bienkiewicz *et al.*, 1993; Letchford and Mehta, 1993; Ho *et al.*, 1995; Holmes *et al.*, 1997; Baker, 1999). The mathematics of this technique is beyond the scope of this book, but the method allows the complexity of the space-time structure of the pressure fluctuations on a complete roof, building or tributary area to be simplified into a series of 'modes', each with its own spatial form. Surprisingly few of these modes are required to describe the complexity of the variations. Invariably, for low-rise buildings, the first, and strongest, mode is 'driven' by the quasi-steady mechanism associated with upwind turbulence fluctuations.

8.4 Buildings with pitched roofs

8.4.1 Cladding loads

Figures 8.11 and 8.12 show contours of the worst minimum pressure coefficients, for any wind direction, measured in wind-tunnel tests on models of single storey houses with gable roofs of various pitches (Holmes, 1994). The simulated approach terrain in the

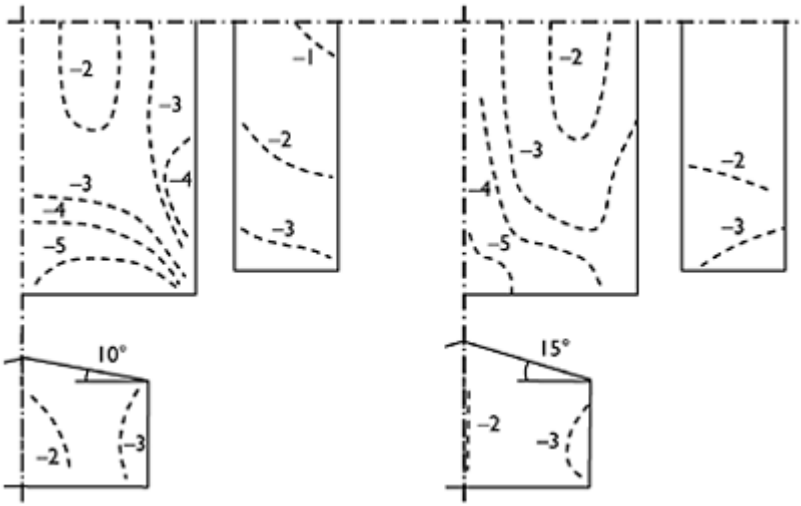

Figure 8.11 Largest minimum pressure coefficients, $\hat{C}_{p-}$ for houses with roofs of 10° and 15° pitch (for any wind direction).

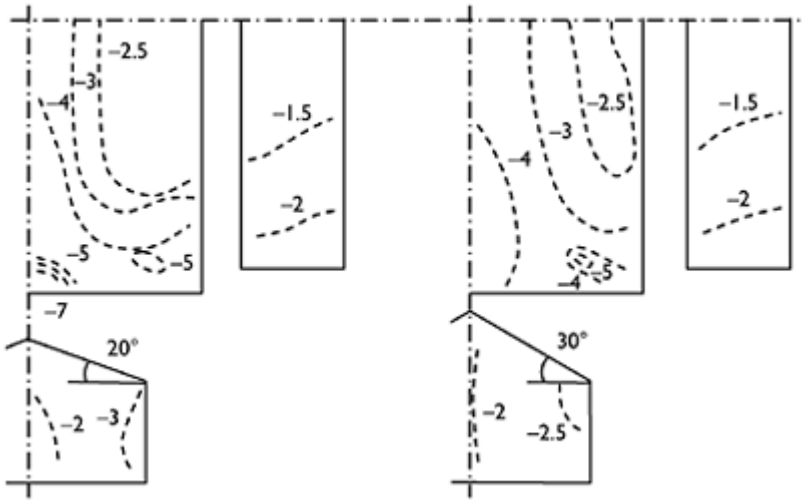

Figure 8.12 Largest minimum pressure coefficients, $\breve{C}_{p'}$ for houses with roofs of 20° and 30° pitch (for any wind direction).

approach boundary-layer flow was representative of open country, and the wind direction was varied at 10° intervals during the tests. The coefficients are all defined with respect to the *eaves* height mean wind speed.

The highest magnitude coefficients occur on the roof. At the lowest pitch (10°), the contours of highest negative pressures converge towards the corner of the roof; the effect of increasing the roof pitch is to emphasize the gable end as the worst loaded region. The worst local negative peak pressures occur on the 20° pitch roof in this area. The highest magnitude minima on the walls occur near the corner.

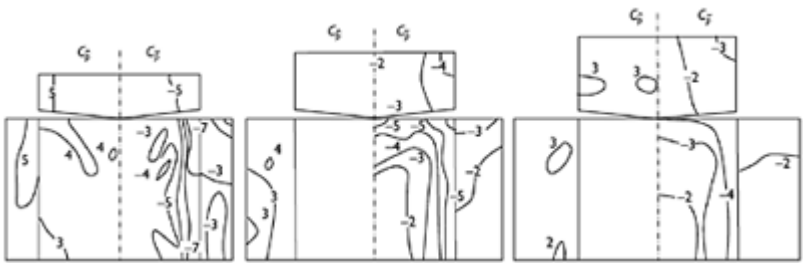

Figure 8.13 Largest maximum and minimum pressure coefficients, $\hat{C}_p$ and $\breve{C}_{p'}$ for industrial buildings with roofs of 5° pitch (for any wind direction) (Davenport *et al.*, 1977).

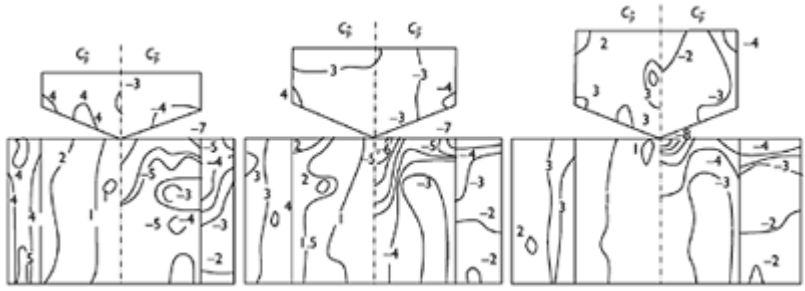

Figure 8.14 Largest maximum and minimum pressure coefficients, $\hat{C}_p$ and $\check{C}_p$, for industrial buildings with roofs of 18° pitch (for any wind direction) (Davenport *et al.*, 1977).

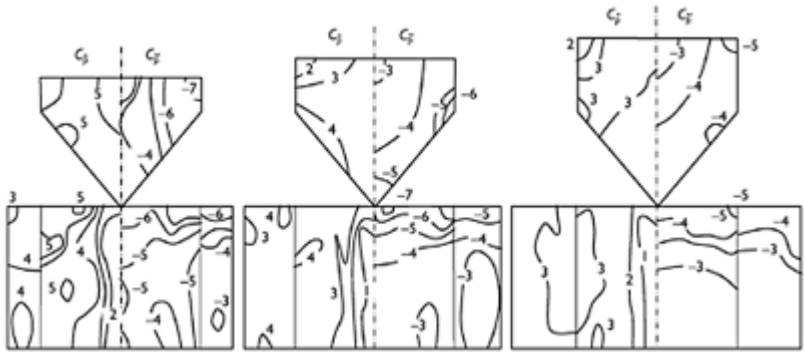

Figure 8.15 Largest maximum and minimum pressure coefficients, $\hat{C}_p$ and $\check{C}_p$, for industrial buildings with roofs of 45° pitch (for any wind direction) (Davenport *et al.*, 1977).

Similar plots for shapes representative of industrial buildings with roof pitches of 5°, 18° and 45° are shown in Figures 8.13–8.15, respectively (Davenport *et al.*, 1977). In these figures, contours of maximum pressure coefficients, as well as minimum pressure coefficients, are plotted. Plots are given for three different eaves heights, for each roof pitch. Results from building models located in simulated urban terrain are shown.

For any given roof pitch, there is no large variation in the magnitudes of the minimum and maximum pressure coefficients with eaves height—however, the pressure coefficients are defined with respect to the mean dynamic pressure at eaves height in each case. As the mean velocity, and hence the dynamic pressure, in a boundary layer increases with increasing height, the pressures themselves will generally increase with the height of the building. As the fluctuating pressure coefficients are closely related to the turbulence intensities in the approach flow, lower magnitudes might be expected at greater eaves heights where the turbulence intensities are lower, and this can be seen in

Figures 8.13– 8.15. However, the local pressure peaks are also influenced by local flow separations, and hence by the relative building dimensions.

The worst minimum pressure coefficients for the 18° pitch roofs (Figure 8.14) occur near the ridge at the gable end (compare also the house with the 20° pitch roof in Figure 8.12). For the 5° pitch case (Figure 8.13), there is a more even distribution of the largest minimum (negative) pressure coefficients around the edge of the roof. For the 45° pitch, the corner regions of the roof generally experience the largest minima; the maximum pressure coefficients are also significant in magnitude on the 45° pitch roof.

Plots such as those in Figures 8.11–8.15 can be used as a guide to the specification of wind loads for the design of cladding. However, it should be noted that if the design wind speeds are non-uniform with direction, as they normally will be, the contours of maximum and minimum *pressures* (as opposed to pressure coefficients) will be different and will depend on the site and the building orientation.

8.4.2 Structural loads and equivalent static load distributions

The effective peak wind loads acting on a major structural element such as the portal frame of a low-rise building are dependent on two factors:

1. The correlation or statistical relationship between the fluctuating pressures on different parts of the tributary surface area ‘seen’ by the frame; this can be regarded as an area-averaging effect.
2. The influence coefficients which relate pressures at points or panels on the surface to particular load effects, such as bending moments or reactions.

Chapter 5 described methods for determining effective static loading distributions, which represent the wind loads that are equivalent in their structural effect to fluctuating (background) wind pressures and to the resonant (inertial) loads when they are significant. For the low-rise buildings under discussion in this chapter, resonant effects can be ignored, but the fluctuating, or background, loading is quite significant because of the high turbulence intensities near the ground. Some examples of the application of the methods discussed in Chapter 5 will be given in this chapter.

To illustrate the problem, consider Figure 8.16. This shows instantaneous external pressure distributions occurring at three different times during a wind storm around a portal frame supporting a low-rise building. These pressure distributions are clearly

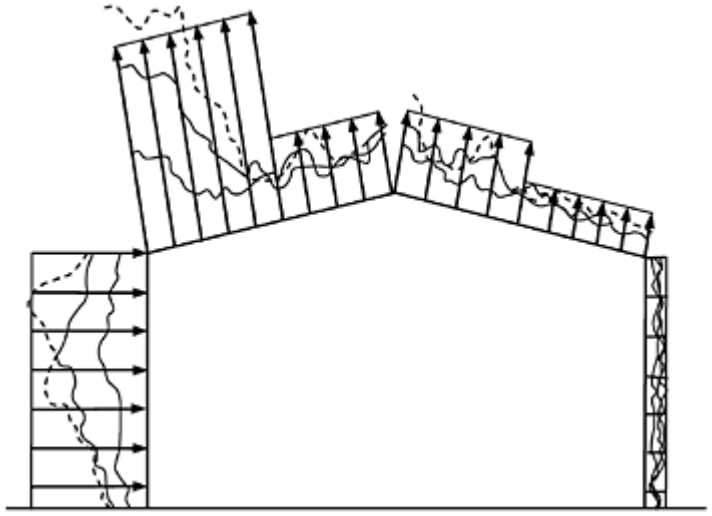

Figure 8.16 Instantaneous external pressure distributions on the frame of a low-rise building and simplified code distributions (Holmes and Syme, 1994).

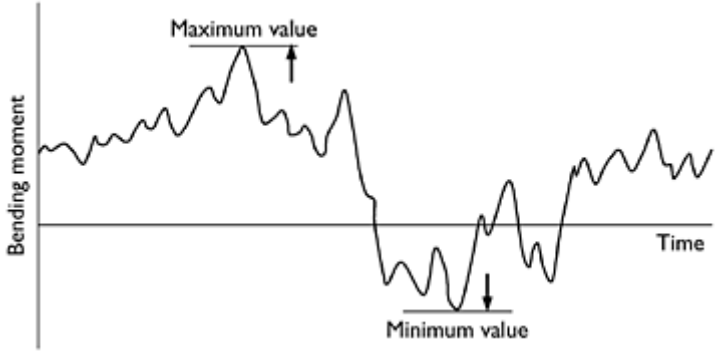

Figure 8.17 Time history of a bending moment (Holmes and Syme, 1994).

different from each other in both shape and magnitude. The value of a load effect such as the bending moment at the knee of the frame will respond to these pressures in a way that might produce the time history of bending moment versus time given in Figure 8.17. Over a given time period, a maximum bending moment will occur. A minimum bending moment will also occur. Depending on the sign of the bending moment produced by the dead loads acting on the structure, one of these extremes will be the critical one for the design of the structure. Methods for the determination of the *expected* pressure distribution which correspond to the maximum or minimum wind-induced bending

moment were discussed in Chapter 5. The effective static pressure distribution so determined must lie between the extreme point pressure limits of the pressures around the frame, as shown in Figure 8.18.

It is of interest to consider the distributions of pressure coefficients given in wind codes and standards. Usually an 'envelope' loading is specified with pressures uniformly distributed in length along the columns and rafters, as shown in Figure 8.16. These are

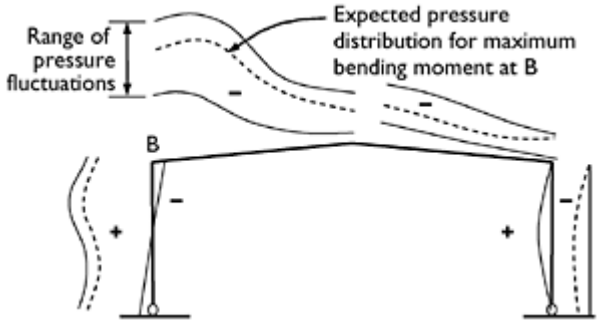

Figure 8.18 Peak load distribution for a corner bending moment (Holmes and Syme, 1994).

usually, but not always, conservative loadings which will give overestimates of load effects such as bending moments.

8.4.3 Hipped roof buildings

It has been observed that, on several occasions in damage investigations following severe wind storms, hipped roof buildings have generally suffered lesser damage. Meecham *et al.* (1991) studied wind pressures on hipped and gable roof buildings of 18.4° pitch in a boundary-layer wind tunnel. Although there is little difference in the largest peak total lift force, or overturning moment, on the two roofs, the gable end region of the gable roof experiences around 50% greater peak negative local pressures, than does the corresponding region on the hipped roof. Furthermore the largest area-averaged full-span truss load was about twice as high on the gable roof.

However, Xu and Reardon (1998), who studied pressures on hipped roofs with three different roof pitches (15°, 20° and 30°), found that the benefits of a hipped configuration compared with a gable roof type reduces as the roof pitch increases. Figure 8.19 shows

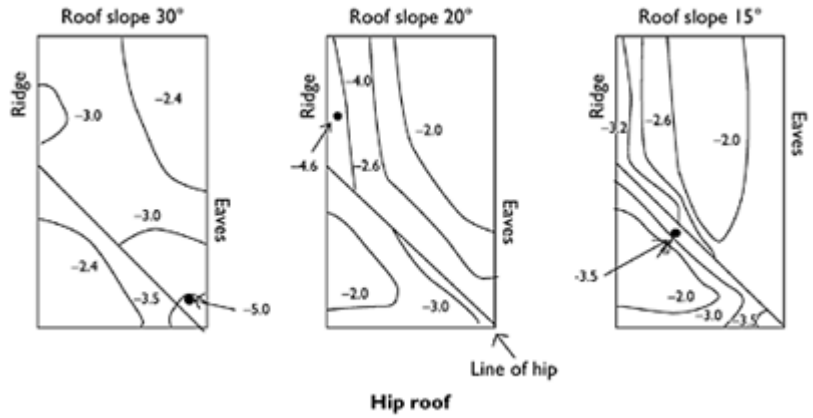

Figure 8.19 Largest minimum pressure coefficients for hipped roofs of 15°, 20° and 30° pitch, for any wind direction (Xu and Reardon, 1998). Reprinted with permission from Elsevier.

contours of worst minimum (negative) peak pressure coefficients, referenced to mean dynamic pressure at eaves height, and can be compared with the equivalent gable roof values in Figures 8.11 and 8.12. Note that, at 30° pitch, the worst negative pressure coefficients of about −5.0 are similar for the two roof types.

8.4.4 Effect of surrounding buildings—shelter and interference

Most low-rise buildings are in an urban situation and are often surrounded by buildings of similar size. The shelter and aerodynamic interference effect of upstream buildings can be very significant on the wind loads. This aspect was the motivation for the studies by Lee and Soliman (1977) and Hussain and Lee (1980) on grouped buildings, as discussed in Section 8.2.1. Three flow regimes were identified based on the building spacing. The study on tropical houses, described by Holmes (1994), included a large number of grouped building situations for buildings with roofs of 10° pitch. This study showed that upstream buildings of the same height reduced the wall pressures and the pressures at the leading edge of the roof significantly, but had less effect on pressures on other parts of the roof. The building height/spacing ratio was the major parameter, with the number of shielding rows being of lesser importance.

A series of wind-tunnel pressure measurements, for both structural loads and local cladding loads, on a flat-roofed building, situated in a variety of ‘random city’ environments was carried out by Ho *et al.* (1990, 1991). It was found that the mean component of the wind loads decreased and the fluctuating component increased, resulting in a less distinct variation in peak wind load with direction. The expected peak loads in the urban environment were much lower than those on the isolated building. It was also found that a high coefficient of variation (60–80%) of wind loads occurred on the building in the urban environment due to the variation in the *location* of the building.

For the isolated building, similar coefficients of variation occurred, but in this case, they resulted from variation due to *wind direction.*

8.5 Multi-span buildings

The arrangement of industrial low-rise buildings as a series of connected spans is common practice for reasons of structural efficiency, lighting and ventilation. Such configurations also allow for expansion in stages of a factory or warehouse.

Wind-tunnel studies of wind pressures on multi-span buildings of the 'saw-tooth' type with 20° pitch were reported by Holmes (1990b), and by Saathoff and Stathopoulos (1992) on 15° pitch buildings of this type. Multi-span gable roof buildings were studied by Holmes (1990b) (5° pitch), and by Stathopoulos and Saathoff (1994) (18° and 45° pitch). The main interest in these studies was to determine the difference in wind loads for multi-span buildings, and the corresponding single-span monoslope and gable roof buildings, respectively.

As for single-span buildings, the aerodynamic behaviour of multi-span buildings is quite dependent on the roof pitch. Multi-span buildings of low pitch (say less than 10°) are aerodynamically flat, as discussed in Section 8.3.3. Consequently, quite low mean and fluctuating pressures are obtained on the downwind spans, as illustrated in Figure 8.20. The pressures on the first windward span are generally similar to those on a single-span building of the same geometry.

For the gable roof buildings and for the saw-tooth roof with the roofs sloping downwards away from the wind, the downwind spans experience much lower magnitude negative mean pressures than the windward spans. For the opposite wind direction on the saw-tooth configuration, the highest magnitude mean pressure coefficients occur on the second span downwind, due to the separation bubble formed in the valley.

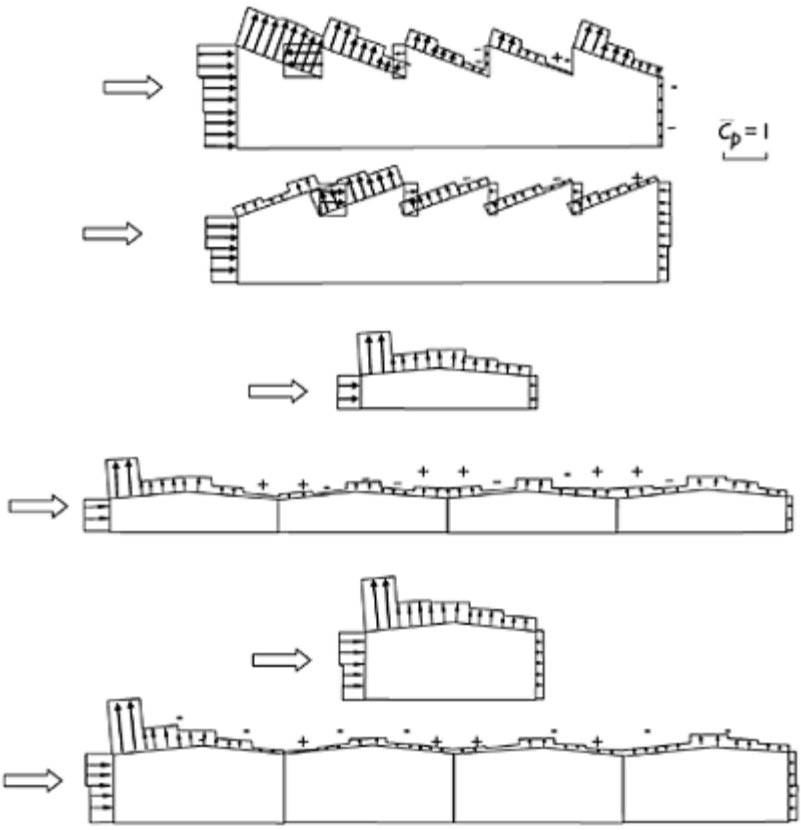

Figure 8.20 Mean pressure distributions on multi-span buildings and comparison with a single span (Holmes, 1990b).

8.6 Effects of parapets on low-rise buildings

A detailed wind-tunnel study of the wind effects of parapets on the roofs of low-rise buildings was carried out by Kopp *et al.* (2005a, b). Earlier work was reviewed by Stathopoulos and Baskaran (1988).

It was found that tall parapets, ($h_p/(h+h_p)>0.2$), where h_p is the parapet height, can reduce peak local negative pressures by up to 50% in corner regions of a roof, when they are installed around the complete perimeter of a roof. Lower parapets, ($h_p/(h+h_p)<0.2$), increase the worst negative peak pressure coefficients, apparently by stabilizing the corner conical vortices that occur on flat or near-flat roofs (see Figure 8.8). However, high parapets increase the positive (downwards) pressure peaks on the roof upwind of leeward parapets.

Isolated parapets, i.e. those installed adjacent to one wall of a building, always increase the corner roof loads, irrespective of their height (Kopp *et al.,* 2005a).

Structural loads on roofs are affected somewhat differently than local loads. For a wind direction normal to a wall, a parapet will move the point of re-attachment (see Figure 8.5) further downwind, thus giving a larger region of separated flow. This increases the structural loads, presumably because of the increased correlations of roof pressures in the separated flow region. The loading on interior bays was increased by about 10% for low parapets, ($h_p/(h+h_p)<0.09$), with greater increases for higher parapets (Kopp *et al.,* 2005b).

8.7 Effect of building length

In codes and standards for wind loading, the effect of the horizontal aspect ratio *(b/d)* on the specified wind pressure coefficients for low-rise buildings is normally neglected. Coefficients are typically based on data obtained from wind-tunnel tests with *b/d* ratios of about 2. However, several studies have shown that horizontal aspect ratio (or building length) is a significant parameter when it becomes large, and particularly for long gable-roofed buildings with very high roof pitches. Such buildings are often used for bulk storage of solids, such as mineral ore or sugar.

The windward ends of these buildings can experience very high loads for oblique wind directions. Very high negative pressures have been observed on the leeward roof surfaces in these situations. The flow and resulting pressures are, in fact, similar to those occurring at the ends of free-standing walls for oblique wind directions (see Section 14.2.1 and Figure 14.3).

A wind-tunnel study of buildings with a 35° pitch (Ginger and Holmes, 2003) showed that some major codes and standards underestimated load effects such as frame bending moments by up to 70%, for a building with a *b/d* ratio of 6. The Australian Standard of 1989 (Standards Australia, 1989) underestimated some bending moments for this case by 50%, but revisions included in the 2002 edition (Standards Australia, 2002) have resulted in much better agreement (Ginger and Holmes, 2003).

8.8 Internal pressures

In Chapter 6, the prediction of internal pressures in buildings in general are discussed. For low-rise buildings in particular, the internal pressure loading may form a high proportion of the total wind loading for both major structural elements and cladding. In severe wind storms, such as hurricanes or typhoons, failures of roofs often occur following window failure on the windward wall, which generates high positive internal pressures acting together with negative external pressures.

8.9 Summary

This chapter has discussed various aspects of the design of low buildings for wind loads. The long history of investigation into wind loads has been discussed, and the use of the modern boundary-layer wind tunnel for determination of design loading coefficients is covered. The characteristics of loads for major structural members and foundations and for local cladding have been considered for buildings with flat and pitched roofs. The effect of shelter and interference from surrounding buildings has been considered. Multi-span building configurations and parapets have also been discussed.

References

American Society of Civil Engineers (1936) Wind-bracing in steel buildings. Fifth Progress Report of Sub-Committee No. 31. *Proceedings ASCE,* March, pp. 397–412.

Bailey, A. and Vincent, N.D.G. (1943) Wind pressure on buildings including the effects of adjacent buildings. *Journal of the Institution of Civil Engineers,* 2:243–75.

Baker, C.J. (1999) Aspects of the use of the technique of orthogonal decomposition of surface pressure fields. *10th International Conference on Wind Engineering,* Copenhagen, 21–24 June, pp. 393–400, Balkema, Rotterdam.

Best, R.J. and Holmes, J.D. (1983) Use of eigenvalues in the covariance integration method for determination of wind load effects. *Journal of Wind Engineering & Industrial Aerodynamics,* 13:359–70.

Bienkiewicz, B., Ham, H.J. and Sun, Y. (1993) Proper orthogonal decomposition of roof pressure. *Journal of Wind Engineering & Industrial Aerodynamics,* 50: 193–202.

Davenport, A.G., Surry, D. and Stathopoulos, T. (1977) Wind loads on low-rise buildings. Final report of Phases I and II. Boundary Layer Wind Tunnel Report, BLWT-SS8–1977, University of Western Ontario.

Eaton, K.J. and Mayne, J.R. (1975) The measurement of wind pressures on two-storey houses at Aylesbury. *Journal of Industrial Aerodynamics,* 1:67–109.

Eaton, K.J., Mayne, J.R. and Cook, N.J. (1975) Wind loads on low-rise buildings—effects of roof geometry. *Fourth International Conference on Wind Effects on Buildings and Structures,* London, September.

Ginger, J.D. and Holmes, J.D. (2003) Effect of building length on wind loads on low-rise buildings with a steep roof pitch. *Journal of Wind Engineering & Industrial Aerodynamics,* 91:1377–400.

Ho, T.C.E., Surry, D. and Davenport, A.G. (1990) The variability of low building wind loads due to surrounding obstructions. *Journal of Wind Engineering & Industrial Aerodynamics,* 36:161–70.

Ho, T.C.E., Surry, D. and Davenport, A.G. (1991) Variability of low building wind loads due to surroundings. *Journal of Wind Engineering & Industrial Aerodynamics,* 38: 297–310.

Ho, T.C.E., Davenport, A.G. and Surry, D. (1995) Characteristic pressure distribution shapes and load repetitions for the wind loading of low building roof panels. *Journal of Wind Engineering & Industrial Aerodynamics,* 57:261–79.

Holmes, J.D. (1981) Non-Gaussian characteristics of wind pressure fluctuations. *Journal of Wind Engineering & Industrial Aerodynamics,* 7:103–8.

Holmes, J.D. (1983) Wind loads on low rise buildings—a review. CSIRO, Division of Building Research, Australia.

Holmes, J.D. (1990a) Analysis and synthesis of pressure fluctuations on bluff bodies using eigenvectors. *Journal of Wind Engineering & Industrial Aerodynamics,* 33:219–30.

Holmes, J.D. (1990b) Wind loading of multi-span buildings. *Civil Engineering Transactions, Institution of Engineers, Australia,* CE32:93–8.

Holmes, J.D. (1994) Wind pressures on tropical housing. *Journal of Wind Engineering & Industrial Aerodynamics,* 53:105–23.

Holmes, J.D. and Carpenter, P. (1990) The effect of Jensen number variations on the wind loads on a low-rise building. *Journal of Wind Engineering & Industrial Aerodynamics,* 36: 1279–88.

Holmes, J.D. and Syme, M.J. (1994) Wind loads on steel-framed low-rise buildings. *Steel Construction (Australian Institute of Steel Construction),* 28:2–12.

Holmes, J.D., Sankaran, R., Kwok, K.C.S. and Syme, M.J. (1997) Eigenvector modes of fluctuating pressures on low-rise building models. *Journal of Wind Engineering & Industrial Aerodynamics,* 69–71:697–707.

Hussain, M. and Lee, B.E. (1980) A wind tunnel study of the mean pressures acting on large groups of low-rise buildings. *Journal of Wind Engineering & Industrial Aerodynamics,* 6: 207–25.

Irminger, J.O.V. (1894) Nogle forsog over trykforholdene paa planer og legemer paavirkede af luftstrominger. *Ingenioren,* 17.

Irminger, J.O.V. and Nokkentved, C. (1930) Wind pressures on buildings. *Ingeniorvidenskabelige Skrifter,* A23.

Jensen, M. (1958) The model law for phenomena in the natural wind. *Ingenioren,* 2:121–8.

Jensen, M. and Franck, N. (1965) *Model-Scale Tests in Turbulent Wind. Part II.* Danish Technical Press, Copenhagen.

Kernot, W.C. (1893) Wind pressure. *Proceedings, Australasian Association for the Advancement of Science,* V, pp. 573–81 and VI, pp. 741–5.

Kopp, G.A., Surry, D. and Mans, C. (2005a). Wind effects of parapets on low buildings: part 1. Basic aerodynamics and local loads. *Journal of Wind Engineering & Industrial Aerodynamics,* 93:817–41.

Kopp, G.A., Surry, D. and Mans, C. (2005b) Wind effects of parapets on low buildings: part 2. Structural loads. *Journal of Wind Engineering & Industrial Aerodynamics,* 93:843–55.

Krishna, P. (1995) Wind loads on low rise buildings—a review. *Journal of Wind Engineering & Industrial Aerodynamics,* 55:383–96.

Lee, B.E. and Soliman, B.F. (1977) An investigation of the forces on three-dimensional bluff bodies in rough wall turbulent boundary layers. *Journal of Fluids Engineering,* 99:503–10.

Letchford, C.W. and Mehta, K.C. (1993) The distribution and correlation of fluctuating pressures on the Texas Tech Building. *Journal of Wind Engineering & Industrial Aerodynamics,* 50:225–34.

Levitan, M.L. and Mehta, K.C. (1992a) Texas Tech Field experiments for wind loads. Part I. Building and pressure measuring system. *Journal of Wind Engineering & Industrial Aerodynamics,* 43:1565–76.

Levitan, M.L. and Mehta, K.C. (1992b) Texas Tech Field experiments for wind loads. Part II. Meteorological instrumentation and terrain parameters. *Journal of Wind Engineering & Industrial Aerodynamics,* 43:1577–88.

Meecham, D., Surry, D. and Davenport, A.G. (1991) The magnitude and distribution of wind-induced pressures on hip and gable roofs. *Journal of Wind Engineering & Industrial Aerodynamics,* 38:257–72.

Mehta, K.C., Levitan, M.L., Iverson, R.E. and Macdonald, J.R. (1992) Roof corner pressures measured in the field on a low-rise building. *Journal of Wind Engineering & Industrial Aerodynamics,* 41:181–92.

Richardson, E.B. and Miller, B.H. (1932) The experimental determination of the pressures and distribution of pressures of an airstream on model buildings. *Journal of the Institution of Engineers Australia,* 4:277–82.

Robertson, A.P. (1992) The wind-induced response of a full-scale portal framed building. *Journal of Wind Engineering & Industrial Aerodynamics,* 43:1677–88.

Saathoff, P. and Stathopoulos, T. (1992) Wind loads on buildings with sawtooth roofs. *ASCE Journal of Structural Engineering*, 118:429–46.

Sill, B.L., Cook, N.J. and Blackmore, P.A. (1989) IAWE Aylesbury Comparative Experiment —preliminary results of wind-tunnel comparisons. *Journal of Wind Engineering & Industrial Aerodynamics*, 32:285–302.

Sill, B.L., Cook, N.J. and Fang, C. (1992) The Aylesbury Comparative Experiment—a final report. *Journal of Wind Engineering & Industrial Aerodynamics*, 43:1553–64.

Simiu, E. and Scanlan, R.H. (1996) *Wind Effects on Structures—An Introduction to Wind Engineering*, 3rd Edition. Wiley, New York.

Standards Australia (1989) SAA loading code. Part 2: wind loads. Australian Standard, AS 1170.2–1989, Standards Australia, North Sydney, New South Wales, Australia.

Standards Australia (2002) Structural design actions. Part 2: wind actions. Australian/New Zealand Standard, AS/NZS1170.2:2002, Standards Australia, Sydney, New South Wales, Australia.

Stathopoulos, T. (1984) Wind loads on low-rise buildings: a review of the state of the art. *Engineering Structures*, 6:119–35.

Stathopoulos, T. (1995) Evaluation of wind loads on low buildings—a brief historical review. In: *A State of the Art in Wind Engineering*, ed. P.Krishna, Wiley Eastern, New Delhi.

Stathopoulos, T. and Baskaran, A. (1988) Turbulent wind loading on roofs with parapet configurations. *Canadian Journal of Civil Engineering*, 29:570–8.

Stathopoulos, T. and Saathoff, P. (1994) Codification of wind-pressure coefficients for multispan gable roofs. *ASCE Journal of Structural Engineering*, 120:2495–519.

Surry, D. (1999) Wind loads on low-rise buildings: past, present and future. *10th International Conference on Wind Engineering*, Copenhagen, 21–24 June, pp. 105–14, Balkema, Rotterdam.

Xu, Y.L. and Reardon, G.F. (1998) Variations of wind pressure on hip roofs with roof pitch. *Journal of Wind Engineering & Industrial Aerodynamics*, 73:267–84.

9
Tall buildings

9.1 Introduction

Tall buildings, now approaching 800 m in height, project well into the atmospheric boundary layer, and their upper levels may experience the highest winds of large-scale wind storms, such as tropical cyclones or the winter gales of the temperate regions. Resonant dynamic response in along-wind, cross-wind and torsional modes are a feature of the overall structural loads experienced by these structures. Extreme local cladding pressures may be experienced on their side walls.

The post-World War II generation of high-rise buildings were the stimulus for the development of the boundary-layer wind tunnel, which remains the most important tool for the establishment of design wind loads on major building projects in many countries. In this chapter, the history of investigations into wind loading of tall buildings, the major response mechanisms and phenomena and the available analytical and semi-analytical techniques will be discussed.

9.2 Historical

Tall buildings or ‘skyscrapers’ are amongst the more wind sensitive of structures, and it was inevitable that their response to wind would be of concern to structural engineers, and attract the interest of early experimenters, both in the wind tunnel and in full scale.

The Empire State Building, at 380m, was the tallest building in the world for 40 years and was the subject of three significant studies in the 1930s (Coyle, 1931; Dry den and Hill, 1933; Rathbun, 1940). These studies have been re-appraised in some detail by Davenport (1975).

Coyle (1931) used a portable horizontal pendulum to record the motion of the building. This clearly revealed resonant dynamic response with a period of around 8 s. Rathbun’s (1940) extensive full-scale measurements were described by Davenport as ‘a monumental piece of full-scale experimentation’. Wind pressures on three floors of the building were measured with 30 m anometers and 28 flash cameras. The pressure coefficients showed considerable scatter, but were clearly much lower than those obtained by Dryden and Hill (1933) on a wind-tunnel model in a uniform flow some years earlier. Rathbun also performed deflection measurements on the Empire State Building using a plumb bob extending from the 86th floor to the 6th floor. These results (as re-analysed by Davenport) indicated the significantly different stiffness of the building in the east-west direction in comparison with the north-south direction (Figure 9.1)

In the 1960s and 1970s, a resurgence in the building of skyscrapers occurred —particularly in North America, Japan and Australia. There was great interest in wind loads on

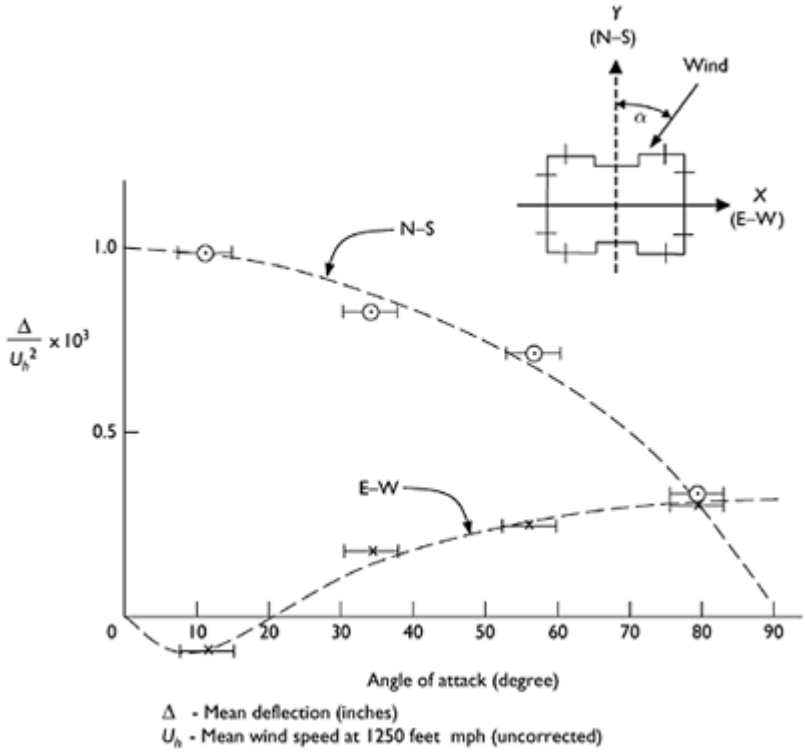

Figure 9.1 Full-scale measurements of mean deflection on the Empire State Building by Rathbun (1940)—re-analysed by Davenport (1975).

tall buildings at this time—this has continued to the end of the twentieth century. The two main problem areas to emerge were

1. the vulnerability of glazed cladding to both direct wind pressures and flying debris in wind storms;
2. serviceability problems arising from excessive motion near the top of tall buildings.

From the early 1970s, many new building proposals were tested in the new boundary-layer wind tunnels (see Chapter 7), and quite a few full-scale monitoring programmes were commenced.

One of the most comprehensive and well-documented full-scale measurement studies, with several aspects to it, which lasted for most of the 1970s, was that on the 239 mtall Commerce Court building in Toronto, Canada (Dalgleish, 1975; Dalgleish *et al.*, 1979,

1983). The full-scale studies were supplemented with wind-tunnel studies, both in the design stage (Davenport *et al.*, 1969) and later on a pressure model (Dalgleish *et al.*, 1979), and a multi-degree-of-freedom aero-elastic model, in parallel with the full-scale studies (Templin and Cooper, 1981; Dalgleish *et al.*, 1983).

The early full-scale pressure measurements on the Commerce Court building showed good agreement with the wind-tunnel study (at 1/400 scale) for mean pressure coefficients, and for the mean base shear and overturning moment coefficients. Not as good agreement with the 1/400-scale wind-tunnel tests was found for the rms fluctuating pressure coefficients for some wind directions (Dalgleish, 1975). The later-reported pressure measurements (Dalgleish *et al.*, 1979) showed better agreement for the fluctuating pressure and peak measurements on a larger (1/200) scale wind-tunnel model, with accurately calibrated tubing and pressure measurement system. The full-scale pressure study on Commerce Court highlighted the importance of short duration peak pressures in separated flow regions (at around this time similar observations were being made from the roof of the low-rise building at Aylesbury—Section 8.2.2). Subsequently, detailed statistical studies of these were carried out for application to glass loading (see Section 9.4.5). Although the Commerce Court pressure measurements were of a high quality, they suffered from the lack of an independent reference pressure for the pressure coefficients—an internal pressure reading from the building was used. For comparison of mean pressure coefficients with the wind-tunnel results, it was necessary to force agreement at one pressure tapping—usually in wake region.

The full-scale study of acceleration response (Dalgleish *et al.*, 1983) showed the following features:

- The significance of the torsional (twisting) motions superimposed on the sway motions for one direction (east–west). This was explained by an eccentricity in the north-south direction between the centre of mass and the elastic axis;
- Generally good agreement between the final aero-elastic model, which included torsional motions, and the full-scale data, for winds from a range of directions;
- Reasonable agreement between the full-scale data and predictions of the National Building Code of Canada for along- and cross-wind accelerations.

The agreements observed occurred despite some uncertainties in the reference velocity measured at the top of the building and in the dynamic properties (frequency and damping) of the building. An interesting observation, not yet clearly explained, but probably an added mass effect, was a clear decrease in observed building frequency as the mean speed increased.

Another important full-scale study, significant for its influence on the development of the British Code of Practice for Wind Loads, was that carried out on the 18-storey Roy ex House in London (Newberry *et al.*, 1967). This study revealed aspects of the transient and fluctuating pressures on the windward and side walls.

The first major boundary-layer wind-tunnel study of a tall building was that carried out for the twin towers of the World Trade Center, New York, in the mid-1960s at Colorado State University. This was the first of many commercial studies, now numbering in thousands, in boundary-layer wind tunnels.

9.3 Flow around tall buildings

Tall buildings are bluff bodies of medium to high aspect ratio and the basic characteristics of flow around this type of body were covered in some detail in Chapter 4.

Figure 9.2 shows the general characteristics of boundary-layer wind flow around a tall building. On the windward face there is a strong downward flow below the stagnation

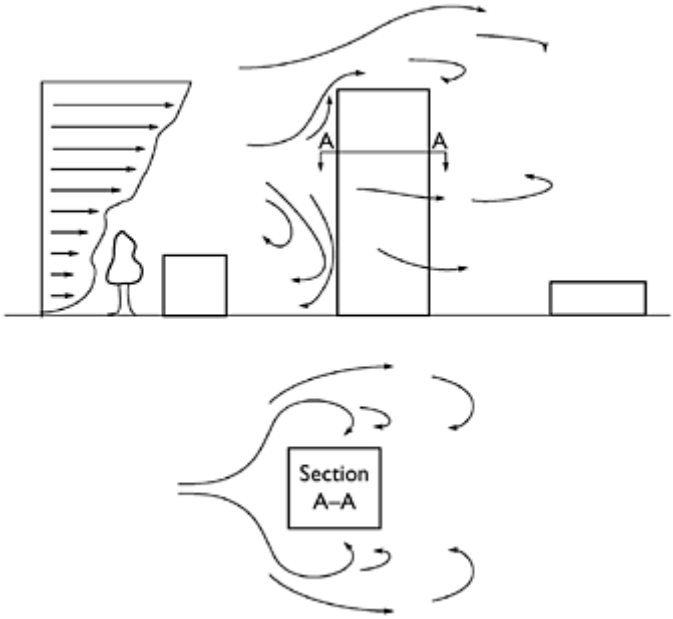

Figure 9.2 Wind flow around a tall building.

point, which occurs at a height of 70–80% of the overall building height. The downward flow can often cause problems at the base, as high velocity air from upper levels is brought down to street level. Separation and re-attachment at the side walls are associated with high local pressures. The rear face is a negative pressure region of lower magnitude mean pressures and a low level of fluctuating pressures.

In a mixed extreme wind climate of thunderstorm downbursts (Section 1.3.5) and synoptic winds, the dominant wind for wind loading of tall buildings will normally be the latter as the downburst profile has a maximum at a height of 50–100 m (Figure 3.3).

9.4 Cladding pressures

9.4.1 Pressure coefficients

As in previous chapters, pressure coefficients in this chapter will be defined with respect to a mean wind speed at the top of the building, denoted by $\bar{U}_h$. Thus, the mean, root-mean-square fluctuating (standard deviation), maximum and minimum pressure coefficients are defined according to Equations (9.1), (9.2), (9.3) and (9.4), respectively:

$$\overline{C}_p = \frac{\overline{p} - p_0}{\frac{1}{2}\rho_a \overline{U}_h^2} \tag{9.1}$$

$$C'_p = \sigma_{C_p} = \frac{\sqrt{\overline{p'^2}}}{\frac{1}{2}\rho_a \overline{U}_h^2} \tag{9.2}$$

$$\hat{C}_p = \frac{\hat{p} - p_0}{\frac{1}{2}\rho_a \overline{U}_h^2} \tag{9.3}$$

$$\check{C}_p = \frac{\check{p} - p_0}{\frac{1}{2}\rho_a \overline{U}_h^2} \tag{9.4}$$

In Equations (9.3) and (9.4), the maximum and minimum pressures, $\hat{p}$ and $\check{p}$, are normally defined as the average or expected peak pressure at a point in a given averaging time, which may be taken as a period between 10 m in and 3 h in full scale. It is not usually convenient, or economic, to measure such average peaks directly in wind-tunnel tests, and various alternative statistical procedures have been proposed. These are discussed in Section 9.4.4.

9.4.2 Pressure distributions on buildings of rectangular cross-section

The local pressures on the wall of a tall building can be used directly for the design of cladding, which is generally supported over small tributary areas.

Figure 4.15 shows the distribution of mean pressure coefficient on the faces of tall prismatic shape, representative of a very tall building, with aspect ratio (height/width) of 8, in a boundary-layer flow.

Figures 9.3, 9.4 and 9.5 show the variation in mean, maximum and minimum pressure coefficients on the windward side and leeward faces for a lower building of square cross-section, with aspect ratio equal to 2.1 (Cheung, 1984). The pressures were measured on a wind-tunnel model which represented a building of 85 m height; the building is isolated, i.e. there is no shielding from buildings of comparable height, and the approaching flow was boundary-layer flow over suburban terrain. The value of Jensen number, h/z_0 (see Section 4.4.5), was then approximately 40.

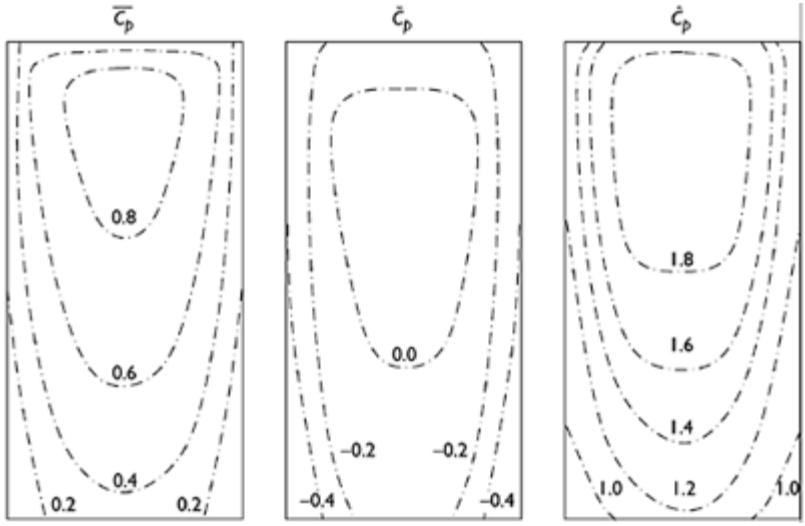

Figure 9.3 Mean, maximum and minimum pressure coefficients—windward wall of a building with square cross-section—height/width=2.1.

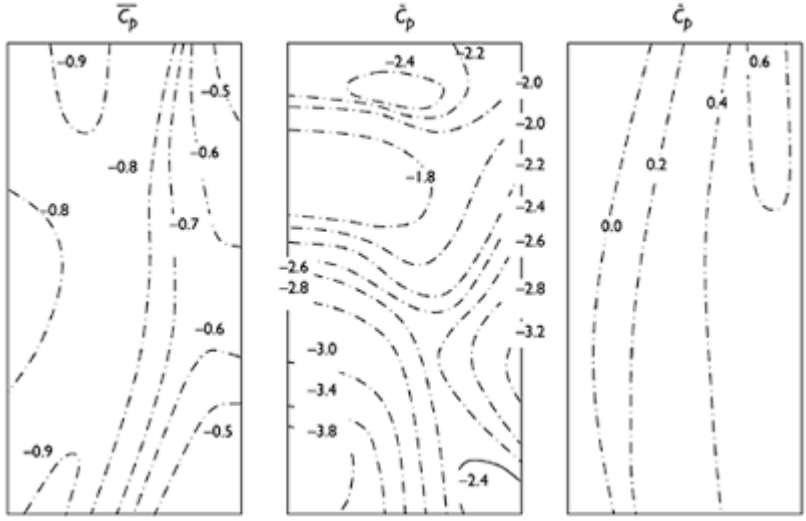

Figure 9.4 Mean, maximum and minimum pressure coefficients—side wall of a building with square cross-section—height/width=2.1.

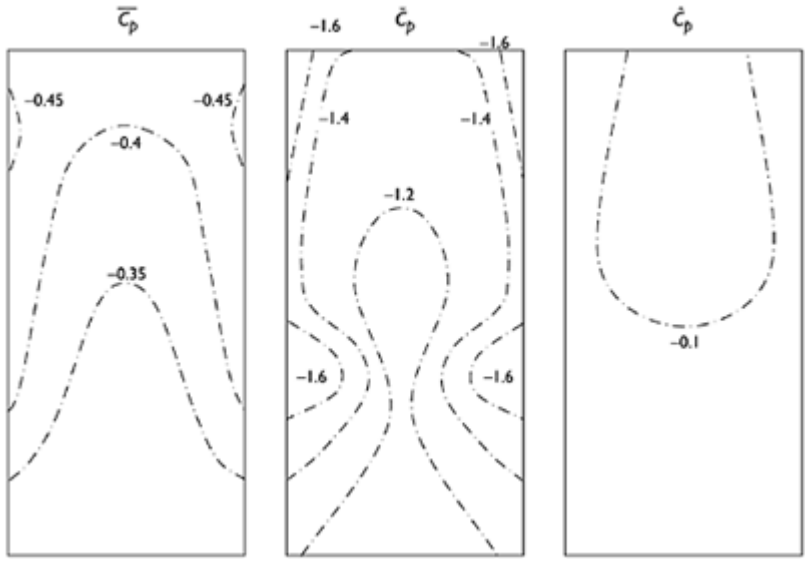

Figure 9.5 Mean, maximum and minimum pressure coefficients—leeward wall of a building with square cross-section—height/width=2.1.

Figure 9.3 shows a stagnation point on the windward face, where the value of $\bar{C}_p$ reaches a maximum, at about 0.8 *h*. The heights for largest maximum pressure coefficient are slightly lower than this.

The side walls (Figure 9.4) are adjacent to a flow which is separated from the front wall, and generates strong vortices (see Figures 4.1 and 9.2). The mean pressure coefficients are generally in the range from −0.6 to −0.8, and not dissimilar to the values on the much taller building in Figure 4.15. The largest magnitude minimum pressure coefficients of about −3.8 occur near the base of the buildings, unlike the windward wall pressures. A wind direction parallel to the side wall produces the largest magnitude negative pressures in this case.

The mean and largest peak pressures on the leeward wall (Figure 9.5) are also negative, but are typically half the magnitude of the side wall pressures. This wall is of course sheltered and exposed to relatively slowly moving air in the near wake of the building.

9.4.3 The nature of fluctuating local pressures and probability distributions

As discussed in Section 9.2, in the 1970s, full-scale and wind-tunnel measurements of wind pressures on tall buildings highlighted the local peak negative pressures that can occur, for some wind directions, on the walls of tall buildings, particularly on side walls at locations near windward corners and on leeward walls. These high pressures generally

only occur for quite short periods of time, and may be very intermittent in nature. An example of the intermittent nature of these pressure fluctuations is shown in Figure 9.6 (from Dalgleish, 1971).

Several studies (e.g. Dalgleish, 1971; Peterka and Cermak, 1975) indicated that the probability densities of pressure fluctuations in separated flow regions on tall buildings were not well fitted by the normal or Gaussian probability distribution (Section C3.1). This is the case even though the latter is a good fit to the turbulent velocity fluctuations in the wind (see Section 3.3.2). The 'spiky' nature of local pressure fluctuations (Figure 9.6) results in probability densities of peaks of five standard deviations, or greater, below the mean pressure, being several times greater than that predicted by the Gaussian distribution.

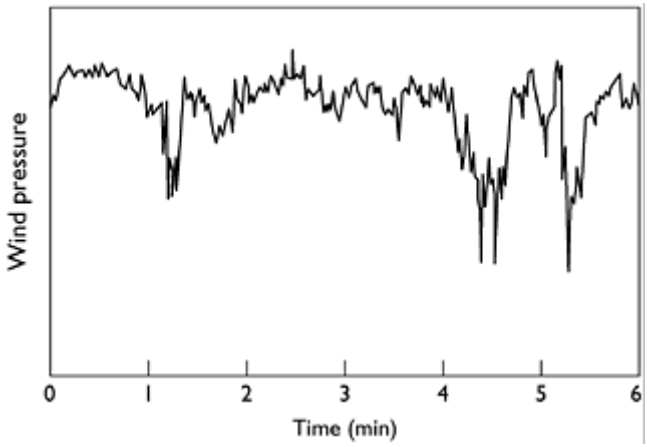

Figure 9.6 Record of fluctuating pressure from the leeward wall of a full-scale office building (Dalgleish, 1971).

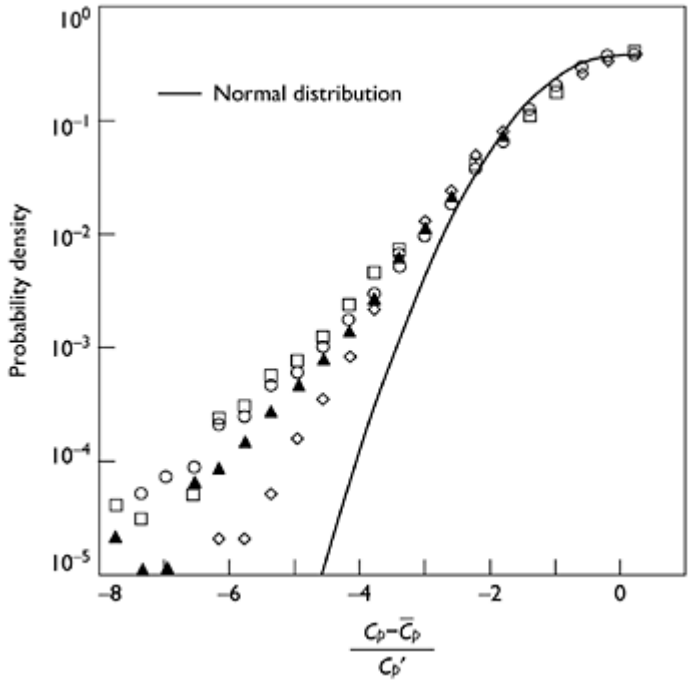

Figure 9.7 Probability densities of pressure fluctuations from regions in separated flow on tall buildings (Peterka and Cermak, 1975).

This is illustrated in Figure 9.7 derived from wind-tunnel tests of two tall buildings (Peterka and Cermak, 1975).

A consequence of the intermittency and non-Gaussian nature of pressure fluctuations on tall buildings is that the maximum pressure coefficient measured at a particular location on a building in a defined time period—say 10 m in in full scale—may vary considerably from one time period to the next. Therefore they cannot be predicted by knowing the mean and standard deviation, as is the case with a Gaussian random process (Davenport, 1964). This has led to a number of different statistical techniques being adopted to produce more consistent definitions of peak pressures for design—these are discussed in Section 9.4.4. A related matter is the response characteristics of glass cladding to short duration peak loads. The latter aspect is discussed in Section 9.4.5.

A detailed study (Surry and Djakovich, 1995) of local negative peak pressures on generic tall building models of constant cross-section, with four different corner geometries, indicated that the details of the corner geometry do not affect the general magnitude of the minimum pressure coefficients, but rather the wind direction at which they occur. The highest peaks were associated with vortex shedding.

9.4.4 Statistical methods for determination of peak local pressures

A simple approach, originally proposed by Lawson (1976), uses the parent probability distribution of the pressure fluctuations, from which a pressure coefficient with a designated (low) probability of exceedence is extracted. The probability of exceedence is normally in the range 1×10^{-4}–5×10^{-4}, with the latter being suggested by Lawson. This method can be programmed 'on the run' in wind-tunnel tests, relatively easily; sometimes a standard probability distribution such as the Weibull type (see Section C3.4) is used to fit the measured data and interpolate, or extrapolate, to the desired probability level.

Cook and Mayne (1979) proposed a method in which the total averaging time, T, is divided into 16 equal parts and the measured peak pressure coefficient (maximum or minimum) within each reduced time period, t, is retained. A Type I extreme value (Gumbel) distribution (see Section 2.2.1 and Section C4) is fitted to the measured data, giving a mode, u_t, and slope, $(1/a_t)$. These can then be used to calculate the parameters of the extreme value Type I distribution appropriate to the maxima (or minima) for the original time period, T, as follows:

$$u_T=u_t+a_t \log_e 16 \tag{9.5}$$

$$a_T=a_t \tag{9.6}$$

Knowing the distribution of the extreme pressure coefficients, the expected peak, or any other percentile, can then be easily determined. The method proposed by Cook and Mayne (1979), in fact, proposes an effective peak pressure coefficient C_p^* given by:

$$C_p^*=u_T+1.4a_T \tag{9.7}$$

Equation (9.7) can be rewritten in terms of the mean and standard deviation of the extremes (Kasperski, 2003). For the extreme value Type I distribution, the mean and standard deviation are related to the mode, u_T, and scale factor, a_T, by Equations (9.8) and (9.9):

$$\text{mean}=m=u_T+0.577a_T \tag{9.8}$$

$$\text{standard deviation}=\sigma=(\pi/\sqrt{6})a_T=1.282a_T \tag{9.9}$$

Hence Equation (9.7) can be written as:

$$C_p^*=u_T+0.577a_T+0.823a_T=m+0.64\ (1.282a_T)$$
$$C_p^*=m+0.64\sigma \tag{9.10}$$

Equation (9.10) can be used to calculate C_p^* by estimating m and σ from the measured extremes without having to fit a distribution. In fact, it does not require an assumption about the distribution of the extremes. An alternative, more conservative, form is Equation (9.11); this corresponds to Equation (9.7) with the 1.4 replaced by 1.5:

$$C_p^* = m + 0.7\sigma \tag{9.11}$$

Peterka (1983) proposed the use of the probability distribution of 100 independent maxima within a time period equivalent to 1 h, to determine C_p^*.

Another approach is to make use of level-crossing statistics. Melbourne (1977) proposed the use of a normalized rate of crossing of levels of pressure (or structural response). A nominal rate of crossing (e.g. 10^{-4} per hour) is chosen to determine a nominal level of 'peak' pressure.

The parameters of the (Type I) extreme value distribution for the extreme pressure in a given time period can also be derived from level-crossing rates as follows. The level crossings are assumed to be uncorrelated events which can be modelled by a Poisson distribution (Section C3.5).

The Poisson distribution gives the probability for the number of events, n, in a given time period, T, when the average rate of occurrence of the events is υ:

$$P(n, \upsilon) = \frac{(\upsilon T)^n}{n!} \exp(-\upsilon T) \tag{9.12}$$

The 'event' in this case can be taken as an upcrossing of a particular level, e.g. the exceedence of a particular pressure level. The probability of getting no crossings of a pressure level, p, during the time period, T, is also the probability that the largest value of the process, $p(t)$, during the time period is less than that level, i.e. the cumulative probability distribution of the largest value in the time period, T.

Thus,

$$F(p) = P(0, \upsilon) = \frac{(\upsilon T)^0}{0!} \exp(-\upsilon T) = \exp(-\upsilon T) \tag{9.13}$$

If we assume that the average number of crossings of level x in time T is given by:

$$\upsilon T = \exp\left[-\frac{1}{a}(p - u_T)\right] \tag{9.14}$$

where a and u_T are constants, then,

$$F(x) = \exp\left\{\exp\left[-\frac{1}{a}(p - u_T)\right]\right\} \tag{9.15}$$

This is the Type I (Gumbel) extreme value distribution with a mode of u_T and a scale factor of a.

From Equation (9.14), taking natural logarithms of both sides,

$$\log_e(\nu T) = -\frac{1}{a}(p - u_T) \tag{9.16}$$

The mode and scale factor of the Type I extreme value distribution of the process *p(t)* can be estimated by the following procedure.

- Plot the natural logarithm of the rate of upcrossings against the level, *p*.
- Fit a straight line. From Equation (9.16), the slope is (−1/*a*), and the intercept (*p*=0) is (u_T/a).
- From these values, estimate u_T and *a*, the mode and scale factor of the Type I extreme value distribution of *p*.

9.4.5 Strength characteristics of glass in relation to wind loads

Direct wind loading is a major design consideration in the design of glass and its fixing in tall buildings. However, the need to design for wind-generated flying debris (Section 1.5)—particularly roof gravel—in some cities also needs to be considered (Minor, 1994).

As has been discussed, wind pressures on the surfaces of buildings fluctuate greatly with time, and it is known that the strength of glass is quite dependent on the duration of the loading. The interaction of these two phenomena results in a complex design problem.

The surfaces of glass panels are covered with flaws of various sizes and orientations. When these are exposed to tensile stresses they grow at a rate dependent on the magnitude of the stress field, as well as relative humidity and temperature. The result is a strength reduction which is dependent on the magnitude and duration of the tensile stress. Drawing on earlier studies of this phenomenon, known as ‘static fatigue’, Brown (1972) proposed a formula for damage accumulation which has the form of Equation (9.17), at constant humidity and temperature:

$$D = \int_0^T [s(t)]^n \, \mathrm{d}t \tag{9.17}$$

where *D* is the accumulated damage, *s(t)* the time varying stress, *T* the time over which the glass is stressed and *n* a higher power (in the range of 12–20).

The expected damage in time, *T*, under a fluctuating wind pressure, *p(t)*, in the vicinity of a critical flaw can be written as Equation (9.18):

$$E\{D\} = K \int_0^T E\{[p(t)]^m\} \, \mathrm{d}t \tag{9.18}$$

where *K* is a constant and *m* a different power, usually lower than *n*, but dependent on the size and aspect ratio of the glass, which allows for the non-linear relationship between load and stress for glass plates due to membrane stresses (Calderone and Melbourne, 1993). *E{}* is the expectation or averaging operation.

Calderone (1999), after extensive glass tests, found a power law relationship between maximum stress anywhere in a plate and the applied pressure, for any given plate; this may be used to determine the value of *m* for that plate. Values fall in the range of 5–20.

The integral on the right-hand side of Equation (9.18) is *T* times the *m*th moment of the pressure fluctuation, so that:

$$E[D] = KT\left(\frac{1}{2}\rho\overline{U}^2\right)^m \int_0^\infty C_p{}^m f_{C_p}(C_p)\mathrm{d}C_p \tag{9.19}$$

where $C_p(t)$ is the time-varying pressure coefficient and $f_{C_p}(C_p)$ the probability density function for C_p.

The integral in Equation (9.19) is proportional to the rate at which damage is accumulated in the glass panel. It can be evaluated from known or expected probability distributions (e.g. Holmes, 1985), or directly from wind-tunnel or full-scale pressure-time histories (Calderone and Melbourne, 1993).

The high weighting given to the pressure coefficient by the power, *m*, in Equation (9.19) means that the main contribution to glass damage comes from isolated peak pressures, which typically occur intermittently on the walls of tall buildings (see Figure 9.6).

An equivalent static pressure coefficient, C_{p_s}, which corresponds to a constant pressure that gives the same rate of damage accumulation as a fluctuating pressure-time history, can be defined:

$$C_{p_s} = \left[\int_0^\infty C_p{}^m f_{C_p}(C_p)\mathrm{d}C_p\right]^{1/m} \tag{9.20}$$

For the structural design of glazing, it is necessary to relate the computed damage caused by wind action to failure loads obtained in laboratory tests of glass panels. The damage integral (Equation (9.17) or (9.18)) can be used to compute the damage sustained by a glass panel under the ramp loading (i.e. increasing linearly with time) commonly used in laboratory testing. In these tests, failure typically occurs in about 1 min.

An equivalent glass design coefficient, C_k, can be defined (Dalgleish, 1979) which, when multiplied by the reference dynamic pressure, $\left(\frac{1}{2}\rho_a\bar{U}^2\right)$, gives a pressure which produces the same damage in a 60 s ramp increase, as in a wind storm of specified duration.

Making use of Equations (9.19) and (9.20), it can be easily shown that for a statistically stationary (synoptic) wind storm of 1 h duration

$$C_k = [60(1+m)]^{1/m} C_{p_s} \tag{9.21}$$

Using typical values of *m* and typical probability distributions, it can be shown (Dalgleish, 1979; Holmes, 1985) that C_k is approximately equal to the expected peak pressure coefficient occurring during the hour of storm wind. This fortuitous result, which is insensitive to both the value of *m* and the probability distribution, means that

measured peak pressure coefficients from wind-tunnel tests are valid for use in calculation of design loads, for comparison with 1 m in loads in glass design charts.

9.5 Overall loading and dynamic response

In Chapter 5, the random, or spectral, approach to the along-wind response of tall structures was discussed. This approach is widely used for the prediction of the response of tall office buildings in simplified forms in codes and standards (see Chapter 15). Dynamic response of a tall building in the along-wind direction is primarily produced by the turbulent velocity fluctuations in the natural wind (Section 3.3). In the cross-wind direction, loading and dynamic response is generated by random vortex shedding (Section 4.6.3)—i.e. it is a result of unsteady separating flow generated by the building itself, with a smaller contribution from cross-wind turbulence.

9.5.1 General response characteristics

In this section, some general characteristics of the dynamic response of tall buildings to wind will be outlined.

By a dimensional analysis, or by application of the theory given in Section 5.3.1, it can be demonstrated (Davenport, 1966, 1971) that the rms fluctuating deflection at the top of a tall building of given geometry in a stationary (synoptic) wind is given to a good approximation for the along-wind response by:

$$\frac{\sigma_x}{h} = A_x \left(\frac{\rho_a}{\rho_b}\right)\left(\frac{\overline{U}_h}{n_1 b}\right)^{k_x} \frac{1}{\sqrt{\eta}} \tag{9.22}$$

and for the cross-wind response by:

$$\frac{\sigma_y}{h} = A_y \left(\frac{\rho_a}{\rho_b}\right)\left(\frac{\overline{U}_h}{n_1 b}\right)^{k_y} \frac{1}{\sqrt{\eta}} \tag{9.23}$$

where h is the building height; A_x, A_y constants for a particular building shape; ρ_a the density of air; ρ_b an average building density; Uh the mean wind speed at the top of the building; b the building breadth; k_x, k_y exponents; n_1 the first mode natural frequency; and η the critical damping ratio in the first mode of vibration.

Equations (9.22) and (9.23) are based on the assumption that the responses are dominated by the resonant components. For along-wind response, the background component is independent of the natural frequency. In the case of the cross-wind response, there is no mean component but some background contribution due to cross-wind turbulence. The assumption of dominance of resonance is valid for slender tall buildings with first mode natural frequencies less than about 0.5 Hz and damping ratios less than about 0.02.

The equations illustrate that the fluctuating building deflection can be reduced by increasing either the building density or the damping. The damping term, η, includes

aerodynamic damping as well as structural damping; however, this is normally small for tall buildings.

The term $(\bar{U}_h/n_1 b)$ is a non-dimensional mean wind speed, known as the *reduced velocity*. The exponent, k_x, for the fluctuating along-wind deflection is greater than 2, since the spectral density of the wind speed near the natural frequency, n_1, increases at a greater power than 2, as does the aerodynamic admittance function (Section 5.3.1 and Figure 5.4) at that frequency. The exponent for cross-wind deflection, k_y, is typically about 3, but can be as high as 4.

Figure 9.8 shows the variation of (σ_x/h) and (σ_y/h) with reduced velocity for a building of circular cross-section (as well as the variation of $\overline{x}$).

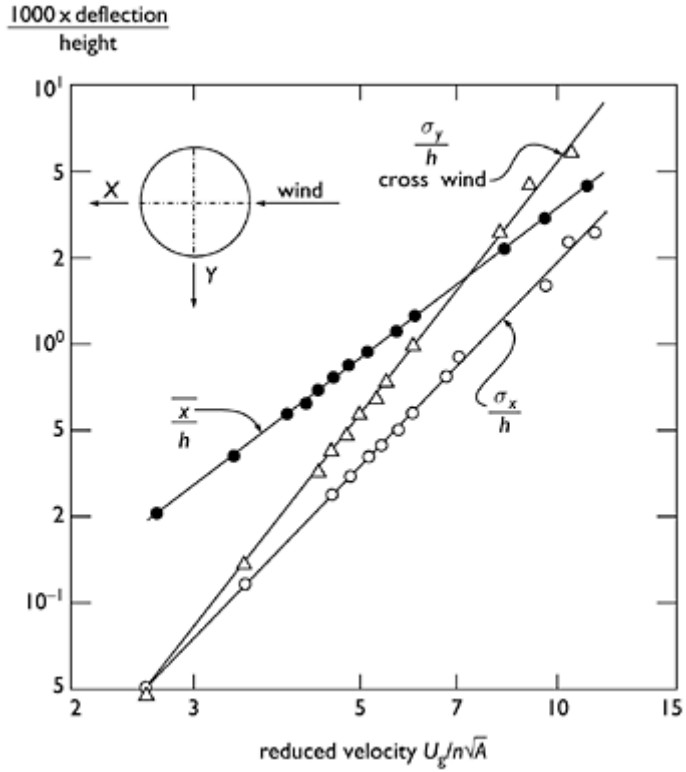

Figure 9.8 The mean and fluctuating response of a tall building of circular cross-section (from Davenport, 1971).

9.5.2 Effect of building cross-section

In a study used to develop an optimum building shape for the US Steel Building, Pittsburgh, the response of six buildings of identical height and dynamic properties but with different cross-sections were investigated in a boundary-layer wind tunnel

(Davenport, 1971). The probability distributions of the extreme responses in a typical synoptic wind climate were determined, and are shown plotted in Figure 9.9. The figure shows a range of 3:1 in the responses with a circular cross-section producing the lowest response and an equilateral triangular cross-section the highest. Deflection across the shortest (weakest) axis of a 2:1 rectangular cross-section was also large.

9.5.3 Corner modifications

Slotted and chamfered corners on rectangular building cross-sections have significant effects on both along-wind and cross-wind dynamic responses to wind (Kwok and Bailey, 1987; Kwok *et al.*, 1988; Kwok, 1995). Chamfers of the order of 10% of the building width produce up to 40% reduction in the along-wind response and 30% reduction in the cross-wind response.

9.5.4 Prediction of cross-wind response

Along-wind response of isolated tall buildings can be predicted reasonably well from the turbulence properties in the approaching flow by applying the random vibration theory methods discussed in Section 5.3.1. Cross-wind response, however, is more difficult to predict, since vortex shedding plays a dominant role in the exciting forces in the cross-wind direction. However, an approach which has been quite successful is the use of the high-frequency base-balance technique to measure the spectral density of the generalized force in wind-tunnel tests (Section 7.6.2). Multiplication by the mechanical admittance and integration over frequency can then be performed to predict the building response.

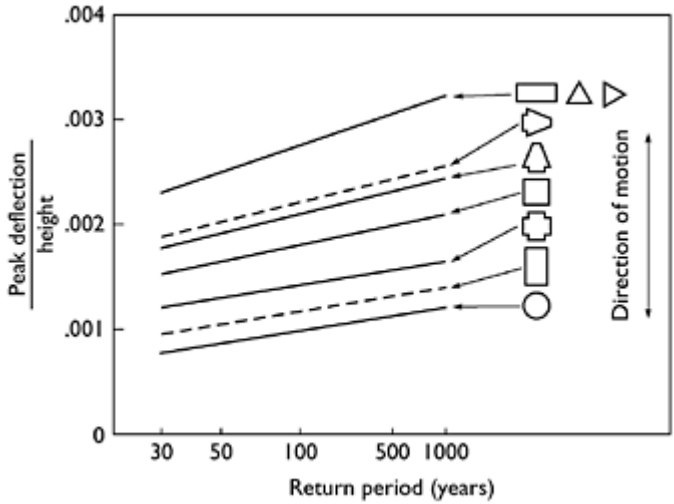

Figure 9.9 Effect of cross-sectional shape on maximum deflections of six buildings (from Davenport, 1971).

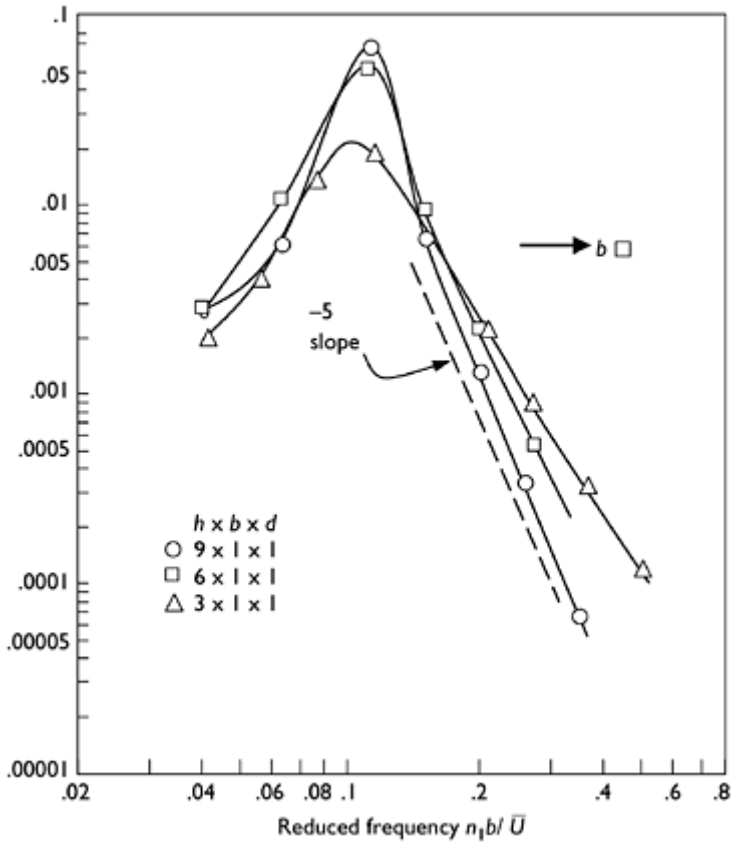

Figure 9.10 Cross-wind generalized force spectra for buildings of square cross-section (from Saunders, 1974).

Examples of generalized force spectra for buildings of square cross-section are shown in Figure 9.10. Non-dimensional spectra for three different height/breadth ratios are shown, and the approach flow is typical of suburban terrain. The mode shapes are assumed to be linear with height. The abscissa of this graph is reduced frequency—the reciprocal of reduced velocity.

For reduced velocities of practical importance (2–8), the non-dimensional spectra vary with reduced velocity to a power of 3–5 or with reduced frequency to a power of −3 to −5 (represented by the slope on the log-log plot). Such data has been incorporated in some standards and codes for design purposes (see Section 15.9).

9.5.5 Database for tall building loading and response

Most tall buildings of 100 m height, or greater, are the subject of special wind-tunnel tests at the later design stages; the techniques for this are well developed and many of these are discussed in Section 7.6. However, the designer usually needs preliminary estimates of overall wind loading early in the design stage. As discussed in Chapter 15, several wind loading codes and standards contain methods for prediction of along-wind and cross-wind responses. A more comprehensive alternative to codes and standards is provided by Internet databases such as the one compiled by the Natural Hazards Modeling Laboratory of Notre Dame University (www.nd.edu/~nathaz/database). The latter provides information on the spectral densities of three components of base moment for 27 different building shapes in two different terrain types. This information has been obtained from a high-frequency base balance (Section 7.6.2). By application of the random vibration, or spectral approach, described in Section 5.3, reasonable preliminary predictions of basic building responses such as base bending moments and accelerations at the top of the building can be obtained. Subsequently, more accurate predictions can be obtained from specific wind-tunnel tests, allowing for accurate reproduction of the building shape, the surroundings, including shielding and interference effects from other buildings, and the mode shapes, including sway-twist coupling effects.

9.6 Combination of along- and cross-wind response

When dealing with the response of tall buildings to wind loading, the question arises: How should the responses in the along-wind and cross-wind directions be combined statistically? Since clearly the along-wind and cross-wind responses are occurring simultaneously on a structure, it would be unconservative (and potentially dangerous!) to treat these as separate load cases. The question arises when applying those wind loading codes and standards which provide methods for calculating both along-wind and cross-wind dynamic responses for tall buildings (See Chapter 15). It also arises when wind-tunnel tests are carried out using either aero-elastic (Section 7.6.1) or base-balance methods (Section 7.6.2). In these cases, predictions are usually provided for each wind direction, with respect to *body*- or building-*axes* rather than *wind axes* (see Section 4.2.2 and Figure 4.2). These axes are usually the two principal axes for sway of the building.

Two cases can be identified:

1. ‘scalar’ combination rules for load effects;
2. ‘vector’ combination of responses.

The former case is the more relevant case for structural load effects being designed for strength, as in most cases structural elements will ‘feel’ internal forces and stresses from both response directions and will be developed in the following. The second case is relevant when axisymmetric structures are under consideration, i.e. structures of circular cross-section such as chimneys.

Load effects (i.e. member forces and internal stresses) resulting from overall building response in two orthogonal directions (x and y) can very accurately be combined by the following formula:

$$\hat{\varepsilon}_t = \overline{\varepsilon}_x + \overline{\varepsilon}_y + \sqrt{(\hat{\varepsilon}_x - |\overline{\varepsilon}_x|)^2 + (\hat{\varepsilon}_y - |\overline{\varepsilon}_y|)^2} \tag{9.24}$$

where $\hat{\varepsilon}_t$ is total combined maximum peak load effect (e.g. the axial load in a column); $\overline{\varepsilon}_x$ the load effect derived from the mean response in the x-direction (usually derived from the mean base bending moment in that direction); $\overline{\varepsilon}_y$ the load effect derived from the mean response in the y-direction; $\hat{\varepsilon}_x$ the peak load effect derived from the response in the x-direction and $\hat{\varepsilon}_y$ the peak load effect derived from the response in the y-direction.

Equation (9.24) is quite an accurate one, as it is based on the combination of uncorrelated Gaussian random processes, for which it is exact. Most responses dominated by resonant contributions to wind have been found to be very close to Gaussian and if the two orthogonal sway frequencies are well separated, the dynamic responses will be poorly correlated.

As an alternative approximation, the following load cases can be studied:

(a) [Mean x load+0.75 (peak − mean)$_x$] with [mean y load+0.75 (peak − mean)$_y$];
(b) [Mean x load+(peak − mean)$_x$] with [mean y load];
(c) [Mean x load] with [mean y load+(peak − mean)$_y$].

The case (a) corresponds to the following approximation to Equation (9.24) for peak load effect:

$$\varepsilon_t = \overline{\varepsilon}_x + \overline{\varepsilon}_y + 0.75((\hat{\varepsilon}_x - |\overline{\varepsilon}_x|) + (\hat{\varepsilon}_y - |\overline{\varepsilon}_y|)) \tag{9.25}$$

Equation (9.25) is a good approximation to Equation (9.24) for the range:

$$1/3 < (\hat{\varepsilon}_x - |\overline{\varepsilon}_x|)/(\hat{\varepsilon}_y - |\overline{\varepsilon}_y|) < 3$$

The other two cases (b) and (c) are intended to cover the cases outside this range, i.e. when $(\hat{\varepsilon}_x - |\overline{\varepsilon}_x|)$ is much larger than $(\hat{\varepsilon}_y - |\overline{\varepsilon}_y|)$ and vice versa.

9.7 Torsional loading and response

The significance of torsional components in the dynamic response of tall buildings was highlighted by the Commerce Court Study of the 1970s (Section 9.2), when a building of a uniform rectangular cross-section experienced significant and measurable dynamic twist due to an eccentricity between the elastic and mass centres. Such a possibility had been overlooked in the original wind-tunnel testing. Now, when considering accelerations at the top of tall building, the possibility of torsional motions increasing the perceptible motions at the periphery of the cross-section may need to be considered.

There are two mechanisms for producing dynamic torque and torsional motions in tall buildings:

1. Mean torque and torsional excitation resulting from non-uniform pressure distributions or from non-symmetric cross-sectional geometries.
2. Torsional response resulting from sway motions through coupled mode shapes and/or eccentricities between elastic (shear) and geometric centres.

The first aspect was studied by Isyumov and Poole (1983), Lythe and Surry (1990) and Cheung and Melbourne (1992). Torsional response of tall buildings has been investigated both computationally, making use of experimentally obtained dynamic pressure or force data from wind-tunnel models (Kareem, 1985; Tallin and Ellingwood, 1985), and experimentally on aero-elastic models with torsional degrees of freedom (Xu *et al.*, 1992a; Beneke and Kwok, 1993; Zhang *et al.*, 1993).

A mean torque coefficient, $\overline{C}_{M_z}$, can be defined as:

$$\overline{C}_{M_z} = \frac{\overline{M}_z}{\frac{1}{2}\rho_a \overline{U}_h^{\,2} b_{\max}^{\,2} h} \tag{9.26}$$

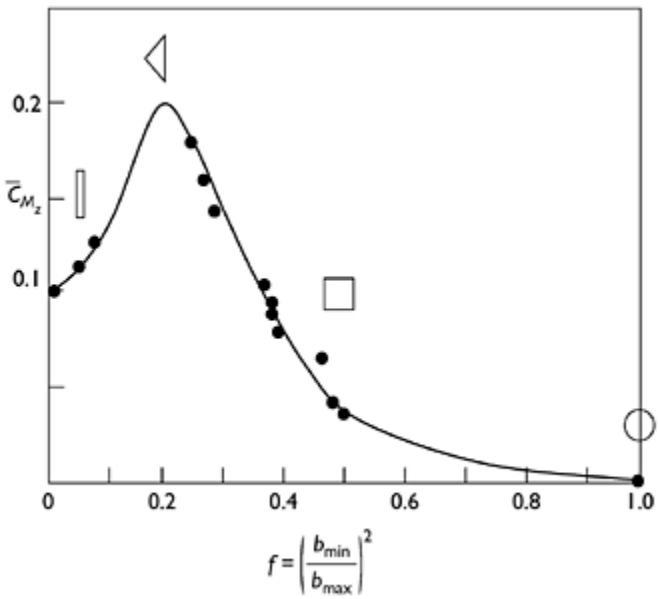

Figure 9.11 Mean torque coefficients on tall buildings of various cross-sections (from Cheung and Melbourne, 1992).

where $\overline{M}_z$ is the mean torque; $b_{\max}$ the maximum projected width of the cross-section and h the height of the building.

Lythe and Surry (1990) from wind-tunnel tests on 62 buildings, ranging from those with simple cross-sections to complex shapes, found an average value of $\overline{C}_{M_z}$ as defined

above, of 0.085 with a standard deviation of 0.04. The highest values appear to be a function of the ratio of the minimum projected width, b_{min}, to the maximum projected width, b_{max}, with a maximum value of $\overline{C}_{M_z}$ approaching 0.2, when (b_{min}/b_{max}) is equal to around 0.45 (Figure 9.11 from Cheung and Melbourne, 1992). The highest value of $\overline{C}_{M_z}$ for any section generally occurs when the mean wind direction is about 60–80° from the normal to the widest building face.

Isyumov and Poole (1983) used simultaneous fluctuating pressures and pneumatic averaging (Section 7.5.2) on building models with a square or 2:1 rectangular cross-section in a wind tunnel to determine the contribution to the fluctuating torque coefficient from various height levels on the buildings and from the various building faces. The main contribution to the fluctuating torque on the square and rectangular section with the wind parallel to the long faces came from pressures on the side faces, and could be predicted from the mean torque by quasi-steady assumptions (Section 4.6.2). On the other hand, for a mean wind direction parallel to the short walls of the rectangular cross-section, the main contribution was pressure fluctuations on the rear face induced by vortex shedding.

A double peak in the torque spectra for the wind direction parallel to the long face of a 2:1 building has been attributed to buffeting by lateral turbulence and by re-attaching flow on to the side faces (Xu *et al.*, 1992a). Measurements on an aero-elastic wind-tunnel tall building model designed only to respond torsionally (Xu *et al.*, 1992a) indicated that aerodynamic damping effects (Section 5.5.1) for torsional motion of cross-section shapes characteristic of tall buildings are quite small in the range of design reduced velocities, in contrast to bridge decks. However, at higher reduced velocities, high torsional dynamic response and significant negative aerodynamic damping have been found for a triangular cross-section (Beneke and Kwok, 1993).

A small amount of eccentricity can increase both the mean twist angle and the dynamic torsional response. For example, for a building with square cross-section, a shift of the elastic centre from the geometric and mass centre by 10% of the breadth of the cross-section is sufficient to double the mean angle of twist and increase the dynamic twist by 40–50% (Zhang *et al.*, 1993).

9.8 Interference effects

High-rise buildings are most commonly clustered together in groups—as office buildings grouped together in a city-centre business district or in multiple building apartment developments, for example. The question of aerodynamic interference effects from other buildings of similar size on the structural loading and response of tall buildings arises.

9.8.1 Upwind building

A single similar upwind building on a building with square cross-section and height/width (aspect) ratio of 6 produces increases of up to 30% in peak along-wind base moment and 70% in cross-wind moment, at reduced velocities representative of design wind conditions in suburban approach terrain (Melbourne and Sharp, 1976). The maximum increases occur when the upwind building is 2–3 building widths to one side of a line taken upwind and about 8 building widths upstream. Contours of percentage

increases in peak cross-wind loading for square section buildings with an aspect ratio of 4 are shown in Figure 9.12. It can be seen that reductions, i.e. shielding, occur when the upstream building is within 4 building heights upstream and ±2 building heights to one side of the downstream building. The effect of increasing turbulence in the approach flow, i.e. increasing roughness lengths in the approach terrain, is to reduce the increases produced by interference.

The effect of increasing aspect ratio is to further increase the interference effects of upstream buildings, with increases of up to 80% being obtained, although this was for

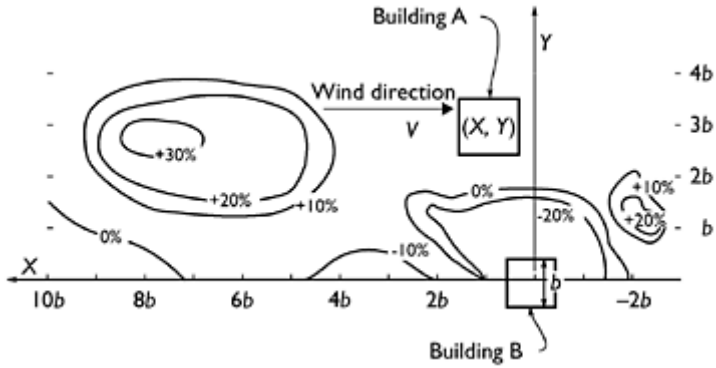

Figure 9.12 Percentage change in cross-wind response of a building (B) due to a similar building (A) at *(X, Y)* (Standards Australia, 1989).

buildings with an atypical aspect ratio of 9, and in relatively low turbulence conditions (Bailey and Kwok, 1985).

9.8.2 Downwind building

As shown in Figure 9.12, *downwind* buildings can also increase cross-wind loads on buildings if they are located in particular critical positions. In the case of the buildings of 4:1 aspect ratio of Figure 9.12, this is about one building width to the side and two widths downwind.

More detailed reviews of interference effects on wind loads on tall buildings are given by Kwok (1995) and Khanduri *et al.* (1998). For a complex of tall buildings in the centres of large cities, wind-tunnel model tests (Chapter 7) will usually be carried out and these should reveal any significant interference effects on *new* buildings such as those described in the previous paragraphs. Anticipated new construction should be included in the models when carrying out such tests. However, existing buildings may be subjected to unpredicted higher loads produced by new buildings of similar size at any time during their future life and this should be considered by designers when considering load factors.

9.8.3 Interference effects on local pressures

Adjacent buildings can also have dramatic effects on local cladding loads on tall buildings. An interesting, unusual example, based on wind-tunnel tests of a commercial high-rise development, was described by Surry and Mallais (1983). In this case, a *downwind* taller building resulted in an increase in the design local pressures by a factor of about three. It was explained by the presence of the adjacent building inducing re-attachment of the separated shear layers (see Section 4.1) on to the wall of the upwind building (Figure 9.13).

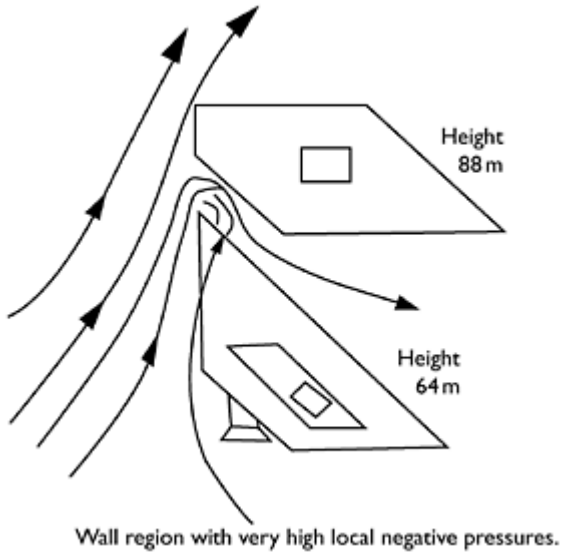

Figure 9.13 Effect of a downwind building on local cladding pressures (Surry and Mallais, 1983). Reproduced by permission from ASCE.

9.9 Damping

The dynamic response of a tall building or other structures, to along-wind or cross-wind forces, depends on its ability to dissipate energy, known as ‘damping’. Structural damping is derived from energy dissipation mechanisms within the material of the structure itself (i.e. steel, concrete, etc.), or from friction at joints, or from movement of partitions, etc. For some large structures constructed in the last 20 years, the structural damping alone has been insufficient to limit the resonant dynamic motions to acceptable levels for serviceability considerations, and auxiliary dampers have been added. Three types of auxiliary damping devices will be discussed in this chapter: visco-elastic dampers, tuned mass dampers (TMD) and tuned liquid dampers (TLD).

9.9.1 Structural damping

An extensive database of free vibration measurements from tall buildings in Japan has been collected (Tamura *et al.*, 2000). This database includes data on frequency as well as damping. More than 200 buildings were studied, although there is a shortage of values at larger heights—the tallest (steel encased) reinforced concrete building was about 170m in height and the highest steel-framed building was 280 m.

For reinforced concrete buildings, the Japanese study proposed the following empirical formula for the critical damping ratio in the first mode of vibration, for buildings less than 100 m in height and for low-amplitude vibrations (drift ratio, (x_t/h) less than 2×10^{-5}):

$$\eta_1 \cong 0.014 n_1 + 470\left(\frac{x_t}{h}\right) - 0.0018 \tag{9.27}$$

where n_1 is the first mode natural frequency and x_t the amplitude of vibration at the top of the building $(z=h)$.

The corresponding relationship for steel-framed buildings is:

$$\eta_1 \cong 0.013 n_1 + 400\left(\frac{x_t}{h}\right) + 0.0029 \tag{9.28}$$

The range of application for Equation (9.28) is stated to be: $h<200$ m and $(x_t/h)< 2\times10^{-5}$.

Equations (9.27) and (9.28) may be applied to tall buildings for serviceability limit states criteria (i.e. for the assessment of acceleration limits). Much higher values are applicable for the high amplitudes appropriate to strength (ultimate) limit states, but unfortunately little, or no, measured data are available.

9.9.2 Visco-elastic dampers

Visco-elastic dampers incorporate visco-elastic material which dissipates energy as heat through shear stresses in the material. A typical damper, as shown in Figure 9.14, consists of two visco-elastic layers bonded between three parallel plates (Mahmoodi, 1969). The force versus displacement characteristic of such a damper forms a hysteresis loop as shown in Figure 9.15. The enclosed area of the loop is a measure of the energy dissipated per cycle and, for a given damper, is dependent on the operating temperature (Mahmoodi and Keel, 1986) and heat transfer to the adjacent structure.

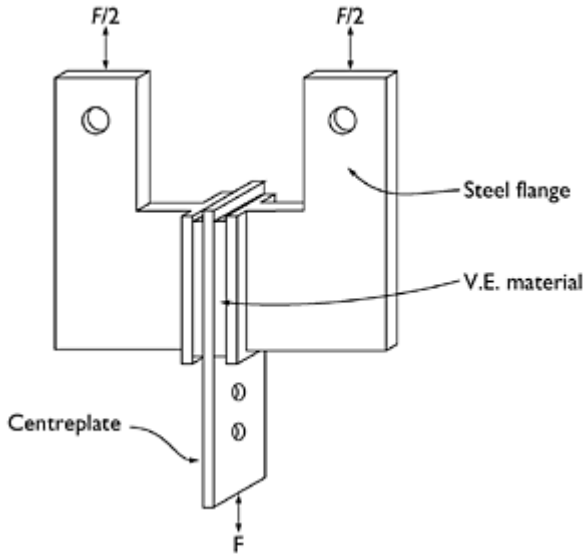

Figure 9.14 A visco-elastic damper (Mahmoodi, 1969).

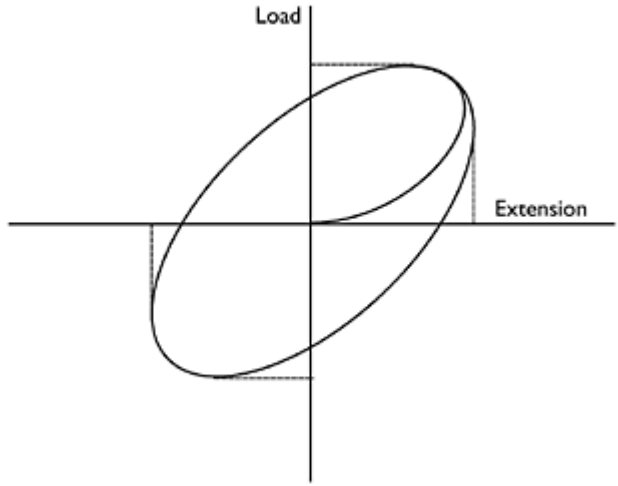

Figure 9.15 Hysteresis loop for visco-elastic dampers.

The World Trade Center buildings in New York City were the first major structures to utilize visco-elastic dampers (Mahmoodi, 1969). Approximately 10,000 dampers were installed in each 110-storey tower, with about 100 dampers at the ends of the floor trusses at each floor from the 7th to the 107th. More recently visco-elastic dampers have been installed in the 76-storey Columbia Seafirst Center Building in Seattle, United States. The

dampers used in this building were significantly larger than those used at the World Trade Center, and only 260 were required to effectively reduce accelerations in the structure to acceptable levels (Keel and Mahmoodi, 1986; Skilling *et al.*, 1986).

A detailed review of the use of visco-elastic dampers in tall buildings has been given by Samali and Kwok (1995).

9.9.3 Tuned mass dampers

A relatively popular method of mitigating vibrations has been the *tuned mass damper* (TMD) or *vibration absorber*. Vibration energy is absorbed through the motion of an auxiliary or secondary mass connected to the main system by viscous dampers. The characteristics of a vibrating system with TMD can be investigated by studying the two-degree-of-freedom system shown in Figure 9.16 (e.g. den Hartog, 1956; Vickery and Davenport, 1970).

Tuned mass damper systems have successfully been installed in the Sydney Tower in Australia, the Citycorp Center, New York (275 m), the John Hancock Building, Boston, United States (60 storeys) and in the Chiba Port Tower in Japan (125 m). In the first and last of these, extensive full-scale measurements have been made to verify the effectiveness of the systems.

For the Sydney Tower, a 180 tonne doughnut-shaped water tank, located near the top of the Tower, and required by law for fire protection, was incorporated into the design of the TMD. The tank is 2.1 m deep and 2.1 m from inner to outer radius, weighs about 200 tonnes, and is suspended from the top radial members of the turret. Energy is dissipated in eight shock absorbers attached tangentially to the tank and anchored to the turret wall. A 40 tonne secondary damper is installed lower down on the tower to further increase the damping, particularly in the second mode of vibration (Vickery and Davenport, 1970; Kwok, 1984).

The system installed in the Citycorp Center building, New York (McNamara, 1977), consists of a 400 tonne concrete mass riding on a thin oil film. The damper stiffness is provided by pneumatic springs, whose rate can be adjusted to match the building frequency. The energy absorption is provided by pneumatic shock absorbers, as for the Sydney Tower. The building was extensively wind-tunnel tested (Isyumov *et al.*, 1975). The aero-elastic model tests included the evaluation of the TMD. The TMD was found to significantly reduce the wind-induced dynamic accelerations to acceptable levels. The effective damping of the model damper was found to be consistent with theoretical estimates of effective viscous damping based on the two-degree-of-freedom model (Vickery and Davenport, 1970).

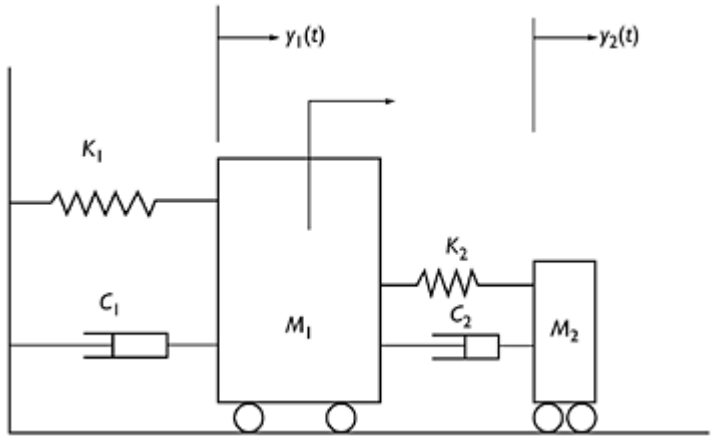

Figure 9.16 Two-degree-of-freedom representation of a tuned mass damper.

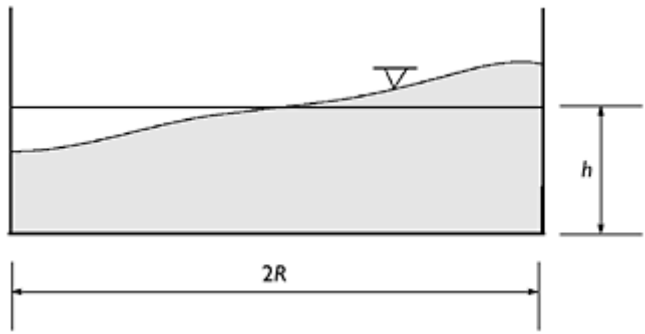

Figure 9.17 Tuned sloshing damper.

Tuned mass damper systems similar to those in the Citycorp Center have been installed in both the John Hancock Building, Boston, and in the Chiba Port Tower. In the case of the latter structure, the system has been installed to mitigate vibrations due to both wind (typhoon) and earthquake. Adjustable coil springs are used to restrain the moving mass, which is supported on frames sliding on rails in two orthogonal directions.

The current (2006) world's tallest building, Taipei 101, has a pendulum type TMD, consisting of a 660 tonne spherical steel mass, suspended at a length to tune it to the building frequency of 0.14 Hz. It is claimed to reduce the accelerations at the top of the building by 30–40%.

The performance of tuned mass dampers in tall buildings and towers under wind loading has been reviewed by Kwok and Samali (1995).

9.9.4 Tuned liquid dampers

Tuned liquid dampers (TLD) are relatively new devices in building and structures applications, although similar devices have been used in marine and aerospace applications for many years. They are similar in principle to the tuned mass damper, in that they provide a heavily damped auxiliary vibrating system attached to the main system. However, the mass, stiffness and damping components of the auxiliary system are all provided by moving liquid. The stiffness is in fact gravitational; the energy absorption comes from mechanisms such as viscous boundary layers, turbulence or wave breaking, depending on the type of system. Two categories of TLD will be discussed briefly here: *tuned sloshing dampers* (TSD) and *tuned liquid column dampers* (TLCD).

The TSD type (Figure 9.17) relies on the motion of shallow liquid in a rigid container for absorbing and dissipating vibrational energy (Fujino *et al.*, 1988; Sun *et al.*, 1989). Devices of this type have already been installed in at least two structures in Japan (Fujii *et al.*, 1990) and on a television broadcasting tower in Australia.

Although a very simple system in concept, the physical mechanisms behind this type of damper are in fact quite complicated. Parametric studies of dampers with circular containers were carried out by Fujino *et al.* (1988). Some of their conclusions can be summarized as follows:

- Wave breaking is a dominant mechanism for energy dissipation but not the only one.
- The additional damping produced by the damper is highly dependent on the amplitude of vibration.
- At small to moderate amplitudes, the damping achieved is sensitive to the frequency of sloshing of liquid in the container. For dampers with circular containers, the fundamental sloshing frequency is given by:

$$n=(1/2\pi)\sqrt{[(1.84g/R)\tanh(1.84h/R)]} \tag{9.29}$$

  where g is the acceleration due to gravity, h the height of the liquid and R the radius of the container, as shown in Figure 9.17.
  This formula is derived from linear potential theory of shallow waves.
- High viscosity sloshing liquid is not necessarily desirable at high amplitudes of vibration, as wave breaking is inhibited. However, at low amplitudes, at which energy is dissipated in the boundary layers on the bottom and side walls of the container, there is an optimum viscosity for maximum effectiveness (Sun *et al.*, 1989).
- Roughening the container bottom does not improve the effectiveness because it has little effect on wave breaking.

The above conclusions were based on a limited number of free vibration tests with only two container diameters. Further investigations are required, including the optimal size of TSD for a given mass of sloshing liquid. However, the simplicity and low cost of this type of damper makes them very suitable for many types of structure.

Variations in the geometrical form are possible, for example Modi *et al.* (1990) have examined TSDs with torus (doughnut)-shaped containers.

The ‘TLCD’ damper (Figure 9.18) comprises an auxiliary vibrating system consisting of a column of liquid moving in a tube-like container. The restoring force is provided by gravity, and energy dissipation is achieved at orifices installed in the container (Sakai *et al.*, 1989; Hitchcock *et al.*, 1997a, b). The same principle has been utilized in anti-rolling tanks used in ships.

The TLCD, like the TSD, is simple and cheap to implement. Unlike the TSD, the theory of its operation is relatively simple and accurate. Sakai *et al.* (1989) has designed a TLCD system for the Citycorp Center Building, New York, as a feasibility study; he found that the resulting damper was simpler, lighter and presumably cheaper than the TMD

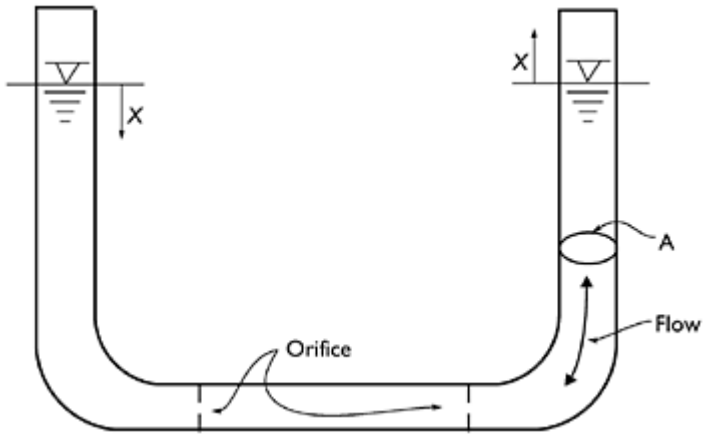

Figure 9.18 Tuned liquid column damper.

system actually used in this building (Section 9.9.3). Xu *et al.* (1992b) have examined theoretically the along-wind response of tall, multi-degree-of-freedom structures, with TMDs, TLCDs and a hybrid damper—the Tuned Liquid Column Mass Damper (TLCMD). They found that the TMD and TLCD, with the same amount of added mass, achieved similar response reductions. The TLCMD—in which the mass of the container, as well as the liquid, is used as part of the auxiliary vibrating system—is less effective when the liquid column frequency is tuned to the same frequency as the whole damper frequency (with the water assumed to remain still). The performance of the latter is improved when the liquid column frequency is set higher than the whole damper frequency.

The effectiveness of tuned liquid structures in several tall structures in Japan has been reviewed by Tamura *et al.* (1995).

9.10 Case studies

Very many tall buildings have been studied in wind tunnels over several decades. These studies include the determination of the overall loading and response, cladding pressures and other wind effects, such as environmental wind conditions at ground level. However, these studies are usually proprietary in nature and not generally available. However, Willford (1985) has described a response study for the Hong Kong and Shanghai Bank Building, Hong Kong. A detailed wind engineering study for a building of intermediate height, including wind loading aspects, is presented by Surry *et al.* (1977).

Relatively few tall buildings have been studied in full scale for wind loads, although many have been studied for their basic dynamic properties (e.g. Tamura *et al.*, 2000). Case studies of wind-induced accelerations on medium height buildings are described by Wyatt and Best (1984) and Snaebjornsson and Reed (1991).

9.11 Summary

This chapter has discussed various aspects of the design of tall buildings for wind loads. The general characteristics of wind pressures on tall buildings and local cladding loads have been considered. The special response characteristics of glass have been discussed. The overall response of tall buildings in along-wind and cross-wind directions and in twist (torsion) has been covered. Aerodynamic interference effects and the application of auxiliary damping systems to mitigate wind-induced vibrations have been discussed.

References

Bailey, P.A. and Kwok, K.C.S. (1985) Interference excitation of twin tall buildings. *Journal of Wind Engineering & Industrial Aerodynamics*, 21:323–38.

Beneke, D.L. and Kwok, K.C.S. (1993) Aerodynamic effect of wind induced torsion on tall buildings. *Journal of Wind Engineering & Industrial Aerodynamics*, 50:271–80.

Brown, W.G. (1972) A load duration theory for glass design. Research paper 508, Division of Building Research, National Research Council of Canada.

Calderone, I.J. (1999) The equivalent wind load for window glass design. Ph.D. thesis, Monash University, Australia.

Calderone, I. and Melbourne, W.H. (1993) The behaviour of glass under wind loading. *Journal of Wind Engineering & Industrial Aerodynamics*, 48:81–94.

Cheung, J.C.K. (1984) Effect of tall building edge configurations on local surface wind pressures. *3rd International Conference on Tall Buildings*, Hong Kong and Guangzhou, 10–15 December.

Cheung, J.C.K. and Melbourne, W.H. (1992) Torsional moments of tall buildings. *Journal of Wind Engineering & Industrial Aerodynamics*, 41–44:1125–26.

Cook, N.J. and Mayne, J.R. (1979) A novel working approach to the assessment of wind loads for equivalent static design. *Journal of Industrial Aerodynamics*, 4:149–64.

Coyle, D.C. (1931) Measuring the behaviour of tall buildings. *Engineering News-Record*, 310–13.

Dalgleish, W.A. (1971) Statistical treatment of peak gusts on cladding. *ASCE Journal of the Structural Division*, 97:2173–87.

Dalgleish, W.A. (1975) Comparison of model/full-scale wind pressures on a high-rise building. *Journal of Industrial Aerodynamics*, 1:55–66.

Dalgleish, W.A. (1979) Assessment of wind loads for glazing design. *IAHR/IUTAM Symposium on Flow-Induced Vibrations*, Karslruhe, September.

Dalgleish, W.A., Templin, J.T. and Cooper, K.R. (1979) Comparison of wind tunnel and full-scale building surface pressures with emphasis on peaks. *Proceedings, 5th International Conference on Wind Engineering*, Fort Collins, CO, pp. 553–65, Pergamon Press, New York.

Dalgleish, W.A., Cooper, K.R. and Templin, J.T. (1983) Comparison of model and full-scale accelerations of a high-rise building. *Journal of Wind Engineering & Industrial Aerodynamics*, 13:217–28.

Davenport, A.G. (1964) Note on the distribution of the largest value of a random function with application to gust loading. *Proceedings of the Institution of Civil Engineers*, 28:187–96.

Davenport, A.G. (1966) The treatment of wind loading on tall buildings. *Proceedings Symposium on Tall Buildings*, Southampton, UK, April, pp. 3–44.

Davenport, A.G. (1971) The response of six building shapes to turbulent wind. *Philosophical Transactions of the Royal Society of London, Series A*, 269:385–94.

Davenport, A.G. (1975) Perspectives on the full-scale measurements of wind effects. *Journal of Industrial Aerodynamics*, 1:23–54.

Davenport, A.G., Hogan, M. and Isyumov, N. (1969) A study of wind effects on the Commerce Court Tower, Part I. Boundary Layer Wind Tunnel Report, BLWT-7–69, University of Western Ontario.

den Hartog, J.P. (1956) *Mechanical Vibrations.* McGraw-Hill, New York.

Dryden, H.L. and Hill, G.C. (1933) Wind pressure on a model of the Empire State Building. *Journal of Research of the National Bureau of Standards*, 10:493–523.

Fujii, K., Tamura, Y., Sato, T. and Wakahara, T. (1990) Wind-induced vibration of tower and practical applications of tuned sloshing damper. *Journal of Wind Engineering & Industrial Aerodynamics*, 33:263–72.

Fujino, Y., Pacheco, B.M., Chaiseri, P. and Sun, L.-M. (1988) Parametric studies on tuned liquid damper (TLD) using circular containers by free-oscillation experiments. *Structural Engineering/Earthquake Engineering, Japan Society of Civil Engineers*, 5:381s–91s.

Hitchcock, P.A., Kwok, K.C.S., Watkins, R.D. and Samali, B. (1997a) Characteristics of liquid column vibration absorbers I. *Engineering Structures*, 19:126–34.

Hitchcock, P.A., Kwok, K.C.S., Watkins, R.D. and Samali, B. (1997b) Characteristics of liquid column vibration absorbers II. *Engineering Structures*, 19:135–44.

Holmes, J.D. (1985) Wind action on glass and Brown's integral. *Engineering Structures*, 7: 226–30.

Isyumov, N., Holmes, J.D., Surry, D. and Davenport, A.G. (1975) A study of wind effects for the First National City Corporation Project—New York, USA. Boundary Layer Wind Tunnel Laboratory, Special Study Report, BLWT-SS1–75, University of Western Ontario.

Isyumov, N. and Poole, M. (1983) Wind induced torque on square and rectangular building shapes. *Journal of Wind Engineering & Industrial Aerodynamics*, 13:183–96.

Kareem, A. (1985) Lateral-torsional motion of tall buildings to wind loads. *ASCE Journal of the Structural Division*, 111:2479–96.

Kasperski, M. (2003) Specification of the design wind load based on wind-tunnel experiments. *Journal of Wind Engineering & Industrial Aerodynamics*, 91:527–41.

Keel, C.J. and Mahmoodi, P. (1986) Design of viscoelastic dampers for Columbia Center Building. In: *Building Motion in Wind*, eds N.Isyumov and T.Tschanz, ASCE, New York.

Khanduri, A.C., Stathopoulos, T. and Bedard, C. (1998) Wind-induced interference effects on buildings—a review of the state-of-the-art. *Engineering Structures*, 20:617–30.

Kwok, K.C.S. (1984) Damping increase in building with tuned mass damper. *ASCE Journal of Engineering Mechanics*, 110:1645–9.

Kwok, K.C.S. (1995) Aerodynamics of tall buildings. In: *A State of the Art in Wind Engineering*, ed. P.Krishna, Wiley Eastern, New Delhi.

Kwok, K.C.S. and Bailey, P.A. (1987) Aerodynamic devices for tall buildings and structures. *ASCE Journal of Engineering Mechanics*, 113:349–65.

Kwok, K.C.S. and Samali, B. (1995) Performance of tuned mass dampers under wind loads. *Engineering Structures*, 17:655–67.

Kwok, K.C.S., Wilhelm, P.A. and Wilkie, B.G. (1988) Effect of edge configuration on wind-induced response of tall buildings. *Engineering Structures*, 10:135–40.

Lawson, T.V. (1976) The design of cladding. *Building and Environment*, 11:37–8.

Lythe, G.R. and Surry, D. (1990) Wind induced torsional loads on tall buildings. *Journal of Wind Engineering & Industrial Aerodynamics*, 36:225–34.

Mahmoodi, P. (1969) Structural dampers. *ASCE Journal of the Structural Division*, 95:1661–72.

Mahmoodi, P. and Keel, C.J. (1986) Performance of viscoelastic dampers for Columbia Center Building. In: *Building Motion in Wind*, eds N.Isyumov and T.Tschanz, ASCE, New York.

McNamara, R.J. (1977) Tuned mass dampers for buildings. *ASCE Journal of the Structural Division*, 103:1785–98.

Melbourne, W.H. (1977) Probability distributions associated with the wind loading of structures. *Civil Engineering Transactions, Institution of Engineers, Australia*, 19:58–67.

Melbourne, W.H. and Sharp, D.B. (1976) Effects of upwind buildings on the response of tall buildings. *Proceedings Regional Conference on Tall Buildings*, Hong Kong, September, pp. 174–91.

Minor, J.E. (1994) Windborne debris and the building envelope. *Journal of Wind Engineering & Industrial Aerodynamics*, 53:207–27.

Modi, V.J., Welt, P. and Irani, P. (1990) On the suppression of vibrations using nutation dampers. *Journal of Wind Engineering & Industrial Aerodynamics*, 33:273–82.

Newberry, C.W., Eaton, K.J. and Mayne, J.R. (1967) The nature of gust loading on tall buildings. *Proceedings, International Research Seminar on Wind Effects on Buildings and Structures*, Ottawa, Canada, 11–15 September, pp. 399–428, University of Toronto Press, Toronto.

Peterka, J.A. (1983) Selection of local peak pressure coefficients for wind tunnel studies of buildings. *Journal of Wind Engineering & Industrial Aerodynamics*, 13:477–88.

Peterka, J.A. and Cermak, J.E. (1975) Wind pressures on buildings—probability densities. *ASCE Journal of the Structural Division*, 101:1255–67.

Rathbun, J.C. (1940) Wind forces on a tall building. *Transactions of ASCE*, 105:1–41.

Sakai, F., Takeda, S. and Tamaki, T. (1989) Tuned liquid column damper—new type device for suppression of building vibrations. *International Conference on High-Rise Buildings*, Nanjing, China, 25–27 March.

Samali, B. and Kwok, K.C.S. (1995) Use of viscoelastic dampers in reducing wind- and earthquake-induced motion of building structures. *Engineering Structures*, 17:639–54.

Saunders, J.W. (1974) Wind excitation of tall buildings. Ph.D thesis, Monash University.

Skilling, J.B., Tschanz, T., Isyumov, N., Loh, P. and Davenport, A.G. (1986) Experimental studies, structural design and full-scale measurements for the Columbia Seafirst Center. In: *Building Motion in Wind*, eds N.Isyumov and T.Tschanz, ASCE, New York.

Snaebjornsson, J. and Reed, D.A. (1991) Wind-induced accelerations of a building: a case study. *Engineering Structures*, 13:268–80.

Standards Australia (1989) Minimum design loads on structures. Part 2: wind loads. Australian Standard, AS1170.2–1989, Standards Australia, North Sydney.

Sun, L.-M., Chaiseri, P., Pacheco, B.M., Fujino, Y. and Isobe, M. (1989) Tuned liquid damper (TLD) for suppressing wind-induced vibration of structures. *2nd Asia-Pacific Symposium on Wind Engineering*, Beijing, 26–29 June.

Surry, D. and Djakovich, D. (1995) Fluctuating pressures on tall buildings. *Journal of Wind Engineering & Industrial Aerodynamics*, 58:81–112.

Surry, D. and Mallais, W. (1983) Adverse local wind loads induced by adjacent building. *ASCE Journal of Structural Engineering*, 109:816–20.

Surry, D., Kitchen, R.B. and Davenport, A.G. (1977) Design effectiveness of wind tunnel studies for buildings of intermediate height. *Canadian Journal of Civil Engineering*, 4: 96–116.

Tallin, A. and Ellingwood, B. (1985) Wind induced lateral-torsional motion of buildings. *ASCE Journal of the Structural Division*, 111:2197–213.

Tamura, Y., Fujii, K., Ohtsuki, T., Wakahara, T. and Kohsaka, R. (1995) Effectiveness of tuned liquid dampers under wind excitation. *Engineering Structures*, 17:609–21.

Tamura, Y., Suda, K. and Sasaki, A. (2000) Damping in buildings for wind-resistant design. *First International Symposium on Wind and Structures for the 21st Century*, Cheju, Korea, 26–28 January.

Templin, J.T. and Cooper, K.R. (1981) Design and performance of a multi-degree-of-freedom aeroelastic building model. *Journal of Wind Engineering & Industrial Aerodynamics* 8: 157–75.

Vickery, B.J. and Davenport, A.G. (1970) An investigation of the behaviour in wind of the proposed Centrepoint Tower, in Sydney, Australia. Boundary Layer Wind Tunnel Laboratory, Research Report, BLWT-1–70, University of Western Ontario.

Willford, M.R. (1985) The prediction of wind-induced responses of the Hong Kong and Shanghai Banking Corporation headquarters, Hong Kong. *Engineering Structures*, 7:35–45.

Wyatt, T.A. and Best, G. (1984) Case study of the dynamic response of a medium height building to wind-gust loading. *Engineering Structures*, 6:256–61.

Xu, Y.L., Kwok, K.C.S. and Samali, B. (1992a) Torsion response and vibration suppression of wind-excited buildings. *Journal of Wind Engineering & Industrial Aerodynamics*, 43: 1997–2008.

Xu, Y.L., Samali, B. and Kwok, K.C.S. (1992b) Control of along-wind response of structures by mass and liquid dampers. *ASCE Journal of Engineering Mechanics*, 118:20–39.

Zhang, W.J., Xu, Y.L. and Kwok, K.C.S. (1993) Torsional vibration and stability of wind-excited tall buildings with eccentricity. *Journal of Wind Engineering & Industrial Aerodynamics*, 50:299–309.

10
Large roofs and sports stadiums

10.1 Introduction

Wind loading is usually the dominant structural loading on the roofs of large buildings such as entertainment or exhibition centres, closed or partially closed sports buildings, aircraft hangars, etc. The wind loads on these structures have some significant differences in comparison with those on the roofs of smaller low-rise buildings that justifies separate treatment:

- The quasi-steady approach (Section 4.6.2), although appropriate for small buildings, is not applicable for large roofs.
- Resonant effects, although not dominant, can be significant.

These roofs are commonly of low pitch and experience large areas of attached flow, with low correlations between the pressure fluctuations acting on different parts. Downward as well as upward external pressures can be significant. These roofs are often arched or domed structures, which are sensitive to the distributions of wind loads, and the possibility of critical 'unbalanced' pressure distributions should be considered.

This chapter will first consider the aerodynamic aspects of wind flow over large roofs, which will facilitate an understanding of the steady and fluctuating components of wind pressures acting on these structures. Then methods of obtaining design wind loads are described, with emphasis on the method of effective static wind load distributions, introduced in earlier chapters. The incorporation of resonant contributions is also discussed.

10.2 Wind flow over large roofs

Figure 8.5 shows the main features of the flow over a low-pitched roof, with the wind blowing normal to one wall. At the top of the windward wall, the flow 'separates' and 're-attaches' further along the roof, forming a separation 'bubble'. The turbulence in the wind flow plays an important role in determining the length of the separation bubble—high turbulence gives a shorter bubble length, low turbulence produces a longer bubble. Even in open country, turbulence intensities in wind storms are equal to 10–20% of the mean or slowly varying wind speed, and in this situation mean separation bubble lengths are equal to 2–3 wall heights.

The separation bubble region is a very important one for large roofs because the upwards pressures are the greatest in this region. In the re-attached flow region, the pressures are quite small. Thus, for very large flat or near-flat roofs, only the edge regions within 2–3 wall heights from the edge will experience large pressures, and large areas of

the roof will experience quite low pressures. The variation of mean uplift pressures, measured in some wind-tunnel tests (Davenport and Surry, 1974) for flat roofs, shown in Figure 10.1, illustrate this point. It should be noted that fluctuations in pressures occur so that downwards as well as upwards pressures can occur for short time periods. Not all codes or standards on wind loads specify these downwards pressure coefficients, as discussed in Chapter 15.

As the roof pitch increases, the point of flow separation moves away from the leading edge of the roof and, in the case of a curved or arched roof, separation usually occurs downstream of the apex (Figure 10.2, from Blessmann, 1991). Upwind of the separation point, the pressures may be downwards (positive) or upwards (negative) near the leading edge, depending on the rise to span ratio, but are always upwards at the apex. Downwind of the separation point, they are upwards with small magnitudes.

The form of the net mean pressure coefficient distribution (i.e. the top surface pressure minus the bottom surface pressure) on a large cantilevered stadium roof is shown in Figure 10.3. Negative values indicate net upwards pressure differences. The largest uplift occurs at the leading edge and reduces to a small pressure difference at the rear. The top surface experiences flow separation, so that the characteristic pressure distribution peaks at the leading edge and reduces quite rapidly downstream. Underneath, the flow stagnates at the back of the grandstand, if there is no gap present, to reach a pressure approaching the dynamic pressure of the free stream. However, the underside pressure will reduce in magnitude with increasing vent gaps at the back of the grandstand.

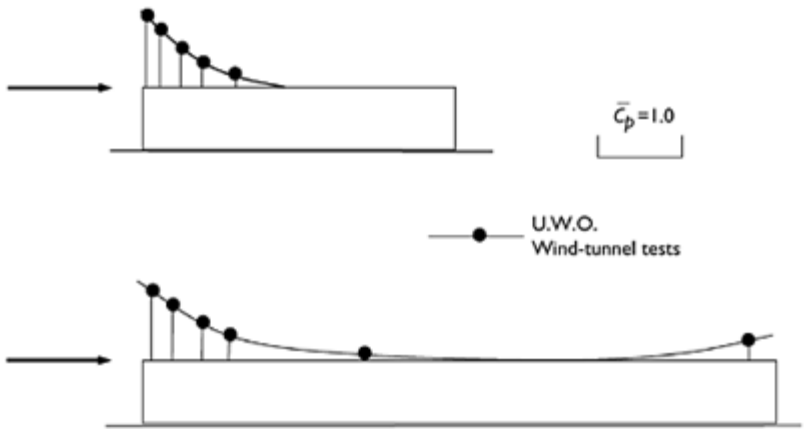

Figure 10.1 Mean pressure distributions on flat roofs.

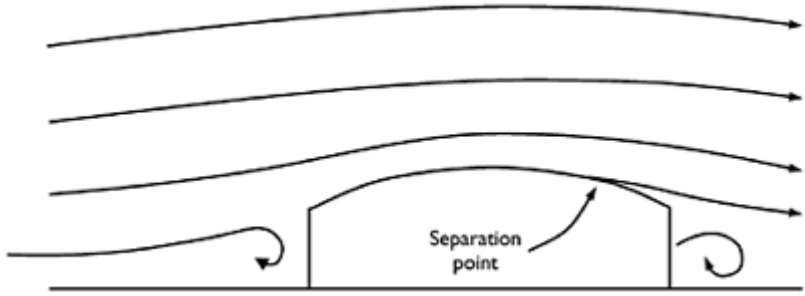

Figure 10.2 Flow separations over arched roofs (from Blessmann, 1991).

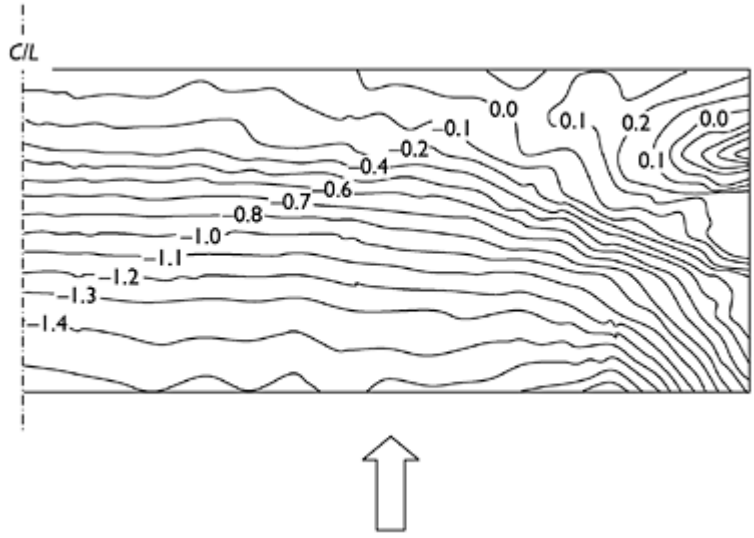

Figure 10.3 Mean net pressure distributions on a cantilevered stadium roof (from Lam and To, 1995).

10.3 Arched and domed roofs

Arched roofs are structurally efficient and are popular for structures like aircraft hangars and enclosed sports arenas, which require large clear spans. Figure 10.4 shows the geometric variables that are relevant to the wind loading of arched-roof buildings. The variables are: the span, *S;* the length, *L;* the rise, *R;* the height of the walls to the eaves level, h_e.

Some very early studies on arched roofs were carried out in an aeronautical wind tunnel in the Soviet Union in the 1920s (Bounkin and Tcheremoukhin, 1928). These data

found their way into a number of national codes and standards on wind loading and are still widely used at the present day, after reference by the American Society of Civil Engineers (1936). Some early full-scale measurements on the Akron Airship Hangar, which had an arched roof of high rise-to-span ratio, were described by Arnstein and Klemperer (1936).

Arched roofs were apparently given very little attention by researchers after 1936 until the 1980s. Grillaud (1981) described full-scale studies of wind loads on an inflatable structure, and Hoxey and Richardson (1983) also measured full-scale loads on film plastic greenhouses. Both these structures had rise/span ratios of 0.5. Holmes (1984) carried out wind-tunnel measurements on a single aircraft hangar model with a rise/span ratio *(R/S)* of 0.20. Although the latter tests were carried out at low Reynolds numbers, the curved roof surface was roughened. The effect of a ridge ventilator on the apex of the roof was also investigated and found to be significant. A significant aspect of the latter work was an early attempt to establish effective static load distributions for load effects such as axial forces and bending moments in the arch.

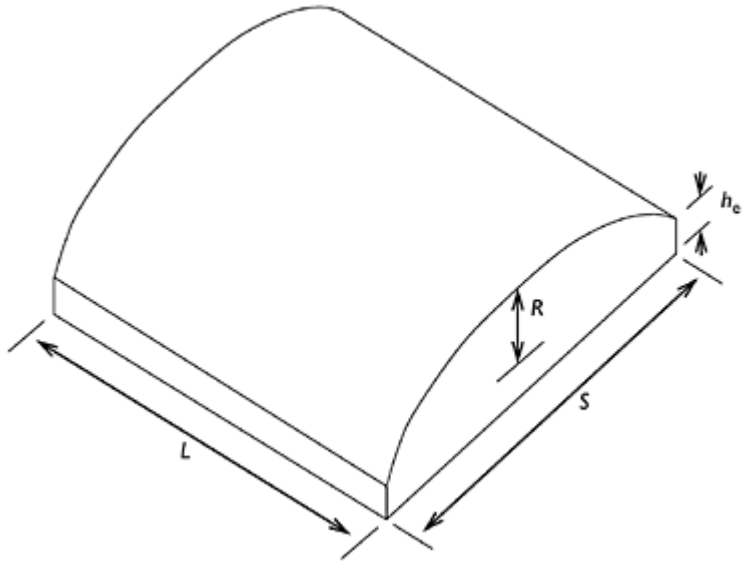

Figure 10.4 Geometric parameters for arched-roof buildings.

Johnson *et al.* (1985) reviewed existing model and full-scale data and described some new wind-tunnel results from the University of Western Ontario. They found significant Reynolds number effects in their wind-tunnel data for models with a rise/span ratio of 0.5.

Toy and Tahouri (1988) carried out measurements on models of semi-cylindrical structures (*R/S*=0.5; *he/R*=0). These wind-tunnel measurements were carried out with a smooth-wall boundary flow (very high Jensen number—see Section 4.4.5), as well as low Reynolds number (6.6×10^4, based on model height), and so the results are questionable in

terms of applicability to full-scale structures. However, the data are useful in illustrating the strong effect of length/span ratio *(L/S)* on the mean pressures near the crest of the roofs. In this study, the effects of lengthening the cross-section to produce a 'flat top' and shortening it to produce a 'ridge' were also investigated. The latter modification has a particularity strong effect in modifying the mean pressure distribution over the roof.

Cook (1990), as well as describing the measurements of Toy and Tahouri in some detail, also discusses some work carried out by Blessmann (1987a,b) on arched roofs mounted on flat vertical walls. It is suggested that flow separations occur at the eave when the roof pitch angle there is less than about 30°.

In a computational study of mean wind pressures (Paterson and Holmes, 1993), 11 separate geometrical configurations were examined. Figures 10.5 and 10.6 show the computed mean external pressure coefficients on a building with a rise/span ratio *(R/S)* of 0.2, a length/span ratio *(L/S)* of 1.0 and a height to eaves/rise ratio (h_e/R) of 0.45, for wind directions of 0° and 45° from the normal to the axis of the arch. Because of symmetry, values on one-half only are shown for the 0° case.

For the 0° direction, positive pressure coefficients occur on the windward wall and the windward edge of the roof, with negative values over the rest of the structure. The highest magnitude negative values occur just upwind of the apex to the roof.

At a wind direction of 45°, positive pressures only occur near the windward corner of the building. The negative pressures on the roof and walls are generally higher than those obtained for the 0° case, with particularly high suctions occurring along the windward end of the arch roof.

The effect of rise/span ratio is illustrated in Figure 10.7. The rise/span ratio of the building in this figure is 0.50, compared with the building in Figures 10.5 and 10.6, which has a rise/span of 0.20. It should be noted that the reference dynamic pressure $(\frac{1}{2}\rho_a\overline{U_h^2})$ is taken as the apex height of the structure in both cases, so that for a fixed span and wall height, the reference dynamic pressure will increase with increasing rise/span ratio.

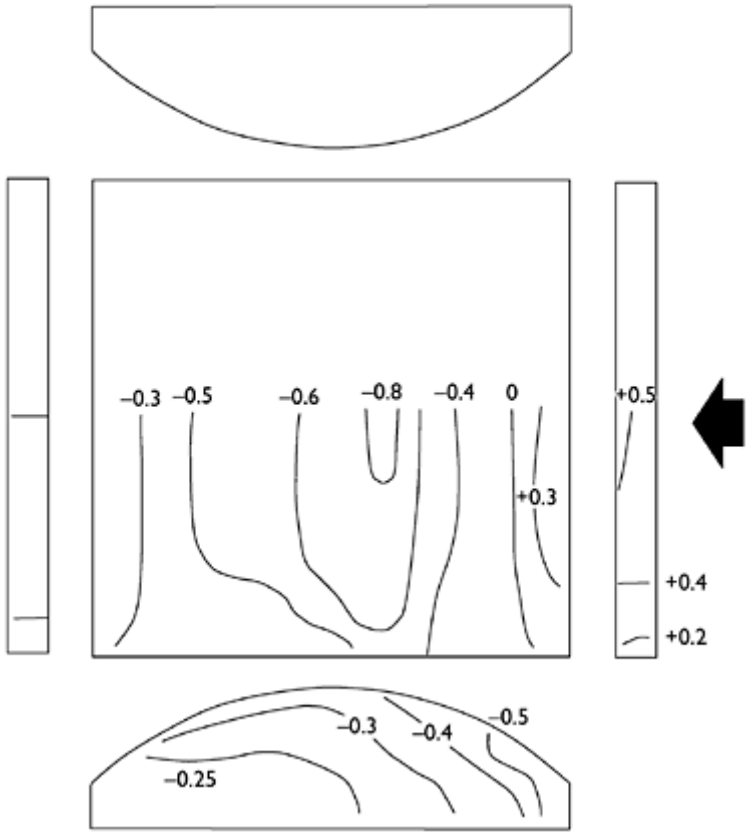

Figure 10.5 Mean pressure coefficients on an arched-roof building—0° (rise/span=0.2).

As for high-pitch gable roofs (Figure 8.6) there is a region of positive pressure on the windward side of the roof.

The effect of increasing length/span ratio is to increase the magnitude of both the positive and negative pressures in the central part of the building as the flow becomes more two dimensional. Increasing wall height to rise ratio (h_e/R) produces more negative values of external pressure coefficient on the roof, side walls and leeward wall (Paterson and Holmes, 1993).

For wind directions parallel to the axis of the arch, arched roofs are aerodynamically flat, with similar pressure distributions as gable roofs, for the same wind direction.

Domed roofs have similar pressure distributions as those on arched roofs, of the same rise/span ratio, for a wind direction normal to the axis.

Values of pressure coefficients for arched and domed buildings, specified in several wind loading codes and standards, are discussed in Chapter 15.

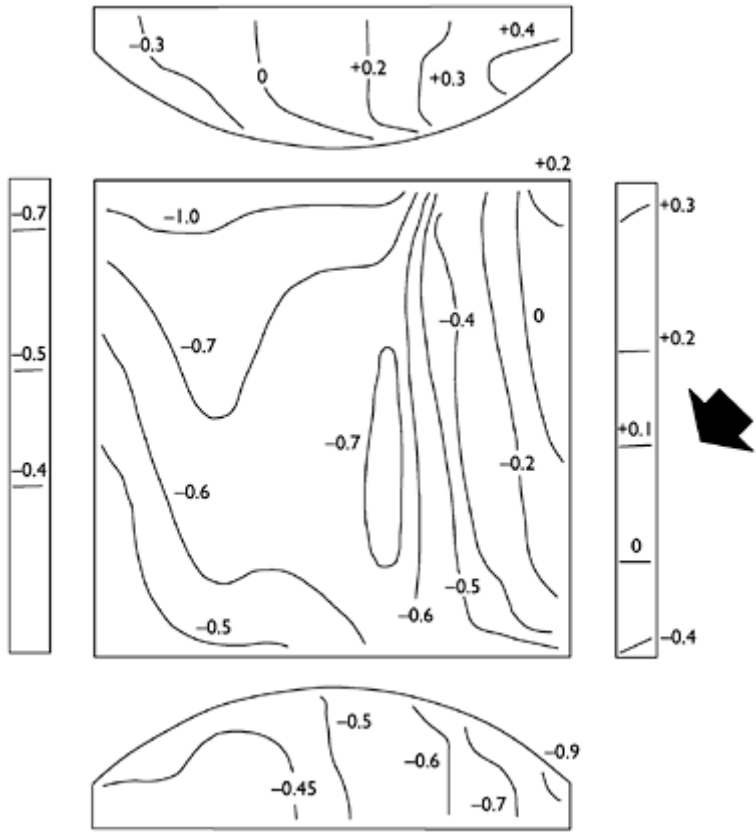

Figure 10.6 Mean pressure coefficients on an arched-roof building—45° (rise/span=0.2).

10.4 Effective static load distributions

Because of the large fluctuating component in the wind loading on large roofs, the statistical correlation between pressures separated by large distances can be quite small. Designers can make use of this, to the advantage of the cost of the structure, by determining effective static load distributions. This approach enables realistic and economical design wind load distributions to be obtained using wind-tunnel tests. Two methods are possible:

- A direct approach in which simultaneous time histories of fluctuating pressures from the whole roof are recorded and stored. These are subsequently weighted with structural influence coefficients to obtain time histories of load effects. The instantaneous pressure distributions coinciding with peak load effects are then identified and averaged.

• In the other approach, correlations between pressure fluctuations at different parts of the roof are obtained, and expected pressure distributions corresponding to peak load effects are obtained using methods discussed in Chapter 5.

The effective static load distribution method, discussed in Section 5.4, tries to simplify the complex time and space variation of wind pressures on structures (produced by upwind turbulence and local building-induced effects) into a number of effective static pressure

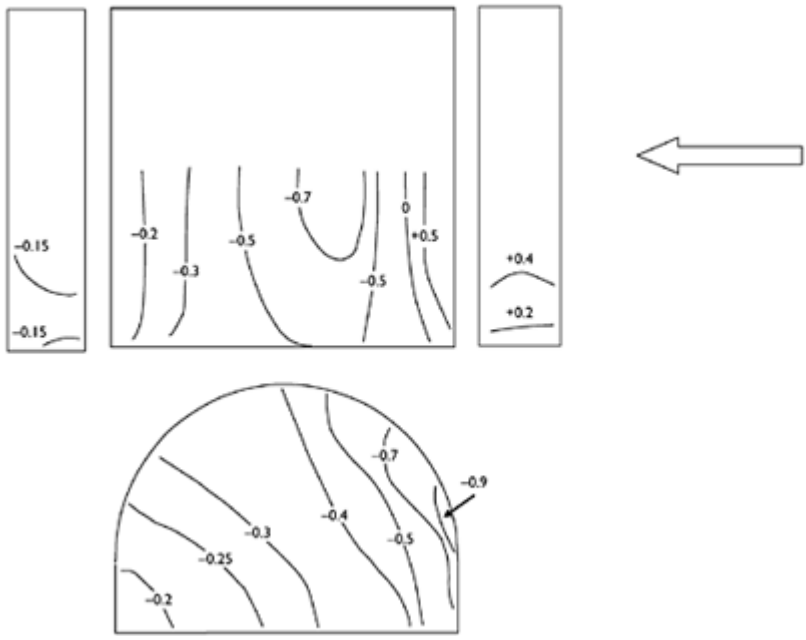

Figure 10.7 Mean pressure coefficients on an arched-roof building (rise/span=0.5).

distributions for structural design. It is a particularly appropriate method for large roofs, over which the pressure fluctuations are not strongly correlated (or statistically related to each other). Significant reductions in design load effects, such as axial forces and bending moments in major structural members, can be obtained by this method, although wind-tunnel tests are normally required to obtain the necessary statistical data.

The principles behind the method as applied to large roofs are illustrated in Figure 10.8. In this figure, a section through a large arched roof is shown and the instantaneous external pressure distributions at three different points in time are shown. Clearly, there are considerable variations from time to time in these loadings. The variations are due to turbulence in the approaching wind flow and local effects such as vortex shedding at the

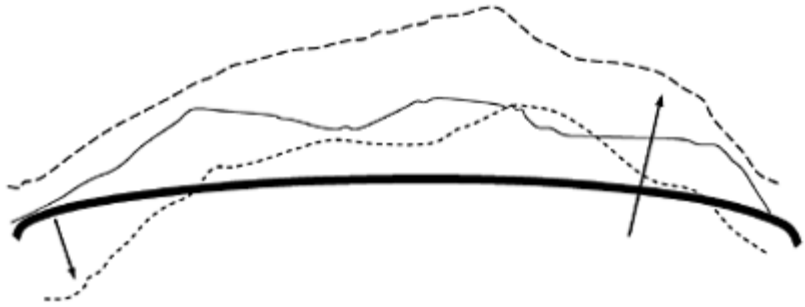

Figure 10.8 Instantaneous pressure distributions at three different times.

leading edge of the roof. The mean pressure distribution indicates only the average pressure at each point, but this distribution usually forms the basis for the design distributions of pressure found in codes. However, the instantaneous pressure distributions producing the largest load effects may be quite different in shape to the mean.

The question of interest to the structural engineer is: what are the critical instantaneous distributions which produce the largest structural load effects in the structure? The maximum and minimum values of each load effect will be produced by two particular expected instantaneous pressure distributions, which can be determined. The main factors determining these distributions are:

- the influence line for the load effect—(an example of the influence line for a bending moment in an arch is given in Figure 5.8); and
- the correlation properties of the wind pressures acting on the roof (both internal and external).

The influence lines can be calculated by the structural engineer, by applying point loads in a static structural analysis, and the correlation information can be obtained easily from wind-tunnel tests.

The effective static loading distributions for the various load effects of interest can be obtained by the formula developed by Kasperski and Niemann (1992) (see also Kasperski, 1992). Examples of two of these distributions are given in Figure 5.10 in Chapter 5. The distributions for a support reaction and a bending moment are shown. Clearly these two distributions differ considerably from each other, due to the different influence lines for the two load effects. They also differ from the mean pressure distribution. The shaded area in Figure 5.10 indicates the limits of the instantaneous maximum and minimum peak pressures around the arch, which form an ‘envelope’ within which the effective static loading distributions must fall.

When applying the effective static wind load distribution approach to large roofs, usually a limited number of load effects are considered and effective static load distributions are computed for them. These are then ‘enveloped’ to give a smaller number of wind pressure distributions, which are then used by the structural engineers to design all the members of the structure. If required by structural designers, the peak values

of critical load effects, such as forces in main members, or deflections can be directly computed.

10.4.1 Contributions of resonant components

When considering dynamic response of any structure to wind, it is necessary to distinguish between the resonant response at or near the natural frequencies of the structure and the fluctuating response at frequencies below the first or lowest frequency, or 'background response', which is usually the largest contributor. As for all structures, the significance of resonant dynamic response to wind for large roofs depends on the natural frequencies of vibration, which are in turn dependent on the mass (inertia) and stiffness properties, and the damping. For roofs which are supported on two or four sides in the case of a rectangular plan or all the way round in the case of a circular plan, the stiffness is usually high enough that resonant response is very small and can be ignored. For totally enclosed buildings, additional stiffness is provided by compression of the air inside the building. Also there is additional positive aerodynamic damping which further acts to mitigate any resonant dynamic response.

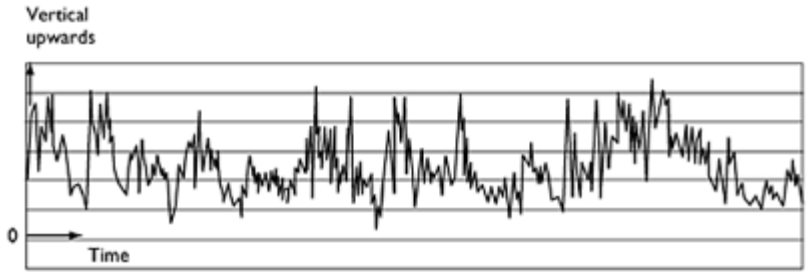

Figure 10.9 Vertical displacement of the leading edge of a cantilevered roof showing some resonant contributions to the response (from Melbourne, 1995).

Extra large stadium roofs may have several natural frequencies below 1 Hz, although these can be expected to have quite high damping.

Roofs supported on one side only, i.e. cantilevered roofs, however, are more prone to significant resonant response due to the lower stiffness. Figure 10.9 shows some resonant response in the time history of vertical deflection at the leading edge of a model cantilevered roof in wind-tunnel tests. The use of stiffening cables often increases the stiffness sufficiently to reduce the resonant contribution to minor proportions.

Most codes and standards do not include the effects of resonant response on large roofs—the Australian Standard AS/NZS1170.2 (Standards Australia, 2002) is an exception—it contains a design load distribution which is dependent on the natural frequency.

If resonant response is anticipated to be substantial on a large roof, wind-tunnel testing with an aeroelastic model is often recommended. These can be very useful but have limitations, in that accurate effective load distributions cannot be determined from them,

and the structural stiffness cannot be altered to accommodate design changes once the model has been built. For important structures, a rigid pressure model test is also advisable to obtain the distributions in pressure for the mean and background components, as discussed earlier. The resonant response can also be computed from the spectra and cross-spectra of the fluctuating pressures at the natural frequency or from the time histories of the generalized forces in the contributing modes of vibration. Either method is computationally complex and requires simultaneous pressure measurement over the entire roof (including the underside pressure for an open stadium roof), but this is certainly feasible and has been used for large projects at wind-tunnel laboratories in Australia and elsewhere.

Usually the resonant response will comprise no more than 10–20% of the peak values of critical load effects (Holmes *et al.*, 1997), and this contribution can be calculated separately and added to the fluctuating background response using a 'root-sum-of-squares approach'. The effective static load distribution corresponding to each peak load effect can then scaled up to match the recalculated peak load effect.

For very large roofs, several resonant modes can contribute, and the evaluation of effective static loads becomes more difficult. In general, it is necessary to adopt the approach of Section 5.3.7 in which the background response is separated from the resonant components, as these components all have different loading distributions. The magnitude of the contribution from each resonant mode depends on the load effect through its influence line. Section 12.3.4 describes the application of the equivalent static load approach to long-span bridges, when more than one resonant mode contributes. This approach can also be applied to very large roofs; in this case, the background contribution is treated as an additional 'mode', for which the effective load distribution is calculated separately.

Thus, the effective static load distribution for the combined background and resonant contributions is:

$$p'_{\text{eff}}(x) = W_{\text{B}}' \cdot p_{\text{eff,back}}(x) + \sum_{j}^{N} W_j' m(x)\phi_j(x) \tag{10.1}$$

where the weighting factors are given by:

$$W'_{\text{B}} = \frac{\sigma_{r,\text{B}}}{\left\{\sigma_{r,\text{B}}{}^2 + \sum_{j=1}^{N} \alpha_j{}^2 \omega_j{}^4 \overline{a_j{}^2}\right\}^{1/2}} \tag{10.2}$$

$$W'_j = \frac{\alpha_j \omega_j{}^4 \overline{a_j{}^2}}{\left\{\sigma_{r,\text{B}}{}^2 + \sum_{j=1}^{N} \alpha_j{}^2 \omega_j{}^4 \overline{a_j{}^2}\right\}^{1/2}} \tag{10.3}$$

where $\sigma_{\text{r,B}}$ is the background component of the load effect, and the other terms are defined in Section 12.3.4. The derivation of the background effective static load distribution, $P_{\text{eff,back}}(x)$, is described in Chapter 5.

10.5 Wind-tunnel methods

As discussed in previous sections, large roofs are usually dominated by the mean wind pressures and the background fluctuating components. Resonant contributions to the wind-induced structural load effects are usually small, even though natural frequencies as low as 0.5 Hz can occur for the largest roofs. The main reason for this behaviour is the nature of the separating-reattaching flow over large roofs of low pitch, and the consequent very low correlations between fluctuating pressures acting on different parts of the roof. Excitation of a dynamic mode requires pressure 'modes' which are coincident with the mode shape, at the modal frequency in question. Usually the excitation energy satisfying these conditions is small. Another reason for low resonant response is high damping with significant positive contributions from aerodynamic damping (Section 5.5.1).

For the reasons given above, modern wind-tunnel testing of large roofs for sports stadiums or arenas is usually carried out with rigid models on which detailed pressure measurements are made. The techniques used are described in Section 7.6.7. Using recorded time histories of fluctuating pressures, computations can be made of the resonant contributions and added to the mean and background fluctuating contributions.

Full aeroelastic models of large roofs, although used quite frequently in the past, are now much less common. They are quite expensive to design and build, are structure dependent and do not lend themselves to changes in the underlying structure during the design process. Also they can only normally be used for deflection measurements. However, for very flexible cantilevered roofs, the use of aeroelastic models may be required in conjunction with tests on rigid models.

10.6 Test cases

The effective static wind load distribution method (Section 10.4), based on the measurement of correlations between fluctuating pressures on panels on different parts of the roof, as applied in conjunction with wind-tunnel tests to two large stadium roofs is described by Holmes *et al.* (1997). This reference also discusses the effects of resonant load components. Some results from that study are given in Figure 10.10.

The alternative approach, based on the direct weighting of the recorded fluctuating pressures by influence coefficients, is described by Xie (2000). This is a case study of a stadium roof consisting of two large cantilevered panels with a complex curvature.

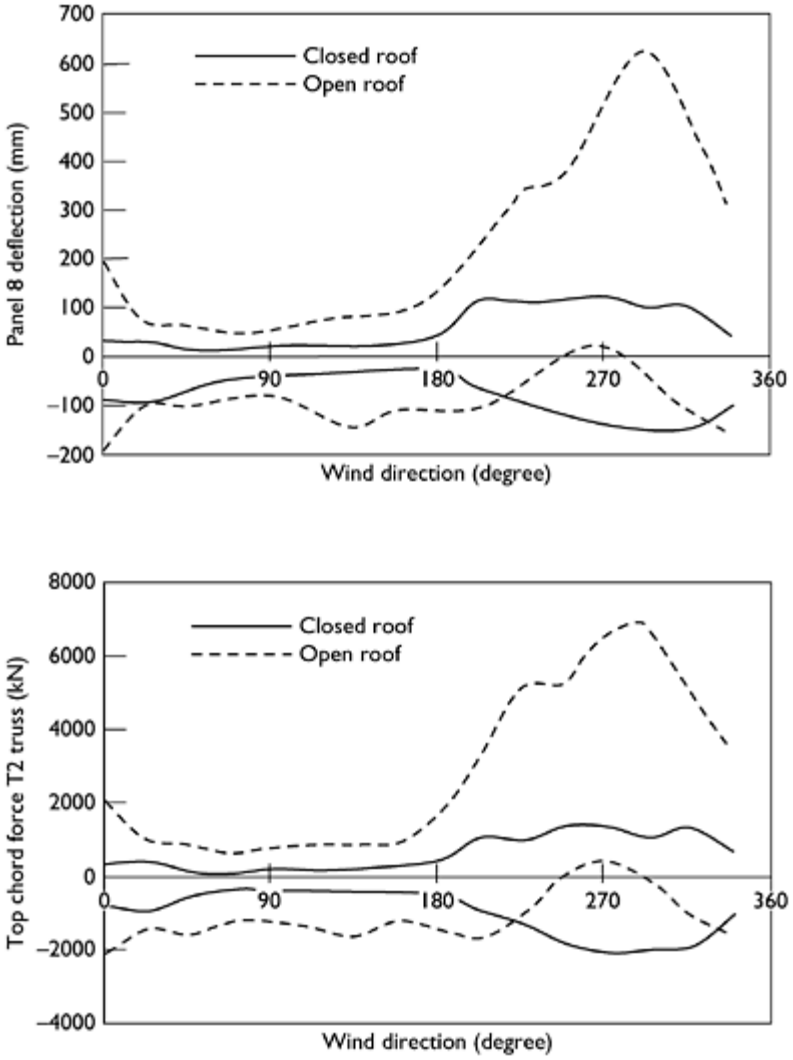

Figure 10.10 Variation of a deflection and a main truss force for a large stadium roof computed from a wind-tunnel pressure model test (from Holmes *et al.*, 1997).

10.7 Summary

This chapter has attempted to cover the main aspects of wind loads on large roofs, including those used increasingly for sports stadiums. The characteristics of air flow and mean pressure distributions on flat, arched and domed roofs are discussed. There is some overlap with Chapter 8, but there are some significant differences namely the large effects of the reduced correlations between fluctuating pressures over large expanses of low-pitch roofs and the possibility of some resonant response contributions.

The application of wind-tunnel methods, using pressure measurements on rigid models, to the determination of effective static wind load distributions is discussed.

References

American Society of Civil Engineers (1936) Wind-bracing in steel buildings. Fifth Progress Report of Sub-Committee No. 31. *Proceedings ASCE*, March, pp. 397–412.

Arnstein, K. and Klemperer, W. (1936) Wind pressures on the Akron Airship-dock. *Journal of the Aeronautical Sciences*, 3:88–90.

Blessmann, J. (1987a) Acao do vento em coberturas curvas, la Parte. Caderno Tecnico CT-86. Universidade Federale do Rio Grande do Sul.

Blessmann, J. (1987b) Vento em coberturas curvas—pavilhoes vizinhos. Caderno Tecnico CT-88. Universidade Federale do Rio Grande do Sul.

Blessmann, J. (1991) Acao do vento em telhados. SAGRA, Porto Alegre, Brazil.

Bounkin, A. and Tcheremoukhin, A. (1928) Wind pressures on roofs of buildings. Transactions, Central Aero- and Hydrodynamical Institute, Moscow, No. 35.

Cook, N.J. (1990) *The Designer's Guide to Wind Loading of Building Structures. Part. 2. Static Structures.* Building Research Establishment, London.

Davenport, A.G. and Surry, D. (1974) The pressures on low-rise structures in turbulent wind. *Canadian Structural Engineering Conference*, Toronto.

Grillaud, G. (1981) Effet du vent sur une structure gonflable. *Colloque, 'Construire avec le vent'*, Nantes, France, June.

Holmes, J.D. (1984) Determination of wind loads for an arch roof. *Civil Engineering Transactions, Institution of Engineers, Australia*, CE26:247–53.

Holmes, J.D., Denoon, R.O., Kwok, K.C.S. and Glanville, M.J. (1997) Wind loading and response of large stadium roofs. *Proceedings, IASS International Symposium '97 on Shell and Spatial Structures*, Singapore, 10–14 November.

Hoxey, R. and Richardson, G.M. (1983) Wind loads on film plastic greenhouses. *Journal of Wind Engineering & Industrial Aerodynamics*, 11:225–37.

Johnson, G.L., Surry, D. and Ng, W.K. (1985) Turbulent wind loads on arch-roof structures: a review of model and full-scale results and the effect of Reynolds number. *5th US National Conference on Wind Engineering*, Lubbock, TX, 6–8 November.

Kasperski, M. (1992) Extreme wind load distributions for linear and nonlinear design. *Engineering Structures*, 14:27–34.

Kasperski, M. and Niemann, H.-J. (1992) The L.R.C. (load-response-correlation) method: a general method of estimating unfavourable wind load distributions for linear and nonlinear structural behaviour. *Journal of Wind Engineering & Industrial Aerodynamics*, 43: 1753–63.

Lam, K.M. and To, A.P. (1995) Generation of wind loads on a horizontal grandstand roof of large aspect ratio. *Journal of Wind Engineering & Industrial Aerodynamics*, 54–55:345–57.

Melbourne, W.H. (1995) The response of large roofs to wind action. *Journal of Wind Engineering & Industrial Aerodynamics*, 54–55:325–35.

Paterson, D.A. and Holmes, J.D. (1993) Mean wind pressures on arched-roof buildings by computation. *Journal of Wind Engineering & Industrial Aerodynamics*, 50:235–43.

Standards Australia (2002) Structural design actions. Part 2: wind actions, AS/NZS 1170.2:2002. Standards Australia, Sydney.

Toy, N. and Tahouri, B. (1988) Pressure distributions on semi-cylindrical structures of different geometrical cross-sections. *Journal of Wind Engineering & Industrial Aerodynamics*, 29: 263–72.

Xie, J. (2000) Gust factors for wind loads on large roofs. *First International Symposium on Wind and Structures*, Cheju, Korea, January.

11
Towers, chimneys and masts

11.1 Introduction

In this chapter the wind loading and wind-induced response of a variety of slender vertical structures will be considered: chimneys of circular cross-section, free-standing lattice towers, observation towers of varying cross-section, poles carrying lighting arrays or mobile telephone antennas and guyed masts. Natural draft cooling towers, although not slender, are large wind-sensitive structures; the loading and response under wind action of these structures will be considered briefly in Section 11.7.

The methodology for determination of the loading and response of slender structures will first be described (making use of the general principles outlined in Chapters 1–7) and then followed by descriptions of several test case examples.

The dynamic response to wind of slender structures is quite similar in nature to that of tall buildings (described in Chapter 9). There are some significant differences, however:

- Fundamental mode shapes are generally non-linear.
- Higher modes are more likely to be significant in the resonant dynamic response.
- As the aspect ratio is higher—i.e. the width is much less than the height, aerodynamic 'strip' theory can be applied. That is total aerodynamic coefficients for the cross-section can be used with the wind properties upstream, at the same height.
- If the mass per unit height is low, aerodynamic damping (Section 5.5.1) will be significant.
- As for tall buildings, cross-wind response can be significant (except for lattice structures). However, because of the smaller cross-wind breadth, the velocity at which the vortex-shedding frequency (or the maximum frequency of the cross-wind force spectrum) coincides with the first mode vibration frequency is usually much lower than for tall buildings, and within the range of frequently occurring mean wind speeds.

11.2 Historical

11.2.1 Lattice towers

When the Eiffel Tower in Paris was completed in 1889, at 300 m it was easily the tallest structure in the world, and one of the first major towers of lattice construction. The designer Gustav Eiffel described the wind loading assumptions used in the design in an address to the Societe′ des Ingenieurs Civils (Eiffel, 1885). He assumed a static horizontal pressure of 2kPa at the base increasing to 4kPa at the top. Over a large part of

the top and base of the tower, he replaced the area of members in the lattice with solid surfaces with the same enclosed area. In the middle section where the tower

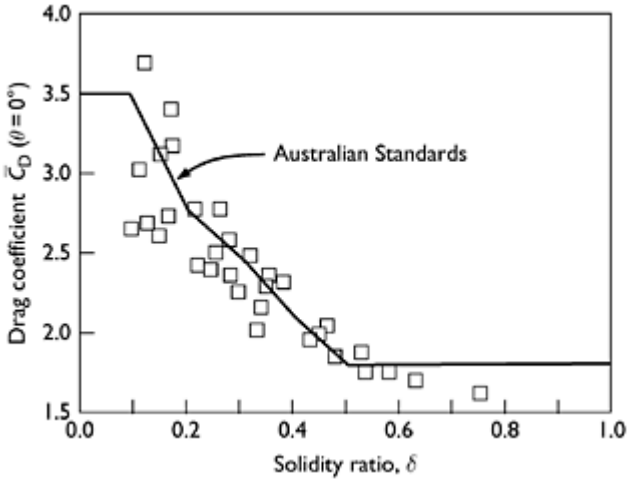

Figure 11.1 Drag coefficients for square towers with flat-sided members.

solidity is lower, he assumed a frontal area equal to 'four times the actual area of iron'. These very conservative assumptions, of course, resulted in a very stiff structure with no serviceability problems in strong winds.

Eiffel constructed a laboratory at the top of the tower and carried out various scientific experiments, including measurements of the deflection of the tower, using a telescope aimed vertically at the target at the top. Some of these measurements were later analysed by Davenport (1975). These indicated that the effective drag coefficient used in the design was approximately 3.5 times that required to produce the measured deflections, and currently used in design for a tower with a solidity of about 0.3 (see Figure 11.1).

Later on the tower, Eiffel, perhaps concerned with the over-conservatism of his designs, carried out some experiments on wind forces on simple plates.

Development of high-voltage power transmission, and radio and television broadcasting, from the 1920s onwards promoted the efficient use of steel for lattice tower construction.

11.2.2 Tall chimneys

In the nineteenth and early twentieth centuries, most factory and power station chimneys were of masonry construction. With the known weakness of masonry joints to resist tension, these structures would have relied on dead load to resist the overturning effect of wind loads. Although undoubtedly many of these failed in severe windstorms, Kernot commented in 1893 that: "…there are thousands of such chimneys in existence, many in very open and exposed situations, which, apart from the adhesion of the mortar, would infallibly overturn with a pressure of not more that 15 pounds per square foot"

(Kernot, 1893). Kernot concluded that the currently used design wind pressures were overconservative (perhaps an early recognition of the effect of correlation) and proceeded to carry out some important early research in wind loads (see Section 7.2.1 and Figure 7.1).

The first full-scale wind pressure measurements on a cylindrical chimney were performed by Dryden and Hill on the newly erected masonry chimney of the power plant of the Bureau of Standards near Washington, DC (Dryden and Hill, 1930). These measurements were carried out together with full-scale measurements on another shorter cylinder (aspect ratio of 3) mounted on a roof and wind-tunnel measurements on circular cylinders. Through comparison of the resulting pressure distributions, this important study recognized, at an early stage, the effects of Reynolds number, surface roughness (Section 4.5.1) and aspect ratio (Section 4.5.2) on the pressure distribution and drag coefficients of slender circular cylinders.

In the 1950s, extensive work on the cross-wind vibration of steel chimneys was carried out at the National Physical Laboratory (NPL) in the United Kingdom under the direction of C. ('Kit') Scruton. This work (e.g. Scruton and Flint, 1964) included some important measurements on circular cylinders obtained in a compressed air wind tunnel and the development of the now-ubiquitous helical strakes for the mitigation of vibration due to vortex shedding on tall chimneys (Section 4.6.3 and Figure 4.23).

11.3 Basic drag coefficients for tower sections

11.3.1 Drag coefficients for solid cross-sections

Many observation towers, communication towers and chimneys have cross-sections which are circular or square. Drag coefficients for these cross-sections were discussed in Chapter 4. The effect of aspect ratios less than 20 is significant on the effective total drag coefficient (see Figures 4.10 and 4.19). Other cross-sections may require wind-tunnel tests to determine drag coefficients.

The mean or time-averaged drag force per unit height, and hence bending moments, can be calculated using an appropriate sectional drag coefficient with a wind speed appropriate to the height, using an appropriate expression for mean wind speed profile (see Equation 5.32).

11.3.2 Drag coefficients for lattice towers

A basic formula for drag force for winds blowing at any angle to a face of a rectangular lattice tower is:

$$D = C_D \cdot A_z \cdot q_z \tag{11.1}$$

where D is the drag force on a complete tower panel section (i.e. all four sides of a square section tower); C_D the drag coefficient for the complete tower section—it depends on the solidity of a face, and the wind direction; A_z the projected area of tower members in one

face of the tower and $q_z (= \frac{1}{2}\rho_a U_z^2)$ the dynamic wind pressure at the average height, z, of the panel under consideration.

Figure 11.1 shows the values of C_D specified in the Australian Standard for steel lattice towers, AS3995 (Standards Australia, 1994) for square sections with flat-sided members, as a function of the solidity, compared with experimental values obtained from windtunnel tests for wind blowing normally to a face. For the range of solidity from 0.1 to 0.5, the following equations are appropriate (from Bayar, 1986):

$$C_D=4.2–1\delta \text{ (for } \delta<0.2) \tag{11.2}$$

$$C_D=3.5–3.5\delta \text{ (for } 0.2<\delta<0.5) \tag{11.3}$$

The ASCE Guidelines (1990) and CSIR Recommendations (1990) for transmission line structures give equations for the wind drag force on a section of a lattice tower for any arbitrary wind direction, θ, with respect to the face of the tower. The CSIR equation may be written as follows:

$$D=q_z[C_{dn1}A_{n1}\cos^2\theta+C_{dn2}\cdot A_{n2}\sin^2\theta]K_\theta \tag{11.4}$$

where C_{dn1}, C_{dn2} are drag coefficients for wind normal to adjacent faces, 1 and 2, of the tower; A_{n1}, A_{n2} the total projected areas of faces 1 and 2, respectively; θ the angle of incidence of the wind with respect to the normal to face 1 of the tower; K_θ a wind incidence factor (derived empirically), given by:

$$K_\theta=1+0.55\cdot\delta\cdot\sin^2(2\theta) \tag{11.5}$$

where δ is the solidity ratio (for $0.2\leq\delta\leq0.5$).

The ASCE Guidelines (1990) give a similar form to Equation (11.4), with a slightly different form for K_θ.

The drag of a lattice tower can also be computed by summing the contributions from every member. However, this is a complex calculation, as the effect of varying pitch and yaw angles on the various members must be considered. This method also cannot easily account for interference and shielding effects between members and faces.

11.4 Dynamic along-wind response of tall slender towers

The application of random vibration theory to the along-wind response of structures with distributed mass is discussed in Sections 5.3.6 and 5.3.7. The application of the equivalent static load distribution method to the along-wind response of tall structures is described in Section 5.4. These methods are applicable to all the structures covered in this chapter. However, a simple gust response factor (Section 5.3.2), in which a single multiplier, G, is applied to the mean pressure distribution or a structural response derived from it, is generally not applicable in its simplest form to slender structures.

Modifications are required to allow for a varying gust response factor, depending on the height, *s*, at which the load effect is required. A similar argument applies when a dynamic response factor approach is used (Section 5.3.4).

Two effects produce an increase in the gust response factor with height of load effect:

- the curved mode shape which gives an increasing contribution from the resonant component as the height, *s*, increases;
- as wind gusts of size equal to, or greater than, the distance *(h−s)* between the height, *s*, and height of the top of the structure, *h*, are fully effective in producing stresses at the level *s*, the background contribution also increases as the height *s* increases.

An analysis for slender towers (Holmes, 1994) gives the following expressions for the gust response factors for shearing force, G_q, and bending moment, G_m, at any arbitrary height level, *s*, on a tower:

$$G_q = 1 + \frac{r\sqrt{g_B^2 B_s F_2 + g_R^2 \left(\frac{SE}{\eta_1}\right) F_3 F_4 F_5}}{F_1} \tag{11.6}$$

$$G_m = 1 + \frac{r\sqrt{g_B^2 B_s F_7 + g_R^2 \left(\frac{SE}{\eta_1}\right) F_3 F_4 F_8}}{F_6} \tag{11.7}$$

where *r* is a roughness factor (=$2I_u$), i.e. twice the longitudinal turbulence intensity at the top of the tower (Section 3.3.1); B_s a background factor reflecting the reduction in correlation of the fluctuating loads between the height level *s* and the top of the tower (Section 4.6.6); g_B and g_R the peak factors (Section 5.3.3) separately calculated for the background and resonant components; *S* a size factor representing the aerodynamic admittance (Section 5.3.1) evaluated at the natural frequency of the tower; $E = \pi n_1 S_u(n_1)/4\sigma_u^2$ a non-dimensional form of the spectral density of longitudinal turbulence (Section 3.3.4) evaluated at the natural frequency of the tower; η_1 the critical damping ratio for the first mode of vibration (this should also include aerodynamic damping contributions) and F_1 to F_8 non-dimensional parameters depending on properties of the approaching wind and geometrical and dynamic properties of the tower such as mean velocity profile, taper ratio, mode shape, mass distribution. They also depend on the ratio *(s/h)*, i.e. the ratio of the height level, *s*, at which the shearing force and bending moments are required, and the height of the top of the tower.

By evaluation of Equations (11.6) and (11.7) for a typical lattice tower (Holmes, 1994), it was shown that the increase in the value of gust response factor over the height of a structure will typically be in the range of 5–15%.

A similar analysis for the deflection at the top of the tower, x, gives a similar expression to Equations (11.6) and (11.7) for the gust response factor for deflection, G_x(Holmes, 1996a):

$$G_x = 1 + \frac{r\sqrt{g_B^2 B_0 F_{11} + g_R^2 \left(\frac{SE}{\eta_1}\right) F_3 F_4 F_{12}}}{F_{10}} \tag{11.8}$$

where B_0 is B_s evaluated at s equal to 0 (the reduction due to correlation over the whole height of the tower is important. F_{10}, F_{11} and F_{12} are additional non-dimensional parameters; F_{12} is a non-dimensional stiffness for the tower.

It can be seen from Equations (11.6), (11.7) and (11.8) that the gust response factor depends on the type of load effect under consideration, as well as the level on the tower at which it is evaluated.

An alternative approach for the along-wind loading and response of slender towers and chimneys is the equivalent (or effective) static load distribution approach discussed in Section 5.4 (see also Holmes, 1996b). This approach allows variations in dimension shape and mass over the height of a tower of complex shape to be easily incorporated. Examples of effective static wind load distributions derived for a 160 m tower are given in Figures 5.11 and 5.12.

11.5 Cross-wind response of tall slender towers

The strength of regular vortex shedding from a tower of uniform or slightly tapered cross-section is often strong enough to produce significant dynamic forces in the cross-wind direction. If the damping of a slender tower of a solid cross-section is low, high-amplitude vibrations can occur if the frequency of vortex shedding coincides with a natural frequency of the structure. The velocity at which this coincidence occurs is known as the *critical velocity*. If the critical velocity is very high, i.e. outside the design range, no problems should arise, as the resonant condition will not occur. Conversely, if the critical velocity is very low, there will also not be a problem as the aerodynamic excitation forces will be low. However, significant vibration could occur if a critical velocity falls in the range 10–40 m/s.

Because of the higher rate of vortex shedding for a circular cross-section compared with that for a square or rectangular section of the same cross-wind breadth, the critical velocity is significantly lower.

Methods of calculation of cross-wind response of slender towers or chimneys fall into two classes:

(i) those based on sinusoidal excitation; and
(ii) those based on random excitation.

In the following sections, methods developed mainly for structures of circular crosssection are described. However, in principle they can be applied to structures of any (constant) cross-section.

11.5.1 Sinusoidal excitation models

The assumption that the vortex-shedding phenomenon generates near-sinusoidal crosswind forces on circular cylinders can be linked to the work of Scruton and co-workers in the 1950s and 1960s (summarized in Scruton, 1981). In this formulation, the excitation forces were treated solely as a form of negative aerodynamic damping, but this is equivalent to sinusoidal excitation by applied forces. Such models are good ones for

situations in which large oscillations occur, and the shedding has 'locked-in' to the cross-wind motion of the structure (Section 5.5.4).

Sinusoidal excitation models were also proposed by Rumman (1970) and Ruscheweyh (1990).

Unlike other loading models in wind engineering, sinusoidal excitation models are *deterministic*, rather than random. The assumption of sinusoidal excitation leads to responses which are also sinusoidal.

To derive a simple formula for the maximum amplitude of vibration of a structure undergoing cross-wind vibration due to vortex shedding, the following assumptions will be made:

- sinusoidal cross-wind force variation with time;
- full correlation of the forces over the height over which they act; and
- constant amplitude of fluctuating cross-wind force coefficient.

None of these assumptions are very accurate for structures vibrating in the turbulent natural wind. However, they are useful for simple initial calculations to determine whether vortex-induced vibrations are a potential problem.

The structure is assumed to vibrate in the jth mode of vibration (in practice *j* will be equal to 1 or 2), so that Equation (5.17) applies:

$$G_j\ddot{a}_j + C_j\dot{a}_j + K_j a_j = Q_j(t)$$

where *Gj* is the generalized mass equal to $\int_0^h m(z)\phi_j^2(z)\mathrm{d}z$; $m(z)$ the mass per unit length along the structure; *h* the height of the structure; *Cj* the modal damping; *Kj* the modal stiffness; ωj the natural undamped circular frequency for the jth mode$(=2\pi n_j = \sqrt{K_j/G_j})$; *Qj(t)* the generalized force, equal to $\int_{z_1}^{z_2} f(z,t)\phi_j(z)\mathrm{d}z$, where *f(z, t)* is the fluctuating force per unit height; Z_1 and Z_2 the lower and upper limits of the height range over which the vortex shedding forces act.

In this case, the applied force is assumed to be harmonic (sinusoidal) with a frequency equal to the vortex-shedding frequency, n_s. The maximum amplitude of vibration will occur at resonance, when n_s is equal to the natural frequency of the structure, n_j.

Thus the generalized force (Section 5.3.6) is given by:

$$Q_j(t) = \int_{z_1}^{z_2} f(z,t)\phi_j(z)\,\mathrm{d}z = \left(\frac{1}{2}\right)\rho_a C_\ell\, b\sin(2\pi n_j t + \varphi)\int_{z_1}^{z_2}\overline{U}^2(z)\phi_j(z)\,\mathrm{d}z$$
$$= \mathrm{Q}_{j,\max}\sin(2\pi n_j t + \varphi)$$

where $Q_{j,\max}$ is the amplitude of the applied generalized force, given by,

$$Q_{j,\max} = \left(\frac{1}{2}\right)\rho_a C_\ell b\int_{z_1}^{z_2}\overline{U}^2(z)\phi_j(z)\,\mathrm{d}z \qquad (11.9)$$

where, C_ℓ is the amplitude of the sinusoidal lift (cross-wind force) per unit length coefficient and ρ_a the density of air.

The result for the maximum amplitude at resonance for a single-degree-of-freedom system can be applied:

$$a_{max} = \frac{Q_{j,max}}{2K_j\eta_j} = \frac{Q_{j,max}}{8\pi^2 n_j{}^2 G_j \eta_j} \tag{11.10}$$

where η_j is the critical damping ratio for the *j*th mode, equal to $C_j/2\sqrt{G_j K_j}$.

Substituting for $Q_{j,max}$ from Equation (11.9) in Equation (11.10),

$$a_{max} = \frac{\left(\frac{1}{2}\right)\rho_a C_\ell b \int_{z_1}^{z_2} \overline{U}^2(z)\phi_j(z)\,dz}{8\pi^2 n_j{}^2 G_j \eta_j} \tag{11.11}$$

$$= \frac{\rho_a C_\ell b^3 \int_{z_1}^{z_2} \phi_j(z)\,dz}{16\pi^2 G_j \eta_j St^2}$$

where *St* is the Strouhal number for vortex shedding (Section 4.6.3), which in this case can be written as:

$$St = \frac{n_s b}{\overline{U}(z_e)} = \frac{n_j b}{\overline{U}(z_e)}$$

where z_e is an average or effective height for the vortex-shedding frequency.

The maximum amplitude of deflection at any height on the structure is given by:

$$y_{max}(z) = a_{max} \cdot \phi_j(z)$$

$$= \frac{\rho_a C_\ell b^3 \phi_j(z) \int_{z_1}^{z_2} \phi_j(z)\,dz}{16\pi^2 G_j \eta_j St^2} \tag{11.12}$$

For a tower with a uniform mass per unit height, the maximum deflection at the tip *(z=h)*, and where $\phi(h)$ is chosen as 1.0, is given by:

$$\frac{y_{max}(h)}{b} = \frac{\rho_a C_\ell b^2 \int_{z_1}^{z_2} \phi_j(z)\,dz}{16\pi^2 G_j \eta_j St^2} = \frac{C_\ell \int_{z_1}^{z_2} \phi_j(z)\,dz}{4\pi\, Sc\, St^2 \int_0^h \phi_j{}^2(z)\,dz}$$

where *Sc* is the *Scruton number* or ‘mass-damping parameter’, defined as:

$$Sc = \frac{4\pi m \eta_j}{\rho_a b^2} \tag{11.14}$$

where *m* is the average mass per unit length along the structure.

The ratio of vibration amplitude at the tip of a uniform cantilevered tower to the tower breadth can thus be evaluated as:

$$\frac{y_{max}}{b} = \frac{k \cdot C_\ell}{4\pi \cdot Sc \cdot St^2} \tag{11.15}$$

where,

$$k\left(=\frac{\int_{z_1}^{z_2}\phi_j(z)\,\mathrm{d}z}{\int_0^h \phi_j^2(z)\,\mathrm{d}z}\right)$$

is a parameter dependent weakly on the mode shape of vibration.

Ruscheweyh (1990) has modified the basic sinusoidal model by the use of a 'correlation length'. The term 'correlation length' is one that is normally applied to random processes or excitation (Section 4.6.5), and a better term would be 'excitation length'. The vortex-shedding forces are applied over a height range less than the total height of the structure in this model.

A simple formula based on Equation (11.13) can be derived to estimate the maximum amplitude of vibration as a fraction of the diameter. The version in the Eurocode (CEN, 2004) is written as follows:

$$\frac{y_{\max}}{b}=\frac{1}{St^2}\cdot\frac{1}{Sc}\cdot K\cdot K_w\cdot C_{\mathrm{lat}} \tag{11.16}$$

where y_{max} is the maximum amplitude of vibration at the critical wind speed; K_w an effective correlation length factor; K a mode shape factor and C_{lat} is a lateral (cross-wind) force coefficient (= C_ℓ).

11.5.2 Random excitation model

A random excitation model for vortex-shedding response prediction was developed by Vickery and Basu (1983). With some approximations, the peak deflection at the tip, as a ratio of diameter, can be written in the following form for a uniform cantilever:

$$\frac{\hat{y}}{b}=g\frac{\left[n_1 S_{C_\ell}(n_1)\right]^{1/2}\left(\rho_a b^2/m\right)}{16\pi^{3/2}\eta^{1/2}St^2}f(\phi) \tag{11.17}$$

where $S_{cl}(n)$ is the spectral density of the generalized cross-wind force coefficient; $f(\phi)$ a function of mode shape; g a peak factor which depends on the resonant frequency, but is usually taken as 3.5–4; and η the critical damping ratio, comprising both structural and aerodynamic components.

Equation (11.17) has some similarities with Equation (11.13), but it should be noted that in the case of random vibration, the response is inversely proportional to the *square root* of the damping, whereas in the case of sinusoidal excitation, the peak response is inversely proportional to the damping. The peak factor (ratio between peak and r.m.s. response) is also much greater than the value of $\sqrt{2}$ in the sinusoidal model. The spectral density includes the effect of correlation length on the fluctuating forces.

In Vickery and Basu's procedure, the spectral density of the local lift force per unit length is represented by a Gaussian function as follows:

$$\frac{n \cdot S_L(n)}{{\sigma_L}^2} = \frac{(n/n_s)}{B\sqrt{\pi}} \exp\left[-\left(\frac{1-n/n_s}{B}\right)^2\right] \tag{11.18}$$

where B is a *bandwidth parameter*.

This function is based on the assumption of a constant Strouhal number and the shedding frequency varying with wind speed, as the large-scale turbulence generates a Gaussian variation in wind speed about the mean value (Vickery and Basu, 1983).

Lock-in (Sections 4.6.3 and 5.5.4), in which the vortex-shedding frequency 'locks-in' to the natural frequency of the structure, results in an increase in the magnitude of the fluctuating cross-wind forces, and an increase in their correlation along the length of the structure. It is dealt in the Vickery and Basu model with a non-linear, amplitude-dependent, aerodynamic damping within the random excitation model.

Equation (11.17) can be written in the form:

$$\frac{\hat{y}}{b} = \frac{A}{[(Sc/4\pi) - K_{ao}(1 - y^2/y_L^2)]^{1/2}} \tag{11.19}$$

where A incorporates all parameters not associated with damping; y is the root-meansquare fluctuating amplitude; y_L is a limiting r.m.s. amplitude; and K_{ao} is a non-dimensional parameter associated with the negative aerodynamic damping.

Equation (11.19) can be used to define three response regimes:

- a randomly 'forced' vibration regime, at high values of Scruton number;
- a 'lock-in' regime for low values of Scruton number, in which the response is driven by the negative aerodynamic damping, and is largely independent of A; and
- a transition regime between the above two regimes.

These three regimes, with an empirical fit based on Equation (11.19), are shown in Figure 11.2 (from Vickery and Basu, 1983), and compared with experimental data from a model chimney (Wooton, 1969).

With appropriate input parameters, the Vickery/Basu method is applicable to any fullscale structure of constant or slightly tapered cross-section, but it has been calibrated to the vortex-induced response of large concrete chimneys.

When making predictions on real towers or chimneys in atmospheric turbulence, it is necessary to include the effect of lateral turbulence. Referring to Figure 11.3, the effect of lateral (horizontal) turbulence is for the instantaneous flow direction to be at an angle to the mean flow direction of θ, where,

$$\sin\ \theta \cong \frac{v}{U}$$

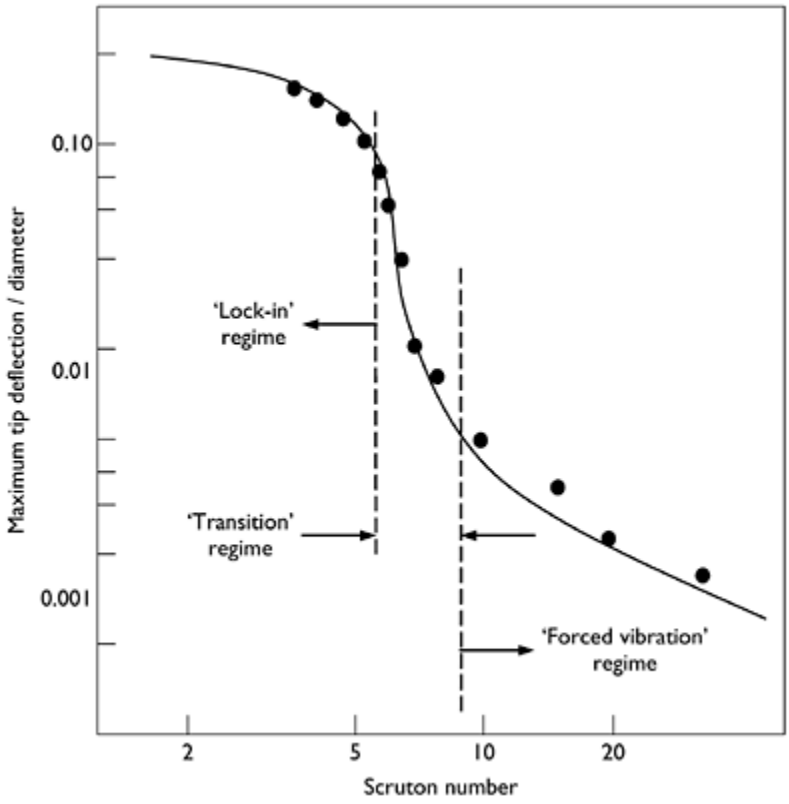

Figure 11.2 Response regimes for cross-wind vibration of circular towers and chimneys (Vickery and Basu, 1983).

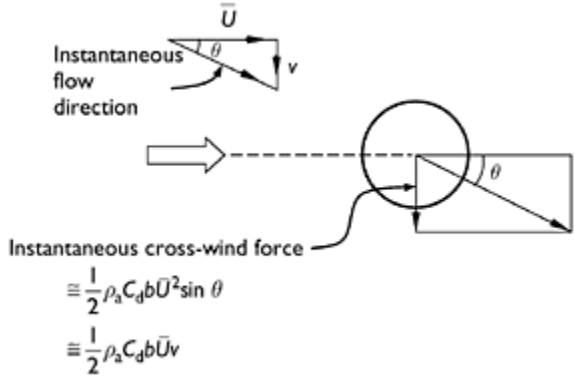

Figure 11.3 Cross-wind forces due to lateral turbulence.

Thus, for a circular cross-section, the instantaneous lateral force per unit length based on quasi-steady assumptions can be written:

$$f_z(z,t) = \frac{1}{2}\rho_a b C_d \overline{U}^2 \sin\theta = \frac{1}{2}\rho_a b C_d \overline{U} v(z,t) \tag{11.20}$$

Basu and Vickery (1983), in developing a method suitable for prediction of the combined cross-wind response of real structures in the atmospheric boundary layer, used the following expression for the mean square modal coordinate in the jth mode:

$$\overline{a_j^2} = \frac{\pi n_j [S_{\ell,v}(n_j) + S_{\ell,t}(n_j)]}{4K_j^2(\eta_s + \eta_a)} = \frac{S_{\ell,v}(n_j) + S_{\ell,t}(n_j)}{(4\pi n_j)^3 G_j^2 (\eta_s + \eta_a)} \tag{11.21}$$

where $S_{\ell,v}(n_j)$, $S_{\ell,t}(n_j)$ are respectively the spectral densities, evaluated at the natural frequency, n_j, of the cross-wind forces due to vortex shedding and lateral turbulence. Equation (11.21) is based on the assumption that the spectral density is constant over the resonant peak, as previously used to derive Equation (5.13).

A comparison of the peak-to-peak cross-wind deflection at the top of the 330m-high Emley Moor television tower computed by the random vibration approach of Vickery and Basu, and compared with measurements, is shown in Figure 11.4. Calculations were made for the first four modes of vibration. There was some uncertainty in the appropriate structural damping for this tower, but generally good agreement was obtained.

Comparisons were also made with full-scale response measurements from several reinforced concrete chimneys (Vickery and Basu, 1984). The average agreement was quite good but some scatter was shown.

11.5.3 Hybrid model

Item 96030 of the Engineering Sciences Data Unit (ESDU, 1996) covers the response of structures of circular and polygonal cross-section to vortex shedding. A computer program and spreadsheet is provided to implement the methods. ESDU 96030 covers uniform, tapered and stepped cylindrical or polygonal structures, and also yawed flow situations.

The method used in ESDU 96030 appears to be a hybrid of the two previously described approaches. For low amplitudes of vibration, a random excitation model similar to that of Vickery and Basu has been adopted. At high amplitudes, i.e. in lock-in situations, a sinusoidal excitation model has been adopted with a cross-wind force coefficient that is non-linearly dependent on the vibration amplitude. The response is postulated to switch intermittently between a random wide-band response and a constant amplitude sinusoidal type as lock-in occurs.

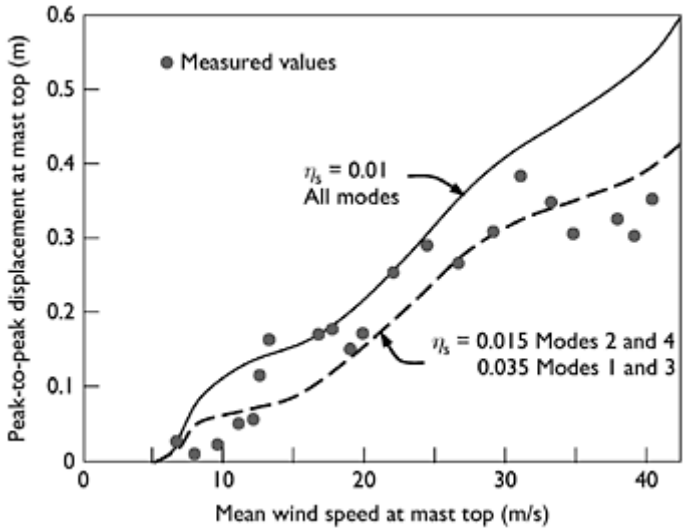

Figure 11.4 Comparison of measured and computed cross-wind response on the Emley Moor television tower (Basu and Vickery, 1983).

The effect of cross-wind turbulence excitation is also included in this method. This contribution becomes more significant with increasing wind speed, and thus is more important for larger cylinders (e.g. large diameter reinforced concrete chimneys with high critical wind speeds).

The ESDU method gives similar results to the Vickery and Basu method, described in the previous section, but with the disadvantage of discontinuities between the two response regimes.

11.5.4 Comparison of predictions of cross-wind response

In this section, a comparison of the computed response to vortex shedding for three representative slender structures with circular cross-section is made:

- a 100 m steel chimney,
- a 250 m reinforced concrete chimney, and
- a 25 m thin-walled, steel lighting pole.

The relevant details of the three structures are given in Table 11.1.

These represent a wide range of structural types for which the cross-wind response needs to be assessed. In all three cases, the structures were assumed to be located in open country terrain, with relevant velocity profile and turbulence properties. In this comparison, only the first mode of vibration was considered.

The maximum r.m.s. ratio of tip deflection/mean diameter for the three structures have been calculated by the following methods and tabulated in Table 11.2: (a) the sinusoidal excitation method given in the European pre-standard (CEN, 2004); (b) Vickery and

Basu's random excitation approach (structures 1 and 2 only) and (c) the hybrid approach of ESDU (1996).

The three methods compared in Table 11.2 clearly give significant variations in estimated response to vortex shedding, for all three structures. In the case of structure 1,

Table 11.1 Structural properties

Property	*Structure 1*	*Structure 2*	*Structure 3*
Height (m)	100	250	25
Diameter (m)	4.9	20	0.55–0.20 (tapered)
Surface roughness (mm)	0.1	1	0.15
Natural frequency (Hz)	0.5	0.3	0.5
Mode shape exponent	2	1.6	2
Mass/unit height (kg/m) (top third)	1700	50,000	30
Critical damping ratio	0.005	0.01	0.005

Table 11.2 Calculated values of maximum rms tip deflection/ diameter (at or near critical velocity)

Method	*Structure 1*	*Structure 2*	*Structure 3*
(a)	0.080	0.032	0.016
(b)	0.214	0.0045	NA
(c)	0.308	0.0054	0.014

all methods predict large amplitudes characteristic of lock-in, although methods (b) and (c) predict higher amplitudes. Method (a), based on sinusoidal excitation, overestimates the response of structure 2 (a large reinforced concrete chimney), which is subject to wide-band excitation with low amplitudes. Methods (b) and (c) predict similar maximum response for structure 2.

Vickery and Basu's model has generally been used for high Reynolds numbers only, and has not been applied to structure 3, which is clearly in the sub-critical regime. The other methods predict a low response amplitude for structure 3 which has a very low critical velocity in the first mode, although this type of low-mass pole or mast has a history of occasional large vortex-shedding responses, sometimes in higher modes, and often producing fatigue problems. One of the main problems in predicting their behaviour is in predicting the structural damping ratio, which is often very amplitude dependent.

11.6 Cooling towers

The vulnerability of large hyperbolic natural draught cooling towers to wind action was emphasized in the 1960s by the collapse of the Ferrybridge Towers in the United Kingdom (Figure 1.11). This event provoked research work on the wind loading and

response of these large structures, especially in Europe. The sensitivity of wind pressures on circular cross-sections to Reynolds number means that, like chimneys, there are some questions about the validity of wind-tunnel tests to produce reliable results.

The main factors affecting wind loading of large cooling towers are:

- the partially correlated nature of fluctuating wind pressures acting on such large bluff structures, which means that quasi-steady design wind pressures are inadequate;
- the non-linear nature of the thin reinforced concrete; and
- aerodynamic interference effects from adjacent similar structures (as illustrated by the Ferrybridge failures).

As the lowest natural frequency in the uncracked state usually exceeds 1 Hz, these structures are not particularly dynamically sensitive to wind, although after cracking of the concrete, the frequencies can apparently reduce significantly, with significant resonant contributions to the response (Zahlten and Borri, 1998).

A detailed discussion of the wind loading of these special structures will not be given in this text, although they are covered in some detail by Simiu and Scanlan (1996). There are a number of specialist design codes for cooling towers which include specification of wind loads (e.g. VGB, 1990; BSI, 1992).

Other useful references are by Shu and Wenda (1991) for soil interaction effects; Niemann and Köpper (1998) for aerodynamic interference; Zahlten and Borri (1998) for resonant amplification effects; and Niemann and Ruhwedel (1980) for wind-tunnel modelling.

11.7 Guyed masts

As most guyed masts are lattice structures (usually with triangular cross-sections), wind-tunnel testing is neither appropriate nor required for this type of structure. Analytical methods are usually used for tall guyed masts.

However, guyed masts are complex structures to analyse for wind loading for a number of reasons:

- Their structural behaviour is non-linear.
- The influence lines for load effects such as bending moments and guy tensions are complex.
- When resonant dynamic response is important (for masts greater than 150 min height) many modes participate, and they are often coupled.

Generally, the dynamic response to wind may be analysed using the methods of random vibration outlined in Chapter 5. However, simple gust response factor approaches are not appropriate, because of the complex influence lines, with alternating positive and negative portions. The non-linear nature of the structure may be readily dealt with by computing the free vibration frequencies and mode shapes, about the deflected position under the mean wind loading, rather than the ‘no-wind’ condition. The effective static load methods outlined in Section 5.4 are very useful to derive effective static load distributions for both the background and the resonant response of these structures.

A simplified approach to the dynamic response of tall guyed masts, in which the responses due to 'patch loads' are scaled to match the response calculated more rigorously from random vibration theory, is described by Davenport and Sparling (1992) and Sparling *et al.* (1996). The patch loads are applied on each span of the mast between adjacent guy levels, and from midpoint to midpoint of adjacent spans. The magnitude of the patch loads is taken as equal to the r.m.s. fluctuating drag force per unit height, at each height level, z:

$$d(z)=\rho_a C_d(z) b(z) \bar{U}(z) \sigma_u(z) \tag{11.22}$$

To simulate the lack of correlation of the fluctuating wind loads, the responses (bending moments, shear, deflections) due to the individual patch loads are combined by a root-sum-of squares as in Equation (11.23):

$$\tilde{r}_{PL} = \sqrt{\sum_{i=1}^{N} r_i^2} \tag{11.23}$$

where $\tilde{r}_{PL}$ is the resultant patch load response, ri the response due to the ith patch load and *N* the total number of patch loads. The design peak response is then determined from Equation (11.24):

$$\hat{r}_{PL} = \tilde{r}_{PL} \cdot \lambda_B \cdot \lambda_R \cdot \lambda_{TL} \cdot g \tag{11.24}$$

where *g* is a peak factor and λ_B, λ_R, λ_{TL} a 'background scaling factor', a 'resonant magnification factor' and a 'turbulent length scale factor', respectively. These factors

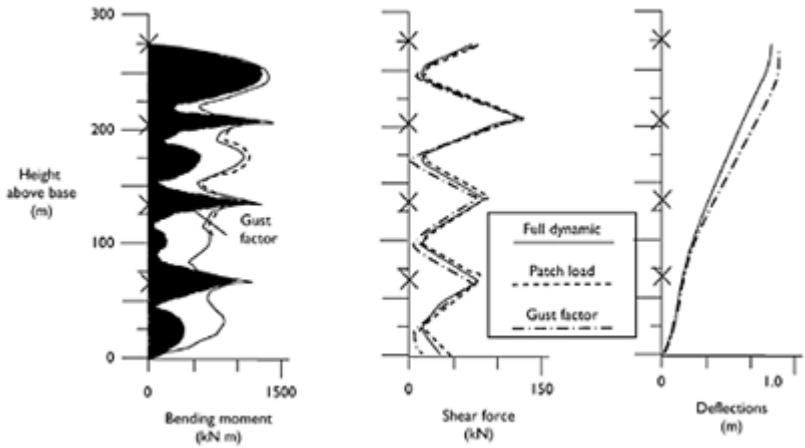

Figure 11.5 Comparison of peak responses for a 295 m guyed mast (Sparling *et al.*, 1996).

were determined by calibrating the method against the results of a full dynamic (random vibration) analysis for eight guyed masts ranging in height from 123 to 622 m. Expressions for these factors resulting from this calibration are given by Sparling *et al.* (1996).

This patch method has been adopted by the British Standard for lattice towers and masts (BSI, 1994). The results from the analysis of a 295 m guyed mast are shown in Figure 11.5. This shows that good agreement is achieved between the patch load method and the full dynamic analysis. The results from a conventional gust response factor approach (Section 5.3.2) are also shown. In this method, the mast is analysed under the mean wind loading, and the resulting responses are factored up by a constant factor (in this case 2.0 was used). Clearly this method grossly underestimates the peak bending moments between the guy levels.

11.8 Wind turbine towers

With the development of wind energy farms in many parts of the world, during the last 20 years, there are now many large wind turbine towers in existence, with heights approaching 100m. These towers are relatively flexible and carry a large mass at the top due to the nacelles and turbine blades. Hence, their frequencies can be quite low (i.e. less than 0.5 Hz) and the towers, which are normally in exposed locations, may be subjected to significant turbulent buffeting (Section 5.3) at high wind speeds. There have been a number of failures of these towers in extreme winds (Figure 11.6)

The along-wind response of a typical wind turbine tower was investigated numerically by Murtagh *et al.* (2005) using simulated turbulent wind forces. The tower and the blades were modelled dynamically as multi-degree-of-freedom systems. The response of the blades themselves were calculated using drag force time histories derived from rotationally sampled wind spectra. The response of the blades and the tower were coupled using compatibility of displacement at the top of the tower. It was found that neglect of the blade-tower interaction can significantly underestimate the response at the top of the tower, especially if the fundamental frequencies of the tower and turbine blades are close to each other.

An overview of the comprehensive wind-tunnel study carried out for the 555-m high CN Tower in Toronto, Canada, with comparisons with full-scale observations is presented by Isyumov *et al.* (1984). The wind-induced response of the Sydney Tower is described by Kwok and Macdonald (1990); the response was found to decrease markedly after a tuned mass damper system (Section 9.9.3) was installed. Numerical and wind-tunnel simulations of the wind-induced response of the 310 mNanjing Tower are described by Kareem *et al.* (1998).

Figure 11.6 A failed wind turbine tower following a typhoon (picture by Dr M.Matsui, Tokyo Polytechnic University).

11.9 Case studies

A case study of the wind loading and response study of the 338-m tall Macau Tower, which incorporates both wind-tunnel studies and calculations, is described by Holmes (2000). The full aeroelastic model (1/150 scale) of the Macau Tower, used for the wind-tunnel testing, is shown in Figure 11.7.

There have also been a number of full-scale studies on the dynamic response of large reinforced concrete chimneys. Notable amongst these are studies by Muller and Nieser (1975), Hansen (1981), Melbourne *et al.* (1983) and Waldeck (1992). Ruscheweyh (1990) reported on some measurements on a number of steel stacks of cross-wind vibration and made comparisons with predictions based on the sinusoidal model (Section 11.5.1).

Measurements on two tall guyed masts have been made by Peil *et al.* (1996) for comparison with theoretical predictions. One of these studies entailed the detailed measurement of turbulent wind speed at 17 height levels up to 340 m height (Peil and Nölle, 1992).

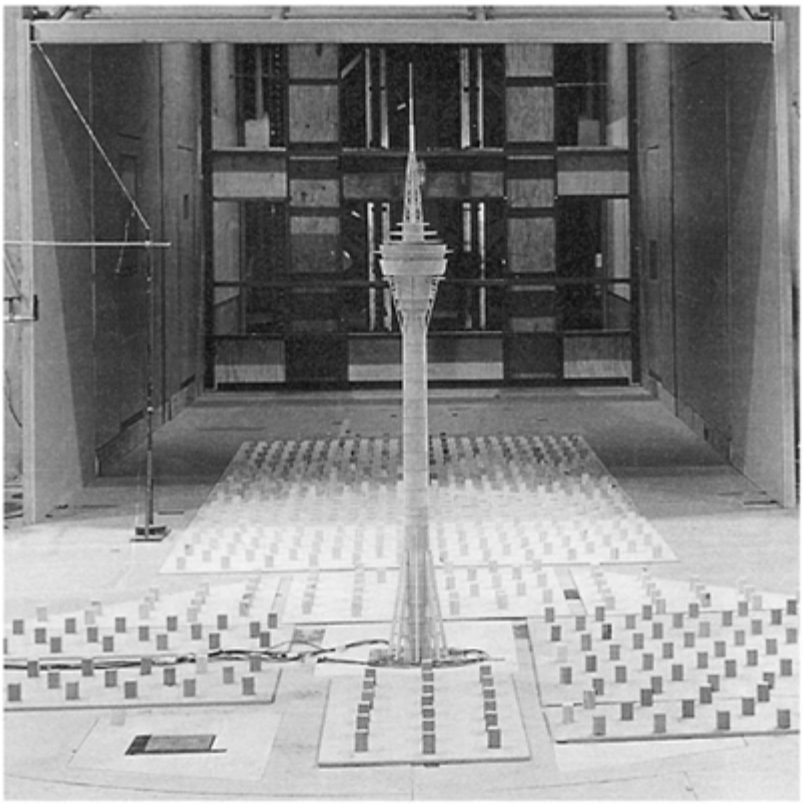

Figure 11.7 Aeroelastic wind-tunnel model of a large free-standing tower.

The wind-induced acceleration response of an air-traffic control tower was investigated by Park *et al.* (2006), using both a high-frequency base balance (Section 7.6.2) and an aeroelastic (Section 7.6.4) test in a wind tunnel. The excessive acceleration response at the top of the tower was controlled using a hybrid active passive tuned mass damper (Section 9.9.3). The effectiveness of the damper system was demonstrated by free vibration tests.

11.10 Summary

In this chapter, the wind loading of slender towers, chimneys and masts of various types has been discussed. These structures are usually dynamically sensitive to wind, and response in both along-wind and cross-wind directions may need to be considered. Theoretical methods for calculating dynamic response, in both directions, are discussed.

The wind loading of hyperbolic cooling towers and guyed masts is complex due to their complex structural behaviour. The main features of the wind loading and response of these structures are discussed.

References

American Society of Civil Engineers (1990) Guidelines for transmission line structural loading. ASCE Manual and Reports on Engineering Practice No. 74, ASCE, New York.

Basu, R.I. and Vickery, B.J. (1983) Across-wind vibrations of structures of circular crosssection. Part II. Development of a mathematical model for full-scale applications. *Journal of Wind Engineering & Industrial Aerodynamics*, 12:75–97.

Bayar, D.C. (1986) Drag coefficients of latticed towers. *ASCE Journal of Structural Engineering*, 112:417–30.

British Standards Institution (1992) Water cooling towers. Part 4. Code of practice for structural design and construction. British Standard, BS 4485: Part 4:1992.

British Standards Institution (1994) Lattice towers and masts. Part 4. Code of practice for lattice masts. British Standard, BS 8100: Part 4:1994.

CEN (European Committee for Standardization) (2004) Eurocode 1: Actions on Structures—Part 1–4: General actions—Wind actions. pr EN 1991–1–4.6, CEN, Brussels.

CSIR (1990) Transmission line loading. Part I: recommendations and commentary. Part II: appendices. Engineering Structures Programme, CSIR Building Technology, South Africa.

Davenport, A.G. (1975) Perspectives on the full-scale measurement of wind effects. *Journal of Industrial Aerodynamics*, 1:23–54.

Davenport, A.G. and Sparling, B.F. (1992) Dynamic gust response factors for guyed masts. *Journal of Wind Engineering & Industrial Aerodynamics*, 44:2237–48.

Dry den, H.L. and Hill, G.C. (1930) Wind pressure on circular cylinders and chimneys. *Journal of Research of the National Bureau of Standards, 5*, 653–93.

Eiffel, G. (1885) Projet d'une tour en fer de 300 m de hauteur. *Memoires de la Societe' des Ingenieurs Civils*, I: 345–70.

ESDU (1996) Response of structures to vortex shedding: structures of circular or polygonal cross-section. ESDU Data Item 96030, Engineering Sciences Data Unit, ESDU International, London, UK.

Hansen, S.O. (1981) Cross-wind vibrations of a 130 m etre tapered concrete chimney. *Journal of Wind Engineering & Industrial Aerodynamics*, 8:145–56.

Holmes, J.D. (1994) Along-wind response of lattice towers: Part I—derivation of expressions for gust response factors. *Engineering Structures*, 16:287–92.

Holmes, J.D. (1996a) Along-wind response of lattice towers: Part II—aerodynamic damping and deflections. *Engineering Structures*, 18:483–8.

Holmes, J.D. (1996b) Along-wind response of lattice towers: Part III—effective load distributions. *Engineering Structures*, 18:489–94.

Holmes, J.D. (2000) Wind loading of the Macau Tower—application of the effective static load approach. *Proceedings, First International Symposium on Wind and Structures for the 21st Century*, Cheju, Korea, 26–28 January, pp. 81–90.

Isyumov, N., Davenport, A.G. and Monbaliu, J. (1984) CN Tower, Toronto: model and full-scale response to wind. *Proceedings, 12th Congress, International Association for Bridge and Structural Engineering*, Vancouver, Canada, 3–7 September, pp. 737–46.

Kareem, A., Kabat, S. and Haan, F.L. (1998) Aerodynamics of Nanjing Tower: a case study. *Journal of Wind Engineering & Industrial Aerodynamics*, 77–78:725–39.

Kernot, W.C. (1893) Wind pressure. *Proceedings, Australasian Society for the Advancement of Science*, V: 573–81.

Kwok, K.C.S. and Macdonald, P.A. (1990) Full-scale measurements of wind-induced acceleration response of Sydney Tower. *Engineering Structures*, 12:153–62.

Melbourne, W.H., Cheung, J.C.K. and Goddard, C. (1983) Response to wind action of 265-m Mount Isa stack. *ASCE Journal of Structural Engineering*, 109:2561–77.

Muller, F.P. and Nieser, H. (1975) Measurements of wind-induced vibrations on a concrete chimney. *Journal of Industrial Aerodynamics*, 1:239–48.

Murtagh, P.J., Basu, B. and Broderick, B.M. (2005) Along-wind response of a wind turbine tower with blade coupling subjected to rotationally sampled wind loading. *Engineering Structures*, 27:1209–19.

Niemann, H.-J. and Köpper, H.-D. (1998) Influence of adjacent buildings on wind effects on cooling towers. *Engineering Structures*, 20:874–80.

Niemann, H.-J. and Ruhwedel, J. (1980) Full-scale and model tests on wind-induced, static and dynamic stresses in cooling tower shells. *Engineering Structures*, 2:81–9.

Park, W., Park, K.-S., Koh, H.-M. and Ha, D.-H. (2006) Wind-induced response control and serviceability improvement of an air traffic control tower. *Engineering Structures*, 28: 1060–70.

Peil, U. and Nölle, H. (1992) Guyed masts under wind load. *Journal of Wind Engineering & Industrial Aerodynamics*, 41–44:2129–40.

Peil, U., Nölle, H. and Wang, Z.H. (1996) Nonlinear dynamic behaviour of guys and guyed masts under turbulent wind load. *Journal of the International Association for Shell and Spatial Structures*, 37:77–88.

Rumman, W.S. (1970) Basic structural design of concrete chimneys. *ASCE Journal of the Power Division*, 96:309–18.

Ruscheweyh, H. (1990) Practical experiences with wind-induced vibrations. *Journal of Wind Engineering & Industrial Aerodynamics*, 33:211–18.

Scruton, C. (1981) *An Introduction to Wind Effects on Structures.* Oxford University Press, Oxford.

Scruton, C. and Flint, A.R. (1964) Wind-excited oscillations of structures. *Proceedings, Institution of Civil Engineers (UK)*, 27:673–702.

Shu, W. and Wenda, L. (1991) Gust factors for hyperbolic cooling towers on soils. *Engineering Structures*, 13:21–6.

Simiu, E. and Scanlan, R.H. (1996) *Wind Effects on Structures—Fundamentals and Applications to Design*, 3rd Edition. Wiley, New York.

Sparling, B.F., Smith, B.W. and Davenport, A.G. (1996) Simplified dynamic analysis methods for guyed masts in turbulent winds. *Journal of the International Association for Shell and Spatial Structures*, 37:89–106.

Standards Australia (1994) Design of steel lattice towers and masts. AS3995–1994, Standards Australia, North Sydney.

VGB (1990) VGB: BTR Bautechnik bei Kültürmen. (Construction guidelines for cooling towers.) VGB Association of Large Powerplant Operators, Essen, Germany.

Vickery, B.J. and Basu, R.I. (1983) Across-wind vibrations of structures of circular crosssection. Part I. Development of a mathematical model for two-dimensional conditions. *Journal of Wind Engineering & Industrial Aerodynamics*, 12:49–73.

Vickery, B.J. and Basu, R.I. (1984) The response of reinforced concrete chimneys to vortex shedding. *Engineering Structures*, 6:324–33.

Waldeck, J.L. (1992) The measured and predicted response of a 300 m concrete chimney. *Journal of Wind Engineering & Industrial Aerodynamics*, 41:229–40.

Wooton, L.R. (1969) The oscillations of large circular stacks in wind. *Proceedings of the Institution of Civil Engineers (UK)*, 43:573–98.

Zahlten, W. and Borri, C. (1998) Time-domain simulation of the non-linear response of cooling tower shells subjected to stochastic wind loading. *Engineering Structures*, 20:881–9.

12
Bridges

12.1 Introduction

As discussed in Chapter 1, bridges have featured in some spectacular failures during wind storms (Figure 1.10). The history of the dynamically wind-sensitive suspension bridge from nineteen century onwards, including the periodic failures that have occurred, has been well documented (e.g. Steinman and Watson, 1957; Billington, 1977; Petroski, 1996).

Most of the early interest was in the drag or along-wind forces, and Baker (1884), Kernot (1893) and others noted that peak wind forces acting on large areas, such as a complete bridge girder, were considerably less than those on a small plate or board. However, the great American builder of suspension bridges, John Roebling, was aware of the dynamic effects of wind as early as 1855. In commenting on the failure of the Wheeling Bridge, Ohio, in the previous year, he wrote: That bridge was destroyed by the momentum acquired by its own dead weight, when swayed up and down by the force of the wind…. A high wind, acting upon a suspended floor, devoid of inherent stiffness, will produce a series of undulations, which will be corresponding from the center each way' (Steinman and Watson, 1957).

However, it took over 80 years for the dramatic failure of the first Tacoma Narrows suspension bridge in 1940 (Section 1.4) to direct serious attention to the dynamic actions of the wind and other wind actions on bridge decks: vertical cross-wind forces and torsional moments.

The cable-stayed bridge emerged in the 1950s in Germany, as an efficient method of spanning intermediate length crossings. Gimsing (1983) and Virlogeux (1999) have reviewed recent developments in the design of bridges of this type.

As the twentieth century ended, the spans of the long-span suspension and cable-stayed bridges have been extended to new limits. The longest bridge in the world at the turn of the century was the suspension bridge across the Akashi-Kaikyo Straits in Japan, which has an overall length of nearly 4km, with a main span of 1990 m(Figure 12.1). The design of this bridge was dominated by its aerodynamic characteristics.

The longest cable-stayed bridge was the Tatara Bridge, also in Japan, with an overall length of 1480 m and a main span of 890 m(Figure 12.2).

As the spans increase, wind actions become more critical in bridge design, and for the longest suspension or cable-stayed bridges, extensive wind studies are normally undertaken. The dynamic wind forces will excite resonant response, often in several modes, and *aeroelastic* forces, in which the motion of the structure itself generates forces, are important. Long-span bridges are usually crossings of large expanses of water and may be exposed to relatively low turbulence flow, at least at low wind speeds. This has contributed to a number of cases of vibrations of bridge decks induced by

Figure 12.1 Akashi-Kaikyo Bridge, Japan.

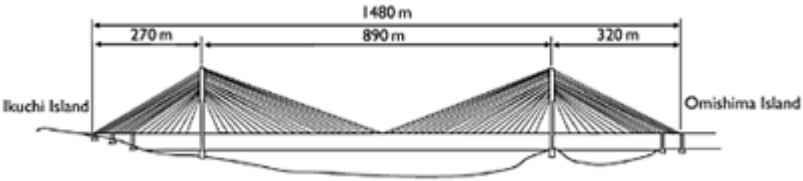

Figure 12.2 Tatara Bridge, Japan.

vortex shedding (Section 4.6.3). Recently the spans of cable-stayed bridges have been limited by problems with cable vibrations, sometimes involving rain, as well as wind (Section 12.5).

In the following sections, a review of the main aspects of wind forces and the windinduced excitation of long-span bridges and their supporting cables is given. The aerodynamics of bridges is a large and specialist topic, and an in-depth treatment will not be given in this book. The reader is referred to other sources (e.g. Larsen, 1992; Simiu and Scanlan, 1996) which treat the subject in more detail.

12.2 Basic force coefficients for bridges

As for other structures, all bridges are subjected to mean and fluctuating wind forces. These may be estimated by the use of mean or steady-state force coefficients, usually determined from wind-tunnel tests. Such coefficients are also required to determine dynamic response from turbulent buffeting.

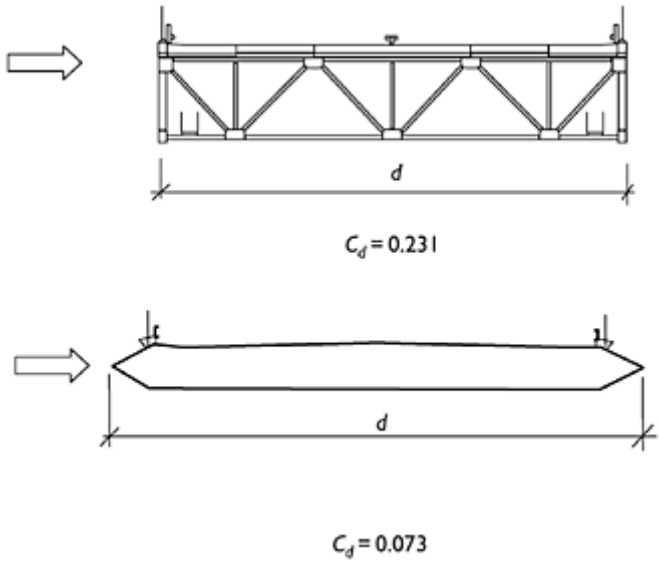

Figure 12.3 Comparison of drag coefficients for two bridge deck cross-sections (Ostenfeld and Larsen, 1992).

Many wind-tunnel section tests of decks for long-span bridges (Section 7.6.3) have been carried out, primarily to determine their aerodynamic stability (Section 12.3.2). Determination of the basic section force coefficients, as a function of wind angle of attack, is also routinely done during the tests.

Most nineteenth century suspension bridges were built with open lattice truss sections. This use has continued, as this type of section has some benefits from the point of view of dynamic response. The open structure prevents the formation of vortices, and dynamic excitation from vortex shedding (Section 4.6.3) is not usually a problem. Provided the torsional stiffness can be made high enough, the critical speed for flutter instability (Sections 5.5.3 and 12.3.2) will be high. However, the drag coefficients for open truss sections are high in comparison with other sections. For example, the drag coefficients for two cross-sections considered for the Little Belt suspension bridge, completed in the 1960s in Denmark, are shown in Figure 12.3 (Ostenfeld and Larsen, 1992). The drag coefficient for the trussed cross-section is more than three times that of the streamlined box girder section; the latter was eventually used for the bridge. However, after extensive aerodynamic testing (Miyata *et al.*, 1992), a truss girder, 11 mdeep, was chosen for the Akashi-Kaikyo suspension bridge—the world's longest (Figure 12.1).

Note that the along-wind *chord* dimension, *d*, rather than the cross-wind dimension, *b*, has been used to define the drag coefficients. This is usually the convention for bridges.

Very slender deck cross-sections, such as the box girder section shown in Figure 12.3, although having very low drag coefficients, will have high lift (cross-wind) force coefficients (Section 4.2.2) when the wind has a significant angle of attack, in a similar way to an airfoil. This situation will occur instantaneously in turbulent flow. This

characteristic makes deck sections of this type prone to buffeting by vertical turbulence (Section 12.3.3).

Examples of the variation of static horizontal and vertical force coefficients, and moment coefficient about the mass centre of a bridge deck section, with angle of attack, are given in Figure 12.4.

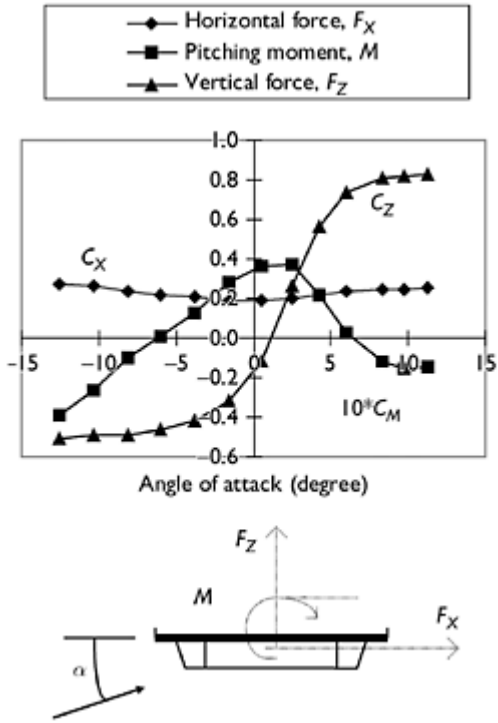

Figure 12.4 Static force coefficients for a typical bridge deck section.

The conventional definition of section force and pitching moments for bridges is as follows:

$$C_X = \frac{F_x}{\frac{1}{2}\rho_a U^2 d} \quad C_Z = \frac{F_z}{\frac{1}{2}\rho_a U^2 d} \quad C_M = \frac{M}{\frac{1}{2}\rho_a U^2 d^2} \tag{12.1}$$

12.3 The nature of dynamic response of long-span bridges

There are several mechanisms, in various wind speed ranges, which can excite resonant dynamic response in the decks of long-span bridges, as follows:

- Vortex-shedding excitation (Section 4.6.3) which usually occurs in low wind speeds and low turbulence conditions (e.g. Frandsen, 2001).
- Flutter instabilities (Section 5.5.3) of several types, which occur at very high wind speeds for *aerodynamically stable* decks, as a result of the dominance of self-excited aerodynamic forces (Sabzevari and Scanlan, 1968). These always involve torsional (rotational) motions and may also involve vertical bending motions.
- Buffeting excitation (Section 4.6.1) caused by the fluctuating forces induced by turbulence (Davenport, 1962; Scanlan and Gade, 1977). This occurs over a wide range of wind speeds and normally increases monotonically with increasing wind speed.

The nature of these mechanisms is discussed in the following sections.

Table 12.1 Some recorded cases of vortex-shedding induced vibrations of bridges

Name	*Natural frequency (Hz)*	*Critical velocity (m/s)*	*Max. amplitude (mm)*	*Reference*
Long's Creek Bridge	0.6	12	100–170	Wardlaw (1971)
Wye Bridge	0.46	7.5	35	Smith (1980)
Waal River	0.44	9–12	50	van Nunen and Persoon (1982)
Great Belt East	0.13–0.21	4.5–9	320	Larsen *et al.* (1999), Frandsen (2001)

12.3.1 Vortex-shedding excitation

Under certain conditions, vortex-shedding excitation can induce significant, but limited, amplitudes of vibration. The conditions required for this to occur are most, or all, of the following:

- wind direction normal to the longitudinal axis of the bridge;
- low turbulence conditions (typically I_u less than 0.05);
- a wind speed in a narrow critical range (5–12 m/s); and
- low damping (1% of critical or less).

The above conditions can be satisfied for both short-to-medium span cable-stayed bridges crossing water and longer span suspension bridges. With Strouhal numbers in the range of 0.1–0.2 (based on the depth of the deck cross section) and natural frequencies in the

range of 0.1–0.6 Hz, critical velocities of 6–15 m/s can produce significant amplitudes. Low turbulence conditions can occur in 'stable' atmospheric conditions, often in the early morning or evening. Recorded examples of this behaviour are listed in Table 12.1.

Section tests carried out in smooth flow in wind tunnels can provide reasonably good predictions of the full-scale behaviour (Wardlaw, 1971; van Nunen and Persoon, 1982). In the case of the Long's Creek Bridge, Canada, where the vibrations were large enough to require remedial action, triangular fairings on the ends and a soffit plate underneath the deck were added to the prototype structure, with satisfactory results (Wardlaw, 1971). Guide vanes were used at the lower corners of the box girder of the Great Belt East suspension bridge, a method known to be successful in suppressing vortex-shedding vibrations, which occurred at four different frequencies and a corresponding wide range of wind speeds. Lock-in effects (Sections 4.6.3 and 5.5.4) were also observed in the vortex-induced vibration on this bridge (Frandsen, 2001).

12.3.2 Flutter instabilities and prediction of flutter speeds

The coupled motion (rotation and vertical displacement) of a suspended bluff body was discussed in Section 5.5.3. Equations (5.46) and (5.47)—the coupled equations of motion are repeated as follows:

$$\ddot{z}+2\eta_z\omega_z\dot{z}+\omega_z^2 z=\frac{F_z(t)}{m}+H_1\dot{z}+H_2\dot{\theta}+H_3\theta \tag{5.46}$$

$$\ddot{\theta}+2\eta_\theta\omega_\theta\dot{\theta}+\omega_\theta^2\theta=\frac{M(t)}{I}+A_1\dot{z}+A_2\dot{\theta}+A_3\theta \tag{5.47}$$

Equations (5.46) and (5.47) are simplified forms of the full equations of motion, which include the horizontal motions of the deck and as many as 18 different aeroelastic derivatives, corresponding to all possible motion-induced forces. Many of these terms are, however, small. The propensity of a bridge deck to flutter instability depends on the magnitudes and signs of some of the aeroelastic derivatives, or *flutter derivatives*, of the particular deck cross-section as a function of the wind speed. For example, a positive value of the derivative, A_2, is an indication of flutter in a pure rotational motion—sometimes known as 'stall flutter' in aeronautical terminology. This can be seen from Equation (5.47) when the term $A_2\theta$ is transposed to the left-hand side of the equation—it then has the form of a negative damping term, with the ability to *extract* energy from the flow. If the magnitude of the negative aerodynamic is greater than the structural damping, then vibrations will grow in amplitude—i.e. an aeroelastic instability will occur.

The most commonly understood use of the term 'flutter', however, is to describe the coupled translational-rotational form of instability, which is largely governed by the signs of the derivatives H_2 and A_1 (see Table 5.1).

Data on the flutter derivatives A_i to H_i are usually obtained experimentally from section tests in wind tunnels (see Section 7.6.3). Tests are usually done in smooth (low turbulence) flow—it has been found that the effects of turbulence on the derivatives are generally small (Scanlan and Lin, 1978). The derivatives are a function of reduced velocity, *(U/nd)*, which incorporates the variation with frequency of vibration, *n*, as well

as the wind speed, *U*. The following non-dimensional forms are usually used for the derivatives (Scanlan and Tomko, 1971):

$$H_1^* = \frac{mH_1}{\rho_a d^2 \omega}; \quad A_1^* = \frac{IA_1}{\rho_a d^3 \omega}$$
$$H_2^* = \frac{mH_2}{\rho_a d^3 \omega}; \quad A_2^* = \frac{IA_2}{\rho_a d^4 \omega} \qquad (12.2)$$
$$H_3^* = \frac{mH_3}{\rho_a d^3 \omega^2}; \quad A_3^* = \frac{IA_3}{\rho_a d^4 \omega^2}$$

where m and I are the mass and moment of inertia per unit length (spanwise), respectively; d the width (chord) of the deck; ρ_a the air density; and ω the circular frequency (= $2\pi n$).

Examples of aeroelastic derivatives determined for two common types of bridge deck—an open truss and a box-girder—are shown in Figure 12.5.

Although the magnitude and sign of the derivatives give some indication of the tendency of a particular section, in the design stage of important long-span bridges to aerodynamic instability, it is usual to attempt to determine a 'critical flutter speed' for the deck crosssection. If this wind speed does not exceed, by a substantial margin, the design wind speed of the site at the deck height (suitably factored for ultimate limit states), then modifications to the deck cross-section are usually made.

Several methods may be used to determine the critical flutter speed:

- empirical formulae (e.g. Selberg, 1963);
- experimental determination by use of section model testing; and
- theoretical stability analysis of the equations of motion (Equations (5.46) and (5.47), with values of A_i and H_i obtained experimentally; e.g. Simiu and Scanlan, 1996).

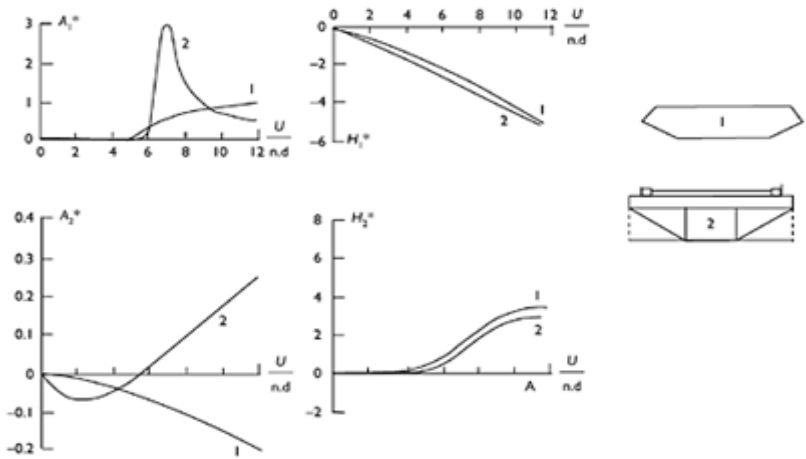

Figure 12.5 Aeroelastic derivatives for two types of bridge deck (Scanlan and Tomko, 1971).

Selberg (1961, 1963) proposed an empirical equation for critical flutter speed, UF, which, in its simplest form, can be written as:

$$U_F = 0.44d\sqrt{(\omega_T^2 - \omega_V^2)\frac{\sqrt{\upsilon}}{\mu}} \tag{12.3}$$

where $\upsilon = 8(r/d)^2$ and $\mu = (\pi\rho_a d^2/2m)$; r is the radius of gyration of the cross-section $(I = mr^2)$; m the mass per unit length. $\omega_T (= 2\pi n_T)$ and $\omega_v (= 2\pi n_v)$ are the circular frequencies in the first torsional mode and first vertical bending modes, respectively.

Alternative ways of expressing the Selberg formula are as follows:

$$U_F = 0.417\omega_T(d/2)\sqrt{\left(1 - \frac{\omega_V^2}{\omega_T^2}\right)\frac{mr}{\rho_a(d/2)^3}} \tag{12.4}$$

where the half chord of the bridge deck $(d/2)$ has been used:

$$\frac{U_F}{n_V d} = 3.72\sqrt{\left(\frac{mr}{\rho_a d^3}\right)\left(1 - \frac{n_V^2}{n_T^2}\right)} \tag{12.5}$$

Figure 12.6 shows measured flutter speeds for several bridge deck sections compared with predictions from the Selberg formula. Reasonable agreement is obtained although there is an overestimation at low angles of attack. It would appear to be unwise to rely on a prediction based on an empirical formula alone.

The analytical estimation of flutter speeds is a specialist function of bridge aerodynamicists, but Ge and Tanaka (2000) have given a useful summary of the available techniques.

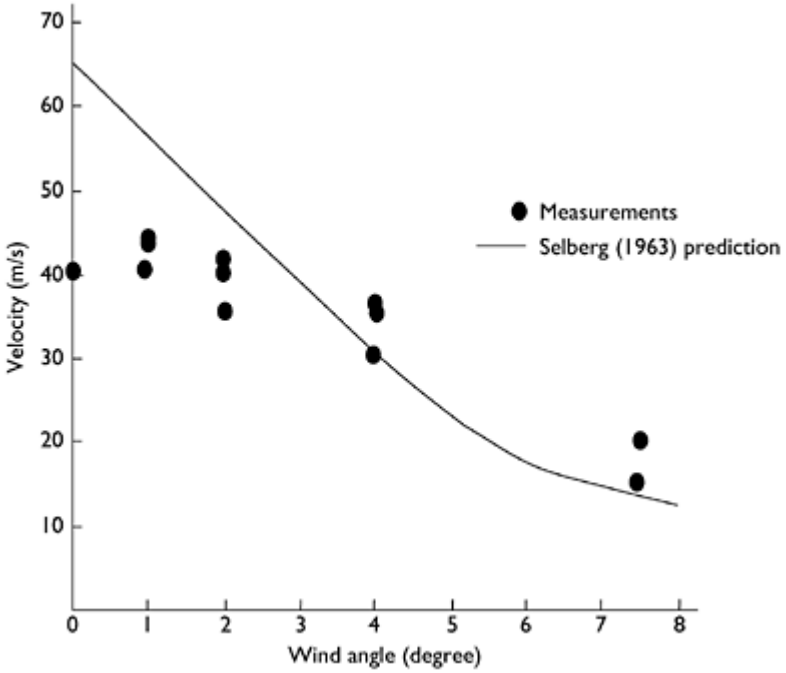

Figure 12.6 Measured critical flutter speeds and comparisons with the Selberg prediction formula (Wardlaw, 1971).

12.3.3 Buffeting of long-span bridges

A bridge that is otherwise stable in flutter up to a high wind speed and does not suffer from vortex-induced vibrations at low wind speeds will still experience dynamic response to atmospheric turbulence, known as *buffeting*, over a wide range of wind speeds. This response will normally determine the size of the structural members and require evaluation at the design stage.

Davenport (1962) was the first to apply random vibration methods to the buffeting of a long-span suspension bridge. These methods were later validated by comparison with model studies in turbulent boundary-layer flow in the 1970s (e.g. Holmes, 1975, 1979; Irwin, 1977).

The methodology described in Section 5.3.6 for the along-wind response of distributed mass structures can be adapted to the *cross-wind* response of bridge decks excited by vertical turbulence components.

The sectional cross-wind force per unit span can be written, applying a 'strip' assumption:

$$f'(z,t) = \rho_a \overline{U} d\left[C_{Z_0} u'(t) + \frac{1}{2}\frac{dC_Z}{d\alpha} w'(t)\right] \tag{12.6}$$

where C_{z0} is the vertical force coefficient at zero angle of attack; ($dC_z/d\alpha$) the slope of the vertical force coefficient versus angle of attack, *α; u'(t)* and *w'(t)* the horizontal and vertical velocity fluctuations upstream of the deck section in question.

C_{z0} and ($dC_z/d\alpha$) can be obtained from static section tests of the deck cross-section (Section 12.2). If there is significant angular rotation of the bridge deck under the mean wind load (as is often the case with suspension bridges), then C_{z0} may need to be replaced by the value of C_z at the mean (non-zero) angle of attack under the mean wind loading.

Following an argument similar to that used in Section 5.3.6, the spectral density of the generalized force for the jth mode of vibration can be obtained:

$$S_{Q_j}(n) = (\rho_a \overline{U} d)^2 \left[C_{Z_0}^2 S_u(n) + \frac{1}{4}\left(\frac{dC_Z}{d\alpha}\right)^2 S_w(n) \right] \chi^2(n) \int_0^L \int_0^L \rho(y_1, y_2, n) \phi_j(y_1) \phi_j(y_2) dy_1 dy_2 \qquad (12.7)$$

In Equation (12.7), $\chi^2(n)$ is an *aerodynamic admittance*, allowing for the fact that smaller gusts (higher frequencies) do not completely envelope the bridge cross-section. Konishi *et al.* (1975), Shiraishi and Matsumoto (1977), Jancauskas (1986) and others have directly measured this function for bridge deck sections and other bluff shapes. Note that this aerodynamic admittance which applies to vertical (cross-wind) aerodynamic forces is similar, but not identical, to that discussed in Section 5.3.1, which relates to along-wind forces and response.

Analysis based on Equation (12.7) and the methods of random vibration analysis outlined in Section 5.3.6 have given good agreement with the measured response on full aeroelastic wind-tunnel models (e.g. Holmes, 1975) and full-scale measurements (Melbourne, 1979). However, for large-span bridges, the towers and cables play important parts in the overall bridge response, and it is the practice to carry out full aeroelastic model studies in simulated turbulent boundary-layer flow, as described in Section 12.4.

12.3.4 Effective static load distributions

The method of equivalent static load distributions discussed in Section 5.4 can be applied to the response of bridges. In many cases of long-span bridges, the background response can be neglected in comparison to the resonant contributions. However, it is often the case that several modes are significant. The following approach (Holmes, 1999) gives the correct method of combining inertial force distributions from more than one resonant mode of vibration. This approach is consistent with the weighting factor method discussed in Section 5.4.5.

The mean-square fluctuating value of a load effect, *r*, resulting from the resonant response in mode *j*, can be written as:

$$\sigma_{rj}^2 = \alpha_j^2 \omega_j^4 \overline{a_j^2} \qquad (12.8)$$

where the displacement response of the deck is written as:

$$y(x, t) = \phi_j(x) \cdot a_j(t)$$

$\phi_j(x)$ is the mode shape and $a_j(t)$ the modal coordinate for the jth mode. ω_j is the circular frequency in mode $j(= 2\pi n_j)$ and a_j is the integral:

$$\int_0^L m(x) \cdot \phi_j(x) \cdot I(x) \mathrm{d}x \tag{12.9}$$

$m(x)$ is the mass per unit length and $I(x)$ the influence line for the load effect in question.

The contribution of the load at each spanwise position to the load effect is the product of the inertial load on a small increment of span, centred at that position, $m(x) \cdot \omega_j^2 \cdot y(x,t) \cdot \delta x$, multiplied by the influence function, $I(x)$. Equation (12.8) is then obtained by integration of the contributions over the span, L, squaring and taking the mean value.

The *total* mean-square fluctuating response is then obtained by summing the contributions from the N contributing modes:

$$\sigma_r^2 = \sum_j^N \alpha_j^2 \omega_j^4 \overline{a_j^2} \tag{12.10}$$

To obtain Equation (12.10), we have assumed that the modes are well separated, and hence the resulting responses can be assumed to be uncorrelated with each other.

The *envelope* of the combined dynamic loadings at each point along the span of a bridge can be obtained by taking the root sum of squares of the inertial loads from the contributing modes along the span and adding to the mean loading. Thus,

$$f_{env}(x) = \bar{f}(x) \pm \left[\sum_j^N \left(m(x) \cdot \omega_j^2 \phi_j(x) \right)^2 \overline{a_j^2} \right]^{1/2} \tag{12.11}$$

where $\bar{f}(x)$ is the mean wind loading at x.

Note that the envelope is independent of the influence line, $I(x)$, of the load effect. It represents the limits within which the effective static load distributions for all load effects must lie.

The contribution of each mode to the total static equivalent load corresponding to a peak load effect (e.g. a bending moment at any point along the span) depends on the shape of the influence line for that load effect. Thus, there is no single static equivalent load. The weighting factor to be applied to obtain the contribution from mode j to the combined inertial load for a *root-mean-square* value of a given load effect, when a total of N modes contribute, is given by:

$$W_j' = \frac{\alpha_j \omega_j^4 \overline{a_j^2}}{\left\{ \sum_j^N \alpha_j^2 \omega_j^4 \overline{a_j^2} \right\}^{1/2}} \tag{12.12}$$

It can be demonstrated that Equation (12.12) will result in the correct mean-square fluctuating response, as given by Equation (12.10).

The effective loading distribution for the root-mean-square fluctuating response, σ_r, obtained by summing over all modes is:

$$p'_{eff}(x) = m(x)\sum_{j}^{N} W_j'\phi_j(x) \tag{12.13}$$

The total root-mean-square fluctuating response is then:

$$\sigma_r = \int_0^L p_{eff}'(x)\cdot I(x)\mathrm{d}x = \int_0^L I(x)\cdot m(x)\sum_{j}^{N} W_j'\phi_j(x)\mathrm{d}x$$

$$= \frac{\sum_{j}^{N}\alpha_j^2\omega_j^4\overline{a_j^2}}{\left\{\sum_{j}^{N}\alpha_j^2\omega_j^4\overline{a_j^2}\right\}^{1/2}} = \left\{\sum_{j}^{N}\alpha_j^2\omega_j^4\overline{a_j^2}\right\}^{1/2}$$

which agrees with Equation (12.10).

The weighting factor for the contribution from mode j to the effective static loading for the *peak* (maximum or minimum) load effect, r, in a specified time period, T, can be written to a good approximation as:

$$W_j = \frac{\left\{\sum_{j}^{N}\alpha_j^2 g_j^2\omega_j^4\overline{a_j^2}\right\}^{1/2}\alpha_j\omega_j^4\overline{a_j^2}}{\sum_{j}^{N}\alpha_j^2\omega_j^4\overline{a_j^2}} \tag{12.14}$$

where g_j is an expected peak factor for the response in mode j.

Equation (12.14) can be obtained from Equation (12.12) as follows:

$$W_j = g_r W_j'$$

where g_r is the peak factor for the response, which can be approximated quite accurately by,

$$g_r \cong \frac{\left\{\sum_{j}^{N}\alpha_j^2 g_j^2\omega_j^4\overline{a_j^2}\right\}^{1/2}}{\left\{\sum_{j}^{N}\alpha_j^2\omega_j^4\overline{a_j^2}\right\}^{1/2}} \tag{12.15}$$

This is a weighted average of the peak factors for the various modes.

When only one mode is significant, Equation (12.14) reduces to:

$$W_j = g_j\omega_j^2(\overline{a_j^2})^{1/2} \tag{12.16}$$

i.e. simply the peak inertial force in the mode j.

Note that Equation (12.16) is independent of α_j, and hence of the influence line $I(x)$.

The contribution to the total inertial loading from mode *j* at a given spanwise position is then given by the product of W_j with the mass/unit length, *m(x)*, and the mode shape at that position. The total effective static loading for the peak load effect, *r*, is then:

$$f_{est}(x) = \overline{f}(x) + m(x)\sum_{j}^{N} W_j \phi_j(x) \qquad (12.17)$$

The effective static loading depends on the influence line for *r* through the parameter α_j. Thus, the effective static loading will be different for load effects, e.g. bending moments at different span wise positions. If the influence line is symmetrical about the centre of the bridge as, for example, that for the bending moment at centre span, then a_j will be zero for antisymmetrical modes, i.e. only symmetrical modes will contribute.

It should also be noted that as g_r from Equation (12.15) can be either positive or negative, the second term on the right-hand side of Equation (12.17) can also be either positive or negative, i.e. it may add or subtract from the mean loading.

12.4 Wind-tunnel techniques

The verification of aerodynamic stability and determination of response to wind of longspan bridges, for structural design, is still largely an experimental process, making use of modern wind-tunnel techniques. Some of the experimental techniques were discussed in Chapter 7 (Sections 7.6.3 and 7.6.4).

A full wind-tunnel test programme for a major long-span bridge might consist of all or some of the following phases:

- Section model tests to determine basic static aerodynamic force and moment coefficients (Section 12.2) for the deck section.
- Section model free or forced vibration tests to determine the aerodynamic or flutter derivatives (Sections 5.5.3 and 12.3.2).
- Section model tests in which the natural frequencies in vertical translation and rotation are scaled to match those of the prototype bridge, and critical flutter speeds are thence determined by slowly increasing the wind-tunnel speed (Section 7.6.3). This may be done in both smooth (low turbulence) and turbulent flow. (An alternative method which better reproduces the mode shapes of the prototype bridge is the ‘taut strip’ method described in Section 7.6.3.)
- Scaled aeroelastic models of the completed bridge, i.e. deck, towers, cables, tested in turbulent boundary-layer flow (Section 7.6.4). The multi-mode aeroelastic modelling scales the various parts of the bridge for elastic properties, mass (inertial), as well as geometric properties. Such tests are quite expensive, with much of the cost in the model design and manufacture.
- Scaled aeroelastic partial models of the bridge in various stages of erection. In most cases, the erection stages find a bridge in its most vulnerable state with respect to wind loading, with lower frequencies making them more prone to turbulent buffeting (Section 12.3.3) and lower flutter speeds, because flutter instabilities tend to occur at constant *reduced* velocity. The erection stage tests may include separate aeroelastic tests of the bridge towers as free-standing structures.

A complete series of tests as outlined above may require two or three different wind tunnels. The wind-tunnel testing of bridges tends to be a specialist activity for wind-tunnel laboratories, with few facilities being capable of carrying out all the above-listed tests. Some facilities restrict their involvement to section testing for bridge decks; others only carry out boundary-layer wind-tunnel tests. However, it should be noted that to satisfactorily carry out aeroelastic tests on full models of the largest suspension bridges, a test section of at least 10 m width (e.g. Figure 12.7) is required. Few boundary-layer wind tunnels are of this size.

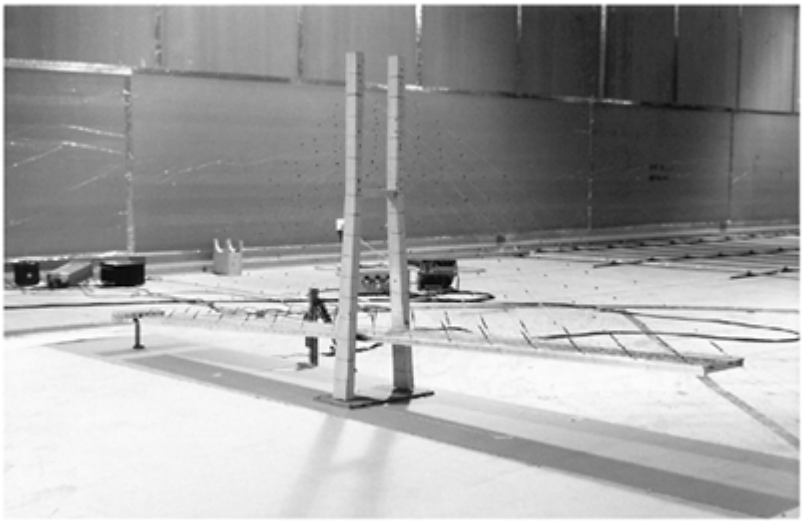

Figure 12.7 A full aeroelastic model of a cable-stayed bridge in a construction stage.

12.5 Vibration of bridge cables

As the spans of cable-stayed bridges have increased and the cables themselves have become longer, cable vibration has become more of a problem. One of the more interesting excitation mechanisms, and until recently, least-understood ones, is the so-called ‘rain—wind’ vibration. In the following sections, the history of occurrences of this phenomenon, suggested excitation mechanisms and methods of mitigating the vibrations are reviewed.

12.5.1 Rain—wind vibration

The first, clearly defined occurrence of wind-induced cable vibration, during which the presence of rain was an essential feature, was observed during the construction of Meiko-Nishi Bridge at Nagoya Harbour, Japan, in 1984. Low-frequency (1–3 Hz) vibrations of some cables, with double amplitudes up to 300mm, were observed, over a 5-month

period. This bridge has a main span of 405 m with cables up to 165 mm in diameter and lengths varying from 65 to 200 m. The vibrations occurred in wind speeds between 7 and 14 m/s; these speeds greatly exceeded the critical wind speeds for vortex shedding at the low frequencies observed. Using a section of polyethylene pipe casing from the prototype structure, wind-tunnel tests were conducted, with and without simulated rain, and it was clearly established that the rain was necessary to induce vibration over a defined range of wind speeds (Hikami and Shiraishi, 1988).

Later, it was found that rain-wind induced vibration had occurred on six bridges in Japan. A common feature was that the vibrating cables were usually sloping down-wards in a downwind direction, with the wind approaching obliquely to the plane of the cable (Figure 12.8). Vibrations were apparently observed only for cables encased in polyethylene.

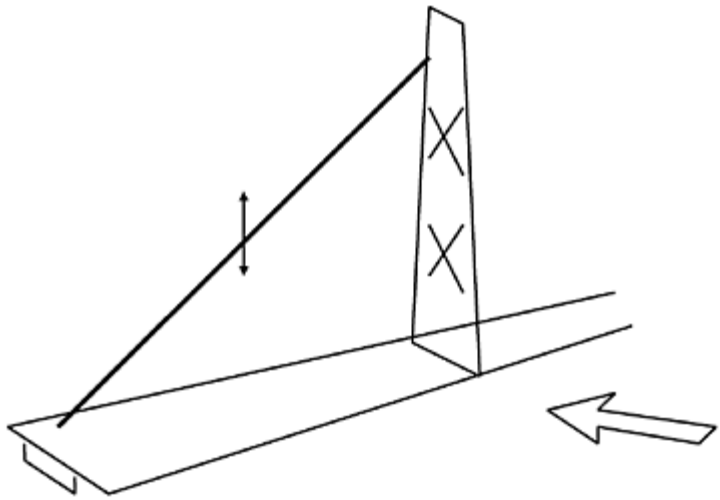

Figure 12.8 Typical cable/wind orientation for rain-wind vibration.

Outside Japan, rain—wind vibration of bridge cables have been observed on the Faroe Bridge (Denmark), Bretonne Bridge (France), Koehlbrand Bridge (Germany), Normandie Bridge (France) and the Fred Hartman Bridge (USA). Many other bridges have experienced cable vibrations—some from different mechanisms such as high-frequency vortex-shedding excitation or from unknown or undefined mechanisms.

12.5.2 Excitation mechanisms

The wind-tunnel studies carried out, following the vibrations observed on the Meiko-Nishi Bridge, indicated that the motion was induced by the presence of two water ‘rivulets’ that oscillated in circumferential position with the cable motion. At low wind speeds, a single rivulet formed on the underside. Motion commenced at higher wind speeds when a second rivulet formed on the upper surface. The rivulets act as trigger

points to promote flow separation on the vibrating cable, as shown in Figure 12.9. In this figure, the effective cross-wind shape is postulated to be elliptical. Other observations have suggested that the circumferential motion was not two-dimensional, and that the width and depth of the rivulet on the upper surface were less than that on the lower surface.

Wind-tunnel tests in France for the Normandie Bridge (Flamand, 1994) showed that carbon combustion products deposited on the surface of the casing were necessary for aerodynamic instability to occur, indicating the role played by surface tension in allowing the water rivulet to be maintained.

Fundamental wind-tunnel model studies of inclined cable aerodynamics, with and without rain, have been made at various angles of pitch (inclination), yaw and rivulet position. It was found that aerodynamic oscillations were of either the 'velocity-restricted' type (i.e. occurring over a narrow range of wind speeds) and produced by vortex shed-ding or of the 'divergent' or galloping type (Section 5.5.2)—i.e. vibration triggered at a particular wind speed and rapidly increasing in amplitude. However, instabilities usually commenced at reduced wind velocity ($U/n_c b$, where U is the wind velocity, n_c the cable frequency and b the diameter) of about 40. In the case of the vortex-induced vibrations,

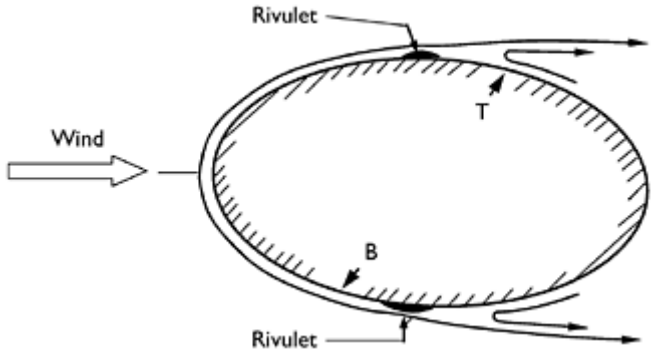

Figure 12.9 Flow separations produced by rivulets of rain water.

these tended to occur in narrow bands of wind speed centred around 40 or multiples of 40, i.e. 80, 120, etc. (Matsumoto *et al.*, 1993).

12.5.3 Solutions

The solutions that have been successful in eliminating or mitigating rain-wind induced vibration of bridge cables can be divided into the following categories:

- aerodynamic treatments—i.e. geometrical modifications of the outer cable casing;
- auxiliary cable ties; and
- auxiliary dampers.

Model measurements were carried out by Miyata *et al.* (1994), on sections of cable models with the same diameter as full-size cables, with a variety of roughened surface treatments (Figure 12.10). Discrete roughness, of about 1% of the diameter, was found to be effective in suppressing rain-wind induced vibration. The explanation was that supercritical flow was promoted at lower Reynolds numbers than would occur on cables with smooth surface finish.

Wind-tunnel tests in France (Flamand, 1994) found that parallel surface projections did stabilize a cable model, but produced a high drag coefficient in the super-critical Reynolds number range. An alternative solution which minimized the drag increase was adopted, namely the use of a double helix spiral, 1.3 mm high, 2 mm wide and with a pitch of 0.6m. This configuration was adopted for the Normandie Bridge.

Usually only one or two stay cables from a harp or fan array will experience rain-wind vibration in particular atmospheric conditions. This observation led to a solution that has been used on several bridges—cable cross-ties. They have also been used on the Normandie Bridge, where they are known as ‘aiguilles’. They have been adopted for the Dane Point Bridge, Florida, USA, the Fred Hartman Bridge, Texas, and the Tatara Bridge, Japan (Figure 12.11).

A fundamental study of damping in stay cables, and of the effectiveness of cross-ties, was carried out by Yamaguchi and Fujino (1994). Measurements on cables of a typical cable-stayed bridge indicated a range of critical damping ratios, from about 0.001 to 0.003, for the first mode, with lower values occurring for the low sag ratios, i.e. a higher pre-stress. A laboratory experiment on cross-ties showed that a ‘stiff’ cross-tie performed

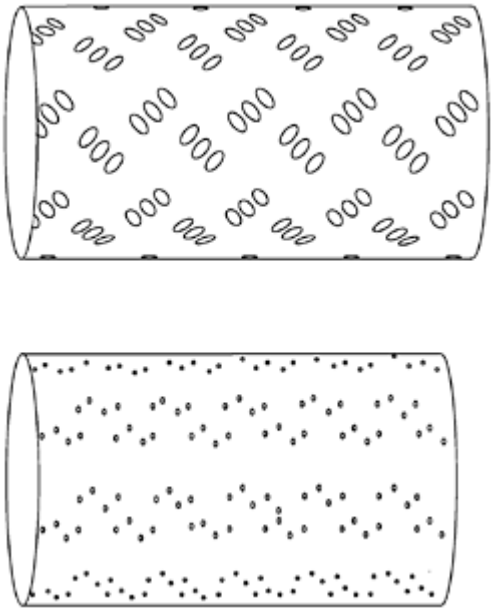

Figure 12.10 Surface roughness treatments for cable vibration mitigation (Miyata *et al.*, 1994).

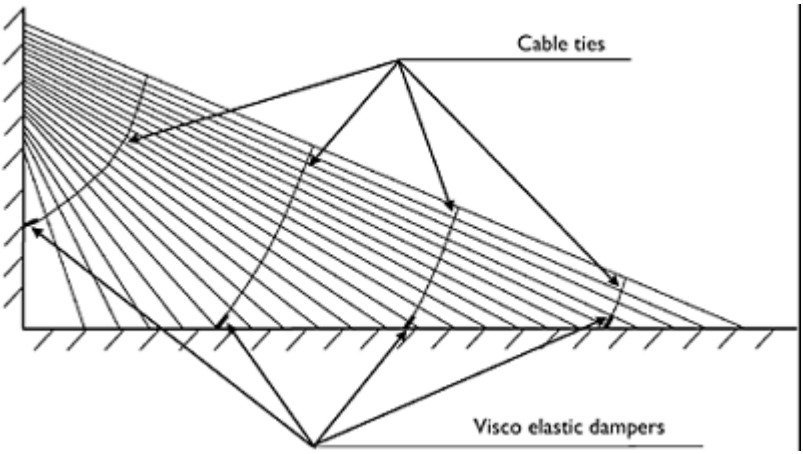

Figure 12.11 Vibration mitigation cable ties used on the Tatara Bridge.

a function of transferring vibration energy from a vibrating cable to its neighbours. By use of 'soft' cross-ties, energy could also be dissipated in the cross-ties, making this system more effective.

Energy dissipation can also be provided by auxiliary damping devices mounted between the cable and the bridge girder, near the connection points. This solution is more expensive than the cross-tie method, but more aesthetically pleasing. Oil dampers and viscoelastic dampers (Section 9.9.2) have been used for this purpose.

12.6 Case studies

The literature on the aerodynamics of long-span bridges is extensive, and many papers on the subject contain references to particular bridges for illustration purposes. Sections 12.3.1 and 12.5 contain several examples in relation to vortex-shedding induced vibrations and cable vibrations, respectively. Holmes (1999) has described the application of the equivalent static load method (Section 12.3.4) to generate design loadings for the Baram River (Malaysia) cable-stayed bridge.

The extensive wind engineering studies carried out for the current (2006) first and second longest bridges in the world are described by Miyata *et al.* (1992) for the AkashiKaikyo Bridge and by Reinhold *et al.* (1992) and Larsen and Jacobsen (1992) for the Great Belt East Bridge (Denmark). The wind design of the Normandie Bridge from the designer's point of view is well covered by Virlogeux (1992).

12.7 Summary

In this chapter, the aerodynamics of bridges have been presented in a summary form. Long-span bridges are probably the most 'wind sensitive' of all structures, and their aerodynamics are complex and are the sphere of specialists. The main phenomena of vortex shedding, flutter and buffeting have been discussed.

The vibration of the cables on cable-stayed bridges has become the limiting factor on their ultimate spans, and this topic, with alleviation measures, has been discussed in some detail.

References

Baker, B. (1884) The Forth Bridge. *Engineering,* 38:213.

Billington, D.P. (1977) History and esthetics in suspension bridges. *ASCE Journal of the Structural Division,* 103:1655–72.

Davenport, A.G. (1962) Buffeting of a suspension bridge by storm winds. *ASCE Journal of the Structural Division,* 88:233–68.

Flamand, O. (1994) Rain-wind induced vibrations of cables. *International Conference on Cable-Stayed and Suspension Bridges,* Deauville, France, 12–15 October.

Frandsen, J.B. (2001) Simultaneous pressures and accelerations measured full-scale on the Great Belt East suspension bridge. *Journal of Wind Engineering & Industrial Aerodynamics,* 89: 95–129.

Ge, Y.J. and Tanaka, H. (2000) Aerodynamic flutter analysis of cable-supported bridges by multi-mode and full-mode approaches. *Journal of Wind Engineering & Industrial Aerodynamics,* 86:123–53.

Gimsing, N.J. (1983) *Cable-Supported Bridges.* Wiley, New York.

Hikami, Y. and Shiraishi, N. (1988) Rain-wind induced vibrations of cables in cable-stayed bridges. *Journal of Wind Engineering & Industrial Aerodynamics, 29:*409–18.

Holmes, J.D. (1975) Prediction of the response of a cable-stayed bridge to turbulence. *Proceedings, 4th International Conference on Wind Effects on Buildings and Structures,* London, 8–12 September, pp. 187–97, Cambridge University Press, Cambridge.

Holmes, J.D. (1979) Monte Carlo simulation of the wind-induced response of a cable-stayed bridge. *Proceedings, 3rd International Conference on Applications of Statistics and Probability in Soil and Structural Engineering (ICASP-3),* Sydney, pp. 551–65, University of New South Wales, Australia.

Holmes, J.D. (1999) Equivalent static load distributions for resonant dynamic response of bridges. *Proceedings, 10th International Conference on Wind Engineering,* Copenhagen, Denmark, 21–24 June, pp. 907–11, Balkema, Rotterdam.

Irwin, H.P.A.H. (1977) Wind tunnel and analytical investigations of the response of Lions' Gate Bridge to a turbulent wind. Laboratory Technical Report, LTR-LA-210, June. National Aeronautical Establishment, Canada.

Jancauskas, E.D. (1986) The aerodynamic admittance of two-dimensional rectangular section cylinders in smooth flow. *Journal of Wind Engineering & Industrial Aerodynamics,* 23: 395–408.

Kernot, W.C. (1893) Wind pressure. *Proceedings, Australasian Society for the Advancement of Science,* V: 573–81.

Konishi, I., Shiraishi, N. and Matsumoto, M. (1975) Aerodynamic response characteristics of bridge structures. *Proceedings, 4th Internal Conference on Wind Effects on Buildings and Structures,* London, 8–12 September, pp. 199–208, Cambridge University Press, Cambridge.

Larsen, A. (ed.) (1992) Aerodynamics of large bridges. *Proceedings of the First International Symposium on Aerodynamics of Large Bridges,* Copenhagen, Denmark, 19–21 February, Balkema, Rotterdam.

Larsen, A. and Jacobsen, A.S. (1992) Aerodynamic design of the Great Belt East Bridge. *Proceedings of the First International Symposium on Aerodynamics of Large Bridges,* Copenhagen, Denmark, 19–21 February, pp. 269–83, Balkema, Rotterdam.

Larsen, A., Esdahl, S., Andersen, J.E. and Vejrum, T. (1999) Vortex shedding excitation of the Great Belt suspension bridge. *Proceedings, 10th International Conference on Wind Engineering,* Copenhagen, Denmark, 21–24 June, pp. 947–54, Balkema, Rotterdam.

Matsumoto, M., Shirato, H., Saito, H., Kitizawa, H. and Nishizaki, T. (1993) Response characteristics of rain-wind induced vibration of stay cables of cable-stayed bridges. *1st European-African Regional Congress on Wind Engineering,* Guernsey, 20–24 September.

Melbourne, W.H. (1979) Model and full-scale response to wind action of the cable-stayed, boxgirder, West Gate Bridge. *IAHR/IUTAM Symposium on Flow-Induced Vibrations,* Karlsruhe, Germany, 3–8 September.

Miyata, T., Yamada, H. and Hojo, T. (1994) Aerodynamic response of PE stay cables with pattern indented surface. *International Conference on Cable-Stayed and Suspension Bridges,* Deauville, France, 12–15 October.

Miyata, T., Yokoyama, Y., Yasuda, M. and Hikami, Y. (1992) Akashi Kaikyo Bridge: wind effects and full model tests. *Proceedings of the First International Symposium on Aerodynamics of Large Bridges,* Copenhagen, Denmark, 19–21 February, pp. 217–36, Balkema, Rotterdam.

Ostenfeld, K.H. and Larsen, A. (1992) Bridge engineering and aerodynamics. *Proceedings of the First International Symposium on Aerodynamics of Large Bridges,* Copenhagen, Denmark, 19–21 February, pp. 3–22, Balkema, Rotterdam.

Petroski, H. (1996) *Engineers of Dreams.* Vintage Books, New York.

Reinhold, T.A., Brinch, M. and Damsgaard, A. (1992) Wind-tunnel tests for the Great Belt link. *Proceedings of the First International Symposium on Aerodynamics of Large Bridges,* Copenhagen, Denmark, 19–21 February, pp. 255–67, Balkema, Rotterdam.

Sabzevari, A. and Scanlan, R.H. (1968) Aerodynamic instability of suspension bridges. *ASCE Journal of the Engineering Mechanics Division,* 94:489–519.

Scanlan, R.H. and Gade, R.H. (1977) Motion of suspended bridge spans under gusty winds. *ASCE Journal of the Structural Division,* 103:1867–83.

Scanlan, R.H. and Lin, W.-H. (1978) Effects of turbulence on bridge flutter derivatives. *ASCE Journal of the Engineering Mechanics Division,* 104:719–33.

Scanlan, R.H. and Tomko, J.J. (1971) Airfoil and bridge flutter derivatives. *ASCE Journal of the Engineering Mechanics Division,* 97:1717–37.

Selberg, A. (1961) Aerodynamic effects on suspension bridges. *Acta Polytechnica Scandinavica,* Engineering and Building Construction Series No. 13, Trondheim, Norway.

Selberg, A. (1963) Aerodynamic effects on suspension bridges. *Proceedings, International Conference on Wind Effects on Buildings and Structures,* Teddington, UK, 26–28 June 1963, pp. 462–86.

Shiraishi, N. and Matsumoto, M. (1977) Aerodynamic responses of bridge structures subjected to strong winds. *Symposium on Engineering for Natural Hazards,* Manila, September.

Simiu, E. and Scanlan, R.H. (1996) *Wind Effects on Structures—Fundamentals and Applications to Design,* 3rd Edition. Wiley, New York.

Smith, I.J. (1980) Wind induced dynamic response of the Wye Bridge. *Engineering Structures,* 2:202–8.

Steinman, D.B. and Watson, S.R. (1957) *Bridges and Their Builders.* Dover Publications, New York,

van Nunen, J.W.G. and Persoon, A.J. (1982) Investigation of the vibrational behaviour of a cable-stayed bridge under wind loads. *Engineering Structures*, 4:99–105.

Virlogeux, M. (1992) Wind design and analysis for the Normandy Bridge. *Proceedings of the First International Symposium on Aerodynamics of Large Bridges*, Copenhagen, Denmark, 19–21 February, pp. 183–216, Balkema, Rotterdam.

Virlogeux, M. (1999) Recent evolution of cable-stayed bridges. *Engineering Structures*, 21: 737–55.

Wardlaw, R.L. (1971) Some approaches for improving the aerodynamic stability of bridge road decks. *3rd International Conference on Wind Effects on Buildings and Structures*, Tokyo, Japan, 6–9 September, Saikon Shuppan, Tokyo.

Yamaguchi, H. and Fujino, T. (1994) Damping in cables in cable-stayed bridges with and without damping control measures. *International Conference on Cable-Stayed and Suspension Bridges*, Deauville, France, 12–15 October.

13
Transmission lines

13.1 Introduction

Electrical transmission lines and their supporting towers are, like other structures, subjected to severe wind storms of various types, and their safe and economic design for wind loading is of concern to the power utilities. There are significant differences between the response of high-voltage transmission towers and other structures to wind:

- They are structurally designed with generally lower safety margins against collapse than other structures.
- The overall length of a transmission line system is relevant when considering the probability and risk of receiving strong winds from localized wind storms such as thunderstorm downbursts and tornadoes.

This chapter deals with the wind loading of the transmission lines themselves and risk issues associated with a long transmission line as a system. The wind loading of the supporting towers and poles is covered elsewhere in the book, in particular, Chapter 11.

13.2 Structural response and calculation of wind loads

Basic design data for wind loads on transmission line conductors in temperate synoptic winds have been compiled by the American Society for Civil Engineers (1990) and CSIR (1990) in South Africa.

13.2.1 Nature of the response

Fortunately, resonant dynamic response does not appear to be a major problem with transmission line systems. Although the suspended lines themselves usually have natural frequencies less than 1 Hz, the resonant response is largely damped out because of the very large aerodynamic damping (Section 5.5.1; e.g. Matheson and Holmes, 1981).

The natural frequencies of supporting towers up to 50 m in height are normally greater than 1 Hz, and hence the resonant response is also negligible. Thus, except for extremely tall supporting towers and long line spans, we can safely compute the peak response of a transmission line system, neglecting the resonant dynamic response. Then the peak response is directly related to the instantaneous gusts upwind, and hence transmission line structures can be designed using gust wind speeds. However, because of the nonuniform spatial gust structure, assumption of the same peak gust along the full span is conservative; this leads to the concept of a *span reduction factor*.

For those cases where resonant response is significant, i.e. very high supporting towers and very long spans, a simplified random response model of the tower-line combination based on the gust response factor concept is available (Davenport, 1979).

13.2.2 Wind forces on conductors

The nominal wind force acting on a single conductor perpendicular to the span can be taken to be:

$$F_c = q_{zc} \cdot C_d \cdot A_c \sin^2 \theta \cdot a \tag{13.1}$$

where q_{zc} is the free-stream dynamic wind pressure $(= \frac{1}{2}\rho_a \hat{U}_{zc}^2)$ at a suitable mean conductor height, z_c. A suitable value for z_c is shown in Figure 13.1, taken from the South African recommendations for transmission line loading (CSIR, 1990). C_d is the drag force coefficient for the conductor. A_c is the reference area, which may be taken as $s \times b$, where s is the wind span (see Figure 13.1) and b the conductor diameter. θ is the horizontal angle of incidence of the wind in relation to the direction of the line, α is a span reduction factor.

The ASCE Guidelines show experimental data for the drag force coefficient as a function of Reynolds number, *Re* (Section 4.2.4), for several conductor types, based on wind-tunnel tests. These data are reproduced in Figure 13.2. The Reynolds number can be calculated by:

$$Re = \frac{U_{zc} b}{15 \times 10^{-6}} \tag{13.2}$$

where U_{zc} is the design gust wind speed in metres per second at the mean conductor height, z_c. The conductor diameter, b, is in metres.

The South African design recommendations (CSIR, 1990) have simplified the data to give the design line shown in Figure 13.3.

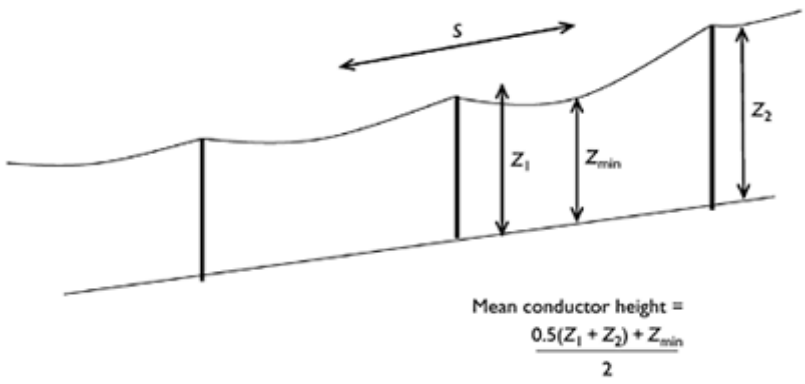

Figure 13.1 Mean conductor height (CSIR, 1990).

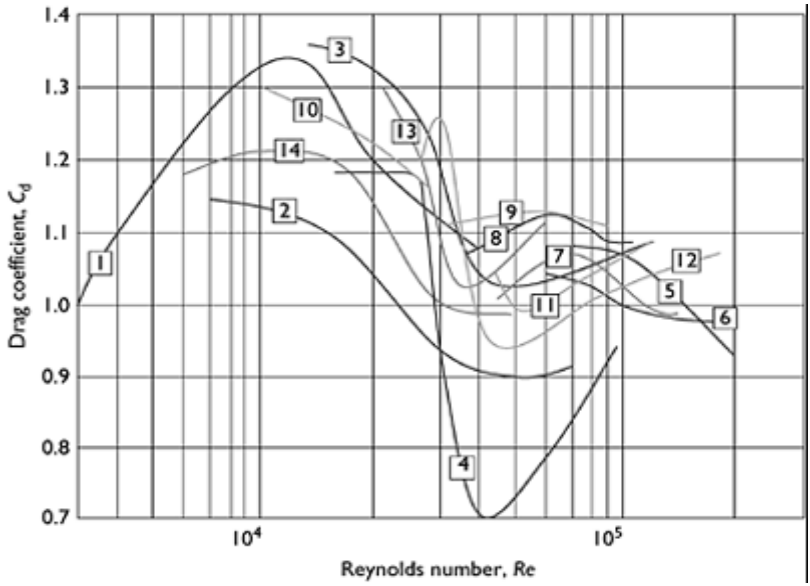

Figure 13.2 Drag force coefficients on conductors from wind-tunnel tests (ASCE, 1990).

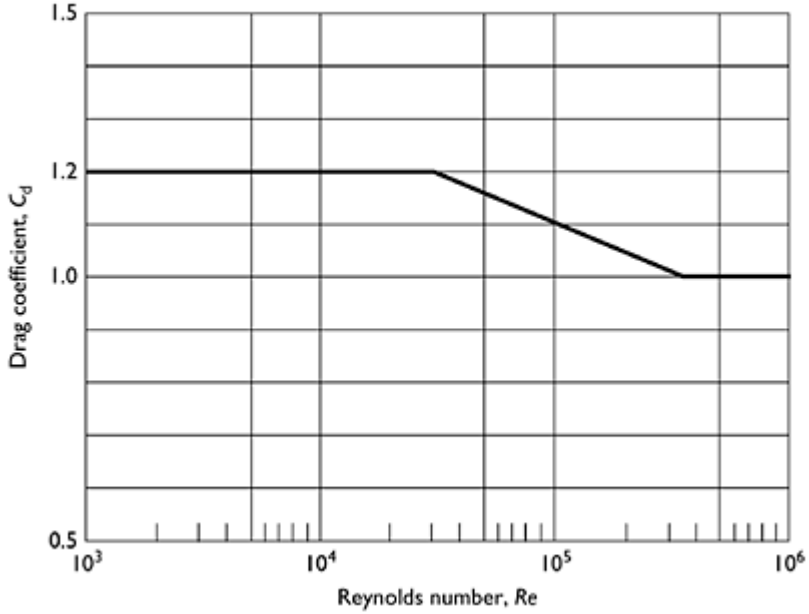

Figure 13.3 Design values of conductor drag coefficient recommended by CSIR (1990).

13.2.3 Span reduction factor

The span reduction factor, a, allows for the reduction in peak wind along the span of a conductor due to the non-simultaneous action of the gusts. As it is determined by the structure of turbulence in the approaching wind flow, the span reduction factor is a function of the approach terrain, the mean conductor height and the span. This factor has a direct relationship with the gust response factor, *G* (Section 5.3.2). The relationship is as follows:

$$\alpha = G\left(\frac{\bar{U}_z}{\hat{U}_z}\right)^2 \tag{13.3}$$

where $\bar{U}_z$ is the mean wind speed at height *z* and $\hat{U}_z$ the gust speed at the same height.

Using Equation (13.3), the values of gust response factors recommended in the ASCE Guidelines for Electrical Transmission Lines (1990) have been converted to span reduction factors for various terrain types, conductor heights and spans. The resulting factors are insensitive to the conductor height, and the following equations can be used to predict values of α:

$$\alpha = 0.58 + 0.42\ \exp\left(\frac{-s}{180}\right) \quad \text{for rural terrain} \tag{13.4}$$

$$\alpha = 0.50 + 0.50\ \exp\left(\frac{-s}{140}\right) \quad \text{for urban terrain} \tag{13.5}$$

where *s* is the span in metres.

In Table 13.1, values of span reduction factor for various spans have been calculated using Equations (13.4) and (13.5). Clearly the span reduction factor reduces with increasing span and with increasing terrain roughness. In the latter case, the reduction occurs because of the increased fluctuating component in the peak load on the line.

13.2.4 Conductor shielding

In both the ASCE Guidelines (1990) and the CSIR Recommendations (1990), no allowance for shielding for individual conductors in a bundle is permitted. Such shielding effects would be small and would not be present for every angle of attack of the instantaneous wind to the line.

Table 13.1 Span reduction factors for transmission line conductors

Conductor span (m)	*Rural terrain ($Z_0 \cong 0.02$ m)*	*Urban terrain ($z_0 \cong 0.2$ m)*
200	0.72	0.62
300	0.66	0.56
400	0.63	0.53
500	0.61	0.51

Note: The above values are applicable to large-scale synoptic winds. Span reduction factors in thunderstorm downbursts are much greater.

13.2.5 Wind forces on lattice supporting towers

The calculation of wind forces on lattice towers typical of those used in high-voltage transmission line system is discussed in Section 11.3.2. The overall drag coefficients for lattice towers depend on the solidity of the towers. Higher solidity results in greater mutual interference and shielding and a reduction in drag coefficient, based on the projected area of members.

13.3 Risk models for transmission line systems

Transmission line systems often extend for several hundred kilometres and are prone to impact by small intense local windstorms such as tornadoes (Section 1.3.4) and downbursts (Section 1.3.5). There has been a history of failures of transmission line systems from these events—especially in large continental countries like Australia, Brazil and Argentina (e.g. Hawes and Dempsey, 1993). Figure 13.4 shows the result of one such event. The risk of failure of *any one tower* along a line is much greater than that for a single isolated structure. Design of the supporting structures requires knowledge of the total risk of the complete line to these small intense windstorms. Knowledge of the risk of failures enables a balance to be made between the cost of failures and the cost of replacement towers. This may vary from country to country, as in some cases there are alternative routes for power transmission.

13.3.1 Tornado risk model

Twisdale and Dunn (1983) describe several tornado risk models for point and ‘lifeline’ targets. Milford and Goliger (1997) developed a tornado risk model for transmission line design which considered normal intersection of a tornado with the line direction.

Figure 13.4 Failure of a high-voltage transmission tower following a local downburst event.

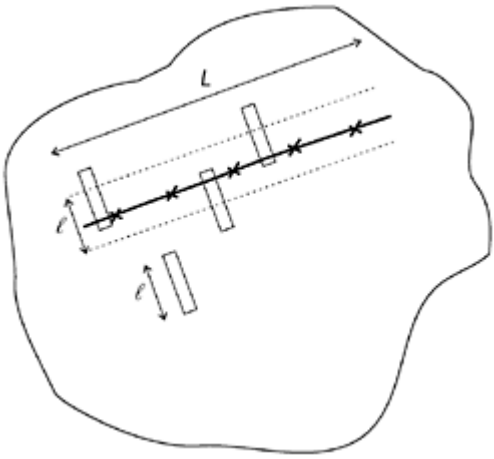

Figure 13.5 Normal intersection of a tornado with a transmission line system.

A simplified probabilistic model is discussed in this section, considering both normal and oblique intersections of tornado tracks with the line target, representing a transmission line.

As the width of tornado tracks (usually less than 100 m) is almost always less than the span length between towers, the critical factor in line failure is the intersection of a

tornado with a tower. Thus, the rate of intersection with a tower is required, rather than with the conductors.

Consider a region specified by its area, A (square kilometres), in which there is an average tornado occurrence of n events per year, so that the per square kilometre rate for the region is:

$$\upsilon = n/A \tag{13.6}$$

Normal intersection of a tornado path of length, ℓ, and width, w, with a line of overall length, L, occurs only for those tracks whose centre falls within the zone of area, $L \times \ell$, adjacent to the line (see Figure 13.5), giving a rate of intersection, r:

$$r = \upsilon L \ell \tag{13.7}$$

This model can be extended to variable intersection angle as follows.

For a tornado path intersecting the transmission line at an angle, β, to normal (Figure 13.6), the width of the zone of intersection reduces to $\ell \cos\beta$ and the rate of intersection (with the line) per annum is now given by:

$$r = \upsilon L \ell \cos\beta \tag{13.8}$$

Now the width of the intersection zone along the line is given by $w/\cos\beta$ and the probability of a *given single point* on the line falling within this zone is $w/(L \cos\beta)$ which may represent a single tower. Thus, the number of intersections of tornadoes with this tower per year is given by:

$$\begin{aligned} r &= \upsilon L \ell \cos\beta \cdot w/(L \cos\beta) \\ &= \upsilon w l \end{aligned} \tag{13.9}$$

If the span length between towers is s, the number of towers along a line of length, L, is equal to L/s, and assuming that intersections are independent (i.e. only one tower is

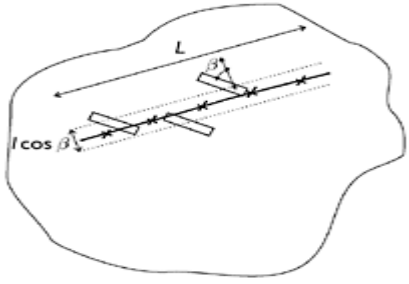

Figure 13.6 Oblique intersection of a tornado with a transmission line system.

intersected by any tornado), then the total number of intersections with *any* tower along the line per year is given by:

$$r_t = (\upsilon w \ell)\ (L/s) \tag{13.10}$$

It should be noted that the rate of intersection is independent of the intersection angle, β. Equation (13.10) may also be written as:

$$r_t = n\ (a/A)N = \upsilon a N \tag{13.11}$$

where n is the number of events per year in an area, A; a the area of tornado path; and N the number of towers in the area.

Example

Assume L=500km; s=0.5 km; ℓ=5 km; w=0.1 km; $\upsilon=10^{-4}$ per km^2 per year. Then, from Equation (13.10), the number of intersections with this line per year=$10^{-4} \times 0.1 \times 5 \times (500/0.5)=0.05$, i.e. an average of 1 intersection every 20 years.

13.3.2 Downburst risk model

Damage 'footprints' produced by severe thunderstorm downbursts (Section 1.3.5) are usually wider than those produced by tornadoes. However, the lengths of the damaged areas produced by downbursts are generally shorter than those of tornadoes. The increased width usually results in several transmission line spans being enveloped by damaging winds, and several adjacent towers often fail as a group. The direct wind load on the conductors themselves is therefore a significant component of the overall wind load in downburst events. This must be incorporated into a risk model.

Oliver *et al.* (2000) describe a downburst risk model for transmission lines, which allows the prediction of an event frequency, where an event is the intersection of a region of wind above a given or design wind speed with a line of some defined length. The probability of such an event is dependent on:

- the overall length of the line, L;
- the relative angle, $\theta - \varphi$, between the direction of the downburst path, θ, and the line orientation, φ;
- the probability of exceedence of the threshold wind speed of interest, U, at any point in the surrounding region, derived from the anemometer records; and
- the width of the path of winds above the threshold, w_u.

The return period, $R_{U,L}$, of the event was shown (Oliver *et al.*, 2000) to be given by:

$$R_{U,L} = (w_u/L) \Big/ \left\{ \sum_{i=1}^{N} \Pr(u > U/|\sin(\theta_i - \varphi)|) \cdot \Pr(\theta_i)|\sin(\theta_i - \varphi)| \right\} \tag{13.12}$$

where it is assumed that:

- there is an average or characteristic downburst damage footprint width associated with each wind speed U, given by w_u;
- for each direction, all downburst tracks can be represented in discrete directional ranges, centred on a characteristic direction, θi, and the summation is over each of these directions;
- the relative probability that the downburst should lie along each of these directions is directly related to the directional frequency of measured gusts; and
- the distribution of wind speed, given a direction, is independent of the directional sector.

The presence of the overall line length, L, in the denominator of Equation (13.12) indicates that, as the overall transmission line length increases, the return period for damaging intersections decreases. Thus, for very long lines orientated at right angles to the prevailing directions of severe thunderstorm winds, the risk of failure may be very high, if these parameters have not been taken account of in the design. This is the experience in large continental countries such as Australia and Argentina, where many failures have occurred (e.g. Hawes and Dempsey, 1993).

An alternative model of downburst risk for transmission line systems has been developed for Argentina by de Schwarzkopf and Rosso (2001).

13.4 Summary

The available data for the specification of wind loads on transmission line structures have been critically reviewed. Risk models which consider the risk of intersection of small intense storms such as tornadoes and downbursts with long transmission line systems are also discussed.

References

American Society of Civil Engineers (1990) Guidelines for transmission line structural loading. ASCE Manual and Reports on Engineering Practice No. 74, ASCE, New York.

CSIR (1990) Transmission line loading. Part I: recommendations and commentary. Part II: Appendices. Engineering Structures Programme, CSIR Building Technology, South Africa.

Davenport, A.G. (1979) Gust response factors for transmission line loading. *Proceedings, 5th International Conference on Wind Engineering*, Fort Collins, CO, pp. 899–909, Pergamon Press, New York,

de Schwarzkopf, M.L.A. and Rosso, L.C. (2001) *A Method to Evaluate Downdraft Risk.* University of Buenos Aires, Argentina.

Hawes, H. and Dempsey, D. (1993) Review of recent Australian transmission line failures due to high intensity winds. Report to Task Force on High Intensity Winds on Transmission Lines, Buenos Aires, 19–23 April.

Matheson, M.J. and Holmes, J.D. (1981) Simulation of the dynamic response of transmission lines in strong winds. *Engineering Structures*, 3:105–10.

Milford, R.V. and Goliger, A.M. (1997) Tornado risk model for transmission line design. *Journal of Wind Engineering & Industrial Aerodynamics*, 72:469–78.

Oliver, S.E., Moriarty, W.W. and Holmes, J.D. (2000) A risk model for design of transmission line systems against thunderstorm downburst winds. *Engineering Structures*, 22:1173–9.

Twisdale, L.A. and Dunn, W.L. (1983) Probabilistic analysis of tornado wind risks. *ASCE Journal of Structural Engineering*, 109:468–88.

14
Other structures

14.1 Introduction

In this chapter the wind loads on some structures not covered in Chapters 8–13, and appendages attached to buildings, will be considered. Some of these structures may be of lesser economic importance, but are often sensitive to wind loads, fail early during a severe wind storm and provide a source of flying debris.

In the following sections wind loads on free-standing walls (including noise barriers along freeways or motorways) and hoardings are discussed. Free-standing paraboloidal antennas for radio telescopes and antennas of various geometries attached to towers or buildings are considered. Wind loading of free-standing roofs or canopies, solar panels attached to the roofs of buildings, as well as appendages attached to buildings such as canopies, awnings and balconies, are also discussed.

14.2 Walls and hoardings

14.2.1 Single walls under normal and oblique winds

In Sections 4.3.1 and 4.3.2, the mean drag coefficients on walls on the ground are discussed in the context of bluff-body aerodynamics. Discussion of wind loads on free-standing walls under normal and oblique winds will be expanded in this chapter.

In Figure 14.1, mean and maximum net pressure difference coefficients acting on complete walls of various breadth/height ratios are shown plotted. These values are based on boundary-layer wind-tunnel measurements (Letchford and Holmes, 1994) in open country terrain (Jensen numbers h/z_0 in the range 50–160). The net pressure coefficient, C_{pn} is defined in Equation (14.1) and, in this case, is equivalent to a drag coefficient:

$$C_{p_n} = \frac{p_W - p_L}{\frac{1}{2}\rho_a \bar{U}_h^2} \tag{14.1}$$

where p_w is the area-averaged pressure coefficient on the windward face of the wall, p_L the area-averaged pressure coefficient on the leeward face of the wall and $\bar{U}h$ is the mean wind speed at the top of the wall.

The maximum values were expected values for periods equivalent to 10 m in in full scale. The mean net pressure coefficients show a small reduction in the range of b/h from 0.5 to 5, as previously shown in Figure 4.5. A larger reduction occurs for the maximum pressure coefficients—this is due to the reduction in spatial correlation for longer lengths

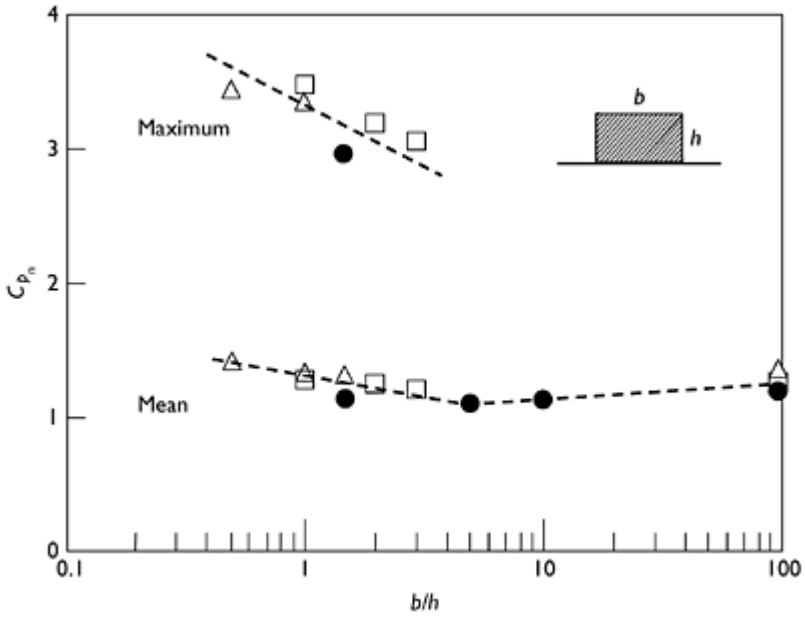

Figure 14.1 Mean and maximum pressure difference coefficients for free-standing walls (normal wind).

of wall. About a 20% reduction in peak net load occurs as the wall length increases from 1 to 4 wall heights.

For a wind direction at 45° to the plane of the walls, the average net pressure coefficients are shown in Figure 14.2. In this case, the net mean pressure coefficient reaches a maximum for a *b/h* ratio of about 3 with lower values for longer walls. For this wind direction, there is a strong separation on the leeward face of the walls of this length ratio. For longer walls, re-attachment occurs and generates lower magnitude pressures on the leeward face.

For mean wind directions normal to the wall, the net pressures do not vary much along the length of the wall. However, this is not the case for the oblique wind direction. Figure 14.3 shows how the mean net pressure coefficient varies along the wall length. The flow separation behind the windward edge generates very high pressures for the first 1 to 2 wall heights from the windward edge. This also occurs for elevated hoardings (Figure 4.8 and Section 14.2.4) and is usually the critical design case for wind loads.

14.2.2 Walls with corners

The effect of a right-angled corner at a free end of a wall for various wind directions on mean pressure coefficients averaged over a vertical line, at a distance *y* from the corner, is shown in Figures 14.4 and 14.5.

For a wind direction of 0°, with the corner running downwind, the effect is small; however, for 180° there is an increase in mean pressure coefficient of up to 30% (Figure 14.4). However, for the 45° wind direction (i.e. blowing from outside the corner), there is a significant reduction in mean pressure coefficients for the region immediately adjacent to the corner (Figure 14.5).

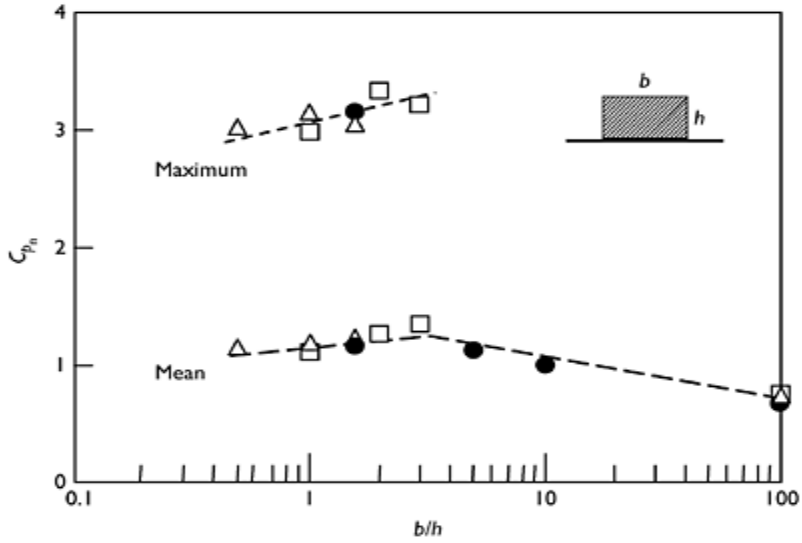

Figure 14.2 Mean and maximum pressure difference coefficients for free-standing walls (oblique wind).

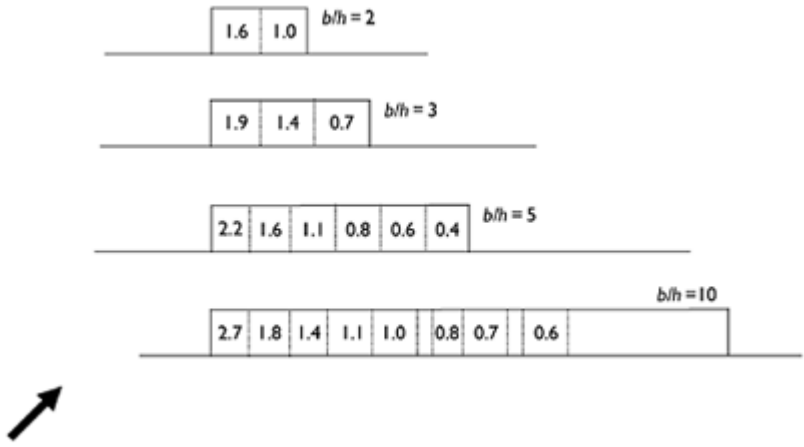

Figure 14.3 Mean pressure difference coefficients for free-standing walls (oblique wind).

14.2.3 Parallel two-dimensional walls

There is an increasing tendency to provide noise barriers along freeways and motorways when they pass through urban areas. These are generally parallel walls spaced at the width of the roadway, so that shielding effects from the opposite wall may be important for certain wind directions. The wind loads on these walls are also affected by other disturbances to the wind flow such as topographic features and elevated bridges.

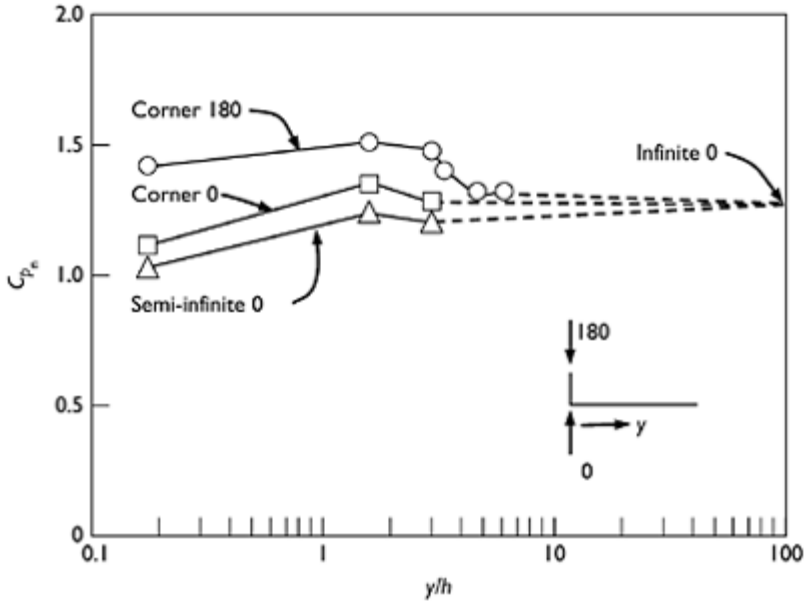

Figure 14.4 Mean pressure difference coefficients for free-standing walls with corners (normal winds).

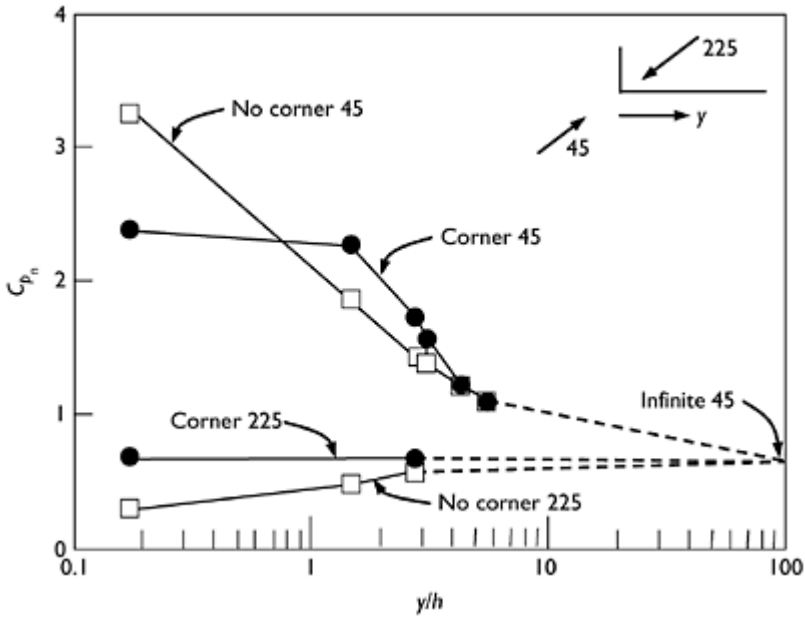

Figure 14.5 Mean pressure difference coefficients for free-standing walls with corners (oblique winds).

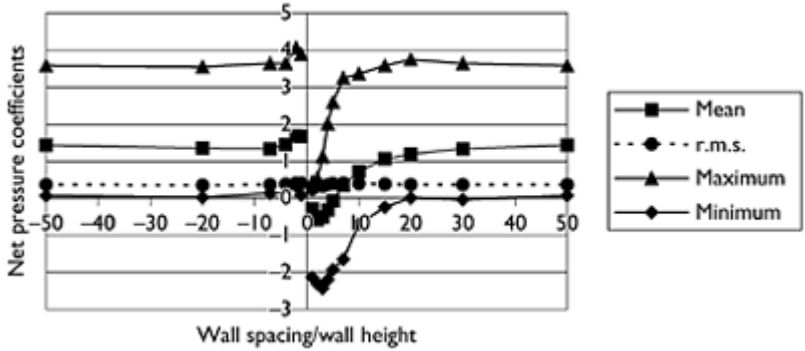

Figure 14.6 Parallel walls on flat level ground—effect of wall spacing.

Figure 14.6 shows the variation of mean, rms, maximum and minimum net pressure coefficients on one wall of a pair of parallel ones, for various spacings. The pressure coefficients are based on the mean wind speed at wall height in the undisturbed flow. A negative value of wall spacing/wall height means the second wall is *downwind*. These measurements were carried out in simulated atmospheric boundary-layer flow in a wind

tunnel. The values of Jensen number, h/z_0, (Section 4.4.5), for the wall heights used in the tests were about 10–20.

The pressure tappings were arranged in vertical rows, with spacings chosen such that the pressures averaged together as a group of four (Section 7.5.2) gave a measure of the bending moment at the base of the wall. Thus, the measurements of base moment coefficients are defined as:

$$C_M = \frac{M}{\frac{1}{4}\rho_a \overline{U}^2 h^2} \tag{14.2}$$

where M is the moment about the base, per unit length of the wall. This is also an effective net pressure coefficient which, when applied uniformly over the wall height, will give the correct base moment. Averaging of peak and fluctuating pressures was carried out over one wall height horizontally along the wall axis.

The mean pressure difference is negative when the upwind wall is about 2 wall heights away from the shielded wall; i.e. it acts *upwind*. Small shielding effects are felt when the upwind wall is as much as 20 wall heights upwind.

Figure 14.7 compares the mean, maximum and r.m.s. net effective pressure coefficients for the windward wall of the pair of parallel walls on a bridge with two different values of clear space underneath (Holmes, 2001). The thickness of the bridge deck was equal to the wall height. Values for *s/h* are equal to 0, 2 and 4, where *s* is the clear spacing under the bridge. All pressure coefficients are calculated with respect to the mean wind speed at the height of the top of the wall (s+2h) in the undisturbed flow.

Figure 14.7 shows there is little difference between the net pressure coefficients for the cases of *s/h* equal to 2 and 4, when there is airflow beneath the bridge. However, when *s/h* is equal to 0—i.e. the 'bridge' forms a flat-topped cliff—the mean and maximum net pressure coefficients are about 90% of the values on the elevated bridges; the r.m.s. pressures are about 80% of those in the elevated case.

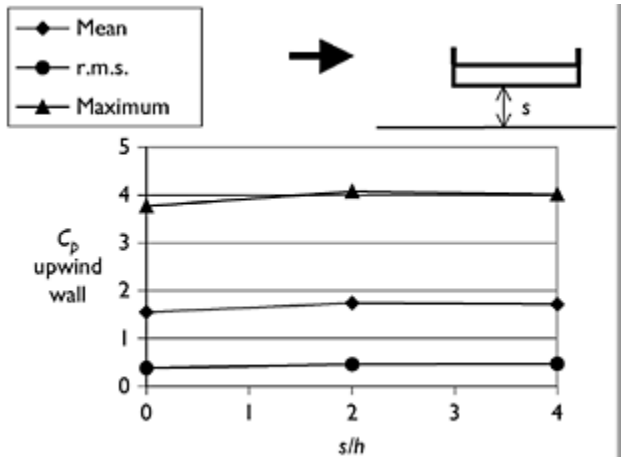

Figure 14.7 Effect of clear space, *s*, for parallel walls on bridges.

14.2.4 Elevated hoardings

The net wind pressure coefficients on elevated hoardings have generally similar characteristics to those on free-standing walls. The effect of elevation is to increase the magnitude of the net pressure coefficient for winds normal to the surface. The average mean pressure coefficient depends on the spacing to the ground beneath the hoarding. For a spacing equal to the depth of the hoarding, a mean net pressure coefficient (with reference to the mean velocity at the top of the hoarding) of about 1.5 occurs.

The oblique wind direction can produce large pressure differences near the windward end, as for free-standing walls (Figure 4.8).

Design data for elevated hoardings and signboards are given in the American (ASCE, 2006), Australian (Standards Australia, 2002) and British Standards (BSI, 1997).

14.2.5 Spanwise averaging

Walls or hoardings supported over long spans will experience lower peak wind loads than those supported over short spans. The following form was proposed for the reduction factor for peak loads on free-standing walls over spans, s (Holmes, 2001):

$$\alpha = 0.5 + 1.35 \exp\left[-\left(\frac{s}{h}\right)^{0.15}\right] \tag{14.3}$$

Equation (14.3) gives the ratio between peak net pressures for a span, s (greater than the wall height, h) and the peak net pressure on a wall with a span, s, equal to the height, h. Thus, for $s=h$, α is equal to 1.0. The equation was derived for both unshielded walls and shielded parallel walls.

14.3 Free-standing roofs and canopies

Free-standing, or ‘canopy’, roofs, without walls, are often used for basic shelter structures—such as those at motor vehicle service stations and railway stations or for coverage of industrial, mineral or agricultural products. The wind loads on roofs of this type attached to buildings are discussed in Section 14.4.1.

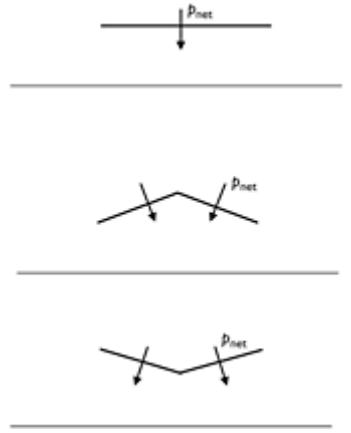

Figure 14.8 Types of free-standing roof, and sign convention for net pressures.

Free-standing roofs, which are completely free of stored material underneath, allow air to flow freely underneath; this generally results in negative, or near-zero, underside pressures with respect to atmospheric pressure. The addition of stored material underneath the roof in sufficient quantity will cause full or partial stagnation of the airflow and positive pressures underneath. The nature of the upper surface pressures depends on the roof pitch and the wind direction.

Wind pressure coefficients on free-standing roofs are usually quoted in the form of net pressure coefficients, as defined in Equation (14.1). The pressures can normally be assumed to act normal to the roof surface. The usual sign convention is that positive net pressures act downwards. This sign convention and the most common three types of free-standing roof geometry are shown in Figure 14.8.

Although the pressures normal to the roof surface are the dominant ones, frictional forces acting parallel to the roof surfaces can also be significant, and it may be necessary to consider them when designing the bracing required to resist horizontal forces.

Free-standing roofs have been studied in both wind-tunnel tests (Gumley, 1984; Letchford and Ginger, 1992; Ginger and Letchford, 1994) and full-scale experiments (Robertson *et al.*, 1985).

Net pressure coefficients along the centreline of a free-standing 'Dutch barn' with 15° roof pitch measured in full scale (Robertson *et al.*, 1985) are shown in Figure 14.9. The roof is completely empty underneath. Positive (downwards) pressure differences exist over the windward quarter of the roof for all wind directions. The largest negative loads occur near the middle of the roof for a wind direction normal to the ridge.

Letchford and Ginger (1992, 1994) carried out extensive wind-tunnel measurements on pitched free roofs (empty under) of approximately square plan, with a range of pitches up to 30°. Mean and fluctuating pressure measurements from single points and area-averaged (Section 7.5.2) over six panels were made. In addition, correlation coefficients

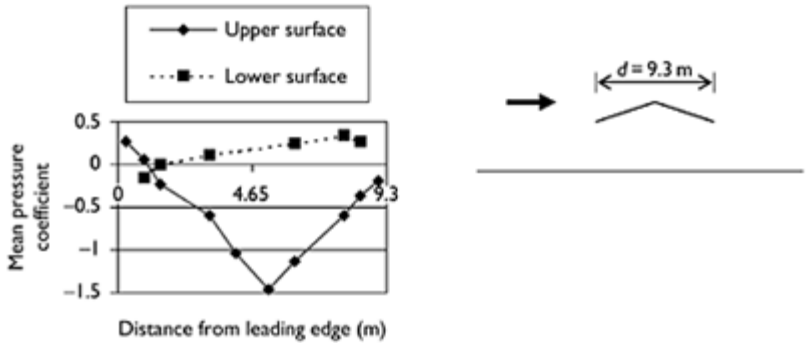

Figure 14.9 Mean pressure difference coefficients along the centre line of a free-standing roof with 15° pitch.

(Section 3.3.5) were measured for the six panel pressures enabling fluctuating total forces (Section 4.6.6), and equivalent static loading distributions to be derived (Section 5.4.3).

Mean area-averaged net pressure coefficients for half the pitched roof are shown in Figure 14.10. For the 0° wind direction, the half roof is on the windward side. Figure 14.10 shows that significant positive pressures (for wind directions of 0°–30°) and negative pressures (for wind directions of 120°–180°) occur for roof pitches of 22.5° and 30°. For roof pitches of 15° or less, the net pressure difference coefficients are not large for any wind direction.

The peak (maximum and minimum) area-averaged pressure difference coefficients generally showed similar behaviour to the mean coefficients shown in Figure 14.10, with the 22.5° and 30° pitch roofs clearly showing larger magnitudes. When peak total uplift and horizontal forces were calculated, substantial reductions of up to 50% from values calculated from the non-simultaneous peaks on windward and leeward halves

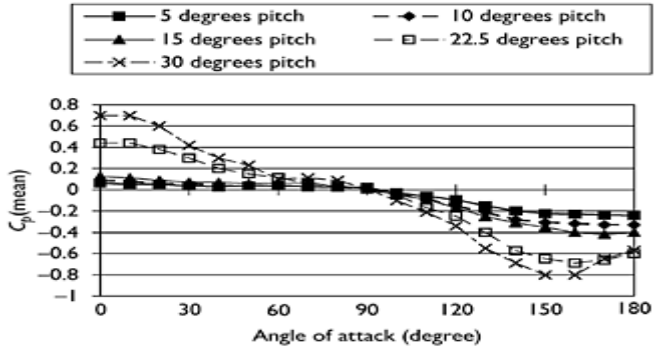

Figure 14.10 Mean pressure difference coefficients for pitched free roofs averaged over a half roof (Letchford and Ginger, 1992).

were obtained, due to the poor correlation between fluctuating wind pressures on the two surfaces (Ginger and Letchford, 1994).

Appendix F gives an example of the calculation of maximum and minimum lift and drag on a pitched free roof, and the effective static pressures producing them, based on data from Ginger and Letchford (1994).

14.4 Attachments to buildings

14.4.1 Canopies, awnings and parapets

Several configurations of horizontal canopy attached to one wall of a low-rise building have been investigated (Jancauskas and Holmes, 1985). The width of the canopy and the height of the canopy position on the wall were the investigated variables. A narrow canopy mounted at the top of the wall behaves similarly to eaves on the roof.

For wind directions normal to the adjacent wall, the peak net force across the canopy is strongly dependent on the non-dimensional ratios, h_c/h, and h_c/w_c.h_c is the height of the canopy above the ground, h the total height of the adjacent wall and w_c the width of the canopy.

For the peak vertical uplift force coefficient, $\hat{C}_Z$, based on the mean wind speed at the height of the canopy, the following conservative relationships were proposed based on the wind-tunnel measurements:

$$\begin{aligned}
&\text{for } \frac{h}{h_c} = 1.0, \quad \hat{C}_Z = 1.0 + 1.3\,(h_c/w_c) \text{ or } 4.0, \text{ whichever is the lesser} \\
&\text{for } \frac{h}{h_c} = 0.75, \quad \hat{C}_Z = 1.0 + 0.4\,(h_c/w_c) \text{ or } 4.0, \text{ whichever is the lesser} \\
&\text{for } \frac{h}{h_c} = 0.5, \quad \hat{C}_Z = 1.0
\end{aligned} \tag{14.4}$$

where,

$$C_Z = \frac{F_z}{\frac{1}{2}\rho_a \overline{U}_c^{\,2} A}$$

and F_z is the net vertical force on the canopy (positive upwards), $\bar{U}_c$ the mean wind speed at the canopy height and A is the plan area of the canopy.

Equation (14.4) can be applied to canopies with pitch angles within 5° of the horizontal. Appropriate adjustment is required if it is applied with gust wind speeds; such adjustment has been made for the rule incorporated in the Australian wind loading standard (Standards Australia, 2002).

The relationships of Equation (14.4) are compared with the experimental data in Figure 14.11.

The higher values obtained for canopies or awnings near the top of the wall (or eaves) can be explained by the high flow velocities occurring on the upper side of the canopy producing significant negative pressures; on the underside of the canopy, stagnation and hence positive pressures occur. When the canopy is mounted part-way up the wall,

stagnation of the flow occurs on the wall, both above and below the canopy. In this situation, the mean net force coefficients are low, but turbulence produces finite peak loads in both directions.

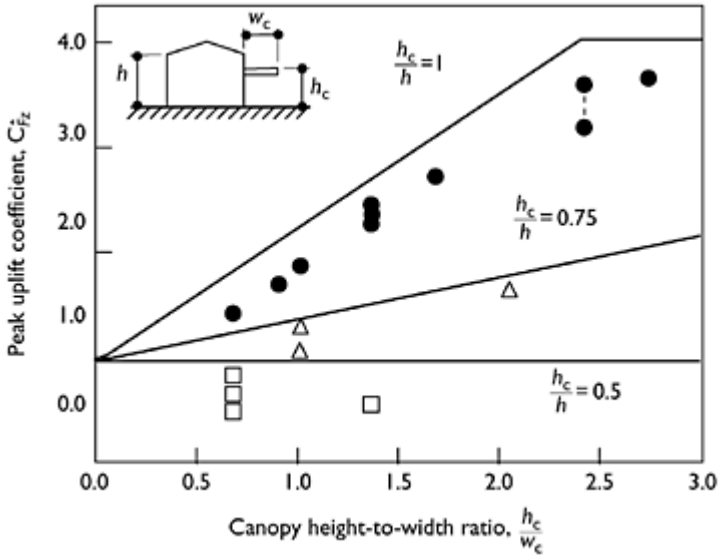

Figure 14.11 Peak uplift force coefficients for attached canopies (Jancauskas and Holmes, 1985).

Parapets and their effect on roof pressures on flat roofs have been the subject of several wind-tunnel studies. In the early work, there were some conflicting conclusions drawn by different laboratories, but the issue was largely resolved using large models and a high density of pressure tappings (Kind, 1988). With or without parapets, the worst suction peaks occur in small zones near the upwind corner of the roof, for wind directions nearly bisecting the corner. The worst suction coefficients decrease monotonically with increasing relative parapet height. The amount of the reduction also depends on the height/width ratio of the building to which the parapet is attached (see also Section 8.6).

14.4.2 Solar panels on roofs

The wind loads on solar panels attached to the roofs of a building are closely related to the flow over the roofs of the building itself, as the latter is a much larger bluff body. Figure 14.12 shows the various geometric variables that are significant in determining the wind loads on solar collector panels on a pitched roof building (Tieleman *et al.*, 1980).

The following summarizes the effects of the various solar panel and building variables on wind loads:

- 'Stand-off' spacing from the roof, *d*,—increasing stand-off appears to reduce net uplift load (normal to roof), but increases the wind force acting on the panel parallel to the roof (Newton, 1983).
- Module shape and size—the combined peak load on a row of panels is significantly less than that on a single panel, due to area reduction effects on the fluctuating pressures.
- Roof pitch—higher roof pitch produces lower uplift loads, but increasing downwards wind loads (as for the loads on the roofs of low-rise buildings generally).

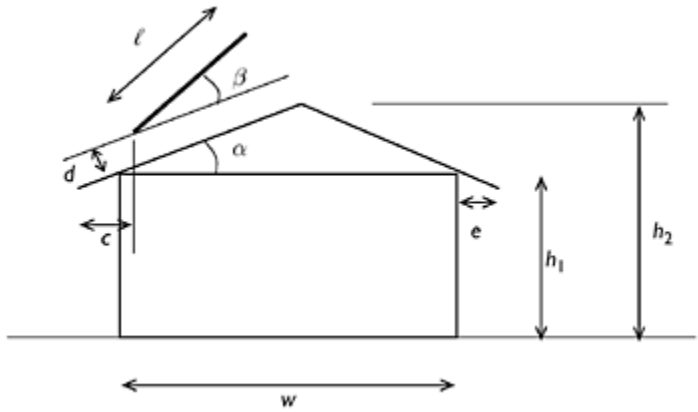

Figure 14.12 The variables affecting wind loads on solar panels (Tieleman *et al.*, 1980).

- Proximity to eaves—the end panel (adjacent to the eaves) experiences considerably higher loads than the interior panel in a row.
- Wind direction—the worst uplifts occur for oblique wind directions to a row of collector panels.
- Roof height—the pressure *coefficients* for panels on two-storey buildings are lower than the equivalent values for single-storey buildings.

To optimize the upwards wind loading on solar panels, it is clearly a good idea to increase the stand-off clearance, as this reduces the net uplift. Increasing the angle, β, so that the inclination of the panel is greater than that of the roof pitch, would appear to increase wind loads. It is better to locate panels away from the roof edges (eaves and ridges), and the uplift loads for parallel-mounted panels (β=0) are lower for higher pitch roofs.

14.5 Antennas

14.5.1 Radio telescopes

Wind loads on the antennas of large steerable radio telescopes—usually with dish reflectors of paraboloidal shape—are of critical importance for several design criteria (Wyatt, 1964):

- overall strength for safety in extreme winds;
- loads on drive system;
- freedom from oscillations;
- pointing accuracy;
- distortion of the reflector.

The last four of the above conditions are serviceability criteria. Very small tolerances are required for the operation of these antennas.

The main source of wind loads is the paraboloidal dish itself. If the dish is impermeable, the pressures acting on it may be assumed to act normal to the surface, with negligible contributions from skin friction. For a paraboloid, the normal to any point on the surface passes through the generating axis, at a point 2*f* measured along the axis from that point, where *f* is the focal length. Therefore, it may be assumed that the resultant aerodynamic force will act through a point on the axis, distant from the vertex by 2*f* plus half the depth of the dish, *d* (Wyatt, 1964).

Consider first the case with the wind direction normal to the altitude axis of rotation of the dish as shown in Figure 14.13. Resolving the aerodynamic forces in body axes (Section 4.2.2), the force coefficients are given by:

$$C_X = \frac{F_x}{\frac{1}{2}\rho_a \overline{U}_h^{\,2} A} \tag{14.5}$$

$$C_Y = \frac{F_Y}{\frac{1}{2}\rho_a \overline{U}_h^{\,2} A} \tag{14.6}$$

where A is the projected area normal to the dish, given by $\pi(b^2/4)$.

Following the arguments in the previous paragraph, the eccentricity, e, of the aerodynamic force can be closely approximated by (Wyatt, 1964):

$$e = 2f + \frac{d}{2} = 2f\left[1 + \left(\frac{b}{8f}\right)^2\right] \tag{14.7}$$

Tests in smooth uniform flow (Wyatt, 1964) indicate maximum values of C_x of about 1.7 when the angle of attack, a, is about 45°. The transverse force coefficient C_Y is approximately constant with f/d when expressed in the form $(f/d)C_Y$, with a maximum value of about 0.05, for a equal to about 135°. The transverse force F_Y generates a moment about the vertex equal to $F_Y \cdot e$.

It is found that the effect of a boundary-layer mean wind profile has a relatively small effect for wind directions facing the wind. However, the effect is greater when the wind

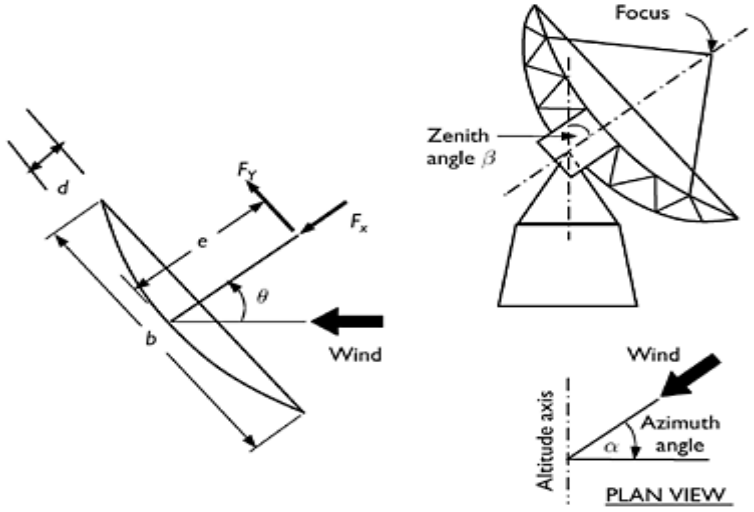

Figure 14.13 Resultant aerodynamic forces on the dish antenna of a radio telescope (Wyatt, 1964).

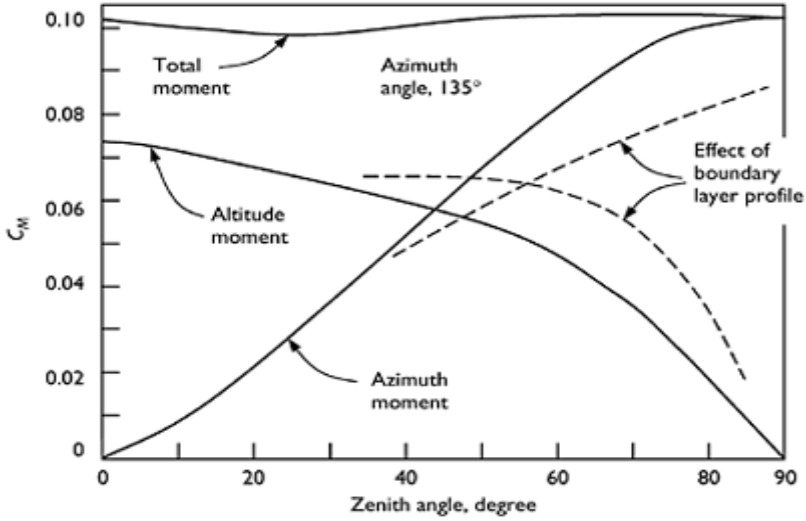

Figure 14.14 The effect of velocity profile on the aerodynamic moments on a radio telescope (Wyatt, 1964).

is blowing obliquely on to the rear of the paraboloid. As shown in Figure 14.14, the effect is to increase the moment about the altitude axis and decrease it about the azimuth axis (Wyatt, 1964).

In Figure 14.14, the moment coefficients are defined as follows:

$$C_M = \frac{M}{\frac{1}{2}\rho_a \overline{U}_h^{\,2} A d} \tag{14.8}$$

14.5.2 Microwave dish antennas

The drag forces acting on small dish antennas used for microwave frequency transmission are of interest for the structural design of the towers supporting them. In the past, total drag forces for tower design have been obtained by simply adding the drag measured on the antennas in isolation to that determined for the tower without antennas. This will overestimate the total drag in many cases, as usually the antennas will shield part of the tower, or vice versa; also the drag on an antenna itself in the presence of the tower will be different to that on the antenna in isolation.

Figure 14.15 shows the drag coefficient for an impermeable unshrouded dish obtained as a function of the wind incidence angle measured from the normal to the plane of the dish, in both smooth (approximately 1% turbulence intensity) and turbulent flows (10% turbulence intensity; Holmes *et al.*, 1993). The reference area is the projected area of the dish, $\pi(b^2/4)$.

The drag coefficient for the isolated dish is maximum with a wind direction normal to the plane of the dish, but does not reduce much in an angular window within 30° to the normal. The maximum drag coefficient based on the disc area is about 1.4. A large reduction occurs for wind directions from 40–80° to the normal. The effect of turbulence intensity is small.

The concept of *interference factor* is illustrated in Figure 14.16. The drag of an isolated antenna should be multiplied by this factor to give the measured incremental contribution to the total tower drag. The sum of the drag on the tower segment, D_t, and the incremental contribution from the antenna, $K_i D_a$, gives a total effective drag, D_e.

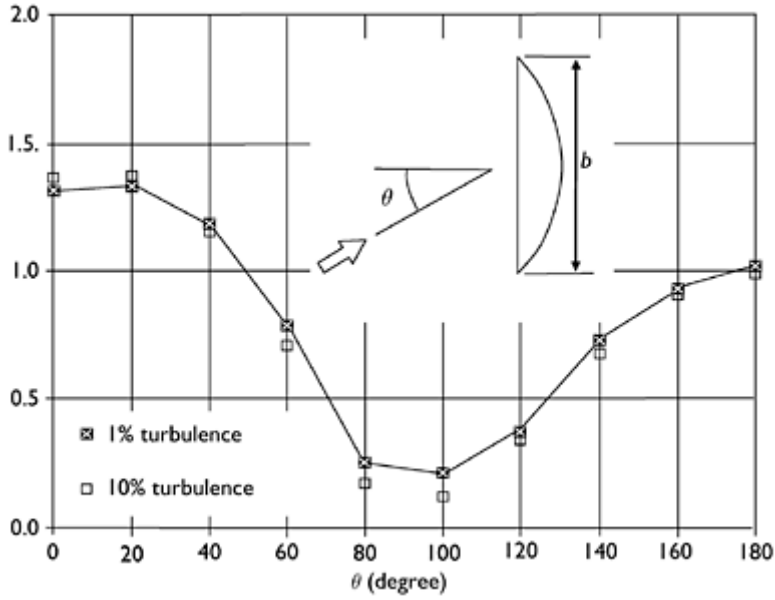

Figure 14.15 Drag coefficient as a function of angle of attack for an isolated dish antenna (Holmes *et al.*, 1993).

The interference factor for a single dish attached to a face of a lattice tower, with square cross-section and a solidity ratio of 0.3, is shown graphically, as a function of wind direction, θ, relative to the tower face in Figure 14.17 (Holmes *et al.*, 1993). The maximum interference factor of about 1.3 occurs at wind directions for which the dish accelerated the airflow over the tower, i.e. for wind directions of 90° and 270°. For wind directions of 0° and 180°, where mutual shielding occurs, interference factors as low as 0.5 can occur.

An empirical form for the interference factor, K_i, based only on the solidity and drag coefficient of the tower which fits the experimental data in Figure 14.17 and data from other cases, takes the form:

$$K_i = \exp\left[-k(C_D\delta)^2\right] \cdot [(1+t) + t\cos 2(\theta - \theta_d - 90°]] \tag{14.9}$$

where C_D is the drag coefficient for the tower or mast section alone, based on the projected area of members in one face, measured normal to the face; δ the solidity of a face of the tower; k a parameter equal to 1.2 for a square tower (ESDU, 1981); t an adjustable parameter (equal to 0.5 in Figure 14.17); and θ_d is the angle of the normal to the dish antenna relative to the tower.

As well as drag (along-wind) forces, there may be significant cross-wind forces acting for wind directions parallel, or nearly parallel, to the plane of a solid dish. These should be taken account of when designing support attachments for the dish. Basic aerodynamic

force coefficients are often obtainable from the antenna manufacturers, although these would not generally include interference effects.

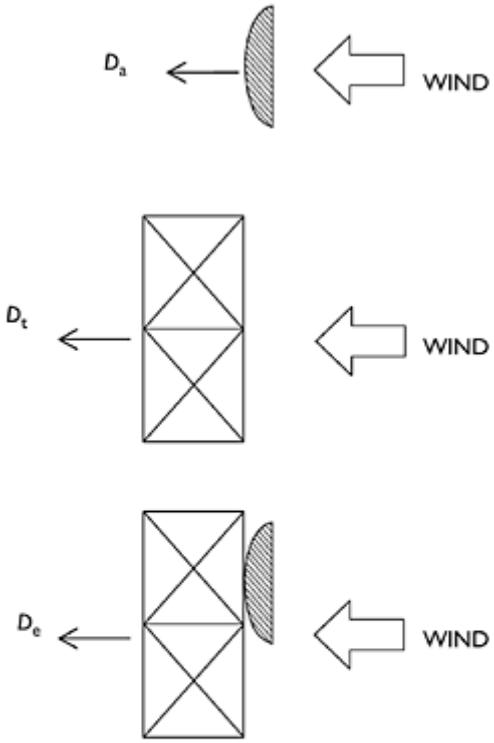

Interference Factor

$$K_i = \frac{D_e - D_t}{D_a}$$

$$D_e = D_t + K_i \cdot D_a$$

Figure 14.16 Concept of interference factor for incremental antenna drag.

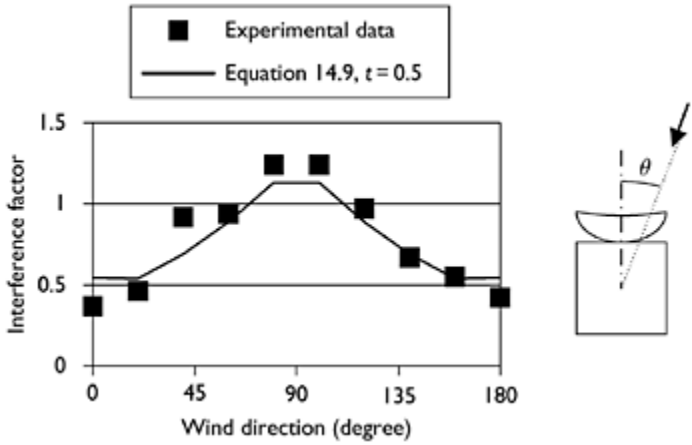

Figure 14.17 Interference factor as a function of wind direction for a single microwave dish added to a square lattice tower (Holmes *et* al., 1993).

14.5.3 Rotating radar antennas

Aerodynamic loads on large rotating radar antennas such as those used at large airports pose a particular serviceability problem due to the variations in torque that arise. The operation of the antennas imposes strict limits on variations in angular velocity, and this in turn limits the variations in torque that the drive motor must overcome. Wind-induced variations in torque arise from two sources:

- variations in the azimuth angle between the wind direction and the antenna; and
- horizontal wind turbulence.

At the rates of rotation used in practice, the first source of aerodynamic torque variation appears to be dominant.

The effect of rotation of the antenna can be treated by a quasi-steady approach. This results in the predicted variation of torque being obtained from static tests in a wind tunnel, in which the azimuth angle is varied. The effect of rotation is assumed to result in a static shift in the fluctuating torque curve obtained from such tests (Sachs, 1978; Lombardi, 1989). However, the quasi-steady theory has been found to be only approximately correct at high rotational speeds (Lombardi, 1991).

The use of small fins on the back of the antenna has been found to be effective in reducing the aerodynamic torque. These are small lifting surfaces which produce a counteracting torque. Figure 14.18 shows measured torque coefficients obtained from a rotating wind-tunnel model with and without fins (Lombardi, 1991).

Unfortunately, all the wind-tunnel measurements on rotating radar antenna have been carried out in smooth uniform flow. The effect of turbulent boundary-layer flow is uncertain, but the most likely effect is to smooth out the torque versus yaw angle graphs, such as those shown in Figure 14.18.

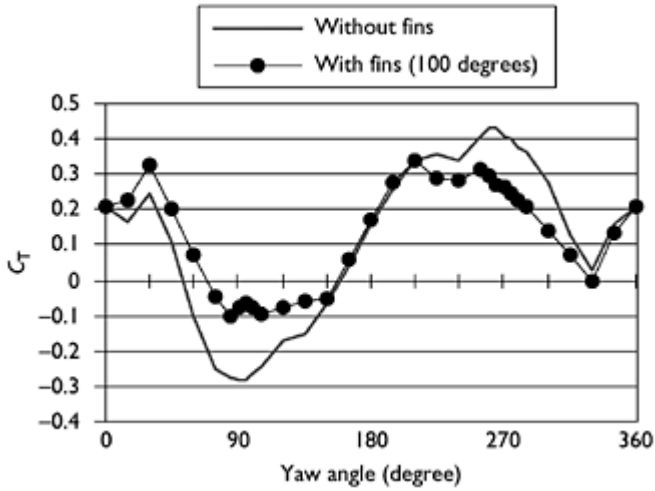

Figure 14.18 Aerodynamic torque coefficient versus yaw angle for rotating radar antennas (Lombardi, 1991).

14.5.4 Mobile telephone antennas

Antennas for mobile telephone cells typically consist of several radiating antennas within fibreglass or plastic radomes, mounted on poles or towers, which may in turn be mounted above buildings or other structures. By their nature they are in exposed positions, and thus the interference, or shelter, effects from other structures is usually small. However, the mutual aerodynamic interference between radomes can be considerable.

Many of these antennas have been tested at full scale in large wind tunnels for aerodynamic force coefficients but the data are usually proprietary in nature, and not freely available. The force coefficients have been found to be dependent on Reynolds number, so that model testing at small scales will produce unreliable results. However, drag coefficients at high Reynolds number from full-scale measurements, typical of these antenna elements, which illustrate the mutual interference effects, are shown in Figure 14.19.

The drag coefficient for wind normal to the curved face of an antenna is around 1.1 based on the projected frontal area. This value is reduced for wind directions in which the frontal area presented to the wind is reduced, as illustrated for the value shown for a wind direction 120° from the normal.

When the antenna elements are grouped in threes, the combined drag coefficient (based on the frontal area of *one* radome element) is greatly reduced. As shown in Figure 14.19, the effect of the two downwind elements in the widely spaced (left side) cluster is neutral—i.e. the drag of the upwind element in isolation is the same as the combined drag of the group of three. For the closely spaced cluster, which resembles a single bluff body with curved surfaces, the overall drag is more than 20% less than that of the upwind radome in isolation.

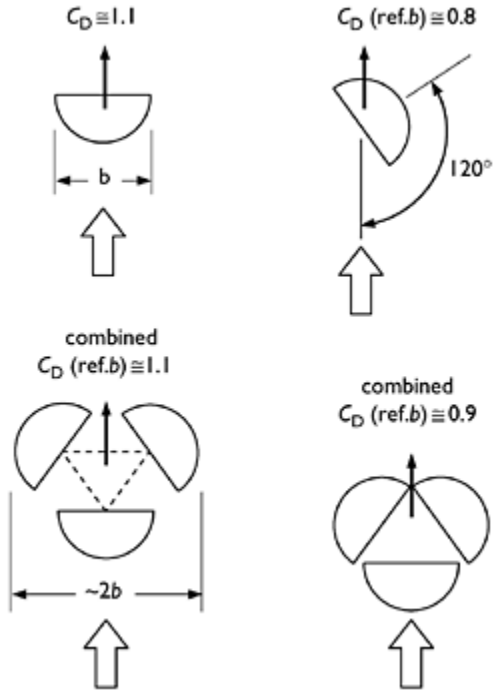

Figure 14.19 Typical drag force coefficients for mobile telephone antenna elements.

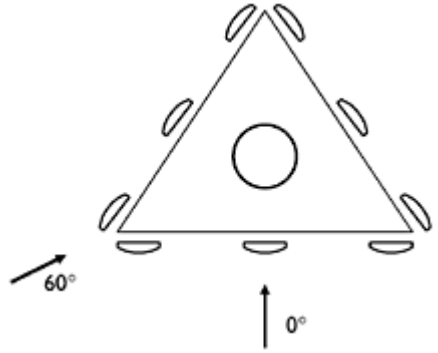

Figure 14.20 A group of mobile telephone antenna elements on a triangular frame.

Sometimes up to nine antennas are grouped together on a triangular frame, as shown in Figure 14.20. For the case shown, the antennas on a single face are well separated to avoid large aerodynamic interference effects, but those at the corners may experience slight increases in drag due to mutual interference (Section 4.3.1, and Marchman and

Werme, 1982). The six downwind antennas are shielded both by the upwind antennas and by the supporting pole. Full-scale wind-tunnel tests on complete antenna headframes indicate an overall reduction of about 30% in the combined drag is obtained, when comparing the combined drag of the group with that obtained by the summation of contributions from individual elements.

Isolated radome elements will also experience cross-wind forces at oblique wind directions. However, these will be largely cancelled by opposite forces from other elements, when they are part of a group.

14.5.5 UHF antennas

Antennas for the transmission of ultra-high-frequency television-broadcasting signals (including digital television) consist of fibreglass or plastic radomes mounted on four or five-sided masts and are usually quite 'solid' cross-sections. They are of the order of 1 m in breadth and about 20 m long. They are usually mounted on the top of free-standing or guyed towers.

The drag coefficient for these cross-sections depends on the porosity of the crosssection—i.e. the ability of the wake to be vented to the windward side. Measurements on full-size antenna sections have yielded drag coefficients in the range of 1.1–1.6, with some dependency on wind direction.

UHF antennas have experienced significant cross-wind response due to vortex shedding (Sections 4.6.3 and 11.4). This has often occurred for antennas on guyed masts, which have a lower damping than free-standing lattice towers. Such responses occur at a critical velocity, which is quite low, and in atmospheric conditions with low turbulence intensities. The prediction of cross-wind response due to vortex shedding for *circular* cross-sections was discussed in Section 11.5. Methods also exist for *non-circular* cross-sections (e.g. ESDU, 1990). These methods require information on the Strouhal number (rate of vortex shedding—see Section 4.6.3) and fluctuating cross-wind force coefficients (Section 4.6.4). These would not be well defined for the complex cross-sections of UHF antennas.

If vibrations occur, they can be mitigated by the use of simple damping devices such as liquid dampers (Section 9.9.4) or *hanging chain* dampers (Koss and Melbourne, 1995).

14.6 Lighting frames and luminaires

Street lighting, flood lighting for railway yards, sporting grounds and industrial areas are bluff bodies of a variety of shapes and porosities. There are considerable interference effects when luminaires are arranged in groups. As for antennas, the drag of many types has been measured in wind tunnels, but is usually commercially sponsored, and the results are not readily obtainable.

The largest drag coefficients of single lights for any wind direction fall in the range of 1.0–1.5, based on the largest frontal area projected vertically. The lower value applies to the more rounded types, and the higher value to sharp-edged lights.

Large rectangular headframes, with many luminaires attached, such as large floodlight systems for sporting grounds, may be treated as porous flat plates (see Section 4.3.1). A

value of drag coefficient of 1.5, based on the projected ‘solid’ or ‘wind’ area, is an appropriate one for solidities of 0.3–0.7.

The wind loads on supporting poles for lighting are discussed in Chapter 11.

14.7 Industrial complexes and offshore platforms

Estimation of wind loads for elements of industrial complexes such as power stations, petroleum refineries or mineral processing plants is an extremely difficult problem. Such complexes consist of a large number of closely spaced bluff bodies, with considerable aerodynamic interference between them. It would normally be extremely conservative to estimate the total wind drag force by summing up the contributions from individual elements, as if they were isolated bluff bodies, although this is often done. The complexity and unique layouts of these plants mean that it is difficult or impossible to give general rules for estimating wind forces, except for some relatively common situations such as closely spaced circular cylinders. One useful approach which avoids gross overestimation of drag forces is to treat a closely spaced complex of bodies in a ‘global’ way as a single ‘porous’ bluff body, for which data are readily available.

Offshore platforms, used for oil exploration and production, are similar in complexity, with the topsides often exposed to severe wind storms (in many cases tropical cyclones), as well as wave action. In these cases, the overall wind forces on the above water exposed structure is of interest in the design of the underwater foundations and supporting structure.

The low frequencies of ‘compliant’ offshore structures, such as tension leg or guyed structures in deep water locations, are of special concern because of the need to consider resonant excitation by dynamic wind forces. The frequencies of some structures of this type can be so low that they are near the peak of the spectrum of wind forces in synoptic winds (Section 3.3.4). However, it appears that hydrodynamic damping, resulting from the underwater motion of the structure (Cook *et al.,* 1986), largely mitigates resonant effects. The special problems of wind effects on compliant offshore structures are discussed in a number of specialist publications (e.g. Smith and Simiu, 1986).

14.8 Summary

In this chapter, wind loads on structures not covered in Chapters 8–13 have been discussed. This category includes free-standing walls and hoardings, attachments to buildings such as canopies and awnings and solar collectors.

Communications and broadcasting antennas of various types, particularly those impermeable enough to attract substantial wind loading, are considered in some detail. Some discussion of wind loads on elements in complex industrial structures, such as oil refineries, and on offshore oil platforms has also been given.

References

American Society of Civil Engineers (2006) Minimum design loads for buildings and other structures. ASCE/SEI 7–05, ASCE, New York.

British Standards Institution (1997) Loading for buildings. Part 2. Code of practice for wind loads. BS 6399: Part 2:1997.

Cook, G.R., Kumarasena, T. and Simiu, E. (1986) Amplification of wind effects on compliant platforms. *Structures Congress '86*, New Orleans, 15–18 September (Proceedings of session: 'Wind effects on compliant offshore structures'), ASCE, New York.

ESDU (1981) Lattice structures. Part 2—mean forces on tower-like space frames. ESDU data items 81028, Engineering Sciences Data Unit, ESDU International PLC, London, UK.

ESDU (1990) Structures of non-circular cross section. ESDU data items 90036, Engineering Sciences Data Unit, ESDU International PLC, London, UK.

Ginger, J.D. and Letchford, C.W. (1994) Wind loads on planar canopy roofs—Part 2: fluctuating pressure distributions and correlations. *Journal of Wind Engineering & Industrial Aerodynamics*, 51:353–70.

Gumley, S.J. (1984) A parametric study of extreme pressures for the static design of canopy structures. *Journal of Wind Engineering & Industrial Aerodynamics*, 16:43–56.

Holmes, J.D. (2001) Wind loading of parallel free-standing walls on bridges, cliffs, embankments and ridges. *Journal of Wind Engineering & Industrial Aerodynamics*, 89:1397–407.

Holmes, J.D., Banks, R.W. and Roberts, G. (1993) Drag and aerodynamic interference on microwave dish antennas and their supporting towers. *Journal of Wind Engineering & Industrial Aerodynamics*, 50:263–9.

Jancauskas, E.D. and Holmes, J.D. (1985) Wind loads on attached canopies. *Fifth US National Conference on Wind Engineering*, Lubbock, TX, 6–8 November.

Kind, R.J. (1988) Worst suctions near edges of flat rooftops with parapets. *Journal of Wind Engineering & Industrial Aerodynamics*, 31:251–64.

Koss, L.L. and Melbourne, W.H. (1995) Chain dampers for control of wind-induced vibration of tower and mast structures. *Engineering Structures*, 17:622–5.

Letchford, C.W. and Ginger, J.D. (1992) Wind loads on planar canopy roofs—Part 1: mean pressure distributions. *Journal of Wind Engineering & Industrial Aerodynamics*, 45: 25–45.

Letchford, C.W. and Holmes, J.D. (1994) Wind loads on free-standing walls in turbulent boundary layers. *Journal of Wind Engineering & Industrial Aerodynamics*, 51:1–27.

Lombardi, G. (1989) Wind-tunnel tests on a model antenna with different fin configurations. *Engineering Structures*, 11:134–8.

Lombardi, G. (1991) Wind-tunnel tests on a model antenna rotating in a cross flow. *Engineering Structures*, 13:345–50.

Marchman, J.F. and Werme, T.D. (1982) Mutual interference drag on signs and luminaires. *ASCE Journal of the Structural Division*, 108:2235–44.

Newton, J.R.H. (1983) Wind effects on buildings—recent studies at Redland wind tunnel. *Journal of Wind Engineering & Industrial Aerodynamics*, 11:175–86.

Robertson, A.P., Hoxey, R.P. and Moran, P. (1985) A full-scale study of wind loads on agricultural canopy roof ridged structures and proposals for design. *Journal of Wind Engineering & Industrial Aerodynamics*, 21:113–25.

Sachs, P. (1978) *Wind Forces in Engineering*, 2nd Edition. Pergamon Press, Oxford, UK.

Smith, C.E. and Simiu, E. (eds) (1986) Wind effects on compliant offshore structures. *Proceedings of a Session at Structures Congress '86*, New Orleans, 15–18 September, ASCE, New York.

Standards Australia (2002) Structural design actions. Part 2: wind actions. Australian/New Zealand Standard, AS/NZS1170.2:2002, Standards Australia, Sydney, New South Wales, Australia.

Tieleman, H.W., Akins, R.E. and Sparks, P.R. (1980) An investigation on wind loads on solar collectors. Report VPI-E-80–1, Virginia Polytechnic Institute and State University, College of Engineering.

Wyatt, T.A. (1964) The aerodynamics of shallow paraboloid antennas. *Annals of the New York Academy of Sciences*, 116:222–38.

15
Wind loading codes and standards

15.1 Introduction

Wind loading codes and standards, although a relatively recent concept (almost all have been produced since World War II), have achieved wide acceptance and are often the practising structural engineer's only contact with information for wind loading calculations. Although often based on extensive research, they are, by necessity, simplified models of wind loading. Thus, great accuracy cannot be expected from them. Often this is consistent with the knowledge of the structure of the wind storms themselves in their country of use. The growth of world trade is expected to reduce the number of loading standards in use and gradually force more consistency in their format and content.

Advanced wind loading codes and standards invariably contain the following features:

- A specification of a basic or reference wind speed for various locations, or zones, within a jurisdiction. Almost always a reference height of 10 m in open country terrain is chosen.
- Modification factors for the effects of height and terrain type, and sometimes for change of terrain, wind direction, topography and shelter.
- Shape factors (pressure or force coefficients) for structures of various shapes.
- Some account of possible resonant dynamic effects of wind on flexible structures.

This chapter reviews the wind loading provisions of several prominent national, multinational and international documents and highlights their similarities and differences. As codes and standards are continually being revised and updated, the overview is, by necessity, time dependent.

Other comparisons between major wind loading codes and standards have been made by Cook (1990), Mehta (1998), and by Kijewski and Kareem (1998) for dynamic effects. A Special Issue of the journal *Wind and Structures* in 2005 included five papers in which all aspects of codification for wind loads were reviewed (Holmes *et al.*, 2005a,b; Letchford *et al.*, 2005; Kasperski and Geurts, 2005; Tamura *et al.*, 2005).

15.2 General descriptions

The following six standards will be described in this chapter:

- ISO 4354—Wind actions on structures—published in 1997.
- prEN 1991–1–4.6 Eurocode 1: Actions on structures—Part 1.4: General actions—Wind actions—published in 2004.

- ASCE Standard ASCE/SEI 7–05. Minimum design loads for buildings and other structures—published in 2006.
- AIJ recommendations for loads on buildings—published in 2004.
- Australian/New Zealand Standard. Structural design actions. Part 2: Wind actions. AS/NZS1170.2—published in 2002.
- British Standard. Loading for buildings. Part 2. Code of Practice for Wind Loads. BS6399: Part 2—published in 1997.

The documents reviewed are those current at the time of writing.

15.2.1 ISO/DIS 4354—Wind actions on structures

ISO International Standard 4354—Wind actions on structures, published by the International Organization for Standardization, was issued in 1997, after remaining in draft form for many years. As described in the Introduction to ISO 4354, the document is intended not as an operating standard, but as a guideline for drafting national codes of practice.

The Standard closely follows the format of the National Building Code of Canada. However, no detailed design basic wind speeds are listed, but guidelines are given for converting wind speeds from one averaging time to another, in particular to the recommended averaging time of 10 min. The main part of the document is quite short and consists largely of definitions of the terms in the expression used to calculate wind pressure:

$$w=(q_{ref})(C_{exp})(C_{fig})(C_{dyn}) \tag{15.1}$$

A'Simplified Method' and a 'Detailed Method' of analysis are given. The latter is intended for dynamically wind-sensitive structures and includes resonant effects in the determination of C_{dyn}. Several Annexes describe these quantities in more detail and give 'representative' values for C_{exp}, C_{fig} and C_{dyn}. The data on the aerodynamic shape factor, C_{fig}, have been reproduced from the National Building Code of Canada and from a former Swiss Norm (of 1956). As stated in the Introduction to ISO 4354, the data in the Annexes are 'only examples and are not intended to be complete'.

The special characteristics of hurricanes (tropical cyclones and typhoons) and thunderstorms winds have also not been considered. This document is not intended as a replacement for national wind loading standards—i.e. it is not a usable code of practice – but rather as a descriptive guidebook for the main features of a wind loading code.

15.2.2 prEN 1991–1–4.6 Eurocode 1. Part 1–4 Wind actions

Eurocode 1 on wind loads, issued in 2004, is the final draft of the European Standard (prEN) which is intended for national committees to prepare 'National Annexes', to enable application in all member countries. It replaces an earlier document ENV 1991–2–4 (CEN, 1994), which was in circulation for about 7 years. It represents several years of work by representatives from many countries of the European Union and two separate committees and is the nearest document to a truly multi-national wind loading standard

currently in existence. In its final form, this code will be mandatory throughout the EEC and eventually replace all existing national documents.

Distinction is made in the document between 'Principles' (denoted by the letter P), comprising general statements, definitions, requirements and analytical models for which there is no alternative, and 'Application Rules' for which it is permissible to use alternatives provided they accord with the relevant Principles.

This is a lengthy document with comprehensive methods of static and dynamic design for wind loads. No basic wind speeds are provided in the standard—these are to be provided separately in each National Annex. The basic wind velocity is a 10-min mean velocity at 10 m height in open country terrain, with an annual probability of exceedence of 0.02 (50-year return period).

15.2.3 ASCE Standard ASCE 7–05. Minimum design loads for buildings and other structures

ASCE/SEI 7–05 is a complete loading standard covering all types of loads, and the wind loading part (Section 6 and its associated Commentary) is a relatively small component of the whole document.

From 1995 onwards, ASCE-7 has incorporated a number of significant changes in the wind load provisions from the 1993 and earlier editions. This includes the use of a 3-s gust wind speed instead of the 'fastest-mile-of wind' as used in the past, a new zoning system for basic wind speeds, the incorporation of topographic factors, some new data on pressure coefficients, a simplified procedure for buildings less than 9 m in height and a revised method for along-wind dynamic response calculation.

The ASCE Standard has no legal standing of its own, but its provisions are cited by many of the regional, city and county building codes. The three major regional building codes in the United States have merged to form a single 'International Building Code'. This draws on the ASCE Standard for wind load provisions.

15.2.4 AIJ Recommendations for loads on buildings

The Recommendations of the Architectural Institute of Japan (AIJ) were revised in 2004 and are a comprehensive loading code including the effects of dead, live, snow, seismic, temperature, earth and hydraulic pressure, as well as wind loads. Chapter 6 on wind loads comprises 54 pages, with 114 pages of Commentary. The derivation of the wind loading section of the 2004 edition of the AIJ, and revisions from the 1993 version, were described in detail by Tamura *et al.* (2004).

Like the ASCE Standard, this is a comprehensive and advanced wind loading document, although the Recommendations have no legally binding standing in Japan. The Building Law of Japan has a separate set of wind loading rules—BSLJ-2000 (Ministry of Land, Infrastructure and Transport, 2000). As the latter does not have a comprehensive set of rules for cross-wind and torsional dynamic response, the AIJ is commonly used by structural designers for buildings greater than 60 m in height.

15.2.5 Australian/New Zealand Standard AS/NZS 1170.2

The current edition of the joint Australian and New Zealand Standard for Wind Loads was issued in 2002 as the first edition of a combined Standard, replacing separate documents from the two countries. It is a comprehensive document of 88 A4 pages and is supported by a separate Commentary, and a Guide for designers is also available (Holmes and King, 2005). It uses a notation and format based on the 1997 International Standard, ISO 4354.

AS/NZS 1170.2:2002 has an indirect legal status by being called up in the Building Codes of Australia and New Zealand. These documents and Part 0 of the joint Standards on Structural design actions must be consulted to obtain the appropriate annual probability of exceedence for the importance and use of the building, before use of Part 2, Wind actions.

The basic wind speed in AS/NZS 1170.2 is a 3-s gust measured at 10 m height in open country terrain, and values are specified for a range of annual probability of exceedence from 1/5 to 1/2000, for four Regions. For most buildings, excluding those with large numbers of occupants and important post-disaster facilities, the annual risk of exceedence for ultimate limit states wind speeds is specified, in the Building Code of Australia, as 1/500.

15.2.6 British Standard BS6399: Part 2:1997

Part 2 of the British Standard BS6399—Loading for buildings is the ‘Code of practice for wind loads’ which replaced CP3: Chapter V: Part 2 in 1995. The significant difference between BS6399: Part 2 and the earlier code of practice is that the basic wind speed is an hourly mean, instead of the 3-s gust speed used in earlier editions. However, the mean wind speed is subsequently converted into a gust speed for calculation of design loads, to take advantage of the quasi-steady model of wind loads. The stated reasons for using the hourly mean are that it allows more accurate treatment of topography and that it provides a starting point for calculations involving fatigue and dynamic response.

BS6399: Part 2 provides two alternative methods of calculating wind loads:

1. a ‘standard method’, which does not use directional wind speed and coefficient data;
2. a ‘directional method’, which is more complex but generally less conservative.

In this comparison, only the standard method will be discussed, as the other standards do not have equivalent methods to the directional method.

15.3 Basic wind speeds or pressures

Table 15.1 summarizes the basic wind speed characteristics used, or recommended, in the six documents. In all cases, the standard meteorological reference position of 10m height in flat, open country is used.

The ISO Standard, as previously discussed, does not give basic wind speeds or dynamic pressures. However, it provides a useful conversion method between wind

speeds averaged in four different ways and the 10-min velocity pressure, q_{ref}, used as a basis for calculation of wind loads (see Equation (15.1)).

Table 15.1 Definitions of basic wind speeds

Code	*Averaging time*	*Basic return period (years)*
ISO 4354	10 min	50 years
prEN 1991–1–4.6	10 min	50 years
ASCE-7	3 s	50 years
AIJ	10 min	100 years
AS/NZS 11 70.2	3 s	500 years
BS6399: Part 2	1 h	50 years

The European pre-Standard prEN 1991 of 2004 also does not give basic wind speeds, although the previous (1994) draft gave 'reference wind velocities', for 18 countries in Europe in an informative Annex. National Annexes will provide basic wind speed information for individual countries in Europe.

The American Standard (ASCE-7) contains maps with two zones in the majority of the country and closely specified contours for Alaska and the coastal regions adjacent to the Gulf of Mexico and the Atlantic Ocean. In the latter case, the effects of hurricanes are of particular concern. The values of basic wind speed given on these maps are peak gust wind speed, with an annual probability of exceedence of 0.02. The methodology for the derivation of the basic wind speed maps for the United States has been described by Peterka and Shahid (1998).

The recommendations of the AIJ gives a detailed map showing contours of the basic wind speed (10-min mean with 100-year return period). Single values are given for outlying territories such as Okinawa. A map of 500-year return period values is also given to enable users to interpolate for intermediate return periods.

In the Australian/New Zealand Standard, basic wind speeds are given in the form of maps with five regions, denoted by A, B, C, D and W. Two of these regions (C and D) comprise a coastal strip exposed to the effects of tropical cyclones (Section 1.3.2). Regional wind speeds are specified for each Region as a function of annual probability of exceedence. The 500-year return period in Table 15.1 applies to the majority of buildings in Australia (Importance Level 2 in the Building Code of Australia). The analysis of extreme wind speeds for Region A, covering most of Australia, in the 2002 Australian Standard was described by Holmes (2002). The analysis of wind speeds for Regions C and D was discussed by Dorman (1984).

In the British Standard, BS6399.2:1997, the basic wind speed, V_b (1-h mean), is given in a map, which covers Ireland as well as the United Kingdom. This has an annual risk of exceedence of 0.02, i.e. a 50-year return period.

15.4 Modification factors on wind velocity

All the documents include modifiers for the effect of terrain/height and topography, although in the case of ISO 4354 and ASCE-7, these act on the dynamic *pressure*, rather than wind *speed*. In the Eurocode, the mean wind speed is modified for terrain and height (roughness factor c_r), and for topography (described as 'orography'), c_0, then converted into a *gust* dynamic pressure at the height of interest, by a factor involving turbulence intensity.

prEN 1991–1–4.6, AS/NZS1170.2 (for regions not affected by tropical cyclones) and BS6399:2 use a logarithmic law (or a modification for gust speeds) to define the terrain/height variation; ASCE-7 and AIJ use a power law variation; and ISO 4354 suggests the use of either and gives parameters for both. AS/NZS 1170.2 allows for changes of terrain upwind of the site, with an interpolation of terrain/ height multipliers. The British Standard allows for this indirectly through an allowance for the distance of the site from the sea.

AS/NZS 1170.2 has special 'Terrain-height Multipliers' for Regions C and D affected by severe tropical cyclones. These reflect the steeper profiles up to 100 m obtained in some measurements in tropical cyclones (Section 3.2.5).

ASCE-7 has an importance factor; this acts on the pressure rather than on the speed. The AIJ Recommendations give a return period conversion factor, and ISO 4354 also has this facility, but not as an explicit factor.

Table 15.2 Calculation formats for velocity, dynamic pressure and building pressure

Code	*Velocity*	*Dynamic pressure*	*Building pressure/force*
ISO 4354 1991–1–4.6	V	$q_{ref}=(1/2)\rho V^2$	$w=(q_{ref})(C_{exp})(C_{fig})(C_{dyn})$
prEN	${}^{v}b=c_{dir}c_{season}v_{b,0}$	$q_p(z)=c_e(z)(1/2)\rho v_b^2$	${}^{w}e=q_p(z)C_{pe}$
ASCE-7	V	$q_Z=(1/2)\rho K_z K_z K_d V^2 I$	$p=q(GCp)$
AIJ	$U_H=U_0 K_D E_H k_{rW}$	$q_H=(1/2)\rho U_H^2$	$W_f=q_H C_f G_f A$*
AS/NZS1170.2	$V_{sit,\beta}=VM_dM_{(z,cat)}M_sM_t$	$q_z=(1/2)\rho_{air}V_{des,\theta}^2$	$P=q_zC_{fig}C_{dyn}$
BS6399: Part 2	$Vc=V_bS_aS_dS_pS_b$	$q_s=(1/2)\rho V_e^2$	$P_s=q_sC_{pe}C_a$

*The subscript f denotes D (for walls) or R for roofs in the AIJ.

The Australian/New Zealand Standard, AS/NZS1170.2, is unique in having a 'Shielding Multiplier', which allows for reductions in velocity when there are buildings upwind of greater or similar height.

The British Standard BS6399: Part 2 has a number of unique features in relation to the calculation of the design wind speed: an 'altitude factor', (S_a), which depends on the

height of the site above sea level and a 'seasonal factor', S_s. The 'terrain and building factor', S_b, includes an allowance for the distance of the site from the sea, as discussed previously; it also incorporates a gust factor to convert the hourly mean wind speed to a peak gust wind speed. A 'site wind speed' is calculated by multiplying the basic wind speed, V_b, by factors for altitude (S_a), wind direction (S_d), season (S_S) and probability (S_p). The seasonal factor, S_s, may be used to reduce loads for temporary structures that are exposed to wind loads for defined periods less than a year. The altitude factor incorporates the aerodynamic effects of topography, as well as the increase of wind speed with height above sea level.

Table 15.2 summarizes the formats for calculation of design wind velocities and dynamic pressures in various documents. ISO 4354 is alone in calculating a basic dynamic pressure from the basic (unfactored) wind velocity. Variation with height and terrain, topography, etc. is incorporated at the stage of calculating building pressure.

15.5 Building external pressures

Table 15.2 also shows the general format for calculation of external pressures on wall or roof surfaces of enclosed buildings.

The formulas (in the right-hand column) appear to be quite different from each other, but they all contain quasi-steady or mean pressure coefficients $(C_{fig}, c_{pe}, C_p, C_f, C_{pe})$ and factors to adjust the resulting pressures to approximate peak values. In the case of ISO 4354 and AIJ, there are gust factors on pressure (C_{dyn} and G_f); in the case of the Eurocode, the function is incorporated in the exposure coefficient, $c_e(z)$, which also includes terrain/height and topographic (orographic) effects through the relationship:

$$c_e(z) = c_r^2(z)c_o^2(z)[1 + 7I_v(z)] \tag{15.2}$$

where $c_r(z)$ and $c_0(z)$ are roughness and orography factors, respectively. $I_v(z)$ is the turbulence intensity.

The term in square brackets can be regarded as a gust factor on pressure.

In ASCE-7, the quantities G and C_p are usually combined together as (GC_p) in tables. In AS/NZS 1170.2, the 'aerodynamic shape factor', C_{fig}, consists of pressure coefficients, multiplied by factors for area reduction, combination of roof and wall surfaces, local pressure effects and porous cladding. The local pressure factor, K_{ℓ}, is always greater than 1, and the area reduction factor, K_a, which allows for correlation effects over large areas in separated flow regions, is less than 1. AS/NZS 1170.2 is alone in having a factor (K_p) for porous cladding.

The tables of shape factors and pressure coefficients of exterior surfaces of buildings given in the various documents are also sources of significant differences. However, in all cases, the nominal wind directions are normal to the walls of buildings of rectangular plan. However, as previously discussed in Section 15.2.6, the British Standard has a directional method, which incorporates pressure coefficients for 15° direction increments.

ISO 4354 gives graphs of $C_{fig}C_{dyn}$ for the cladding on walls and roofs and the frames of low-rise buildings (widths>2×height, and height <15m) with flat and gabled roofs. There are strong similarities between these figures and the ones for GC_p for buildings less

than 18 m height in ASCE-7. Both documents give graphs of shape (and gust) factor as a function of tributary area. There are numerical differences, however, such that the values in ASCE-7 are 50–60% of those in ISO 4354. This is because, as shown in Table 15.1, ASCE uses a 3-s gust wind speed rather than a 10-min mean. However, as $\left(\overline{U}_{10\,\mathrm{min}}/\hat{U}_{3\,\mathrm{s}}\right)^2$ is 0–35−0.40, it appears that ISO 4354 will give peak loads on low-rise buildings about two-thirds of those specified in ASCE-7. However, ASCE-7 allows a further reduction of up to 15% through the use of a 'wind directionality factor', K_d. ISO 4354 does not consider any variation of load with terrain for low-rise buildings designed by the 'Simplified Method'.

The tables in ISO 4354 and ASCE-7 for low-rise buildings do not allow for variation with height—to width ratio. However, an alternative figure for C_p in ASCE-7 (for buildings of all heights), which has been derived from equivalent tables in the Australia/New Zealand Standard AS/NZS 1170.2, does allow for the variation with height/width ratio. The ASCE-7 Standard and AS/NZS 1170.2 require alternative positive roof pressure coefficients to be considered. These are important values for the design of frames, especially for those in colder climates where dead loads are often high, as pointed out by Kasperski (1993).

prEN 1991–1–4.6 gives tables of external pressure coefficients, c_{pe}, which are comparable to those in ASCE-7 and AS/NZS 1170.2, as they are effectively applied to gust dynamic pressure through the use of the exposure coefficient, $c_e(z)$. The tables give two values: $c_{pe\,1,}$ intended for tributary areas less than $1\mathrm{m}^2$, i.e. local cladding design; and $c_{pe,10}$ intended for major structural members. It appears that the numerical values for flat and gable ('duopitch') roofs in prEN 1991–1–4.6 are comparable to those in ASCE-7 and AS/NZS 1170.2, and alternative (positive or lower negative) values are given for most roof pitches. However, no variation with height/width ratio is given.

The factors incorporated into the shape factor in the Australia/New Zealand Standard AS/NZS 1170.2 for flat and gable-roofed buildings have already been discussed. However, it should also be mentioned that the effect of tributary area and correlation effects is dealt with by the use of the three factors: K_a (area reduction factor), K_c (action combination factor) and K_ℓ (local pressure factor). The action combination factor, K_c, a new feature in the Australian and New Zealand Standard, allows for a reduction when wind pressures from more than one building surface, e.g. walls and roof, contribute significantly to a load effect.

The AIJ Recommendations also separate the specification of loads on the structural frames and on the 'components and cladding' of buildings. The specification of pressure coefficients is separated from the specification of the gust factor. Unlike any of the other documents, the gust factor, G_R, for the loads on the roofs of low-rise buildings has a dependency on natural frequency. Buildings are classified as those with heights less than or greater than 45 m, a somewhat greater height than used in the other documents.

The 'size effect factor', C_a, in the British Standard BS6399: Part 2, is specified in a graph. It depends on the diagonal dimension of the 'load-sharing area', with a minimum value of 5 m. When overall loads involving wind pressures on both windward and leeward facing surfaces are being calculated, a reduction factor of 0.85, to allow for the 'nonsimultaneous' action between faces, is allowed.

15.6 Building internal pressures

The treatment of internal pressures varies considerably from one document to another. ISO 4354 gives a general description of the nature of internal pressures and then suggests ranges of $C_{fig,i}$ for three situations: buildings with large openings, buildings with small openings not uniformly distributed, buildings with small openings uniformly distributed.

For buildings with uniformly distributed openings, prEN 1991–1–4.6 gives a graph of c_{pi}, varying from +0.35 to −0.5, as a function of an opening ratio, μ For a dominant opening, the internal pressure coefficient is expressed as a fraction of the external pressure coefficient on the face with the opening. This document also gives fairly detailed guidance on pressures on walls and roofs, with more than one skin.

ASCE-7 specifies three different situations: open, partially enclosed and enclosed buildings, and specifies values of GC_{pi} between +0.55 and −0.55. A feature not found in the other standards is a reduction factor, R_i, for large building volumes.

AS/NZS1170.2 gives two tables with various positive and negative values of internal pressure coefficients, $C_{p,i}$. For one of these tables, the values depend on the ratio of dominant openings on the windward wall to the total open area on other walls and roof.

The AIJ Recommendations does not specify a positive internal pressure, i.e. the possibility of dominant openings is not considered. For buildings without dominant openings, values of C_{pi} of 0 or −0.5 are specified.

In the British Standard, only three possible cases are specified, and these also do not include the possibility of a dominant opening, with a large positive internal pressure.

15.7 Specified pressure coefficients for roofs

As a series of examples for comparison of shape factors or pressure coefficients, the specification for various kinds of medium to large roofs of low-rise buildings by the various codes will be considered. The following cases will be examined:

(a) A flat or near-flat roof for an enclosed building with a square planform and wall height to width ratio of 0.2. Nominal width and height are 25 and 5 m, respectively.
(b) As for (a), but a free-standing roof or canopy, i.e. the space under the roof is assumed to be open.
(c) As for (a), but with an arched roof with a rise-to-span ratio of 0.2.
(d) As for (c), but for a domed roof on a circular planform with a rise-to-span ratio of 0.2.

As discussed in Section 15.3, some of the Standards under review are based on wind speeds with mean wind speeds averaged over 10min or 1h, and conversion to peak velocities or to peak pressures is accomplished by means of gust factors or an exposure factor (prEN 1991–1–4.6). Thus, the basic pressure coefficients discussed are ultimately factoring a gust pressure, and are thus directly comparable with each other. However, the method of dealing with area-averaging effects varies considerably between the documents, as previously discussed. For example, the Australian Standard (AS/NZS1170.2) has an ‘area reduction factor’, K_a, based on the tributary area of the structural system; in the present comparisons, this area will be taken as the total plan area

of the roof. The British Standard specifies a 'size effect factor', C_a, which depends upon the diagonal dimension of the tributary area and also on the terrain and height.

The comparisons will be separated into loads in major structural members and loads on small elements of cladding. In these comparisons, external pressures only will be considered for the enclosed buildings. Internal pressures are an important part of the net pressure, but are much less dependent on the building shape, being mainly affected by the number and size of openings in the building envelope.

Case (a)—Square plan enclosed building with flat roof

The effective pressure coefficients for the structural loads on the roof are given in Figure 15.1 and for areas of cladding of the order of $1m^2$ are given in Figure 15.2. In Figure 15.1, K_a in the Australia/New Zealand Standard is taken as 0.8, and C_a in the British Standard is 0.85. In the case of the American (ASCE) Standard, Figures 6.10 and 6.11b have been used to obtain values of GC_p.

Figure 15.1 shows that the largest magnitude negative pressure coefficients, which occur at the windward end of the roof, are reasonably similar in magnitude in all the codes; however, the zoning systems are quite different from each other. The American (ASCE-7) and International (ISO 4354) Standards give very similar pressure coefficients to each other for structural loads. The British Standard and the Eurocode also give similar values to each other. Only AS/NZS1170.2, prEN 1991–1–4.6 and BS6399.2 allow for the possibility of positive pressures occurring on the leeward half of the roof, and only AS/NZS1170.2 allows for alternative negative pressures on the windward end. As discussed in earlier chapters, the nature of the fluctuating and turbulent flow over large roofs can produce large fluctuations in the instantaneous pressures.

There are bigger differences in both the zonal system and the specified pressures for small areas of cladding between the various codes, as shown in Figure 15.2. All the codes specify higher pressures along the edge regions of the roof, i.e. the regions mainly affected by the separated flow from the walls. All except the Australian Standard (AS/NZS1170.2) give higher pressures at the corners, with the largest values being specified by the Eurocode and the American Standard.

Case (b)—Square plan canopy with flat free roof

Five documents of the group specify pressures for canopies or free roofs. In all these cases, *net* pressure difference coefficients are given. Figures 15.3 and 15.4 give the pressure coefficients for structural and cladding loads, respectively. The Eurocode gives the same pressure coefficients for main structural loads and cladding and applies them over the whole roof—obviously very much a simplification. AS/NZS 1170.2 specifies pressures for zones based on distance from the windward edge as for the enclosed building. ASCE-7

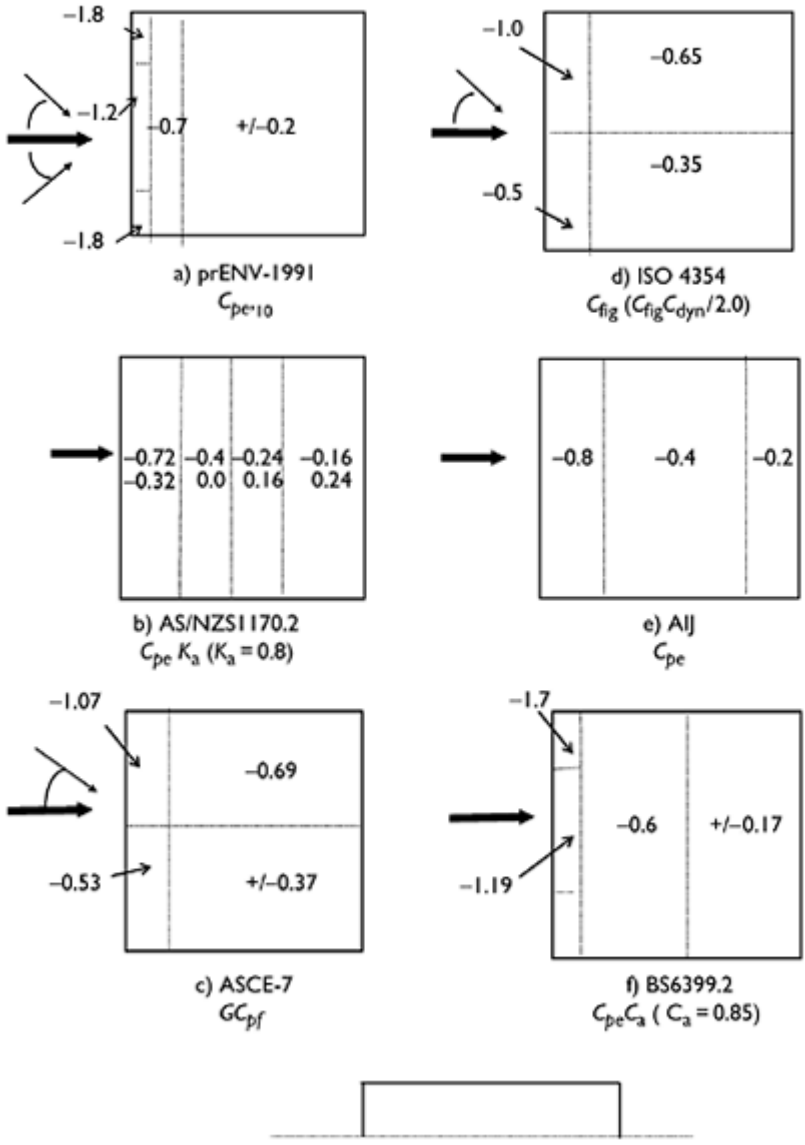

Figure 15.1 Comparison of pressure coefficients for a flat roof (main structural loads), h/d=0.2.

and the AIJ specify coefficients for the two halves of the roof. In all codes, upwards (negative) and downwards (positive) pressures are specified. Higher upwards net pressures are specified for cladding along the roof edges and at the corners in the Australian, British and American Standards and in the AIJ Recommendations

(Figure 15.4). The British Standard specifies higher positive (downwards) net pressure coefficients than negative values for local cladding loads, along the edges. ASCE-7 specifies higher local pressures than any other document.

Case (c)—Square plan enclosed building with arched roof

Figure 15.5 shows the pressure coefficients for an enclosed building with an arched roof, which is covered in all codes except the British Standard. The ISO Standard only

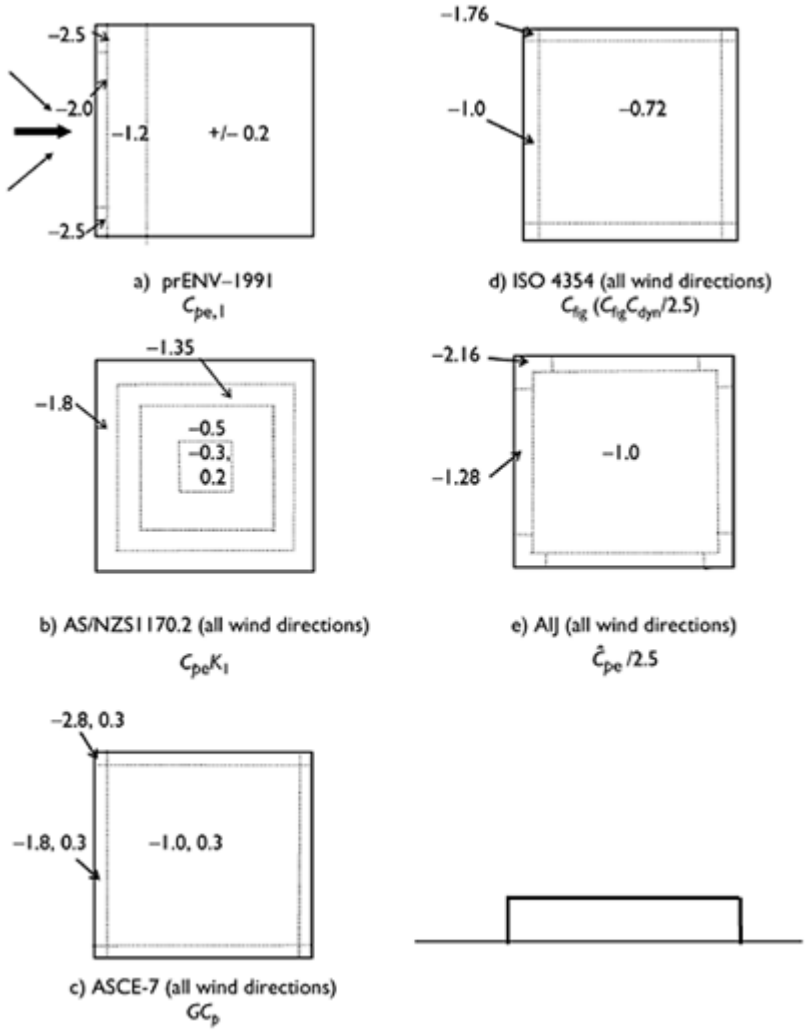

Figure 15.2 Comparison of pressure coefficients for a flat roof local cladding loads (< 1 m^2), *h/d=0.2.*

gives loads for one geometrical shape of arched roof—this has a lower wall height and a slightly lower rise/span ratio, but is shown in Figure 15.5 for completeness. The zone system in prEN 1991–1–4.6 and AIJ is the same as AS/NZS1 170.2 and ASCE-7, but the coefficients are different. The largest magnitude negative pressure coefficients in the central part of the roof are in the range −0.6 to −1.15.

Note that the reference heights for the pressure coefficients for arched roofs vary between the various codes: ISO 4354 appears to use the eaves height (but this is not clearly specified); ASCE-7, AIJ and AS/NZS1 170.2 use the average roof height; and prEN 1991–1–4.6 uses the top of the roof. No adjustments have been made for this in Figure 15.5, as these depend on the velocity profile assumed.

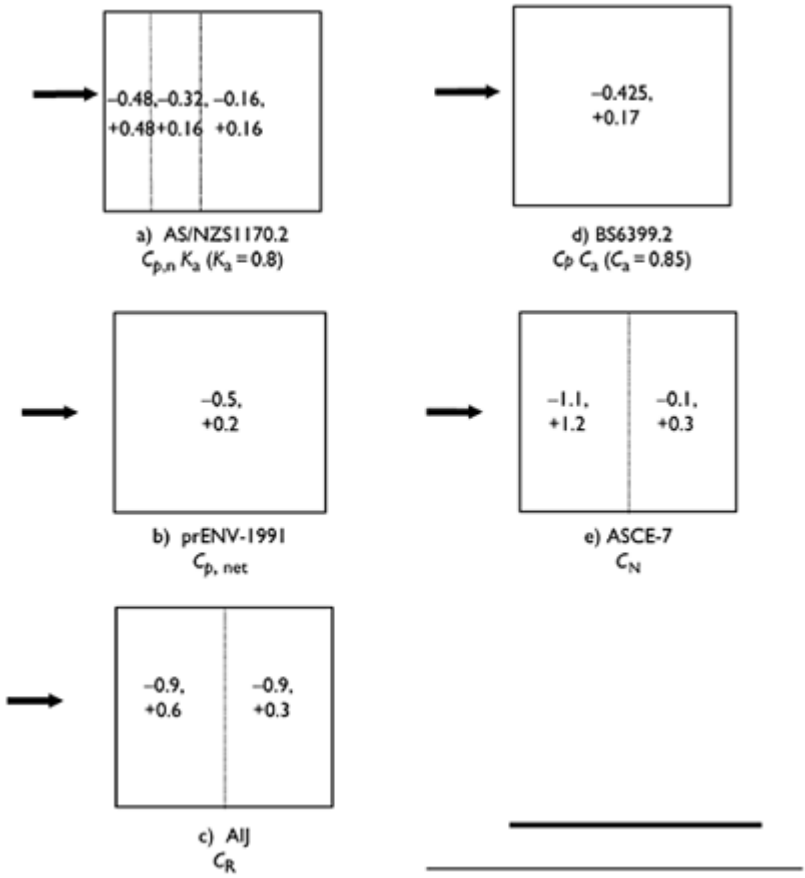

Figure 15.3 Comparison of pressure coefficients for a flat free roof (empty under—main structural loads), h/d=0.2.

Case (d)—Circular plan enclosed building with domed roof

prEN 1991–1–4.6, the AIJ and ASCE-7 are the only documents to give pressure coefficients specifically for a domed roof (although AS/NZS1170.2 gives values for curved roofs, applicable to both arches and domes). Values are shown in Figure 15.6. The values in ASCE-7 are identical to those in prEN 1991–1–4.6. Values at the windward and leeward points on the roof and along a line perpendicular to the apex of the roof are given. Interpolation between the values shown along the arcs of circles parallel to the wind is recommended. Generally, the values are similar in magnitude to the arched roof.

In ASCE-7, a separate table gives values of GC_p for components and cladding on domed roofs. A negative value of GC_p of −0.9 is specified, and positive values of +0.9($0<\theta<60°$) and +0.5($61°<\theta<90°$) are given, where θ is the angle to the horizontal of the line from the centre of the building at eaves height to the roof surface.

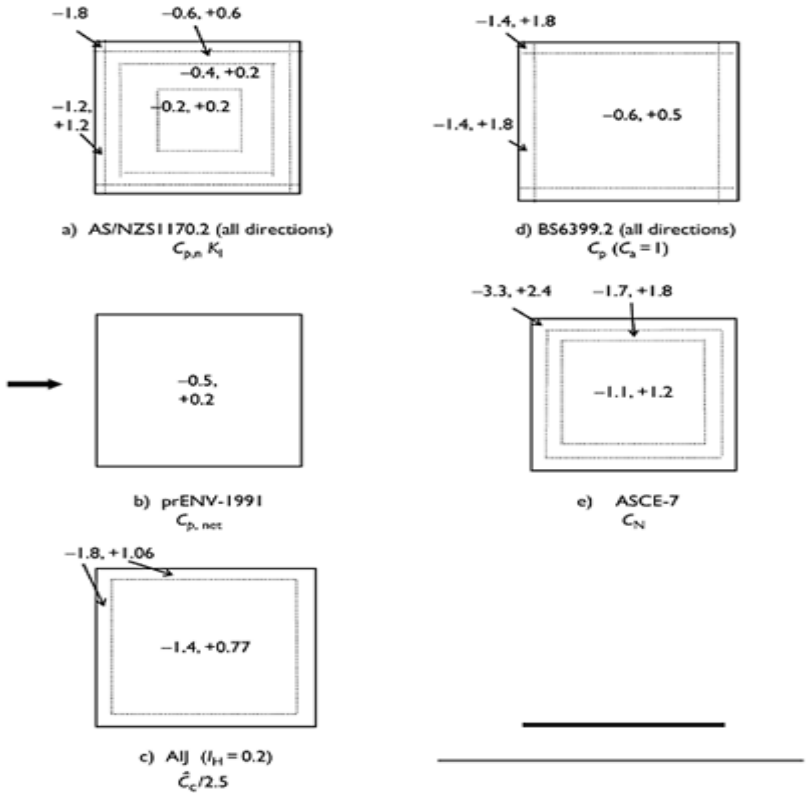

Figure 15.4 Comparison of pressure coefficients for a flat free roof (empty under—local cladding loads), h/d=0.2.

15.8 Other shapes and sectional force coefficients

Apart from the AIJ Recommendations, which is intended exclusively for buildings, all the surveyed documents contain shape, or force, coefficients for a variety of structure shapes and cross-sections. Table 15.3 summarizes the given data.

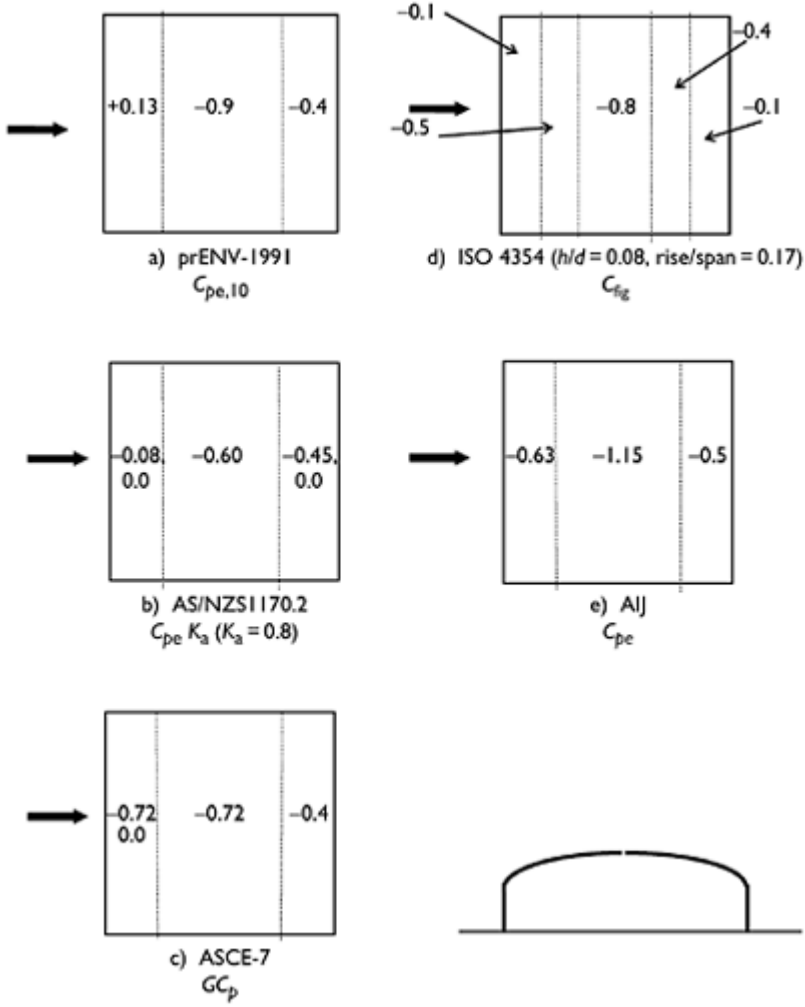

Figure 15.5 Comparison of pressure coefficients for an arched roof (main structural loads), h/d=0.2, rise/span=0.2.

The data in ISO 4354 (non-rectangular buildings) are quite old and pre-date boundarylayer wind tunnels. The data in the other documents appear to be based on modern wind-tunnel measurements for the most part. prEN 1991–1–4.6 clearly contains the most comprehensive set of data.

15.9 Dynamic response calculations

The first five standards contain procedures for the calculation of dynamic response for wind-sensitive structures such as slender, flexible, lightly damped tall buildings. ASCE-7 and AS/NZS 1170.2 classify wind-sensitive structures as those with a first-mode natural frequency less than 1 Hz; ASCE-7 also requires a height to breadth (or depth) ratio greater than four. ISO 4354 considers a structure slender if the height to diameter ratio exceeds six.

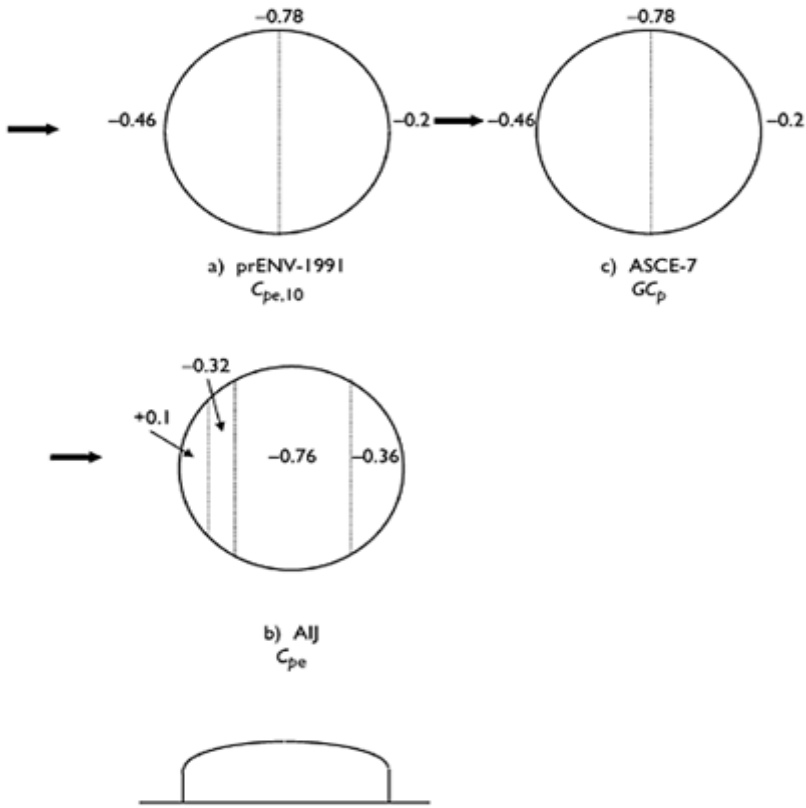

Figure 15.6 Comparison of pressure coefficients for a domed roof (main structural loads), h/d=0.2, rise/span=0.2.

ISO 4354 recommends the use of a 'dynamic response factor', C_{dyn}, to account for the dynamic wind action caused by random wind gusts acting in the along-wind direction. Fluctuating wind pressures induced by the wake of the structure, including vortexshedding forces, and other fluctuating forces induced by the motion of the structure are also discussed. However, the recommended procedure for the calculation of the dynamic response factor is only available for the along-wind response to gusts. In this case, the 'dynamic response factor' is defined as the ratio of the maximum load effect to the mean load effect. That is, it is actually a *gust response factor* (Section 5.3.2):

$$C_{dyn}=1+2g_{w}I_{u}\sqrt{(B^2+R^2)} \qquad (15.3)$$

where g_w is a peak factor, I_u the turbulence intensity, B a background response factor (dependent on the size of the building) and R a resonant response factor (note that in ISO 4354, B and R are the square roots of the background and resonant factors used in Chapter 5 of this book).

Representative values of structural damping ratio for typical steel and concrete structures are also given, together with a suggested acceptance criterion for habitable buildings.

Table 15.3 Shape factors contained in the various documents (excluding rectangular enclosed buildings)

Type	*ISO 4354*	*prEN 1991*	*ASCE-7*	*AIJ*	*AS/NZS1170.2*	*BS6399*
Stepped roofs	No	No	Yes	No	No	Yes
Free-standing walls, hoardings	Yes	Yes	Yes	No	Yes	Yes
Parapets	No	Yes*	Yes	No	No	Yes*
Free-standing roofs (canopies)	No	Yes	Yes	Yes	Yes	Yes
Attached canopies	No	No	No	No	Yes	Yes
Multi-span roofs (enclosed)	No	Yes	Yes	Yes†	Yes	Yes
Multi-span canopies	No	Yes	No	No	No	No
Arched roofs	Yes	Yes	Yes	Yes†	Yes	No
Domes	No	Yes	Yes	Yes†	Yes‡	No
Bins, silos, tanks	Yes	Yes	Yes	No	Yes	No
Circular sections	Yes	Yes	Yes	Yes	Yes	Yes
Polygonal sections	No	Yes	Yes	No	Yes	No
Structural angle sections	Yes	Yes	No	No	Yes	Yes
Bridge decks	No	Yes	No	No	No	No
Lattice sections	Yes	Yes	Yes	No	Yes	No

Flags	No	Yes	No	No	Yes	No
Sphere	No	Yes	No	No	Yes	No

* Treated as free-standing walls.
†Given in commentary section of Japanese language version.
‡ Treated as arched roofs.

Although ISO 4354 recognizes the importance of vortex shedding in causing dynamic cross-wind effects in slender prismatic and cylindrical structures, only circular cylindrical structures are dealt with in detail. Strouhal numbers for circular and near-circular cylinders are given to enable the calculation of critical wind speed at which large amplitude motions may result. The sign and magnitude of an equivalent aerodynamic damping is required to further assess the potential for large amplitude vortex-induced motions. Expressions for the amplitude of stable motion and an equivalent static wind force distribution are also given.

prEN 1991–1–4.6 has adopted a structural factor, $c_s c_d$, for the design of dynamically sensitive structures. Using the same notation as that in Equation (15.3), but not the same as in prEN 1991–1–4.6, $c_s c_d$ can be written as:

$$c_s c_d = \frac{1 + 2gI_u\sqrt{B^2 + R^2}}{1 + 2gI_u} \tag{15.4}$$

This form is intended for use with a *gust* dynamic pressure, not a mean dynamic pressure, and is the *dynamic response factor* discussed in Section 5.3.4. Values greater than one indicate significant resonant dynamic response, *R*.

In prEN 1991–1–4.6, the structural factor is actually specified as a combination of a size factor with a dynamic factor to form the combined structural factor, $c_s c_d$. The size factor separately takes account of correlation effects.

Using the notation of Equation (15.4),

$$c_s = \frac{1 + 2gI_u\sqrt{B^2}}{1 + 2gI_u} \quad \text{and} \quad c_d = \frac{1 + 2gI_u\sqrt{B^2 + R^2}}{1 + 2gI_u\sqrt{B^2}} \tag{15.5}$$

A comprehensive set of graphs of dynamic coefficient is given in prEN 1991–1–4.6, for a full range of structures, including buildings, chimneys and bridges. A detailed procedure is recommended for buildings and structures with values of dynamic coefficient in the range 1.0–1.2, with relevant information in Annexes B, C and D. Expressions for maximum along-wind displacement and standard deviation of along-wind acceleration are also given.

Comprehensive information, including working equations, regarding vortex excitation and other aeroelastic effects such as vortex-induced large amplitude lock-in type vibrations, galloping (Section 5.5.2), various types of interference excitations and flutter (Section 5.5.3), is included in Annex C of prEN 1991–1–4.6. Recommended calculation procedures for dynamic structural properties, including natural frequencies, mode shapes, equivalent masses and logarithmic decrement, are given in Appendix D of prEN 1991–1–4.6.

In ASCE-7, an analytical procedure for the determination of a ‘gust effect factor’, G_f, for the along-wind vibrations of flexible buildings and other structures is presented, in the

commentary. The development of this factor was described by Solari and Kareem (1998). The gust effect factor is, in fact, a *dynamic response factor* (Section 5.3.4), defined in the same way as the structural factor, $c_s c_d$, in prEN 1991–1–4.6, i.e. it is based on Equation (15.4) for use with dynamic pressure based on a 3-s gust wind speed. The calculation procedure is nearly identical to that in prEN 1991–1–4.6, making use of the closed form equations of Solari (1983). Expressions for maximum along-wind displacement and standard deviation and maximum along-wind acceleration are also given. However, no analytical procedure for cross-wind response is given.

In the AIJ Recommendations, a detailed procedure is applied to estimate the dynamic response of wind-sensitive structures. For along-wind response, a standard gust response factor approach along the lines of Equation (15.3) is used to determine a gust effect factor, G_D. A mode shape correction for prediction of peak base bending moments for buildings with non-linear mode shapes is provided (Tamura *et al.,* 2004).

Vortex-induced cross-wind vibration and wind loads can also be determined from the AIJ, based on rms cross-wind base moment data obtained from wind-tunnel tests. Expressions for effective cross-wind load distributions, displacement and acceleration are given. However, the cross-wind response calculations are restricted to prismatic cross-sections with a height to breadth ratio no greater than six and to wind directions normal to a face of the building. Expressions for torsional angular acceleration and torsional wind load distribution are also given. Guidelines for assessing potential aeroelastic instabilities including lock-in type vortex resonance and galloping instabilities are presented.

The dynamic along-wind and cross-wind responses of tall buildings and towers are dealt with through a dynamic response factor, C_{dyn}, in Section 6, of AS/NZS1170.2. An approach based on Equation (15.4) is adopted for along-wind response calculations. The methodology is a modified version of that originally described by Vickery (1971).

Cross-wind base overturning moment and acceleration can be determined from crosswind force spectrum coefficients, derived from wind-tunnel test data for a series of square and rectangular section buildings, with the incident wind normal to a face. Suggested values of damping for a range of steel and concrete structures under different stress levels are given. The importance of aeroelastic instabilities such as lock-in, galloping, flutter and interference are discussed separately in the Commentary to AS/NZS1170.2. However, a 'diagnostic' method for the cross-wind response of chimneys, masts and poles of circular cross-section is provided in the Standard itself.

The British Standard, BS6399: Part 2, contains a 'dynamic augmentation factor', C_r, which is, in fact, not applied directly as a factor, but in the form $(1+C_r)$ to the overall horizontal loads on buildings. It is intended for application to 'mildly dynamic structures'. If the value of C_r obtained from the graph in BS6399 exceeds 0.25 or if the height of the structure exceeds 300 m, the user is referred to other codes, and other references, for further information.

15.10 Future developments

This chapter has reviewed the provisions of six major and current (at the time of writing) standards for wind loading. Considerable differences exist in both the format and the type of information presented in these documents.

At present, there is no generally used international standard on wind loading, although shortly the final version of Eurocode 1 will be adopted in most of Europe. At the time of writing the International Standard, ISO 4354, is being re-drafted. Hopefully then national and regional standards will gradually be amended to be of similar format. The first requirement is a common format and notation. For wide international acceptance in tropical and subtropical as well as temperate climates, the special requirements of regions affected by typhoons (tropical cyclones or hurricanes) and thunderstorms will need to be incorporated.

References

American Society of Civil Engineers (2006) Minimum design loads for buildings and other structures. ASCE/SEI 7–05, ASCE, New York.

Architectural Institute of Japan (2004) AIJ recommendations for loads on buildings. AIJ, Tokyo.

British Standards Institution (1997) Loading for buildings. Part 2. Code of practice for wind loads. BS 6399: Part 2:1997.

CEN (European Committee for Standardization) (1994) Eurocode 1: Basis of design and actions on structures. Part 2–4: Wind actions. ENV-1991–2–4, CEN, Brussels.

CEN (European Committee for Standardization) (2004) Eurocode 1: Actions on structures Part 1–4: General actions—Wind actions. prEN 1991–1–4.6, CEN, Brussels.

Cook, N.J. (1990) *The Designer's Guide to Wind Loading of Building Structures. Part 2 Static Structures.* Building Research Establishment and Butter worths, London.

Dorman, C.M.L. (1984) Tropical cyclone wind speeds in Australia. *Civil Engineering Transactions, Institution of Engineers, Australia,* CE26:132–9.

Holmes, J.D. (2002) A re-analysis of recorded wind speeds in Region A. *Australian Journal of Structural Engineering,* 4:29–40.

Holmes, J.D. and King, A.B. (2005) *A Guide to AS/NZS1170.2:2002—Wind Actions.* Warreen Publishing, Mentone, Australia.

Holmes, J.D., Baker, C.J., English, E.G. and Choi, E.C.C. (2005a) Wind structure and codification. *Wind and Structures,* 8:235–50.

Holmes, J.D., Kasperski, M., Miller, C.A., Zuranski, J.A. and Choi, E.C.C. (2005b) Extreme wind structure and zoning. *Wind and Structures,* 8:269–81.

International Standards Organization (1997) Wind actions on structures. ISO International Standard. ISO 4354.

Kasperski, M. (1993) Aerodynamics of low-rise buildings and codification. *Journal of Wind Engineering & Industrial Aerodynamics,* 50:253–63.

Kasperski, M. and Geurts, C. (2005) Reliability and code level. *Wind and Structures,* 8: 295–307.

Kijewski, T. and Kareem, A. (1998) Dynamic wind effects: a comparative study of provisions in codes and standards with wind tunnel data. *Wind and Structures,* 1:77–109.

Letchford, C.W., Holmes, J.D., Hoxey, R.P. and Robertson, A.P. (2005) Wind pressure coefficients on low-rise structures and codification. *Wind and Structures,* 8:283–94.

Mehta, K.C. (1998) Wind load standards. *Proceedings, Jubileum Conference on Wind Effects on Buildings and Structures,* Porto Alegre, Brazil, 25–29 May.

Ministry of Land, Infrastructure and Transport, Japan (2000) Building Standard Law of Japan, Enforcement Orders Regulations and Notifications.

Peterka, J.A. and Shahid, S. (1998) Design gust wind speeds in the United States. *ASCE Journal of Structural Engineering,* 124:207–14.

Solari, G. (1983) Gust buffeting II: dynamic along-wind response. *ASCE Journal of Structural Engineering,* 119:383–98.

Solari, G. and Kareem, A. (1998) On the formulation of ASCE-7–95 gust effect factor. *Journal of Wind Engineering & Industrial Aerodynamics*, 77–78:673–84.

Standards Australia and Standards New Zealand (2002) Structural design actions. Part 2: wind actions. Australian/New Zealand Standard, AS/NZS 1170.2:2002. Standards Australia, Sydney, and Standards New Zealand, Wellington.

Tamura, Y., Kawai, H., Uematsu, Y., Okada, H. and Ohkuma, T. (2004) Documents for wind resistant design of buildings in Japan. *Workshop on Regional Harmonization of Wind Loading and Wind Environmental Specifications in Asia-Pacific Economies*, Atsugi, Japan, 19–20 November.

Tamura, Y., Kareem, A., Solari, G., Kwok, K.C.S., Holmes, J.D. and Melbourne, W.H. (2005) Aspects of the dynamic wind-induced response of structures and codification. *Wind and Structures*, 8:251–68.

Vickery, B.J. (1971) On the reliability of gust loading factors. *Civil Engineering Transactions, Institution of Engineers, Australia*, CE13:1–9.

Appendix A: Terminology

Aerodynamic admittance Transfer function relating the gust spectral density to the spectral density of an aerodynamic force (Sections 5.3, 5.3.1, 12.3.3)

Aerodynamic damping Aerodynamic forces proportional to the velocity of a structure, and additional to (or subtractional from) the structural damping (Section 5.5.1)

Background response That part of dynamic response to wind excluding the effects of resonant amplifications

Bernoulli's equation Equation describing irrotational and inviscid fluid flow (Section 4.2.1)

Blockage effect Distortion effect of wind-tunnel walls on measurements, particularly force and pressure measurements (Section 7.7)

Bluff body Body with a large frontal dimension, from which the airflow separates

Body axes Axes defined by the body or structure (Section 4.2.2)

Boundary layer Region of reduced air velocities near the ground or the surface of a body (Section 3.1)

Cauchy number Ratio of internal forces in a structure to inertial forces in the air (Chapter 7)

Coriolis force Apparent force on moving air due to the rotation of the earth

Correlation Statistical relationship between two fluctuating random variables (Section 3.3.5)

Downburst Severe downdraft of air occurring in thunderstorms (Sections 1.3.5, 3.2.6, 3.3.7)

Drag Along-wind force

Dynamic response factor Ratio of expected maximum structural response including resonant and correlation effects, to that ignoring both effects (Section 5.3.4)

Ekman Spiral Turning effect of the wind vector with height in the atmospheric boundary layer (Chapter 3)

Flutter One or two degrees of freedom aeroelastic instability, involving rotational motion (Section 5.5.3)

Friction velocity Non-dimensional measure of surface shear stress (Section 3.2.1)

Froude number Ratio of inertial forces in the air to gravity forces (Chapter 7)

Galloping Single degree of freedom translational aeroelastic instability (Section 5.5.2)

Geostrophic drag coefficient Ratio of friction velocity to geostrophic wind speed (Section 3.2.4)

Gradient wind Upper level wind that can be calculated from the gradient wind equation (Section 1.2.4)

Gust factor Ratio of expected maximum to mean value of wind speed, pressure or force

Gust response factor Ratio of expected maximum to mean structural response (Section 5.3.2)

Helmholtz resonance Resonance in internal pressure fluctuations associated with the compressibility of the air within a building, and the mass of air moving in and out of a dominant opening

Inviscid Fluid flow in which the effects of viscosity are non-existent or negligible

Isotach Contour of constant basic design wind speed

Jensen number Ratio of building dimension (usually height) to roughness length in atmospheric boundary-layer flow (Section 4.4.5)

Lift Cross-wind force, usually but not necessarily, vertical

Limit states design A method of structural design, which separately considers structural failure through collapse or overturning, from the functional (serviceability) aspects

Lock-in The enhancement of fluctuating forces produced by vortex shedding due to the motion of the vibrating body (Section 5.5.4)

Logarithmic law A mathematical representation of the profile of mean velocity with height in the lower part of the atmospheric boundary layer

Manifold A device for averaging pressure measurements from several measurement positions (Section 7.5.2)

Mechanical admittance Transfer function relating the spectral density of aerodynamic forces to the spectral density of structural response (Section 5.3.1)

Peak factor Ratio of maximum minus mean value, to standard deviation, for wind velocity, pressure, force or response (Section 5.3.3)

Peak gust Maximum value of wind speed in a defined time period

Pressure coefficient Surface pressure made non-dimensional by the dynamic pressure in the wind flow (Section 4.2.1)

Quasi-steady A model of wind loading that assumes that wind pressures on buildings fluctuate directly with the fluctuations in wind speed immediately upstream

Return period Inverse of probability of exceedence of an extreme value (Chapter 2)

Reynolds number Ratio of inertial forces to viscous forces in fluid flow (Section 4.2.4)

Roughness length A measure of the aerodynamic roughness of a surface, which affects the boundary-layer flow over it (Section 3.2.1)

Safety index A measure of probability of failure of a structure. ‘Reliability Index’ is also used (Section 2.6.2)

Scruton number A non-dimensional parameter incorporating the ratio of structural mass to fluid mass, and structural damping, which is a measure of the propensity of a structure to resonant dynamic response (Section 11.5.1)

Shear stress (fluid flow) The force per unit area exerted by a layer of moving fluid on the adjacent layer

Spectral density A measure of the contribution to a fluctuating quantity (e.g. wind velocity, wind pressure, deflection) within a defined frequency bandwidth

Stagnation point Point on a body where the approaching flow is brought to rest

Stationary Description of a random process whose statistical properties do not change with time

Strouhal number Non-dimensional vortex-shedding frequency (Section 4.6.3)

Synoptic winds Winds created by large-scale meteorological systems, especially gales produced by extra-tropical depressions

Thunderstorm Thermally driven local storm capable of producing strong downdraft winds (Section 1.3.3)

Tornado Local intense storm formed from thunderclouds, with intense winds rotating around a vortex structure (Sections 1.3.4, 3.2.7)

Tropical cyclone An intense tropical storm that can occur over warm tropical oceans. A generic name which incorporates 'hurricane' (used for Caribbean and north-west Atlantic storms) and 'typhoon' (used in the north-west Pacific) (Section 1.3.2)

Turbulence Fluctuations in fluid flow. In meteorology and wind engineering the term 'gustiness' is also used

von Karman's constant Dimensionless constant in the logarithmic law for the profile of mean velocity in a turbulent boundary layer

Vortex shedding The periodic shedding of eddies formed from the rolling-up of the boundary layer shed from a bluff body

Wake The region of low velocity and turbulent flow in the region downstream of a body

Wind axes Axes parallel and normal to the mean wind direction (Section 4.2.2)

Appendix B:
List of symbols

Note: symbols that are specific to particular wind loading codes and standards described in Chapter 15 are not listed in this appendix.

a (i) Coriolis acceleration (Chapter 1)

(ii) scale factor (Chapter 2)

(iii) empirical constant (Equation (3.9))

(iv) modal (generalized) coordinate

(v) parameter in wide-band fatigue (Equation (5.56))

a_s speed of sound

b (i) cross-wind breadth of bluff body

(ii) parameter in wide-band fatigue (Equation (5.56))

(iii) diameter of antenna dish (Chapter 14)

c (i) ground clearance of elevated hoarding

(ii) damping constant

(iii) scale factor in Weibull distribution

(iv) distance of solar panel from roof edge (Chapter 14)

d (i) effective diameter of rod-type objects (Chapter 1)

(ii) along-wind dimension of building or bluff body, chord of bridge deck

(iii) stand-off of solar panel from roof surface (Chapter 14)

(iv) depth of antenna dish

(v) diameter of pole (Appendix E)

d() drag force per unit length

e (i) eccentricity

(ii) eaves overhang

(iii) wall thickness of pole (Appendix E)

f (i) Coriolis parameter ($=2\Omega \sin \lambda$)

(ii) force per unit length

(iii) focal length of parabolic antenna dish (Chapter 14)

$f()$ probability density function

$f(\phi)$ function of mode shape (Equation (11.17))

g (i) gravitational constant

(ii) peak factor

h height of building or bluff body

$h(t)$ unit impulse response function (Chapter 5)

h_c height of canopy (Chapter 14)

h_e height to eaves

h_i depth of inflow in tornado (Chapter 7)

h_p height of parapet (Chapter 8)

i, j indices

k (i) $(\rho_a C_F)/(2\rho_m \ell)$ (Chapter 1)

(ii) shape factor in generalized extreme value distribution (Chapter 2, Appendix C)

(iii) von Karman's constant (Chapter 3)

(iv) constant for type of topographic feature

(v) spring stiffness

(vi) average surface roughness height (Chapter 4)

(vii) orifice constant (Chapter 6)

(viii) mode shape parameter (Equation (11.15))

(ix) parameter (Equation (14.9))

(x) parameter in generalized Pareto distribution (Appendix C)

k_x exponent (Equation (9.22))

k_y exponent (Equation (9.23))

ℓ (i) characteristic dimension for compact objects

(ii) correlation length

(iii) length of tornado path (Chapter 13)

(iv) length of solar panel (Chapter 14)

$\ell()$ lift (cross-wind) force per unit length (Chapter 11)

m (i) mass or mass per unit length

(ii) exponent in fatigue *s-N* relationship

(iii) exponent (Equation (9.18))

n (i) frequency

(ii) stress cycle

(iii) mean value (Chapter 9)

(iv) number of events e.g. number of tornado occurrences in a region (Chapter 13)

(v) exponent (Equation (9.17))

n_c characteristic frequency for internal pressure fluctuations

n_s vortex shedding frequency

p (i) pressure

(ii) probability (Chapter 2)

p_0 (i) central pressure of a tropical cyclone (Chapter 1)

(ii) ambient (static) pressure

p_f probability of failure (Chapter 2)

p_n (i) atmospheric pressure at the edge of a storm (Chapter 1)

(ii) net pressure (Chapter 14)

p_L leeward face pressure

p_w windward face pressure

q dynamic pressure

r (i) radius of curvature—of isobars (Chapter 1), or square section (Chapter 4)

(ii) risk (Chapter 2)

(iii) radius in downburst (Equation (3.13))

(iv) general structural response, or load effect

(v) ratio A_L/A_W (Chapter 6)

(vi) roughness factor ($=2I_u$)

(vii) radius of gyration (Chapter 12)

(viii) rate of intersection of tornadoes with a transmission line

r_c radius of core in tornado (Chapter 7)

r_u radius of updraft region in tornado (Chapter 7)

s (i) position factor (Equation (3.33))

(ii) stress

(iii) height for calculation of load effects

(iv) span length of a transmission line or free-standing wall (Chapters 13, 14)

(v) clear space under bridge (Chapter 14)

(vi) skewness (Appendix C)

t	(i) time
	(ii) thickness of sheet objects (Chapter 1)
	(iii) parameter for interference factor (Equation (14.9))
u, v, w	orthogonal velocity components
u	mode of extreme value distribution (Chapter 2)
u_0	wind speed level (Chapter 2)
u_*	friction velocity (Chapter 3)
v_m	velocity of flying debris
w	(i) shape factor in Weibull Distribution (Chapter 2)
	(ii) width of building (Figure 14.12)
	(iii) width of tornado or downburst path (Chapter 13)
w_a	average width of tower (Appendix E)
w_b	base width of tower (Appendix E)
w_c	width of canopy (Chapter 14)
w_0	assumed wind load per unit height (Equation (7.11))
x, y, z	Cartesian coordinate system (z is vertical)
$x(t)$	random process, structural response
x_i	distance to inner boundary layer
z	variable of integration, or transformed random variable (Appendix C)
z_h	zero-plane displacement
z_0	roughness length
z^*	characteristic height (Equation (3.13))
A	(i) scaling parameter (Equation (1.10))
	(ii) reference or frontal area
	(iii) parameter in cross-wind response (Equation (11.19))
	(iii) area of a region (Chapter 13)
A	flutter derivative for rotational motion (Chapters 5, 12)
A_j^*	normalised flutter derivative for rotational motion (Chapter 12)
A_L	area of openings on leeward wall
A_w	area of openings on windward wall
B	(i) exponent (Equation (1.10))
	(ii) background factor (also B_s)

(iii) bandwidth parameter (Equation (11.18))

C (i) decay constant (Equation (3.30))

(ii) modal damping

C_d coefficient of drag force per unit length

C_D drag coefficient

Cf coefficient of aerodynamic force per unit length

C_F aerodynamic force coefficient

C_k equivalent glass design coefficient

C_M moment coefficient

C_N normal force coefficient

C_p pressure coefficient

C_p* effective peak pressure coefficient (Equation (9.7))

C_{pn} net pressure coefficient (Chapter 14)

C_{ps} equivalent pressure coefficient for glass loading (Equation (9.20))

C_T torque coefficient

C_x coefficient of X force

C_Y coefficient of Y force

C_z coefficient of Z force

Co() co-spectral density

D (i) damage index (Chapter 1)

(ii) drag

(iii) nominal dead load (Chapter 2)

(iv) accumulated damage (Chapters 5, 9)

D_a antenna drag (Chapter 14)

D_e effective tower drag with antenna attached (Chapter 14)

D_t tower drag (Chapter 14)

E (i) Young's Modulus

(ii) non-dimensional spectral density (Chapter 11)

F (i) force

(ii) non dimensional parameter (Section 11.4)

$F()$ cumulative probability distribution function

F_i parameter in along-wind response (Chapter 11)

G (i) generalised mass

(ii) gust factor, gust response factor

(iii) shear modulus

$G()$ complementary cumulative probability distribution (Appendix C)

H_i flutter derivative for vertical motion (Chapters 5, 12)

Hi^* normalised flutter derivative for vertical motion (Chapter 12)

$H()$ dynamic amplification factor; square root of mechanical admittance

I (i) fixing strength integrity parameter (Chapter 1)

(ii) influence coefficient

(iii) mass moment of inertia (Chapters 7, 12)

(iv) second moment of area

I_u, I_v, I_w - turbulence intensities

Je Jensen Number

K (i) $\frac{1}{2}\frac{\rho_a}{\rho_m}\frac{U^2}{gl}\frac{\ell}{t}$ (Tachikawa Number) (Chapter 1)

(ii) modal stiffness

(iii) constant in fatigue *s*-*N* relationship

(iv) bulk modulus (Chapter 6)

(v) constant (Equation (7.1))

(vi) constant (Equation (9.18))

(vii) mode shape factor (Equation (11.16))

K_{ao} parameter for negative aerodynamic damping (Equation (11.19))

K_i interference factor

K_p porosity factor

K_A bulk modulus of air (Chapter 6)

K_B bulk modulus of building (Chapter 6)

K_w correlation length factor (Equation (11.6))

K_θ wind incidence factor (Equation (11.5))

L (i) lifetime of a structure (Chapter 2)

(ii) lift (cross-wind) force

(iii) general length (Chapter 7)

(iv) length of building (Figure 10.4)

(v) length of a transmission line (Chapter 13)

L_N parameter to calculate frequency of lattice tower (Appendix E)

L_s span of bridge (Appendix E)

M moment

M_b base bending moment

M_t topographic multiplier

N (i) number of wind direction sectors (Chapters 2, 13)

(ii) cycles to failure by fatigue

(iii) number of patch loads for a guyed mast (Chapter 11)

(iv) number of samples of a random variable (Appendix C)

Q (i) generalized force

(ii) volume flow rate

R (i) return period

(ii) structural resistance

(iii) characteristic radius (Equation (3.13))

(iv) radius of maximum wind in a tornado (Figure 3.4)

(v) resonant response factor

(vi) radius of liquid damper (Chapter 9)

(vii) rise of arch (Figure 10.4)

R_c combined return period for winds from more than one storm type

Rj structural response (load effect) due to unit modal coordinate, in mode, j

Re Reynolds number

S (i) structural load effect (Chapter 2)

(ii) size factor

(iii) span of arch

$S()$ spectral density

Sc Scruton number

St Strouhal number

T (i) time of flight of missile

(ii) time period

U wind speed

U_f wind speed for threshold of flight of debris

U_R wind gust speed corresponding to return period, R

V wind speed (in some code notations—Chapter 15)

V_0 internal volume

W (i) nominal wind load (Chapter 2)

(ii) weighting factor

X general random variable (Appendix C)

$X(t)$ deflection of a structure

Superscripts:

– mean (time averaged) value

′ fluctuating value

. differentiation with respect to time

∧ maximum value

∨ minimum value

Subscripts:

a air

b base of building, tower or pole

c tornado core, canopy, cable, conductor

d drag force per unit length, (antenna) dish

e (i) external

(ii) eaves

(iii) effective (Chapter 6)

eff effective

env envelope

f (i) flight speed (Chapter 1)

(ii) failure (Chapter 2)

g geostrophic (Chapter 3)

i (i) index of position or wind direction

(ii) internal

(iii) inflow layer of tornado (Chapter 7)

j index of mode of vibration

ℓ lift (cross-wind) force per unit length

lat lateral

m (i) missile (Chapter 1)

(ii) model (Chapter 7)

(iii) bending moment (Chapter 11)

max maximum

n net (pressure)

ni normal to face *i* (Chapter 11)

P (i) Peak

(ii) prototype (Chapter 7)

(iii) parapet (Chapter 8)

q shearing force

r (i) radial wind velocity component in a tornado (Chapter 3),

(ii) ratio of model to prototype value (Chapter 7)

s (i) structure, (ii) shedding, (iii) sloshing

t top of building, tower or pole

u updraft region in tornado (Chapter 7)

v vertical wind velocity component in a tornado (Chapter 3)

x x-direction response

y y-direction response

B (i) background response

(ii) barrier (Figure 7.4)

D drag force

F flutter (Chapter 12)

H Helmholtz resonance

L leeward, lift (cross-wind) force

P1 patch load (Equation (11.23))

R resonant response

T (i) top of wind tunnel (Figure 7.3)

(ii) torsional (frequency) (Chapter 12)

TL turbulence length scale (Equation (11.24))

v vertical bending (frequency) (Chapter 12)

w windward

1 first mode of vibration

θ tangential wind velocity component in a tornado (Chapter 3)

Greek symbols:

a (i) angle of attack

(ii) span reduction factor for transmission lines or walls (Chapters 13, 14)

(iii) roof pitch angle

aj coefficient for influence of resonant mode, j, on a structural load effect

β (i) safety index (Chapter 2)

(ii) mode shape exponent (Chapter 7)

(iii) angle of intersection of tornado path width with transmission line (Chapter 13)

(iv) angle of solar panel to roof surface (Figure 14.12)

γ ratio of specific heats

δ solidity of porous body

ε (i) characteristic height (Equation (3.13))

(ii) spectral bandwidth parameter (Equation (5.59))

ϕ upwind slope of topographic feature

$\phi()$ mode shape

γ ratio of specific heats of air (Chapter 6)

γ_D dead load factor

γ_W wind load factor

η ratio of damping to critical

φ (i) resistance factor (Chapter 2)

(ii) wall porosity (Chapter 6)

(iii) phase angle (Chapter 11)

(iv) transmission line direction (Chapter 13)

K surface drag coefficient

λ (i) angle of latitude (Chapter 1)

(ii) crossing rate (Chapter 2)

(iii) scaling factor (Equation (3.13))

(iv) parameter in wide-band fatigue (Equation (5.56))

(v) factor for guyed mast response (Equation (11.24))

(vi) parameter in Poisson distribution (Appendix C)

(vii) parameter for pole frequency calculation (Appendix E)

μ (i) dynamic viscosity

(ii) moment of spectral density (Chapter 5)

π (i) ratio of circumference to diameter of a circle

(ii) (with subscript) non-dimensional group

θ (i) angular rotation

(ii) angle of incidence

(iii) (as a subscript) tangential velocity component in a tornado (Chapter 3)

(iv) angle of downburst path to transmission line (Chapter 13)

ρ correlation coefficient

$\rho(n)$ normalised co-spectral density

ρ_a air density

ρ_b average building density

σ (i) scale factor (Chapter 2)

(ii) standard deviation

(iii) parameter in lognormal distribution (Appendix C)

(iv) parameter in generalized Pareto distribution (Appendix C)

τ (i) equilibrium, or response, time for internal pressure (Chapter 6)

(ii) dummy time variable for integration (Chapter 5)

(iii) averaging time (Chapter 7)

τ_0 surface shear stress

υ (i) kinematic viscosity of air

(ii) cycling rate of a random process

(iii) rate of occurrence of tornadoes per unit area (Chapter 13)

w circular frequency

Δ mean deflection (Figure 9.1)

$\Phi()$ cumulative distribution function of a normal (Gaussian) random variable (zero mean and unit standard deviation)

$\Gamma()$ Gamma function

Γ imposed circulation on tornado (Chapter 7)

Ω angular velocity of rotation of the earth

Π repeated multiplication

Σ repeated summation

$\chi^2(n)$ aerodynamic admittance

Appendix C:
Probability distributions relevant to wind engineering

C1 Introduction

Probability distributions are an essential part of wind engineering as they enable the random variables involved such as wind speeds, wind directions, surface pressures and structural response (e.g. deflections and stresses) to be modelled mathematically. Some of these variables are random *processes*, i.e. they have time-varying characteristics, as shown in Figure C1. The probability density describes the distribution of the magnitude or amplitude of the process, without any regard to the time axis.

The Appendix will cover first some basic statistical definitions. Second, a selection of probability distributions for the complete population of a random variable—the normal (Gaussian), lognormal, Weibull, Poisson, will be considered. Third, the three types of extreme value distributions and the closely related Generalized Pareto distributions will be discussed.

C2 Basic definitions

C2.1 Probability density function (pdf)

The probability density function, $f_x(x)$, is the limiting probability that the value of a random variable, X, lies between x and $(x+\delta x)$. Thus, the probability that X lies between a and b is:

$$Pr\{a < X < b\} = \int_a^b f_X(x)\mathrm{d}x \qquad \text{(C1)}$$

As any value of X must lie between $-\infty$ and $+\infty$:

$$\int_{-\infty}^{\infty} f_X(x)\mathrm{d}x = Pr\{-\infty < X < \infty\} = 1$$

Thus, the area under the graph of $f_x(x)$ versus x must equal 1.0.

C2.2 Cumulative distribution function (cdf)

The cumulative distribution function $F_x(x)$ is the integral between $-\infty$ and x of $f_x(x)$:

$$\text{i.e. } F_X(x) = \int_{-\infty}^{x} f_X(x)\,dx = Pr\{-\infty < X < x\} = Pr\{X < x\} \tag{C2}$$

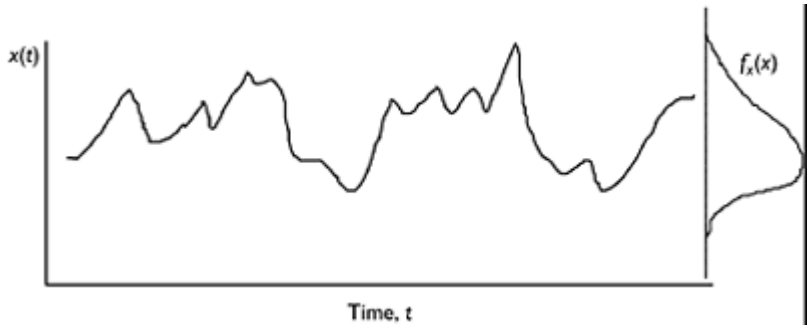

Figure C1 A random process and amplitude probability density.

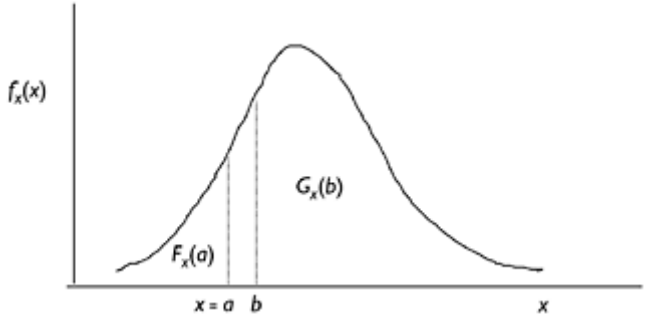

Figure C2 Probability density function and cumulative distribution functions.

The complementary cdf usually denoted by $G_x(x)$ is:

$$G_x(x)=1-F_x(x)=Pr\{X>x\} \tag{C3}$$

$F_x(a)$ and $G_x(b)$ are equal to the areas indicated on Figure C2.

Note that:

$$f_X(x) = \frac{dF_X(x)}{dx} = -\frac{dG_X(x)}{dx} \tag{C4}$$

The following basic statistical properties of a random variable are defined and their relationship to the underlying probability distribution given.

Mean:

$$\begin{aligned}\overline{X} &= (1/N)\ \Sigma_i x_i \\ &= \int_{-\infty}^{\infty} x f_X(x)\ dx\end{aligned} \tag{C5}$$

Thus, the mean value is the first moment of the pdf (i.e. the x coordinate of the centroid of the area under the graph of the pdf).

Variance:

$$\sigma_X^2 = (1/N)\ \Sigma_i [x_i - \overline{X}]^2 \tag{C6}$$

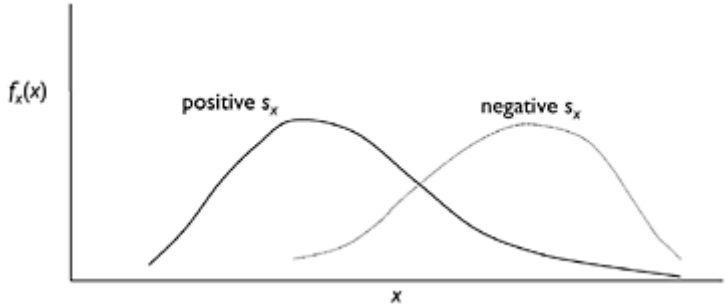

Figure C3 Positive and negative skewness.

σx (the square root of the variance) is called the standard deviation:

$$\sigma_X^2 = \int_{-\infty}^{\infty} (x - \overline{X})^2\ f_x(x)\ dx \tag{C7}$$

Thus, the variance is the second moment of the pdf about the mean value. It is analogous to the second moment of area of a cross-section about a centroid.

Skewness:

$$\begin{aligned}s_X &= [1/(N\sigma_X^3)]\ \Sigma_i\ [x_i - \bar{X}]^3 \\ &= (1/\sigma_X^3) \int_{-\infty}^{\infty} (x - \overline{X})^3\ f_X\ (x)\ dx\end{aligned} \tag{C8}$$

The skewness is the normalized third moment of the pdf. Positive and negative skewness are illustrated in Figure C3. A distribution that is symmetrical about the mean value has a zero skewness.

C3 Parent distributions

C3.1 Normal or Gaussian distribution

For $-\infty<X<\infty$,

$$f_X(x) = \frac{1}{\sqrt{2\pi}\sigma_X} \exp\left[\frac{-(x-\overline{X})^2}{2\sigma_X{}^2}\right] \tag{C9}$$

where $\overline{X}$, σ_x are the mean and standard deviation, respectively.

This is the most commonly used distribution. It is a symmetrical distribution (zero skewness) with the familiar bell shape (Figure C4).

$$F_X(x) = \Phi\left(\frac{x-\overline{X}}{\sigma_X}\right) \tag{C10}$$

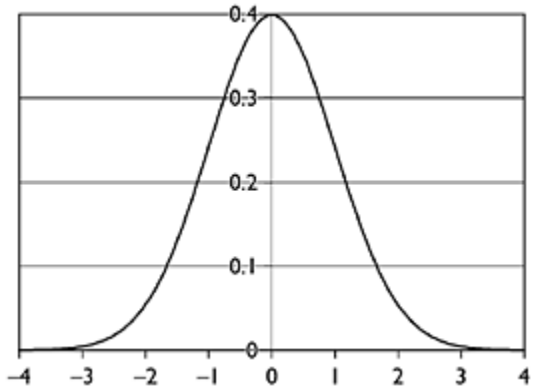

Figure C4 Normal distribution.

where Φ() is the cumulative distribution function of a normally distributed variable with a mean of zero and a unit standard deviation,

$$\text{i.e. } \Phi(u) = \left(\frac{1}{\sqrt{2\pi}}\right)\int_{-\infty}^{u} \exp\left(\frac{-z^2}{2}\right) dz \tag{C11}$$

Tables of Φ(u) are readily available in statistics textbooks, etc.

If $Y=X_1+X_2+X_3+\ldots X_N$, where X_1, X_2, $X_3\ldots X_N$, are random variables with any distribution, the distribution of Y tends to become normal as N becomes large. If $X_1, X_2,\ldots$ themselves have normal distributions, then Y has a normal distribution for any value of N.

In wind engineering, the normal distribution is used for turbulent velocity components and for response variables (e.g. deflection) of a structure undergoing random vibration. It

should be used for variables that can take both negative and positive values, so it would not be suitable for scalar wind speeds that can only be positive.

C3.2 Lognormal distribution

$$f_X(x) = \frac{1}{\sqrt{2\pi}\sigma x} \exp\left[-\frac{-\left\{\log_e\left(\frac{x}{m}\right)\right\}^2}{2\sigma^2} \right] \tag{C12}$$

where the mean value $\overline{X}$ is equal to m exp ($\sigma 2/2$) and the variance σ_x^2 is equal to $m^2\exp(\sigma^2)[\exp(\sigma^2)-1]$.

$\log_e x$ in fact has a normal distribution with a mean value of $\log_e m$ and a variance of σ^2.

If a random variable $Y=X_1 \cdot X_2 \cdot X_3 \ldots X_N$, where $X_1, X_2, X_3, \ldots X_N$, are random variables with any distribution, the distribution of Y tends to become lognormal as N becomes large. Thus, the lognormal distribution is often used for the distribution of a variable that is itself the product of a number of uncertain variables—for example, wind speed factored by multipliers for terrain, height, shielding, topography, etc.

The lognormal distribution has a positive skewness equal to $[\exp(\sigma^2)+2][\exp(\sigma^2) - 1]^{1/2}$.

C3.3 'Square-root-normal' distribution

Now consider the distribution of $Z=X^2$, where X has the normal distribution:

$$f_Z(z) = \frac{1}{2\left(\frac{\sigma_X}{\overline{X}}\right)\sqrt{2\pi z}} \left\{ \exp\left[-\left(\frac{1}{2}\right)\left(\frac{\sqrt{z}-1}{\left(\frac{\sigma_X}{\overline{X}}\right)} \right)^2 \right] + \exp\left[-\left(\frac{1}{2}\right)\left(\frac{\sqrt{z}+1}{\left(\frac{\sigma_X}{\overline{X}}\right)} \right)^2 \right] \right\} \tag{C13}$$

and the cdf is:

$$F_Z(z) = \Phi\left(\frac{\sqrt{z}-1}{\left(\frac{\sigma_X}{\overline{X}}\right)} \right) + \Phi\left(\frac{\sqrt{z}+1}{\left(\frac{\sigma_X}{\overline{X}}\right)} \right) - 1 \tag{C14}$$

This distribution is useful for modelling the pressure fluctuations on a building which are closely related to the square of the upwind velocity fluctuations, which can be assumed to have a normal distribution (e.g. Holmes, 1981).

C3.4 Weibull distribution

$$f_X(x) = \left(\frac{w x^{w-1}}{c^w} \right) \exp\left[-\left(\frac{x}{c}\right)^w \right] \tag{C15}$$

$$F_X(x) = 1 - \exp\left[-\left(\frac{x}{c}\right)^w \right] \tag{C16}$$

where c (>0) is known as the scale parameter with the same units as *x* and w (>0) is the shape parameter (dimensionless).

The shape of the pdf for the Weibull distribution is quite sensitive to the value of the shape factor, *w*, as shown in the Figure C5. The Weibull distribution can only be used for random variables that are always positive. It is often used as the parent distribution for wind speeds, with *k* in the range of about 1.5–2.5. The Weibull distribution with *w*=2 is a special case known as the Rayleigh distribution. When *k*=1, it is known as the exponential distribution.

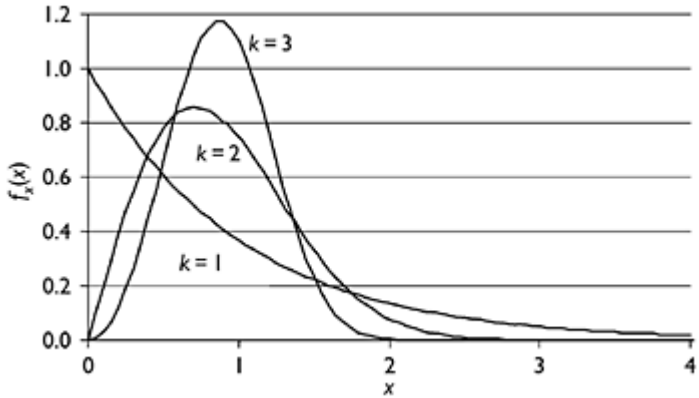

Figure C5 Probability density functions for Weibull distributions (*c*=1).

C3.5 Poisson distribution

The previous distributions are applicable to *continuous* random variables, i.e. *x* can take any value over the defined range. The Poisson distribution is applicable only to positive *integer* variables, e.g. number of cars arriving at an intersection in a given time, number of exceedences of a defined pressure level at a point on a building during a wind storm.

In this case, there is no probability density function but instead a probability function:

$$p_X(x) = \lambda^x \frac{\exp(-\lambda)}{x!} \tag{C17}$$

where A is the mean value of *X*. The standard deviation is $\lambda^{1/2}$.

The Poisson distribution is used quite widely in wind engineering to model exceedences or upcrossings of a random process such as wind speed, pressure or structural response, or events such as number of storms occurring at a given location. It can also be written in the form:

$$p_X(x) = (vT)^x \frac{\exp(-vT)}{x!} \tag{c18}$$

where υ is now the mean rate of occurrence per unit time and T the time period of interest.

C4 Extreme value distributions

In wind engineering, as in other branches of engineering, we are often concerned with the largest values of a random variable (e.g. wind speed) rather than the bulk of the population.

If a variable Y is the maximum of n random variables, $X_1, X_2,\ldots X_n$ and X_i are all independent,

$$F_Y(y) = F_{X_1}(y) \cdot F_{X_2}(y) \cdots F_{X_n}(y),$$

as $P[Y<y]=P[$all n of the $X_i<y]=P[X_1<y] \cdot P[X_2<y]\ldots P[X_n<y]$

In the special case that all the X_i are identically distributed with cdf $F_x(x)$,

$$F_Y(y)=[F_X(X)]^n \tag{C19}$$

If the assumptions of common distribution and independence of X_i hold, the shape of the distribution of Y is insensitive to the exact shape of the distribution of X_i. In this case, three limiting forms of the distributions of the largest value Y, as n becomes large may be identified (Fisher and Tippett, 1928; Gumbel, 1958). However, they are all special cases of the generalized extreme value distribution.

C4.1 Generalized extreme value distribution

The cdf may be written,

$$F_Y(y) = \exp\left\{-\left[1-\frac{k(y-u)}{a}\right]^{1/k}\right\} \tag{C20}$$

In this distribution, k is a shape factor, a a scale factor and u a location parameter. There are thus three parameters in this generalized form.

The three special cases are:

Type I (k=0). This is also known as the Gumbel distribution.

Type II (k<0). This is also known as the Frechet distribution.

Type III (k>0). This is a form of the Weibull distribution.

The Type I can also be written in the form:

$$F_Y(y)=\exp\{-\exp[-(y-u)/a]\} \tag{C21}$$

The GEV is plotted in Figure 2.1 in Chapter 2, with k equal to –0.2, 0 and 0.2 such that the Type I appears as a straight line with a reduced variate, z, given by:

$$z=-\log_e\{-\log_e[F_Y(y)]\}$$

As can be seen the Type III (k=+0.2) curves in a way to approach a limiting value at high values of the reduced variate (low probabilities of exceedence). Thus, the Type III distribution is appropriate for phenomena that are limited in magnitude for geophysical reasons, including many applications of wind engineering. The Type I can be assumed to be a conservative limiting case of the Type III, and it has only two parameters (a and u), as k is predetermined to be 0. For that reason, the Type I (Gumbel distribution) is easy to fit to actual data, and is very commonly used as a model of extremes for wind speeds, wind pressures and structural response.

C4.2 Generalized Pareto distribution

The complementary cumulative distribution function is:

$$G_X(x)=\left[1-\left(\frac{kx}{\sigma}\right)\right]^{1/k} \tag{C22}$$

The pdf is:

$$f_X(x)=\left(\frac{1}{\sigma}\right)\left[1-\left(\frac{kx}{\sigma}\right)\right]^{(1/k)-1}$$

where k is the shape parameter and a a scale parameter. The range of X is $0<X<\infty$ when $k<0$ or $k=0$. When $k>0$, $0<X<(\sigma/k)$. Thus, positive values of k only apply when there is a physical upper limit to the variate, X. The mean value of X is as follows:

$$\overline{X}=\frac{\sigma}{k+1} \tag{C24}$$

The probability density functions for various values of k are shown in Figure C6.

The generalized Pareto has a close relationship with the generalized extreme value distribution (Hosking and Wallis, 1987), so that the three types of the GEV are the distributions for the largest of a group of N variables that have a generalized Pareto

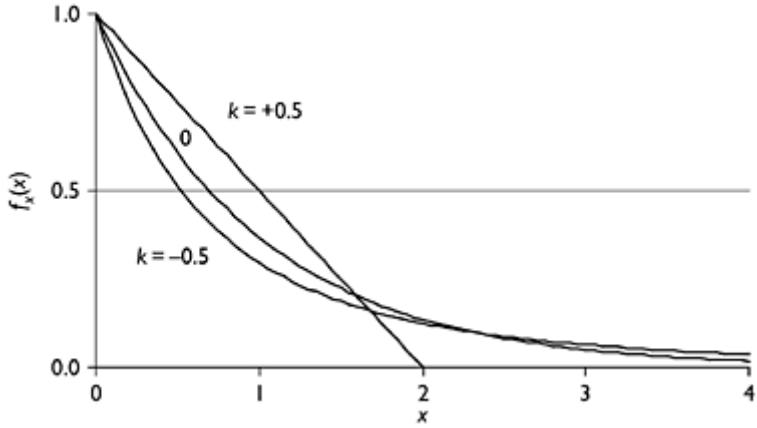

Figure C6 Probability density functions for generalized Pareto distributions (σ=1).

parent distribution with the same shape factor, *k.* It also transpires that the generalized Pareto distribution is the appropriate one for the excesses of independent observations above a defined threshold (Davison and Smith, 1990). This distribution is used for the excesses of maximum wind speeds in individual storms over defined thresholds (Holmes and Moriarty, 1999 and Section 2.4). From the mean rate of occurrence of these storms, which are assumed to occur with a Poisson distribution, predictions can be made of wind speeds with various annual exceedence probabilities.

C5 Other probability distributions

There are many other probability distributions. The properties of the most common ones are listed by Hastings and Peacock (1974).

The general application of probability and statistics in civil and structural engineering is discussed in specialized texts by Benjamin and Cornell (1970) and Ang and Tang (1975).

References

Ang, A.H.-S. and Tang, W.H. (1975) *Probability Concepts in Engineering Planning and Design—Volume I—Basic Principles.* Wiley, New York.

Benjamin, J.R. and Cornell, C.A. (1970) *Probability, Statistics and Decision for Civil Engineers.* McGraw-Hill, New York.

Davison, A.C. and Smith, R.I. (1990) Models for exceedances over high thresholds. *Journal of the Royal Statistical Society, Series B,* 52:393–442.

Fisher, R.A. and Tippett, L.H.C. (1928) Limiting forms of the frequency distribution of the largest or smallest member of a sample. *Proceedings of the Cambridge Philosophical Society,* 24(pt 2): 180–90.

Gumbel, E.J. (1958) *Statistics of Extremes.* Columbia University Press, New York.

Hastings, N.A.J. and Peacock, J.B. (1974) *Statistical Distributions.* Wiley, New York.

Holmes, J.D. (1981) Non-Gaussian characteristics of wind pressure fluctuations. *Journal of Wind Engineering & Industrial Aerodynamics,* 7:103–8.

Holmes, J.D. and Moriarty, W.W. (1999) Application of the generalized Pareto distribution to extreme value analysis in wind engineering. *Journal of Wind Engineering & Industrial Aerodynamics,* 83:1–10.

Hosking, J.R.M. and Wallis, J.R. (1987) Parameter and quantile estimation for the generalized Pareto distribution. *Technometrics,* 29:339–49.

Appendix D:
Extreme wind climates—a world survey

In this Appendix, an attempt has been made to describe the general type of extreme wind climate, and to catalogue reliable design wind speed information available, from many countries in the world. Classification is done on a national basis, although of course extreme wind climates do not follow national boundaries. For small countries without wind loading standards, or building codes with wind loading information, it would be appropriate to use information from neighbouring countries.

It should be noted that wind loading codes and standards are constantly under revision, and the values of design wind speed, zoning systems, etc. given in this Appendix may change periodically.

D1 Severe wind strength classification system

There have been cases where major errors have been made in the general level of design wind speeds used for a particular country or region, by engineers from other parts of the world. This is most likely to happen in the tropical and equatorial regions, where the interface between very severe winds produced by tropical cyclones (typhoons, hurricanes), and the low extreme winds near the Equator where tropical cyclones do not occur, may not be clearly defined. It is very useful to have a general idea of the level of design wind speeds in a country or parts of a large country. This information may in fact be sufficient for the design of small buildings, and less important structures such as signs or poles.

Table D1 presents a simple classification system, which can be used to ‘grade’ any country or region in terms of its general level of wind speed. Nothing is stated in this table with regard to the type of windstorm that is dominant in a country. A dominant storm type in one country can produce similar extreme value statistics to another storm type in a different country. Note that for some storm types, such as downbursts generated by thunderstorms, the 3-s gust may be a more relevant indicator than the 10-min mean.

Table D1 A classification system for design wind speeds (50-year return period wind speeds at 10 mheight)

Level	*3-s gust (m/s)*	*10-min mean (m/s)*
I	<35	<22
II	35–45	22–30
III	45–55	30–35
IV	55–65	35–40
V	>65	>40

D2 Country by country survey

Unless stated otherwise, all design wind data in the following is referred to 10-m height, in flat, open country, terrain.

D2.1 Antigua (see Leeward Islands)

D2.2 Argentina

Argentina is a large country and is affected by a range of different types of windstorms, although tropical cyclones do not occur. Large extra-tropical depressions are the dominant winds in the south (Patagonia and Tierra del Fuego). In the north-east (Cordoba region), the dominant winds are caused by severe thunderstorms; tornadoes and downbursts ('tormentas') have caused failures of several high voltage transmission lines. Downslope and 'fonda' winds with severe gustiness occur in the Andes.

Early extreme value analyses (Riera and Reimundin, 1970; Viollaz *et al.*, 1975) used the Frechet (Type II) Extreme Value Distribution to fit data from 63 stations in Argentina. This distribution (Section 2.2.1) is known to give excessively conservative predictions at high return periods. More recent extreme value analysis, based on the Gumbel Distribution, for six stations in the north east of the country, gave 50-year return period gusts of 44–47 m/s. Thunderstorm winds were dominant in these records (de Schwarzkopf, 1995). *Extreme wind classifications: II, III.*

D2.3 Australia

This large continental country has a variety of severe wind types with large extra-tropical gales along the south coast and Tasmania moving from the west, and 'East Coast lows' in the Tasman Sea affecting the eastern coastline. Thunderstorm-generated downbursts originating from local convection are the dominant windstorms in the interior. The strongest recorded winds, at 10 m height, in the four major capitals of Sydney, Melbourne, Adelaide and Brisbane are also caused by local downbursts from thunderstorms. Severe tropical cyclones can affect the coastline within about 100km from

the sea between 25° and 10° S latitudes. The most common and most severe occur on the west coast between 20° and 25° S (Table D2).

Analyses of extreme wind speeds for Australia have been carried out by Whittingham (1964), Gomes and Vickery (1976a,b), Dorman (1983) and Holmes (2002). Wind speeds for structural design are given in Australian Standard AS/NZS 1170.2 (Standards Australia, 2002). Four regions are defined: these are labelled from A to D with increasing basic design wind speeds. Regions C-D are considered dominated by severe to very

Table D2 Australia

Region	*Description*	*Classification*
A	Thunderstorm downbursts and synoptic winds (gales)	II
B	Weakening tropical cyclones	III
C	Moderately severe to severe tropical cyclones	IV
D	Severe tropical cyclones	V

severe tropical cyclones. In Region B (covering Brisbane), and the tropical coastal strip between 50 and 100km inland, weaker tropical cyclones can occur.

D2.4 Austria

No values were specified in the draft Eurocode (CEN, 1994). However, wind climate should be similar to southern Germany and Switzerland. *Extreme wind classification: II.*

D2.5 Bahamas

This island group is subjected to frequent Atlantic hurricanes. The US Department of Defense gives 50-year return period gust speeds of 66–72 m/s. *Extreme wind classification: V.*

D2.6 Barbados (see Windward Islands)

D2.7 Belgium

The draft Eurocode (CEN, 1994) specified a single value of 10min mean wind speed with a 50-year return period of 26.2 m/s. *Extreme wind classification: II.*

D2.8 Belize

Belize in Central America experiences severe winds from hurricanes. Analysis of extreme wind speeds for the Commonwealth Caribbean was carried out by Shellard (1972). These results have been used by the Caribbean Uniform Building Code (Caribbean Community Secretariat, 1986). This code specifies a 50-year return period

10min mean wind speed of 36 m/s for the north of the country, and 30.5 m/s for the south. *Extreme wind classifications: IV (north); III (south).*

D2.9 Brazil

In Brazil, extreme winds are produced primarily by a mixture of large extra-tropical depression systems and local thunderstorm downdrafts (Riera and Nanni, 1989). The coastline of the South Atlantic normally does not experience tropical cyclones due to the low water temperature; however, a cyclonic system (named 'Catarina') with the characteristics of a weak hurricane, formed off the coastline of southern Brazil in January 2004 (Loredo-Souza and Paluch, 2005).

Salgado Vieira Filho (1975) carried out extreme value analyses of wind speeds for 49 Brazilian stations, but used the conservative Frechet Distribution for predictions, and apparently the data were not separated by storm type. Later analyses by Riera and Nanni (1989) indicate that thunderstorm winds are dominant in most locations. Jeary (1997b) lists 10 years of recorded wind speeds (from 3 mheight) for three stations in Rio de Janeiro. The Brazilian wind loading code (NBR-6123, 1987) gives isotachs of 3-s gust speeds with 50-year return period varying from 30 m/s (north half of country) to 50 m/s (extreme south). *Extreme wind classifications: I (north of 20°); II (south central); III (extreme south).*

D2.10 Canada

Extreme winds in Canada are primarily generated by large-scale synoptic systems, and surface extreme winds can be quite well predicted from gradient wind observations (Davenport and Baynes, 1972). An appendix to the National Building Code of Canada (NRC, 1995) gives values of dynamic pressures. The equivalent hourly mean wind speeds with a 30-year return period range from 24–28 m/s in the main populated area around the Great Lakes (including Toronto, Montreal and Ottawa) to 30–35 m/s in Newfoundland, and in the Hudson's Bay area. *Extreme wind classifications: III (Newfoundland and north); II (rest of Canada).*

D2.11 China (including Taiwan)

China is a large country with a range of extreme wind types ranging from severe gales arising from synoptic systems in Siberia in the north-west to typhoons along the southern coastline. There is a region with downslope winds.

There is a combined loading code published by the Department of Standards and Norms, Ministry of Construction, which includes a wind loading section. This is also available as an English translation (GBJ-9—Department of Standards and Norms, 1994). A map is included with this standard, which gives contours of dynamic pressure in kN/m^2 (kPa). The standard states that the 'wind reference pressure' is calculated from the 10-min mean wind speed at 10 m height by the formula, $w_o = v_o^2/1600$. These values have a 50-year return period (recently revised from 30-year return period). Values of dynamic pressure on these contours range from 0.30 to 0.90kPa. For most of the country, the values are in the range from 0.30 to 0.50 kPa (Table D3).

D2.12 Croatia

The extreme wind climate in Croatia is described by Bajic and Peros (2005). Most of the country has been assigned a value of 25 m/s for the 10-min mean wind speed with a return period of 50 years. The exceptions are some valleys and mountain passes with accelerated *bura* (downslope) winds (see Section 1.3.6). In these regions it is stated that values of 38–55 m/s were obtained. *Extreme wind classification: II (most of country); IV-V (downslope wind areas).*

Table D3 China

Region	*Description*	*Classification*
Central Mainland	Pressure contours from 0.30 to 0.50 kPa	II
North-west and inner southern coast	Pressure contours from 0.60 to 0.70 kPa	III
Outer southern coast and islands,	Pressure contours from 0.80 to 0.90 kPa	IV
Hainan Taiwan	Severe typhoons	V

D2.13 Denmark

Wind speed observations have been made in Denmark since the 1870s. The dominant source of extreme winds in Denmark is severe extra-tropical depressions moving in from the North Atlantic Ocean. Extreme value analyses of extreme wind speeds have been made by Jensen and Franck (1970) and several others.

The draft Eurocode (CEN, 1994) specified a single value of 10-min mean wind speed with a 50-year return period, for Denmark, of 27.0 m/s. *Extreme wind classification: II.*

D2.14 Dubai

See United Arab Emirates.

D2.15 Egypt

Locations on the coast have a similar extreme winds to other Mediterranean locations e.g. the 50-year gust for Alexandria is given as 38 m/s by the US Department of Defense. Inland values appear to be significantly lower. *Extreme wind classifications: I, II.*

D2.16 Fiji

The Fijian islands are subject to periodic visits from tropical cyclones (e.g. ‘Kina’ in 1993, ‘Ami’ in 2003) and consequent high winds. *Extreme wind classification: IV.*

D2.17 Finland

The draft Eurocode (CEN, 1994) specified a single value of 10-min mean wind speed with a 50-year return period, for Finland, of 23 m/s. *Extreme wind classification: II.*

D2.18 France

Like other Western European countries, the extreme wind climate of France is dominated by synoptic gales from large depression systems moving in from the Atlantic Ocean.

The draft Eurocode (CEN, 1994) specified four value of 10-min mean wind speed with a 50-year return period, for four zones in metropolitan France, ranging from 24 to 30.5 m/s. The highest values occur for Zone 4, which includes parts of Brittany and Normandy, the Mediterranean coastline and Eastern Corsica. *Extreme wind classification: II (Zones 1–3); III (Zone 4).*

D2.19 French Caribbean (see also Leeward and Windward islands)

The draft Eurocode (CEN, 1994) specified a value of 10-min mean wind speed with a 50-year return period, of 34 m/s, for the French territories of Guadeloupe and Martinique in the southern Caribbean. These territories experience visits from hurricanes, although apparently less frequently than the islands of the northern Caribbean. *Extreme wind classification: III (Martinique); IV (Guadeloupe).*

Table D4 Germany

Zone	*Description*	*Classification*
1	Southern Germany	II
2	Northern Germany	II
3	North Sea coast	III
4		III

D2.20 Germany

The draft Eurocode ENV-1991–2–4 gave a map with a system of 4 zones. The highest wind speed zone, 3, is on the North Sea coast. The main source of strong winds is gales accompanying large-scale depressions moving into Germany from the west. The zone system given differs from an earlier zoning system for the Federal Republic (West Germany) by Caspar (1970).

Analyses by Schueller and Panggabean (1976) for stations in West Germany gave distributions for gust speeds, which give 50-year return period values between 35 and 50 m/s. An exception was Feldberg with 60 m/s; this is a mountain station, with topographic influences (Table D4).

D2.21 Greece

The draft Eurocode ENV-1991–2–4 specified a 50-year return period 10-min mean wind speed for Greece, of 36 m/s for the islands and coastal areas of the mainland within 10km of the coastline. For the rest of the country, the value is 30 m/s. *Extreme wind classification: III.*

D2.22 Greenland

The US Department of Defense recommends 50-year gust wind speeds between 54 m/s and 74 m/s for US Air Force Bases in Greenland. *Extreme wind classification: IV.*

D2.23 Guam (U.S.)

This Pacific island has experienced some of the strongest recorded tropical cyclones. The ASCE-7 Loading Standard specifies a 50-year return period gust speed of 76 m/s. *Extreme wind classification: V.*

D2.24 Guyana

This country has an equatorial climate with low wind speeds. Analysis of extreme wind speeds for the Commonwealth Caribbean was carried out by Shellard (1972). These results have been used by the Caribbean Uniform Building Code (Caribbean Community Secretariat, 1986) and by the Code of Practice of the Barbados Association of Professional Engineers (1981). The former specifies a 50-year return period 10-min mean speed of 18 m/s, and the latter gives a 50-year return period 3-s gust speed of 22 m/s. *Extreme wind classification: I.*

D2.25 Hong Kong and Macau

As for the rest of the south China coastline, Hong Kong and Macau are subjected to frequent visits from moderate to severe typhoons. Hong Kong has good quality recorded wind speed data extending more than a 100 years from 1884 to 1957, from the Royal Hong Kong Observatory, and since 1957, from Waglan Island. Analyses of extreme winds from typhoons has been carried out by a number of authors including Faber and Bell (1967), Chen (1975), Davenport *et al.* (1984), and Melbourne (1984), Jeary (1997a) and Holmes *et al.* (2001). Most of these studies have normalized the wind speeds to a height of 50m, rather than 10m. Design wind speeds in Hong Kong and Macau are set by the respective building departments.

The Hong Kong Code of Practice (Buildings Department, 2004) implies a 50-year return period 3-s gust wind speed at 50 m height of about 65 m/s. This compares with the values obtained by Chen (1975) of 70.5 m/s using annual maxima, and by Melbourne (1984) of 63.5 m/s, using only recorded typhoon data; both used the Type I (Gumbel) Extreme Value Distribution. Lower values are obtained if the Generalized Extreme Value Distribution is used to fit the typhoon data. *Extreme wind classification: IV.*

D2.26 Iceland

Iceland is subject to Atlantic gales. The draft Eurocode ENV-1991–2–4 specified a 50-year return period 10-min mean at 10 mheight, of 39 m/s for coastal areas within 10km of the coastline. For inland areas, the value is 36 m/s (ENV-1191–2–4 incorrectly describes these values as 3-s gusts). *Extreme wind classification: II.*

D2.27 India

India, a large sub-continental tropical country, has a range of extreme wind zones, with extreme tropical cyclones being dominant on the east (Bay of Bengal) coast, and less frequent ones on the west coast. In inland areas, thunderstorms and monsoon winds are prevalent.

India has a good network of meteorological stations, and there have been a number of extreme value analyses of wind speeds for the country. The Indian Standard for Wind Loads IS875 Part 3 (Bureau of Indian Standards, 1987) divides the country into six zones, giving 50-year return period gust wind speeds ranging from 33 to 55 m/s (Table D5).

D2.28 Indonesia

Like Malaysia and Singapore, Indonesia is entirely in the equatorial zone, does not experience typhoons, and design wind speeds from weak thunderstorms and monsoonal winds are low. *Extreme wind classification: I.*

D2.29 Ireland

Ireland is a small island nation exposed to severe Atlantic gales on its west coast. A map showing contours of extreme wind speeds for Ireland appears in the British Code of Practice (British Standards Institution, 1997). The map in the draft Eurocode (CEN, 1994) had higher values, although nominally also 10-min mean wind speeds with a 50-year return

Table D5 India (refer to map in IS 875: Part 3 for details of zones)

Zone	*Description*	*Classification*
1	Tripura, Mizoram, Ladakh	IV
2	Coastal strips of Tamil Nadu (including Madras), Andhra Pradesh, Orissa, Gujarat, West Bengal (including Calcutta), Assam	III
3	Northern India including Delhi, central Tamil Nadu	III
4	Coastal strip on Arabian Sea, including Bombay, inland Madhya Pradesh, Orissa	II
5	Most of southern India	II
6	Inland Karnataka, including Bangalore	I

Table D6 Italy (refer to map in ENV 1991–2–4 for details of zones)

Zones	*Description*	*Classification*
1,2	Northern Italy (25 m/s)	II
3	Central and southern Italy (27 m/s)	II
4, 5, 6	Sardinia and Sicily (28 m/s)	II
7	Liguria (29 m/s)	II
8,9	Trieste and islands (31 m/s)	III

period. The values in the British Standard are believed to be more reliable. *Extreme wind classification: II.*

D2.30 Italy

Italy was divided into nine zones with five basic wind speeds in the draft Eurocode (CEN, 1994). These are 10-min mean speeds with a 50-year return period, ranging from 25 to 31 m/s (Table D6).

D2.31 Jamaica

Jamaica is in a region of hurricane tracks in the Caribbean, and experiences severe winds from these events. Analysis of extreme wind speeds for the Commonwealth Caribbean was carried out by Shellard (1972). These results have been used by the Caribbean Uniform Building Code (Caribbean Community Secretariat, 1986) and by the Code of Practice of the Barbados Association of Professional Engineers (1981). The former specifies a 50-year return period 10-min mean wind speed of 36.5 m/s, and the latter a 56 m/s peak gust. *Extreme wind classification: IV.*

D2.32 Japan

Japan is subject to typhoons from the Pacific in Kyushu and Okinawa, and temperate synoptic systems in the north of the country. The Architectural Institute of Japan has a contour map of design wind speeds (10-min mean, 100-year return period) in its wind load recommendations. Values range from 26–44 m/s on the main islands to 50 m/s on Okinawa which is subject to frequent severe typhoons. *Extreme wind classifications: II, III, IV, V.*

D2.33 Korea

The coastline of South Korea has some influence from typhoons on the south and east coasts and the island of Cheju, but these are relatively infrequent.

The Architectural Institute of Korea has a map of 10-min mean 100-year return period wind speeds varying from 25 m/s in the inland centre to 40 m/s at some points on the eastern and southern coastline. Seoul is specified as 30 m/s. *Extreme wind classifications: II, III, IV.*

D2.34 Leeward Islands

This group of islands is affected by hurricanes in the Caribbean. Analysis of extreme wind speeds for Commonwealth countries in the Caribbean was carried out by Shellard (1972). These results have been used by the Caribbean Uniform Building Code (Caribbean Community Secretariat, 1986) and by the Code of Practice of the Barbados Association of Professional Engineers (1981). The latter specifies a 50-year return period 3-s gust speed of 64 m/s, based on studies for Antigua. This value is also applicable to St. Kitts-Nevis, Montserrat, and the Virgin Islands. *Extreme wind classification: IV.*

D2.35 Luxembourg

The draft Eurocode (CEN, 1994) specified a single value of 10-min mean wind speed with a 50-year return period, of 26 m/s. *Extreme wind classification: II.*

D2.36 Madagascar

No direct information is available, but the eastern coast can be assumed to have a similar extreme wind climate to Reunion Island and Mauritius. *Extreme wind classification: III.*

D2.37 Malaysia

Malaysia is entirely in the equatorial zone, does not experience typhoons, and has very low extreme winds from weak thunderstorms and monsoonal winds. Monthly maximum wind data are available from more than 30 stations in the country, including Miri and Kuching in East Malaysia (Sarawak).

Analysis of this data for 50-year return period gust values for 20 stations by the Malaysian Meteorological Service gave values between 24 and 32 m/s. There is evidence of higher wind speeds in the highland stations away from the coastal plains. *Extreme wind classification: I.*

D2.38 Mauritania

An investigation of design wind speeds for offshore oil and gas platforms indicated strong winds caused by severe thunderstorm events with a 50-year return period gust wind speed of around 55 m/s. *Extreme wind classification: III.*

D2.39 Mauritius

Like neighbouring Reunion, Mauritius in the Indian Ocean experiences land fall from a tropical cyclone about once every 5 years (Sites and Peterson, 1995). *Extreme wind classification: III.*

D2.40 Mexico

Mexico experiences extreme winds from hurricanes on both its Pacific and Caribbean coasts. For inland areas, thunderstorms are dominant. Extreme value analyses were carried out by Vilar *et al.* (1991) (also Lopez and Vilar, 1995) for the Mexican Electrical Utility (CFE) using the Generalized Extreme Value Distribution, for data from 57 stations. An isotach map resulting from this study shows 50-year return period 3-s gusts ranging widely from 28 m/s in the Mexico City area to 61 m/s on the Pacific coast.

Table D7 is not official but describes zones based on the isotach map.

D2.41 Morocco

The 50-year gust for Casablanca on the Atlantic coast is given as 40 m/s by the US Department of Defense. Inland mountainous regions may have higher values. *Extreme wind classifications: II, III.*

D2.42 Netherlands

The Netherlands is exposed to gales from the North Sea on the coast. The draft Eurocode ENV-1991–2–4 specified three ‘areas’ with 50-year return period 10-min wind speeds,

Table D7 Mexico

Description	*Classification*
South of 24° S excluding coastline	I
North of 24° S excluding coastline	II
Within 50 km of Caribbean coast,	III
5 0–100 km from Pacific coast	
Within 50 km of Pacific coast	IV

of 25, 27.5 and 30 m/s. Amsterdam and Rotterdam are in Area 2 (27.5 m/s). *Extreme wind classification: II.*

D2.43 New Caledonia

New Caledonia in the South Pacific Ocean is affected by tropical cyclones (Holmes and Weller, 2002). *Extreme wind classification: IV.*

D2.44 New Zealand

The main extreme winds in New Zealand are temperate synoptic systems, although the north of the country can experience the effects of decaying tropical cyclones. The map of basic wind speeds in the Australian/New Zealand Standard (Standards Australia, 2002) shows three wind regions. These have similar all-directional basic wind speeds (1000year return period gusts) ranging between 46 and 53 m/s, but differ in their directional wind speeds. There are a number of mountain areas, especially in the South Island, where downslope winds occur—for these the wind speed is increased by a 'Lee Multiplier' of up to 1.35. *Extreme wind classifications: II, III (some mountain areas).*

D2.45 Norway

The draft Eurocode, ENV-1991–2–4, specified several wind velocity profiles of 3- to 5-s gust wind speeds, which incorporate terrain effects as well as height variation. Two of these curves, E and F, incorporate gust speeds at 10 m height in open terrain of 45 and 50 m/s, respectively. Curves A and B correspond to 35 and 40 m/s, respectively (Curves C and D apply to built up areas, corresponding to open country exposure for Curves A and B, respectively). *Extreme wind classifications: II (A and B); III (E and F).*

D2.46 Oman

The U.S. Department of Defense recommends 50-year gust wind speeds of 47 m/s for south-west inland areas and the Batinah coast, 51 m/s for central and southern inland areas, and the north and east coasts, and 54 m/s for offshore islands. *Extreme wind classification: III.*

D2.47 Papua-New Guinea

The majority of Papua-New Guinea (including Port Moresby) is in the equatorial zone, and the design winds, originating from thunderstorms produced by local convective activity, are quite low. An extreme value (Gumbel) analysis for Port Moresby by Whittingham (1964) using only 11 years of data gives a 50-year return period gust of 31 m/s. The addition of some extra years gives even lower values. The P-NG loading code gives a contour map with 50-year return period gust wind speeds ranging from 24 to 32 m/s. For the south-west tip 40 m/s is specified. Values for major centres are: Port Moresby 28 m/s, Lae 23 m/s, Rabaul 26 m/s; 34 m/s is specified for Honiara (Solomons).

The islands on the south west are occasionally exposed to developing Coral Sea cyclones, and should have higher design wind speeds. *Extreme wind classifications: I (most of country), II (south-west tip).*

Table D8 Philippines

Zone in structural code	*Description*	*Classification*
I	Eastern Luzon	V
II	Remainder of Philippines	IV
III	Western Mindanao, Palawan	III

D2.48 Philippines

The Philippines experiences typhoons from the south-west Pacific Ocean, which often cross the northern Philippines (Luzon) and re-form in the south China sea. On the other hand, the southern island of Mindanao has little or no influence from typhoons, and effectively has an equatorial extreme wind climate. An extreme value analysis of 1-min average extreme wind speeds in the Philippines was carried out in the early 1970s by Kintenar (1971). This gave widely ranging 50-year return period values, and probably suffering from sampling errors due to short records.

The National Structural Code of the Philippines specifies three extreme wind zones with 1-min sustained wind speeds of 200 kph (55.5 m/s), 175 kph (48.6 m/s) and 150 kph (41.7 m/s), respectively. These values have been used for the Table D8, but are probably conservative for Mindanao.

D2.49 Poland

The Polish wind loading standard PN-77/B-02011 gives ‘characteristic’ wind speeds of 20, 24, 27 and 30 m/s for four zones. In the largest zone, 20 m/s is specified. These values are 10-min mean speeds, with a return period of 50 years. *Extreme wind classifications: II, III.*

D2.50 Portugal

The draft Eurocode (CEN, 1994) specified a value of 10-min mean wind speed with a 50-year return period, of 31 m/s, for the Azores, Madeira, and the 5 km coastal strip of the mainland; 28 m/s is specified for the rest of the country. *Extreme wind classifications: II, III.*

D2.51 Puerto Rico

As for other Caribbean islands, Puerto Rico is subjected to hurricane winds. The ASCE Standard (ASCE, 2006) gives a basic design wind speed (3-s gust with 50-year return period) of 65 m/s. *Extreme wind classification: IV.*

D2.52 Reunion I

This small French island in the southern Indian Ocean has a design wind speed (10-min mean, 50-year return period) of 34.0 m/s specified in the draft Eurocode (CEN, 1994).

According to Sites and Peterson (1995), Reunion experiences landfall of a tropical cyclone about once every 5 years. *Extreme wind classification: III.*

D2.53 Romania

The Romanian Standard STAS 10101/20–78 on Actions on Structures specifies five zones for design wind pressures. These pressures correspond to peak gust wind speeds (10-year return period) ranging from 27 to 37 m/s. *Extreme wind classifications: I, II.*

D2.54 Russia

Russia has a vast land area, with a range of extreme wind climates. The Russian loading code SniP 2.01.07.85 specifies 8 zones for design wind pressures. The specified values are 5-year return period pressures with a 10-min averaging time, and range from 240 Pa for the central part of the country to 1200 Pa on the coastal part of the Far East, and the islands of the Barents Sea (Popov, 2001). *Extreme wind classifications: II, III, IV, V.*

D2.55 Samoa

Samoa in the South Pacific (latitude 13–14°S) is affected by tropical cyclones (Holmes and Weller, 2002). Cyclones 'Ofa' (1990) and 'Val' (1991) did significant damage. The US Department of Defence recommends a 50-year gust wind speed of 67 m/s for the capital, Apia. *Extreme wind classification: IV.*

D2.56 Saudi Arabia

The national oil company has an Engineering Standard (Saudi Aramco, 2005) containing meteorological and seismic design data intended for use with the American Loading Standard ASCE-7–02; this contains 50-year return period gust data for many locations in the country. These range from 41 to 51 m/s, with a value of 46 m/s for the capital, Riyadh. *Extreme wind classifications: II, III.*

D2.57 Singapore

Like Malaysia, Singapore in the equatorial zone does not experience typhoons, and has very low extreme winds from weak thunderstorms and monsoonal winds (Choi, 1999). Good quality corrected monthly maximum extreme gust data are available from Tengah and Changi airfields. A Gumbel extreme value analysis for data up to 1997 from these data (Holmes, unpublished) gives 50-year return period gusts of 33 and 25 m/s, respectively. (However, a gust of 40.1 m/s was recorded at Tengah in 1984.) *Extreme wind classification: I.*

D2.58 South Africa

South Africa is subjected to severe thunderstorms on the inland high plains, and synoptic winds in the south. The Code of Practice for Loading of the South African Bureau of

Standards (SABS 0160–1989) has a map showing design wind speeds for the country (50-year return period, 3-s gust). This map is based on the analysis of annual maximum

Table D9 Sri Lanka

Zone in building code	*Description*	*Classification*
1	50km from east coast	III
2	Inland strip	II
3	South and west (including Colombo)	I

wind speeds by Milford (1987). The value given for the majority of the country is 40 m/s. This value is specified for the main cities of Johannesburg, Pretoria, Cape Town and Durban. A small zone around Beaufort West has a value of 50 m/s. *Extreme wind classifications: II, III.*

D2.59 Spain

No data was given in the draft Eurocode (CEN, 1994), but the map in the ECCS Recommendations for the Calculation of Wind Effects on Structural Steelwork (ECCS, 1978) gives values of 10-min mean wind speeds (50-year return period) of 22–26 m/s for Spain. There are some downslope wind areas in the Pyrenees. *Extreme wind classification: II.*

D2.60 Sri Lanka

The east coast of Sri Lanka is exposed to relatively weak tropical cyclones. A Building Code was prepared by an Australian consulting group in the 1970s. Three design wind zones are specified (Table D9).

D2.61 Sweden

The draft Eurocode (CEN, 1994) gave a contour map with values of 10-min mean wind speed with a 50-year return period, between 22 m/s (north-east) and 26 m/s (south and west). For Stockholm, the value is 24 m/s. *Extreme wind classification: II.*

D2.62 Switzerland

The draft Eurocode (CEN, 1994) specified values of 10-min mean wind speed with a 50-year return period, of 27.2 m/s over the vast majority of the country, including Zurich, Basel, Bern and Lausanne. There are a number of mountain areas where downslope wind occur, and for which higher values of 30 and 33.3 m/s are specified. *Extreme wind classifications: II, III (some mountain areas).*

D2.63 Thailand

Thailand has a particularly mixed wind climate. Most of the country appears to be dominated by extreme winds from thunderstorms and monsoons. However, occasionally typhoons have impacted on southern Thailand, as did Typhoon 'Gay' in 1989, inflicting considerable damage. Post-landfall typhoons can also affect north-west Thailand.

An analysis of historical gust data for 60 m eteorological stations is described by Davenport *et al.* (1995), using Type I (Gumbel) Extreme Value Distributions. There were apparently siting problems for many of the anemometers, and although extreme winds caused by typhoons were separated, those from thunderstorms apparently were not.

The analysis by Davenport *et al.* (1995) proposed two design wind speeds based on 50-year return period 10-min means of 26.5 and 30 m/s. The latter value applies to small zones on the east and north-west of Thailand. In recent proposals for a new Thailand loading code (Lukkunaprasit, 1997), these values were converted to nominal mean hourly speeds of 24.9 and 28.2 m/s, respectively. *Extreme wind classification: II.*

D2.64 Tonga

Tonga, an island group in the South Pacific, suffers regular visits by tropical cyclones (Holmes and Weller, 2002), including 'Isaac' (1982), 'Hina' (1997), 'Cora' (1998) and 'Waka' (2001), all of which did significant damage. *Extreme wind classification: IV.*

D2.65 Trinidad and Tobago

Analysis of extreme wind speeds for the Commonwealth Caribbean was carried out by Shellard (1972). These results have been used by the Caribbean Uniform Building Code (Caribbean Community Secretariat, 1986) and by the Code of Practice of the Barbados Association of Professional Engineers (1981). The former specifies 50-year return period 10-min mean speeds of 20–28 m/s, and the latter gives a 50-year return period 3-s gust speed of 45 m/s for Trinidad and 50 m/s for Tobago. The latter values are based on a Frechet (Type II) Extreme value distribution (Section 2.2.1) and may be conservative. *Extreme wind classification: II.*

D2.66 Turkey

The extreme wind climate of Turkey can be assumed to be similar to that of Greece. The U.S. Department of Defense recommends a 50-year return period gust of 44 m/s for Ankara. *Extreme wind classification: II.*

D2.67 Ukraine

Horokhov and Nazim (2001) give a zoning map of wind velocities for the Ukraine. The values have an averaging time of 2-min, with a 10-year recurrence interval. Values range between 20 and 45 m/s. The higher values are primarily in mountainous regions or adjacent to the Black or Azof Seas. *Extreme wind classifications: II, III, IV.*

D2.68 United Arab Emirates

U.A.E. along the south-eastern tip of the Arabian Peninsula is a federation of seven emirates: Abu Dhabi, Dubai, Sharjah, Ajman, Umm al-Qaiwain, Ras al-Khaimah and Fujairah. Analyses by various wind-tunnel laboratories for building projects in Dubai gives predictions of 50-year gust speed between 35 and 39 m/s. The dominant wind directions for the extreme winds are in the north to west quadrant. *Extreme wind classification: II.*

D2.69 United Kingdom

The United Kingdom has a close network of meteorological stations and high quality data. The main strong wind source is severe gales moving in from the Atlantic on the west. Design winds are generally stronger on the west, reducing further east.

Analyses of extreme winds for the UK have been carried out by Shellard (1958, 1962) and Cook and Prior (1987). The latter work was used for the design wind speed data in the British Standard BS6399:2.

BS6399:2 contains a map of 1-h mean wind speeds (50-year return period) ranging from 20 to 30 m/s. The latter values occur only for the Shetland Islands in the north. The map also covers the whole of Ireland. The map in the draft Eurocode (CEN, 1994) was identical, with Ireland omitted. *Extreme wind classification: II.*

D2.70 United States

The United States has a vast array of meteorological stations operated by the U.S. Weather Bureau, and other agencies, such as those involved in defence. Until 1995 the standard extreme wind was the ‘fastest mile of wind’, calculated from the time taken by a cup anemometer to rotate through one mile. The introduction of automatic weather stations has seen this measure replaced by a peak gust wind speed.

There have been many extreme value analyses for the United States, including those by Thom (1960, 1968), Simiu *et al.* (1979) and Peterka and Shahid (1998). The latter analysis has resulted in the design wind map in the ASCE Loading Standard (ASCE, 2006). The latter contains two main zones, with 50-year return period gust speeds of 40 and 38 m/s. The lower value applies to the west coast states. The Atlantic Ocean and Gulf of Mexico coastlines have isotachs ranging from 67 to 45 m/s. Alaska has contours from 40 to 58 m/s. Hawaii has a basic wind speed of 47 m/s (Table D10).

D2.71 Vanuatu

Vanuatu is an island group in the South Pacific, often affected by tropical cyclones (Holmes and Weller, 2002), including ‘Uma’ (1987), ‘Dani’ (1999) and ‘Ivy’ (2004), which did significant damage. *Extreme wind classification: IV.*

D2.72 Vietnam

Vietnam is influenced by typhoons over most of its coastline, although the influence is weaker on the southern provinces. For design wind speeds, Vietnam is divided into five

zones with 20-year return period gust speeds ranging from 33 to 55 m/s, in the national loading code TCVN-2737 (values of dynamic pressure are given in the code). The zones

Table D10 United States

Description	*Classification*
Central and Western States	II
Atlantic and Texas coasts	III
Southern Florida and Louisiana, Alaska coasts	IV

Table D11 Vietnam

Zone in loading code	*Description*	*Classification*
I	Inland north and south	II
II	Inland north and southern coast	II
III	Central and northern coastline	III
IV, V	Offshore islands in north	IV

of higher wind speeds occur close to the coast and reflect different degrees of influence from typhoons (Table D11).

D2.73 Windward Islands

These islands in the Caribbean are visited by developing hurricanes, and weaker tropical storms. Analysis of extreme wind speeds for the former British colonies in the Caribbean was carried out by Shellard (1972). These results have been used by the Caribbean Uniform Building Code (Caribbean Community Secretariat, 1986) and by the Code of Practice of the Barbados Association of Professional Engineers (1981). The latter specifies a 50-year return period 3-s gust speed of 58 m/s, based on studies for Barbados. This value is also applicable to St. Vincent, St. Lucia, Grenada and Dominica. *Extreme wind classification: III.*

D2.74 Zimbabwe

Zimbabwe is an elevated land-locked country with most land at 1000 m above sea level or greater. The country falls between 15° and 22° S in latitude. The expected dominant windstorm in this environment would be thunderstorm winds created by local convection. The code of practice for wind loads (Central African Standards Institution, 1977) specifies a basic design wind speed (50-year return period gust) of 35 m/s, for the whole country. The analysis by Lewis (1983) for five different locations found higher and lower values than this. *Extreme wind classifications: I and II.*

References

American Society of Civil Engineers (2006) Minimum design loads for buildings and other structures. ANSI/ASCE 7–05, ASCE, New York.

Barbados Association of Professional Engineers (1981) Code of practice for wind loads for structural design. Consulting Engineers Partnership Ltd. and Caribbean Meteorological Institute.

Bajic, A. and Peros, B. (2005) Meteorological basis for wind loads calculation in Croatia. *Wind and Structures*, 8:389–405.

British Standards Institution (1997) Loading for buildings. Part 2. Code of practice for wind loads. BS 6399: Part 2.

Building Department, Hong Kong (2004) Code of practice on wind effects—Hong Kong, Hong Kong Special Administrative Region, China.

Bureau of Indian Standards (1987) Indian Standard IS: 875 (Part 3) Bureau of Indian Standards, New Delhi.

Caribbean Community Secretariat (1986) Caribbean uniform building code. Part 2. Section 2. Wind Load. Caribbean Community Secretariat, Georgetown, Guyana.

Caspar, W. (1970) Maximale windgeschwindigkeiten in der BRD. *Bautechnik*, 47:335–40.

CEN (European Committee for Standardization) (1994) Eurocode 1: basis of design and actions on structures. Part 2–4: Wind actions. ENV-1991–2–4, CEN, Brussels.

Central African Standards Institution (1977) Wind loads on buildings. CASI 160, Part 2. Central African Standards Institution, Harare.

Chen, T.Y. (1975) Comparison of surface winds in Hong Kong. Hong Kong Royal Observatory, Technical Note 41.

Choi, E.C.C. (1999) Extreme wind characteristics over Singapore—an area in the equatorial belt. *Journal of Wind Engineering & Industrial Aerodynamics*, 83:61–9.

Cook, N.J. and Prior, M.J. (1987) Extreme wind climate of the United Kingdom. *Journal of Wind Engineering & Industrial Aerodynamics*, 26:371–89.

Davenport, A.G. and Baynes, C.J. (1972) An approach to the mapping of the statistical properties of gradient winds over Canada. *Atmosphere*, 10:80–92.

Davenport, A.G., Georgiou, P.N., Mikitiuk, M., Surry, D. and Lythe, G. (1984) The wind climate of Hong Kong. *Proceedings, Third International Conference on Tall Buildings*, Hong Kong and Guangzhou.

Davenport, A.G., Lukkunaprasit, P., Ho, T.C.E., Mikitiuk, M., and Surry, D. (1995) The design of transmission line towers in Thailand. *Proceedings, Ninth International Conference on Wind Engineering*, New Delhi, 9–13 January, pp. 57–68.

Department of Standards and Norms (China) (1994) Load code for the design of building structures (English Translation). GBJ-9–87. New World Press, Beijing,

de Schwarzkopf, M.L.A. (1995) Meteorological weather patterns and wind storm types. Course notes. 'Design Loadings on Transmission Lines', Brisbane, Queensland, Australia, 5–7 July.

Dorman, C.M.L. (1983) Extreme wind gust speeds in Australia, excluding tropical cyclones. *Civil Engineering Transactions, Institution of Engineers, Australia*, CE25: 96–106.

European Committee for Structural Steelwork (ECCS) (1978) Recommendations for the calculation of wind effects on buildings and structures. Technical Committee T12. ECCS, Brussels.

Faber, S.E. and Bell, G.J. (1967) Typhoons in Hong Kong and building design. Hong Kong Royal Observatory, Reprint No. 37.

Gomes, L. and Vickery, B.J. (1976a) On thunderstorm wind gusts in Australia. *Civil Engineering Transactions, Institution of Engineers, Australia*, CE18:33–9.

Gomes, L. and Vickery, B.J. (1976b) Tropical cyclone gust speeds along the northern Australian coast. *Civil Engineering Transactions, Institution of Engineers, Australia*, CE18: 40–8.

Holmes, J.D. (2002) A re-analysis of recorded wind speeds in Region A. *Australian Journal of Structural Engineering*, 4:29–40.

Holmes, J.D. and Weller, R. (2002) Design wind speeds for the Asia-Pacific Region. Handbook, HB212, Standards Australia, Sydney, NSW, Australia.

Holmes, J.D., Hitchcock, P., Kwok, K.C.S. and Chim, J.K.S. (2001) Re-analysis of typhoon wind speeds in Hong Kong. *5th Asia-Pacific Conference on Wind Engineering*, Kyoto, Japan, 21–24 October.

Horokhov, Y.V. and Nazim, Y.V. (2001) Wind and sleet loads on the aerial power lines in Ukraine. *Journal of Wind Engineering & Industrial Aerodynamics*, 89:1409–19.

Jeary, A.P. (1997a) The wind climate of Hong Kong. *Journal of Wind Engineering & Industrial Aerodynamics*, 72:433–44.

Jeary, A.P. (1997b) *Designer's Guide to the Dynamic Response of Structures.* E.F. and N. Spon, London.

Jensen, M. and Franck, N. (1970) The climate of strong winds in Denmark. Danish Technical Press, Copenhagen.

Kintenar, R.L. (1971) An analysis of annual maximum wind speeds in the Philippines. UNESCO, Manila.

Lewis, G. (1983) Probabilistic estimation of extreme climatological parameters over Zimbabwe. *Proceedings, Institution of Engineers (U.K.), Part* 2, 75:551–5.

Lopez, A. and Vilar, J.I. (1995) Basis of the Mexican wind handbook for the evaluation of the dynamic response of slender structures. *Proceedings, Ninth International Conference on Wind Engineering*, New Delhi, 9–13 January, pp. 1890–1900.

Loredo-Souza, A.M. and Paluch, M.J. (2005) Brazil storm Catarina: hurricane or extratropical cyclone? *Proceedings, Tenth Americas Conference on Wind Engineering*, Baton Rouge, 31 May-4 June.

Lukkunaprasit, P. (1997) Seismic and wind loading codes in Thailand. *International Workshop on Harmonization in Performance-Based Building Structural Design*, Tsukuba, Japan, 1–3 December.

Melbourne, W.H. (1984) Design wind data for Hong Kong and surrounding coastline. *Proceedings, Third International Conference on Tall Buildings*, Hong Kong and Guangzhou.

Milford, R.V. (1987) Annual maximum wind speeds for South Africa. *The Civil Engineer in South Africa*, 15–19 January.

National Research Council (Canada) (1995) Climatic information for building design in Canada. Appendix C to the National Building Code of Canada. NRC, Ottawa.

Peterka, J.A. and Shahid, S. (1998) Design gust wind speeds in the United States. *ASCE Journal of Structural Engineering*, 124:207–14.

Popov, N.A. (2001) Wind load codification in Russia and some estimates of a gust load accuracy provided by various codes. *Journal of Wind Engineering & Industrial Aerodynamics*, 88:171–81.

Riera, J.D. and Nanni, L.F. (1989) Pilot study of extreme wind velocities in a mixed climate considering wind orientation. *Journal of Wind Engineering & Industrial Aerodynamics*, 32: 11–20.

Riera, J.D. and Reimundin, J.C. (1970) Sobre la distribucion de velocidades maximas de viento en la Republica Argentina. *Simposio sobre Acciones en Estructuras.* National University of Tucuman, Argentina.

Salgado Vieira Filho, J.M. (1975) Velocidades maximas do vento no Brasil. Master's thesis, Federal University of Rio Grande do Sul, Brazil.

Saudi Aramco (2005) Meteorological and seismic data. Engineering Standard SAES-A-112. Environmental Protection Department, Saudi Aramco, Dharan, Saudi Arabia, December.

Schueller, G.I. and Panggabean, H. (1976) Probabilistic determination of design wind velocity in Germany. *Proceedings, Institution of Engineers (U.K.), Part 2*, 61:673–83.

Shellard, H.C. (1958) Extreme wind speeds over Great Britain and Northern Ireland. *Meteorological Magazine*, 87:257–65.

Shellard, H.C. (1962) Extreme wind speeds over the United Kingdom for periods ending 1959. *Meteorological Magazine*, 91:39–47.

Shellard, H.C. (1972) Extreme wind speeds in the Commonwealth Caribbean. *Journal of the Barbados Association of Professional Engineers*, December.

Sites, J.S. and Peterson, R.E. (1995) Climatology of Southwest Indian Ocean tropical cyclones (1962–1987). *Proceedings, Ninth International Conference on Wind Engineering*, New Delhi, 9–13 January.

Simiu, E., Changery, M.J. and Filliben, J.J. (1979) Extreme wind speeds at 129 stations in the contiguous United States. NBS Building Science Series 118, National Bureau of Standards, Washington, DC.

South African Bureau of Standards (1989) The general procedures and loadings to be adopted in the design of buildings. South African Standard SABS 0160–1989.

Standards Australia (2002) Structural design actions. Part 2: wind actions. Standards Australia, Australian/New Zealand Standard, AS/NZS1170.2:2002, Sydney, New South Wales, Australia.

Thom, H. (1960) Distributions of extreme winds in the United States. *ASCE Journal of the Structural Division*, 85:11–24.

Thom, H. (1968) New distributions of extreme winds in the United States. *ASCE Journal of the Structural Division*, 94:1787–1801.

Vilar, J.I. *et al.* (1991) Analisis estadistico de dates de vientos maximos. Reporte Interno 42/2929/I/02/P. Departamento de Ingenieria Civil. Institute de Investigaciones Electricas, Mexico.

Viollaz, A., Riera, J.D. and Reimundin, J.C. (1975) Estudio de la distribucion de velocidades maximas de viento en la Republica Argentina, Informe I-75–1, Structures Laboratory. National University of Tucuman, Argentina.

Whittingham, H.E. (1964) Extreme wind gusts in Australia. Bureau of Meteorology, Bulletin No. 46.

Appendix E:
Some approximate formulas for natural structural frequencies

A necessary prerequisite for dynamic response estimation is knowledge of the natural frequencies in the lowest sway modes of the structure. It is also useful to know these values to determine whether or not dynamic response calculations to wind are, in fact, necessary.

Most modern frame analysis or finite element computer programs will, of course, give this information. However, if the structure is still in the early design stage, application of simple empirical formulae may be useful. Some of these are given here:

- For multi-storey office buildings, approximately uniform in plan (Jeary and Ellis, 1983):

$$n_1 \approx 46/h \tag{E1}$$

where h is the height of the building in metres.

- For cantilevered masts or poles of uniform cross-section (in which bending action dominates):

$$n_1 = \frac{0.56}{h^2}\sqrt{\frac{EI}{m}} \tag{E2}$$

where EI is the bending stiffness of the section and m is the mass/unit height (this of course is an exact formula for uniform masts or towers; it can be used for those with a slight taper, with average values of EI and m).

- An approximate formula for cantilevered, *tapered*, circular poles (European Convention for Structural Steelwork, 1978) is:

$$n_1 \approx \frac{\lambda}{2\pi \cdot h^2}\sqrt{\frac{EI}{m}} \tag{E3}$$

where h is the height, and E, I, m are calculated for the cross-section *at the base*. A depends on the wall thicknesses at the tip and base, e_t and e_b, and external diameter at the tip and base, d_t and d_b, according to the following formula:

$$\lambda = \left[1.9 \exp\left(\frac{-4d_t}{d_b}\right)\right] + \left[\frac{6.65}{0.9 + \left(\frac{e_t}{e_b}\right)^{0.666}}\right] \qquad \text{(E4)}$$

Note that for $(d_t/d_b)=(e_t/e_b)=1.0$, i.e. a uniform cylindrical tube, $\lambda=3.52$, and Equation (E2) results.

- For free-standing lattice towers (without added ancillaries such as antennas, lighting frames, etc.) (Standards Australia, 1994):

$$n_1 \approx 1500\, w_a/h^2 \qquad \text{(E5)}$$

where w_a is the average width of the structure in metres and h is the tower height. An alternative formula for lattice towers (with added ancillaries) is (Wyatt, 1984):

$$n_1 \approx \left(\frac{L_N}{h}\right)^{2/3} \left(\frac{w_b}{h}\right)^{1/2} \qquad \text{(E6)}$$

where w_b is the tower base width and L_N=270 m for square base towers or 230 m for triangular base towers.

- A formula which seems to fit data on bridges, with spans between 20 and 1000m (Pretlove *et al.*, 1995; Jeary, 1997) is:

$$n_1 \approx 40\,(L_s)^{-3/4} \qquad \text{(E7)}$$

where L_s is the span in metres (main span in the case of a multi-span structure).

References

European Convention for Structural Steelwork (ECCS) (1978) Recommendations for the calculation of wind effects on buildings and structures. Technical Committee T12. ECCS, Brussels.

Jeary, A.P. (1997) *Designer's Guide to the Dynamic Response of Structures.* E.F. and N. Spon, London.

Jeary, A.P. and Ellis, B.R. (1983) On predicting the response of tall buildings to wind excitation. *Journal of Wind Engineering & Industrial Aerodynamics*, 13:173–82.

Pretlove, A.J., Rainer, J.H. and Bachmann, H. (1995) Pedestrian bridges. In: *Vibration Problems in Structures*, Birkhäuser, Basel.

Standards Australia (1994) Design of steel lattice towers and masts. Australian Standard, AS3995–1994. Standards Australia, North Sydney, Australia.

Wyatt, T.A. (1984) Sensitivity of lattice towers to fatigue induced by wind gusts. *Engineering Structures*, 6:262–7.

Appendix F:
Application of the effective static load method to a simple structure

F1 Introduction

In this Appendix, the formula of Kasperski (1992) is applied to a simple structure a pitched free roof—to illustrate the method of determining the effective static wind pressures. Data were obtained from wind-tunnel tests carried out by Ginger and Letchford (1991).

F2 Wind pressure data

A model of a pitched free roof (i.e. no walls), with a roof pitch of 22.5° at a geometric scaling ratio of 1/100, was tested in a boundary-layer wind tunnel by Ginger and Letchford (1991). Net area-averaged pressures across the windward and leeward roof slopes were measured. Three panels per roof half were used, but the data used here applies to the central panels, i.e. the central third of the roof.

Figure F1(b) shows the mean and standard deviation pressure coefficients for a wind direction normal to the ridge as shown; the latter values are in brackets. Maximum and minimum panel pressure coefficients were also recorded, and are shown in Figure F1(c). The directions for positive net panel pressures are shown in the figure.

F3 Effective static loads for total lift and drag

At first, one might assume that the maximum total lift force should be obtained from the two recorded minimum pressures on the two roof panels. Similarly, the maximum drag could be obtained from the maximum on panel 1 and the minimum on panel 2. However, this would be incorrect and conservative, as these values do not occur simultaneously. The *expected* pressure coefficients coinciding with the maximum and minimum lift and drag are derived in the following.

F3.1 Mean lift and drag

The mean lift force (positive upwards) is obtained as follows:

$$\overline{L} = (-1)(0.46)q_h(d/2) + (-1)(-0.60)q_h(d/2) = 0.14q_h(d/2)$$

where q_h is the reference mean dynamic pressure at roof height $(=\frac{1}{2}\rho_a \overline{U}_{h^2})$ and d the along-wind length of the roof.

In this case, the *influence coefficients* for the *lift force* are both equal to $-(d/2)$.

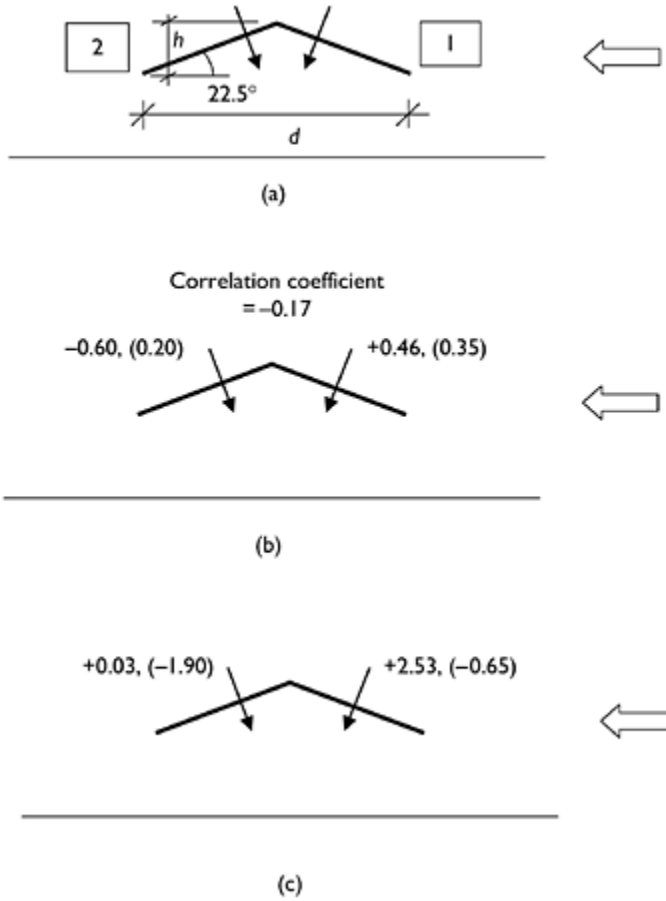

Figure F1 Pressure coefficients for a pitched free roof, (a) Roof geometry, (b) Mean (standard deviation) pressure coefficients and correlation coefficient, (c) Maximum and (minimum) pressure coefficients.

The mean drag force is given by:

$$\overline{D} = (+1)(0.46)q_h(h) + (-1)(-0.60)q_h(h) = 1.06q_h(h) = 0.44q_h(d/2)$$

as, $h/(d/2)$=tan 22.5°=0.414.

The *influence coefficients* for the *drag force* are equal to $+h=(d/2)$ tan 22.5° for panel 1, and $-h=-(d/2)$ tan22.5°, for panel 2.

F3.2 Standard deviations of lift and drag

The rms fluctuating or standard deviation, lift and drag forces can be obtained by *covariance integration* (Holmes and Best, 1981; Ginger and Letchford, 1991, 1994).

The standard deviation of the lift force, σL, is obtained as follows:

$$\begin{aligned}\sigma_{\mathrm{L}} &= q_{\mathrm{h}}(d/2)[(0.35)^2+(0.20)^2+2(-0.17)\cdot(0.35)(0.20)]^{1/2}\\ &= 0.372 q_{\mathrm{h}}(d/2)\end{aligned}$$

The standard deviation of the drag force, σ_{D}, is:

$$\begin{aligned}\sigma_{\mathrm{D}} &= q_{\mathrm{h}}(d/2)\tan\ 22.5°[(0.35)^2+(0.20)^2-2(-0.17)\cdot(0.35)(0.20)]^{1/2}\\ &= 0.432 q_{\mathrm{h}}(d/2)\ \tan\ 22.5° = 0.179 q_{\mathrm{h}}(d/2)\end{aligned}$$

F3.3 Effective pressures for peak lift force

The expected pressure on panel 1 when the *lift* is a maximum is given by Kasperski (1992):

$$(p_1)_{\hat{L}} = q_{\mathrm{h}}[\overline{C}_{p1} + g\rho_{p1,L}\sigma_{Cp1}]$$

where g is a peak factor for the lift (it will be taken as 4), and $\rho_{p1,L}$ is the correlation coefficient between the pressure $p_1(t)$ and the lift $L(t)$.

The *covariance* between the pressure $P_1(t)$ and the lift $L(t)$ is given by:

$$\begin{aligned}-q_{\mathrm{h}}^2(d/2)[\sigma_{Cp1}^2+\overline{p'_1p'_2}] &= -q_{\mathrm{h}}^2(d/2)[(0.35)^2+(-0.17)(0.35)(0.20)]\\ &= -(0.111)q_{\mathrm{h}}^2(d/2)\end{aligned}$$

Then,

$$\rho_{p1,L} = \frac{-0.111}{(0.35)(0.372)} = -0.853$$

Hence,

$$(p_1)_{\hat{L}} = q_{\mathrm{h}}[\overline{C}_{p1} + g\ \rho_{p1,L}\ \sigma_{Cp1}] = q_{\mathrm{h}}[(0.46)+4(-0.853)(0.35)] = -0.73 q_{\mathrm{h}}$$

Similarly, the *covariance* between the pressure $p_2(t)$ and the lift $L(t)$ is given by:

$$\begin{aligned}-q_{\mathrm{h}}^2(d/2)[\sigma_{Cp2}^2+\overline{p'_1p'_2}] &= -q_{\mathrm{h}}^2(d/2)[(0.20)^2+(-0.17)(0.35)(0.20)]\\ &= -(0.028)q_{\mathrm{h}}^2(d/2)\end{aligned}$$

Then,

$$\rho_{p2,L} = \frac{-0.028}{(0.20)(0.372)} = -0.376$$

Hence,

$$(p_2)_{\hat{L}} = q_h[\overline{C}_{p2} + g\rho_{p2,L}\sigma_{Cp2}] = q_h[(-0.60) + 4(-0.376)(0.20)] = -0.90\ q_h$$

Thus, the expected pressure coefficients corresponding to the maximum lift (acting upwards) are:

$$(C_{p1})_{\hat{L}} = \mathbf{-0.73} \quad (C_{p2})_{\hat{L}} = \mathbf{-0.90}$$

The pressures corresponding to the *minimum* lift force (downwards) are also of interest.

In this case,

$$(p_1)_{\check{L}} = q_h[\overline{C}_{p1} - g\rho_{p1,L}\sigma_{Cp1}] = q_h[(0.46) - 4(-0.853)(0.35)] = +1.65\ q_h$$

and,

$$(p_2)_{\check{L}} = q_h[\overline{C}_{p2} - g\rho_{p2,L}\sigma_{Cp2}] = q_h[(-0.60) - 4(-0.376)(0.20)] = -0.30\ q_h$$

Hence,

$$(C_{p1})_{\check{L}} = \mathbf{+1.65} \quad (C_{p2})_{\check{L}} = \mathbf{-0.30}$$

These pressure coefficients are shown in Figure F2(a) and (b).

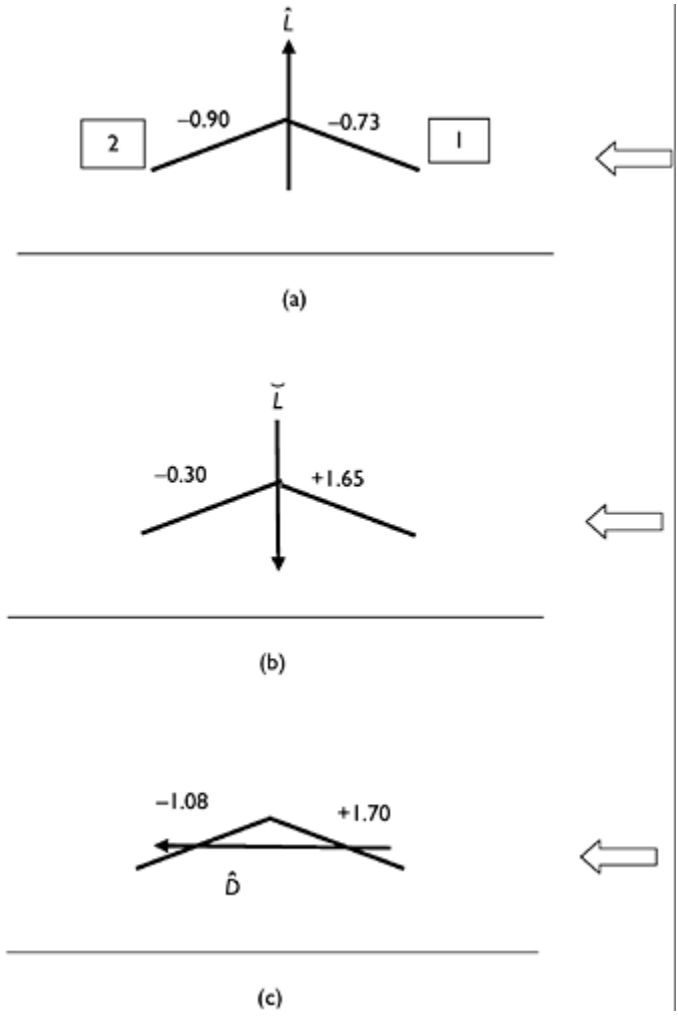

Figure F2 Pressure coefficients for a pitched free roof, (a) Effective pressures for maximum lift force, (b) Effective pressures for minimum lift force, (c) Effective pressures for maximum drag force.

F3.4 Effective pressures for maximum drag force

The expected pressures for the maximum *drag* force can be determined in a similar way as the lift force, as follows.

The *covariance* between the pressure $P_1(t)$ and the drag $D(t)$ is given by:

$$q_h^2(d/2)\tan\ 22.5°[\sigma_{Cp1}^2 - \overline{p'_1 p'_2}] = q_h^2(d/2)\tan\ 22.5°[(0.35)^2 - (-0.17)(0.35)(0.20)]$$
$$= (0.134)q_h^2(d/2)\tan\ 22.5°$$

Then,

$$\rho_{p1,D} = \frac{0.134}{(0.35)(0.432)} = 0.886$$

Hence,

$$(p_1)_{\hat{D}} = q_h[\overline{C}_{p1} + g\rho_{p1,D}\sigma_{Cp1}] = q_h[(0.46) + 4(0.886)(0.35)] = 1.70q_h$$

(again taking a peak factor of 4).

Similarly, the *covariance* between the pressure $p_2(t)$ and the drag $D(t)$ is given by:

$$-q_h^2(d/2)\tan\ 22.5°[\sigma_{Cp2}^2 - \overline{p'_1 p'_2}] = -q_h^2(d/2)\tan\ 22.5°[(0.20)^2 - (-0.17)(0.35)(0.20)]$$
$$= -(0.052)q_h^2(d/2)$$

Then,

$$\rho_{p2,D} = \frac{-0.052}{(0.20)(0.432)} = -0.602$$

Hence,

$$(p_2)_{\hat{D}} = q_h[\overline{C}_{p2} + g\rho_{p2,D}\sigma_{Cp2}] = q_h[(-0.60) + 4(-0.602)(0.20)] = -1.08q_h$$

Thus, the expected pressure coefficients corresponding to the maximum drag are:

$$(C_{p1})_{\hat{D}} = +\mathbf{1.70} \quad (C_{p2})_{\hat{D}} = -\mathbf{1.08}$$

These pressure coefficients are shown in Figure F2(c).

F4 Discussion

The effective pressure coefficients for maximum and minimum lift, and maximum drag, as summarized in Figure F2, are clearly quite different to each other, and indicate the difficulty in specifying a single set of pressure coefficients in a code or standard, for a structure such as this.

It can be checked that the values obtained in the previous section will in fact give the correct values of the peak load effects. For example, the maximum lift can be obtained in two ways as follows.

From the effective static pressure coefficients:

$$\hat{L} = (-1)\cdot(-0.73)q_h(d/2) + (-1)\cdot(-0.90)q_h(d/2) = 1.63q_h(d/2)$$

Directly from the mean and standard deviation:

$$\hat{L} = \overline{L} + 4\sigma_L = 0.14q_h(d/2) + 4 \times 0.372q_h(d/2) = 1.63q_h(d/2)$$

The effective static pressure coefficients for each panel should lie between the limits set by the maximum and minimum pressure coefficients for each panel. This is the case here (see Figures F1 and F2), except the value on panel 1 for $\hat{L} = -0.73$, is slightly more negative that the measured minimum value of −0.65. This could result from a sampling error in the measured peak or the choice of a slightly conservative peak factor of 4 for the lift force.

F5 Conclusions

This example has explained, using a simple 2-panel case, the methodology for determining the expected pressure distributions corresponding to peak load effects based on correlations. More complex cases, such as large roofs, require a large number of panels and a matrix of correlation coefficients, but the principles of the calculation are the same.

References

Holmes, J.D. and Best, R.J. (1981) An approach to the determination of wind load effects on low-rise buildings. *Journal of Wind Engineering & Industrial Aerodynamics,* 7:273–87.

Ginger, J.D. and Letchford, C.W. (1991) Wind loads on canopy roofs. Department of Civil Engineering, Research Report, CE132, June, University of Queensland.

Ginger, J.D. and Letchford, C.W. (1994) Wind loads on planar canopy roofs—Part 2: fluctuating pressure distributions and correlations. *Journal of Wind Engineering & Industrial Aerodynamics,* 51:353–70.

Kasperski, M. (1992) Extreme wind load distributions for linear and nonlinear design. *Engineering Structures,* 14:27–34.

Index